JULY 2009 VOLUME 11 NO.7
www.nature.com/naturecellbiology

nature cell biology

Protein translation
eIF4GI triggers metastasis

Transmitting tauopathy

Light limits plant cell division

nature cell biology

EDITORIAL OFFICES

LONDON: cellbio@nature.com
The Macmillan Building, 4 Crinan Street, London N1 9XW
Telephone: +44 207 843 4924; Fax: +44 207 843 4794
EDITOR: Bernd Pulverer
SENIOR EDITORS: Alison Schuldt, Sowmya Swaminathan & Nathalie Le Bot
ASSOCIATE EDITORS: Silvia Grisendi & Christina Karlsson Rosenthal
PRODUCTION EDITOR: Karl Smart
ART EDITOR: Denis Mallet
COPY EDITOR: Tamra Poorun
EDITORIAL ASSISTANT: Alice Fuller

MANAGEMENT OFFICES

NPG LONDON: nature@nature.com
The Macmillan Building, 4 Crinan Street, London N1 9XW
Telephone: +44 207 833 4000; Fax: +44 207 843 4596/7
MANAGING DIRECTOR: Steven Inchcoombe, PUBLISHING DIRECTOR: Alison Mitchell
ASSOCIATE DIRECTORS: Jenny Henderson, Tony Rudland
EDITOR-IN-CHIEF, NATURE PUBLICATIONS: Philip Campbell
EDITORIAL PRODUCTION DIRECTOR: James McQuat
MANAGING PRODUCTION EDITOR: Donald McDonald
PRODUCTION DIRECTOR: Yvonne Strong
PRODUCTION CONTROLLER: Kelly Hopkins
SENIOR MARKETING MANAGER: Tim Redding

NPG NEW YORK: nature@natureny.com
75 Varick St F1 9, New York, NY 10013-1917
Telephone: +212 726 9200; Fax: +212 696 9006
EXECUTIVE EDITOR: Linda Miller
CHIEF TECHNOLOGY OFFICER: Howard Ratner

NPG TOKYO: nature@natureasia.com
Nature Japan K.K., Chiyoda Building 2–37 Ichigayatamachi, Shinjuku-Ku, Tokyo, 162-0843, Japan
Telephone: +81 3 3267 8751; Fax: +81 3 3267 8746
ASIA-PACIFIC PUBLISHER: Antoine E. Bocquet, MANAGER: Koichi Nakamura
ASIA-PACIFIC SALES DIRECTOR: Kate Yoneyama
ASIA-PACIFIC SALES: Ken Mikami
MARKETING/PRODUCTION MANAGER: Takeshi Murakami

DISPLAY ADVERTISING

display@natureny.com (US/Canada)
display@nature.com (Europe)
nature@natureasia.com (Asia)

GLOBAL HEAD OF DISPLAY ADVERTISING:
Andrew Douglas, Tel: 44 207 843 4960, Fax: 44 207 843 4996
ASIA-PACIFIC SALES MANAGER:
Ken Mikami, Tel: 81 3 3267 8765, Fax: 81 3 3267 8746

DISPLAY ACCOUNT MANAGERS:
WESTERN REGIONAL SALES MANAGER, WEST COAST SOUTH/WEST COAST CANADA:
George Lui, Tel: (415) 781 3804, Fax: (415) 781 3805
WEST COAST NORTH: Bruce Shaver, Tel: (415) 781 6422, Fax: (415) 781 3805
NEW ENGLAND/EAST COAST CANADA:
Sheila Reardon, Tel: (617) 399 4098, Fax: (617) 426 3717
NEW YORK, MID-ATLANTIC, SOUTHEAST:
Jim Breault, Tel: (212) 726 9334, Fax: (212) 696 9481
MIDWEST: Mike Rossi, Tel: (212) 726 9255, Fax: (212) 696 9481
GERMANY/SWITZERLAND/AUSTRIA:
Sabine Hugi-Fürst, Tel: 41 52761 3386, Fax: 41 52761 3419
UNITED KINGDOM/IRELAND/FRANCE/BELGIUM/EASTERN EUROPE:
Jeremy Betts, Tel: 44 207 843 4968, Fax: 44 207 843 4749
SCANDINAVIA/DENMARK/THE NETHERLANDS/ITALY/SPAIN/PORTUGAL/ISRAEL/ICELAND:
Graham Combe, Tel: 44 207 843 4914, Fax: 44 207 843 4749
GREATER CHINA/SINGAPORE: Gloria To, Tel: (852) 2811 7191, Fax: (852) 2811 0743

WORLD WIDE WEB

www.nature.com/naturecellbiology
WEB PRODUCTION MANAGER: Alex Thurrell
WEB PRODUCTION EDITOR: Deborah Anthony
WEB SERVICES: Anthony Barrera

NATUREJOBS

Please refer to panel at the start of the naturejobs section at the back of the issue.

VOLUME 11 NUMBER 7 JULY 2009

nature cell biology

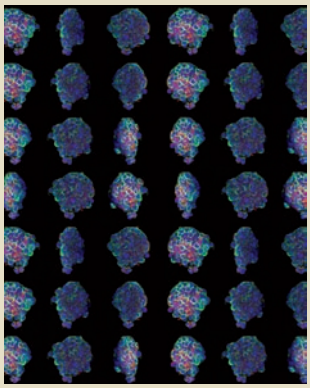

A 3D image of inflammatory breast cancer tumour cell emboli that form tight spherical non-adherent clusters responsible for highly efficient passive metastasis.

[letter p903]

EDITORIAL

TURNING POINTS

NEWS AND VIEWS

ARTICLES

Nature Cell Biology® (ISSN 1465-7392) is published monthly by Nature Publishing Group (Porters South, 4 Crinan Street, London N1 9XW, UK). Editorial Office: Porters South, 4 Crinan Street, London N1 9XW, UK. Telephone: +44 (0)20 7843 4924. Fax: +44 (0)20 7843 4794. Email: cellbio@nature.com. North American Advertising: Nature Cell Biology, 75 Varick Street F19, New York NY 10013-1917, US. Telephone: +1(212) 726-9200. Fax: +1(212) 696-9006. European Advertising: Nature Cell Biology, Porters South, Crinan Street, London N1 9XW, UK. Telephone: +44 (0)20 7833 4000. Fax: +44 (0)20 7843 4596. New subscriptions/renewals/changes of address/back issues and all other customer service questions should be addressed to – North America: Nature Cell Biology, Subscription Dept, P.O. Box 5055, Brentwood, TN 37024-5055, USA. Outside North America: Subscriptions Department, Brunel Road, Basingstoke, Hants. RG21 6XS, UK. Annual subscription rates: Americas: US$225 (personal), US$3,060 (institutional); Europe: €287 (personal), €2,430 (institutional); UK: £185 (personal), £1,570 (institutional); Japan: ¥40,000 (personal), ¥345,000 (institutional). Back issues: US/Canada. $45 (Canada add 7% GST); Rest of World: surface US$43, air mail US$45. Application for periodical postage rate submitted and paid by New York, NY 10010 and additional mailing offices. Reprints: Nature Cell Biology Reprints Department, Porters South, Crinan Street, London N1 9XW, UK. Subscription information is available at the Nature Cell Biology homepage at http://www.nature.com/naturecellbiology POSTMASTER: Send address changes to Nature Cell Biology Subscriptions Department, Brunel Road, Basingstoke, Hants. RG21 6XS, UK or Nature Cell Biology Subscriptions Department PO Box 5054, Brentwood, TN 37024-5054, USA.

npg
nature publishing group

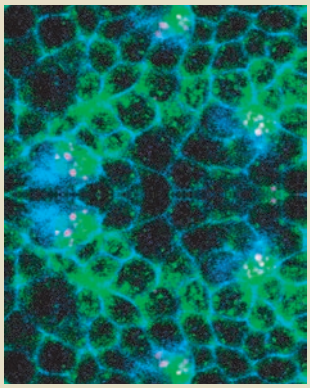

Delta vesicles (magenta) colocalize with a new apical actin-rich structure (green) in sensory organ cells (blue nuclei).

[article p815]

LETTERS

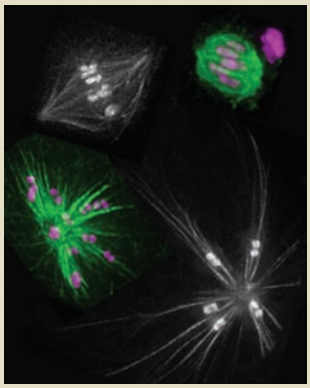

Acentrosomal structures formed during *C. elegans* oocyte meiosis. Bipolar spindles (top) and monopolar spindles (bottom) are visualized using GFP-labelled tubulin (green), histone (black and white). DNA in magenta.

[letter p839]

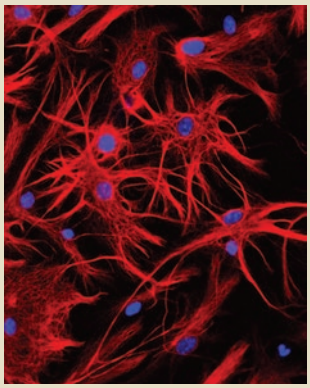

Astrocytes differentiating from neural stem cells in culture (GFAP staining in red and DAPI staining in blue).

[letter p873]

EDITORIAL

nature cell biology

Freedom of scientific expression

An English High Court judgement highlights the need for reform of a libel law that discourages open scientific discourse.

A visitor to the UK can easily witness the penchant of its citizens for open debate in any pub or by attending that quintessentially British institution, the debating society. Indeed, it is no coincidence that animated discussions by interested scientific amateurs during the age of enlightenment in this country paved the way for our present scientific culture. On the other hand, England has evolved one of the strictest libel laws anywhere, maybe because debate tends to get personal and spill over into the media.

The protection of persons and institutions against malicious slander is as essential in science as it is elsewhere. However, a recent libel case serves as a stark reminder that open scientific discourse can all too easily enter the courts. In April 2008, the well respected popular science writer Simon Singh published a 'comment' in the Guardian, a UK broadsheet, criticizing alleged claims by members of the British Chiropractic Association (BCA) that spinal manipulation can treat conditions such as colic, asthma and ear infections in children. The court ruled against Singh, stating that the language used implied that BCA promoted treatments they knew did not work. Singh argued that his intended meaning was that "alternative therapists who offer treatments unsupported by reasonable evidence are deluded rather than deliberately dishonest". Whatever the language used, Singh raised an issue of significant public interest. It is lamentable that the BCA did not publish a defence based on scientific arguments and the peer reviewed literature, which would have ensured that the evidence could be judged by the same readers. In our view, falling back on legal proceedings may instead appear defensive, although the BCA stated "To stifle scientific debate would clearly be wrong… However, scientists must realize that they cannot simply publish with impunity what they know to be untrue."

The case is raising widespread support for Singh, who is planning to appeal. Signatories to a statement entitled 'we the undersigned believe that it is inappropriate to use the English libel laws to silence critical discussion of medical practice and scientific evidence', published by the charity Sense about Science, include Martin Rees, President of the Royal Society, the present and former directors of the Wellcome trust, Mark Walport and Bridget Ogilvie, and the presidents of a number of scientific societies. David King, former chief scientific advisor to the UK government, commented "It is ridiculous that a legal and outdated definition of a word has been used to hinder and discourage scientific debate. We must be able to fairly and reasonably challenge ideas without the fear of legal intimidation." Numerous scientific editors, journalists, lawyers, politicians, novelists, poets and comedians have also expressed their solidarity. Another disturbing case that took 17 months and cost half a million pounds to defend before it was dropped was that of columnist Ben Goldacre, who was sued by a businessman allegedly promoting vitamin tablets as a cure for AIDS. A central concern about English libel law is that it favours the plaintiff in that the burden of proof rests with the defendant. This is in marked contrast to other countries, including the US, where the plaintiff generally has to disprove the allegations, and it has already resulted in a number of books not being published in the UK. A second issue is that the enormous costs in defending libel allegations in court will make any writer think twice before criticizing powerful interest groups. Tracey Brown, director of Sense about Science, says "it is not only about the rights of scientists to inform the public, but about the right of the public to hear their voices. We have had a long battle to get scientists to speak up and share with the public their reasoning. There was a time when some people did not deign to. Now I think there is a real danger that people won't dare to."

The law also has a direct impact on the scientific literature: it can in principle be used by pharmaceutical companies to block opinions critical of their products. Such censorship can preclude access to information that is clearly in the public interest. Liberal Democrat science spokesman Evan Harris commented in an editorial in the *British Medical Journal* "it is essential in the scientific sphere, and in particular the world of medicine, for claims of efficacy to be subject to the most stringent examination and criticism… all practitioners need to be able to justify their claims in a transparent and scientific way. If that debate is chilled, then the medical profession, patients' interests, and scientific discourse are severely undermined." Importantly, libel law applies just as much to online commenting and blogs, which can be written in a much more casual style. As the *Nature* journals enable commenting on primary papers, we have to consider the legal options and mechanisms for doing this. We could in principle face a claim over user-generated content of which we had no knowledge or control. In the meantime, we have added functionality for readers to efficiently flag up libellous statements and may have to remove potentially defamatory content since we did not write, let alone research, it. The law will also affect decisions such as whether to publish referee reports, as for example already practiced by the *EMBO Journal*. We hope the current legislation does not discourage informed commenting. Purely factual information is not a cause for concern, but extrapolation to individuals and institutions must be considered carefully (also in referee reports).

It is essential that the law does not dampen open scientific debate and the scrutinizing of claims, irrespective of the commercial or personal value attached to them. As it stands, English law discourages critical discussion, impeding the constitutional right to freedom of expression. The web has dramatically facilitated and democratized this open discourse and it would be tragic if outdated laws destroy this core value of our scientific culture.

The House of Commons did launch an inquiry into libel law last year, which is pending. It is encouraging that three senior parliamentarians sent a letter of support to Sense about Science, arguing for a change in the law. The hope is that concrete recommendations for a more balanced law will emerge. Reform is not only in the interest of people living in England: any text, including online content, accessed in England is also subject to the law, which has led to what Evan Harris has called 'libel tourism'.

Further reading: Connotea.org/user/ncb/tag/Englishlibellaw

Building confidence: the transition from student to professor

Elaine Fuchs

My turning point as a scientist was the offer of an assistant professorship to join 15 male colleagues in the Biochemistry Department at the University of Chicago. How I arrived at this position is more circuitous.

Like many other kids who grew up in the cornfield suburbs outside Chicago, playing in swamps and fields was far more interesting than organized sports, particularly when only three other kids lived within earshot of our house. Unlike those kids' parents, my father was a geochemist and my aunt, a biologist at Argonne National Labs. Both were graduates of the University of Chicago, where I later received an offer.

My father encouraged me to be an elementary school teacher; it was my mother — a homemaker with artistic, musical and gardening talents — who contended that since I cooked well, I'd make a fine chemist. I didn't believe her. However, I did major in Chemistry at the University of Illinois. As one of three women in a class of 200 physics students, I felt that I had to study hard to be recognized. I pestered the graduate teaching assistants, who explained the science and also taught me how to juggle tennis balls. After each exam, I always anticipated failure, but usually received the best grade and became a good juggler.

On graduating, I hoped to enter the Peace Corps, an American programme for volunteer work in the developing world. I applied to graduate school as a default pathway, exerting my creativity by submitting a two page essay outlining my reasons for refusing to take the graduate school entrance examinations. My options turned out to be graduate school or Idi Amin, Uganda and the Peace Corps.

Without having any college biology, I began Princeton's graduate programme in Biochemistry. Marc Kirschner's lectures on differentiation were counter to my maths professors' views. Bruce Alberts only took the best students — I wasn't among them. So I chose Charles Gilvarg, an exceptionally smart but demanding advisor researching bacterial sporulation.

Biological equations had too many variables. I worked day and night without solving any problems. I was, however, developing my tennis backhand and broadening my horizons with inexpensive trips to India, Nepal, Bolivia, Peru, Egypt and Turkey. Closer to Princeton, I tasted the pleasures of New York City, discovering restaurants, art and music.

Every now and then an experiment worked, yielding a fresh and exciting way to counter the agony of defeat. I began to enjoy designing my own experiments. I defended my PhD with a modicum of confidence and with a determination to work at the interface of biology and medicine. I chose to work at Massachusetts Institute of Technology (MIT) with Howard Green, who devised methods to culture human stem cells — epidermal keratinocytes — under conditions where they could be maintained and propagated straight from tissue.

On arrival, I was handed a bucket of rat submaxillary glands and asked to purify EGF (epidermal growth factor) for the lab. I was then asked to search through urine for new growth factors. Perhaps Howard misinterpreted 'P-Chem' on my resume. Left to my own devices, I began to identify keratins, their mRNAs and their program of gene expression, as a means to explore epidermal differentiation. I began embarking upon my own trajectory.

I ventured upstairs, downstairs and across the street. Sheldon Penman's postdocs were the mRNA experts. Gobind Khorana's postdocs taught me to make Oligo dT cellulose. London's postdocs were skilled at isolating rabbit reticulocytes for *in vitro* translations. Jim Rothman was the ^{32}P-labelling expert, Richard Hynes shared my interest in comparing vimentin and keratin, Bryan Roberts at Brandeis was Zen master of methyl mercury gels and the David Baltimore and Phil Sharp labs were embarking on DNA recombinant technology. I thrived in the environment at MIT. My experiments were working. While maintaining my interests in music, art and travelling, I fuelled my passion for science.

In my second year at MIT, Charlie Gilvarg nominated me for a faculty position at the University of Chicago. I was flabbergasted, but overjoyed. An even bigger surprise was the invitation for an interview: a free trip home and a chance to practice being interviewed!

Snow was everywhere. I always disliked Chicago's cold weather, but when the city is hit by a major snowstorm, it is beautiful. My seminar seemed to go smoothly. My discussions with famous scientists were a treat. The lack of expectations was a recipe for relaxation.

Months passed. Fellow MIT postdocs received rejection notices. I wondered if mine had been lost in the mail. After receiving an offer that year, I wondered whether Chicago had been impressed with my 'confidence' in not having applied elsewhere.

My father always inspired me to strive to do better. Charlie Gilvarg instilled in me the importance of designing a well-controlled experiment. Marc Kirschner, Bruce Alberts and my other professors at Princeton inspired in me the excitement of the looming revolution in recombinant DNA technology. They exemplified why originality and unconventional thinking are so critical in moving science forward. Howard Green reinforced these lessons. MIT generated an exhilarating environment that stimulated every brain cell I had. It made it easy for those with initiative to thrive. But the offer from the University of Chicago gave me the opportunity to have my own lab, affording me the possibility to pursue my passion.

Elaine Fuchs is the Rebecca C. Lancefield Professor of Mammalian Cell Biology and Development, Howard Hughes Medical Institute, The Rockefeller University, NY 10065, USA. E-mail: fuchslb@rockefeller.edu

Chromosome congression: on the bi-orient express

Emily A. Foley and Tarun M. Kapoor

Errors in chromosome–spindle attachments during cell division can lead to an irreversible change in chromosome number. Proper connections between chromosomes and spindle microtubules can be promoted by both chromosome-intrinsic and extrinsic mechanisms during mitosis and meiosis.

Accurate chromosome segregation requires that chromosomes bi-orient, or attach to microtubules emanating from opposite ends of a bipolar spindle, such that at anaphase, when the molecular glue holding chromosome pairs together (cohesion) is dissolved, chromosomes are flawlessly segregated into each daughter cell. Chromosomes attach to the spindle through kinetochores, proteinaceous structures that assemble on centromeric DNA. The fast-growing (plus) ends of microtubules are typically buried in the kinetochore; in humans 20–30 such microtubules are bundled to form a kinetochore fibre (K-fibre), which provides the driving force for chromosome segregation at anaphase[1].

Although bi-orientation can potentially occur solely through microtubule plus-end 'search-and-capture', in which microtubules nucleated from centrosomes are captured and stabilized by kinetochores to create K-fibres[1], other routes towards bi-orientation must exist because in plants and some animal oocytes spindles assemble and chromosomes bi-orient in the absence of centrosomes. Within the last two decades, it has become clear that, like centrosomes, chromosomes also direct microtubule formation and stabilization[2,3]. Microtubules can then be sorted into bundles, forming K-fibres whose minus-ends can be 'captured' by the spindle[4]. Additionally, mechanisms not directly linked to microtubule dynamics also contribute to proper chromosome alignment at metaphase. On pages 832 and 839 of this issue, two groups show that metaphase alignment can be achieved in the absence of normal K-fibres, through the transport of chromosomes to the spindle equator along the sides of microtubules by plus-end-directed motors[5,6]. In addition, a recent study published in *Nature* has revealed that cohesion at centromeres drives chromosomes towards proper microtubule attachments by influencing the geometry of sister kinetochore (or homologous chromosome) pairs[7].

A straightforward way to increase the rate of bi-orientation is to introduce a positional bias by actively transporting chromosomes to the spindle equator (or metaphase plate), the region where capture of microtubule plus-ends from opposite poles is most probable. Such a mechanism was recently described in mammalian cells[8], where chromosome transport to the spindle equator (congression) precedes bi-orientation. This mode of chromosome movement involves interactions between kinetochores and the sides, rather than the tips, of microtubules, similar to the transport of other organelles along cytoskeletal filaments. In the cases analysed, the chromosome movements were along K-fibres of other chromosomes already aligned at the spindle equator, suggesting a model in which congression is a cooperative process and where the probability of a chromosome being positioned at the centre of the spindle increases as more chromosomes align and properly oriented K-fibres provide tracks. This type of chromosome movement is most likely driven by CENP-E (kinesin-7), a motor that walks towards microtubule plus-ends[9].

However, it remained unclear whether K-fibres were necessary for chromosome congression. In the first of the new studies, Cai *et al.*[5] devised a clever trick, based on previous work[10], to investigate this question: they used RNAi to simultaneously knock down both a protein essential for K-fibre formation and a minus-end-directed motor, thereby creating conditions in which chromosome movement would have to be driven by microtubules other than K-fibres. Remarkably, chromosomes were able to align at the spindle equator in the absence of detectable K-fibres. This alignment depended on CENP-E, the motor protein previously implicated in transporting chromosomes to the spindle equator along K-fibres[8].

The studies by Cai *et al.* reveal that in the absence of plus-end 'search-and-capture', a positional bias towards bi-orientation, arising from lateral interactions between any microtubules, not just K-fibres, and plus-end-directed motors at the kinetochore is sufficient to transport chromosomes to the metaphase plate (Fig. 1). However, congression in the absence of K-fibres required simultaneous removal of a minus-end motor, indicating that spindle forces within human tissue culture cells are not optimal to facilitate this congression mechanism.

Although there is no doubt that future studies will build on these interesting findings to determine how prevalent this type of motor-driven chromosome transport is during congression in unperturbed mitotic cells, in the second of the new studies, Wignall and Villeneuve[6] provide strong evidence that this mode of chromosome movement can be the main route towards chromosome alignment during meiosis.

During mitosis, sister chromatids attach to opposite spindle poles. In contrast,

Emily A. Foley and Tarun M. Kapoor are at Rockefeller University, 1230 York Avenue, NY 10065, USA.
e-mail: kapoor@mail.rockefeller.edu
Published online 16 June 2009;
DOI:10.1038/ncb1902

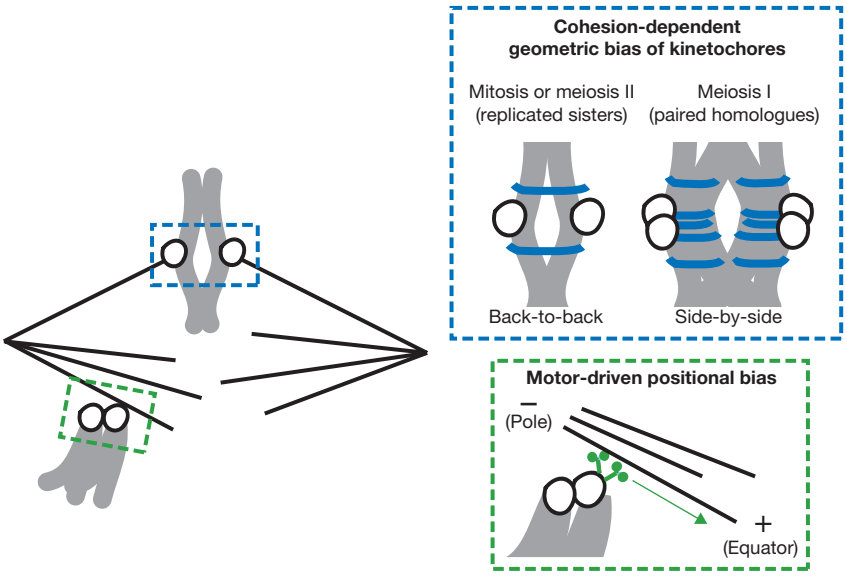

Figure 1 Two routes to bi-orientation. Chromosomes (grey) become bi-oriented when kinetochores (circles) capture microtubule (black lines) plus-ends emanating from opposite spindle poles. Bi-orientation is facilitated by lateral interactions between chromosomes and microtubules which generate a positional bias by transporting chromosomes to the spindle equator (green box). Kinetochore-associated motors (green) walk towards microtubule plus-ends, promoting congression. Differential establishment of sister-chromatid cohesion at chromosome regions underlying kinetochores establishes kinetochore geometry (blue box). During mitosis and meiosis II, cohesion (blue) adjacent to kinetochores generates a back-to-back kinetochore geometry and influences sister kinetochores to capture microtubules from opposite spindle poles. In contrast, during meiosis I, additional cohesion at the site where the kinetochore assembles promotes a side-by-side sister kinetochore orientation and promotes attachment of homologous chromosomes to opposite spindle poles.

during meiosis paired homologous chromosomes (meiosis I) and then sister chromatids (meiosis II) must bi-orient. Using high-resolution live-cell imaging, Wignall and Villeneuve discovered that chromosomes in *Caenorhabditis elegans* oocyte meiotic spindles aligned at the spindle equator while ensheathed in microtubule bundles that ran laterally along their length, in the apparent absence of normal K-fibres. Interestingly, ensheathment of chromosomes by microtubule bundles resulted in chromosomes aligning on the spindle with homologues pointing towards opposite spindle poles in meiosis I, thus poised to segregate to opposite poles at anaphase. This mode of chromosome alignment required the plus-end-directed motor Klp-19, whose localization is restricted to the regions between paired homologues (in meiosis I) or sister chromatids (in meiosis II), the precise sites where cohesion is released at anaphase. Unlike mitosis, the localization of this motor does not overlap with that of the core kinetochore, which is holocentric (extends over the chromosome) in worms. Similar chromosome–microtubule arrangements have been observed in mouse and *Drosophila melanogaster* oocytes[11,12], suggesting that lateral microtubule interactions may be the predominant mechanism of chromosome alignment in oocyte meiotic spindles.

Whereas interactions between the microtubule lattice and chromosome-associated motor proteins can provide external forces to influence chromosome position towards bi-orientation, chromosome-intrinsic properties, such as kinetochore geometry, may specify modes of chromosome–microtubule attachment. The potential importance of establishing back-to-back sister kinetochore geometries in mitosis versus side-by-side configurations in meiosis I has been appreciated for several decades[13]. Recent work by Sakuno *et al.*[7], however, provides the first molecular insight into the link between mechanisms controlling kinetochore geometries and chromosome bi-orientation. They show that sister-chromatid cohesion alters the kinetochore geometry in *Schizosaccharomyces pombe*, biasing chromosomes to bi-orient in mitosis and meiosis.

These authors developed an ingenious assay, excising from whole chromosomes the precise region where the kinetochore is assembled, to visualize cohesion at this site *in vivo*. This assay revealed that subtle differences in where sister-chromatid cohesion is established relative to where the kinetochore is assembled correlate with the bi-orientation of sister chromatids (in mitosis and meiosis II) or homologous chromosomes (in meiosis I; Fig. 1). Next, in a series of experiments using artificial links in place of normal cohesion, the authors examined the effects of site-specific tethering on the promotion of chromosome–microtubule attachments *in vivo*. Without any tether, chromosomes segregated randomly. However, engineering the tether to link DNA sequences at the core centromere (adjacent to the kinetochore) strongly influenced sister kinetochores to attach to the same spindle pole. Significantly, when the tether was repositioned to the peri-centromere (only ~ 1 kb away), sister kinetochores showed a strong tendency to attach to opposite spindle poles. Thus, the tethering of sister DNA molecules (through establishment of cohesion) at chromosomal loci immediately surrounding kinetochores establishes kinetochore geometries and provides a molecular explanation for bias in the modes of chromosome–microtubule attachment in mitosis and meiosis.

Together, these three studies raise a number of interesting questions. In particular, if kinetochore geometry is fixed by cohesion before spindle assembly, how, if at all, do kinetochores convert between different modes of microtubule attachments?

In somatic cells, every chromosome, even if it starts with lateral attachments, is likely to require a K-fibre, with microtubule tips buried end-on at the kinetochore, before anaphase. In mammalian cells, CENP-E, the plus-end motor required for lateral microtubule-driven congression, is depleted from kinetochores as they form mature K-fibres[14]. It will be interesting to determine whether this reflects a requirement to turn off the capacity to make lateral microtubule connections after end-on attachments are generated. Moreover, if motor proteins such as CENP-E pull chromosomes to the metaphase plate, might they also subsequently push kinetochores off the end of microtubule bundles? It will be important to determine if there are mechanisms, possibly linked to encounters with microtubules from the opposite pole, which prevent a kinetochore from 'falling off' a microtubule plus end.

Wignall and Villeneuve raise the intriguing possibility that lateral microtubule–chromosome attachments may not need to be converted to end-on attachments to drive anaphase chromo-

some movements in oocyte spindles. They speculate that these attachments could drive meiotic chromosome segregation because Klp-19, the plus-end motor driving congression in oocyte spindles, is removed from chromosomes at anaphase[15], potentially resulting in a net increase in minus-end-directed lateral chromosome movement towards spindle poles. To prevent chromosome segregation errors, however, chromosomes would have to bi-orient, with homologues (meiosis I) or sister chromatids (meiosis II) establishing lateral interactions with microtubules that extend from opposite spindle poles, before anaphase. It is possible that the site-specific and overlapping localizations of Klp-19 and the chromosomal passenger complex (Aurora kinase), which is known to regulate chromosome–microtubule attachments[16], could contribute to establishing bi-orientation in meiosis in *C. elegans*. Additional studies should shed light on how the restricted localization of factors that mediate bi-orientation ensures accurate chromosome spindle attachments.

The powerful assays developed by Sakuno *et al.*, which allow different sister chromosome geometries to be engineered through artificial tethers, may need to be combined with electron microscopy analysis and, in the future, extended to other systems, to fully explore how chromosome geometry influences different attachment modes and how inter-conversions between these attachment states are possible. Tracking the different routes chromosomes take to the spindle equator during cell division will no doubt continue to intrigue and surprise us.

1. Maiato, H., DeLuca, J., Salmon, E. D. & Earnshaw, W. C. *J. Cell Sci.* **117,** 5461–5477 (2004).
2. Wadsworth, P. & Khodjakov, A. *Trends Cell Biol.* **14,** 413–419 (2004).
3. Karsenti, E. & Vernos, I. *Science* **294,** 543–547 (2001).
4. Khodjakov, A., Copenagle, L., Gordon, M. B., Compton, D. A. & Kapoor, T. M. *J. Cell Biol.* **160,** 671–683 (2003).
5. Cai, S., O'Connell C. B., Kohdjakov, A. & Walczak, C. E. *Nature Cell Biology* **11,** 832–838 (2009).
6. Wignall, S. M. & Villeneuve, A. M. *Nature Cell Biology* **11,** 839–844 (2009).
7. Sakuno, T., Tada, K. & Watanabe, Y. *Nature* **458,** 852–858 (2009).
8. Kapoor, T. M. *et al. Science* **311,** 388–391 (2006).
9. Wood, K. W., Sakowicz, R., Goldstein, L. S. & Cleveland, D. W. *Cell* **91,** 357–366 (1997).
10. Manning, A. L. & Compton D. A. *Curr. Biol.* **17,** 260–265 (2007).
11. Skold, H. N., Komma, D. J. & Endow, S. A. *J. Cell Sci.* **118,** 1745–1755 (2005).
12. Brunet, S. *et al. J. Cell Biol.* **146,** 1–12 (1999).
13. Hauf, S. & Watanabe, Y. *Cell* **119,** 317–327 (2004).
14. Hoffman, D. B., Pearson, C. G., Yen, T. J., Howell, B. J. & Salmon, E. D. *Mol. Biol. Cell* **12,** 1995–2009 (2001).
15. Powers, J. *et al. J. Cell Biol.* **166,** 991–1001 (2004).
16. Kelly, A. E. & Funabiki, H. *Curr. Opin. Cell Biol.* **21,** 51–58 (2009).

Cavin fever: regulating caveolae

Ivan R. Nabi

SDPR is a new regulator of caveolae biogenesis. SDPR overexpression results in increased caveolae size and leads to the formation of caveolae-derived tubules containing Shiga toxin. SDPR may therefore be a membrane curvature-inducing component of caveolae.

Caveolae are morphologically defined plasma membrane invaginations of a relatively constant size (50–100 nm) that function as endocytic carrier vesicles. Formation of caveolae is dependent on expression of the caveolar coat protein, caveolin-1 (Cav1) or, in muscle, Cav3 (ref. 1). Recently, PTRF (polymerase I and transcript release factor, also known as cavin-1), was found to be required for caveolae formation[2,3]. However, regulators of caveolae dynamics remain poorly characterized. On page 807 of this issue, Hansen *et al.*, show that a PTRF-related protein, SDPR (serum deprivation protein response; also known as cavin-2), is required for caveolae formation and that it regulates caveolae morphology and dynamics by inducing membrane tubules, similar to those induced by the glycosphingolipid-binding Shiga toxin[4].

As reported previously for PTRF[2,3], Hansen *et al.* found that depletion of SDPR, which is known to associate with caveolae[5], reduces Cav1 expression levels and limits caveolae formation[4]. Furthermore, knockdown of *SDPR* reduces PTRF levels and vice versa. SDPR, PTRF and Cav1 were found to co-immunoprecipitate, suggesting that they form a protein complex in which expression of one member critically regulates expression of the other complex members. The dependence of Cav1 expression on these two cytoplasmic proteins could explain the requirement of these adaptor proteins for caveolae formation. However, in cells overexpressing both Cav1 and PTRF, and concomitantly presenting increased caveolae, SDPR depletion still reduced caveolae formation. More importantly, whereas overexpression of PTRF did not affect caveolae morphology, overexpression of SDPR resulted in the formation of larger caveolae and also induced caveolae-associated tubule formation. These findings not only define a clear role for SDPR in caveolae biogenesis that is distinct from that of PTRF, but they also demonstrate a role for this protein in caveolae morphology[4].

Another PTRF homologue, SRBC (sdr-related gene product that binds to c-kinase; also known as cavin-3), has recently been shown to regulate caveolae endocytosis[6]. A fourth member of this family, MURC (muscle restricted coiled-coiled protein; also known as cavin-4), is muscle specific, but whether it interacts with Cav3 and regulates caveolae function in muscle remains to be determined[7,8]. Knockdown of *SRBC* does not affect Cav1 levels, but limits budding and intracellular trafficking of Cav1-positive vesicles from the plasma membrane[6]. Importantly, Hansen

Ivan R. Nabi is in the Department of Cellular and Physiological Sciences, Life Sciences Institute, University of British Columbia, Vancouver, BC V6T 1Z3, Canada.
e-mail: irnabi@interchange.ubc.ca

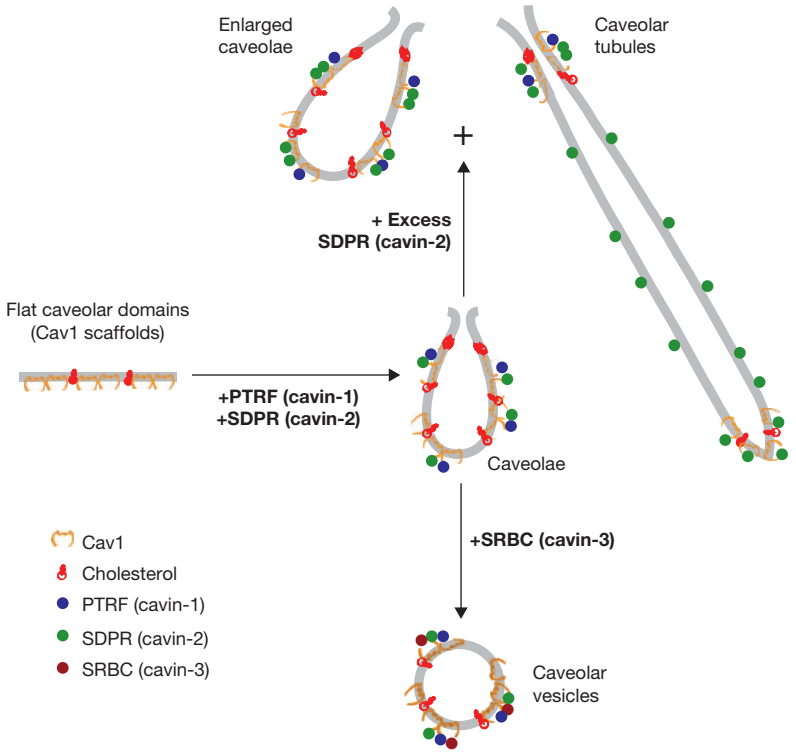

Figure 1 Regulation of caveolae morphology and dynamics by cavin family members. Cav1 is associated with both flat caveolar domains and Cav1 scaffolds[11] as well as invaginated smooth plasmalemmal vesicles or caveolae. PTRF (cavin-1) and SDPR (cavin-2) are required for caveolae invagination and SRBC (cavin-3) for caveolae budding to form caveolar vesicles. Overexpression of SDPR induces enlarged caveolae and caveolar tubules, defining critical roles for cavin family members in caveolae formation, morphology and dynamics.

et al.[4] show that all four cavins, PTRF, SDPR, SRBC and MURC, are recruited to caveolae. Overexpression of individual complex members alters caveolae biogenesis, suggesting that altered stoichiometry of these members may affect caveolae formation, morphology, dynamics and function (Fig. 1).

A requirement for PTRF and SDPR in caveolae formation is consistent with functional roles for Cav1 that are independent of caveolae[9]. In cells that do not express PTRF or SDPR, Cav1, even at reduced expression levels, will necessarily adopt caveolae-independent functions. Indeed, in cells expressing reduced levels of Cav1, oligomerized Cav1 domains or scaffolds regulate EGFR (epidermal growth factor receptor) signalling and dynamics independently of caveolae[10,11]. In addition, PC3 prostate cancer cells lack PTRF and caveolae, yet express elevated Cav1 levels as well as tyrosine phosphorylated Cav1 that regulates focal adhesion turnover and cell migration[2,12]. Indeed, Cav1 is a multifunctional protein that has specific functions in different tissues and can function as both tumour suppressor and promotor, in cancer[1,13]. By affecting the ability of Cav1 to form caveolae, as well as the nature and stability of the caveolae formed, tissue-specific expression of regulatory cavin proteins may selectively modulate Cav1 function in different cell types.

Caveolae function as endocytic carriers for various ligands, including the SV40 virus. In *Cav1*$^{-/-}$ fibroblasts, SV40 and the cholera toxin-b subunit are internalized through cholesterol-dependent, lipid raft-associated tubular endocytic carriers that necessarily form independently of caveolae[14,15]. Hansen *et al.* demonstrate that SDPR induces tubules that are similar to Shiga toxin-induced membrane tubules[16] and can be labelled with Cav1 (ref. 4). SDPR may recruit the Shiga toxin receptor Gb3 to caveolar domains and therefore to SDPR-induced tubules. The requirement of SDPR, PTRF and Cav1 for Shiga toxin recruitment to tubules suggests that Shiga toxin is internalized through a caveolar domain[4]. Internalization of Shiga toxin through caveolae-derived tubules in SDPR-overexpressing cells therefore expands the repertory of raft-derived endocytic intermediates[17], suggesting that vesicular and tubular endocytic intermediates can derive from both Cav1-positive and Cav1-negative raft domains. Together with the ability of SRBC to regulate caveolae-derived vesicle formation[6], these data indicate that cavins may prove to be critical regulators of the endocytic potential of caveolae.

The ability of SDPR overexpression to increase caveolae size as well as to induce elongated Cav1-containing tubules suggests that caveolae morphology is not immutable[4]. How the oligomeric caveolar coat can change size and give rise to dynamic tubules remains unclear. Cav1 forms stable oligomers, is immobile at the plasma membrane and has been proposed to form a stable coat of ~150 monomers on individual caveolae[1]. Indeed, if Cav1 oligomers form a stable vesicular coat, SDPR must in some way be altering Cav1 oligomeric structure, perhaps by disrupting larger caveolae-associated Cav1 oligomers, causing them to form smaller, less stable oligomers or monomers that permit tubule formation. The recent observations from electron microscopy tomography of a spiked caveolar coat[18] may be suggestive of a more flexible coat structure conducive to changes in caveolar size, shape and tubulation.

It remains to be determined whether tubules derive directly from caveolae, flat caveolar domains or disrupt Cav1 oligomeric structure. Using immunofluorescence, Hansen *et al.* found that overexpressed SDPR was distributed along elongated membrane tubules that were enriched for Cav1 at either the plasma membrane-associated origin or at the distal end of a long tube. Electron microscopy showed that these tubules were labelled for Cav1 throughout their length. However, the discrete distribution of SDPR and Cav1 along the tubules indicates that these proteins are not forming stochiometric complexes along the length of the tubule. The region of SDPR responsible for membrane tubulation is a coiled-coiled domain followed by a conserved basic domain that is distinct from its PTRF-binding site. Hansen *et al.* speculate that the coiled-coiled domain is responsible for homo- and/or hetero-oligomerization, whereas the basic domain promotes interaction with the inner leaflet of the plasma membrane, perhaps through binding to phosphatidyl serine[4]. The lack of homology between these domains and other curvature-inducing proteins suggests that SDPR induces membrane curvature through a new mechanism. Furthermore,

how the formation of Shiga toxin-containing tubules, which are apparently derived from and are dependent on caveolae and Cav1, in intact cells can be reconciled with the ability of Shiga toxin to induce tubules in cell-free liposomes[16] is unclear. It does, however, suggest that complex mechanisms underlie membrane curvature in biological membranes, including endocytic events associated with lipid raft domains. Whereas the specific impact of SDPR on caveolae function remains to be determined, its ability to regulate caveolae expression, morphology and endocytosis implicates it, and other cavin family members, as critical regulators of both caveolae and Cav1 function.

1. Parton, R. G. & Simons, K. *Nature Rev. Mol. Cell Biol.* **8,** 185–194 (2007).
2. Hill, M. M. *et al. Cell* **132,** 113–124 (2008).
3. Liu, L. *et al. Cell Metabolism* **8,** 310–317 (2008).
4. Hansen, C., Bright, N., Howard, G. & Nichols, B. *Nature Cell Biol.* **11,** 807–814 (2009).
5. Mineo, C., Ying, Y. S., Chapline, C., Jaken, S. & Anderson, R. G. *J. Cell Biol.* **141,** 601–610 (1998).
6. McMahon, K.-A. *et al. EMBO J.* **28,** 1001–1015 (2009).
7. Ogata, T. *et al. Mol. Cell. Biol.* **28,** 3424–3436 (2008).
8. Tagawa, M. *et al. Am. J. Physiol. Cell Physiol.* **295**, C490–498 (2008).
9. Head, B. P. & Insel, P. A. *Trends Cell Biol.* **17,** 51–57 (2007).
10. Lajoie, P. *et al. J. Cell Biol.* **179,** 341–356 (2007).
11. Lajoie, P., Goetz, J. G., Dennis, J. W. & Nabi, I. R. *J. Cell Biol.* **185,** 381–385 (2009).
12. Joshi, B. *et al. Cancer Res.* **68,** 8210–8220 (2008).
13. Goetz, J. G., Lajoie, P., Wiseman, S. M. & Nabi, I. R. *Cancer Metastasis Rev.* **27,** 715–735 (2008).
14. Kirkham, M. *et al. J. Cell Biol.* **168,** 465–476 (2005).
15. Damm, E. M. *et al. J. Cell Biol.* **168,** 477–488 (2005).
16. Romer, W. *et al. Nature* **450,** 670–675 (2007).
17. Lajoie, P. & Nabi, I. R. *J. Cell. Mol. Med.* **11,** 644–653 (2007).
18. Richter, T. *et al. Traffic* **9,** 893–909 (2008).

Delta traffic takes a sh-Arp turn

Eyal D. Schejter

In the Notch pathway, the transmembrane ligand Delta is internalized and then re-established on the surface of signal-sending cells to allow the productive binding and activation of the Notch receptor on neighbouring cells. Arp2/3-dependent actin polymerization directs Delta trafficking through this circuit.

The Notch signalling pathway uses a broad array of basic cellular machineries to convey instructions between cells throughout metazoan development[1,2]. At first glance, the molecular mechanisms for signal transduction involving this pathway appear relatively simple. The Notch receptor and its transmembrane ligands (DSL-family, Delta, Serrate and Lag-2) are expressed on the surface of neighbouring signal-receiving and signal-sending cells, and associate through their extracellular domains. This interaction results in proteolytic release of the intracellular portion of Notch, which then enters the nucleus where it functions as a transcriptional co-activator of target genes.

Closer examination, however, has revealed a far more complex picture. The Notch receptor undergoes extensive post-translational modification and several cleavage events; Notch receptor trafficking through endocytosis also has a critical role in modulation of signalling levels[3–5]. Regulation of the activity of the Notch ligands seems just as complex[6]. In particular, there is an intriguing requirement for ligand endocytosis into the signal-sending cell, which has been the focus of intensive recent research[7,8]. On page 815 of this issue, Bellen and colleagues[9] describe an essential involvement of the WASp–Arp2/3 (Wiskott-Aldrich syndrome protein and actin-related protein 2/3, respectively) actin polymerization machinery in DSL-ligand trafficking and signalling.

The authors studied the assignment of distinct fates to the four cell types that constitute the numerous sensory organs located along the cuticle of the adult *Drosophila melanogaster* fly, and which are characterized by their external mechanosensory bristle. This process relies on asymmetric cell divisions, mediated by the Notch signalling pathway[10,11]. Single sensory organ precursors (SOPs) are selected within a neurogenic field[12] and enter a program of three rounds of cell division[13,14]. Each division generates a pair of daughter cells that interact in a stereotypic fashion: one of the daughters assumes the signal-sending role and uses DSL-type ligands[15] to activate Notch in its sibling, the signal-receiving cell. Preferential activation of a Notch-induced genetic program in the signal-receiving cell results in the acquisition of cell features and functions that are distinct from those shown by the signal-sending cell. Disruption of Notch-based signalling in this context leads the siblings to assume an identical 'default' cell fate, normally only shown by the signal-sending cell.

The evolutionarily conserved Arp2/3 system is a primary mediator of the dynamic organization of the actin cytoskeleton. When stimulated by actin nucleation-promoting factors such as WASp, the seven-subunit Arp2/3 complex induces the formation of extensive, branched arrays of microfilaments, which can be used for cell motility, intracellular movement of membrane-bound particles and endocytosis[16]. The single *Drosophila* WASp homologue has been implicated previously in Notch-mediated sensory organ development[17,18]. However, the nature of the branched microfilament structures involved, as well as the mechanistic basis for their function, remained unknown.

In their recent study, Bellen and colleagues concentrated on the regulation of the DSL- ligand Delta in the pair of cells generated by division of the SOP cell itself, pIIb (signal-sending) and pIIa (signal-receiving; Fig. 1). They took advantage of a newly-identified mutant allele of *Arp3*, which encodes one of the subunits of the Arp2/3 complex, as well as existing mutant alleles of a second Arp2/3 subunit and WASp. The authors show that regions of the adult fly cuticle lacking Arp2/3 function show sensory organ cell-fate transformations that are highly similar to those observed following disruption of Notch signalling. They obtained genetic evidence that Arp2/3 is required upstream of Notch, within the signal-sending cell. The authors rule out two possible explanations for the observed phenotypes; they show that cell-fate determinants are

Eyal D. Schejter is in the Department of Molecular Genetics, Weizmann Institute of Science, Rehovot 76100, Israel.
e-mail: eyal.schejter@weizmann.ac.il

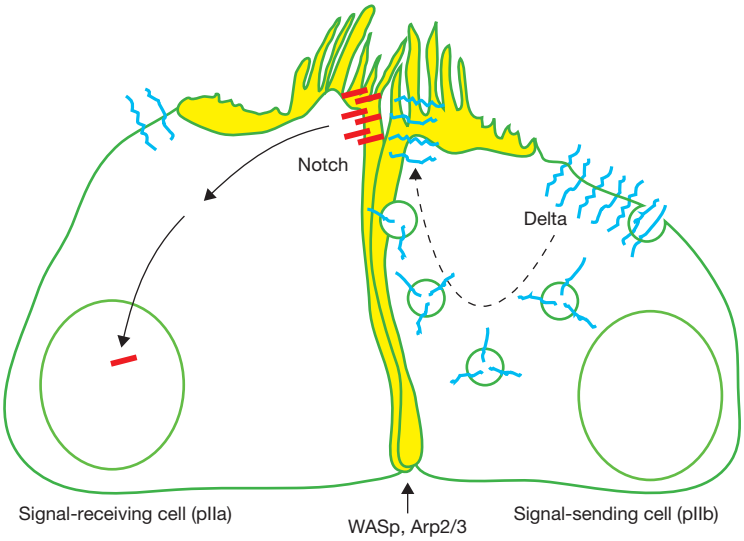

Figure 1 Drosophila sensory organ cells use an actin-rich structure to promote Notch pathway signalling. During sensory organ development, asymmetric signalling between neighbouring cells via the Notch pathway, leads to assignment of distinct cell identities. The Delta ligand (blue), expressed by the signal-sending cell (right), binds Notch (red) on the neighbouring signal-receiving cell (left), leading to the release of the intracellular domain of the receptor, which acts to promote target gene expression and influence cell fate. Proper display of the ligand requires internalization of Delta-containing vesicles into the signal-sending cell, followed by transport along an actin-rich structure (yellow) to apical, microvilli-rich sites of Delta–Notch interaction. Construction of the actin-rich structure requires the activity of the WASp-Arp2/3 actin polymerization system.

distributed normally between pIIa and pIIb, and that the Delta ligand is internalized properly within the signal-sending cells in the absence of Arp2/3 function. The latter observation is particularly surprising given the well-established involvement of Arp2/3 in endocytosis[19].

Complementing their genetic analysis, Bellen and colleagues visualized sensory organ cell components and structures using both light and electron microscopy, and here they make a pair of striking observations. A previously undescribed, filamentous actin-rich structure (termed ARS) is found to form within the pIIa and pIIb cells following SOP division. In addition, long finger-like microvilli associated with the ARS are shown to protrude from the apical side of the cells. The ARS warrants particular interest as the possible link between Arp2/3 microfilament-nucleating activity and Delta ligand function. When the neighbouring pIIa and pIIb cells are viewed along their apical-basal axis, the ARS resembles an open umbrella in which the umbrella 'top' lies just beneath the apical membrane of the cells, and the umbrella 'shaft' lines the apposing basolateral cell membranes (Fig. 1). Bellen and colleagues found that intracellular Delta-containing particles tend to cluster near the ARS, and they revealed an intriguing dynamic sequence using a pulse-chase approach: Delta particles, internalized from the apical cell surface, travel basally but then re-localize apically to the microvilli-rich portion at the top of the ARS umbrella. Impairment of Arp2/3 function results in defects in size and morphology of the ARS and the associated microvilli. Significantly, internalized Delta particles reach the basal portion of the mutant sensory organ cells but fail to travel back apically.

Bellen and colleagues seem, therefore, to have cracked the structural basis for Arp2/3 involvement in sensory organ Notch signalling: the ARS, a new actin-based structure, which is formed through the action of WASp and the Arp2/3 complex, serves as a means for trafficking the Delta ligand to apical membrane domains, from where it can productively interact with the Notch receptor. However, although a significant step forward has been made, several important questions remain open, especially regarding the mechanism by which the ARS is used for apical trafficking of Delta particles. One appealing model would involve basal-to-apical travel along the ARS 'shaft'. However, microfilament-based transport is more commonly attributed to myosin-motor activity along parallel actin bundles than along the branched arrays nucleated by the Arp2/3 complex[20]. One possibility is that an Arp2/3-initiated array is restructured and gives rise to a bundled-filament arrangement, as has been proposed in other contexts[21]. Refined electron microscopy analysis of the ARS structure should shed light on this matter. An alternative mechanism may involve acquisition of polymerization-based motility by the internalized Delta-containing vesicles, in keeping with traditional roles for Arp2/3 microfilament nucleation.

Whether the Arp2/3-based sensory organ trafficking mechanism is used in additional developmental settings involving Notch-mediated signalling remains to be addressed. Bellen and colleagues provide initial indications that this may be the case, by showing that Arp2/3 is required for Delta activity during *Drosophila* wing development and oogenesis. It remains to be seen, however, if structures resembling the sensory organ ARS mediate Notch signalling in these distinct tissues as well. Finally, the significance of the newly described apical microvilli for Notch-mediated signalling between sensory organ cells is yet to be determined. Bellen and colleagues discuss the intriguing possibility that these membrane projections serve as a platform for Delta ligand presentation by the signalling cell. Appropriate genetic backgrounds, which specifically interfere with the formation of microvilli, should be sought for further investigation. Despite this range of open issues, the study by Bellen and colleagues provides new insights in the context of cellular regulation of Notch signalling and, furthermore, constitutes a significant contribution to our knowledge of the role of Arp2/3-mediated actin polymerization during the development of multicellular organisms.

1. Artavanis-Tsakonas, S., Rand, M. D. & Lake, R. J. *Science* **284,** 770–776 (1999).
2. Lai, E. C. *Development* **131,** 965–973 (2004).
3. Bray, S. J. *Nature Rev. Mol. Cell Biol.* **7,** 678–689 (2006).
4. Fiuza, U. M. & Arias, A. M. *J. Endocrinol.* **194,** 459–474 (2007).
5. Tien, A. C., Rajan, A. & Bellen, H. J. *J. Cell Biol.* **184,** 621–629 (2009).
6. D'Souza, B., Miyamoto, A. & Weinmaster, G. *Oncogene* **27,** 5148–5167 (2008).
7. Emery, G. & Knoblich, J. A. *Curr. Opin. Cell Biol.* **18,** 407–415 (2006).
8. Le Borgne, R. *Curr. Opin. Cell Biol.* **18,** 213–222 (2006).
9. Rajan, A., Tien, A. C., Haueter C. M., Schulze, K. L. & Bellen, H. J. *Nature Cell Biol.* **11,** *815–824* (2009).
10. Bellaiche, Y. & Schweisguth, F. *Curr. Opin. Genet. Dev.* **11,** 418–423 (2001).
11. Gonczy, P. *Nature Rev. Mol. Cell Biol.* **9,** 355–366 (2008).
12. Pi, H. & Chien, C. T. *J. Biomed. Sci.* **14,** 467–473 (2007).
13. Gho, M., Bellaiche, Y. & Schweisguth, F. *Development* **126,** 3573–3584 (1999).
14. Reddy, G. V. & Rodrigues, V. *Development* **126,** 4617–4622 (1999).

15. Zeng, C., Younger-Shepherd, S., Jan, L. Y. & Jan, Y. N. *Genes Dev.* **12,** 1086–1091 (1998).
16. Goley, E. D. & Welch, M. D. *Nature Rev. Mol. Cell Biol.* **7,** 713–726 (2006).
17. Ben-Yaacov, S., Le Borgne, R., Abramson, I., Schweisguth, F. & Schejter, E. D. *J. Cell Biol.* **152,** 1–13 (2001).
18. Tal, T., Vaizel-Ohayon, D. & Schejter, E. D. *Dev. Biol.* **243,** 260–271 (2002).
19. Kaksonen, M., Toret, C. P. & Drubin, D. G. *Nature Rev. Mol. Cell Biol.* **7,** 404–414 (2006).
20. Pruyne, D., Legesse-Miller, A., Gao, L., Dong, Y. & Bretscher, *Annu. Rev. Cell Dev. Biol.* **20,** 559–591 (2004).
21. Svitkina, T. M. *et al. J. Cell Biol.* **160,** 409–421 (2003).

A reader for centromeric chromatin

Nikolina Sekulic and Ben E. Black

For nucleosome-encoded epigenetic information to be transmitted, an epigenetic mark requires a 'reader' for its physical recognition. CENP-N has now been identified as a reader of the centromere-specifying epigenetic mark that is generated by incorporation of the histone H3 variant CENP-A into centromeric nucleosomes.

Centromeres are defined epigenetically, and nucleosomes containing the histone H3 variant CENP-A are thought to provide the epigenetic information required to specify centromere location on the chromosome. As for other chromatin marks, it is important to understand how the epigenetic information is physically transmitted from the chromatin. On page 896 of this issue, Straight and colleagues take a step towards our understanding of the centromere by identifying CENP-N as a reader of the centromere mark comprising CENP-A-containing nucleosomes[1].

How centromeres work has been a long-standing target of investigation due to their central role in directing the stable inheritance of the chromosome and all the genes present on it. Furthermore, the epigenetic centromere mark is perhaps the longest lived of all epigenetic marks, surviving through the germ line and (with rare exceptions) maintaining its location at the same chromosomal locus on the evolutionary timescales of speciation events. Yet, our understanding of the centromere mark lags behind its shorter-lived counterparts elsewhere on the chromosome, which are involved in other biological processes. In the case of its nearest neighbour, pericentromeric heterochromatin, the identity of the critical nucleosomal mark (di- or tri-methylated K9 on the tail of histone H3) and reader (HP1) helped to develop early models for the spread and propagation of a chromosome domain[2]. Relative to our understanding of the epigenetic pathways at the pericentromere, our knowledge of the centromere lags behind; however, the centromeric field is catching up with the identification of CENP-N as a reader[1], along with other notable recent progress in describing the physical basis for marking the centromere[3] and characterizing candidate molecules involved in cell-cycle-coupled replenishment of the mark[4–7].

Before considering the reader itself, what is the nature of the CENP-A-generated mark? Many nucleosome-encoded marks elsewhere on the chromosome involve post-translational modification of the tails of conventional histones, with the tail of histone H3 serving as a particularly common target[8]. H3 is replaced by CENP-A in the centromeric nucleosome, which removes most of the common H3 tail modification sites and supplies a related but structurally distinct histone fold domain[9]. Many lines of evidence support the notion that the structural core of the CENP-A nucleosome is key to marking centromeres. An engineered histone H3 chimaera ($H3^{CATD}$), which contains the intact tail from H3 but harbours 22 amino-acid substitutions in the Loop 1 and α2 helix regions within the histone fold of CENP-A, is sufficient to target H3 to the centromere and replace the mitotic function of CENP-A[9,10]. This domain, termed CATD (CENP-A targeting domain), confers nucleosomal rigidity to CENP-A-containing nucleosomes at the centromere[3], providing a unique structure, which enables the reader to distinguish CENP-A-containing nucleosomes from bulk nucleosomes elsewhere on the chromosome that contain conventional H3 (Fig. 1a). The CATD may also provide a subset of exposed side-chains within its Loop 1, specific to the CENP-A nucleosome, which could be directly recognized by the reader (Fig. 1b). In either case, the centromere reader is predicted to bypass the histone tails and hone in on the core of the CENP-A-containing nucleosome (Fig. 1c).

To investigate the reading of the centromere mark, Straight and colleagues rounded up the usual suspects, screening each of the 14 known constitutive non-histone human centromere proteins, one-by-one, for their ability to bind to CENP-A-containing mononucleosomes assembled from recombinant purified components[1]. While centromeres comprise a polynucleosome array of CENP-A-containing nucleosomes, the authors reasoned that one or more known centromere components could directly recognize CENP-A-containing mononucleosomes, which represent the fundamental unit of centromere-specifying chromatin. The most likely candidates were the centromere proteins (CENP-B, CENP-C, CENP-H, CENP-M, CENP-N, CENP-T and CENP-U) that co-purify with CENP-A-containing nucleosomes, but not with their canonical counterparts containing conventional H3 (ref. 11).

There are several possible means by which each of these proteins could associate with the centromere-specifying nucleosome: by directly recognizing the α-satellite DNA sequence that wraps most CENP-A nucleosomes in the cell (as is well-established in the case of CENP-B association); by association with nucleosomes containing H3 that are directly adjacent to CENP-A-containing nucleosomes at the centromere (as has been proposed for CENP-T and its close binding partner CENP-W[12]); by direct recognition of, and binding to, CENP-A nucleosomes independently of DNA sequence; or by indirect interaction (that is, in an arrangement bridged by another constitutive centromere component). Of the 14 candidates, only two, CENP-B and CENP-N, directly bound to the reconstituted CENP-A-containing mononucleosomes[1]. The association of CENP-B was, as expected, dependent on the α-satellite

Nikolina Sekulic and Ben E. Black are in the Department of Biochemistry and Biophysics, University of Pennsylvania, PA 19104–6059, USA.
e-mail: blackbe@mail.med.upenn.edu

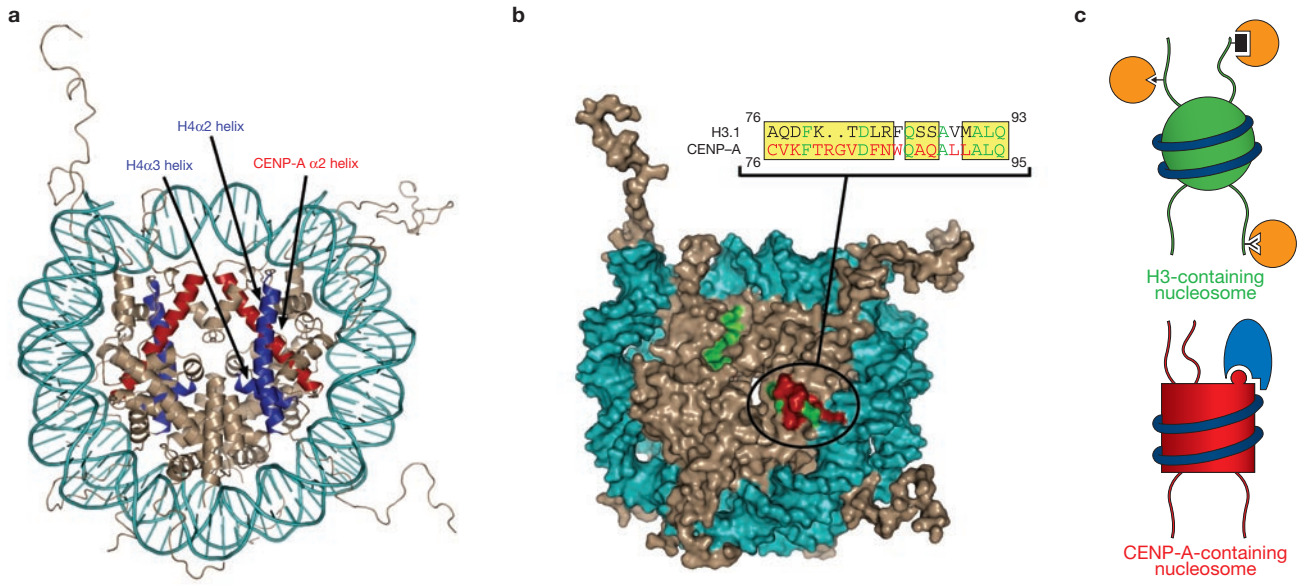

Figure 1 Physical features that could be recognized by a reader of centromere-specifying nucleosomes. (**a**) Conformational rigidity of the CENP-A-containing nucleosome. The α2 helix within the CATD of CENP-A (red) and the α2 and α3 helices of H4 (blue) are protected from amide proton exchange[3] indicative of structural rigidity that a reader could use to distinguish centromere-specifying nucleosomes from their conventional counterparts containing H3. (**b**) Surface-exposed side chains from a subset of residues of Loop 1 within the CATD of CENP-A in a molecular surface representation of a canonical nucleosome in the same orientation as in **a** with DNA in blue and histones in tan. Exposed regions corresponding to the predicted location of the CATD are coloured in red (CENP-A specific substitutions) and green (conserved between H3 and CENP-A). Note that only a small part of the C-terminal α2 helix is predicted to be solvent exposed (upper left green patch) where the surface residues are identical between H3 and CENP-A. A larger exposed area mostly consists of Loop 1 (circled). In the alignment (top), exposed positions in this region of the canonical nucleosome are highlighted in yellow, red letters indicate CENP-A-specific residues, black letters indicate H3-specific residues, and green letters indicate residues conserved between the two proteins. These side chains may be recognized by a centromere reader. Models in **a** and **b** are based on the crystal structure of a canonical nucleosome; PDB ID 1KX5. (**c**) Diagrams depicting distinct modes of reading tail modifications on conventional nucleosomes versus the predicted requirements for a candidate reader of CENP-A-containing nucleosomes. While epigenetic mark readers (orange) for conventional nucleosomes commonly recognize modified tail residues (black), a centromere mark reader (blue) is likely to recognize the rigid core of the CENP-A-containing nucleosome and/or specific residues protruding from its surface.

sequences present in the nucleosomal DNA, but independent of the presence of CENP-A. On the other hand CENP-N, bound to CENP-A-containing nucleosomes independently of DNA sequence. This critical finding makes CENP-N a prime candidate to represent a chromatin reader that specifically recognizes centromere-specifying nucleosomes from the presence of CENP-A in place of H3.

Straight and colleagues used SNAP pulse labelling, an approach used in earlier experiments to identify the telophase/G1 phase of new CENP-A assembly[13], to demonstrate that CENP-N is required for the robust assembly of CENP-A nucleosomes[1]. The mechanism by which CENP-N and other constitutive centromere-associated network (CCAN) proteins participate in centromere reinforcement remains unclear, but may involve a high order of centromeric chromatin organization; possibly required for efficient CENP-A nucleosome assembly and telophase recruitment (directly or indirectly) of the Mis18 centromere licensing complex[4,5] or telophase/G1 recruitment of the HJURP chromatin assembly complex[6,7]. Disruption of CENP-N by mutation or depletion yields mislocalization of some, but not all, CCAN constituents, culminating in defective kinetochores[1]. All of this supports the notion that the role of CENP-N in reading the centromere mark is a critical step in ensuring accurate chromosome segregation at cell division.

In considering CENP-N as a candidate chromatin reader, it is important to distinguish it from proteins that recognize a pre-nucleosomal histone complex destined for the centromere, as such proteins would be more likely to represent chromatin assembly proteins, chaperoning CENP-A–H4 complexes before incorporation into centromeric DNA. Recent candidates to represent the CENP-A-specific chromatin assembly proteins include HJURP in mammals[6,7] and Sim3 and Scm3 in fission yeast[14,15]. Several lines of evidence argue against a role for CENP-N in chaperoning pre-nucleosomal CENP-A complexes: CENP-N is present at the centromere throughout the cell cycle[11] (as opposed to transient association following mitotic exit when new CENP-A nucleosomes are assembled), it is absent from the soluble HJURP-containing complex that chaperones newly expressed CENP-A to the centromere[6,7] and it does not seem to selectively bind to non-nucleosomal CENP-A[1]. Instead, CENP-N selectively binds to CENP-A-containing nucleosomes with an apparent K_d of 169 nM (ref. 1).

To determine how CENP-N reads the centromere-specifying nucleosome, Straight and colleagues compared its binding to three types of nucleosomes: conventional nucleosomes containing the canonical histone octamer, nucleosomes in which the two copies of H3 are replaced by CENP-A and those in which they are replaced by the chimaeric $H3^{CATD}$. Although only background levels of binding to conventional nucleosomes were detected, CENP-N bound to CENP-A- and $H3^{CATD}$-containing nucleosomes with nearly identical affinity[1]. Thus, CENP-N recognition of CENP-A-containing nucleosomes involves not the tail of CENP-A, but instead the unique physical properties imparted by the CATD. It will be interesting to determine whether CENP-N reads the centromere-specifying nucleosome by recognizing CATD-directed nucleosomal

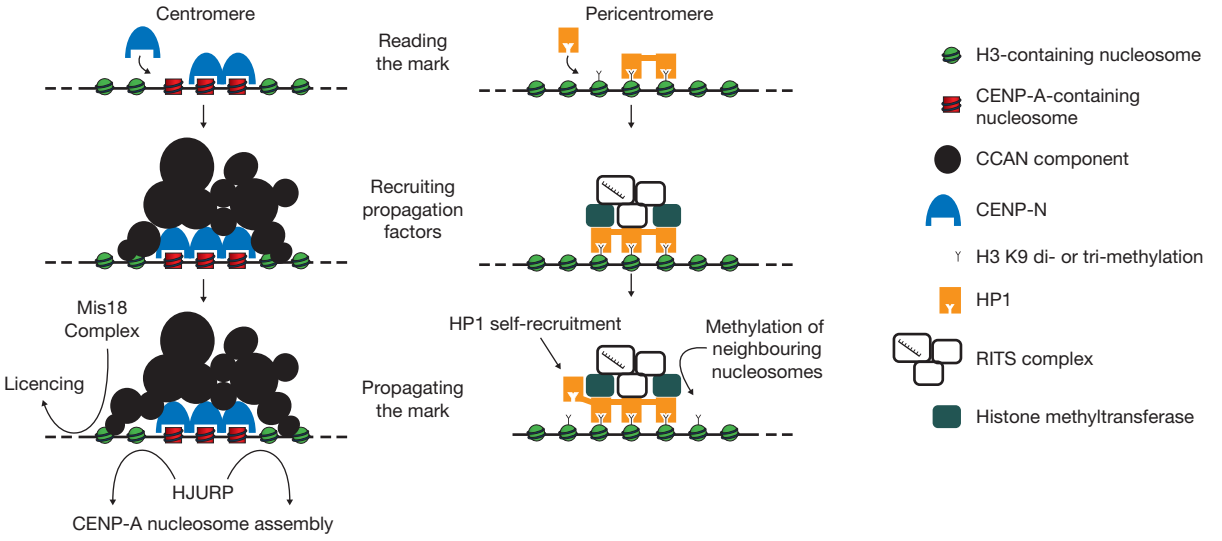

Figure 2 Distinct modes of epigenetic propagation at the pericentromere and centromere. At centromeric chromatin, CENP-A nucleosome are read by CENP-N. CCAN components are recruited by interactions with CENP-N, adjacent nucleosomes, and other CCAN components. To propagate the centromeric mark, the Mis18 complex is recruited to the centromere in telophase, followed by the recruitment of a prenucleosomal CENP-A/H4 histone complex chaperoned by HJURP to assemble new CENP-A-containing nucleosomes following mitotic exit every cell cycle. At pericentromeric heterochromatin, nucleosomes, marked by di- or tri-methylation of histone H3, are read by HP1-related proteins. Propagation factors, including histone methyltransferases and the siRNA-containing RITS complex are recruited by interactions with HP1 and each other, as well as by potential modes of recruitment not shown in this diagram including direct binding of the RITS complex by its Chp1 subunit and base pairing between the RITS-bound siRNA and nascent pericentromeric transcripts in fission yeast. To propagate the pericentromeric mark, neighbouring nucleosomes are methylated and local recruitment of additional HP1 molecules is facilitated by its self–self interactions.

rigidity (Fig. 1a), exposed side-chains specific to the CATD (Fig. 1b) or a combination of these unique physical signatures of CENP-A-containing nucleosomes.

Centromere-specific chromatin uses a different strategy for its propagation than that used at the pericentromere (Fig. 2). In pericentromeric heterochromatin propagation, the HP1 reader recruits the siRNA-containing RITS complex and a methyltransferase (Clr4 in fission yeast, for instance) to methylate neighbouring nucleosomes on H3 K9, as well as undergoing self–self interactions to recruit additional HP1 molecules[2]. In centromere-specifying chromatin propagation, the CENP-N reader directly interacts with a network of constitutive centromere proteins that together generate a chromatin compartment that is competent to recruit the Mis18 licensing complex and subsequently recruit the HJURP-containing centromeric chromatin assembly complex to load new CENP-A nucleosomes following mitotic exit.

In the context of centromeric chromatin — where there remain many biochemically uncharacterized components — this study provides the first glimpse at the reading of the mark generated by CENP-A nucleosomes, adding a key piece to our understanding of centromere identity and the assembly of a functional kinetochore. These findings will undoubtedly serve as a bridge to future studies to elucidate the mechanisms used to mark, read and propagate centromeric chromatin.

1. Carroll, C. W., Silva, M. C. C., Godek, K. M., Jansen, L. E. T. & Straight, A. F. *Nature Cell Biol.* **11,** *896–902* (2009).
2. Cam, H. P., Chen, E. S. & Grewal, S. I. *Cell* **136,** 610–614 (2009).
3. Black, B. E., Brock, M. A., Bédard, S., Woods, V. L. & Cleveland, D. W. *Proc. Natl Acad. Sci. USA* **104,** 5008–5013 (2007).
4. Fujita, Y. *et al. Dev. Cell* **12,** 17–30 (2007).
5. Maddox, P. S., Hyndman, F., Monen, J., Oegema, K. & Desai, A. *J. Cell Biol.* **176,** 757–763 (2007).
6. Foltz, D. R. *et al. Cell* **137,** 472–484 (2009).
7. Dunleavy, E. M. *et al. Cell* **137,** 485–497 (2009).
8. Taverna, S. D., Li, H., Ruthenburg, A. J., Allis, C. D. & Patel, D. *J. Nature Struct. Mol. Biol.* **14,** 1025–1040 (2007).
9. Black, B. E. *et al. Nature* **430,** 578–582 (2004).
10. Black, B. E. *et al. Mol. Cell* **25,** 309–322 (2007).
11. Foltz, D. R. *et al. Nature Cell Biol.* **8,** 458–469 (2006).
12. Hori, T. *et al. Cell* **135,** 1039–1052 (2008).
13. Jansen, L. E., Black, B. E., Foltz, D. R. & Cleveland, D. W. *J. Cell Biol.* **176,** 795–805 (2007).
14. Pidoux, A. L. *et al. Mol. Cell* **33,** 299–311 (2009).
15. Williams, J. S., Hayashi, T., Yanagida, M. & Russell, P. *Mol. Cell* **33,** 287–298 (2009).

RESEARCH HIGHLIGHTS

Sorting lipids at the Golgi

The trans-Golgi network (TGN) is the main hub in the secretory pathway for sorting proteins. Now, Simons and colleagues report that in *Saccharoymyces cerevisiae*, the TGN can also sort lipids (*J. Cell Biol*. **185,** 601–612).

The authors purified TGN-derived secretory vesicles bearing a raft marker. These vesicles were found to contain other raft proteins destined for the plasma membrane but lacked soluble secreted proteins that are delivered in different vesicles. Comparative lipidomics between secretory vesicles, TGNs and endosomes revealed that ergosterol and sphingolipids — lipids typical of raft domains — were enriched in the vesicles, whereas other lipids were under-represented. Moreover, the authors found that the vesicle membrane was more ordered relative to the TGN, potentially reflecting the coalescence of lipid raft domains in the vesicles.

These findings demonstrate not only that lipids can be sorted at the TGN, but also that sorting may rely on a raft-based clustering mechanism during the biogenesis of secretory vesicles at the TGN. Identifying factors that facilitate raft clustering at the TGN will be the next important step in understanding how rafts may assist in cargo sorting. SS

Pom1 sets size limit

Two studies in *Nature* from the groups of Sophie Martin and Paul Nurse find that the polarized distribution of the kinase Pom1 functions as a cell size sensor that controls mitotic entry through the Wee1-inhibitory kinase Cdr2 (*Nature,* doi:10.1038/nature08074 and doi:10.1038/nature08054).

Pom1 regulates polarized cell growth at the tips of *Schizosaccharomyces pombe* cells. Both groups noticed that *pom1* mutants divide at a smaller size than wild-type cells do and found that Pom1 acts as a dose-dependent inhibitor of mitotic entry. It localizes Cdr2 medially and negatively regulates Cdr2, perhaps through direct phosphorylation.

The gradient of Pom1 levels emanating from cell tips only reaches the cell centre to overlap with Cdr2 in small cells. When cells reach a threshold size, Pom1 no longer inhibits Cdr2, resulting in Wee1 inhibition and hence mitotic entry. Consistent with this, both groups found that expressing Pom1 at higher levels in the middle of the cell can trigger a delay in mitotic entry.

Thus, these studies provide an elegant example of how the intracellular gradient of a polarity protein can regulate a cell size checkpoint. AS

oskar moved by myosin V

In *Drosophila* oocytes, posterior accumulation of *oskar* mRNA is required for embryonic development. *oskar* localization requires the microtubule-based motor kinesin, but the precise mechanism is unclear. Ephrussi and colleagues now demonstrate that the actin-based motor myosin V has two functions in oocyte polarization: it directly modulates kinesin activity and it targets *oskar* mRNA to the posterior cortex (*Curr. Biol.,* doi:10.1016/j.cub.2009.04.062). A previous screen identified mutants with anterior–posterior patterning defects, which are now shown to be due to mutations in the myosin V gene, *didium*. Both *oskar* mRNA and Staufen, which mediates posterior oskar localization, are mislocalized in *didium*-mutant oocytes, or when dominant-negative myosin V peptides are expressed. Genetic experiments suggest that kinesin activity is upregulated when myosin V is deficient, which may cause accumulation of *oskar* mRNA in the middle of the oocyte. Consistent with the direct regulation of kinesin, myosin V is found to interact with kinesin, confirming data from mammalian cells. Myosin V also colocalizes with *oskar* mRNA at the posterior cortex, biochemically interacts with *oskar* mRNA and is required for the cortical localization of *oskar* mRNA and protein. Thus, in addition to the microtubule-based and kinesin-dependent cytoplasmic transport mechanism, *oskar* mRNA is translocated to the posterior cortex in an actin-based and myosin V-dependent manner. CKR

Chemical iPS cocktails

Overexpression of the transcription factors Oct4, Sox2 and either Klf4, c-Myc or Nanog, Lin28 is sufficient to reprogram somatic cells into embryonic stem (ES) cell-like induced pluripotent stem (iPS) cells. Whereas fine-tuning culture conditions has obviated the requirement for c-Myc, the other potentially oncogenic factors still have to be overexpressed from viral vectors, limiting clinical applications. Transient transfection and excisable vectors also represent viable approaches, albeit less efficient ones. A number of recent studies have identified small-molecule compounds that allow efficient iPS induction with only Oct4 and either Klf4 or Sox2, raising the possibility that a chemical cocktail can be derived that allows iPS induction in a more clinically relevant setting. The laboratories of Jaenisch and Schultz now report the results of a screen of 500,000 compounds designed to select for replacements for Klf4 (*Proc. Natl Acad. Sci. USA* **106,** 8912–8917; 2009). The broad-spectrum kinase inhibitor kenpaullone in combination with Oct4, Sox2 and c-Myc yielded iPS cells that were indistinguishable from ES cells. siRNA depletion of combinations of known kenpaullone targets did not reproduce the effect. Although the compound is less efficient and does not completely recapitulate the role of Klf4 overexpression, future screens to replace Oct4 may provide a chemical protocol for iPS generation. BP

Viral-induced polyadenylation mediates decay

mRNA polyadenylation usually correlates with increased mRNA stability in metazoan eukaryotes, but has been linked to mRNA decay in *Escherichia coli* and yeast. Herpesviruses induce a global shut-off of their hosts transcriptome to evade immune surveillance and the Kaposi's herpesviral protein SOX (shut off and exonuclease) mediates global mRNA decay in eukaryotic cells, although it has no homology to ribonucleases. Glaunsinger and colleagues now show that SOX induces aberrant mRNA polyadenylation to stimulate transcriptome turnover (*PLoS Biol.,* doi:10.1371/journal.pbio.1000107).

The authors observed that SOX expression in cells triggers polyadenylation and rapid turnover of the *GFP* (green fluorescent protein) mRNA reporter. Knockdown of polyA polymerase (PAPII) by siRNA impairs *GFP* mRNA hyperadenylation and SOX-induced decay. In addition, SOX promotes the relocation of the cytoplasmic polyA-binding protein PAPBC to the nucleus, correlating with the destabilization of the cytoplasmic *GFP* mRNA, and siRNA silencing of *PAPBC* prevents SOX action.

Thus, the Kaposi herpesvirus uses a new mechanism based on aberrant polyadenylation to trigger host transcriptome shut-off. How exactly SOX regulates PAPBC relocation and how viral mRNA escapes this process will be the focus of future studies. NLB

By Nathalie Le Bot, Bernd Pulverer, Christina Karlsson Rosenthal, Alison Schuldt and Sowmya Swaminathan

nature cell biology

Arabidopsis cortical microtubules position cellulose synthase delivery to the plasma membrane and interact with cellulose synthase trafficking compartments

Ryan Gutierrez[1,2], Jelmer J. Lindeboom[3], Alex R. Paredez[4], Anne Mie C. Emons[3,5] and David W. Ehrhardt[1,2,6]

Plant cell morphogenesis relies on the organization and function of two polymer arrays separated by the plasma membrane: the cortical microtubule cytoskeleton and cellulose microfibrils in the cell wall. Studies using *in vivo* markers confirmed that one function of the cortical microtubule array is to drive organization of cellulose microfibrils by guiding the trajectories of active cellulose synthase (CESA) complexes in the plasma membrane, thus orienting nascent microfibrils. Here we provide evidence that cortical microtubules also position the delivery of CESA complexes to the plasma membrane and interact with small CESA-containing compartments by a mechanism that permits motility driven by microtubule depolymerization. The association of CESA compartments with cortical microtubules was greatly enhanced during osmotic stress and other treatments that limit cellulose synthesis. On recovery from osmotic stress, delivery of CESA complexes to the plasma membrane was observed in association with microtubule-tethered compartments. These results reveal multiple functions for the microtubule cortical array in organizing CESA in the cell cortex.

Plant cells have microtubule arrays that are organized without a centrosome or other central organizing body. Acentrosomal arrays are common in many organisms, including mammals, but the mechanisms by which these arrays are organized and their precise cellular functions are often poorly understood[1]. In plant cells undergoing axial growth, interphase microtubules form highly organized arrays at the cell cortex, with microtubules lying in parallel to the plasma membrane and transverse to the cell's axis of elongation, as both single and bundled polymers[2,3]. New polymers arise from dispersed nucleation sites in the cell cortex and show dynamics at both polymer ends that result in net migration of microtubules in the direction of their plus ends, thus creating a highly dynamic array that undergoes constant remodelling[3,4]. Disruption of microtubule organization by genetic or pharmacological means has demonstrated that these arrays are essential for acquisition of differentiated cell shape[5]. A central question in plant cell development is how these distinctive microtubule arrays function to guide cell morphogenesis.

It has long been hypothesized that one essential function of the cortical microtubule array is to control the material anisotropy of the cell wall by interacting with CESA complexes to guide the orientation of cellulose microfibrils, the key load-bearing constituent of the cell wall[6–8]. CESA complexes are molecular machines thought to be composed of 36 catalytic subunits and arranged in symmetrical rosettes with diameters of 25–30 nm, as observed in freeze-fractured plasma membranes[9–13]. In *Arabidopsis thaliana*, genetic studies have suggested that simultaneous expression of at least three of ten isoforms is necessary for a functional complex, with *CESA1*, *3* and *6* being involved in primary cell wall synthesis[14–16]. A functional YFP::CESA6 fusion protein revealed a patterned distribution of active CESA complexes in the plasma membrane, which localized to and tracked along individual elements of the cortical microtubule array[17]. Changes in microtubule organization were observed to precede changes in the organization of CESA complexes in the plasma membrane, confirming the microtubule guidance hypothesis for cellulose deposition.

Although dynamic YFP-labelled CESA complexes are observed to be positioned along cortical microtubules[17], it is not known how CESA is delivered to the plasma membrane and how this association is established. Are CESA complexes delivered at addresses defined by cortical microtubules, or are they delivered at random locations, subsequently forming associations with cortical microtubules? Rosettes have been observed by freeze-fracture electron microscopy in the membranes of vesicles and Golgi cisternae, suggesting that CESA complexes are assembled before they reach the plasma membrane[18]. Consistent with this observation, YFP::CESA6 protein prominently labels Golgi bodies and also labels a population of smaller compartments[17], henceforward termed small CESA compartments (SmaCCs). Here we have used live-cell imaging of labelled CESA and tubulin proteins to investigate the role of the cortical microtubule cytoskeleton in the spatial control of CESA trafficking and delivery to the plasma membrane of *Arabidopsis*.

[1]Department of Plant Biology, Carnegie Institution for Science, 260 Panama St, Stanford, CA 94305, USA. [2]Department of Biology, Stanford University, Stanford, CA 94305, USA. [3]Laboratory of Plant Cell Biology, Wageningen University, Droevendaalsesteeg 1, 6708 PB Wageningen, The Netherlands. [4]Department of Molecular and Cellular Biology, University of California, Berkeley, CA 94720, USA. [5]Department of Biomolecular Systems, FOM Institute for Atomic and Molecular Physics, Kruislaan 407, 1098 SJ Amsterdam, The Netherlands.
[6]Correspondence should be addressed to D.W.E. (e-mail: ehrhardt@stanford.edu)

Received 31 March 2009; accepted 20 May 2009; published online 14 June 2009; DOI: 10.1038/ncb1886

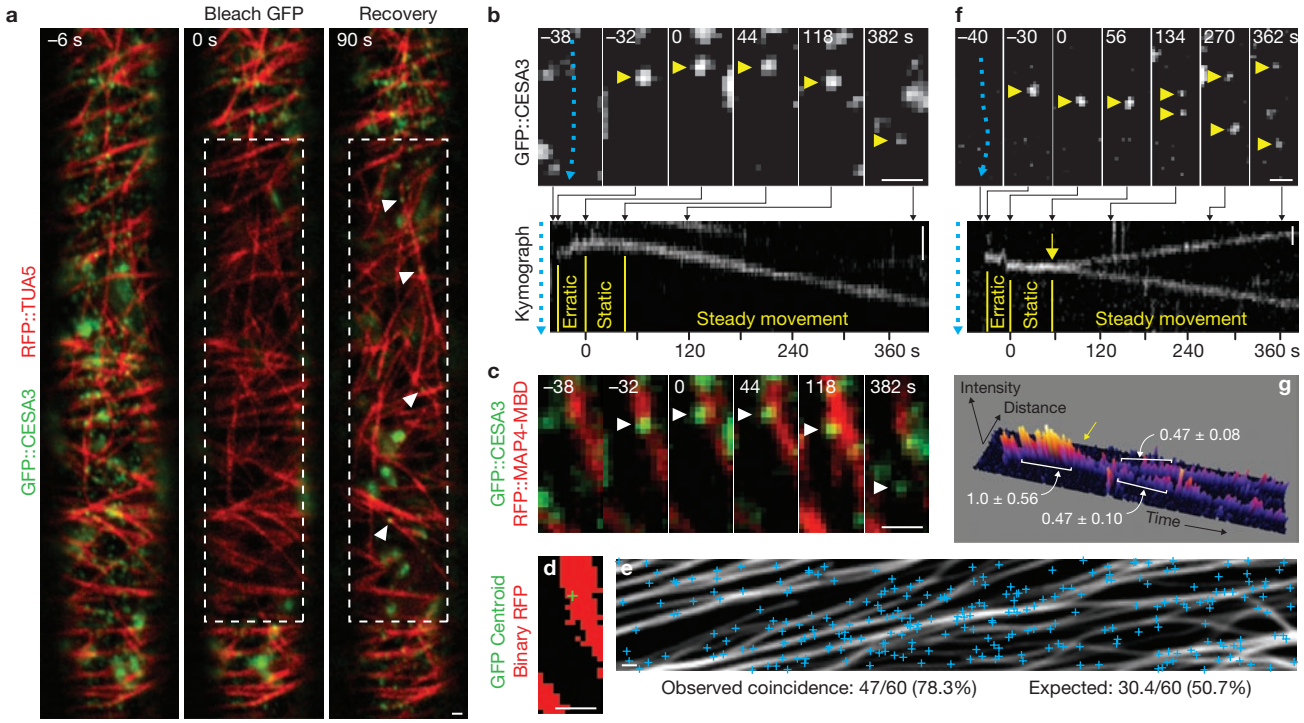

Figure 1 Delivery of CESA complexes to the plasma membrane is coincident with microtubules. *Arabidopsis* seedlings expressing markers for CESA (GFP::CESA3) and microtubules (mCherry::TUA5 or mCherry::MAP4–MBD) were grown in the dark for 3 days. Epidermal cells in the upper hypocotyl were imaged by confocal microscopy at 2-s intervals. (**a**) Photobleaching was used to visualize delivery of GFP-labelled CESA complexes (arrowheads). A delivery rate of 4.8 events μm^{-2} h^{-1} was measured from observations of 811 events in 3 cells from 3 seedlings. (**b**) Delivery of a GFP::CESA3 particle. The CESA particle (arrowhead) undergoes three stages of behaviour seen on a kymograph taken along its path of movement (cyan line): erratic motility, static localization and steady movement. (**c**) Colocalization of the GFP::CESA3 particle in **b** with a microtubule. (**d**) Determination of coincidence between a CESA complex delivery site and microtubules. At the start of the static phase ($t = 0$), the centroid of the particle (cross) is coincident with the thresholded microtubule signal. (**e**) Map of CESA complex delivery sites in one cell overlaid on a 10-min average projection of microtubule signal (mCherry::MAP4–MBD). This panel illustrates the relationship of the two patterns without correction for microtubule dynamics. Sixty delivery events (from 3 cells) were analysed for colocalization of CESA insertion into the plasma membrane with cortical microtubules as in **d**; results are summarized in the panel. Events of CESA complex appearance were associated with microtubules at a frequency significantly higher than chance ($P < 0.001$, binomial test). (**f**) Delivery of multiple CESA particles at the same time and position. A GFP::CESA3 particle arrives at the plasma membrane and splits into two punctae, seen as bifurcation of signal (yellow arrow) on the kymograph taken along the cyan line. (**g**) Surface plot of kymograph in **f**. Mean intensity above background was measured along the trunk (before split) and both branches (after split) and reported as relative values ± s.d. Each daughter particle contains roughly half the intensity of the original particle. A yellow arrow marks the bifurcation point. Scale bars, 1 μm.

RESULTS

Observation of CESA complex delivery events to the plasma membrane

Epidermal cells in the upper hypocotyl of seedlings expressing pCESA3::GFP::CESA3 to label cellulose synthase complexes, and either 35S::mCherry::TUA5 or 35S::mCherry::MAP4-MBD to label cortical microtubules, were observed by spinning disk confocal microscopy (Fig. 1). To more easily reveal newly delivered CESA complexes, we bleached existing GFP::CESA3 in a large region of the plasma membrane. Delivery events had to meet two criteria: first, *de novo* appearance of a GFP::CESA3 puncta in the optical plane of the plasma membrane that could not be attributed to migration of existing plasma membrane localized complexes or a focal shift, and second, steady movement in subsequent frames consistent with active CESA complexes[14,15,17,19,20] (Fig. 1; Supplementary Information, Movie 1). On the basis of these criteria, 4.8 ± 0.7 CESA-complex delivery events μm^{-2} h^{-1} were observed.

Individual delivery events typically showed three phases of behaviour. First, in most events (37 of 60), a labelled particle appeared in the focal plane and showed erratic motility with rapid and short dislocations (Fig. 1b, f; Supplementary Information, Movies 2, 3). Second, the particle stabilized and remained in a fixed position for 62 ± 23 s ($n = 60$ events). Finally, the particle was observed to move at a slow and steady velocity of approximately 200–400 nm min^{-1}, typically on a linear path. In some cases (7 of 60), a bifurcation of signal was seen to coincide with the onset of steady motility (Fig. 1f), with daughter particles moving in opposite directions and with approximately half the intensity each of the initial, stabilized particle (Fig. 1g). We interpret these events to be consistent with arrival of a trafficking compartment with erratic motility behaviour in the optical plane and the subsequent delivery of one or two CESA complexes with slow and steady motility behaviour. From these observations alone, it is not known whether the static phase represents stabilization of the delivering compartment adjacent to the plasma membrane or whether it represents CESA complexes that have been inserted into the plasma membrane but have yet to synthesize enough cellulose to drive complex motility[17,19].

CESA complexes are delivered at sites coincident with microtubules

The positions of all delivery events within a sub-region of the bleached area were determined for the first 10 min of fluorescence recovery. These

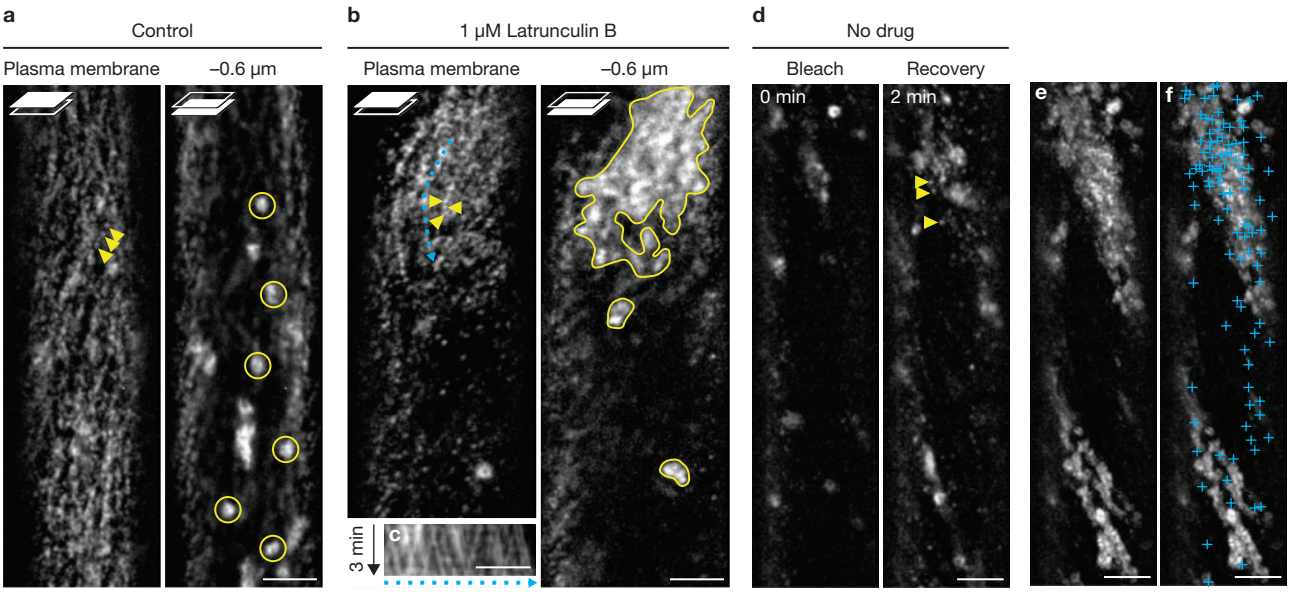

Figure 2 CESA complex delivery is correlated with cortical Golgi body distribution. (**a**, **b**) Latrunculin B induces stable clustering of Golgi bodies and active CESA complexes. Seedlings expressing YFP::CESA6 were treated with 0.05% DMSO (**a**) or latrunculin B (1 μM) in 0.05% DMSO (**b**) for 4 h. After latrunculin B treatment for 4 h, cytoplasmic streaming was severely diminished. Focal planes at the plasma membrane and lower cell cortex are shown. In cells treated with latrunculin B, the non-uniform distribution of CESA complexes (arrowheads) in the plasma membrane coincided with underlying Golgi bodies (circled) in the cell cortex. (**c**) Kymograph along the cyan trace in **b**. Particles show slow (~300 nm min^{-1}) and steady velocities, consistent with motility of active CESA complexes. (**d**–**f**) Transient clustering of Golgi bodies in the cell cortex leads to spatially concentrated delivery of CESA complexes to the plasma membrane. (**d**) GFP::CESA3 signal in a cell was bleached. After 2 min, labelled CESA complexes (arrowheads) accumulated non-uniformly. (**e**) A 2-min brightest point projection (61 frames) of GFP signal in **d**. (**f**) Map of CESA complex delivery sites overlaid on **e**. Cortical regions visited by Golgi bodies (light areas) show a higher density of deliveries (crosses) than regions bereft of Golgi bodies (dark areas). Scale bars, 5 μm.

positions were defined as the centroids of GFP::CESA3 particles during the static phase of delivery (Fig. 1e). Sixty delivery events were then mapped onto segmented images of mCherry::MAP4–MBD (Fig. 1d, e). Forty-seven events (78%) were observed to be coincident with microtubules, a frequency significantly greater than the 30 events expected by chance alone ($P < 0.001$, binomial test). Thus, CESA complexes are preferentially delivered to the plasma membrane at sites coincident with microtubules.

To determine whether CESA delivery to the plasma membrane requires microtubule function, we measured the rate of delivery events in cells treated with the microtubule depolymerizing drug oryzalin. A delivery rate of 4.2 ± 1.3 events $\mu m^{-2}\ h^{-1}$ was observed ($n = 3$ cells from 3 seedlings), a rate not significantly different from that in controls ($P = 0.57$, t-test). Therefore, cortical microtubules seem to guide CESA complex delivery, but they are not required for the act of delivery.

Perturbation of actin disrupts the global distribution of CESA at the plasma membrane

Wightman and Turner reported recently that in xylem vessels, actin filaments—not microtubules—mark CESA delivery sites at the cell surface[21]. To investigate the role actin might have in CESA distribution in epidermal cells, we treated seedlings with 1 μM latrunculin B to disassemble the actin cytoskeleton. Cytoplasmic streaming was severely inhibited, as assayed by Golgi body motility, but YFP::CESA6 punctae characteristic of active complexes remained visible in the plasma membrane (Fig. 2b, c) indicating that delivery to the plasma membrane was not prevented. However, the global distribution of CESA complexes was severely disrupted and many cells showed large areas bereft of signal (Fig. 2a, b). A clumped distribution of Golgi bodies was observed in these cells, which showed close correlation with the patchy CESA signal at the plasma membrane (Fig. 2b). In control cells, patchy distribution of Golgi bodies was also observed occasionally for short periods lasting 1–3 min. Photobleaching recovery experiments revealed that CESA delivery in these cells was biased to regions of higher Golgi body density (Fig. 2d–f). Taken together, these results suggest that motility and distribution of Golgi bodies by the actin cytoskeleton[22] may be required for proper global organization and distribution of CESA complexes in the plasma membrane, whereas the microtubule cytoskeleton seems important for fine-scale positioning of CESA delivery.

Isoxaben and osmotic stress cause cortical tethering of SmaCCs

To explore CESA trafficking further, we examined the behaviour of Golgi bodies and SmaCCs. Golgi bodies, SmaCCs and active CESA complexes were distinguished by characteristic motility, morphology and localization (Fig. 3a–c). We had previously shown that the cellulose synthesis inhibitor isoxaben caused the rapid disappearance of YFP::CESA6 complexes from the cell surface[17]. When isoxaben treatment was carried out for longer periods of time, a striking additional response was observed: SmaCCs accumulated in the cell cortex (Fig. 3a, e) and showed a marked reduction in motility, with sustained episodes of positional stability (Fig. 3; Supplementary Information, Movie 4). Golgi bodies in the cell cortex (labelled with YFP::CESA6 or YFP::SYP32; ref. 23) also showed reduced motility (Fig. 3g; Supplementary Information, Movie 4). The disappearance of YFP:CESA6 punctae was accompanied by a quantitative loss of YFP signal from the plasma membrane (Supplementary Information, Fig. S1), indicating that isoxaben caused net removal of YFP::CESA6 from the membrane rather than simply dispersing the protein by disruption

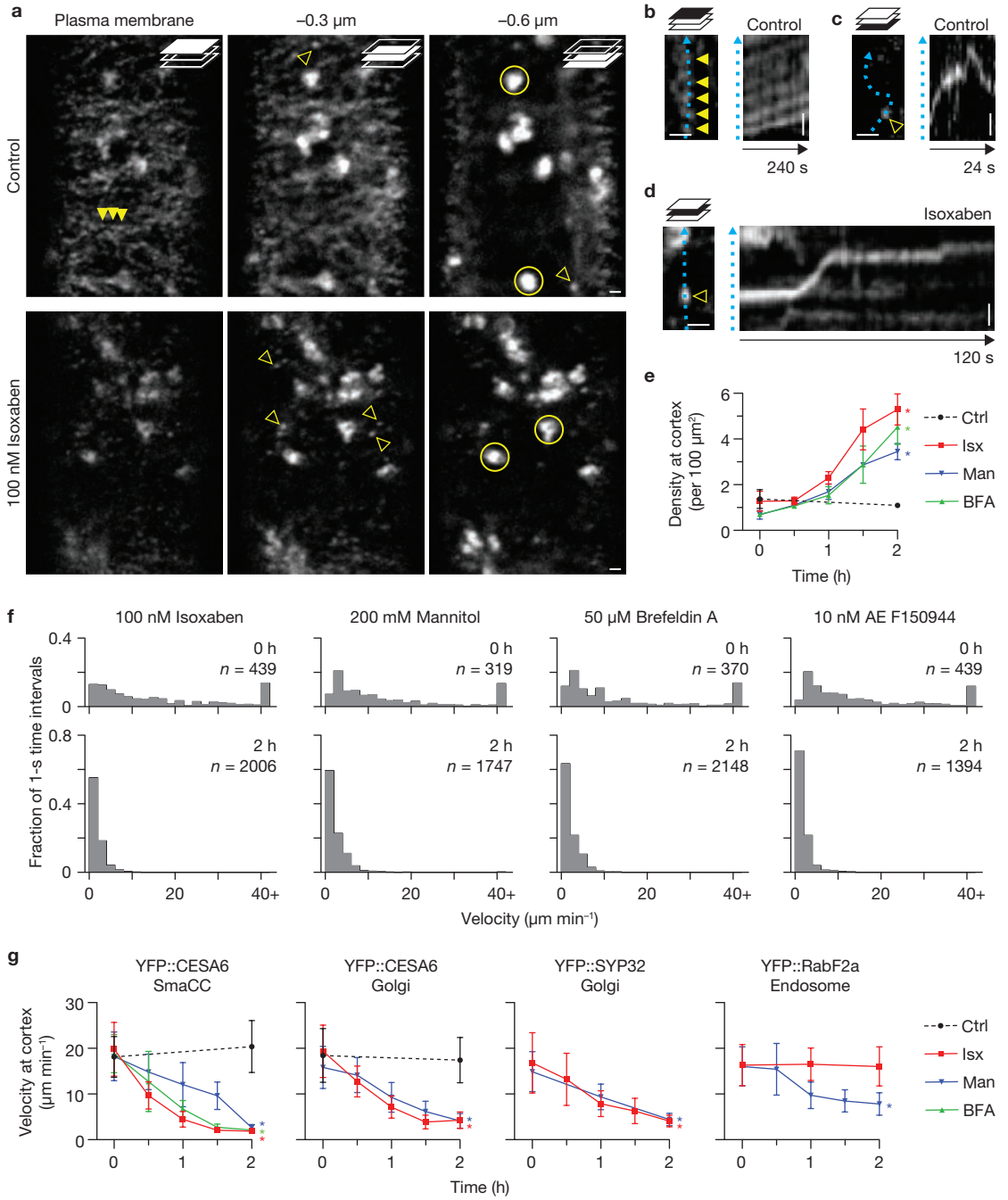

Figure 3 Isoxaben, osmotic stress and brefeldin A redistribute CESA protein and alter the location and dynamics of compartments containing CESA. (**a**–**f**) Seedlings expressing YFP::CESA6 were treated with 0.05% DMSO (control), 100 nM isoxaben in 0.01% DMSO, 200 mM mannitol, 50 µM brefeldin A in 0.05% DMSO or 10 nM AE F150944 in 0.01% DMSO for 2 h. (**a**) Confocal *z*-series of the cell cortex. Propidium iodide staining of the cell wall provided a fiducial marker for the start of the series. In controls, YFP punctae (closed arrowheads) corresponding to active CESA complexes are visible in the plasma membrane. Lower optical planes reveal Golgi bodies (circled) and small CESA compartments (SmaCCs, open arrowheads). Isoxaben removed most punctae from the plasma membrane and caused accumulation of labelled organelles in the cell cortex. (**b**–**d**) Kymographs of YFP::CESA6 structures taken along cyan traces. In controls, punctae (**b**) travel at slow and constant rates, whereas SmaCCs (**c**) move at higher velocities and change directions frequently. (**d**) With isoxaben treatment, changes in SmaCC velocity and direction were less frequent, compared with **c**. (**e**) SmaCCs accumulate in the cortex under treatment with isoxaben, mannitol or brefeldin A. Measurements (mean ± s.e.m.) were taken from 3 cells (from 3 seedlings). (**f**) Histograms of SmaCC velocity in the cell cortex before and after chemical treatment, measured in the same 3 seedlings per treatment. (**g**) Organelle velocity in the cell cortex. Seedlings expressing the indicated fluorescent protein fusion were imaged, and velocity was measured for the indicated organelle. Time courses show the weighted average of $n = 18$ organelles in 3 cells from 3 seedlings (data are mean ± s.e.m.). Linear regression slopes significantly different than zero are marked with asterisks ($P < 0.05$). Scale bars, 1 µm.

of complex structure[13]. The cellular pathology of isoxaben treatment described above was mimicked by several other small molecules that disrupt cellulose biosynthesis (data not shown), including AE F150944 (ref. 24; Fig. 3f; Supplementary Information, Fig. S2).

As isoxaben and other cellulose synthesis inhibitors are pharmacological agents, we sought to determine whether there are physiological conditions that perturb CESA complex trafficking. Previous studies have shown that osmotic stress downregulates synthesis of cell wall polysaccharides, including cellulose[25], and rosettes were depleted in the plasma membrane of freeze-fractured plant cells that were not turgid[9]. Treatment with 200 mM mannitol, a concentration of osmoticum that did not induce plasmolysis (Supplementary Information, Fig. S3), caused cortical accumulation and tethering of SmaCCs (Fig. 3; Supplementary Information, Fig. S2, Movie 4). The density of punctae in the plasma membrane was also reduced, but the extent of this clearing was variable.

Although both isoxaben and osmotic stress caused tethering of SmaCCs and Golgi bodies in the cell cortex, the motility of endosomes labelled with YFP::RabF2a[26] was not affected by isoxaben and was slowed but not stopped by mannitol treatment (Fig. 3g). Furthermore, isoxaben did not alter the localization of the brassinosteriod receptor BRI1 (ref. 27) and the t-SNARE NPSN12 (ref. 28; Supplementary Information, Fig. S3), suggesting that the drug neither disrupts trafficking of plasma membrane proteins in general nor causes bulk internalization of plasma membrane proteins. Similarly, both of these markers remained at the plasma membrane during treatment with 200 mM mannitol, although some evidence for internalization of label was observed (Supplementary Information, Fig. S3). The effects of isoxaben and osmotic stress were reversible after a washout with water (Supplementary Information, Fig. S2). Together, these results suggest that isoxaben causes a specific perturbation in the localization and motility of compartments involved in the trafficking of CESA6, whereas osmotic stress causes a similar syndrome of responses but may affect membrane trafficking more generally.

Treatment with brefeldin A, which blocks secretion and other membrane trafficking events by inhibiting the Sec7/BIG class of guanine nucleotide exchange factors[29], also caused cortical SmaCC accumulation and tethering (Fig. 3; Supplementary Information, Fig. S2, Movie 4), suggesting that the responses observed with isoxaben and osmotic stress might be caused by specific disruption of membrane trafficking.

Osmotic stress inhibits CESA delivery to the plasma membrane

The disappearance of CESA label at the plasma membrane and the cortical accumulation of SmaCCs might be caused by a reduction in the rate of CESA complex insertion into the plasma membrane, stimulation of CESA complex recycling from the plasma membrane, or both. CESA delivery rate was reduced over 100-fold in cells treated with 200 mM mannitol for 3 h: 0.04 ± 0.04 events $\mu m^{-2}\ h^{-1}$ (5 cells, 5 seedlings), compared with 4.8 ± 0.7 events $\mu m^{-2}\ h^{-1}$ for controls (3 cells, 3 seedlings). Addressing the rate of internalization is more challenging, but experiments using the lipophilic tracer dye FM4-64 (ref. 30) showed that dye endocytosed after initial mannitol treatment did not label SmaCCs, although SmaCCs could be labelled after the dye had time to redistribute to other internal membranes, including Golgi bodies (Supplementary Information, Fig. S4).

Tethered SmaCCs colocalize with cortical microtubules

Time-lapse imaging revealed that cortically localized SmaCCs, which were often stationary, also showed saltatory movement along linear paths (Fig. 3d; Supplementary Information, Movie 4), a pattern of movement consistent with cytoskeletal motility. Imaging of cells expressing markers for both CESA and microtubules revealed that during treatment with isoxaben, mannitol or brefeldin A, cortically tethered SmaCCs were substantially colocalized with microtubules (Fig. 4a; Supplementary Information, Fig. S5a, Movies 5–8). Oryzalin treatment prevented accumulation of SmaCCs at the cell cortex (Fig. 4b), indicating that microtubules are also necessary for cortical tethering of SmaCCs.

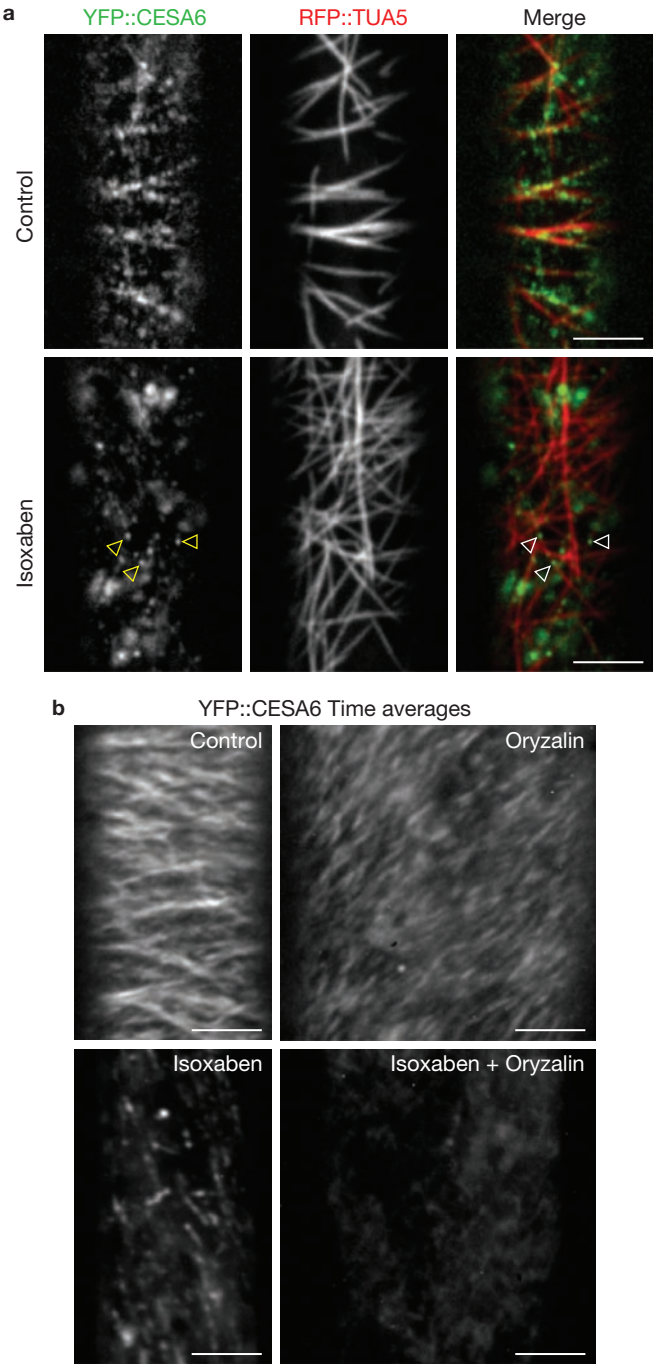

Figure 4 SmaCCs associate with cortical microtubules in cells treated with isoxaben. (**a**) Seedlings expressing YFP::CESA6 and mCherry::TUA5 were treated with 0.01% DMSO (control) or 100 nM isoxaben in 0.01% DMSO. SmaCCs (arrowheads) colocalize with microtubules. (**b**) Depolymerization of microtubules by oryzalin prevents cortical accumulation of CESA6 under isoxaben treatment. Seedlings expressing YFP::CESA6 were incubated in 0.01% DMSO + 0.1% methanol alone (control) or together with 100 nM isoxaben, 20 μM oryzalin or 100 nM isoxaben + 20 μM oryzalin for 8 h. Averages of 61 frames representing 5 min. Scale bars, 5 μm.

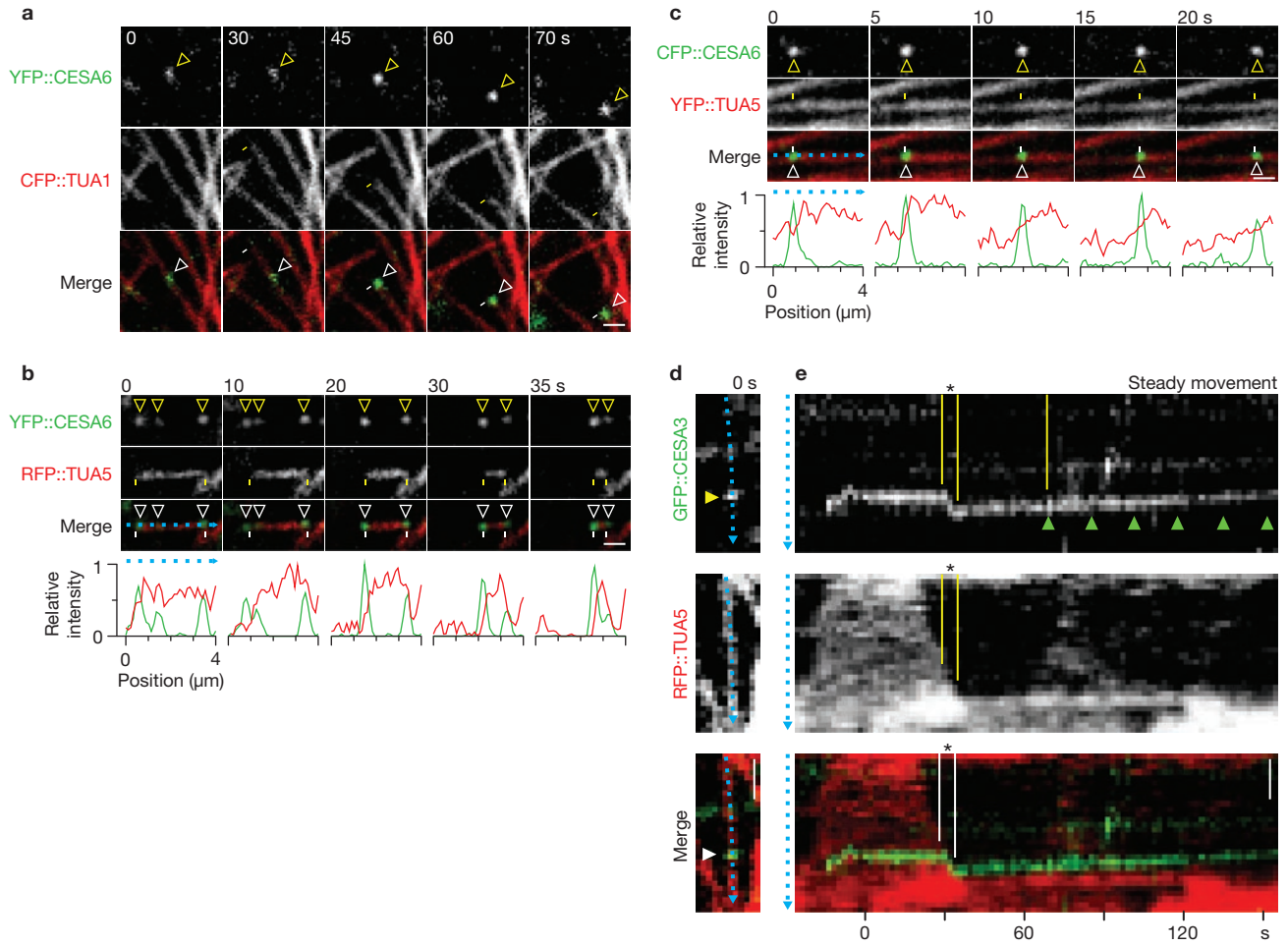

Figure 5 CESA tracks depolymerizing microtubule ends. (**a**–**c**) Cortically tethered SmaCCs frequently show tip-tracking behaviour during isoxaben treatment or osmotic stress. Time series showing dynamic association between SmaCCs (arrowheads) and microtubule ends (dashes). Seedlings expressing markers for CESA (green) and microtubules (red) were treated with 100 nM isoxaben or 200 mM mannitol. (**a**) A microtubule-associated SmaCC is initially stationary and then moves along the microtubule when encountering a depolymerizing microtubule end. (**b**) SmaCCs track with the depolymerizing plus and minus ends of the same microtubule. Two SmaCCs on the left are collected on the depolymerizing end. The increase in CESA signal suggests that both compartments maintain association with the depolymerizing end. (**c**) A SmaCC moves with a shrinking microtubule end in a microtubule bundle. For **b** and **c**, intensity from both channels was measured along the cyan trace for each time point. (**d**, **e**) CESA undergoes brief tip-tracking events under normal conditions. A labelled CESA complex is delivered to the plasma membrane in the absence of drugs. (**d**) Still images at $t = 0$ showing GFP::CESA3 (arrowhead) and an associated microtubule. (**e**) Kymograph along the cyan trace in **a**. The static phase of CESA complex delivery is interrupted by a depolymerizing microtubule end. GFP::CESA3 moves with the depolymerizing end for several frames (*), becomes static again and then moves steadily. Green arrowheads mark the position of GFP::CESA3 where steady movement starts. The transitory nature of the tip-tracking event makes it difficult to identify the tracking object as a SmaCC or possibly a membrane-embedded CESA complex, although the former possibility is the more parsimonious hypothesis. Scale bars, 1 μm.

SmaCC motility is driven by depolymerizing microtubule ends

To further elucidate SmaCC behaviour, we analysed the joint dynamics of microtubules and 50 SmaCCs from 8 cells treated with isoxaben. Only SmaCCs that were traceable for at least five continuous frames (that is, 20 s) were analysed. SmaCCs moved along paths defined by microtubules 43.0% of the time, were stationary and coincident with a labelled microtubule for 55.1% of the time (frame-to-frame displacement <50 nm s^{-1}), and were not associated with microtubules 1.9% of the time. Of the SmaCCs observed to move, 37 moved processively in coincidence with depolymerizing ends (Fig. 5a; Supplementary Information, Movie 9). Of the remaining 14, 9 were stationary and the other four showed movement along microtubule bundles where individual polymers and polymer ends could not be distinguished (see below). In this data set and others, comprising at least 100 observations, SmaCCs were never observed to move along the lattice of an unambiguously single microtubule—a behavior characteristic of translocation by motor proteins such as kinesins—or to track with growing polymer ends. To further test whether SmaCC motility was driven by microtubule depolymerization, microtubules were stabilized by taxol. SmaCC velocity was reduced significantly (Supplementary Information, Fig. S5b, c), indicating that SmaCCs require dynamic ends for microtubule-dependent motility. Observation of tip-tracking motility suggests that tethered SmaCCs are physically associated with microtubules.

Multiple SmaCCs associated with the same microtubule were observed to be collected by depolymerizing ends (Fig. 5b; Supplementary Information, Movie 10), with total signal increasing in a stepwise fashion with the addition of each SmaCC. The movement of SmaCCs associated with depolymerizing ends was not confined to single cortical microtubules, but was also observed within microtubule bundles (Fig. 5c; Supplementary Information, Movie 11), suggesting that the architecture of bundles does not prevent this form of organelle motility. Finally, SmaCCs were observed

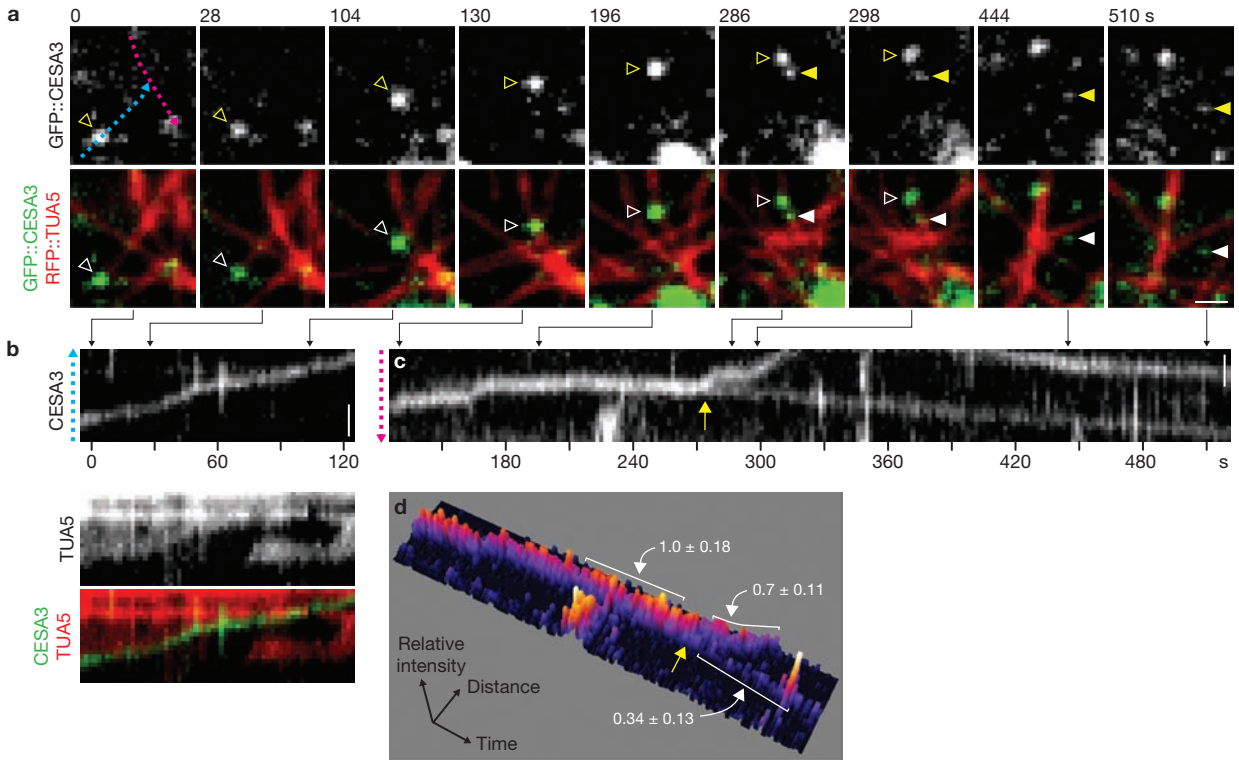

Figure 6 SmaCCs are associated with CESA complex delivery to the plasma membrane. (**a**–**c**) Seedlings were treated with 200 mM mannitol for 3 h and then washed with water for 0.5 h. (**a**) A SmaCC (open arrowhead) tracks a depolymerizing microtubule end for the first 120 s and then jumps to an adjacent microtubule. At 274 s, the SmaCC begins to split into two structures of unequal intensity. The brighter compartment (open arrowhead) leaves the focal plane (at 314 s) in a manner consistent with SmaCC motility. The dimmer compartment (closed arrowhead) moves at a slow and steady velocity, consistent with CESA complex motility in the plasma membrane. (**b**) Kymograph along the cyan line in **a**, showing prolonged tip-tracking by the SmaCC. (**c**) Kymograph along the magenta line in **a**, showing the SmaCC-associated delivery event. A yellow arrow marks the bifurcation point. (**d**) Surface plot of **c**. Mean intensity above background was measured in the indicated regions and reported as relative values ± s.d. A yellow arrow marks bifurcation. The sum of signal intensity from both branches roughly equals the trunk, suggesting both daughter particles originated from the same structure. Scale bars, 1 μm.

to track both plus and minus ends of microtubules (Fig. 5b), indicating that these organelles use a mechanism of microtubule end tracking motility that is independent of polarity.

Observation of sustained interaction of SmaCCs with cortical microtubules was uncommon in cells under normal conditions, but close examination of image sequences acquired at 2-s intervals revealed brief microtubule tip-tracking events (6 events in 4 cells from 4 seedlings; Fig. 5d, e; Supplementary Information, Fig. S6, Movie 12).

CESA delivery is associated with microtubule-tethered SmaCCs

To explore the functional nature of tethered SmaCCs, we followed the fate of CESA protein as osmotic stress was lifted. We observed two classes of events in these experiments. First, we observed CESA complex delivery associated with microtubule-tethered SmaCCs (n = 18 events in 7 cells; Fig. 6; Supplementary Information, Fig. S7, Movie 13). These SmaCCs could show microtubule tip-tracking behaviour before complex delivery (Fig. 6). Second, we observed the successive break-up of SmaCCs into more numerous and less bright cytoplasmic components. These break-up products did not show the slow, steady and constrained trajectories of active CESA complexes but rather, the more erratic motility behaviour of SmaCCs (Fig. 7; Supplementary Information, Movie 14). As 'collection' behaviour of SmaCCs was often observed (Fig. 5b), it is possible that these break-up events represent the dispersal of tethered SmaCC aggregates.

Microtubule-associated SmaCCs are heterogeneous in identity

The observations consistent with quantitative delivery of one or two CESA complexes under normal conditions (Figs 1, 5d, e) suggest that these compartments are large enough to contain 1 or 2 CESA complexes and thus are probably vesicular. Some Golgi bodies were observed to associate with SmaCCs under normal conditions and to show physical tethering to microtubule-associated SmaCCs during osmotic stress or isoxaben treatment (Supplementary Information, Fig. S8, Movie 15). Consistent with these observations, three putative markers for the *trans*-Golgi network—SYP41, SYP42 and SYP61[23,31]—showed significant overlap with freely motile SmaCCs under both normal conditions and during osmotic stress or isoxaben treatment. However, the population of cortically-tethered SmaCCs showed no significant colocalization with SYP41 or SYP42, although a minority (20 of 60 in 3 cells) colocalized with SYP61 (Fig. 8; Supplementary Information, Fig. S9). Thus, microtubule-associated SmaCCs seem to constitute a heterogeneous population of organelles. A survey of 9 additional fluorescent markers for various endomembrane structures did not reveal a definitive marker for most of the tethered SmaCCs (Supplementary Information, Table 1 and data not shown). Further elucidation of SmaCC diversity will probably require isolation of SmaCCs and analysis of constituent proteins other than CESA.

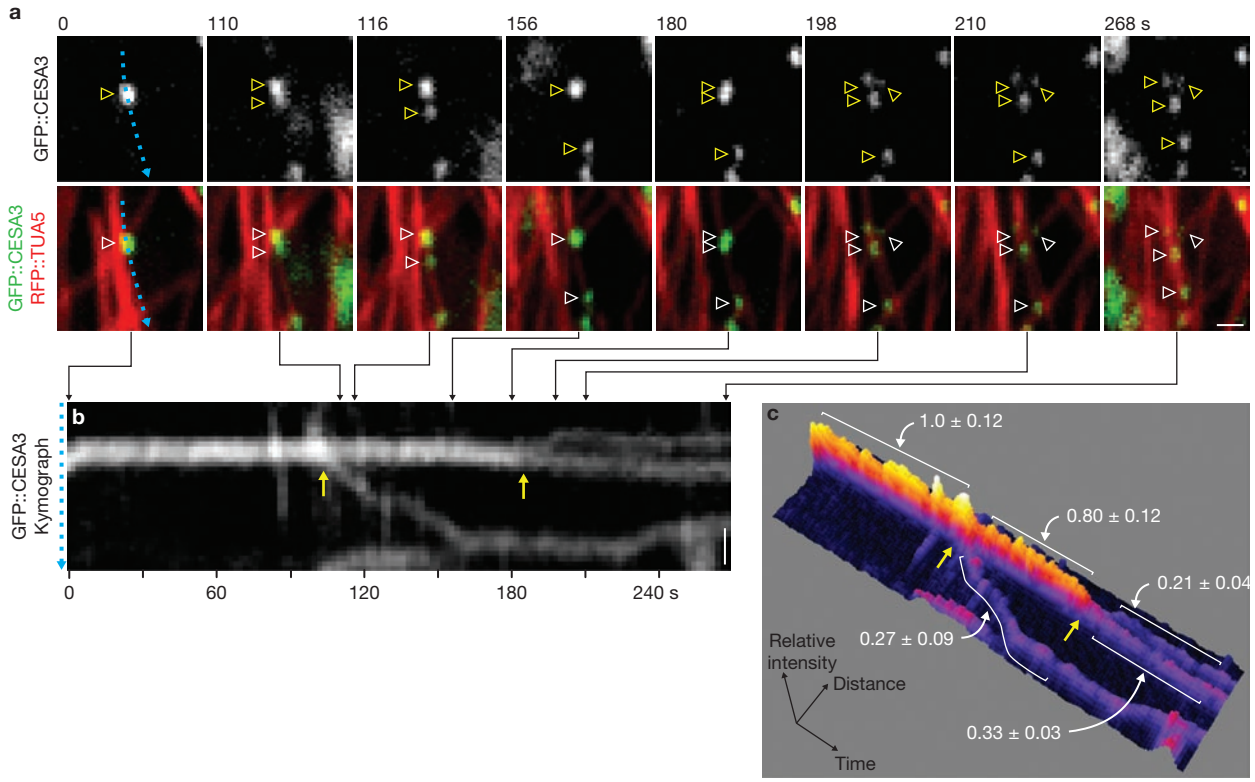

Figure 7 Successive break-up of one SmaCC into multiple cytoplasmic compartments. Seedlings were treated with 200 mM mannitol for 3 h and then washed with water for 0.5 h. (**a**) A SmaCC (arrowhead) splits into two compartments, clearly visible at 116 s. The brighter daughter SmaCC then proceeds to split into 3 compartments, clearly visible at 198 s. All structures show motility characteristic of SmaCCs. (**b**) Kymograph along the cyan trace in **a**. Yellow arrows mark the bifurcation events. (**c**) Surface plot of **b**. Mean intensity above background was measured in the indicated regions and reported as relative values ± s.d. Yellow arrows mark the bifurcation points. The sum of intensity values after each bifurcation event roughly equals the intensity of the originating compartment. The second break-up event has three daughter particles, only two of which move along the kymograph trace in **a**. Mean intensity for the third daughter particle, measured along a different kymograph line, is 0.18 ± 0.05. Scale bars, 1 μm.

DISCUSSION

Interphase microtubule arrays have important roles in the vectorial trafficking of membranes and proteins in many organisms, but the function of the acentrosomal cortical array of higher plant cells in trafficking and targeting has remained little explored. Bundles of cortical microtubules have long been observed to underlie thickenings in specialized secondary cell walls[32,33] and recently were shown to colocalize with mucilage secretion in seed coat cells[34]. Here we assayed protein delivery by observing single delivery events of CESA complexes to the plasma membrane and found that most of the newly arrived complexes were optically coincident with labelled microtubules. This result suggests two possible mechanisms. First, microtubules might interact with and organize exocytotic machinery, creating a pattern of vesicle docking sites that is coincident with the microtubule array. Second, CESA-containing delivery compartments might preferentially dock and pause at microtubules, as actinomyosin-driven cytoplasmic streaming carries them through the cortex, thus promoting interaction with export sites located adjacent to microtubules. These models are not mutually exclusive. Support for the latter mechanism is provided by our observations of SmaCC interaction with cortical microtubules and of CESA delivery events coinciding with microtubule-associated SmaCCs during recovery from osmotic stress. Although sustained pausing of SmaCCs on microtubules was not observed in untreated cells, observation of brief tip-tracking events suggest that perturbations of CESA activity might cause prolongation of a SmaCC–microtubule interaction that is normally short-lived.

Two classes of hypotheses can be envisioned for the function of microtubule-dependent positioning of CESA delivery to the plasma membrane. Positioning of CESA delivery might ensure efficient association of CESA with cortical microtubules at the time of microfibril initiation. This mechanism would ensure that most microfibrils are initiated in the appropriate positions and orientations as determined by cortical microtubule array organization. Alternatively, microtubules might help to coordinate the location or timing of CESA delivery with other proteins or polysaccharides required for cell wall biogenesis.

The mechanism for SmaCC tethering to microtubules and tip-tracking motility seems to be unusual for a membranous compartment. SmaCC motility could possibly be driven by a tip-tracking kinesin[35]; however, the observation that both polymer ends are tracked would require two such motors with opposite polarity, each activated by depolymerization. The tip-tracking behaviour of SmaCCs more closely resembles the behaviour of the Dam1 complex in yeast[36], a part of the kinetochore required for chromosome segregation. The Dam1 complex forms a ring structure around microtubules, which move processively on depolymerizing microtubule ends *in vitro*[36]. Non-encircling Dam1 oligomers are also observed to track shrinking microtubule ends[37]. However, a search of the *Arabidopsis* genome reveals no clear Dam1 homologues. Biochemical and genetic investigations will be required to reveal if there are in fact dual motors acting on the same cargo, if there are other proteins that function similarly to

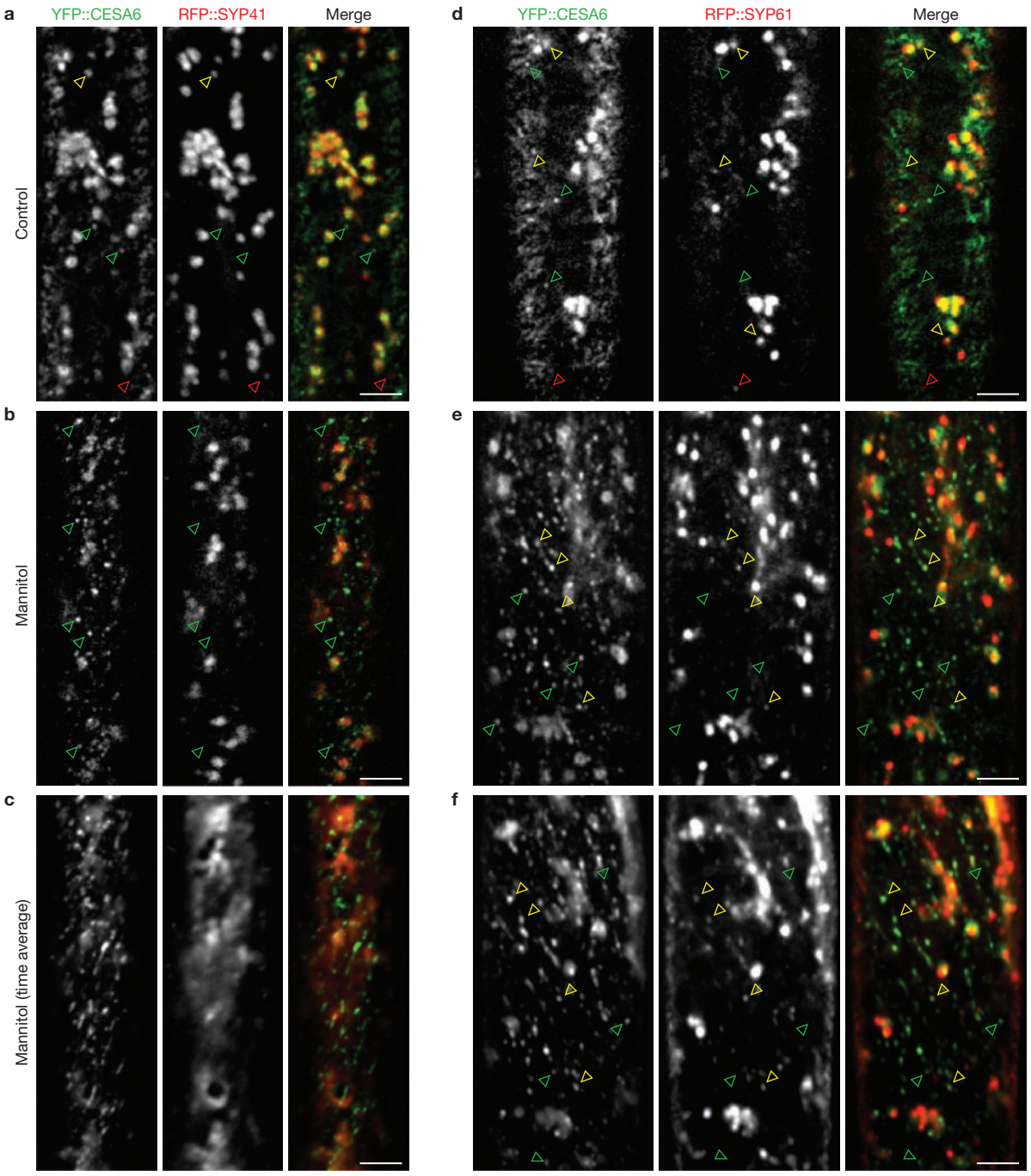

Figure 8 SYP41 and SYP61 label a subset of SmaCCs. (**a**–**f**) Seedlings expressing YFP::CESA6 and mCherry::SYP41 (**a**–**c**) or mCherry::SYP61 (**d**–**f**) were incubated in water (**a**, **c**) or 200 mM mannitol (**b**, **c**, **e**, **f**) for 3 h and imaged at the cell cortex. (**a**, **d**) Some small compartments are labelled with YFP only (green arrowheads), mCherry only (red arrowheads) or both (yellow arrowheads). (**b**, **c**) SYP41 fails to label cortically tethered SmaCCs (green arrowheads) after mannitol treatment. (**e**, **f**) SYP61 labels some tethered SmaCCs (yellow arrowheads) but not all (green arrowheads). Of 60 tethered SmaCCs, 20 were labelled by mCherry::SYP61 (observations from 3 cells from 3 mannitol-treated seedlings). These results suggest that SmaCCs are a heterogeneous population of membranous compartments, with one class being identified by SYP41 colocalization, a second by SYP61 colocalization and microtubule association, and a third class by the absence of SYP41/61 colocalization but with microtubule association. This latter class makes up the majority of observed SmaCCs that show sustained microtubule interaction. (**a**, **b**, **d**, **e**) Still images. (**c**, **f**) Averages of 61 frames representing 1 min. Scale bars, 5 μm.

Dam1, or if there is a new mechanism for microtubule-based motility waiting to be discovered.

Microtubule tip-tracking motility might help to distribute SmaCCs on the cell cortex, although prolonged cytoskeletal association of SmaCCs does not seem to be prevalent during normal cell growth. Another possibility is that motility is simply a consequence of a more fundamental microtubule attachment mechanism. Cortical microtubules are highly dynamic polymers that show treadmilling behaviour[4]. To maintain attachment to this

dynamic substrate, an organelle or vesicle must either be able to remain associated with a shrinking end or undergo quick re-association with another microtubule when depolymerization destroys the site of attachment. SmaCC movement on shrinking ends may therefore represent a mechanism for maintaining attachment to a treadmilling array.

The observation that cellulose biosynthesis inhibitors, osmotic stress and brefeldin A all caused cortical accumulation and tethering of SmaCCs suggests that these treatments may impinge on a common pathway regulating CESA trafficking. Previous work on osmotic stress provides a physiological context for this distinctive response. During severe osmotic stress, soluble sugars and amino acids accumulate at high intracellular concentrations to counteract water efflux[38], and the biosynthesis of cellulose and hemicellulose is reduced[25]. Our observations suggest that the CESA complex itself is depleted from the plasma membrane during this metabolic shift and that its insertion into the plasma membrane is inhibited. Sequestration of either recycled or outgoing CESA in cytoplasmic reservoirs adjacent to the cell surface might provide an effective mechanism of blocking cellulose biosynthesis to increase the cytosolic concentration of sugar precursors, as well as allow for efficient redeployment of CESA to the plasma membrane on relief from the stress. Evidence for such deployment was in fact observed during recovery from osmotic stress.

Here we present evidence that, in addition to guidance of CESA complexes, the cortical microtubule array also acts to position delivery of CESA complexes to the plasma membrane and interacts with CESA trafficking compartments. The relative contributions of these cortical array functions to plant cell growth and morphogenesis can now be investigated through use of the expanding collection of mutants and small molecule effectors that perturb cellulose synthesis and cell growth. □

METHODS

Methods and any associated references are available in the online version of the paper at http://www.nature.com/naturecellbiology/

Note: Supplementary Information is available on the Nature Cell Biology website.

ACKNOWLEDGEMENTS

We thank S. Vernhettes, E. Nielsen and N. Geldner for providing transgenic *Arabidopsis* seeds; V. Kirik for help with vector construction; B. Busse for modifying the ImageJ frame alignment plugin; and S. Debolt, V. Kirik, R. Brown, T. Ketelaar and H. Höfte for helpful discussions. This work was supported by grants from the National Science Foundation (0524334) and the EU Commission (FP6-2004-NEST-C1-028974).

AUTHOR CONTRIBUTIONS

R.G., J.L. and D.E. designed, carried out and analysed experiments; A.P. created the pCESA6::CFP::CESA6 and 35S::YFP::TUA5 transgenic lines; R.G. made all figures and movies; R.G., D.E. and A.M.E. wrote the manuscript.

COMPETING INTERESTS

The authors declare that they have no competing financial interest.

Published online at http://www.nature.com/naturecellbiology/
Reprints and permissions information is available online at http://npg.nature.com/reprintsandpermissions/

1. Bartolini, F. & Gundersen, G. G. Generation of noncentrosomal microtubule arrays. *J. Cell Sci.* **119,** 4155–4163 (2006).
2. Barton, D. A., Vantard, M. & Overall, R. L. Analysis of cortical arrays from *Tradescantia virginiana* at high resolution reveals discrete microtubule subpopulations and demonstrates that confocal images of arrays can be misleading. *Plant Cell* **20,** 982–994 (2008).
3. Ehrhardt, D. W. Straighten up and fly right: microtubule dynamics and organization of non-centrosomal arrays in higher plants. *Curr. Opin. Cell Biol.* **20,** 107–116 (2008).
4. Shaw, S. L., Kamyar, R. & Ehrhardt, D. W. Sustained microtubule treadmilling in *Arabidopsis* cortical arrays. *Science* **300,** 1715–1718 (2003).
5. Paradez, A., Wright, A. & Ehrhardt, D. W. Microtubule cortical array organization and plant cell morphogenesis. *Curr. Opin. Plant Biol.* **9,** 571–578 (2006).
6. Green, P. B. Mechanism for plant cellular morphogenesis. *Science* **138,** 1404–1405 (1962).
7. Heath, I. B. A unified hypothesis for the role of membrane bound enzyme complexes and microtubules in plant cell wall synthesis. *J. Theor. Biol.* **48,** 445–449 (1974).
8. Staehelin, L. A. & Giddings, T. H. Membrane mediated control of microfibrillar order, in *Developmental order, its origin and regulation*. (eds. S. Subtelny & P. B. Green) 133–147 (Alan R. Liss, New York; 1982).
9. Emons, A. M. Plasma-membrane rosettes in root hairs of *Equisetum hyemale*. *Planta* **163,** 350–359 (1985).
10. Herth, W. Arrays of plasma-membrane 'rosettes' involved in cellulose microfibril formation of *Spirogyra*. *Planta* **159,** 347–356 (1983).
11. Kimura, S. *et al.* Immunogold labeling of rosette terminal cellulose-synthesizing complexes in the vascular plant *Vigna angularis*. *Plant Cell* **11,** 2075–2086 (1999).
12. Mueller, S. C. & Brown, R. M., Jr Evidence for an intramembrane component associated with a cellulose microfibril-synthesizing complex in higher plants. *J. Cell Biol.* **84,** 315–326 (1980).
13. Somerville, C. Cellulose synthesis in higher plants. *Annu. Rev. Cell Dev. Biol.* **22,** 53–78 (2006).
14. Desprez, T. *et al.* Organization of cellulose synthase complexes involved in primary cell wall synthesis in *Arabidopsis thaliana*. *Proc. Natl Acad. Sci. USA* **104,** 15572–15577 (2007).
15. Persson, S. *et al.* Genetic evidence for three unique components in primary cell-wall cellulose synthase complexes in *Arabidopsis*. *Proc. Natl Acad. Sci. USA* **104,** 15566–15571 (2007).
16. Taylor, N. G., Howells, R. M., Huttly, A. K., Vickers, K. & Turner, S. R. Interactions among three distinct CESA proteins essential for cellulose synthesis. *Proc. Natl Acad. Sci. USA* **100,** 1450–1455 (2003).
17. Paredez, A. R., Somerville, C. R. & Ehrhardt, D. W. Visualization of cellulose synthase demonstrates functional association with microtubules. *Science* **312,** 1491–1495 (2006).
18. Haigler, C. H. & Brown, R. M. Transport of rosettes from the golgi apparatus to the plasma membrane in isolated mesophyll cells of *Zinnia elegans* during differentiation to tracheary elements in suspension culture. *Protoplasma* **134,** 111–120 (1986).
19. Debolt, S. *et al.* Morlin, an inhibitor of cortical microtubule dynamics and cellulose synthase movement. *Proc. Natl Acad. Sci. USA* **104 (14),** 5854–5859 (2007).
20. DeBolt, S., Gutierrez, R., Ehrhardt, D. W. & Somerville, C. Nonmotile cellulose synthase subunits repeatedly accumulate within localized regions at the plasma membrane in *Arabidopsis* hypocotyl cells following 2, 6-dichlorobenzonitrile treatment. *Plant Physiol.* **145,** 334–338 (2007).
21. Wightman, R. & Turner, S. R. The roles of the cytoskeleton during cellulose deposition at the secondary cell wall. *Plant J.* **54,** 794–805 (2008).
22. Nebenfuhr, A. *et al.* Stop-and-go movements of plant Golgi stacks are mediated by the acto-myosin system. *Plant Physiol.* **121,** 1127–1142 (1999).
23. Uemura, T. *et al.* Systematic analysis of SNARE molecules in *Arabidopsis*: dissection of the post-Golgi network in plant cells. *Cell Struct. Funct.* **29,** 49–65 (2004).
24. Kiedaisch, B. M., Blanton, R. L. & Haigler, C. H. Characterization of a novel cellulose synthesis inhibitor. *Planta* **217,** 922–930 (2003).
25. Iraki, N. M., Bressan, R. A., Hasegawa, P. M. & Carpita, N. C. Alteration of the physical and chemical structure of the primary cell wall of growth-limited plant cells adapted to osmotic stress. *Plant Physiol.* **91,** 39–47 (1989).
26. Preuss, M. L., Serna, J., Falbel, T. G., Bednarek, S. Y. & Nielsen, E. The *Arabidopsis* Rab GTPase RabA4b localizes to the tips of growing root hair cells. *Plant Cell* **16,** 1589–1603 (2004).
27. Friedrichsen, D. M., Joazeiro, C. A., Li, J., Hunter, T. & Chory, J. Brassinosteroid-insensitive-1 is a ubiquitously expressed leucine-rich repeat receptor serine/threonine kinase. *Plant Physiol.* **123,** 1247–1256 (2000).
28. Zheng, H. *et al.* NPSN11 is a cell plate-associated SNARE protein that interacts with the syntaxin KNOLLE. *Plant Physiol.* **129,** 530–539 (2002).
29. Nebenfuhr, A., Ritzenthaler, C. & Robinson, D. G. Brefeldin A: deciphering an enigmatic inhibitor of secretion. *Plant Physiol.* **130,** 1102–1108 (2002).
30. Bolte, S. *et al.* FM-dyes as experimental probes for dissecting vesicle trafficking in living plant cells. *J. Microsc.* **214,** 159–173 (2004).
31. Bassham, D. C., Sanderfoot, A. A., Kovaleva, V., Zheng, H. & Raikhel, N. V. AtVPS45 complex formation at the trans-Golgi network. *Mol. Biol. Cell* **11,** 2251–2265 (2000).
32. Hepler, P. K. & Newcomb, E. H. Microtubules and fibrils in the cytoplasm of coleus cells undergoing secondary wall deposition. *J. Cell Biol.* **20,** 529–532 (1964).
33. Oda, Y., Mimura, T. & Hasezawa, S. Regulation of secondary cell wall development by cortical microtubules during tracheary element differentiation in *Arabidopsis* cell suspensions. *Plant Physiol.* **137,** 1027–1036 (2005).
34. McFarlane, H. E., Young, R. E., Wasteneys, G. O. & Samuels, A. L. Cortical microtubules mark the mucilage secretion domain of the plasma membrane in *Arabidopsis* seed coat cells. *Planta* **227,** 1363–1375 (2008).
35. Wu, X., Xiang, X. & Hammer, J. A. 3rd. Motor proteins at the microtubule plus-end. *Trends Cell Biol.* **16,** 135–143 (2006).
36. Westermann, S. *et al.* The Dam1 kinetochore ring complex moves processively on depolymerizing microtubule ends. *Nature* **440,** 565–569 (2006).
37. Grishchuk, E. L. *et al.* Different assemblies of the DAM1 complex follow shortening microtubules by distinct mechanisms. *Proc. Natl Acad. Sci. USA* **105,** 6918–6923 (2008).
38. Handa, S., Bressan, R. A., Handa, A. K., Carpita, N. C. & Hasegawa, P. M. Solutes contributing to osmotic adjustment in cultured plant cells adapted to water stress. *Plant Physiol.* **73,** 834–843 (1983).

METHODS

Transgenic lines. All *Arabidopsis* lines were ecotype Columbia. Five lines were used for dual imaging of CESA and microtubules: 1) pCESA3::GFP::CESA3 and 35S::mCherry::TUA5, 2) pCESA3::GFP::CESA3 and 35S::mCherry::MAP4-MBD, 3) pCESA6::YFP::CESA6 and 35S::mCherry::TUA5, 4) pCESA6::CFP::CESA6 and 35S::YFP::TUA5 and 5) pCESA6::YFP::CESA6 and 35S::CFP::TUA1 (ref. 17). All lines produced similar results.

To generate all mCherry constructs, mCherry was amplified from a donor vector[39] with primers 5′-TTGGATCCATGGTGAGCAAGGGCGAGGA-3′, and 5′-GGTCCGGACTTGTACAGCTCGTCCATGC-3′, which contained *Bam*HI and *Bsp*EI sites, respectively. This fragment was cut with *Bam*HI and ligated to an HA tag containing a linker sequence. The HA tag was made using complementary oligonucleotides 5′-GGCCATGGGCTACCCATACGATGTTCCAGATTACGC-TTCACTAGGAGGACCTTCAG-3′ and 5′-GATCCTGAAGGTCCTCCTA-GTGAAGCGTAATCTGGAACATCGTATGGGTAGCCCATGGCC-3′, which featured flanking *Nco*I and *Bam*HI sites. The YFP sequence in the pEG104 binary vector[40] was then exchanged with the HA::mCherry fragment via *Nco*I and *Bsp*EI sites. TUA5, SYP41, SYP42 or SYP61 was amplified from Col-0 genomic DNA and inserted into the resulting vector using Gateway cloning technology (Invitrogen) as described previously[41]. The microtubule-binding domain (MBD) of MAP4 was amplified from the genomic DNA of GFP::MAP4-MBD plants[42]. The mCherry fusion constructs were then introduced into YFP::CESA6 plants[17] or GFP::CESA3 plants[14] by *Agrobacterium*-mediated transformation to generate the double-labelled lines. CFP::CESA6 plants were constructed as described previously[17] and crossed with YFP::TUA5 plants[19] to create a double-labelled line.

GFP::CESA3 (ref. 14) and GFP::KOR1 (ref. 43) seeds were provided by S. Vernhettes (Institut National de la Recherche Agronomique, Versailles, France). YFP::RabF2a, YFP::RabA4b and YFP::RabG3c[26] seeds were provided by E. Nielsen (University of Michigan, USA). YFP::SYP32, YFP::RabF2b, YFP::RabC1, YFP::RabA1g, YFP::RabA5d and YFP::RabG3f seeds were provided by N. Geldner (Salk Institute, CA, USA; Geldner and Chory, unpublished data).

Growth. Seeds were surface sterilized, stratified for 3 days at 4 °C, and sown on 0.8% agar containing 0.5× Murashige and Skoog (MS) salts and 1× Gamborg's vitamin solution (Sigma-Aldrich) at pH 5.7. After 1 h of light exposure, the seedlings were grown in darkness for 60–72 h at 22 °C.

Specimen mounting. Seedlings were mounted between a 24 × 60 mm cover glass and a 1-mm thick 0.8% agar pad affixed to a 22 × 22 mm cover glass. The agar cushion stabilized the specimen for sustained time-lapse imaging, minimized compression and mechanical damage, and allowed greater reproducibility in mounting conditions.

Drug treatments. For time-courses, seedlings were mounted in solution containing the chemical agent(s) and imaged at various time points. For other experiments, seedlings were submerged in 2 ml of solution in 12-well cell culture plates (Becton Dickinson) and incubated in darkness. Isoxaben, brefeldin A, latrunculin B, taxol, oryzalin (Sigma-Aldrich) and AE F150944 (Bayer CropScience) were dissolved in dimethyl sulfoxide (DMSO) or methanol to create stock solutions. Working solutions of chemicals were freshly diluted in water from these stocks immediately before use. Propidium iodide (PI) and FM4-64 were dissolved in water and used at a concentration of 10 μg ml^{-1} and 20 μM, respectively.

Confocal microscopy. Imaging of plants expressing GFP:CESA3 and mCherry:TUA5 or MAP4–MBD was performed on a system featuring a CSU-X1 spinning disk head (Yokogawa), Axiovert 200 inverted microscope (Zeiss), ×100/1.4 NA oil immersion objective, QuantEM:512SC CCD camera (Roper Scientific) and ×1.2 lens between the spinning disk unit and camera. Excitation switching and shuttering was performed by a multi-channel AOTF device (AA Opto-Electronic Company), and emission filtering was accomplished with band pass filters (530/50 nm for GFP, and 640/50 nm for mCherry; Chroma Technology). GFP and mCherry were excited at 491 nm and 561 nm, respectively, by solid-state lasers. Typical exposure times were 600 ms for GFP and 300 ms for mCherry.

Photobleaching was performed by a FRAP/PA system (Roper Scientific) integrated into the setup above. Focused laser light was scanned on the image plane by a pair of galvometer-driven mirrors inside the FRAP/PA unit. Scanner positions were calibrated to image coordinates using an automated procedure. GFP photobleaching was performed with a 491 nm laser (5 ms per scan point of 4 pixels in diameter) for plants expressing GFP::CESA3 and mCherry::MAP4-MBD or a 405 nm laser (10 ms per scan point) for plants expressing GFP::CESA3 and mCherry::TUA5.

Imaging of seedlings expressing YFP::CESA6 and mCherry::SYP41/42/61 or labelled with FM4-64 was performed on a system similar to the one described above, except a DMI6000 B inverted microscope (Leica) was used and an AOTF from Crystal Technologies was used to select and attenuate excitation light. YFP was imaged using the same settings as GFP, and FM4-64 used the same settings as mCherry.

All other imaging was performed on a system as described previously[17]. Fluorescent markers were excited at 442 nm (CFP), 488 nm (GFP/YFP), 514 nm (YFP) or 568 nm (PI). Emission was collected through band-pass filters (Chroma Technologies): 480/40 nm (CFP), 525/50 nm (GFP/YFP), 570/65 nm (YFP) and 620/60 nm (RFP and PI). Acquisitions were typically performed with 500-ms exposures (with two-frame averaging).

For all imaging experiments, focal shift was monitored by tracking other objects in the same focal plane as the object under study.

General image processing. All image processing was performed using ImageJ software[44]. For analyses involving measurement of signal intensity, only linear adjustments to pixel values were made. For other images, background signal was reduced using the 'Subtract Background' tool (rolling ball radius of 20–30 pixels) in ImageJ. Image drift was corrected using ImageJ plugins: StackReg[45] and MultiStackReg (http://www.stanford.edu/~bbusse/work/downloads.html). Post-acquisition frame averaging (http://valelab.ucsf.edu/~nico/IJplugins/Running_ZProjector.html) was applied to time series where indicated.

Colocalization analysis of CESA delivery sites and cortical microtubules. GFP signal in seedlings expressing GFP::CESA3 and mCherry::MAP4–MBD was bleached at the plasma membrane and imaged at 2-s intervals. The CESA channel was scanned for delivery events defined by punctae appearing at the plasma membrane and then moving steadily. Sixty events from 3 cells were selected arbitrarily and analysed. For each putative delivery event, previous frames were studied to ensure that the puncta of interest appeared *de novo* and could not be attributed to other particles nearby. At the start of the static phase ($t = 0$), the centroid of the particle was determined by eye. A 3-frame running average was applied to the microtubule channel. The frame representing $t = 0$ was then thresholded using the Isodata algorithm in ImageJ to create a binary image of microtubule signal. The particle centroid was then mapped onto the binary image to determine colocalization.

A binomial test was used to determine whether CESA delivery was coincident with microtubules at a frequency higher than chance. The expected colocalization between delivery events and microtubules, according to the null hypothesis, was dependent on the optical coverage of microtubule signal at the cell cortex. To calculate this value, the microtubule channel was converted into a binary image stack, and averaged over the time series. The mean pixel intensity in this time average projection represented the optical coverage. Overall, microtubules occupied approximately 50.7% of the cell cortex. From our analysis, 47 of 60 delivery events were coincident with microtubules. The observed frequency is significantly higher than chance according to the binomial test ($P < 0.001$).

Delivery rate analysis of CESA complexes. Seedlings expressing GFP::CESA3 and mCherry::MAP4–MBD or TUA5 were treated with control, oryzalin (20 μM) or mannitol (200 mM) for 3–8 h and bleached as described above. All observable CESA delivery events within a large area (277–569 μm^2) of the bleach region were counted over a 3- to 10-min window per cell. For control, 811 events in 1031 μm^2 were observed in 3 cells over a combined 30 min. For oryzalin, 1011 events in 1458 μm^2 were observed in 3 cells over a combined 30 min. For mannitol, 8 events in 1778 μm^2 were observed in 5 cells over a combined 22 min.

Measurement of particle intensity in kymographs. CESA-labelled particles occasionally appeared to split into two or more daughter particles. To confirm that the CESA signal was conserved before and after putative splitting events, individual particle intensities were measured in a background-subtracted kymograph. For each time-point, a 5-pixel (0.67 μm) portion of the kymograph line, centred on the particle, was measured. Mean intensity from multiple time points was then

DOI: 10.1038/ncb1886

calculated. Surface plots of kymographs were generated using the Interactive 3D Surface Plots plugin (http://rsbweb.nih.gov/ij/plugins/surface-plot-3d.html).

Measurement of SmaCC density at cell cortex. Time series imaging of YFP::CESA6 labelled cells was performed in the optical plane of the cell cortex. SmaCCs in the first frame of the time series were tallied. SmaCCs were identified by optical size and dynamic behaviour as revealed in subsequent frames. The area of the visible cortex was also measured, and density was calculated (number of compartments per 100 μm^2).

Organelle velocity analysis. Frame-to-frame velocities of objects were measured using the ImageJ SpotTracker plugin[46]. A Gaussian blur filter (2 pixel radius) was applied to time series of Golgi body images to identify centroids with greater ease. For each time point, multiple objects were tracked in at least 3 cells in 3 plants. The set of frame-to-frame velocities for one object was treated as a statistical subgroup. The weighted average of subgroups for each time point was calculated, as well as the standard error of this value. Linear regression was performed using Prism 5 (GraphPad software) to determine whether organelle velocity decreased significantly over time (that is, slope less than zero). Two-level nested ANOVA was also performed to determine whether organelle velocity differed significantly between two treatments.

39. Shaner, N. C. *et al.* Improved monomeric red, orange and yellow fluorescent proteins derived from *Discosoma* sp. red fluorescent protein. *Nature Biotechnol.* **22,** 1567–1572 (2004).
40. Earley, K. W. *et al.* Gateway-compatible vectors for plant functional genomics and proteomics. *Plant J.* **45,** 616–629 (2006).
41. Kirik, V. *et al.* CLASP localizes in two discrete patterns on cortical microtubules and is required for cell morphogenesis and cell division in *Arabidopsis*. *J. Cell Sci.* **120,** 4416–4425 (2007).
42. Marc, J. *et al.* A GFP–MAP4 reporter gene for visualizing cortical microtubule rearrangements in living epidermal cells. *Plant Cell* **10,** 1927–1940 (1998).
43. Robert, S. *et al.* An *Arabidopsis* endo-1**,** 4-β-D-glucanase involved in cellulose synthesis undergoes regulated intracellular cycling. *Plant Cell* **17,** 3378–3389 (2005).
44. Rasband, W. S. ImageJ, *US National Institutes of Health*, Bethesda, MD, USA <http://rsbweb.nih.gov/ij/plugins/surface-plot-3d.html>.
45. Thevenaz, P., Ruttimann, U. E. & Unser, M. A pyramid approach to subpixel registration based on intensity. *IEEE Trans Image Process* **7,** 27–41 (1998).
46. Sage, D., Neumann, F. R., Hediger, F., Gasser, S. M. & Unser, M. Automatic tracking of individual fluorescence particles: application to the study of chromosome dynamics. *IEEE Trans Image Process* **14,** 1372–1383 (2005).

nature cell biology

DOI: 10.1038/ncb1886

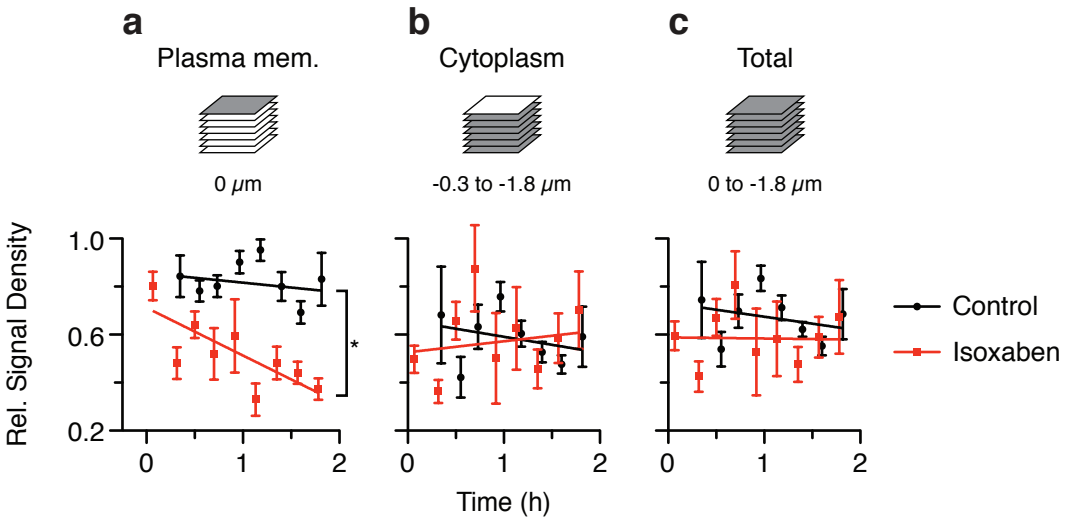

Figure S1 Isoxaben causes loss of YFP::CESA6 signal from the plasma membrane. Seedlings expressing YFP::CESA6 were treated with 0.01% DMSO (control) or 100 nM isoxaben in 0.01% DMSO. Z-series of 10 optical planes, spaced 0.3 μm apart, were acquired. Propidium iodide was used to stain the cell wall, providing a fiducial marker for the start of the z-series. Based on examination of many images, we determined that the outer three planes (z = +0.3 to +0.9 μm) represented the extracellular space and the fourth (z = 0 μm) represented the plasma membrane. The next six planes (z = -0.3 to -1.8 μm) sampled the cellular space interior to the plasma membrane. Relative YFP::CESA6 signal densities were measured in background-subtracted images representing the plasma membrane (**a**), cytoplasm (**b**) and total (**c**). Each data point represents signal density (relative intensity per unit volume) from at least 3 cells from 3 unique plants. Isoxaben significantly decreases YFP::CESA6 signal at the plasma membrane (**a**) compared to control ($P = 0.027$, F-test for equality of slopes of regression lines). Total integrated signal does not change significantly (**c**), suggesting there is no net loss of CESA6. Since most of the total CESA6 protein resides in cytoplasmic organelles, and measured values for cytoplasmic signal have high variance (**b**), it is not possible to determine if the protein lost at the plasma membrane could be accounted for in cytoplasmic pools. Measurements in **a** were corrected for out-of-focus signal caused by Golgi bodies and small compartments. First, the planes representing the cytoplasm were summed and thresholded by eye. Structures larger than 12 square pixels were identified using the "Analyze particles" tool in ImageJ. Regions of the plasma membrane that were directly above these structures were eliminated from analysis. Thus the reported intensities in **a** primarily represent signal from CESA punctae in the plasma membrane. Error bars represent s.e.m.

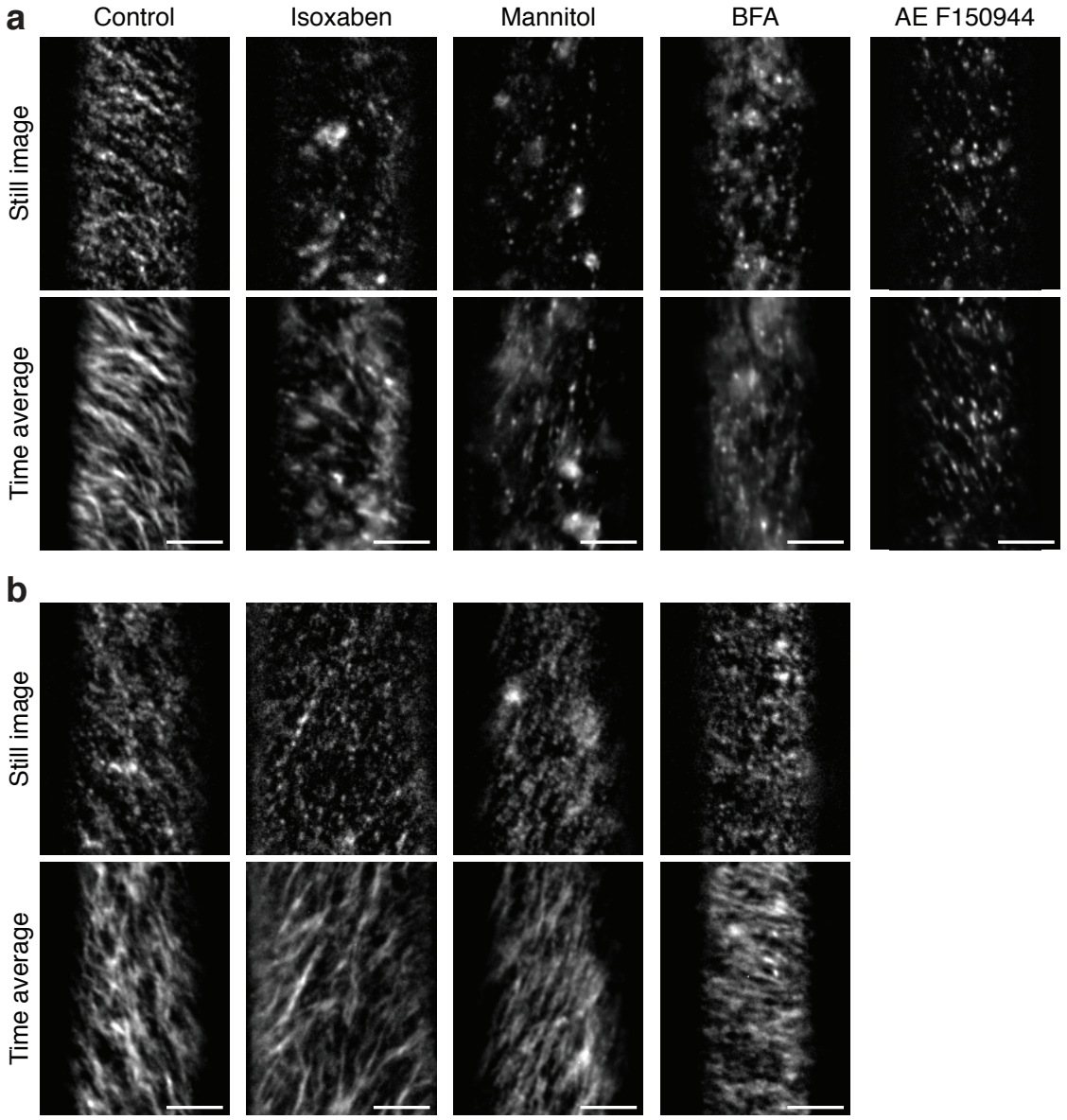

Figure S2 Effects of isoxaben, mannitol or BFA treatment on CESA6 are reversible. Seedlings expressing YFP::CESA6 were treated with 0.05% DMSO (control), 100 nM isoxaben in 0.01% DMSO, 200 mM mannitol, 50 μM BFA in 0.05% DMSO or 10 nM AE F150944 in 0.01% DMSO for 3 h (**a**). In all non-control treatments, few punctae are visible in the plasma membrane, and many SmaCCs are observed in the cell cortex. The plants were then incubated in water for 5 h. After washing, CESA6 complexes accumulate in the plasma membrane and are motile in all treatments (**b**). Observations were performed on three plants per treatment. Representative images are shown. Washout was not performed for AE F150944-treated plants. Time-averaged projections were made from 61 images collected over 5 min. Scale bar, 5 μm.

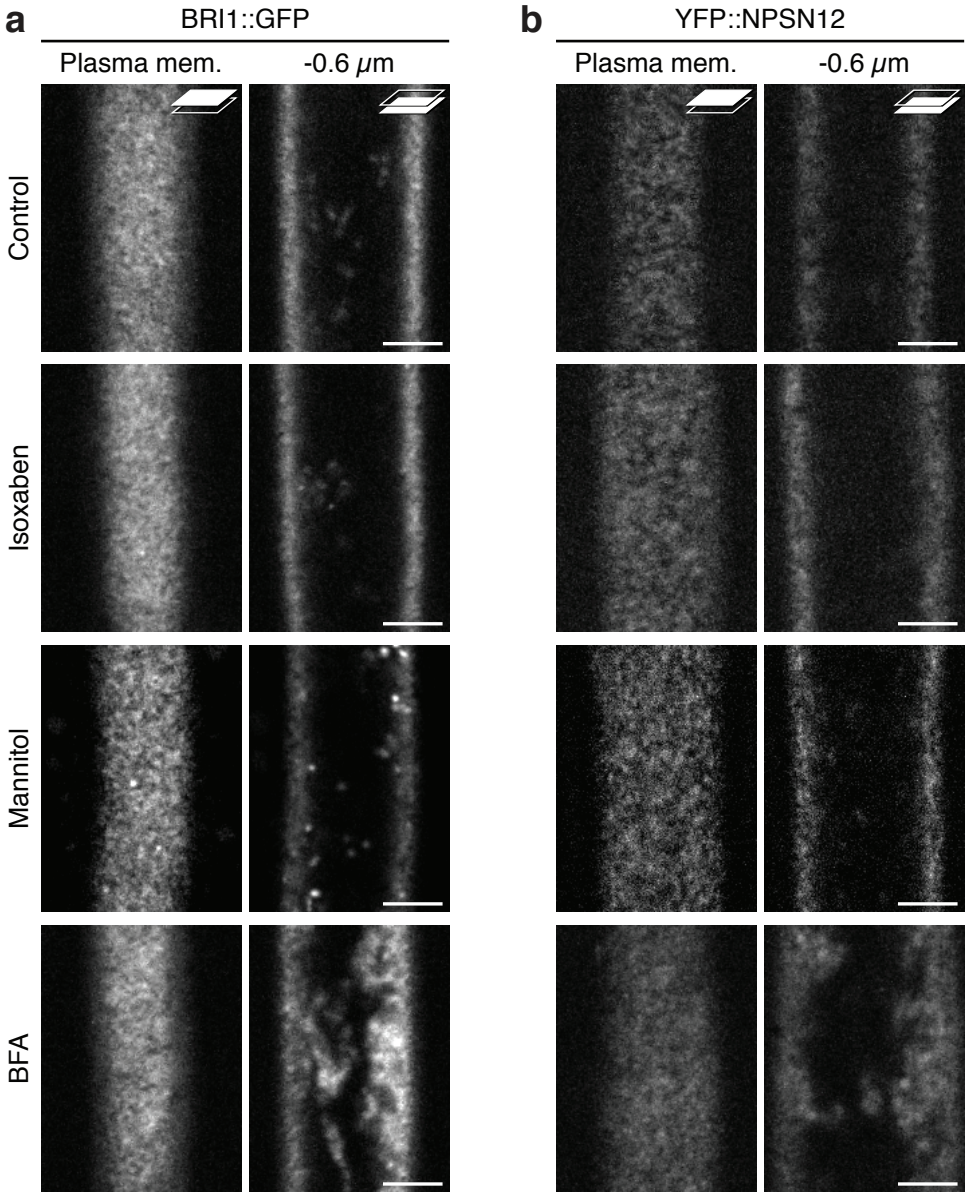

Figure S3 Isoxaben does not generally affect the localization of plasma membrane proteins. Seedlings expressing plasma membrane markers BRI1::GFP (**a**) or YFP::NPSN12 (**b**) were treated with 0.05% DMSO (control), 100 nM isoxaben in 0.01% DMSO, 200 mM mannitol or 50 μM BFA in 0.05% DMSO. Focal planes at the plasma membrane and lower cell cortex are shown. Isoxaben does not noticeably disrupt localization of either labeled protein.Mannitol causes some detectable internalization of BRI1 signal but does not induce plasmolysis at the concentration used. BFA causes intracellular accumulation of labeled BRI1 and NPSN12. Scale bar, 5 μm.

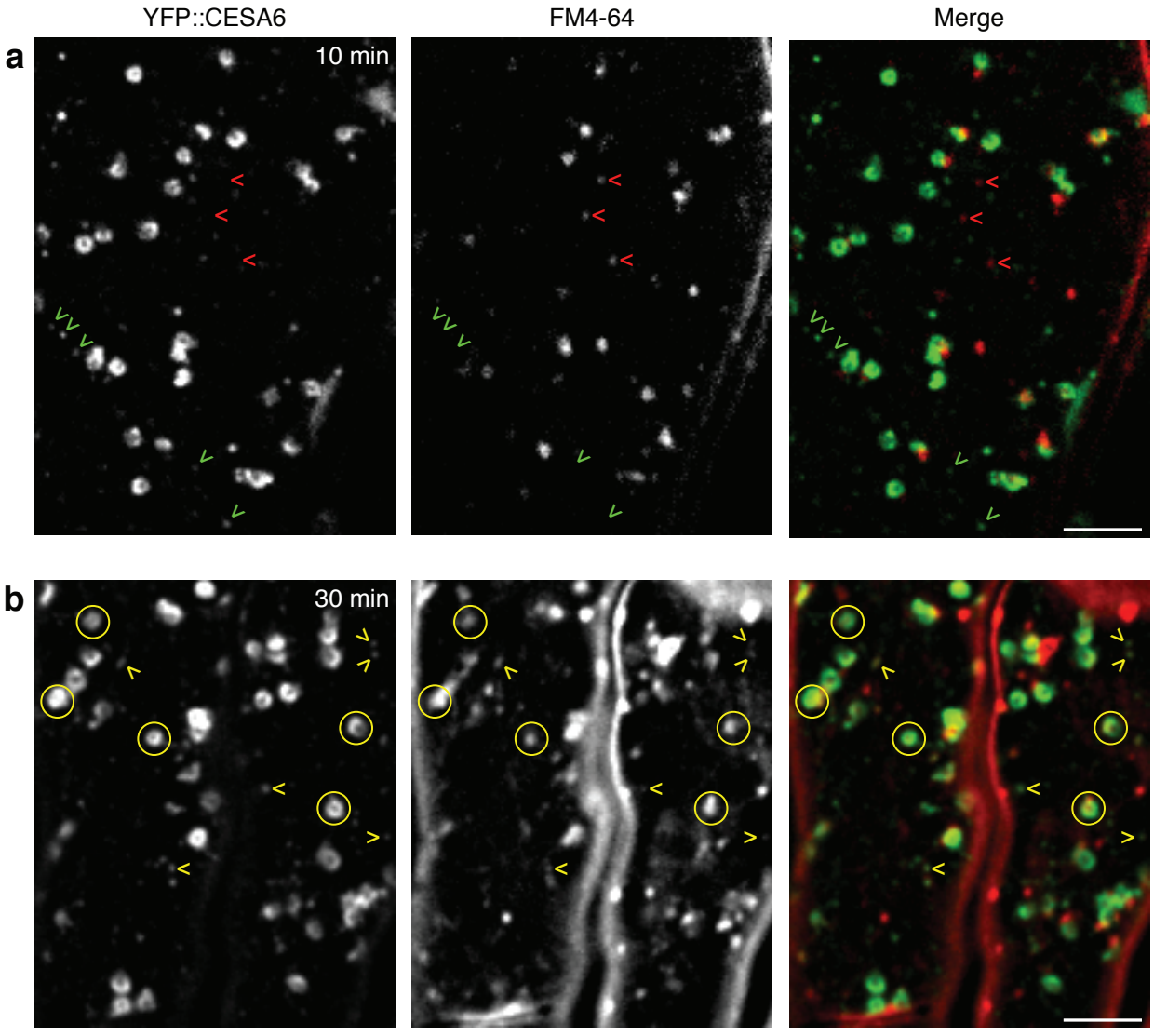

Figure S4 FM4-64 dye is internalized into SmaCCs slowly. YFP::CESA6 seedlings were light-grown for 3 days and incubated in 200 mM mannitol and 20 μM FM4-64 for 10 min (**a**) or 30 min (**b**). Epidermal hypocotyl cells were imaged. (**a**) At 10 min, the dye labels endosomes[1] (red arrowheads) that are not coincident with cortically tethered SmaCCs (green arrowheads), which were identified based on their dynamics. (**b**) After 30 min, the dye labels Golgi bodies (circles) and some SmaCCs (yellow arrowheads), indicating that it is possible to eventually load enough dye into SmaCC membranes for positive detection. The fact that dye is not detected in SmaCCs at earlier time points, although the plasma membrane is well labeled, suggests that most observed SmaCCs are not directly formed by endocytosed plasma membrane. Scale bar, 5 μm.

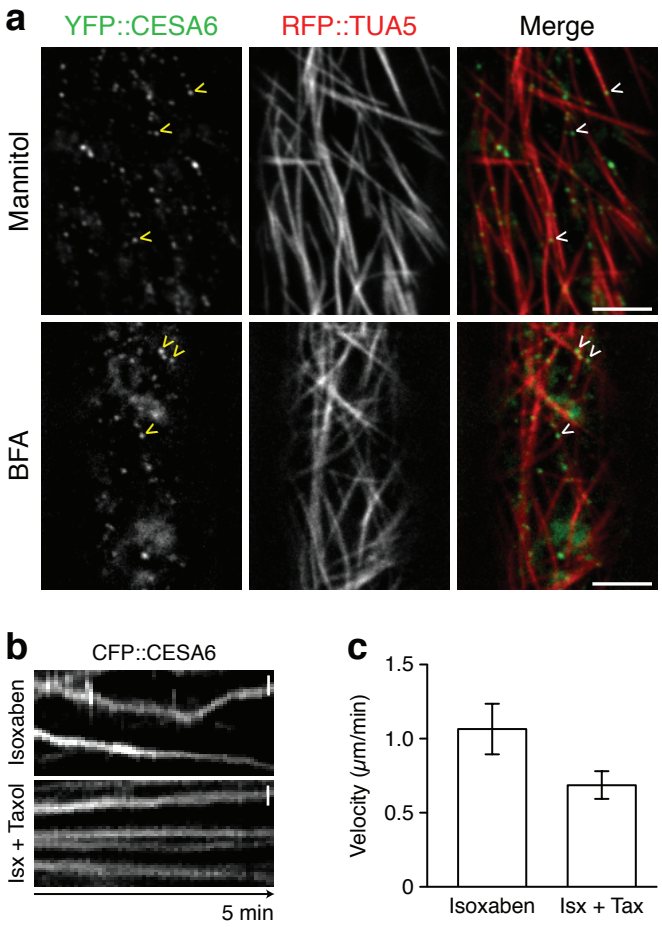

Figure S5 (**a**) SmaCCs colocalize with cortical microtubules in cells treated with BFA or mannitol. Seedlings expressing YFP::CESA6 and mCherry::TUA5 were treated with 200 mM mannitol or 50 μM BFA for 3 h. SmaCCs (arrowheads) show colocalization with microtubules. Scale bar, 5 μm. (**b**, **c**) Stabilization of cortical microtubules by taxol lowers SmaCC velocity under isoxaben treatment. Seedlings expressing CFP::CESA6 and YFP::TUA5 were treated with 100 nM isoxaben in 0.11% DMSO or 100 nM isoxaben + 20 μM taxol in 0.11% DMSO for 2 h. Visualization of labeled microtubules confirmed that taxol slowed down depolymerization of microtubules. (**b**) Representative kymographs of SmaCCs. (**c**) Velocities of SmaCCs in the cell cortex. For each treatment, n = 24 SmaCCs from 4 cells (from 4 seedlings). Application of isoxaben and taxol together reduces SmaCC velocity more than isoxaben does alone ($P < 0.001$, two-level nested ANOVA). Error bars represent s.e.m. Scale bar, 1 μm.

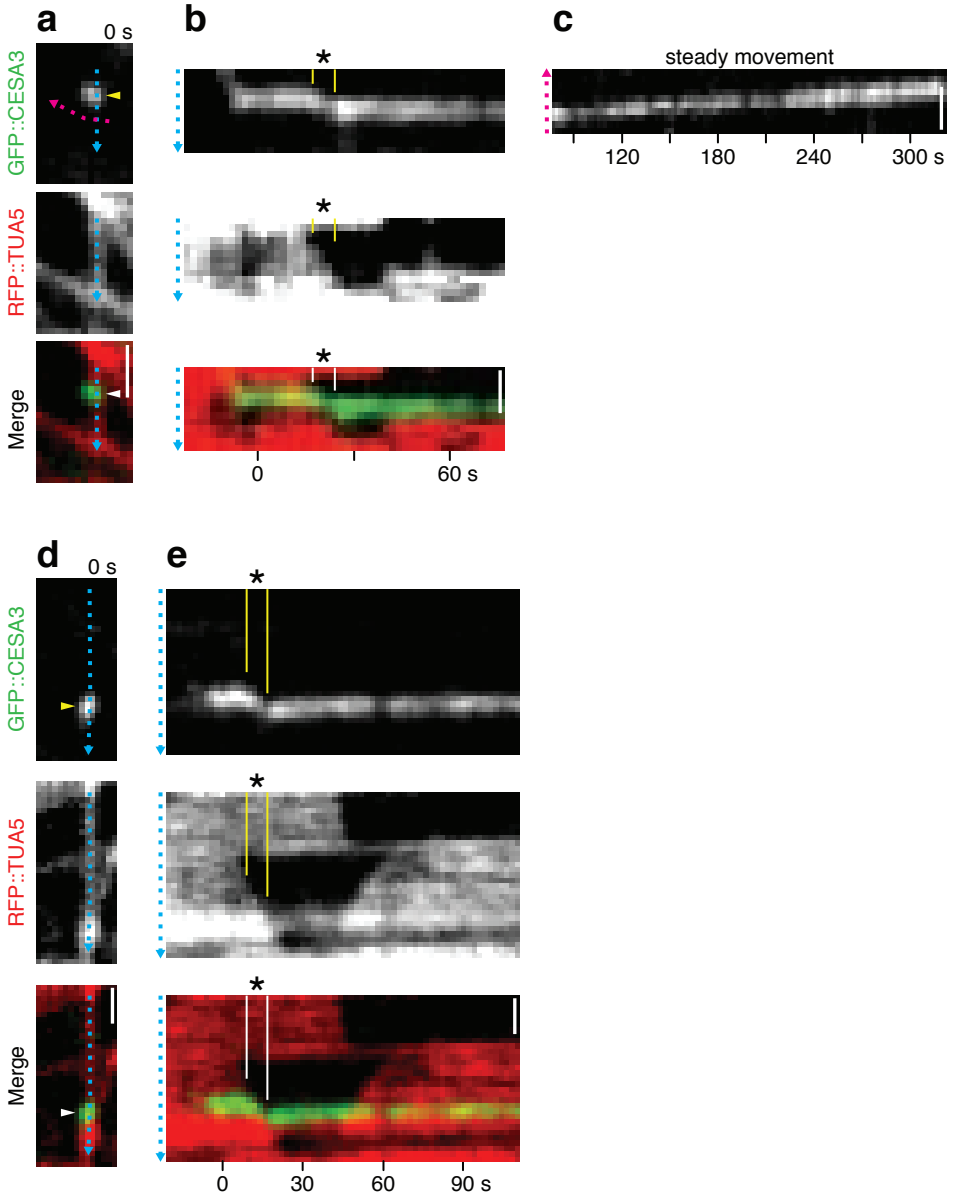

Figure S6 Two additional examples of CESA tip tracking under normal conditions. Seedlings expressing GFP::CESA3 and mCherry::TUA5 were imaged in the absence of drugs. (**a**-**c**) First example. (**a**) Still images at t = 0 showing GFP::CESA3 (arrowhead) and an associated microtubule. (**b**) Kymograph along cyan trace in **a**. A CESA particle appears in the focal plane of the plasma membrane and becomes stationary. This static behavior is interrupted by a depolymerizing end. GFP::CESA3 tracks with the end for several frames (*) and then becomes static again. (**c**) Kymograph along magenta trace in **a**. At 78 s, the CESA particle moves steadily. (**d**, **e**) Second example. (**d**) Still images at t = 0 showing GFP::CESA3 (arrowhead) and an associated microtubule. (**e**) Kymograph along cyan trace in **d**. As in **b**, GFP::CESA3 tracks on a depolymerizing end (*). Scale bar, 1 μm.

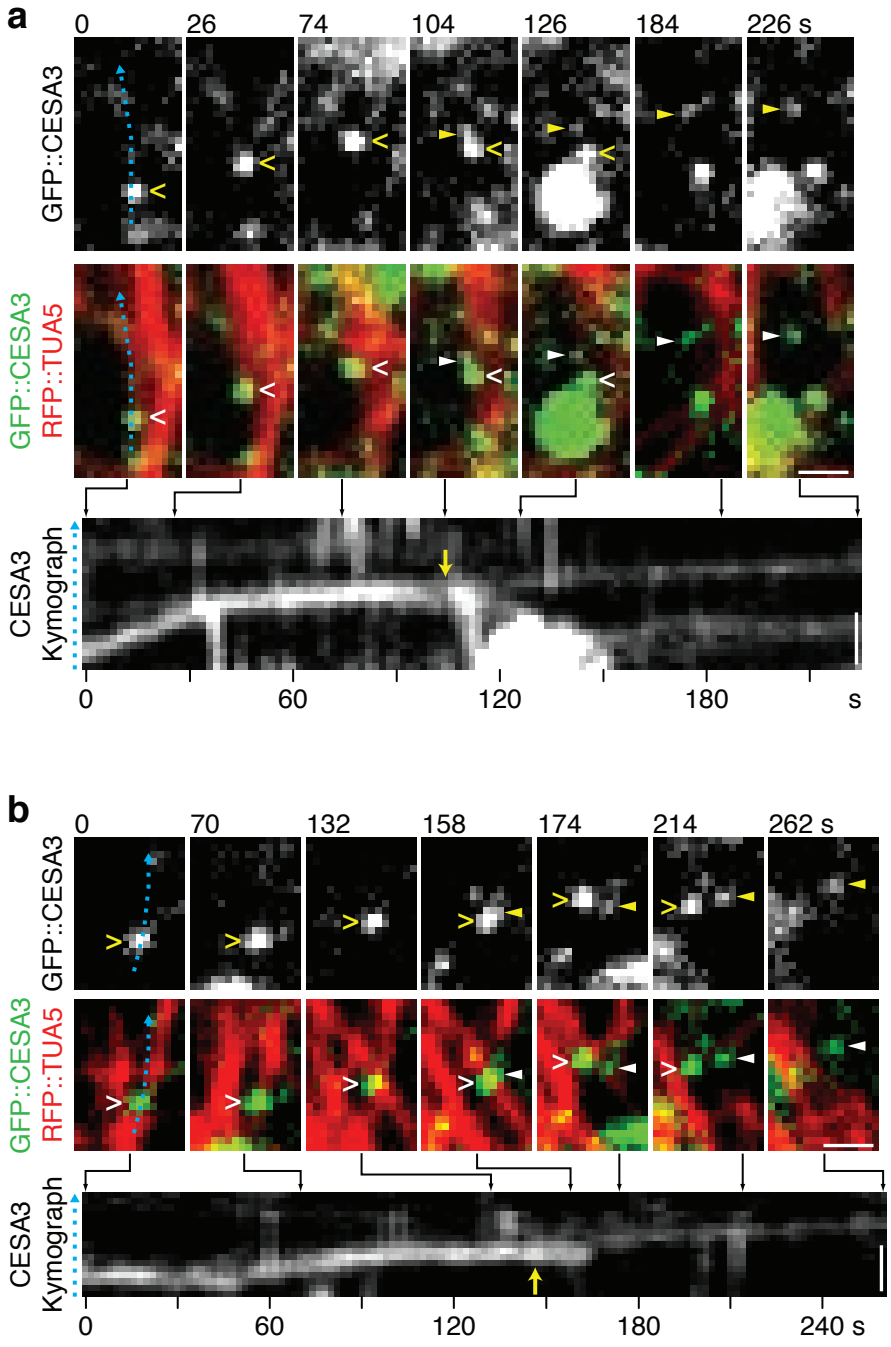

Figure S7 Two additional examples of CESA delivery events that are associated with SmaCCs. Seedlings were treated with 200 mM mannitol for 3 h and then washed with water for 0.5 h. Kymographs were taken along the cyan trace. Yellow arrows mark bifurcation on the kymographs. (**a**) First example. A SmaCC (open arrowhead) tracks on a depolymerizing end before splitting into two structures of unequal intensity at 104 s. The brighter particle (open arrowhead) moves in a manner consistent with SmaCC motility. The dimmer particle (closed arrowhead) moves at a slow and steady rate, consistent with CESA complex motility in the plasma membrane. (**b**) Second example. A similar event occurs in a different cell. The splitting event occurs at around 146 s. Scale bar, 1 μm.

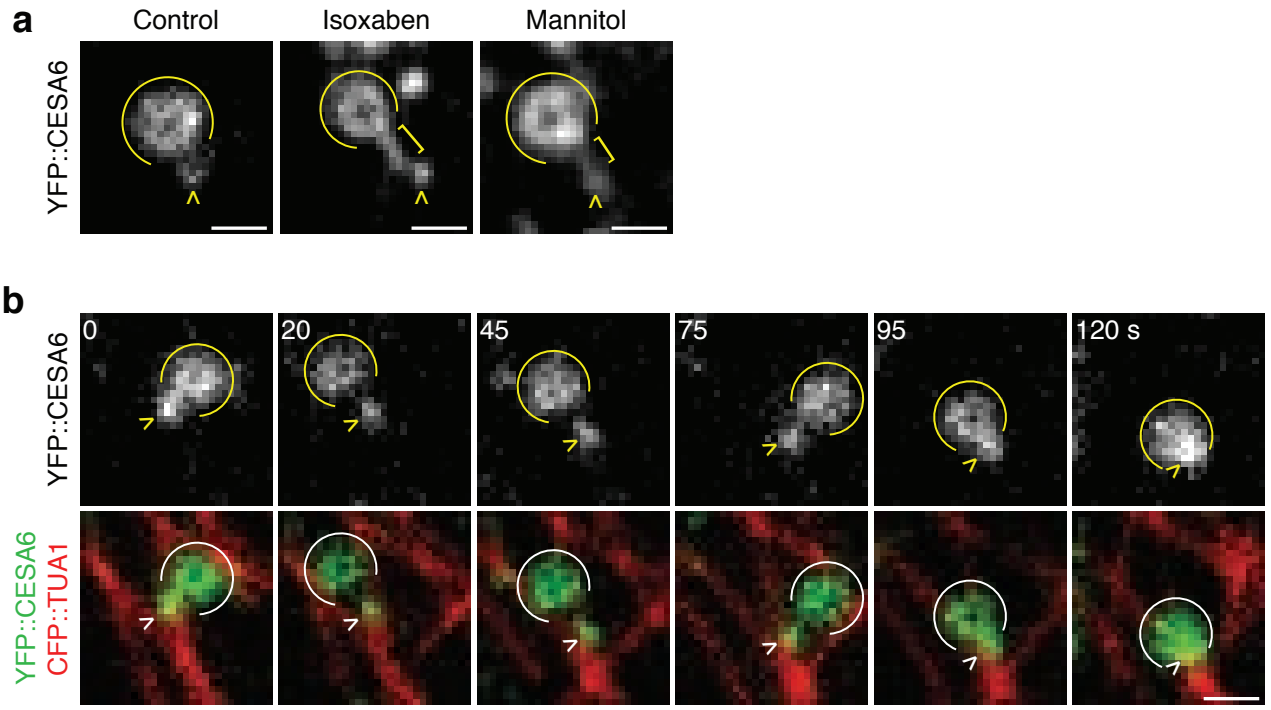

Figure S8 Golgi bodies associate with SmaCCs. (**a**) YFP::CESA6 seedlings were treated with 0.01% DMSO (control), 100 nM isoxaben in 0.01% DMSO or 200 mM mannitol for 3 h. In the control, physical association between Golgi bodies (arcs) and SmaCCS (arrowheads) is frequently observed. With isoxaben or mannitol treatment, this association is more conspicuous: the two structures are sometimes observed to be connected by a detectable strand of YFP::CESA6 signal (bracket), which may represent a membrane bridge. (**b**) Association between Golgi bodies and cortically localized SmaCCs persists for up to several minutes in the presence of cytoplasmic streaming. Seedlings expressing YFP::CESA6 and CFP::TUA1 were treated with 100 nM isoxaben for 2 h. A short distance (< 1.3 μm) is maintained between a Golgi body and a moving SmaCC for 120 s, suggesting the two are physically tethered. These observations suggest that some SmaCCs can form tight associations with Golgi bodies, which might be the case if these SmaCCs are derived from them or interact closely with them to exchange cargo. Scale bar, 1 μm. See Movie 15.

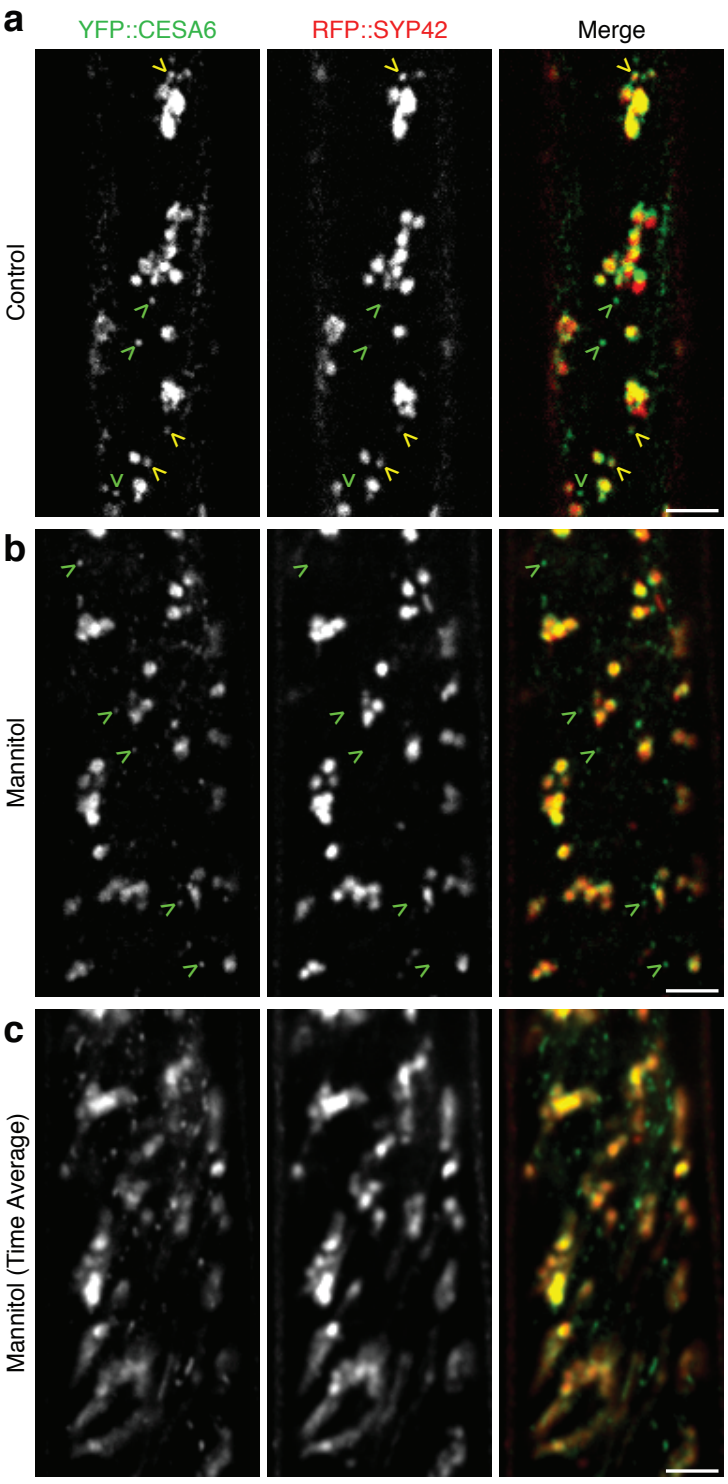

Figure S9 SYP42 labels a subset of SmaCCs. Seedlings expressing YFP::CESA6 and mCherry::SYP42 were incubated in water (**a**) or 200 mM mannitol (**b**, **c**) for 3 h and imaged at the cell cortex. (**a**) Some small compartments are labeled by YFP only (green arrowheads) or both YFP and mCherry (yellow arrowheads). (**b**, **c**) SYP42 fails to label cortically tethered SmaCCs (green arrowheads) after mannitol treatment. (**a**, **b**) Still images. (**c**) Averages of 61 frames representing 1 min. Scale bar, 5 μm.

Marker	Putative localization
GFP::KOR1	KOR1-containing compartments[2]
YFP::RabA4b	TGN-like compartments[3]
YFP::RabF2a	Early endocytic compartments[3]
YFP::RabG3c	Prevacuolar compartment/vacuole[3]
YFP::RabF2b	Endosome[4]
YFP::RabC1	Endosome[5]
YFP::RabA1g	Endosome[5]
YFP::RabA5d	TGN[5]
YFP::RabG3f	Late endosome/vacuole[5]

Supplementary Table 1 Visualized endomembrane markers. Arabidopsis seedlings expressing different fluorescent fusion proteins were dark-grown for 3 days, treated with 100 nM isoxaben for 2 h, and visualized. The lines were assayed for the labeling of small compartments that become tethered to the cell cortex in response to isoxaben. None of the lines were observed to display such behavior; however, it is possible that one or more of these markers label a subset of SmaCCs.

Supplementary Movie Legends

All movies were acquired in epidermal cells of the upper hypocotyl of Arabidopsis seedlings that were dark-grown for 3 days (see Methods).

Movie 1 Photobleaching used to visualize delivery of GFP-labeled CESA complexes to the plasma membrane. A cell expressing GFP::CESA3 and mCherry::TUA5 was imaged in the plane of the plasma membrane. At t = 0 s, GFP is bleached. During the recovery, several CESA particles (arrowheads) are delivered to plasma membrane. The majority of delivery sites are coincident with cortical microtubules. A 2-frame running average was applied to the time series. Scale bar, 5 µm.

Movie 2 Delivery of a single CESA particle to the plasma membrane. A cell expressing GFP::CESA3 and mCherry::MAP4-MBD was imaged in the plane of the plasma membrane. The CESA particle (arrowhead) undergoes three stages of behavior: erratic motility (t = -26 to 0 s), static localization (t = 0 to 44 s), and steady movement (t = 44 to 490 s). At the start of the static phase, the particle colocalizes with microtubule signal. A 2-frame running average was applied to the time series. Scale bar, 1 µm.

Movie 3 Delivery of multiple CESA particles at the same time and position. A cell expressing GFP::CESA3 and mCherry::MAP4-MBD was imaged in the plane of the plasma membrane. A CESA particle (large arrowhead) arrives at the plasma membrane and splits into two punctae (small arrowheads) at t = 56 s. A 2-frame running average was applied to the time series. Scale bar, 1 µm.

Movie 4 Dynamics of CESA6-containing organelles are affected by isoxaben, osmotic stress or BFA. Seedlings expressing YFP::CESA6 were treated with 0.05% DMSO (**a** and **e**), 100 nM isoxaben in 0.01% DMSO (**b**), 50 µM BFA in 0.05% DMSO (**c**) or 200 mM mannitol (**d**). Time series were acquired at the plasma membrane or lower cell cortex, as indicated. (**a**) In the controls, SmaCCs (open arrowheads) and Golgi bodies (crosses) move rapidly through the cell cortex. These two structures are often in close proximity and move together in a coordinated fashion (red arrowhead and cross). (**b**-**d**) With the other treatments, organelles show reduced velocity and altered dynamics at the cortex. SmaCCs, in particular, exhibit saltatory movement along linear paths. (**e**) These structures are distinguished from active CESA complexes (closed arrowhead) in the plasma membrane, which move at slow and steady rates along linear trajectories. A 3-frame running average was applied to **b**-**e**. Scale bar, 5 µm.

Movies 5-8 SmaCCs are coincident with cortical microtubules. Seedlings expressing YFP::CESA6 and mCherry::TUA5 were treated with 0.05% DMSO (**5**), 100 nM isoxaben in 0.01% DMSO (**6**), 200 mM mannitol (**7**) or 50 µM BFA in 0.05% DMSO (**8**) for 3 h. (**5**) In the control, CESA complexes (closed arrowheads) in the plasma membrane move slowly along paths coincident with microtubules. (**6**-**8**) With the other treatments, CESA complexes are predominantly cleared from the plasma membrane. The SmaCCs (open arrowheads) accumulate at the cortex, displaying colocalization with microtubules. The motility of these SmaCCs is often observed to be coincident with depolymerizing microtubule ends (dashes). A 3-frame running average was applied to **5**. Scale bar, 5 µm.

Movies 9-11 Cortically tethered SmaCCs move with depolymerizing ends of microtubules. Seedlings expressing markers for CESA (green) and microtubules (red) were treated with 100 nM isoxaben or 200 mM mannitol. Microtubule-bound SmaCCs (arrowheads) move in concert with depolymerizing ends (dashes). (**9**) A SmaCC is initially stationary and then moves along the microtubule when encountering a depolymerizing end. (**10**) SmaCCs track with the depolymerizing plus and minus ends of the same microtubule. Two SmaCCS on the left are collected by the depolymerizing end. The increase in CESA signal at that end suggests both SmaCCs remain associated with the microtubule. (**11**) A SmaCC moves with a shrinking end in a microtubule bundle. Scale bar, 1 µm.

Movie 12 CESA exhibits tip-tracking behavior under normal conditions. A cell expressing GFP::CESA3 and mCherry::TUA5 was imaged in the plane of the plasma membrane. During delivery, a GFP::CESA3 particle (arrowhead) moves with the depolymerizing end of a microtubule (dash). A 3-frame running average was applied to the time series. Scale bar, 1 µm.

Movie 13 SmaCCs are associated with CESA delivery to the plasma membrane. Seedlings were treated with 200 mM mannitol for 3 h and then washed with water for 0.5 h. A SmaCC (open arrowhead) tracks a depolymerizing end (dash) for the first 136 s and then jumps to an adjacent microtubule. At approximately t = 308 s, the SmaCC begins to split into two structures of unequal intensity. The brighter structure (open arrowhead) leaves the focal plane (at 348 s) in a manner consistent with SmaCC motility. The dimmer particle (closed arrowhead) moves at a slow and steady rate, consistent with CESA complex motility in the plasma membrane. A 3-frame running average was applied to the time series. Scale bar, 1 µm.

Movie 14 Successive breakup of one SmaCC into multiple compartments. Seedlings treated with 200 mM mannitol for 3 h and then washed with water for 0.5 h. A SmaCC (arrowhead) splits into two compartments, clearly visible at 116 s. The brighter daughter SmaCC then proceeds to split into 3 compartments, clearly visible at 198 s. All structures exhibit motility characteristic of SmaCCs. Scale bar, 1 µm.

Movie 15 Golgi body tethering to a SmaCC under isoxaben treatment. Seedlings expressing YFP::CESA6 and CFP::TUA1 were treated with 100 nM isoxaben for 2 h. A Golgi body (cross) shows apparent tethering to a moving SmaCC (arrowhead). A short distance is maintained between these structures for 120 s. Scale bar, 1 µm.

REFERENCES

1. Bolte, S. *et al.* FM-dyes as experimental probes for dissecting vesicle trafficking in living plant cells. *J Microsc* **214**, 159-173 (2004).
2. Robert, S. *et al.* An Arabidopsis endo-1,4-beta-D-glucanase involved in cellulose synthesis undergoes regulated intracellular cycling. *Plant Cell* **17**, 3378-3389 (2005).
3. Preuss, M.L., Serna, J., Falbel, T.G., Bednarek, S.Y. & Nielsen, E. The Arabidopsis Rab GTPase RabA4b localizes to the tips of growing root hair cells. *Plant Cell* **16**, 1589-1603 (2004).
4. Ueda, T., Uemura, T., Sato, M.H. & Nakano, A. Functional differentiation of endosomes in Arabidopsis cells. *Plant J.* **40**, 783-789 (2004).
5. Rutherford, S. & Moore, I. The Arabidopsis Rab GTPase family: another enigma variation. *Curr. Opin. Plant Biol.* **5**, 518-528 (2002).

nature cell biology

SDPR induces membrane curvature and functions in the formation of caveolae

Carsten G. Hansen[1], Nicholas A. Bright[2], Gillian Howard[1] and Benjamin J. Nichols[1,3]

Caveolae are plasma membrane invaginations with a characteristic flask-shaped morphology. They function in diverse cellular processes, including endocytosis. The mechanism by which caveolae are generated is not fully understood, but both caveolin proteins and PTRF (polymerase I and transcript release factor, also known as cavin) are important. Here we show that loss of SDPR (serum deprivation protein response) causes loss of caveolae. SDPR binds directly to PTRF and recruits PTRF to caveolar membranes. Overexpression of SDPR, unlike PTRF, induces deformation of caveolae and extensive tubulation of the plasma membrane. The B-subunit of Shiga toxin (STB) also induces membrane tubulation and these membrane tubes also originate from caveolae. STB colocalizes extensively with both SDPR and caveolin 1. Loss of caveolae reduces the propensity of STB to induce membrane tubulation. We conclude that SDPR is a membrane-curvature-inducing component of caveolae, and that STB-induced membrane tubulation is facilitated by caveolae.

Various endocytic pathways operate in mammalian cells. The number, mechanism and specific functions of these pathways are currently under investigation[1]. Current models describing the generation of endocytic vesicles are based on three features: reversible association of cytosolic coat proteins leads to the formation of clathrin-coated pits[2,3], stable membrane association of caveolin proteins leads to the formation of morphologically stable caveolae and caveolar vesicles[4–9] and tubulation of the plasma membrane can result in endocytosis via processes that are not well defined in molecular terms[1,10,11]. Recently, it was shown that extracellular ligands such as glycosphingolipid-binding STB induce their own endocytosis in tubular membrane invaginations[12–14]. Several important questions remain to be addressed. The biogenesis of caveolae requires both caveolin and PTRF proteins[15–20], but the identity, function and molecular interactions of further caveolar components remain unresolved. STB induces the formation of membrane tubes even in ATP (adenosine tri-phosphate)-depleted cells[12], but whether such tubes arise solely from the interaction of the toxin with membrane lipids or whether they require additional membrane or cytosolic proteins remains unclear. Here we provide new data to address both of these questions. We show that loss of SDPR, a caveolar protein homologous to PTRF[21–23], causes loss of caveolae. SDPR binds directly to PTRF and recruits PTRF to caveolar membranes. Overexpression of SDPR, unlike PTRF, induces deformation of caveolae and extensive tubulation of the plasma membrane. SDPR-induced tubes originate from caveolae and incorporate STB. Membrane tubes induced by STB also originate from caveolae, and STB colocalizes extensively with both SDPR and caveolin 1. STB-induced membrane tubulation is diminished in cells expressing reduced levels of SDPR, PTRF or caveolin 1. We propose that SDPR induces membrane curvature within caveolae and that cellular STB-induced tubes reflect the interaction of toxin–glycosphingolipid complexes with caveolar proteins.

RESULTS

PTRF is a caveolar protein required for the formation of characteristic flask-shaped caveolar membrane invaginations[15–18,20]. There are three proteins in the human genome with a primary structure that is > 20% identical to PTRF (Supplementary Information, Fig. S1; http://www.treefam.org, accession number TF331031): SDPR[22–24], SRBC (sdr-related gene product that binds to C-kinase, also known as PRKCDBP)[22,25] and MURC (muscle-restricted coiled-coil protein)[26,27]. SDPR colocalizes with caveolin 1 (refs 23, 25). We constructed plasmids to express fluorescent chimaeras of PTRF, SDPR, SRBC and MURC in mammalian cells. All four chimaeras colocalized well with caveolin 1 in HeLa cells, and thus are likely to be recruited to caveolae (Supplementary Information, Fig. S2). This study focuses on SDPR, because of its ability to induce membrane tubulation as detailed below.

SDPR is required for stable expression of PTRF and caveolin 1

A polyclonal antibody raised against peptides corresponding to amino-acids 9–23 and 312–325 of human SDPR was generated in rabbits. After affinity purification, the anti-SDPR antibodies recognized a band of relative molecular mass 49,000 (M_r 49K) on western blots of HeLa cell

[1]MRC-LMB, Hills Road, Cambridge CB2 0QH, UK. [2]University of Cambridge, Cambridge Institute for Medical Research, Addenbrooke's Hospital, Hills Road, Cambridge CB2 0XY, UK.
[3]Correspondence should be addressed to B.J.N. (e-mail: ben@mrc-lmb.cam.ac.uk)

Received 13 February 2009; accepted 14 May 2009; published online 14 June 2009; DOI: 10.1038/ncb1887

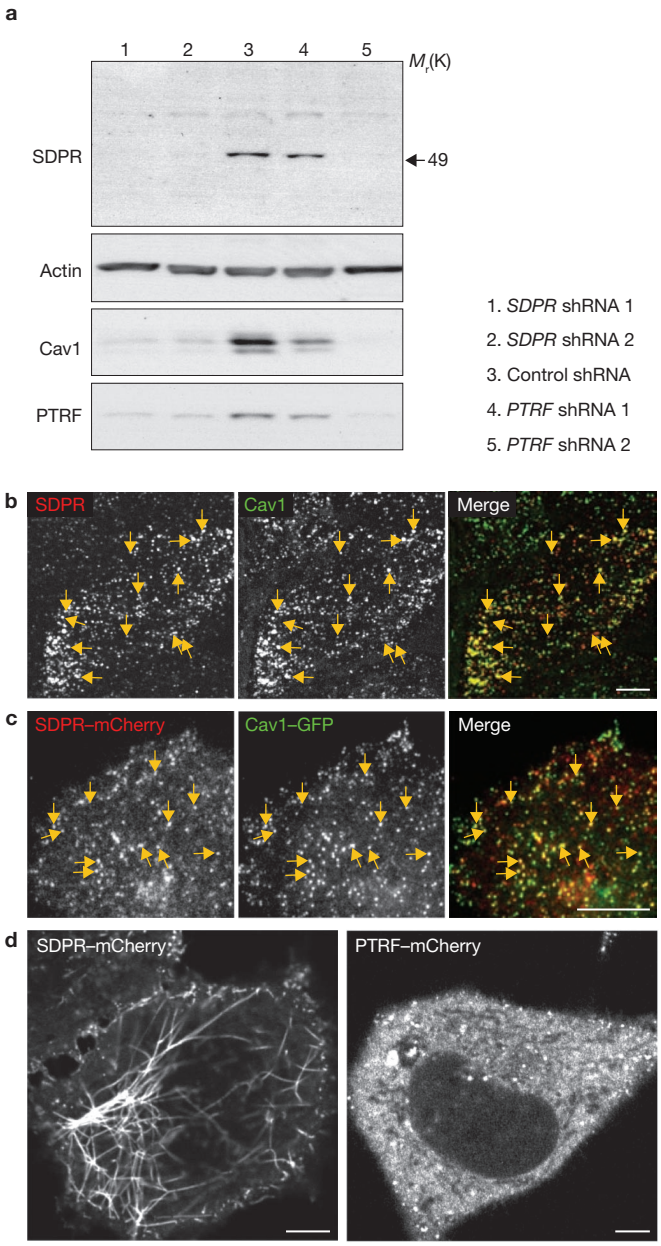

Figure 1 SDPR is a caveolar protein, but forms tubes at high expression levels. (**a**) Western blots show expression levels of SDPR, actin, caveolin 1 and PTRF in HeLa cell lines stably transfected with plasmids expressing shRNAs as shown. The arrow indicates the position of a 49K marker (ovalbumin, not visible; cav1: caveolin 1). Full scans are shown in Supplementary Information, Fig. S6. (**b**) Confocal image of a HeLa cell labelled using indirect immunofluorescence with monoclonal anti-caveolin 1 and polyclonal anti-SDPR antibodies. Yellow arrows highlight colocalization. Scale bar, 10 μm. (**c**) TIR microscopy images of caveolin 1–GFP and SDPR–mCherry expressed in a HeLa cell. Yellow arrows highlight colocalization. Scale bar, 10 μm. (**d**) Overexpression of SDPR–mCherry, at approximately 10 × the level of endogenous protein, results in the formation of extensive tubes. PTRF overexpressed at the same levels has a predominantly cytosolic distribution. Confocal images show live HeLa cells. Scale bars, 10 μm.

extracts. This corresponds to the predicted M_r of SDPR; a higher M_r band was also observed (Fig. 1a). Two HeLa cell lines stably transfected with plasmids expressing short hairpin RNAs (shRNAs) specific to different regions of *SDPR* mRNA were generated. In both cell lines the 49K band was reduced to less than 15% of the levels observed in control cells (cells stably transfected with an empty shRNA vector or non-targeting shRNA— only the latter is shown). Thus, the *SDPR* shRNA cell lines provide a good system to investigate SDPR function. Cell lines expressing shRNAs against *PTRF* were also generated (Fig. 1a).

Western blotting of control, *SDPR* shRNA and *PTRF* shRNA cells showed that reduction in SDPR expression causes loss of PTRF protein, and vice versa (Fig. 1a). Reduction in either PTRF or SDPR expression also caused a loss of caveolin 1 expression. *SDPR* shRNA cell lines were transiently transfected with a plasmid expressing SDPR–CFP (cyan fluorescent protein) with silent mutations to the nucleotides recognized by the shRNA. Protein expression levels in transfected and non-transfected cells were compared after FACS (fluorescence-activated cell sorting) analysis. Expression of the non-targeted SDPR–CFP was sufficient to rescue expression of PTRF and caveolin 1 (Supplementary information, Fig. S3A), confirming that loss of PTRF and caveolin 1 expression in these cells is due to reduced expression of SDPR, thereby implying that SDPR, PTRF and caveolin 1 are functionally inter-dependent.

Indirect immunofluorescence labelling of HeLa cells with the anti-SDPR antibody revealed a high degree of colocalization of SDPR with caveolin 1 in some cells (Fig. 1b), but in others non-specific background labelling (as judged by labelling of *SDPR* shRNA cell lines) was apparent, presumably because SDPR expression was lower in these cells. Labelling of both transfected and neighbouring untransfected cells with the antibody allowed us to obtain an estimate of the minimum fold overexpression of SDPR–mCherry (Supplementary Information, Fig. S3B). Expression of SDPR–mCherry at low levels (more than three times endogenous levels) resulted in a high degree of colocalization with caveolin 1. We used total internal reflection (TIR) microscopy to illuminate the bottom 100 nm of the cells[28], and confirmed that over 80% of plasma membrane puncta containing caveolin 1 also contained SDPR–mCherry (Fig. 1c). When overexpressed by more than fivefold, SDPR was observed in profuse membrane tubes as well as puncta (Fig. 1d). SDPR–GFP (green fluorescent protein) behaved in the same way as SDPR–mCherry. When expressed at equivalent levels to SDPR–GFP, PTRF-mCherry accumulated in the cytosol, (Fig. 1d).

PTRF and SDPR bind to each other and form complexes also containing caveolin 1

The findings that SDPR, like PTRF[15–18], colocalizes with caveolin 1 and that when expression of either SDPR or PTRF is reduced the expression of the other two members of this trio also decreases, suggested that SDPR, PTRF and caveolin 1 may be present in the same complex. Our antibodies did not efficiently precipitate endogenous SDPR, so immunoprecipitation of either PTRF–GFP or SDPR–GFP from cell lysates with anti-GFP antibodies was performed. Both cases resulted in specific co-precipitation of epitope-tagged SDPR (Fig. 2a). Immunoprecipitation of SDPR–GFP also resulted in specific co-precipitation of endogenous PTRF and caveolin 1 (Fig. 2b). The simplest explanation for these results is the presence of a complex containing all three proteins.

We used bacterially expressed and purified PTRF and SDPR to test whether these proteins bind to each other. Full-length PTRF was degraded within the bacterial cells, but we found that a construct containing the conserved coiled-coil and basic regions (6-His–PTRF$^{47–268}$) could be isolated intact. Full-length GST (glutathione *S*-transferase)–SDPR was also slightly degraded, as was GST–SDPR$^{49–274}$ (comprising

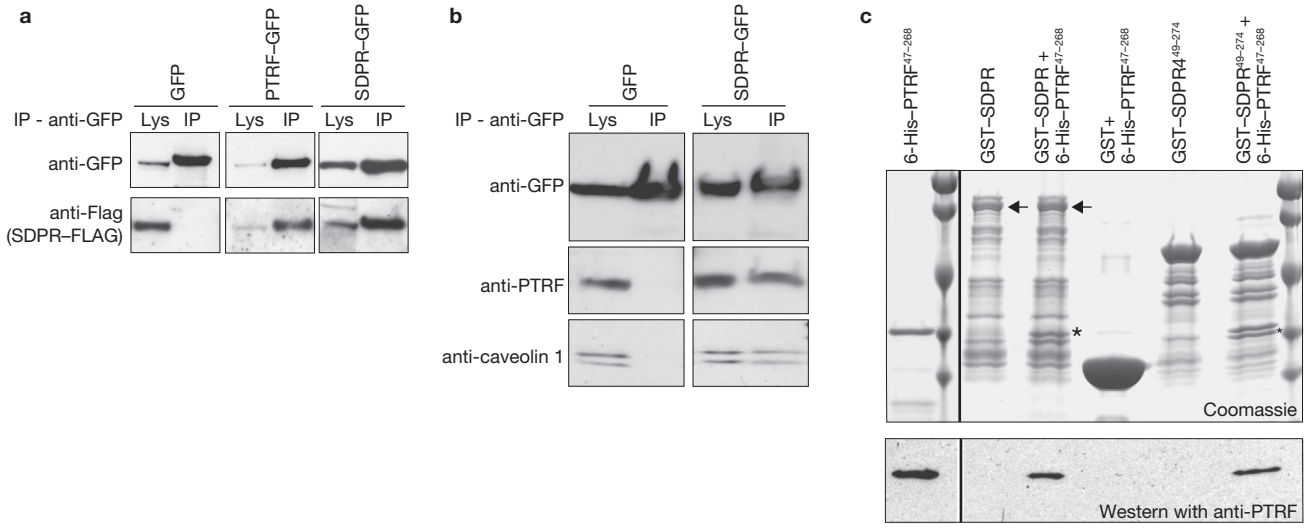

Figure 2 SDPR is present in protein complexes with PTRF and caveolin 1 and can bind directly to PTRF *in vitro*. (**a**) Immunoprecipitation of PTRF–GFP or SDPR–GFP from HeLa cells using anti-GFP antibodies results in co-precipitation with SDPR–Flag, as shown. Immunoprecipitation of GFP did not result in co-precipitation (IP: immunoprecipitate; Lys, cell lysate). (**b**) Immunoprecipitation of SDPR–GFP expressed in HeLa cells using an anti-GFP antibody results in specific co-precipitation of endogenous PTRF and caveolin 1, detected by western blotting as shown. (**c**) After purification on Ni-Agarose, 6-His–PTRF$^{47–268}$ (left hand lane) was applied to GST–SDPR, GST–SDPR$^{49–274}$ or GST immobilized on glutathione sepharose as indicated. Eluted proteins were analysed by SDS–PAGE and Coomassie staining or western blotting. The bands marked with arrows are intact GST–SDPR, other bands in the GST–SDPR lane are predominantly degradation products as determined by western blotting with an anti-SDPR antibody (data not shown). The asterisks highlight 6-His–PTRF$^{47–268}$ specifically bound to SDPR and SDPR$^{49–274}$. Full scans of all blots and gels are shown in Supplementary Information, Fig. S6.

the minimal region required for membrane targeting and tubulation). Nevertheless, 6-His–PTRF$^{47–268}$ clearly bound efficiently and specifically to both GST–SDPR and GST–SDPR$^{49–274}$ (Fig. 2c). To confirm that the Coomassie-stained band with a size corresponding to 6-His–PTRF$^{47–268}$ that was eluted bound to the SDPR constructs was PTRF, we used western blotting with anti-PTRF antibodies (Fig. 2c). PTRF and SDPR therefore do indeed bind to each other directly and specifically, and this interaction does not require the presence of caveolin 1.

SDPR has a direct role in the biogenesis of caveolae

PTRF is required for the production of normal levels of caveolae[15,16,20]. As a reduction in SDPR expression causes concomitant reductions in the expression of PTRF and caveolin 1, the same phenotype would be expected in *SDPR* shRNA cell lines. We counted the number of plasma membrane caveolae in electron micrographs representing complete sections through cells from control and *SDPR* shRNA cell lines (Supplementary Information, Fig. S4), and observed the predicted loss of caveolae (Fig. 3a).

To address whether the role of SDPR is limited to stabilizing PTRF and caveolin 1 expression, we first compared the number of caveolae in a control shRNA cell line with *SDPR* shRNA cells, after transfection of both cell lines with PTRF–mCherry and caveolin 1–GFP and FACS isolation of transfected cells. Transfection with PTRF and caveolin 1 caused an increase in the number of caveolae relative to untransfected cells, but there were markedly less caveolae in the *SDPR* shRNA cells compared to the control cells (Fig. 3a). Therefore, not only does SDPR function during the biogenesis of caveolae, but it probably has specific roles in this process beyond that of regulating PTRF and caveolin 1 expression levels. Additionally, immuno-labelling in cryo-sections of SDPR–GFP-expressing cells and subsequent electron microscopy revealed clear colocalization between caveolin 1 and SDPR in caveolae (Fig. 3b). SDPR and caveolin 1 were additionally present in larger tubulo-vesicular structures, as analysed below (Fig. 3c).

Comparison of the effects of overexpression of PTRF with those of SDPR provided an initial way to further dissect their function within caveolae. Overexpression of PTRF–GFP caused an increase in the number of caveolae as compared with untransfected cells (Fig. 3a), but did not alter the morphology of these invaginations (Fig. 3d). In contrast, overexpression of SDPR–GFP did not significantly alter the total number of caveolae, but rather altered their morphology, with many showing distended and elongated profiles (Fig. 3a, d). Thus, although both SDPR and PTRF are directly involved in caveolar biogenesis and morphology, they have differing and specific properties.

SDPR recruits PTRF to plasma membrane caveolae

We expressed PTRF–mCherry and caveolin 1–GFP in control and *SDPR* shRNA cell lines. A reduction in SDPR-expression caused a visible decrease in the amount of PTRF–mCherry present in caveolin 1–GFP puncta in confocal images (Fig. 4a). To confirm the loss of PTRF–mCherry from the plasma membrane in cells with reduced levels of SDPR, we mechanically lysed appropriately transfected *SDPR* shRNA and control cells, and the post-nuclear supernatant was subjected to centrifugation at 100,000*g* to form membrane pellets. There was far less PTRF–mCherry in the membrane fraction (P100) of the *SDPR* shRNA cells (Fig. 4b). In contrast, the amount of SDPR found in the membrane fraction was not altered in *PTRF* shRNA cells (Fig. 4b).

Overexpression of PTRF and SDPR fused with GFP or mCherry in mouse embryonic fibroblasts (MEFs) from caveolin 1-knockout mice (*cav1*$^{-/-}$; ref. 29) was used to further investigate their function in the absence of caveolin 1. Confocal images showed that, when expressed alone, PTRF had a predominantly cytosolic distribution, whereas SDPR was found associated

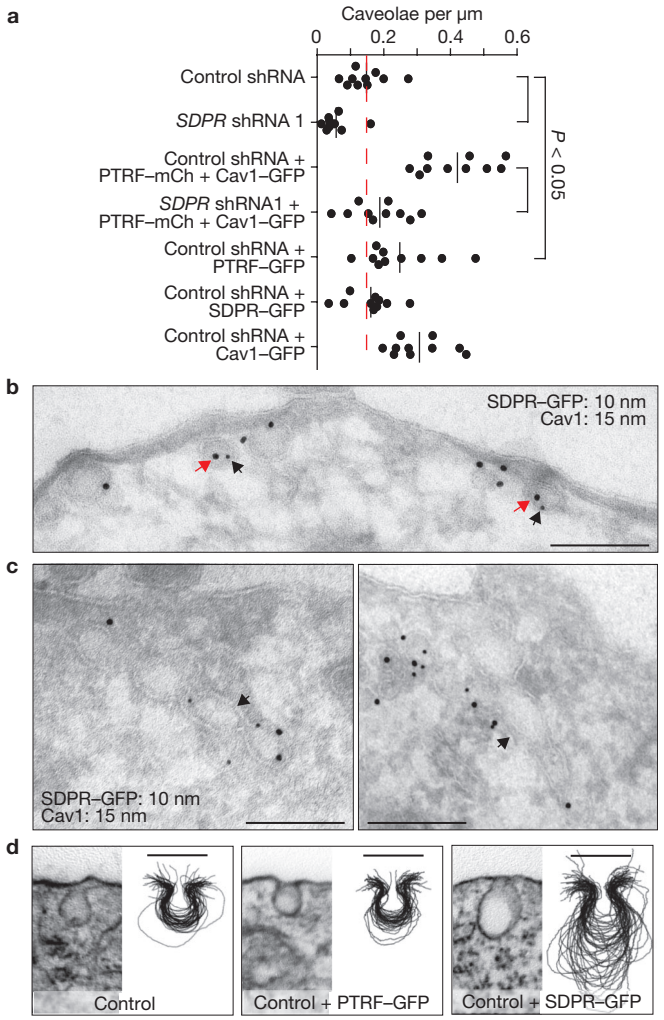

Figure 3 SDPR is required for the formation of caveolar membrane invaginations, and induces formation of elongated caveolae when overexpressed. (**a**) The frequency of caveolae formation in HeLa cell lines stably transfected with different shRNAs and transiently transfected with various plasmids is shown (cav1, caveolin 1; mCh, mCherry). Transiently transfected cells were selected using FACS. For each cell line, electron micrographs showing complete sections through ten cells were analysed (Supplementary Information, Fig. S5). Black bars represent the mean for each sample and the dashed red line shows the mean for control cells. *P* values were determined using unpaired student's *t* test. (**b**) Immunolabelling of cryo-sections of SDPR–GFP-expressing cells with antibodies against caveolin 1 (15 nm gold; red arrow) and GFP (10 nm gold; black arrows). Scale bar, 200 nm. (**c**) Immunolabelling of cryo-sections of SDPR–GFP-expressing cells with antibodies against caveolin 1, as in **b**. Examples of extended caveolae and tubulo-vesicular structures containing SDPR and caveolin 1 are shown. Scale bar, 200 nm. (**d**) Morphology of caveolae in cells overexpressing PTRF or SDPR. Electron micrographs of typical caveolae from each cell line are shown, together with manually superimposed caveolar membrane profiles from 50 caveolae (Supplementary Information, Fig. S5). Scale bars, 100 nm.

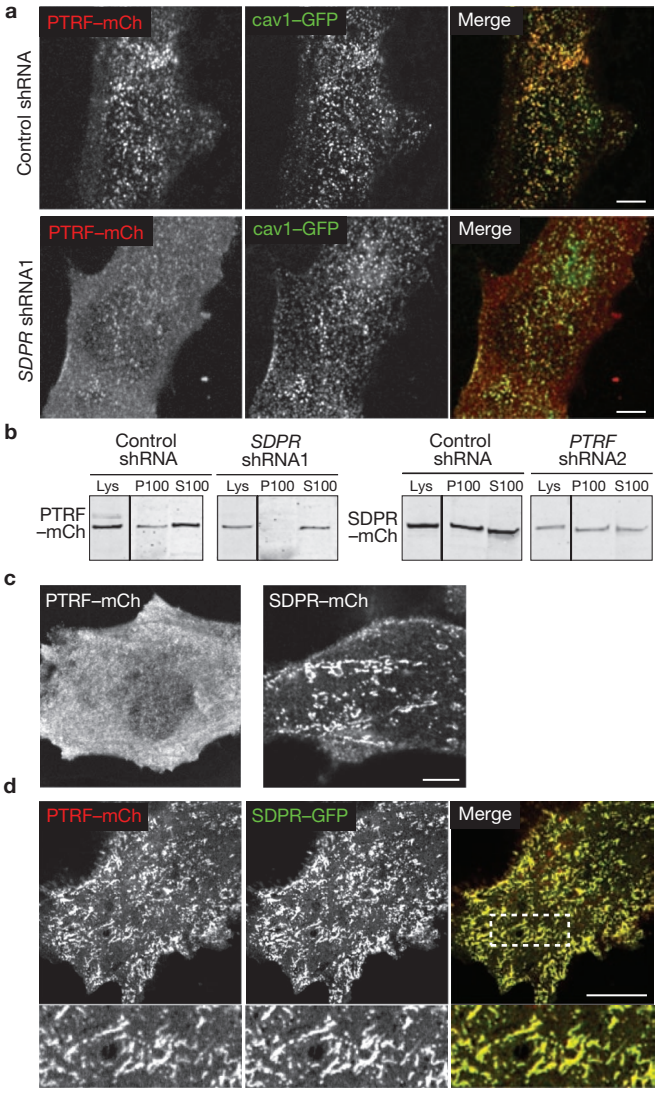

Figure 4 SDPR recruits PTRF to caveolae and the plasma membrane. (**a**) Recruitment of PTRF–mCherry to caveolin 1–GFP puncta in cells stably transfected with control and *SDPR* shRNAs were visualized by confocal microscopy. Cells expressing equivalent amounts of PTRF–mCherry (PTRF–mCh) and caveolin 1–GFP (Cav1–GFP) are shown. Scale bars, 10 µm. (**b**) Fractionated samples of post-nuclear supernatants from control, *SDPR* and *PTRF* shRNA cell lines transfected with PTRF–mCherry and caveolin 1–GFP (left) or SDPR-mCherry and caveolin 1-GFP (right) were subjected to western blotting. Cell lysates (Lys) were prepared by solubilization of the post-nuclear supernatant in SDS–PAGE sample buffer. P100 represents a membrane pellet formed at 100,000*g* and S100 represents the supernatant at 100,000*g*. Blots were probed with an anti-mCherry antibody and fluorescent secondary antibodies, and analysed using a Licor Odyssey fluorescence scanner for linear detection. Full scans of blots are shown in Supplementary Information, Fig. S6. (**c**) Confocal images showing the distribution of PTRF–mCherry and SDPR–mCherry expressed individually at similar levels in *cav1*$^{-/-}$ MEFs. Scale bar, 10 µm. (**d**) Co-expression of PTRF–mCherry and SDPR–GFP in *cav1*$^{-/-}$ MEFs results in the recruitment of PTRF–mCherry to SDPR–GFP membrane patches and tubes. Scale bar, 10 µm. Lower panels are a magnified view of the region delineated by a dashed line.

with the plasma membrane in patches and tubes (Fig. 4c). Co-expression of PTRF and SDPR resulted in translocation of PTRF from the cytosol to the same membrane patches and tubes as SDPR (Fig. 4d). PTRF–mCherry and SDPR–GFP colocalized in *cav1*$^{-/-}$ MEFs even at the lowest detectable expression levels (data not shown). These data confirm that PTRF associates with protein complexes that also contain SDPR, and that the assembly of these complexes is sufficient to recruit PTRF to membranes.

SDPR-overexpression generates membrane tubes

Overexpression of SDPR causes accumulation of pronounced tubes in both HeLa cells and *cav1*$^{-/-}$ MEFs, suggesting that SDPR may be able to stablize or generate membrane curvature. Labelling of HeLa cells with

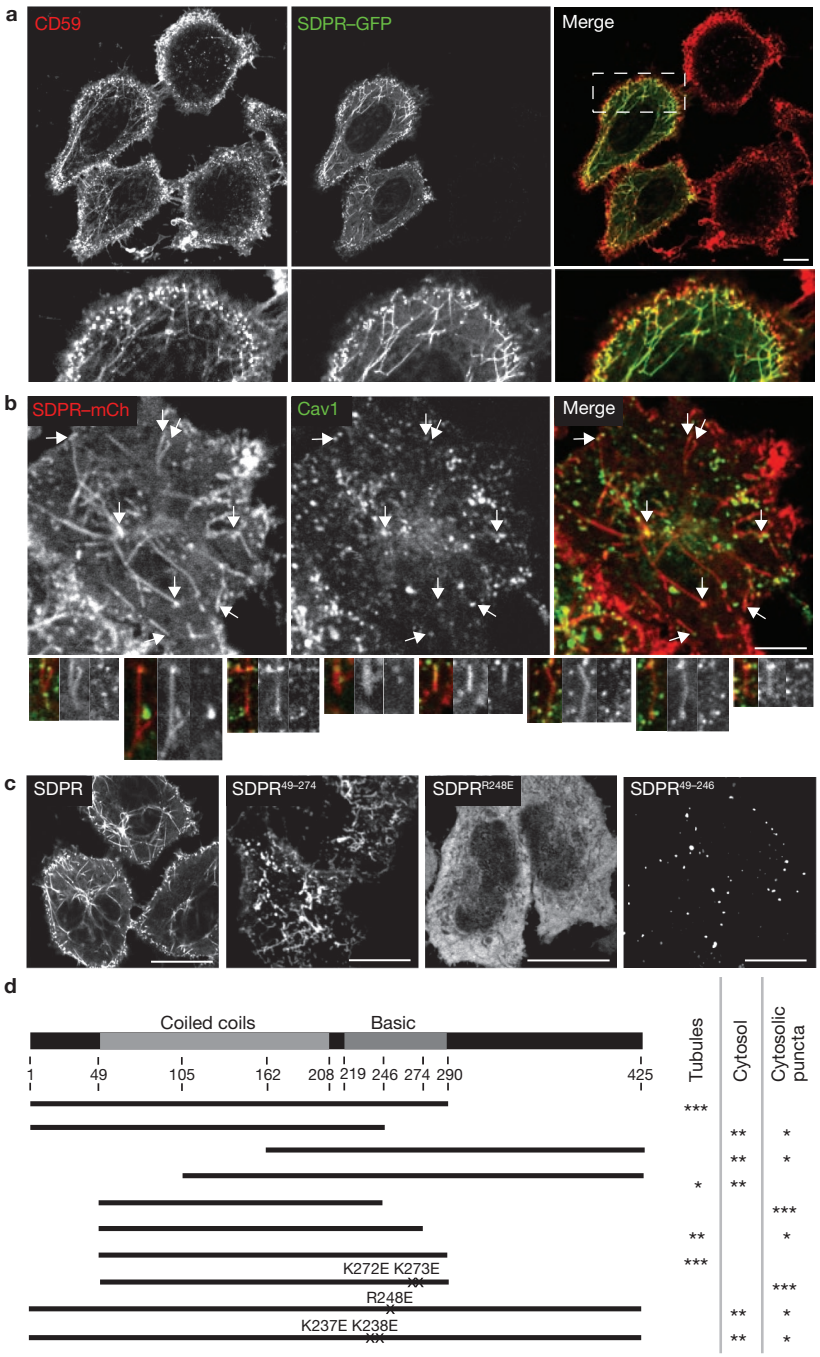

Figure 5 SDPR overexpression induces membrane tubes derived from caveolae. (**a**) Live HeLa cells, some of which overexpressed SDPR–GFP, were labelled with fluorescent antibodies against the GPI (glycosylphosphatidylinositol)-linked protein CD59, 20 min before confocal imaging. Lower panels show a magnified view of the region denoted by the dashed line. Scale bar, 20 μm. (**b**) Caveolin 1 (Cav 1) localizes to the ends of SDPR–mCherry (SDPR–mCh)-positive membrane tubes, as highlighted by arrows. Caveolin 1 was detected with polyclonal antibodies using indirect immunofluorescence. Scale bar, 10 μm. Lower panels show further examples of SDPR-induced membrane tubes with caveolin 1-puncta at one end. All images are confocal. (**c**) Different distributions of overexpressed SDPR mutants. Various GFP-tagged mutants of SDPR, as indicated, were overexpressed at similar levels in live HeLa cells and imaged using confocal microscopy. Scale bars, 20 μm. (**d**) Mapping of the region of SDPR required for membrane targeting and tubulation. The diagram indicates a selected subset of all constructs analysed, with a score representing their subcellular distribution based on up to three asterisks (aa, amino acid). Only overexpressing cells were analysed — some mutants that are not membrane targeted when overexpressed are still found in caveolae when expressed at low levels, presumably because of binding to endogenous SDPR or another caveolar component. Construct 105–425 was occasionally observed in the nucleus as well as the cytosol.

fluorescent antibodies against the plasma membrane marker CD59 confirmed that the SDPR-positive tubes are composed of plasma membrane derived membrane and that these tubes are induced by SDPR expression, as they were not observed in non-transfected cells (Fig. 5a). Expression of untagged SDPR also resulted in extensive membrane tubulation (Supplementary Information, Fig. S5b).

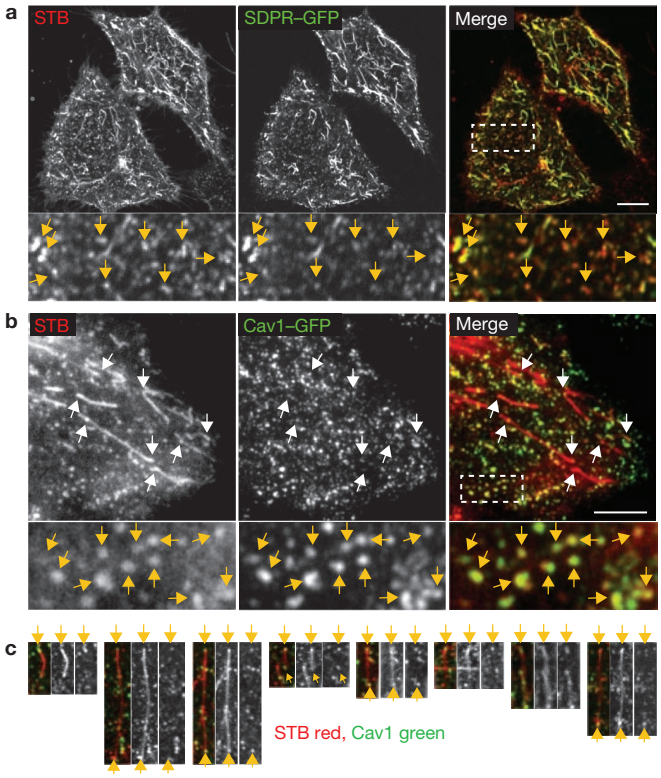

Figure 6 Membrane tubes induced by STB colocalize with SDPR and caveolin 1. (**a**) Colocalization between overexpressed SDPR–GFP and STB–Cy3 (Cy3, cyanine dye) in energy-depleted HeLa cells. Confocal image of live cells. Scale bar, 20 μm. Lower panels show a magnified view of the region delineated by the dashed line. Yellow arrows highlight extensive colocalization in membrane puncta. (**b**). Confocal images showing localization of caveolin 1–GFP (Cav1–GFP) to the ends of STB-induced tubes and colocalization between caveolin 1 and STB puncta in unfixed energy-depleted cells. Scale bar, 10 μm. White arrows indicate localization of caveolin 1 to the end of STB-positive tubes. Lower panels show a magnified view of the region delineated by the dashed line. Yellow arrows indicate colocalization in membrane puncta. (**c**) Further examples of localization of caveolin 1 (Cav 1) to the ends of STB tubes are shown. Tubes are lined up using caveolin 1 puncta at one end of the tube, indicated with large arrows. Some tubes also have caveolin 1 puncta at the other end of the tube, indicated with small arrows.

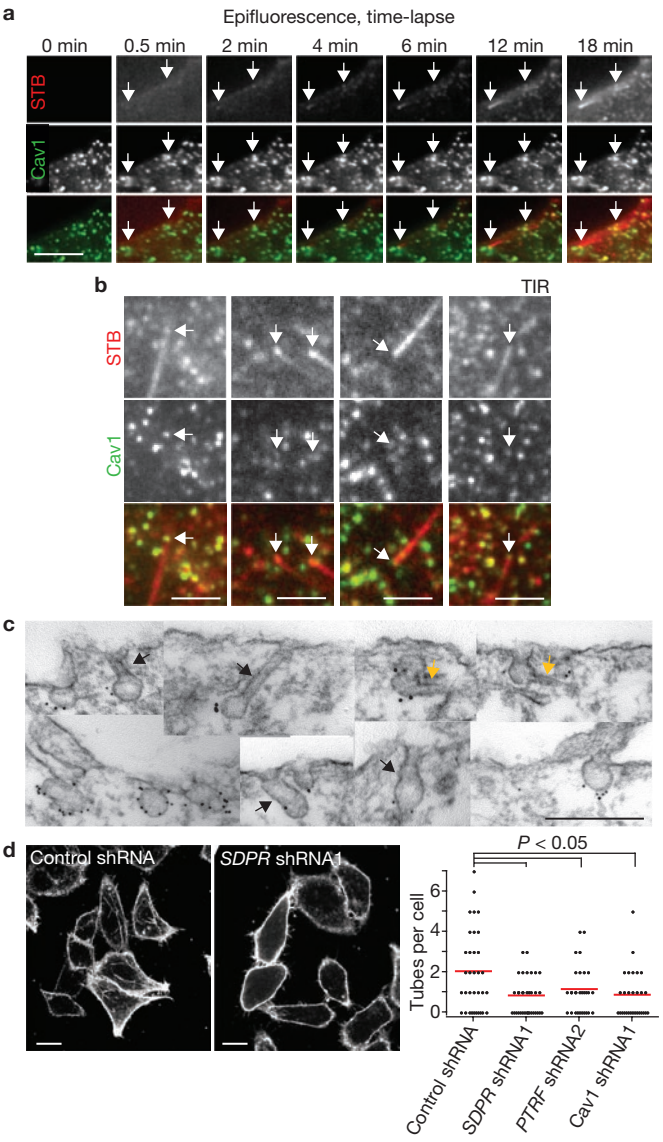

Figure 7 STB-induced membrane tubes grow from caveolae, and their formation is facilitated by caveolar proteins. (**a**) Time-lapse epifluorescence images of an energy-depleted HeLa cell expressing caveolin 1–GFP to which STB has been added (at 0 min). Arrows indicate STB-induced tubules growing from caveolin 1-positive puncta. See also Supplementary Information, Movies 1 and 2. Scale bar, 2 μm. (**b**) Montage of TIR microscopy images of STB-labelled, energy-depleted, unfixed HeLa cells expressing caveolin 1–GFP. Arrows indicate caveolin 1 (Cav1) puncta at the membrane-proximal end of STB-induced tubes. Each series of panels is from a different cell. Scale bars, 2 μm. (**c**) Pre-embedding immuno-electron microscopy of energy-depleted cells after treatement with STB. Cells were labelled with a polyclonal anti-caveolin 1 antibody and 10 nm gold-conjugated secondary antibodies. Black arrows indicate caveolae with STB-induced membrane tubes connecting them to the plasma membrane and yellow arrows indicate caveolae at the plasma membrane with STB-induced membrane tubes emanating from them. Normal caveolae (no arrows) are also shown for comparison. Scale bar, 200 nm. (**d**) The effect of reduced SDPR, PTRF and caveolin 1 expression on STB-induced membrane tubulation in energy-depleted cells. Images are of live HeLa cell lines stably transfected with the shRNAs shown. Data were quantified (right) and the number of STB-positive membrane tubes in the different cell lines is shown. The red bars denote the mean for each sample. *P* values were determined using unpaired Student's *t*-test.

We labelled HeLa cells overexpressing SDPR–mCherry with antibodies against caveolin 1 and examined them using confocal microscopy. There was little detectable alteration in the distribution of caveolin 1 in these cells, but 64% of SDPR-positive tubes (in the 20 cells analysed) had a caveolin 1-positive punctum at one end (Fig. 5b), and caveolin 1 puncta were also observed along the tube. This is consistent with the observation of SDPR–GFP and caveolin 1 in tubulo-vesicular structures by cryo-electron microscopy (Fig. 3c), and suggests that, in cells expressing caveolin 1, SDPR tubes frequently originate from caveolae.

We mutated SDPR to define the minimal region of this protein required to associate with the plasma membrane and generate membrane tubes (Fig. 5c). Both the conserved region (amino-acids 49–208) that contains putative coiled coils and the adjacent region characterized by abundant basic residues (amino-acids 219–274) were required for membrane targeting and tubulation. Figure 5d shows the SDPR mutants that support this conclusion. Notably, we did not find membrane-targeted mutants that did not induce tubulation, and replacement of pairs of basic residues in the region 219–274 with glutamate was generally sufficient to abolish

membrane targeting (Fig. 5c, d). The mutations R248E, K237E + K238E, K243E + K244E, K257E + K261E and K272E + K273E all abolished membrane targeting of full-length SDPR. Furthermore, mutants such as SDPR$^{49–290}$ K272E + K273E that contain the coiled-coil region and accumulated in the cytoplasm as puncta could recruit endogenous PTRF to these puncta, thereby confirming that SDPR binds to and recruits PTRF (Supplementary Information, Fig. S5A).

SDPR and other caveolar components facilitate STB-induced tubulation of the plasma membrane

Tubular membrane structures have been implicated in the endocytosis of STB, and STB induces extensive membrane tubulation in energy-depleted cells[12,14]. As it is not known whether cytosolic or membrane proteins participate in the formation of these tubes, we asked whether they could be related to the tubes induced by SDPR overexpression. When HeLa cells overexpressing SDPR–GFP were depleted of ATP and labelled with STB there was a high degree of colocalization between STB and SDPR in both tubes and membrane puncta (Fig. 6a). We compared cells expressing equivalent quantities of SDPR–GFP and found the number and appearance of SDPR-positive tubes was not altered by a combination of energy poisons and STB (Supplementary Information, Fig. S5C). This implies that although STB induces the formation of tubes in energy-depleted, non-transfected cells[12], it may preferentially enter SDPR tubes that are already present.

SDPR tubes originate in caveolae (Fig. 5), and in energy-depleted cells, SDPR puncta colocalize with STB (Fig. 6a). As SDPR puncta colocalize with caveolin 1 (Fig. 1b, c), we looked for colocalization between caveolin 1 and STB in energy-depleted cells. STB in membrane puncta colocalized extensively with caveolin 1–GFP (Fig. 6b), and STB-positive membrane tubes frequently had caveolin 1 puncta at one or both ends (Fig. 6b, c). These data suggest that the tubes induced by SDPR overexpression and the tubes induced by STB-labelling of energy-depleted cells both originate in caveolae.

To better define the caveolar origin of STB-induced tubes in energy-depleted cells we used a combination of time-lapse imaging, TIR imaging and electron microscopy. The STB-induced tubulation of the plasma membrane was followed in real time with an epifluorescence microscope. Tubes could readily be observed growing from caveolin 1-containing puncta (Fig. 7a, Supplementary Information, Movies 1, 2). TIR imaging, with its very limited depth of illumination, provides a way of observing the plasma membrane-proximal end of STB-induced tubes. Analysis of TIR images revealed that 88% of STB-induced tubes had a caveolin 1-positive punctum at the proximal end (n = 148 tubes in 24 individual cells; Fig. 7b). These puncta were not always as bright as neighbours that did not form the origin of an STB tube. As caveolae contain a defined amount of caveolin 1 (ref. 30), this is consistent with the idea that caveolin 1 can also be distributed in puncta elsewhere along the tube (as shown by confocal microscopy in Fig. 6c). Indeed, when energy-depeleted, STB-labelled cells were analysed by immuno-electron microscopy two different types of STB-induced caveolar deformations were observed: caveolin 1-containing caveolae at the plasma membrane-distal end of long tubular invaginations, and membrane tubes emanating from caveolin 1-containing caveolae at the plasma membrane (Fig. 7c). STB-induced membrane tubes are at least ten times less abundant than caveolae (Fig. 6b), and accordingly most anti-caveolin 1 antibody labelling was of morphologically normal caveolae (Fig. 7c). Together, these data strongly support the conclusion that STB-induced tubes in energy-depleted cells are derived from caveolae.

To assess the role of caveolae in STB uptake without energy depletion, we looked for colocalization between caveolin 1 and STB. Although we did observe some, the extent of this colocalization was less than that observed after energy depletion (Fig. 6b; Supplementary Information, Fig. S5d). Tubular intermediates containing STB were observed, albeit markedly less frequently than in energy-depleted cells, and these tubes also originated in caveolin 1 puncta (Supplementary Information, Fig. S5D). This suggests that in unperturbed HeLa cells, uptake in tubular intermediates may account for a minor fraction of total STB internalization, but again the tubes detected are likely to be derived from caveolar membrane invaginations.

As STB-positive tubes were most abundant in energy-depleted cells we used that system to assay the functional requirement for SDPR and the other components of caveolae in STB-induced membrane tubulation. ShRNA cell lines, as well as control cells, were energy depleted and labelled with STB so as to induce formation of membrane tubes. The number of tubes over 2 μm in length per cell was counted (Fig. 7d). Reduction in SDPR-, PTRF- or caveolin 1-expression (Supplementary Information, Fig. S5E) resulted in a decrease in the amount of STB-induced tubulation (Fig. 7d). Cells included in this analysis were selected to have the same amount of bound STB, so reduced tubulation in shRNA cell lines cannot be explained solely by a reduction in STB binding. We conclude that the presence of functional caveolae facilitates the formation of STB-induced membrane tubes in cells.

DISCUSSION

Our data show that SDPR is present in a complex with PTRF. SDPR promotes recruitment of PTRF to caveolae and has a direct role in the formation of caveolar invaginations. Thus, the formation of caveolae is not solely dependent on oligomerization of caveolin proteins[5], but requires association of other factors. The structure of the multi-molecular assemblies required for characteristic caveolar morphology, with its defined combination of positive and negative membrane curvature, remains to be fully understood. One theory is that the recruitment or modification of PTRF + SDPR-containing complexes is important for changes in caveolar morphology[8,31,32].

Overexpressed SDPR can bind to the plasma membrane and induce membrane tubulation, implying that its role within caveolae is directly related to generating curvature. The region of SDPR responsible for membrane tubulation comprises a potentially helical, coiled-coil forming region adjacent to another conserved domain containing multiple basic amino acids (Fig. 5d). There is no obvious sequence similarity between SDPR and known curvature-inducing protein domains, so SDPR may induce curvature using a new mechanism[33]. Further insights will require structural information. SDPR can be recruited to membranes independently from caveolin 1 and binds to phosphatidylserine *in vitro*, making this lipid a good candidate for the plasma membrane receptor of SDPR[21,22,24]. PTRF has also been reported to bind to phosphatidylserine[16]. However, our data implies that this interaction alone is not of sufficiently high affinity to confer plasma membrane localization on PTRF.

STB can enter the cell by multiple mechanisms including through clathrin-coated pits; different mechanisms may predominate in different cell types, and it is not clear how the behaviour of the toxin in energy-depleted cells relates to its uptake under physiological conditions[13,34,35].

Our data show that, at least in energy-depleted HeLa cells, STB is concentrated in caveolae; other reports highlight its concentration in clathrin-coated pits[13,35]. We found the colocalization between caveolin 1 and STB to be reduced when cells were not depleted of energy. STB can induce membrane deformations in liposomes[12], but our data reveals that in cells STB-induced tubes originate from caveolae and that formation of these tubes is less efficient in the absence of caveolar proteins. These results are not incompatible. Caveolae, either because of their lipid composition or the fact that they are pre-curved, are clearly favoured binding sites for STB. The tubulation induced by STB can then be seen as a deformation of caveolae that uses curvature-inducing caveolar proteins. □

METHODS

Methods and any associated references are available in the online version of the paper at http://www.nature.com/naturecellbiology/.

Note: Supplementary Information is available on the Nature Cell Biology website.

ACKNOWLEDGEMENTS

We thank K. Riento, H. Pelham and S. Munro for comments on the manuscript. C.G.H. is supported by the MRC, Cowi Foundation, Ulla og Mogens Andersens Fond, Oticon Fonden, Julie Von Mullens Fond, Fuhrmann-Fonden, Krista og Viggo Petersen's Fond, Reinholdt W Jorck og Hustrus Fond, Christian og Ottilia Brorsons Rejselegat for Yngre Videnskabsmænd- og Kvinder, Niels Bohr Fond and Henry Shaw's Legat. N.A.B. is supported by the MRC.

AUTHOR CONTRIBUTIONS

C.G.H. carried out the majority of experiments and data analysis, and participated in project planning; N.A.B. carried out cryo-electron microscopy; G.H. carried out all other electron microscopy and B.J.N. carried out some experiments and data analysis, participated in project planning, and wrote the paper.

COMPETING FINANCIAL INTERESTS

The authors declare no competing financial interests.

Published online at http://www.nature.com/naturecellbiology/
Reprints and permissions information is available online at http://npg.nature.com/reprintsandpermissions/.

1. Mayor, S. & Pagano, R. E. Pathways of clathrin-independent endocytosis. *Nature Rev. Mol. Cell Biol.* **8,** 603–612 (2007).
2. Kirchhausen, T. Three ways to make a vesicle. *Nature Rev. Mol. Cell Biol.* **1,** 187–198 (2000).
3. Stagg, S. M., LaPointe, P. & Balch, W. E. Structural design of cage and coat scaffolds that direct membrane traffic. *Curr. Opin. Struct. Biol.* **17,** 221–228 (2007).
4. Lajoie, P. & Nabi, I. R. Regulation of raft-dependent endocytosis. *J. Cell Mol. Med.* **11,** 644–653 (2007).
5. Bauer, M. & Pelkmans, L. A new paradigm for membrane-organizing and -shaping scaffolds. *FEBS Lett.* **580,** 5559–5564 (2006).
6. Le Lay, S. & Kurzchalia, T. V. Getting rid of caveolins: phenotypes of caveolin-deficient animals. *Biochim. Biophys. Acta* **1746 (3),** 322–333(2005).
7. Parton, R. G. & Richards, A. A. Lipid rafts and caveolae as portals for endocytosis: new insights and common mechanisms. *Traffic* **4,** 724–738 (2003).
8. Stan, R. V. Structure and function of endothelial caveolae. *Microsc. Res. Tech.* **57,** 350–364 (2002).
9. Pelkmans, L., Burli, T., Zerial, M. & Helenius, A. Caveolin-stabilized membrane domains as multifunctional transport and sorting devices in endocytic membrane traffic. *Cell* **118,** 767–780 (2004).
10. Kirkham, M. *et al.* Ultrastructural identification of uncoated caveolin-independent early endocytic vehicles. *J. Cell Biol.* **168,** 465–476 (2005).
11. Kumari, S. & Mayor, S. ARF1 is directly involved in dynamin-independent endocytosis. *Nature Cell Biol.* **10,** 30–41 (2008).
12. Romer, W. *et al.* Shiga toxin induces tubular membrane invaginations for its uptake into cells. *Nature* **450,** 670–675 (2007).
13. Lauvrak, S. U. *et al.* Shiga toxin regulates its entry in a Syk-dependent manner. *Mol. Biol. Cell* **17,** 1096–1109 (2006).
14. Sandvig, K. *et al.* Pathways followed by protein toxins into cells. *Int. J. Med. Microbiol.* **293,** 483–490 (2004).
15. Liu, L. & Pilch, P. F. A critical role of cavin (polymerase I and transcript release factor) in caveolae formation and organization. *J. Biol. Chem.* **283,** 4314–4322 (2008).
16. Hill, M. M. *et al.* PTRF-Cavin, a conserved cytoplasmic protein required for caveola formation and function. *Cell* **132,** 113–124 (2008).
17. Vinten, J., Johnsen, A. H., Roepstorff, P., Harpoth, J. & Tranum-Jensen, J. Identification of a major protein on the cytosolic face of caveolae. *Biochim. Biophys. Acta* **1717,** 34–40 (2005).
18. Aboulaich, N., Vainonen, J. P., Stralfors, P. & Vener, A. V. Vectorial proteomics reveal targeting, phosphorylation and specific fragmentation of polymerase I and transcript release factor (PTRF) at the surface of caveolae in human adipocytes. *Biochem. J.* **383,** 237–248 (2004).
19. Vinten, J. *et al.* A 60-kDa protein abundant in adipocyte caveolae. *Cell Tissue Res.* **305,** 99–106 (2001).
20. Liu, L. *et al.* Deletion of Cavin/PTRF causes global loss of caveolae, dyslipidemia, and glucose intolerance. *Cell Metab.* **8,** 310–317 (2008).
21. Gustincich, S. & Schneider, C. Serum deprivation response gene is induced by serum starvation but not by contact inhibition. *Cell Growth Differ.* **4,** 753–760 (1993).
22. Gustincich, S. *et al.* The human serum deprivation response gene (*SDPR*) maps to 2q32-q33 and codes for a phosphatidylserine-binding protein. *Genomics* **57,** 120–129 (1999).
23. Mineo, C., Ying, Y. S., Chapline, C., Jaken, S. & Anderson, R. G. Targeting of protein kinase Cα to caveolae. *J. Cell Biol.* **141,** 601–610 (1998).
24. Burgener, R., Wolf, M., Ganz, T. & Baggiolini, M. Purification and characterization of a major phosphatidylserine-binding phosphoprotein from human platelets. *Biochem. J.* **269,** 729–734 (1990).
25. Izumi, Y. *et al.* A protein kinase Cδ-binding protein SRBC whose expression is induced by serum starvation. *J. Biol. Chem.* **272,** 7381–7389 (1997).
26. Ogata, T. *et al.* MURC, a muscle-restricted coiled-coil protein that modulates the Rho/ROCK pathway, induces cardiac dysfunction and conduction disturbance. *Mol. Cell Biol.* **28,** 3424–3436 (2008).
27. Tagawa, M. *et al.* MURC, a muscle-restricted coiled-coil protein, is involved in the regulation of skeletal myogenesis. *Am. J. Physiol. Cell Physiol.* **295**, C490–498 (2008).
28. Merrifield, C. J., Feldman, M. E., Wan, L. & Almers, W. Imaging actin and dynamin recruitment during invagination of single clathrin-coated pits. *Nature Cell Biol.* **4,** 691–698 (2002).
29. Razani, B. *et al.* Caveolin-1 null mice are viable but show evidence of hyperproliferative and vascular abnormalities. *J. Biol. Chem.* **276,** 38121–38138 (2001).
30. Pelkmans, L. & Zerial, M. Kinase-regulated quantal assemblies and kiss-and-run recycling of caveolae. *Nature* **436,** 128–133 (2005).
31. Kirkham, M. *et al.* Evolutionary analysis and molecular dissection of caveola biogenesis. *J. Cell Sci.* **121,** 2075–2086 (2008).
32. Rothberg, K. G. *et al.* Caveolin, a protein component of caveolae membrane coats. *Cell* **68,** 673–682 (1992).
33. Zimmerberg, J. & Kozlov, M. M. How proteins produce cellular membrane curvature. *Nature Rev. Mol. Cell Biol.* **7,** 9–19 (2006).
34. Nichols, B. J. *et al.* Rapid cycling of lipid raft markers between the cell surface and Golgi complex. *J. Cell Biol.* **153,** 529–541 (2001).
35. Sandvig, K. & van Deurs, B. Entry of ricin and Shiga toxin into cells: molecular mechanisms and medical perspectives. *EMBO J.* **19,** 5943–5950 (2000).

METHODS

Constructs. cDNA for PTRF from *Rattus norvegicus* was a gift from J. Vinten[17] (University of Copenhagen, Denmark). The cDNA encoding PTRF was PCR amplified with suitable forward (5'-GGACTCGAGATGGAGGATGT-CACGCTCCATATCGTC-3') and reverse (5'-TGCGAATTCCGTCGCTGTCGCT-CTTGTCCACCAG-3') primers and was subcloned in the *Xho*I and *Eco*RI sites of pEGFP–N1 (Clontech) generating PTRF–EGFP. EGFP was exchanged with mCherry using *Bam*HI and *Not*I sites to generate PTRF–mCherry.

Human SRBC and SDPR were obtained as cDNA (I.M.A.G.E. Consortium, clone IDs 3882155 and 4620139, respectively) and PCR amplified with appropriate primers for insertion into the *Sal*1 and *Bam*HI sites in the pEGFP–N1 vector. Primers used for amplification were: SRBC, forward primer 5'-CTTGTCGACA-TGAGGGAGAGTGCGTTGGAGCCGGGGC-3' and reverse primer 5'-CACG-GATCCGCTCCGGCTACACTCTCCA TTTGGAGCAG-3'; SDPR, forward primer 5'-CTTGTCGACATGGGAGAG GACGCTGCACAGGCCGAAAAG-3' and reverse primer 5'-CTTGGATCCG CTCCGGAGGTCTGGTGCACCTGG-AGCACGGCG-3'. Versions of these constructs that were tagged at the carboxy-terminal with mCherry were generated by swapping EFGP for mCherry using *Age*I and *Bsr*GI. An SDPR construct Flag-tagged at the C-terminal was also generated in the pEGFP–N1 vector by using the same gene-specific forward primers, but by engineering two stop codons following an engineered Flag (5'-CTAGGATCC-TATTACTTATCGTCGTCATCCTT GTAATCACCTGCCCCGGGTCCGGA-GGTCTGGTGCACCTGGAGCACGGCGGGCTGCACG-3') as the reverse primer. MURC (TrueClone, Origene; accession number XM_294592) was cloned into the *Eco*RI and *Sal*I sites in pEGFP–N3 (Clontech), resulting in MURC–GFP.

SDPR–CFP that contained silent mutations to avoid targeting by *SDPR* shRNA 2 was produced by site-directed mutagenesis of *SDPR* cDNA inserted in a pECFP–N1 vector. Five silent nucleotide substitutions were introduced, 5'-961AGTGAG-CAG969-3' to 5'-961TCCGAACAA969-3'.

Generation of SDPR truncation mutants was performed by PCR amplification of SDPR using appropriate primers with engineered *Sal*I and *Bam*HI restriction sites. The PCR products were then inserted into pEGFP–N1 or pmCherry–N1. Single and double point-mutants were generated using site directed mutagenesis.

All PCR-generated constructs were sequenced by Geneservice in their entirety to ensure that no PCR-generated artefacts were present. Plasmids were transfected into HeLa cells or MEFs maintained in DMEM and 10% FCS, using Fugene 6 (Roche).

ShRNAs. Stable knockdown cell lines were generated using HUSH technology (Origene). A pRS vector expressing an appropriate shRNA 29mer from the U6 promoter was transfected into HeLa cells growing in DMEM. One day after transfection the DMEM was supplemented with puromycin (0.7 μg ml^{-1}). After 14 days in selection media, the cells were re-seeded at an appropriate dilution to ensure that single clones could be selected. After a further 21 days under selection the isolated clones were assayed for knockdown of expression levels of the protein of interest by western blotting. The constructs targeting PTRF, 5'-CACCTTC-CACGTCAAGAAG ATCCGCGAGG-3' (*PTRF* shRNA1) and 5'-CTGCTGGA-GATCACCGAGGAG TCGGACGC-3' *PTRF* shRNA2) were from Origene. An empty pRS vector (control) and a pRS vector with a non-targeting shRNA cassette 5'-TGACCACCCTGACCTACGGCGTGCAGTGC-3' (control shRNA) were also from Origene. No difference in the expression levels of the proteins assayed or any other characteristics between cell lines generated from the two different control constructs was observed, therefore the control shRNA cell line was used in all figures. ShRNA constructs targeting human *SDPR* were generated by ligating two complementary primers and insert them into BamH1 and HINDIII sites in the empty pRS vector. The sequences targeted were 5'-CCAGCCTGAA-GAAGTGGATAG CCTCAAG-3' (*SDPR* shRNA 1) and 5'-AGTGAGCAGAT-GCCAAATGACCAG GAAGA-3' (*SDPR* shRNA 2). Caveolin 1 shRNA HeLa cell lines were produced as described for *SDPR*. Two separate cell lines targeting 5'-TGGAAGGCCAGCTTCACCACCTTCACTGT-3' (caveolin 1 shRNA1) and 5'-AGAGCTTCCTGATTGAGATTCAGTGCATC-3' (caveolin 1 shRNA2) of human caveolin 1 mRNA were generated.

Bacterial expression and purification of PTRF and SDPR. A pGEX-6P-2 vector was used for amino-terminal GST expression of SDPR constructs that were inserted into the *Eco*RI and *NOT*I sites. A pET28 vector was used for N-terminal 6-His-tagged expression of $PTRF^{47–268}$, which was inserted into the *Nde*I and *Eco*RI sites. This construct proved superior in terms of both expression and stability compared with full-length PTRF. Protein expression was carried out using the BL21 strain of *Escherichia coli* grown in Luria–Bertani medium. Expression was induced in bacteria at an optical density (OD) at 600nm of 0.4–0.5 at 18 °C with IPTG (isopropyl-β-D-thiogalactopyranoside; 0.5 mM). The next day the bacteria were spun down, washed in cold PBS, sonicated and spun down again for 10 min at 3,800*g*. The post-nuclear supernatant was spun down at 100,000*g* for 45 min. The resulting supernatant was used in a one-step batch purification with glutathionine sepharose or Ni-NTA agarose as appropriate.

Immunoprecipitations. HeLa cells were transfected with constructs of interest 36 h before collection. Immunoprecipitations were carried out using the μMacs Epitope Tag Protein Isolation Kit (Miltenyi Biotec). Cells were lysed directly into the provided lysis buffer (which included 1% Triton X-100), supplemented with protease inhibitors and OG (n-β-Octylglycoside; 1%). Solubilization was carried out for 2 h on a roller at 4 °C. Non-solubilized material was removed by ultracentrifugation at 400,000*g* in a Beckman TL120.2 rotor. Magnetic beads conjugated to anti-GFP antibodies were added to the remaining samples, which were incubated at 4 °C for 1 h. Samples were added to μMACS magnetic columns and OG (0.2%) was added to the provided washing buffer. Protein complexes were eluted by a pH shift (0.1 M triethylamine and 0.1% Triton X-100, pH 11).

Antibodies. Peptides against amino-acids 9–23 and 312–325 of human SDPR were used to immunise the same rabbit. The resultant anti-serum was purified using immobilised peptides. This was carried out by Eurogentec. Sources for other antibodies were as follows: mouse monoclonal anti-c-Myc 9E10 (Sigma), rabbit polyclonal anti-PTRF (Abcam), mouse monoclonal anti-PTRF (Abnova), polyclonal rabbit anti-GFP (Abcam), polyclonal rabbit anti-Flag (Sigma), polyclonal rabbit anti-caveolin 1 and monoclonal mouse anti-caveolin 1 (BD Biosciences) and polyclonal anti-dsRed (against mCherry, Clontech). Primary antibodies were generally used at a 1:200 dilution for immunofluorescence and a 1:1000 dilution for western blotting. HRP-conjugated secondary antibodies were from DAKO and the ECL western blotting detection kit was from GE Healthcare. Protein A conjugated to 10 nm and 15 nm colloidal gold was from the Department of Cell Biology, University of Utrecht.

Light Microscopy. TIR microscopy images were acquired with an Olympus TIR illumination system with a ×100 1.45 NA objective. Confocal microscopy images were acquired with a Zeiss LSM510. Standard FITC (fluorescein isothiocyanate) and rhodamine filter sets were used for imaging GFP and mCherry fluorescence.

Electron microscopy. For both resin-embedded and cryo-electron microscopy, transfected cells were sorted away from untransfected cells by FACS. They were then re-plated and allowed to grow overnight to regain normal cell morphology. For microscopy of resin-embedded sections, cells grown in Petri dishes were briefly washed twice with PBS and then fixed in paraformaldehyde (PFA; 2%) and glutaraldehyde (2.5%) in sodium cacodylate (0.1 M at pH 7.2). They were scraped off and centrifuged in a horizontal rotor and then the pellets were embedded in agar (2%), cut into blocks (1 mm^3) and placed in fresh fixative. Cells were fixed at room temperature for 1 h and then stored at 4 °C. Samples were washed thoroughly in sodium cacodylate buffer (0.1 M) and post fixed in OsO4 (1% in 0.1 M sodium cacodylate) for 1 h and then washed with distilled water. Samples were then en bloc stained with uranyl acetate (2%) in ethanol (30%) before dehydration in a graded ethanol series followed by 1,2, epoxy propane (propylene oxide) and then infiltrated and embedded in CY212 resin (Agar Scientific).

For pre-embedding immunogold electron microscopy, cells were washed with PBS and fixed in a paraformaldehyde (4%), sodium cacodylate (0.1 M) buffer (pH 7.4) for 2 h at room temperature. After three 10 min washes in cacodylate buffer, the cells were pelleted in Eppendorf tubes at 1500*g* for 8 min (this applied to each subsequent step when changing buffers) and washed twice in Tris (0.05 M), HCl (0.05 M) NaCl (0.15 M) and TBS (tris buffered saline at pH 7.4). Cells were then permeabilised in TBS containing saponin (0.05%), BSA (3%) and glycine (0.02 M), for 30 mins. Note that saponin was added to all subsequent TBS incubation and wash steps. The cells were then incubated in rabbit anti-caveolin antisera (1:20 dilution) for 2 h at room temperature, washed in TBS and incubated with goat anti-rabbit IgG (immunoglobulin G) conjugated to 10 nm gold (BB International) for 1 h. Cells were then washed and finally fixed in glutaraldehyde (2%) in cacodylate buffer, post fixed and embedded in CY212.

DOI: 10.1038/ncb1887

Ultrathin (50–70 nm) sections were cut on a Reichert Ultracut E microtome and collected on uncoated 200 mesh grids. Sections were post stained with saturated uranyl acetate before staining with Reynolds lead citrate. Images were acquired using a Philips EM208 microscope, with an operating voltage of 80 kV, and a CCD camera.

Immunogold cryo-electron microscopy was carried out as follows: HeLa cells expressing GFP-tagged SDPR were washed with PBS, fixed with paraformaldehyde (4%) and glutaraldehyde (0.1%) in a sodium cacodylate buffer (0.1 M at pH 7.2) and pelleted in an eppendorf tube (16,000*g* for 5 min). The fixative was aspirated and the cell pellet was re-suspended in warm gelatin (10%) in PBS. The cells were then pelleted (16,000*g* for 5 min) and the gelatin-coated cells were set on ice, trimmed into blocks (1 mm^3) and infused with sucrose (1.7 M) in poly vinyl pyrolidone (15%) for 24 h at 4 °C. The blocks were subsequently mounted on cryotubes and snap-frozen in liquid nitrogen. Frozen ultrathin sections were cut using a diamond knife in an ultramicrotome with a cryochamber attachment (Leica) at –120 °C, collected from the knife-edge with 50:50 methyl cellulose (2%): sucrose (2.3 M)[37] and mounted on formvar carbon-coated electron microscopy grids.

Sequential immunolabelling of caveolin and EGFP was performed using the protein A-gold technique at room temperature[38]. The sections were compared by embedding in methyl cellulose(1.8%) and uranyl acetate (0.3%) and air-dried before observation with a Philips CM100 transmission electron microscope with an operating voltage of 80kV.

Cell labelling and indirect immunofluorescence. STB–Cy3 was a gift from F. Barr[36] (University of Liverpool, UK). STB–Cy3 was used at a final concentration of 0.5 μg ml^{-1}. ATP depletion was carried out by incubating cells with NaN_3 (10 mM) and 2-deoxyglucose (10 mM) in PBS^{++}, as described previously[12]. For indirect immunofluorescence, cells were fixed in formaldehyde (4%) and pre-warmed to 37 °C, as we found this improved the preservation of membrane tubes. Antibody incubations were performed in PBS with FCS (10%) and saponin (0.2%).

36. Fuchs, E. *et al*. Specific Rab GTPase-activating proteins define the Shiga toxin and epidermal growth factor uptake pathways. *J. Cell Biol.* **177,** 1133–1143 (2007).
37. Liou, W., Geuze, H. J.& Slot, J. W. Improving structural integrity of cryosections for immunogold labeling. *Histochem. Cell Biol.* **106,** 41–58 (1996).
38. Slot, J. W., Geuze, H. J., Gigengack, S., Lienhard, G. E. & James, D. E. Immunolocalization of the insulin regulatable glucose transporter in brown adipose tissue of the rat. *J. Cell Biol.* **113,** 123–135 (1991).

nature cell biology

DOI: 10.1038/ncb1887

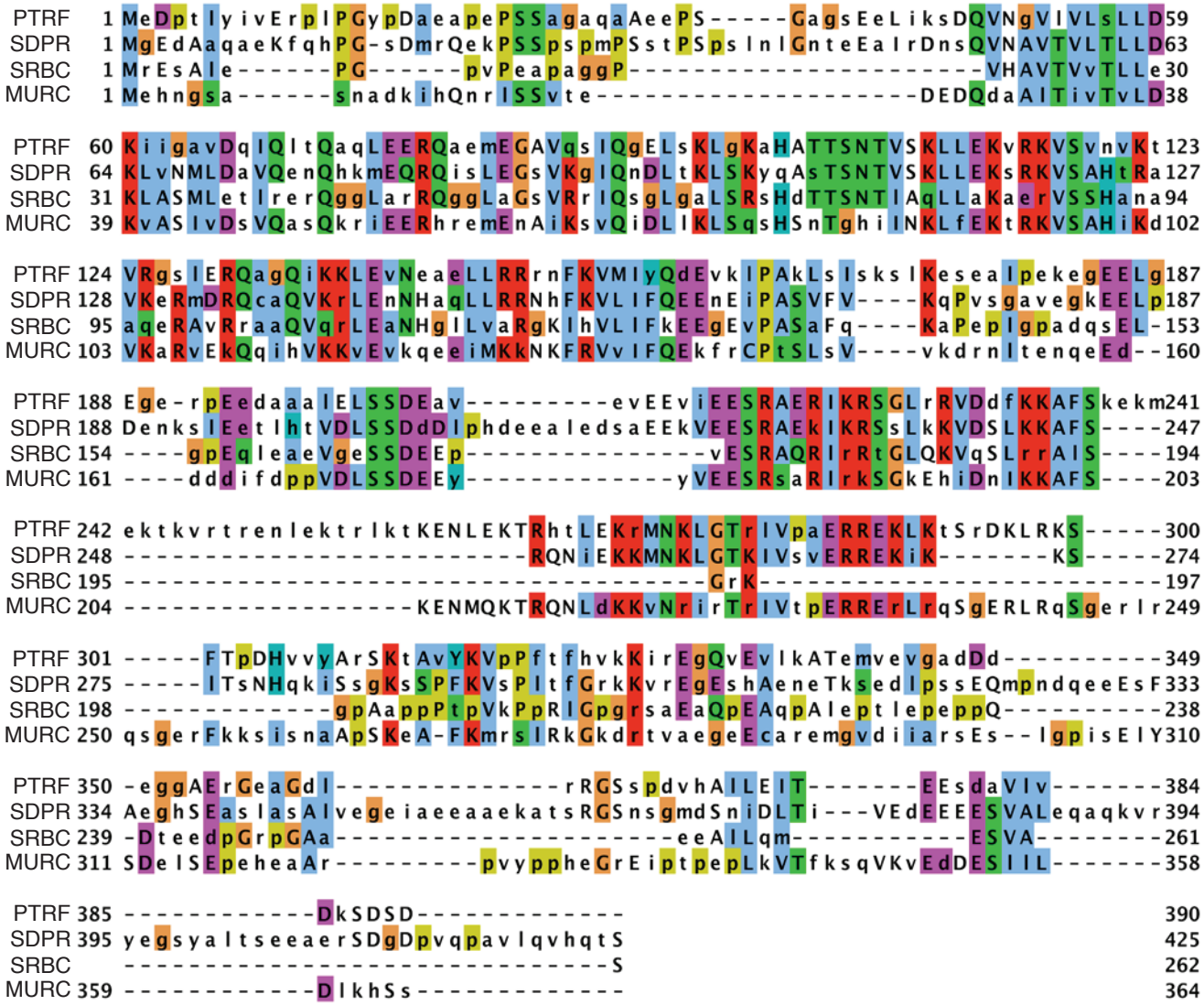

Figure S1 Alignment of the amino acid sequences of human PTRF, SDPR, SRBC and MURC. Generated using Jalview [1].

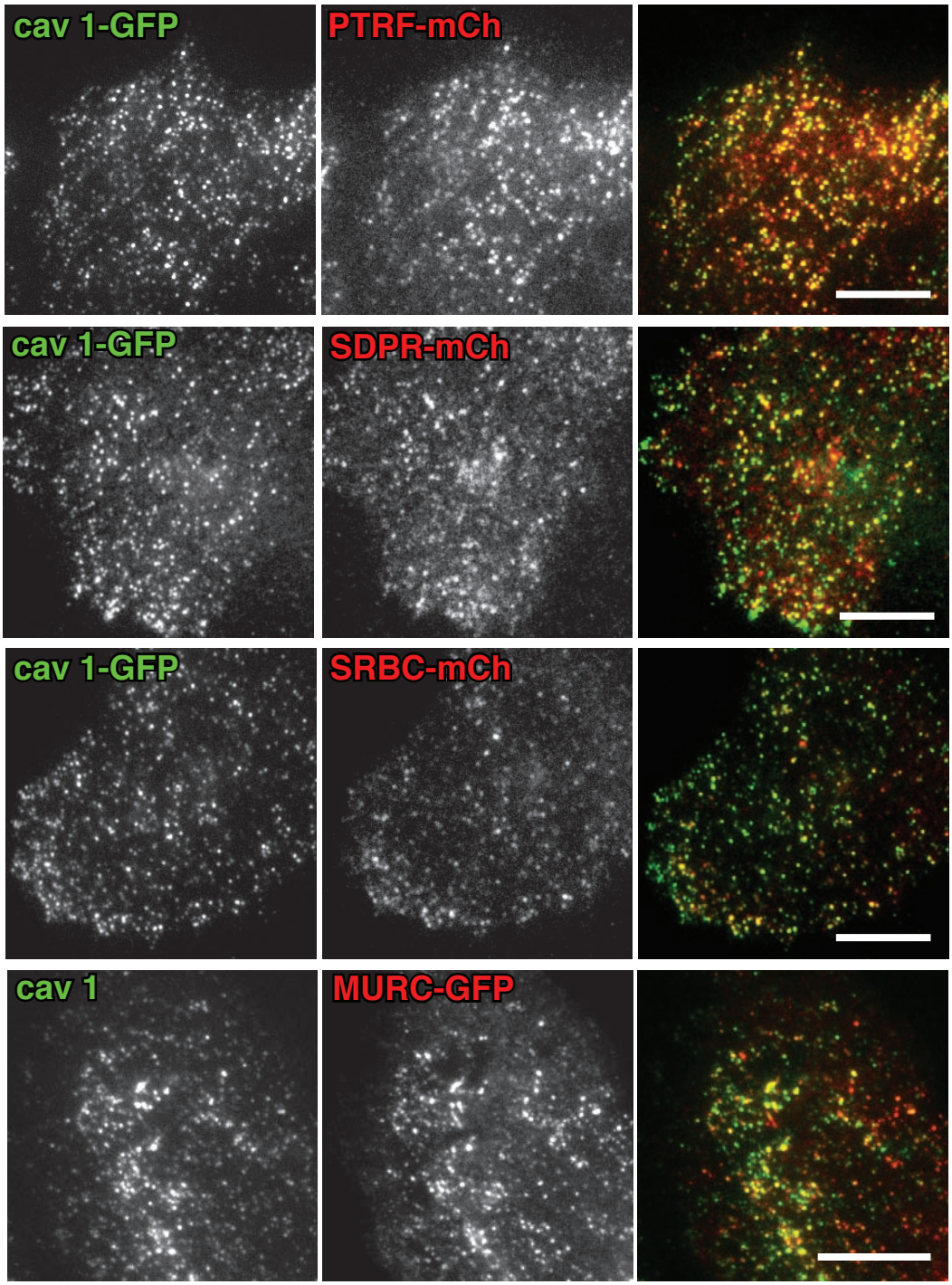

Figure S2 Localization of PTRF-mCh, SDPR-mCh, SRBC-mCh and MURC-GFP to caveolae. Total internal reflection images of HeLa cells fixed and stained using indirect immunofluorescence with antibodies against caveolin 1. Cells were expressing the constructs shown. Bars 10μm.

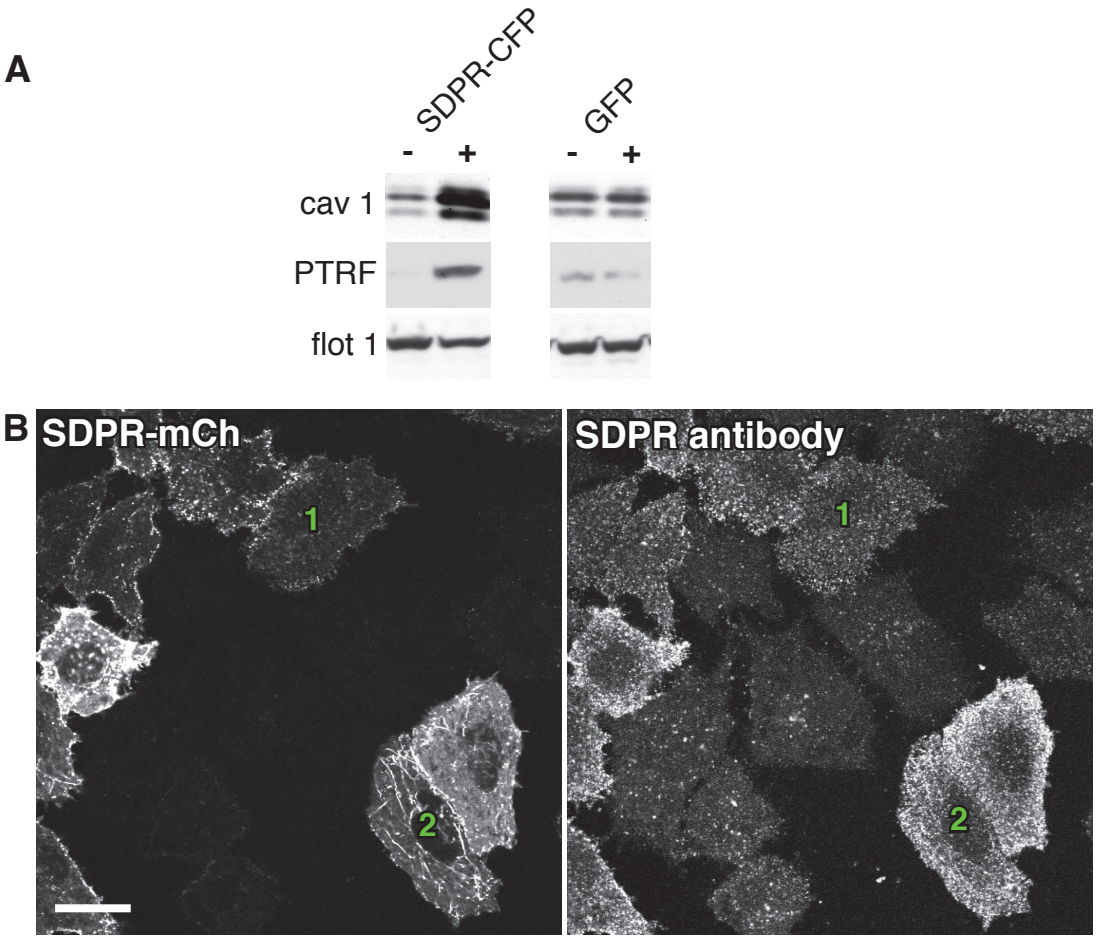

Figure S3 (**A**) Rescue of loss of PTRF and caveolin 1 expression in SDPR shRNA cell line upon re-expression of non-targeted SDPR. SDPR-CFP with silent mutations to avoid targeting by the shRNA was expressed in cell line SDPR shRNA 2 by transient transfection. As a control, a separate population of cells was transfected with plasmid expressing GFP. FACS was used to select and separate equal numbers of transfected from untransfected cells, extracts of which were then analyzed by Western blotting with antibodies against the proteins indicated in the figure. Antibodies against flotillin 1 were used to provide a control for equal loading. (**B**) Estimation of the extent of over-expression of SDPR-mCh in different cells. HeLa cells expressing SDPR-mCh, and neighboring untransfected cells, were fixed and stained using indirect immunofluorescence with antibodies against SDPR. Comparison of the mean fluorescence intensity from SDPR antibody staining between transfected and untransfected cells allow estimation of minimum fold over-expression of SDPR-mCh. In the cell labeled 1, where SDPR-mCh is punctate, over-expression is approximately 2x, in the cell labeled 2, where SDPR is in tubes, over-expression is approximately 10x. These are minimum estimates because in un-transfected cells a significant fraction of total fluorescence signal may come from non-specific labeling. Bar 20μm.

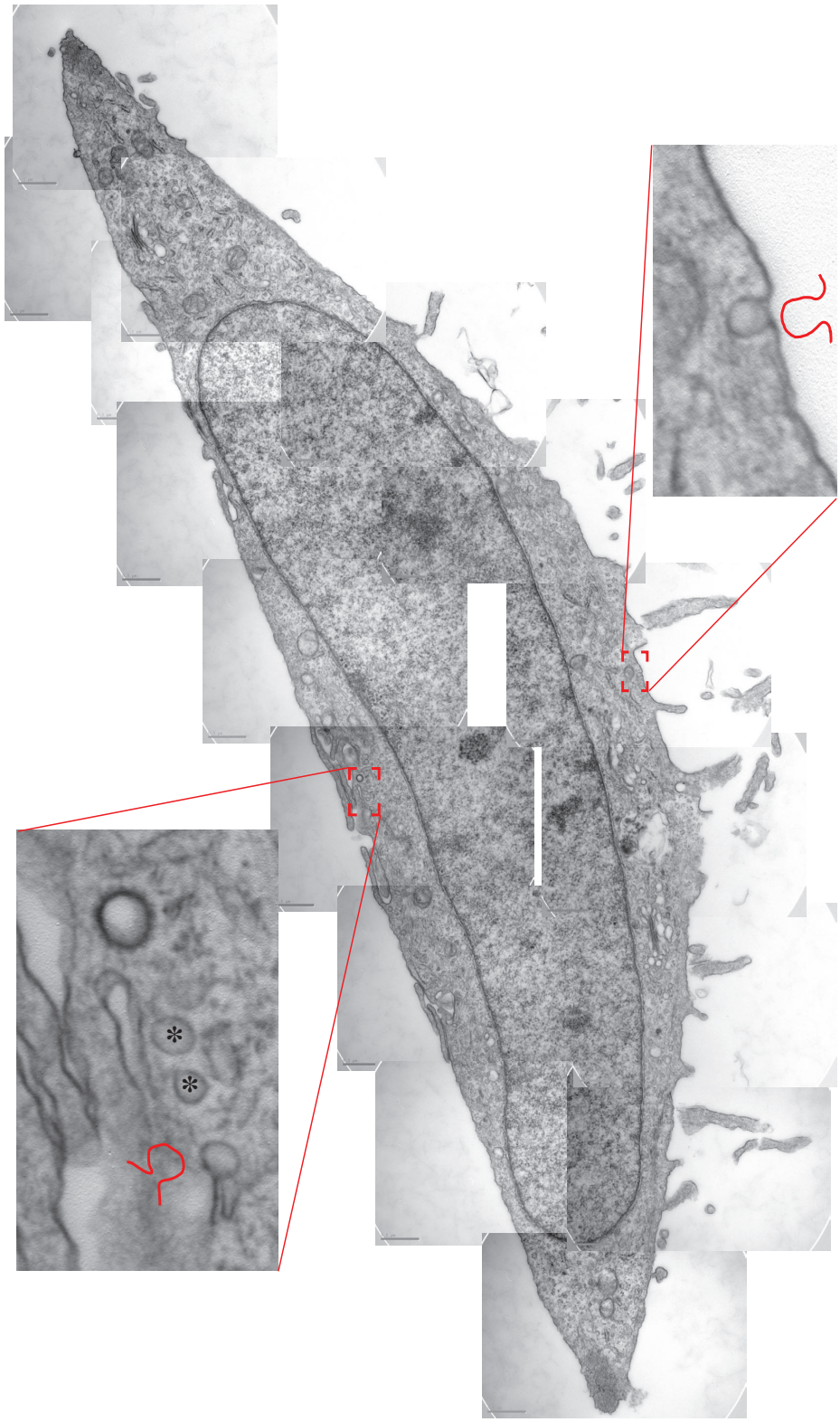

Figure S4 Quantification of the number and morphology of caveolae in reconstructed cell sections by electron microscopy. Images at 36,000 x magnification were acquired using a CCD camera, so as to completely track the perimeter of selected cells. Typically this required 20-30 images per cell. The number of caveolae clearly connected to the cell surface in each cell was counted, and their outline traced by hand and shown in the enlarged panels. Potential caveolae not open at the plasma membrane, such as the vesicular structures marked * in the left hand inset were not counted. Clathrin coated structures could be readily identified. The bars are 500nm.

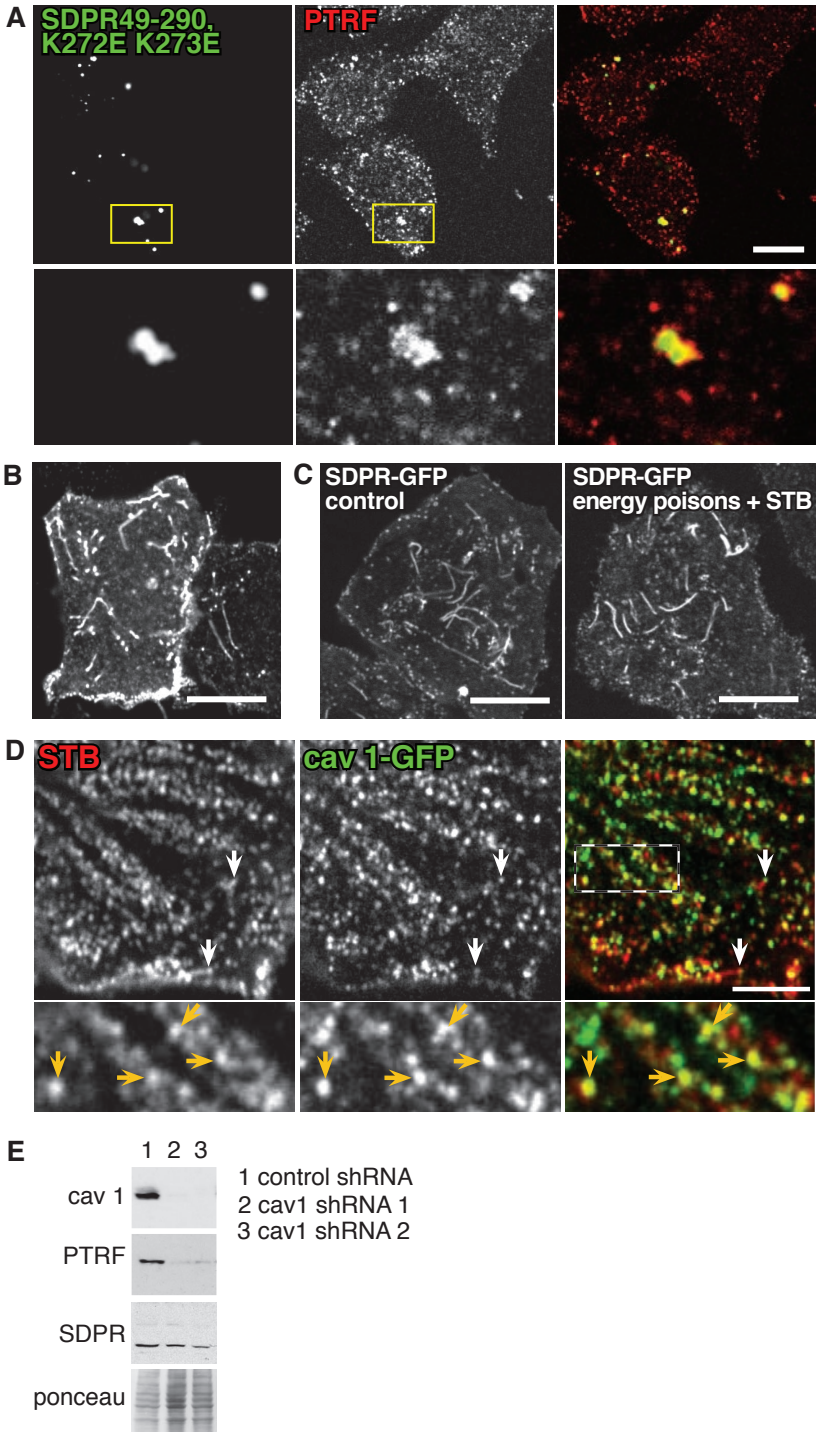

Figure S5 (**A**) Recruitment of endogenous PTRF to cytosolic puncta composed of SDPR49-290, K272E K273E. The SDPR mutant was GFP-tagged at the C-terminus. PTRF was detected by indirect immunofluorescence. The lower panels show a zoomed view of the region outlined with a white box. Bar 20μm. (**B**) SDPR over-expression induces membrane tubulation. Cells over-expressing non-tagged SDPR, fixed and labeled with anti-SDPR antibody. Bar 20μm. (**C**) Comparison of membrane tubulation in cells over-expressing the same amount of SDPR-GFP, with and without STB. Confocal sections of live cells. Bars 20μm. (**D**) Co-localization between STB and caveolin 1 without energy depletion. Confocal image. Bar 10μm. White arrows highlight localization of caveolin 1 at the end of STB-positive tubes, yellow arrows highlight co-localization in membrane puncta. The lower panels show a magnified view of the region delineated by the dashed line. Note that both the abundance of STB tubes and the extent of co-localization between STB and caveolin 1 in puncta are less than in energy depleted cells (Figure 6B). (**E**) Western blots showing down-regulation of caveolin 1 in caveolin 1 shRNA cell lines. Blots of whole cell lysates were probed with the antibodies shown. The anti-caveolin 1 blot was Ponceau stained to provide an indication of total protein levels in each sample.

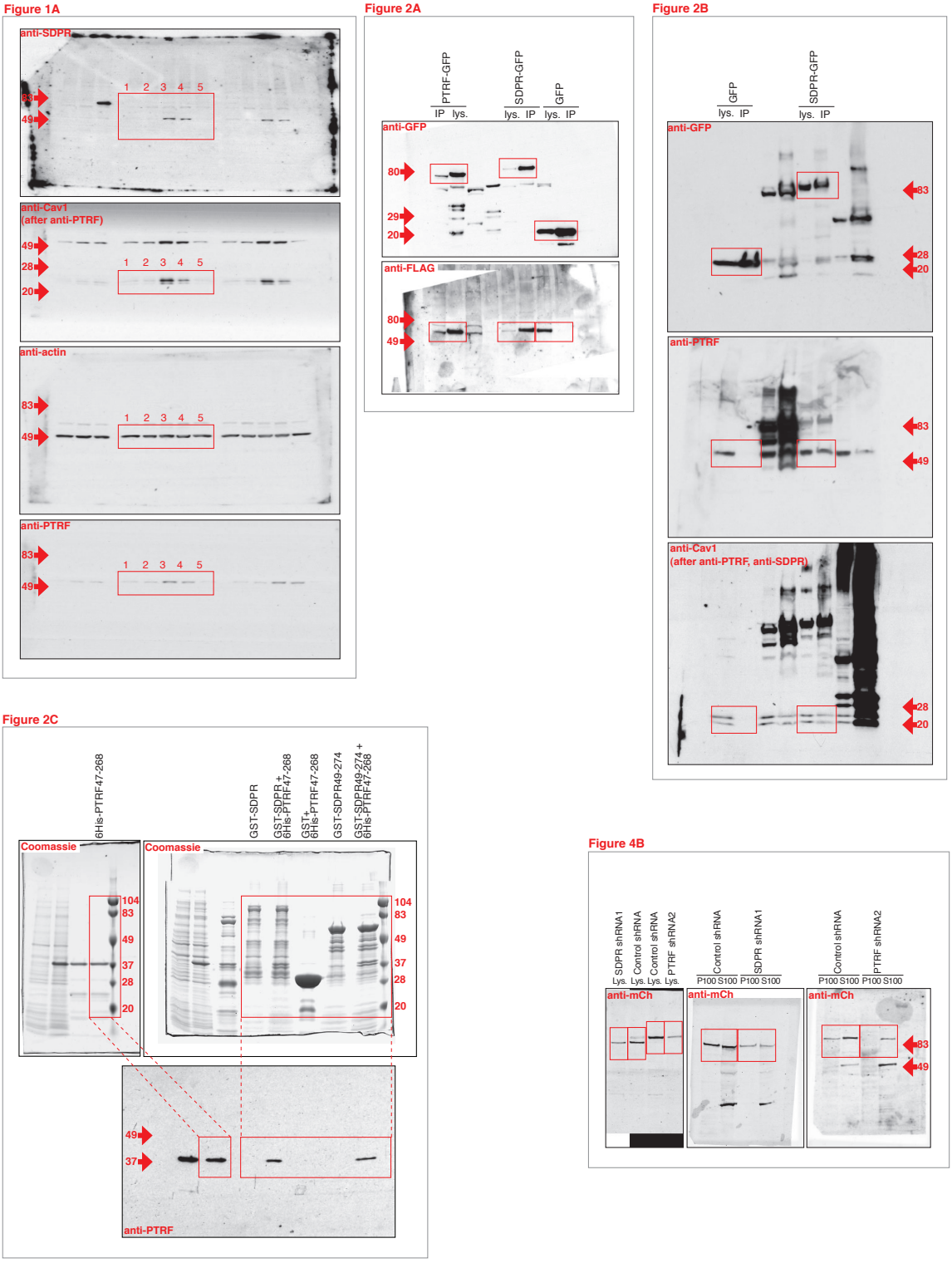

Figure S6 Full scans of all blots and gels from main figures. Red text indicates which main figure each panel relates to, which antibodies were used in blots, and positions of relevant size markers. Red boxes indicate the regions shown in the main figure. Black text is the labeling of the relevant lanes used in the main figure.

Movies 1 and 2 Both movies show time-lapse images of an energy-depleted cell expressing caveolin 1-GFP during addition of STB conjugated to Cy3. Movie 1 provides a lower resolution view of the whole cell, Movie 2 a zoomed in view of a region in the upper left hand corner of the cell. In both images the lefthand monochrome panel is STB-Cy3, right hand is caveolin1-GFP, and in the color overlay GFP is green and Cy3 red. Images were acquired at 4 images per minute, and play back at 15 images per second (i.e. 225x real time).

1. Clamp, M., Cuff, J., Searle, S.M., and Barton, G.J. (2004). The Jalview Java alignment editor. Bioinformatics *20*, 426-427.

nature cell biology

The Arp2/3 complex and WASp are required for apical trafficking of Delta into microvilli during cell fate specification of sensory organ precursors

Akhila Rajan[1,5,7], An-Chi Tien[2,6,7], Claire M. Haueter[3], Karen L. Schulze[3] and Hugo J. Bellen[1,2,3,4,8]

Cell fate decisions mediated by the Notch signalling pathway require direct cell–cell contact between adjacent cells. In *Drosophila melanogaster*, an external sensory organ (ESO) develops from a single sensory organ precursor (SOP) and its fate specification is governed by differential Notch activation. Here we show that mutations in *actin-related protein-3 (Arp3)* compromise Notch signalling, leading to a fate transformation of the ESO. Our data reveal that during ESO fate specification, most endocytosed vesicles containing the ligand Delta traffic to a prominent apical actin-rich structure (ARS) formed in the SOP daughter cells. Using immunohistochemistry and transmission electron microscopy (TEM) analyses, we show that the ARS contains numerous microvilli on the apical surface of SOP progeny. In *Arp2/3* and *WASp* mutants, the surface area of the ARS is substantially reduced and there are significantly fewer microvilli. More importantly, trafficking of Delta-positive vesicles from the basal area to the apical portion of the ARS is severely compromised. Our data indicate that WASp-dependent Arp2/3 actin polymerization is crucial for apical presentation of Delta, providing a mechanistic link between actin polymerization and Notch signalling.

Notch signalling is an evolutionarily conserved pathway used by metazoans to control cell fate decisions[1,2]. The Notch receptor and its ligands Delta and Serrate (Jagged in vertebrates) are single-pass transmembrane proteins. Cell–cell communication begins when the extracellular domain of the ligand on the signal-sending cell interacts with the extracellular domain of the Notch receptor on the signal-receiving cell. This interaction triggers a series of proteolytic cleavages that releases the intracellular domain of Notch, which enters the nucleus and functions as a transcriptional regulator[3].

Notch signalling mediates key decisions during nervous system development[4], including patterning and fate specification of the ESOs[5]. Each ESO is composed of four cell types (shaft, socket, sheath and neuron) and is derived from a single cell, the SOP (also called the pI cell), which is selected through Notch-mediated lateral inhibition at about 8–12 h after puparium formation (APF; Fig. 1a). The stage when the SOP has not yet undergone cell division is referred to as the 1-cell stage (15–18 h APF). During the 2-cell stage (~18–18.30 h APF) the SOP undergoes asymmetric cell division to generate the anterior pIIb and posterior pIIa (Fig. 1a). Because of the asymmetric distribution of cell fate determinants such as Numb and Neuralized[6,7], Notch signalling is differentially activated in pIIa and pIIb. The pIIa divides to create the external cells of the ESO, the shaft and socket cells. The pIIb divides twice to create the internal cells of the ESO, the neuron and sheath cell[8]. These four differentiated cells are collectively called the sensory cluster.

Delta and Serrate act redundantly to activate Notch during specification of pIIa and pIIb[9]. Recent studies indicate that endocytosis of Delta in the signal-sending cell is crucial for its ability to activate Notch[10]. An alternative, but not mutually exclusive model, is that ligand endocytosis promotes trafficking of the ligand to an endocytic recycling compartment, resulting in its activation[11,12]. In addition, apical trafficking of Delta seems to be important for proper fate specification in the SOP lineage[13]. However, the nature of ligand activation or the requirement for apical trafficking of the ligand remains unclear.

Here, we report that there is an apical actin-enriched structure in the pIIa and pIIb cells that contains numerous microvilli. The surface area of the actin-rich region and the number of microvilli are markedly reduced in *Arp2/3* complex and *WASp* mutants. More importantly, we found that the Arp2/3 complex and WASp have crucial roles in trafficking of endocytosed Delta vesicles to an apical ARS.

RESULTS

Mutations in *Arp3* result in a pIIa-to-pIIb cell fate transformation in *Drosophila* ESO lineages

Notch loss-of-function results in a pIIa-to-pIIb transformation, leading to loss of bristles[14]. Previous genetic screens based on assaying mitotic clones on the adult *Drosophila* thorax for bristle abnormalities[13,15,16] have

[1]Department of Molecular and Human Genetics, [2]Program in Developmental Biology, [3]Howard Hughes Medical Institute, [4]Department of Neuroscience, Baylor College of Medicine, Houston, TX 77030, USA. [5]Current address: Department of Genetics, Harvard Medical School, Boston, MA 021155, USA.[6]Current address: University of California, San Francisco, CA 94143, USA.
[7]These authors contributed equally to the work.
[8]Correspondence should be addressed to H.J.B. (e-mail: hbellen@bcm.tmc.edu)

Received 9 February 2009; accepted 17 March 2009; published online 21 June 2009; DOI: 10.1038/ncb1888

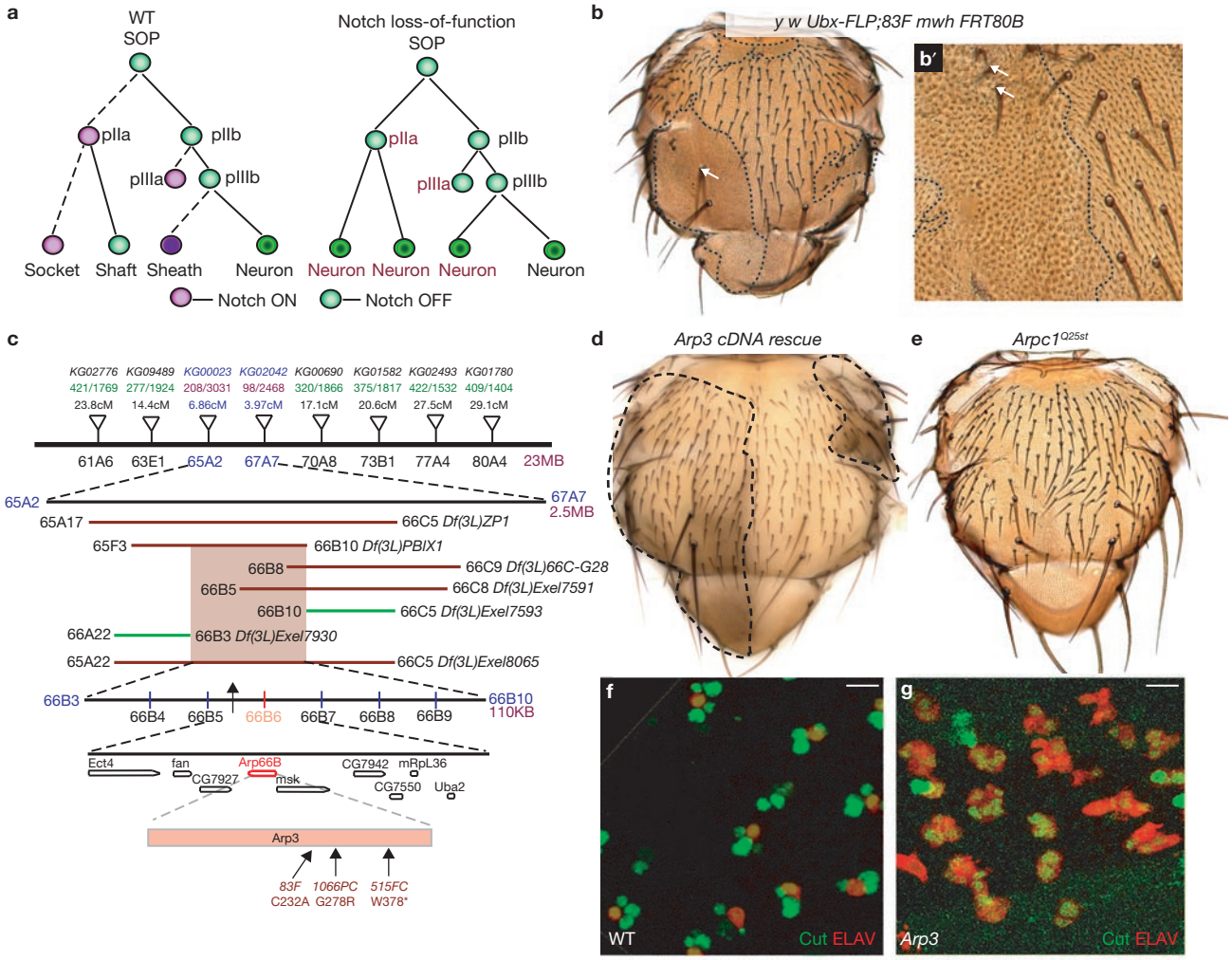

Figure 1 *Arp3* mutations cause a pIIa-to-pIIb transformation in the ESO lineage (**a**) A diagram of the ESO lineage in wild-type (WT) and in *Notch* loss-of-function background. Each cell is represented by a circle; the cells in which Notch is activated are in purple and the signal-sending cells are in green. The dashed lines indicate daughter cells in which Notch is activated. (**b**) Homozygous clones of $Arp3^{83F}$ on an adult thorax induced by *Ubx–FLP*. The clone (dashed lines) is identified by an epithelial cell marker *multiple wing hair (mwh)*, which marks the trichomes (small hair-like structures) on epithelial cells. Mutant clones show loss of external structures, socket and shaft cells, of the microchaetae. Macrochaetae (arrow) sometimes show a double-shaft phenotype in $Arp3^{83F}$ clones. (**b′**) Higher magnification of an $Arp3^{83F}$ clone shows that rarely there are shaft and sockets (arrows) in the mutant clone. Most of the $Arp3^{83F}$ clones show a balding phenotype. (**c**) Schematic representation of the mapping strategy. The inverted triangles represent *P* elements that were used for recombination mapping. Deficiencies represented by lines: those in red failed to complement the alleles, whereas those in green complement our alleles. (**d**) Rescue of the *Arp3* phenotype by overexpression of an *Arp3* cDNA construct in the mutant clones. An image of a pupal notum of an adult thorax which harbours *Arp3* clones; the mutant clones (dashed lines) do not show bristle loss (compare with **b**). (**e**) Flies that harbour clones of $Arpc1^{Q25st}$ show bald patches. The clones were not generated in a *Minute* background and hence appear smaller than *Arp3* clones (compare with **b**). We have not outlined the clones in $Arpc1^{Q25st}$ as they are unmarked clones. (**f**, **g**) A projection of confocal slices show part of the notum at 24–26 h APF stained for ELAV (red) and Cut (green). All cells in the wild-type (**f**) sensory clusters are positive for Cut and one of the cells is ELAV-positive. In *Arp3* (**g**) mutant clones all of the cells in the sensory clusters are positive for Cut and ELAV, indicating the transformation of all SOP progeny to neurons. Scale bar, 10 μm.

identified components in the Notch pathway[14]. We performed a similar F1 mitotic recombination screen on chromosome arm 3L[16] and isolated one complementation group consisting of three homozygous lethal alleles (*83F*, *515FC* and *1066PC*) that cause bristle loss in clones (Fig. 1b, b′). Using a recombination-based mapping strategy[17], the lethality of these alleles was mapped to the 66B cytological region (Fig. 1c). We obtained a *P* element *EP(3)3640* (ref. 18) inserted upstream of the *Arp3* gene that failed to complement our alleles, and identified molecular lesions in *Arp3* for the three alleles (Fig. 1c). Overexpression of the *Arp3* cDNA in *Arp3* mutant clones rescued the lethality and ESO phenotype (Fig. 1d), demonstrating that the observed phenotypes are caused by loss of *Arp3*.

Arp3 is part of the seven-protein Arp2/3 complex, which functions together for polymerization of branched actin filaments[19]. Another component of the Arp2/3 complex, Arpc1, was shown to be involved in ring canal formation during oogenesis in *Drosophila*[18]. As with *Arp3* alleles, $Arpc1^{Q25st}$ clones also cause bristle loss (Fig. 1e)[20]. Bristle loss in *Arp3* clones does not result from a failure to specify SOPs (Supplementary Information, Fig. S1a, a′). To examine whether bristle loss in *Arp3* clones is associated with a *Notch* loss-of-function defect, SOP progeny

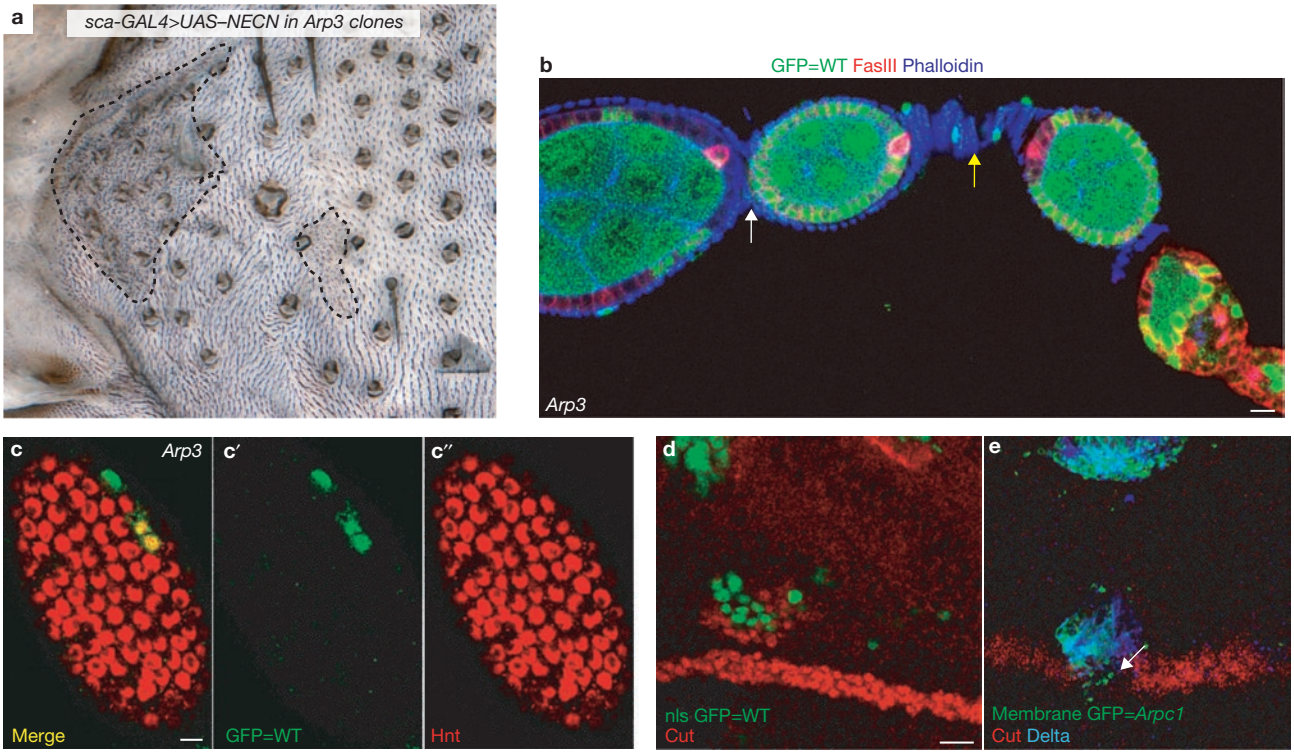

Figure 2 Arp3 is required in the signal sending cells during Notch signalling (**a**) Overexpression of N^{ECN} in wild-type SOPs using the sca^{109-68}-*GAL4* driver results in a multiple socket phenotype in the majority of the sensory clusters. We generated *Arp3* clones (dashed line) using *Ubx–FLP* in this N^{ECN} overexpression background. We did not observe a region of bald cuticle in the *Arp3* clones. (**b**) Clones of $Arp3^{515FC}$ induced by *hs-FLP* in follicle cells are marked by the absence of GFP (green). FasciclinIII (red) marks the follicle cells and is upregulated in polar follicle cells. Phalloidin (blue) marks the membrane of all cells. When polar follicle cells are wild-type (WT), stalk cells (yellow arrow) are formed normally, separating two cysts, whereas, when the polar follicle cells are mutant for *Arp3,* we found a loss of stalk cells between the cysts, resulting in a partial fusion of cysts (white arrow). (**c**–**c**′′) The follicle cells of the cyst harbour mutant clones of *Arp3* induced by *hs-FLP* at stage 7 of oogenesis. *Arp3* mutant clones are marked by the absence of nuclear GFP (green). The cyst was immunostained for Hnt (red), a Notch downstream target gene in the follicle cells. Note that Hnt is still expressed in the *Arp3* mutant follicle cell clones (non-green cells). (**d**) Overexpression of Delta in WT cells (green) near the dorsal-ventral boundary of the wing can induce Cut expression (red) in the adjacent cells near the dorsal-ventral boundary at the dorsal compartment. (**e**) Overexpression of Delta (blue) in *Arpc1* mutant cells (green) cannot induce Cut expression (red) in the adjacent cells near the dorsal-ventral boundary at the dorsal compartment. Note the loss of Cut expression when the clone crosses the dorsal-ventral boundary (arrow). Scale bars, 10 μm (**b**, **d**) and 5 μm (**c**).

at 24 h APF were labelled with differentiation markers. In wild-type sensory clusters, all four cells expressed the homeodomain protein Cut and one expressed the neuronal marker ELAV (Fig. 1f). In contrast, sensory clusters in both *Arp3* and $Arpc1^{Q25st}$ mutant clones contained 4–6 ELAV-positive cells (Fig. 1g and data not shown), suggesting that there is a pIIa-to-pIIb fate transformation.

Although a pIIa-to-pIIb transformation might result from disruption of asymmetric localization of cell fate determinants[6,7], both Neuralized and Numb were asymmetrically localized in *Arp3* mutant SOPs (Supplementary Information, Fig. S1c, e). One of the activators of the Arp2/3 complex, Wiskott-Aldrich syndrome protein (WASp)[21], is also involved in a similar fate specification process in *Drosophila*[22]. Together these observations suggest a specific requirement for WASp-regulated Arp2/3-complex function in Notch signalling.

Arp3 functions in the signal-sending cell during Notch signalling

Is Arp2/3 function required in the signal-sending or the signal-receiving cell during Notch signalling? We first determined the epistatic relationship between *Notch* and *Arp3* with a constitutively active Notch that is independent of ligand activation (N^{ECN})[23]. Expression of N^{ECN} in the ESO lineage causes a *Notch* gain-of-function phenotype, which results in generation of extra socket cells[13]. Overexpression of N^{ECN} in *Arp3* clones, as in wild-type cells, resulted in a *Notch* gain-of-function phenotype, indicating that a ligand-independent form of *Notch* is epistatic to *Arp3* (Fig. 2a). This places the function of Arp3 upstream of Notch activation, possibly in the signal-sending cell.

To gather evidence for a requirement of *Arp3* in the signal-sending cell, we examined its function in oogenesis. Egg chambers are individual units, consisting of germline cells surrounded by somatic follicle cells. The follicle cells can be further divided into three distinct populations: main body follicle cells (phalloidin-positive cells, Fig. 2b), which encapsulate the germline cyst; polar cells, which function as signalling centres (FasIII-positive cells, Fig. 2b); and stalk cells that connect neighbouring cysts (yellow arrow, Fig. 2b). The role of Notch signalling is well-documented in oogenesis[24,25], and signal-sending and receiving cells are spatially well-segregated. *Notch* loss-of-function causes the inability of the follicle cells to encapsulate germline cysts and leads to the formation of giant compound egg chambers[25]. However, *Delta* loss-of-function in follicle cells does not result in an encapsulation defect[25] but rather, loss of stalk cells and partial fusion of the cysts. Delta is required in the anterior polar follicle cells of the posterior egg chamber to specify stalk cells[25,26]. Generating follicle cell clones of *Notch* and *Delta*, therefore, results in

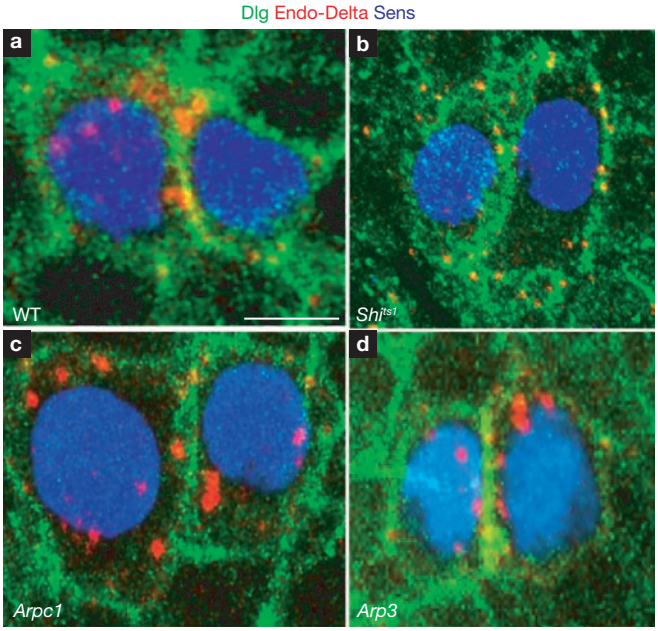

Figure 3 Delta is normally endocytosed in *Arp3* and *Arpc1* mutant pIIa-pIIb. (**a**–**d**) Endocytosis assay for Delta ligand (red) performed at the 2-cell stage in pIIa-pIIb. Sens (blue) labels the nucleus and Dlg (green) marks the sub-apical membrane. A projection of optical slices shows that in the negative control (*shi*^{ts1} (**b**), Delta (red) is found only on the membrane and not in cytoplasmic vesicles between the nucleus and membrane. However, in the wild-type (WT, **a**), *Arpc1* (**c**) and *Arp3* (**d**) pIIa-pIIb, endocytosed Delta vesicles (red) are present in the cytoplasm, indicating that Arp2/3 function is not required for Delta endocytosis. Note small punctae in **b** when Delta is not endocytosed. Scale bar, 5 μm.

distinct phenotypes. We found that loss of *Arp3* phenocopied loss-of-function of *Delta*. Mutant clones of *Arp3* ($n = 14$) in anterior polar follicle cells resulted in loss of stalk cells and partial fusion of adjacent cysts (white arrow, Fig. 2b). At later stages of oogenesis, Delta signals from the germ cells (signal-sending cells) activate Notch in the overlying somatic follicle cells (signal-receiving cells), resulting in expression of a Notch downstream target, Hindsight (Hnt)[27]. Arp3 does not seem to be required in the signal-receiving cell for Notch function, as expression of Hnt was normal in *Arp3* mutant follicle cell clones (Fig. 2c, c′).

To further examine whether Arp2/3 function is required in the signal-sending cell during wing formation, a Delta overexpression assay was performed. During wing development, pre-patterning signals, including Notch, are required to compartmentalize the immature wing imaginal disc at the third-instar larva[28]. Notch signalling is required to activate Cut expression at the dorsal-ventral boundary[29,30]. Previous studies have shown that overexpression of Delta in wild-type clones near the dorsal-ventral boundary results in ectopic Cut expression in the neighbouring cells (Fig. 2d)[11,16,29,30]. However, similar overexpression of Delta in *Arpc1* clones failed to activate Cut expression and resulted in loss of endogenous Cut expression when the clone crossed the dorsal-ventral boundary (Fig. 2e). These data suggest that Arp2/3 complex function is required for the normal function of Delta in the signal-sending cell.

The Arp2/3 complex is not required for Delta endocytosis

Delta must be endocytosed in the signal-sending cell to activate Notch on the receiving cell[6,31]. As Arp2/3 and WASp have been shown to be required for clathrin-mediated endocytosis in yeast[32,33], Arp2/3 might be required for Delta endocytosis during fate specification. However, by performing a Delta endocytosis assay[6] at the 2-cell stage, we found that Delta is endocytosed similarly to wild-type cells (Fig. 3a) in *Arpc1* and *Arp3* mutant tissue (Fig. 3c, d). By contrast, in *shibire* (*Dynamin*) mutant cells kept at the restrictive temperature (Fig. 3b), Delta is not endocytosed[34,35]. This indicates that the Arp2/3 complex is not required for ligand endocytosis during Notch signalling.

A specific ARS forms during fate specification in the ESO lineage

As Arp2/3 is required for polymerization of branched actin filaments[19], we visualized filamentous actin (F-actin) in the ESO lineage with phalloidin. In the wild-type, a prominent apical ARS was present in the pIIa and pIIb (pIIa-pIIb) cells (Fig. 4a, a′′). Co-staining of phalloidin and E-cadherin (*D*E-Cad), which highlights the apical-most stalk region of the pIIb cell that is engulfed by the pIIa cell[36], indicates that the ARS is present in both pIIa-pIIb cells apically (Supplementary Information, Fig. S1f, f′). However, no specialized apical actin enrichment was observed at the earlier 1-cell stage (Supplementary Information, Fig. S1g, g′). In *Arpc1* (yellow arrows, Fig. 4a, a′′), *Arp3* and *WASp* (data not shown) pIIa-pIIb cells, the ARS was formed. However, the apical area of the ARS was markedly reduced in *Arp3* (9.57 ± 5.32 μm^2; mean ± s.e.m, $n = 22$), *Arpc1* (12.25 ± 6.89 μm^2; $n = 19$) and *WASp* (21.86 ± 7.74 μm^2; $n = 19$) pIIa-pIIb cells when compared with the wild-type (43.48 ± 13.79 μm^2; Fig. 4b; $n = 18$). The ARS in wild-type pIIa-pIIb cells formed an umbrella shape along the *xy* axis, whereas in about 50% of the mutant ARS, the stalk of the umbrella was not formed properly (Fig. 4a′′, d).

To test whether the ARS is affected in other mutants, *α-Adaptin*[15] and *numb*[7], which regulate Notch signalling during pIIa-pIIb specification, were examined. In mutant clones of *α-Adaptin* (Fig. 4e) and *numb* (Fig. 4f) the ARS was formed normally, suggesting that the ARS defect is specific to *Arpc1*, *Arp3* and *WASp*. In *neuralized* clones, where both lateral inhibition and fate specification[37] are affected, the ARS was clearly observed in all SOP progeny (Fig. 4 g, g′′). This suggests that most, if not all, SOP progeny at the 2-cell stage are instructed to form an ARS.

To examine whether the Arp2/3 complex colocalizes with the ARS, we overexpressed a GFP-tagged *Arp3* cDNA construct (*UAS–Arp3–GFP)* by *neuralized–GAL4*. We observed that much of the GFP-tagged Arp3 protein colocalized with the ARS (Supplementary Information, Fig. S1h, h′′). The presence of the ARS in the pIIa-pIIb cells during fate specification and the fact that the ARS is morphologically affected in the *Arp3, Arpc1* and *WASp* mutants indicate that it has a role in Notch signal transduction.

Abundant actin-rich microvilli are present at the apical surface of pIIa-pIIb

The ARS was further analysed using TEM to visualize the actin cytoskeleton at the ultracellular level[38]. To distinguish the pIIa-pIIb cell-membrane from that of epithelial cells, HRP was overexpressed in the pIIa-pIIb cells using *neuralized–GAL4* and *UAS–CD2::HRP* (Fig. 5a). On DAB staining, HRP labelling was visualized as a darker cell membrane outline in the SOPs. The serial apical cross-sections (0–2520 nm) of the pIIa-pIIb cells revealed numerous membrane protrusions (Fig. 5b; Supplementary Information, Fig. S2). At high magnification (×10,000), we clearly observed actin bundles within these membranous extensions (Fig. 5c), which was confirmed by immuno-electron microscopy with phalloidin (Fig. 6a, a′). TEM analysis of *Arp3* pIIa-pIIb cells (Fig. 5d–f)

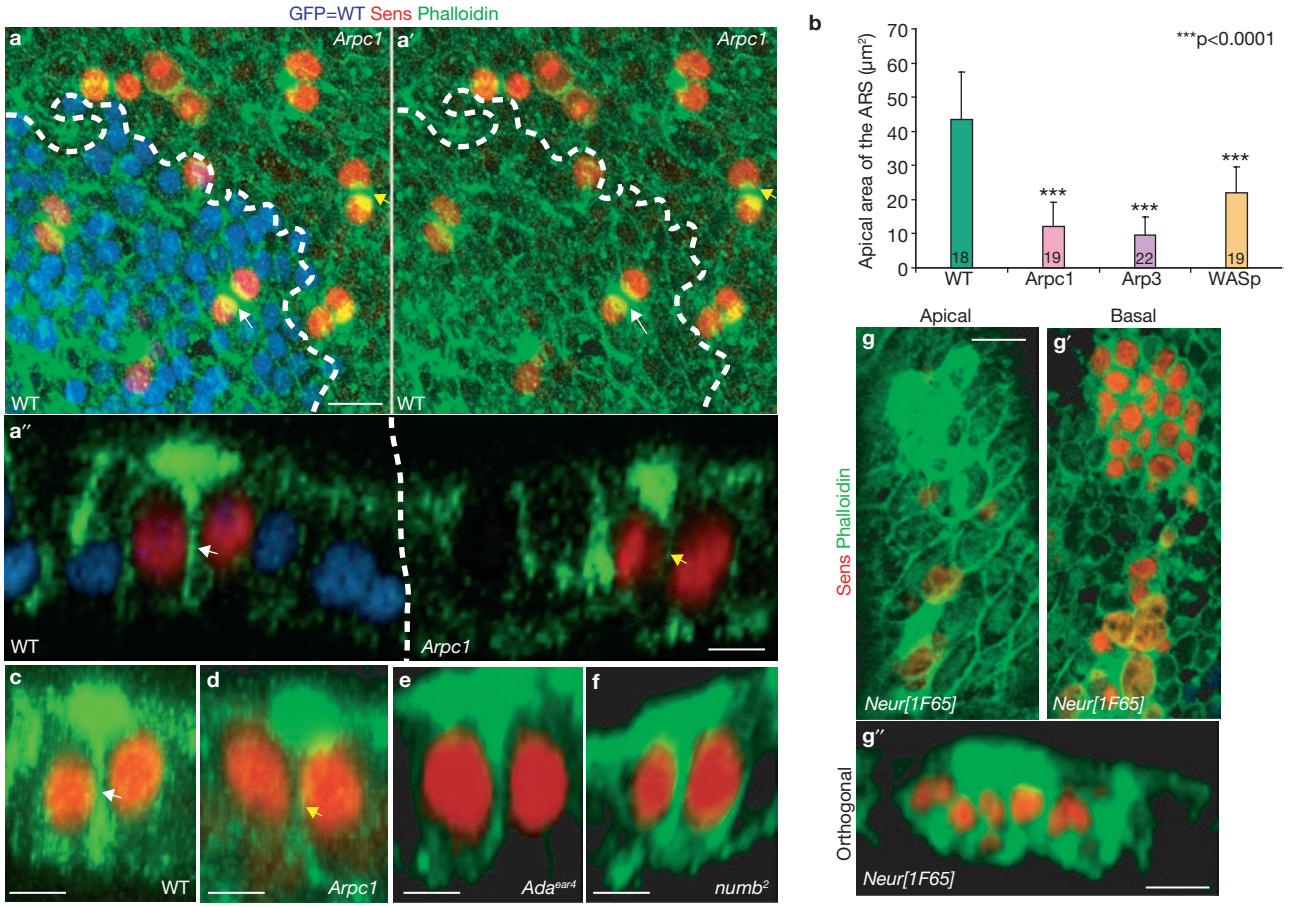

Figure 4 The ARS forms specifically in the pIIa-pIIb progeny and is reduced in *Arp3*, *Arpc1* and *WASp* mutant SOP progeny. (**a**, **a**′) A projection of confocal sections shows that the ARS identified by phalloidin (green) staining is present in both wild-type (WT, white arrow) pIIa-pIIb and *Arpc1* (yellow arrow) mutant pIIa-pIIb cells marked by Sens (red). *Arpc1* homozygous mutant clones (dotted lines) are marked by the absence of nuclear GFP (blue). (**a**′′) An orthogonal confocal section shows that the ARS is quite broad in the WT pIIa-pIIb (white arrow) and has an umbrella-shaped structure, whereas the ARS in the *Arpc1* homozygous clones (yellow arrow) seems compressed and the lateral 'stalk' of the ARS is malformed. (**b**) Quantification of the apical area of the ARS in different genotypes. The ARS area was quantified using the Measure function of ImageJ software. The measurements were analysed using a Student's *t*-test (***P <0.0001). Data are mean ± s.e.m. and the number of SOP progeny pairs used for quantification per genotype is indicated in the bars. (**c**–**g**′′) Pupal nota stained with Sens (red) and phalloidin (green) reveal ARS in pIIa-pIIb. Projections of orthogonal slices show the ARS in WT (**c**, white arrow), *Arpc1* (**d**, yellow arrow), *α-adaptin* (**e**), *numb* (**f**) and *neuralized* (**g**–**g**′′) pIIa-pIIb. An apical section (**g**) reveals apical (0.5 μm) actin enrichment whereas a basal section (**g**′) of the sample (~6 μm) shows the nuclei of the SOP progeny. Scale bars, 10 μm (**a**, **a**′′, **g**, **g**′′) and 5 μm (c–f).

revealed fewer finger-like projections than in wild-type cells (Fig. 5g), consistent with the marked reduction in apical surface area of the ARS in *Arp3*, *Arpc1* and *WASp* mutants (Fig. 4b). Finger-like projections were present on the epithelial cells, but there were fewer and they were markedly shorter (only about 60 nm in length), compared with those of pIIa-pIIb (Supplementary Information, Fig. S3a, c).

The finger-like actin projections on the pIIa-pIIb cells resemble microvilli, which are typically observed to be densely packed in intestinal and kidney epithelial cells[39], and circulating leukocytes[40]. Microvilli on the intestinal and kidney epithelial cells are thought to increase the surface area for absorption, whereas in leukocytes they have been implicated in receptor presentation, which enables leukocyte adhesion[41,42]. To examine whether the finger-like projections are microvilli, the ARS was immunostained with a microvilli marker myosin 1B (Myo1B), which forms lateral tethers between the microvillar membrane and underlying actin filament core[43]. We found that Myo1B is indeed enriched in the apical region of pIIa-pIIb cells (Fig. 6b, b′), specifically at the base of the 'umbrella' region of the ARS (Fig. 6b′′′). This localization of Myo1B was unaffected in *Arp3* mutant pIIa-pIIb cells (Supplementary Information, Fig. S3e, e′). These data indicate that microvilli are present on the apical region of pIIa-pIIb cells.

Delta traffics to the ARS

Intracellular vesicular trafficking of Delta is emerging as a key regulatory step in the activation of Notch[44,45]. We investigated Delta trafficking by co-staining of phalloidin and Delta. In wild-type pIIa-pIIb cells, Delta vesicles colocalized with the apical microvillar region of the ARS (Fig. 7a and transverse section in 7a′). In *Arpc1* (Fig. 7b and transverse section in Fig. 7b′) and *Arp3* (data not shown) pIIa-pIIb, fewer Delta vesicles were colocalized with the ARS. Furthermore, when serial sections were projected to visualize the whole cell (Fig. 7c, c′′), the Delta vesicles were clustered close to the wild-type ARS, whereas the vesicles were widely distributed in the cytoplasm of *Arpc1* pIIa-pIIb cells. The marked reduction of Delta vesicles colocalizing with the ARS in the mutant pIIa-pIIb cells suggests that Arp2/3 has a role in Delta trafficking to the ARS.

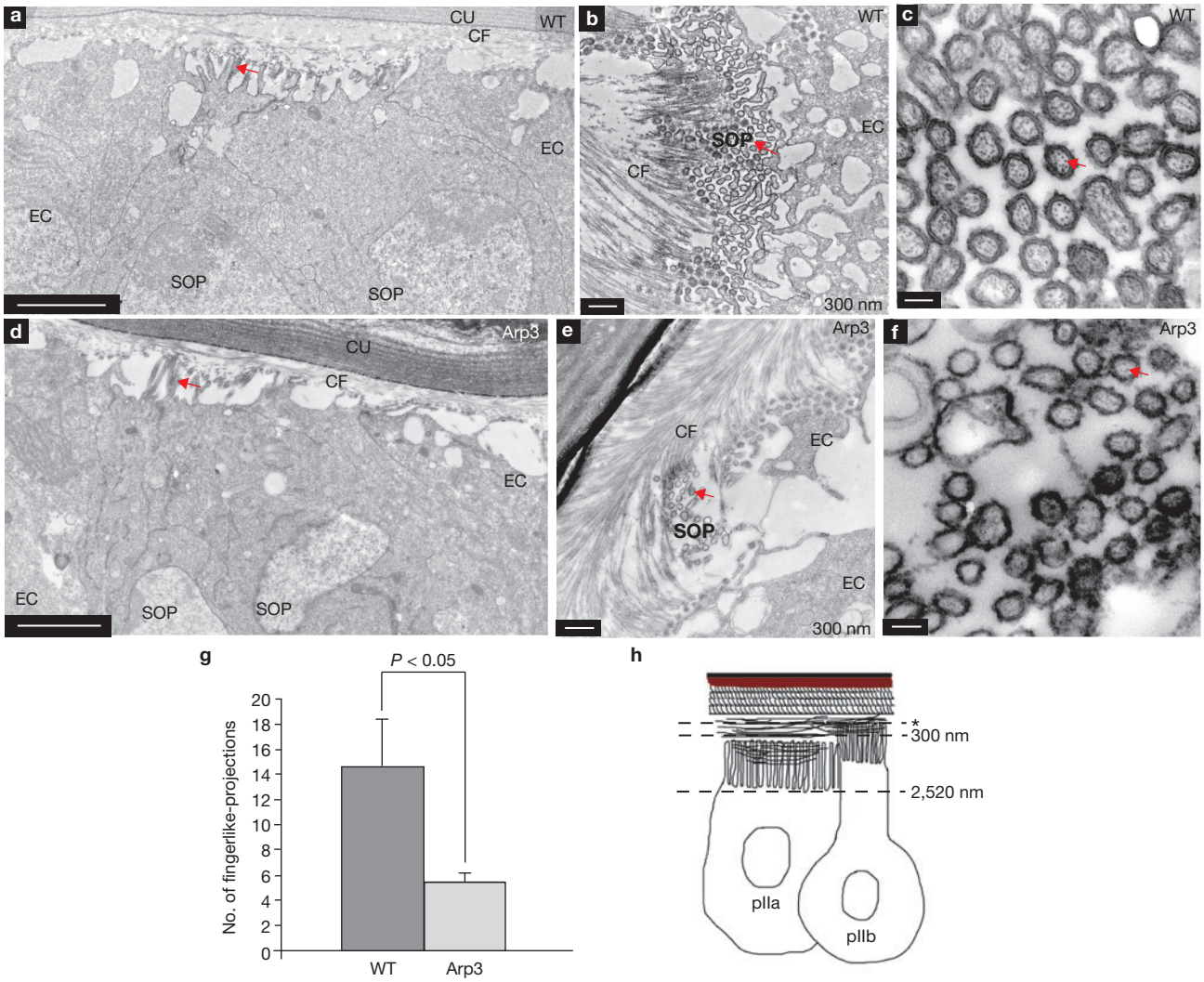

Figure 5 TEM analysis reveals enrichment of actin-filled finger-like projections in pIIa-pIIb cells at 18 h APF. (**a**, **d**) Orthogonal sections of wild-type (WT, **a**) and *Arp3* (**d**) pIIa-pIIb cells show finger-like projections (arrows) at the apical domain of the cells. (**b**–**f**) Cross-section of WT (**b**) and *Arp3* (**e**) pIIa-pIIb cells show finger-like projections (arrows). (**c**, **f**) Higher magnification of the apical surface of WT (**c**) and *Arp3* (**f**) pIIa-pIIb cells shows actin bundles (arrows) inside the finger-like projections. (**g**) Quantification of the number of finger-like projections at the 2-cell stage in WT and *Arp3*. The total number of microvilli in SOP and epithelial cells were quantified using ImageJ. The data are mean ± s.e.m and measurements were analysed using Student's *t*-test. Three SOP progeny pairs were used for this quantification per genotype. (**h**) Schematic representation of pIIa-pIIb in the prepupal thorax epithelium. The asterisk represents the level of the first electron microscopy section at 60 nm. Abbreviations: cuticle (Cu), chitin fibre (CF), epithelial cell (EC), sensory organ precursor cell (SOP). Scale bars, 0.5 μm (**a**, **b**, **d**, **e**) and 0.1 μm (**c**, **f**).

Arp2/3 and WASp are required for trafficking of endocytosed Delta to the apical ARS

To investigate Delta trafficking in *Arp2/3* and *WASp* mutants, we performed pulse-chase labelling experiments[12] to monitor the internalization of Delta in living pupae. Internalization of Delta vesicles with respect to ARS was examined at three different time-points (0, 30 and 60 min). At 0 min Delta vesicles were present apically (~0.5 μm into the sample) and colocalized with ARS in wild-type (Fig. 8a, a′′), *Arp3* (Fig. 8b, b′′), *Arpc1* and *WASp* (data not shown) SOP progeny. At 30 min post-internalization, Delta vesicles were localized basally (~6 μm) in wild-type (Fig. 8c, c′′) and *Arp3* (Fig. 8d, d′′) SOP progeny, indicating that the Delta vesicles had trafficked intracellularly at this time-point. However, 60 min after internalization, localization of Delta vesicles in mutants differed from the wild-type. In the wild-type, about 6–10 Delta-positive vesicles colocalized apically on the ARS (Fig. 8e, e′′), suggesting that endocytosed Delta traffics back to the apical microvilli. In *Arp3* (Fig. 8f, f′′), *Arpc1* (Supplementary Information, Fig. S4a, a′′) and *WASp* (Supplementary Information, Fig. S4b, b′′) mutants, Delta vesicles were not localized apically on the ARS. Instead, they were found basally in the cytoplasm (~6 μm into the cell; Fig. 8f′, f′′; Supplementary Information, Fig. S4a′–b′′), suggesting a defect in Delta trafficking. Indeed, the number of Delta vesicles that traffic to the microvillar region of the ARS at 60 min post-chase was significantly lower in the *Arpc1*, *Arp3* and *WASp* pIIa-pIIb than in wild-type cells (Fig. 8g). However, the total number of internalized Delta vesicles and the intensity of Delta signal in the SOP progeny at 60 min post-chase were very similar in wild-type and mutants (Supplementary Information, Fig. S4c, d). In summary, initially Delta is properly targeted apically at the ARS and endocytosed (Fig. 8a–b′′). Delta traffics basally in both wild-type and mutants (Fig. 8c–d′′) 30

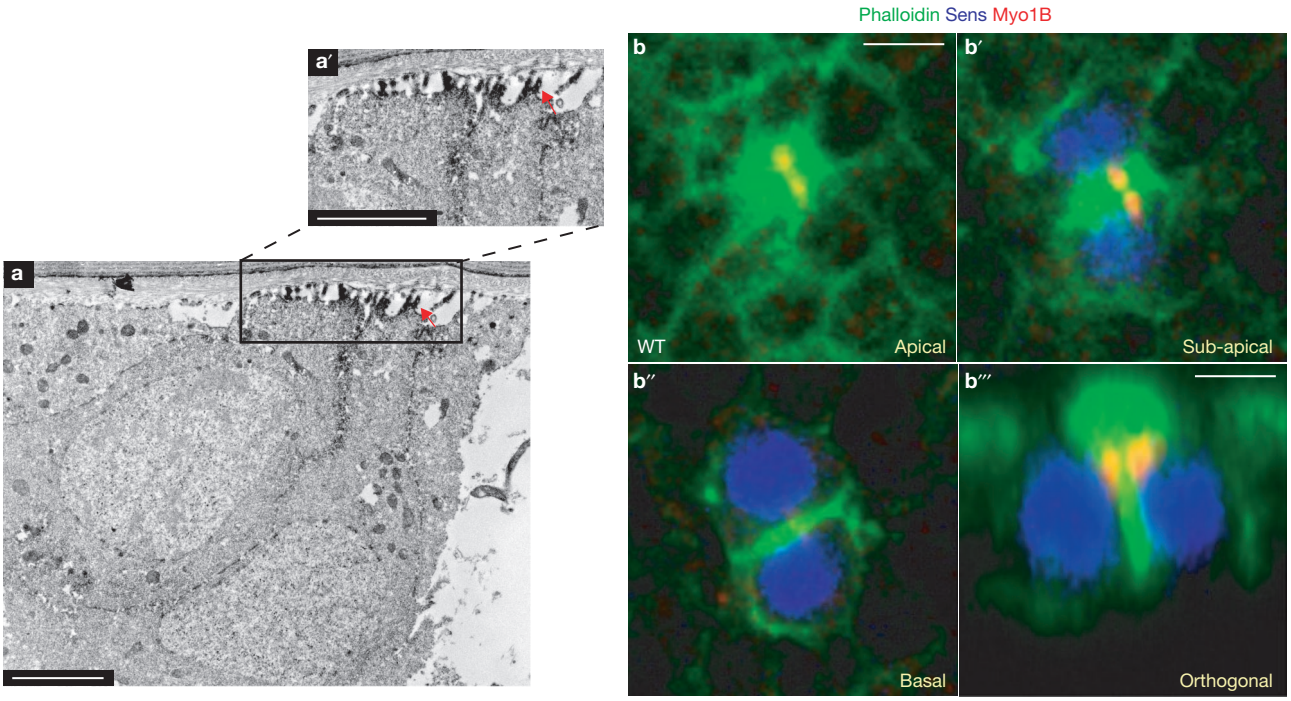

Figure 6 Finger-like projections in pIIa-pIIb cells are enriched with F-actin bundles and are marked by a microvillar marker Myo1B. (**a**, **a**′) Immuno-electron microscopy image of an orthogonal section through the wild-type pIIa-pIIb of a pupal notum shows an enrichment of phalloidin (electron-dense material) in the finger-like projections along the apical region of the ARS. (**a**′) A higher magnification view of the boxed region in **a** is shown in **a**′. The arrow points to the enrichment of phalloidin in the finger-like projections (**b**–**b**‴) Confocal images of single optical (*xy* axis) sections (**b**–**b**″) and orthogonal section (**b**‴) of wild-type (WT) pIIa-pIIb cells immunostained for Myo1B (red), phalloidin (green) and Sens (blue). Scale bars, 0.5 μm (**a**, **a**′) and 5 μm (**b**, **b**‴).

min after internalization. However, endocytosed Delta is not targeted back to the microvillar region in *Arp3*, *Arpc1* and *WASp* SOP progeny 60 min post-chase.

It has been proposed that Delta must be endocytosed and targeted to a specific endosomal compartment to become activated[11], possibly through Rab11-positive recycling endosomes[12,13]. By examining the distribution of the vesicular compartments, we found that the early endosome and the recycling endosome were enriched on the ARS (Supplementary Information, Fig. S4e–h′). Pulse-chase of endocytosed Delta through these compartments (Supplementary Information, Figs S5, S6), showed no significant defects in the localization and abundance of these endosomal compartments or the ability of Delta to traffic through these endosomal compartments in *Arpc1* mutant SOP progeny. The internalized Delta is thought to be proteolytically cleaved in an unknown compartment[11]. We found that Delta processing in *Arp3* mutants is similar to that in the wild-type (Supplementary Information, Fig. S7).

In summary, we surmise that a defect in trafficking of endocytosed Delta to the apical microvillar portion of the ARS leads to a failure in Delta signalling. We conclude that this defect underlies the pIIa-to-pIIb fate transformation phenotype in *Arp3, Arpc1* and *WASp* mutants.

DISCUSSION

Previous reports have suggested that trafficking of a subset of endocytosed Delta to the apical membrane in the pIIb cell is required for its ability to activate Notch in the pIIa cell[12,13]. We have uncovered a highly stereotyped ARS that consists of apical microvilli and a lateral 'stalk' region. In *Arp2/3* and *WASp* pIIa-pIIb cells, the apical surface area of the ARS was significantly reduced and the number of microvilli on the apical region was also reduced. In addition, trafficking of endocytosed Delta to the apical microvilli-rich region of the ARS was severely impaired in *Arp3* mutants. Although numerous studies have focused on the SOP daughter cells, the ARS and the microvilli have not been described previously. These microvillar structures are very different from filopodia[46], which have been reported to have a role in lateral inhibition[47] at an earlier stage. Our data indicate that apical trafficking of Delta to the ARS is required for its ability to signal.

Given the role of Arp2/3 in forming branched actin filaments, one of the primary roles of the Arp2/3 complex and WASp during Notch signalling is probably to form actin networks[48], and to enable and/or to promote the trafficking of Delta vesicles to the ARS (Fig. 8h). This requirement for endocytosed Delta localization to the microvilli during Notch signalling is akin to findings showing that localization of Smoothened to primary cilia is important for its activation during Hedgehog (Hh) signal transduction[49,50]. An interesting study performed in circulating lymphocytes has demonstrated a crucial requirement for microvillar receptor presentation in leukocyte adhesion to the endothelial membrane[41]. In an analogous manner to findings in leukocytes, microvillar presentation of Delta might enhance its ability to contact Notch on the surface of the adjacent cell. As Notch signalling is a major contact-dependent signalling pathway, microvilli might therefore increase the surface area of contact between the signal-sending and receiving cells, enhancing the ability of the ligand to interact with the receptor.

On the basis of the well-characterized role for WASp and Arp2/3 in clathrin-mediated endocytosis[32], it was speculated that Arp2/3 and

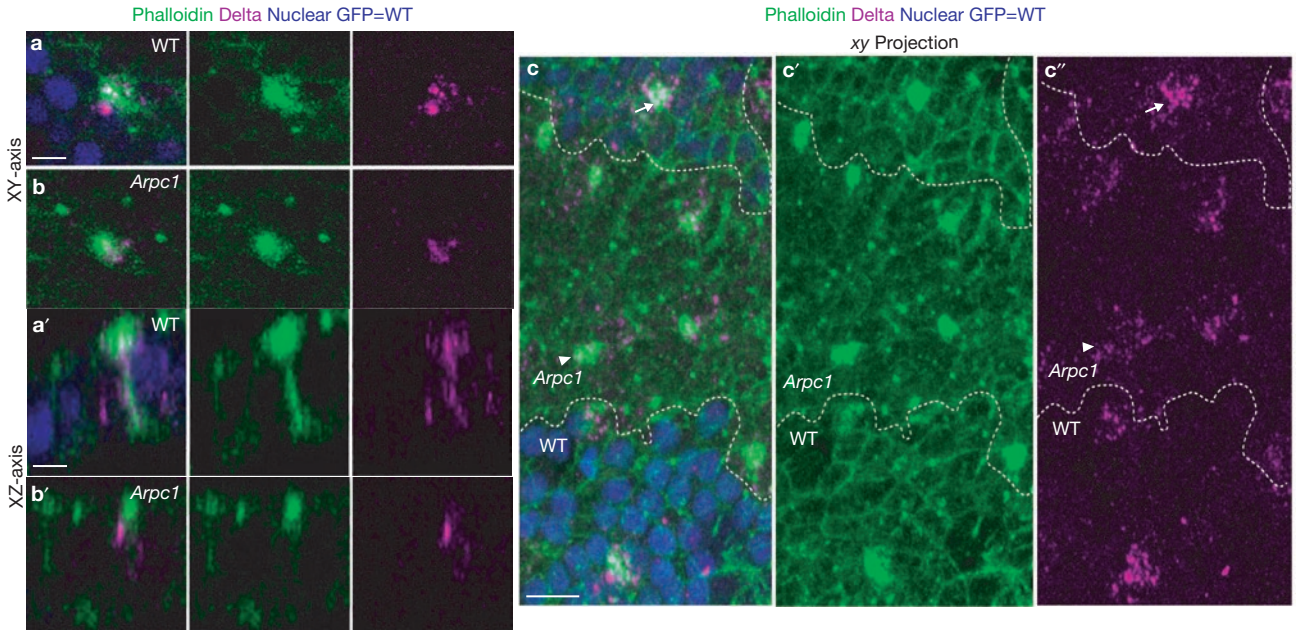

Figure 7 Delta localization to the ARS is reduced in *Arpc1* mutants. (**a**–**c**′′) Pupal wing nota at the 2-cell SOP stage (18.30 h APF) were immunostained with phalloidin (green) and Delta (magenta). *Arpc1* homozygous mutant cells are marked by the absence of GFP (blue). (**a**, **b**) A single section along the *xy* axis through pIIa-pIIb cells shows an enrichment of Delta on the ARS in wild-type (WT, **a**) and this enrichment is much reduced in *Arpc1* (**b**). (**a**′, **b**′) A single section along the *xy* axis of pIIa-pIIb shows that the Delta vesicles colocalize along the lateral stalk of the ARS in WT and in the basal portion of the umbrella region of the ARS (**a**′). In *Arpc1* (**b**′), the lateral stalk of the ARS is malformed and there is a reduction in the number of Delta vesicles that colocalize on the apical portion of the ARS. (**c**–**c**′′) A projection of confocal sections of a pupal notum harbouring an *Arpc1* mutant clone (dashed line). In the WT region, a high density of Delta vesicles are clustered on and around the ARS, whereas in the mutant clones, the Delta vesicles are more widely distributed and do not cluster around the ARS; compare arrowheads (*Arpc1*) with arrows (WT). Scale bars, 5 μm (**a**, **a**′) and 10 μm (**c**).

WASp might be required for endocytosis of Delta and/or Notch during signalling[51]. However, our data indicate that the Arp2/3 complex is not required for Notch in the signal-receiving cell. Our data also indicate that the Arp2/3 complex is not required to endocytose Delta. It is possible that endocytosis of Delta occurs in a clathrin-independent manner[52,53].

The involvement of *WASp* during Notch-mediated fate decisions might have implications for its mammalian homologue in Wiskott-Aldrich syndrome, an X-linked immunodeficiency[54]. Given that Notch signalling is required for proper T-cell development[55] and differentiation of peripheral T-cells[56], defects in Delta trafficking caused by WASp-mediated actin polymerization might underlie the loss and aberrant function of T cells in patients with Wiskott-Aldrich syndrome. Interestingly, microvilli on the surface of lymphocytes might also have a central role in receptor presentation in macrophages and T cells[41,42]. It will be interesting to investigate whether WASp has a role in Notch signalling during T-cell development and activation. □

METHODS

Methods and any associated references are available in the online version of the paper at http://www.nature.com/naturecellbiology/

Note: Supplementary Information is available on the Nature Cell Biology website.

ACKNOWLEDGEMENTS

We are grateful to W. Theurkauf, L. Cooley, E. Schejter, J. Skeath, D. F. Ready, P. Badenhorst, Y. N. Jan, P. Bryant, M. González Gaitán, G. Struhl, E. C. Lai, M. Muskavitch, A. L. Parks, F. B. Gertler, L. M. Lanier, J. Knoblich, F. Schweisguth, R. Dubreuil, W. Sullivan, M. S. Mooseker, G.M. Guild, the Bloomington Stock Center and the Developmental Studies Hybridoma Bank for reagents. We thank G. Emery for advice regarding the Delta endocytosis assay. We would like to thank H. Jafar-Nejad for suggestions and advice during the screen and comments on the manuscript. We thank P. Verstreken and C. V. Ly for their help with the screen, and R. Atkinson for advice on imaging. Confocal microscopy was supported by the BCM Mental Retardation and Developmental Disabilities Research Center. H.J.B. is an investigator of the Howard Hughes Medical Institute.

AUTHOR CONTRIBUTIONS

A.R., A.T. and H.B. conceived the project. A.R. and A.T. carried out the screen, mapped the genes and executed the project. K.S. was involved in the screen and mapping of the genes. C.M.H. in collaboration with A.R. and A.T. designed the TEM experiments and C.M.H. carried out the TEM experiments.

COMPETING INTERESTS

The authors declare that they have no competing financial interest.

Published online at http://www.nature.com/naturecellbiology/Reprints and permissions information is available online at http://npg.nature.com/reprintsandpermissions/

1. Tien, A. C., Rajan, A. & Bellen, H. J. A Notch updated. *J. Cell Biol.* **184 (5),** 621–629 (2009).
2. Bray, S. J. Notch signalling: a simple pathway becomes complex. *Nature Rev. Mol. Cell Biol.* **7,** 678–689 (2006).
3. Schweisguth, F. Regulation of Notch signaling activity. *Curr. Biol.* **14,** R129–138 (2004).
4. Louvi, A. & Artavanis-Tsakonas, S. Notch signalling in vertebrate neural development. *Nature Rev.* **7,** 93–102 (2006).
5. Bray S. Notch signalling in *Drosophila*: three ways to use a pathway. *Sem. Cell Dev. Biol.* **9,** 591–597 (1998).
6. Le Borgne, R. & Schweisguth, F. Unequal segregation of Neuralized biases Notch activation during asymmetric cell division. *Dev. Cell* **5,** 139–148 (2003).
7. Rhyu, M. S., Jan, L. Y. & Jan, Y. N. Asymmetric distribution of numb protein during division of the sensory organ precursor cell confers distinct fates to daughter cells. *Cell* **76,** 477–491 (1994).
8. Gho, M., Bellaiche, Y. & Schweisguth, F. Revisiting the *Drosophila* microchaete lineage: a novel intrinsically asymmetric cell division generates a glial cell. *Development* **126,** 3573–3584 (1999).
9. Zeng, C., Younger-Shepherd, S., Jan, L. Y. & Jan, Y. N. Delta and Serrate are redundant Notch ligands required for asymmetric cell divisions within the *Drosophila* sensory organ lineage. *Genes Dev.* **12,** 1086–1091 (1998).

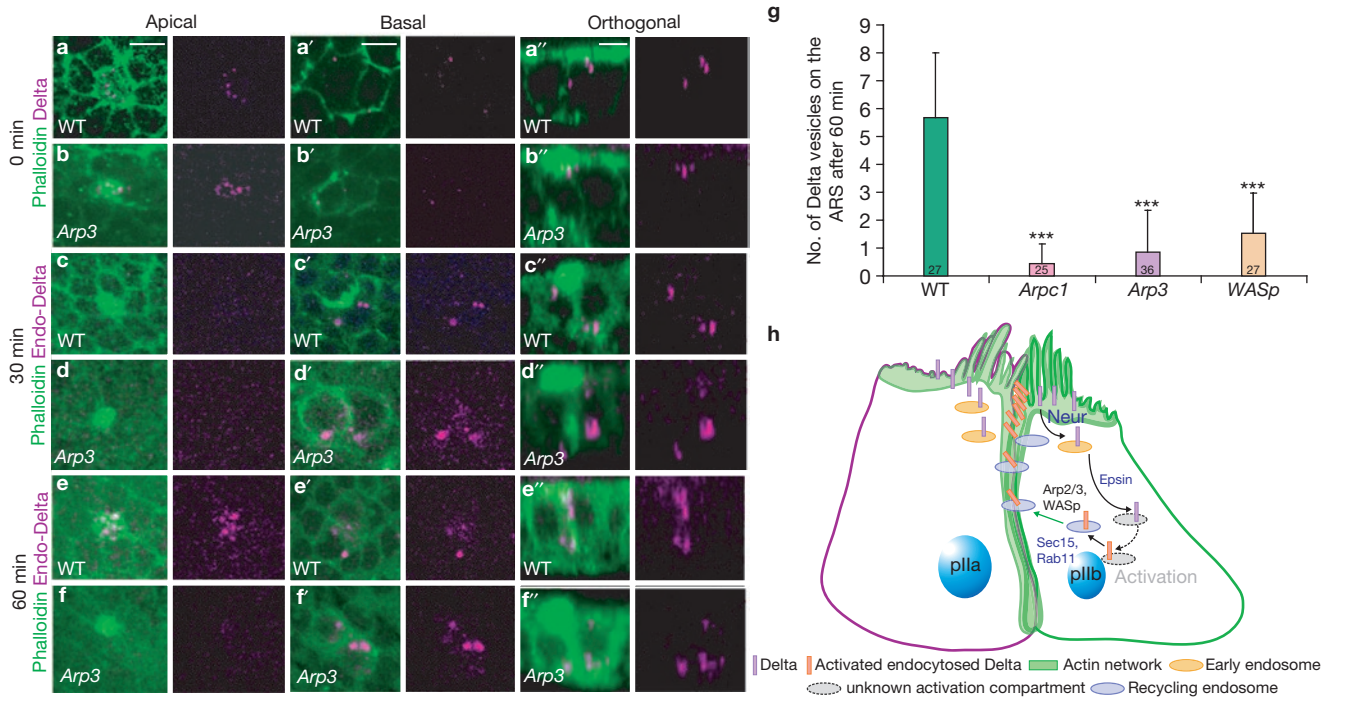

Figure 8 Arp2/3 and WASp are required for trafficking of endocytosed Delta to the apical ARS 1 h post-endocytosis. (**a**–**f**′′) A pulse-chase assay for the trafficking of endocytosed Delta (magenta) at different time-points with respect to the ARS (green) was performed in live pupal nota of wild-type (WT) and *Arp3* mutants. Confocal images show apical (0.5 μm), basal (6 μm) and orthogonal sections of the pIIa-pIIb cells of the WT notum (**a**–**a**′′, **c**–**c**′′, **e**–**e**′′), and *Arp3* mutant clones (**b**–**b**′′, **d**–**d**′′, **f**–**f**′′). The pulse-chase assays for three different time-points, 0 min, 30 min and 60 min, are shown. (**g**) Quantification of the number of internalized Delta vesicles that are present apically and colocalize with the ARS. Measurements of total number of Delta vesicles that traffic to the ARS 1 h after chase were analysed using a Student's *t*-test (***$P < 0.0001$). Data are mean ± s.e.m. and the number of SOP progeny pairs quantified per genotype is indicated in the bars. Note that fewer vesicles that colocalize in mutants when compared with the WT control and the difference is statistically significant. (**h**) Proposed model. In the pIIb cell, Delta is endocytosed by Neuralized (Neur)[6] and trafficked by Epsin[11] to an endocytic compartment where it undergoes activation, probably by a proteolytic cleavage event. It is trafficked back to the membrane in a compartment positive for Rab11 (ref. 12) and the exocyst complex member Sec15 (ref. 13). Arp2/3 and WASp are required for the formation of branched actin networks to form the 'stalk' of the ARS and enables endocytosed vesicles containing activated Delta to traffic back to the dense actin-rich microvilli at the apical membrane of the pIIb cell, where it can signal. Scale bars, 5 μm.

10. Parks, A. L., Klueg, K. M., Stout, J. R. & Muskavitch, M. A. Ligand endocytosis drives receptor dissociation and activation in the Notch pathway. *Development* **127,** 1373–1385 (2000).
11. Wang, W. & Struhl, G. *Drosophila* Epsin mediates a select endocytic pathway that DSL ligands must enter to activate Notch. *Development* **131,** 5367–5380 (2004).
12. Emery, G. *et al.* Asymmetric Rab 11 endosomes regulate delta recycling and specify cell fate in the *Drosophila* nervous system. *Cell* **122,** 763–773 (2005).
13. Jafar-Nejad, H. *et al.* Sec15, a component of the exocyst, promotes notch signaling during the asymmetric division of *Drosophila* sensory organ precursors. *Dev. Cell* **9,** 351–363 (2005).
14. Hartenstein, V. & Posakony, J. W. A dual function of the Notch gene in *Drosophila* sensillum development. *Dev. Biol.* **142,** 13–30 (1990).
15. Berdnik, D., Torok, T., Gonzalez-Gaitan, M. & Knoblich, J. A. The endocytic protein α-Adaptin is required for numb-mediated asymmetric cell division in *Drosophila*. *Dev. Cell* **3,** 221–231 (2002).
16. Tien, A. C. *et al.* Ero1L, a thiol oxidase, is required for Notch signaling through cysteine bridge formation of the Lin12-Notch repeats in *Drosophila melanogaster*. *J. Cell Biol.* **182,** 1113–1125 (2008).
17. Zhai, R. G. *et al.* Mapping *Drosophila* mutations with molecularly defined P element insertions. *Proc. Natl Acad. Sci. USA* **100,** 10860–10865 (2003).
18. Hudson, A. M. & Cooley, L. A subset of dynamic actin rearrangements in *Drosophila* requires the Arp2/3 complex. *J. Cell Biol.* **156,** 677–687 (2002).
19. Machesky, L. M. & Gould, K. L. The Arp2/3 complex: a multifunctional actin organizer. *Curr. Opin. Cell Biol.* **11,** 117–121 (1999).
20. Tal, T., Vaizel-Ohayon, D. & Schejter, E. D. Conserved interactions with cytoskeletal but not signaling elements are an essential aspect of *Drosophila* WASp function. *Dev. Biol.* **243,** 260–271 (2002).
21. Machesky, L. M. & Insall, R. H. Scar1 and the related Wiskott-Aldrich syndrome protein, WASP, regulate the actin cytoskeleton through the Arp2/3 complex. *Curr. Biol.* **8,** 1347–1356 (1998).
22. Ben-Yaacov, S., Le Borgne, R., Abramson, I., Schweisguth, F. & Schejter, E. D. Wasp, the *Drosophila* Wiskott-Aldrich syndrome gene homologue, is required for cell fate decisions mediated by Notch signaling. *J. Cell Biol.* **152,** 1–13 (2001).
23. Struhl, G., Fitzgerald, K. & Greenwald, I. Intrinsic activity of the Lin-12 and Notch intracellular domains *in vivo*. *Cell* **74,** 331–345 (1993).
24. Ruohola, H. *et al.* Role of neurogenic genes in establishment of follicle cell fate and oocyte polarity during oogenesis in *Drosophila*. *Cell* **66,** 433–449 (1991).
25. Lopez-Schier, H. & St Johnston, D. Delta signaling from the germ line controls the proliferation and differentiation of the somatic follicle cells during *Drosophila* oogenesis. *Genes Dev.* **15,** 1393–1405 (2001).
26. Assa-Kunik, E., Torres, I. L., Schejter, E. D., Johnston, D. S. & Shilo, B. Z. *Drosophila* follicle cells are patterned by multiple levels of Notch signaling and antagonism between the Notch and JAK/STAT pathways. *Development* **134,** 1161–1169 (2007).
27. Sun, J. & Deng, W. M. Hindsight mediates the role of notch in suppressing hedgehog signaling and cell proliferation. *Dev. Cell* **12,** 431–442 (2007).
28. de Celis, J. F., Garcia-Bellido, A. & Bray, S. J. Activation and function of Notch at the dorsal-ventral boundary of the wing imaginal disc. *Development* **122,** 359–369 (1996).
29. de Celis, J. F. & Bray, S. Feed-back mechanisms affecting Notch activation at the dorsoventral boundary in the *Drosophila* wing. *Development* **124,** 3241–3251 (1997).
30. Micchelli, C. A., Rulifson, E. J. & Blair, S. S. The function and regulation of cut expression on the wing margin of *Drosophila*: Notch, Wingless and a dominant negative role for Delta and Serrate. *Development* **124,** 1485–1495 (1997).
31. Seugnet, L., Simpson, P. & Haenlin, M. Requirement for dynamin during Notch signaling in *Drosophila* neurogenesis. *Dev. Biol.* **192,** 585–598 (1997).
32. Kaksonen, M., Toret, C. P. & Drubin, D. G. A modular design for the clathrin- and actin-mediated endocytosis machinery. *Cell* **123,** 305–320 (2005).
33. Galletta, B. J., Chuang, D. Y. & Cooper, J. A. Distinct roles for Arp2/3 regulators in actin assembly and endocytosis. *PLoS Biol.* **6,** e1 (2008).
34. Chen, M. S. *et al.* Multiple forms of dynamin are encoded by *shibire*, a *Drosophila* gene involved in endocytosis. *Nature* **351,** 583–586 (1991).
35. van der Bliek, A. M. & Meyerowitz, E. M. Dynamin-like protein encoded by the *Drosophila shibire* gene associated with vesicular traffic. *Nature* **351,** 411–414 (1991).
36. Le Borgne, R., Bellaiche, Y. & Schweisguth, F. *Drosophila* E-cadherin regulates the orientation of asymmetric cell division in the sensory organ lineage. *Curr. Biol.* **12,** 95–104 (2002).
37. Lai, E. C. & Rubin, G. M. neuralized functions cell-autonomously to regulate a subset of notch-dependent processes during adult *Drosophila* development. *Dev. Biol.* **231,** 217–233 (2001).

38. Maupin, P. & Pollard, T. D. Improved preservation and staining of HeLa cell actin filaments, clathrin-coated membranes, and other cytoplasmic structures by tannic acid-glutaraldehyde-saponin fixation. *J. Cell Biol.* **96,** 51–62 (1983).
39. Heintzelman, M. B. & Mooseker, M. S. Assembly of the intestinal brush border cytoskeleton. *Curr. Top. Dev. Biol.* **26,** 93–122 (1992).
40. Majstoravich, S. *et al.* Lymphocyte microvilli are dynamic, actin-dependent structures that do not require Wiskott-Aldrich syndrome protein (WASp) for their morphology. *Blood* **104,** 1396–1403 (2004).
41. von Andrian, U. H., Hasslen, S. R., Nelson, R. D., Erlandsen, S. L. & Butcher, E. C. A central role for microvillous receptor presentation in leukocyte adhesion under flow. *Cell* **82,** 989–999 (1995).
42. Singer, II. *et al.* CCR5, CXCR4, and CD4 are clustered and closely apposed on microvilli of human macrophages and T cells. *J. Virol.* **75,** 3779–3790 (2001).
43. Morgan, N. S., Heintzelman, M. B. & Mooseker, M. S. Characterization of myosin-IA and myosin-IB, two unconventional myosins associated with the *Drosophila* brush border cytoskeleton. *Dev. Biol.* **172,** 51–71 (1995).
44. Le Borgne, R. Regulation of Notch signalling by endocytosis and endosomal sorting. *Curr. Opin. Cell Biol.***18,** 213–222 (2006).
45. Emery, G. & Knoblich, J. A. Endosome dynamics during development. *Curr. Opin. Cell Biol.* **18,** 407–415 (2006).
46. Chhabra, E. S. & Higgs, H. N. The many faces of actin: matching assembly factors with cellular structures. *Nature Cell Biol.* **9,** 1110–1121 (2007).
47. De Joussineau, C. *et al.* Delta-promoted filopodia mediate long-range lateral inhibition in *Drosophila*. *Nature* **426,** 555–559 (2003).
48. Mullins, R. D., Heuser, J. A. & Pollard, T. D. The interaction of Arp2/3 complex with actin: nucleation, high affinity pointed end capping, and formation of branching networks of filaments. *Proc. Natl Acad. Sci. USA* **95,** 6181–6186 (1998).
49. Rohatgi, R., Milenkovic, L. & Scott, M. P. Patched1 regulates hedgehog signaling at the primary cilium. *Science* **317,** 372–376 (2007).
50. Kiprilov, E. N. *et al.* Human embryonic stem cells in culture possess primary cilia with hedgehog signaling machinery. *J. Cell Biol.* **180,** 897–904 (2008).
51. Ilagan, M. X. & Kopan, R. SnapShot: notch signaling pathway. *Cell* **128,** 1246 (2007).
52. Chen, H. & De Camilli, P. The association of epsin with ubiquitinated cargo along the endocytic pathway is negatively regulated by its interaction with clathrin. *Proc. Natl Acad. Sci. USA* **102,** 2766–2771 (2005).
53. Sigismund, S. *et al.* Clathrin-independent endocytosis of ubiquitinated cargos. *Proc. Natl Acad. Sci. USA* **102,** 2760–2765 (2005).
54. Imai, K., Nonoyama, S. & Ochs, H. D. WASP (Wiskott-Aldrich syndrome protein) gene mutations and phenotype. *Curr. Opin. Allergy Clin. Immunol.* **3,** 427–436 (2003).
55. Tanigaki, K. & Honjo, T. Regulation of lymphocyte development by Notch signaling. *Nature Immunol.* **8,** 451–456 (2007).
56. Osborne, B. A. & Minter, L. M. Notch signalling during peripheral T-cell activation and differentiation. *Nature Rev. Immunol.* **7,** 64–75 (2007).

METHODS

***Drosophila* genetics.** Stocks used in this study were: 1) y w; FRT80B (isogenized), 2) y w Ubx–FLP; RpS17[4] Ubi–GFP.nls FRT80B/TM3 Ser, 3) y w hs-FLP; UAS–N$^{ECN(NEXT)}$/CyO; MKRS/TM2 (ref. 57), 4) y w; UAS-Arp3::GFP[58], 5) w; Wsp[3]/TM6B Tb[59], 6) Df(3R)3450/TM6B Tb, 7) y w; Arpc1^{Q25St} FRT40A /CyO Kr-GAL4, UAS–GFP[60], 8) y w Ubx–FLP; Ubi–GFP.nls FRT40A/CyO, 9) y w hs-FLP; RpS17[4] Ubi–GFP FRT80B/ TM6B Tb, 10) y hs-FLP tubα1–GAL4 UAS–GFP.nls-6×Myc; tub–GAL80 RpS17[4] FRT80B/TM6B Tb, 11) w*; UAS–CD2::HRP/CyO (Bloomington Stock Center)[61], 12) w^{1118}; neur^{A101}–GAL4 Kg^{V}/TM3 Sb^{1} (Bloomington Stock Center)[62], 13) y w; numb^{2} ck FRT40A/CyO[63], 14) y w ey-FLP; Ada^{ear4} FRT40A/CyO y^{+} (ref. 64), 15) w; FRT82B neur^{1F65}/TMB6B Tb[65] 16) y w; sca$^{109-68}$-GAL4 (ref. 66).

Rescue experiments were performed using the MARCM technique. Flies of genotype *y hs-FLP tubα1–GAL4 UAS–GFP.nls-6×Myc; UAS–Arp3::GFP/+; tub–GAL80 RpS17[4] FRT80B/ Arp3^{515FC} FRT80B* were examined. The homozygous mutant bristles with longer and thicker appearance were differentiated from the short and thin *RpS17[4] (Minute* phenotype) bristles.

Epistasis analysis of *Arp3* with the ligand-independent form of Notch[57], *N^{ECN}* was performed by examining flies of the genotype *y w Ubx–FLP; sca$^{109-68}$-GAL4/ UAS-N^{ECN}; y^{+} w^{+} FRT80B/mwh Arp3^{83F} FRT80B. Arp3* follicle cell clones in egg chambers were generated by heat-shocking virgin females of genotype *y w hs-FLP/+; FRT80B Arp3^{515FC}/ RpS17[4] Ubi–GFP FRT80B* for 90 min at 38 °C for 3 consecutive days. Ovaries of heat-shocked females were dissected after 2–3 days of mating on medium supplemented with yeast.

The wing-disc signal-sending cell assay was performed as described previously[67,68] and flies of the genotype *y w hs-FLP UAS–GFP.CD8; tub–GAL80 FRT40A/ Arpc1 FRT40A; tub–GAL4/ UAS-Dl* were examined.

Immunohistochemistry. For conventional immunostaining, ovaries, wing discs from third instar larvae or pupal nota were dissected in PBS and fixed with 4% formaldehyde for 20 min. The samples were then permeabilized in PBS + 0.2% Triton X-100 (PBST) for 20 min and blocked with 5% normal donkey serum in PBST for 1 h. Samples were incubated with primary antibodies at 4 °C overnight. The following primary antibodies were used: chicken anti-GFP (1:2,000, Abcam), mouse anti-Cut (1:500; 2B10; Developmental Studies Hybridoma Bank, University of Iowa (DSHB))[69], rat anti-ELAV (1:200; 7E8A10; DSHB)[70], guinea pig anti-Sens (1:1,000; ref 71), mouse anti-Dl^{ECD} (1:1,000; C594.9B; DSHB)[72], guinea pig anti-Delta (1:3,000; M. Muskavitch and A. L. Parks)[73], mouse anti-Fasciclin III (1:10; 7G10; DSHB)[74], mouse anti-Hnt (1:10; 1G9; DSHB)[75], Alexa Fluor 488- and 546-conjugated phalloidin (1 unit per reaction, Invitrogen), rabbit anti-Dlg (1:1,000; P. Bryant)[76], rat anti-Myo1B (1:500; M.S. Mooseker)[77]. The following antibodies were used in the experiments included in the Supplementary Information: rabbit anti-Numb (1:1,000; Y. N. Jan)[78], rabbit anti-Neuralized (1:600; E. C. Lai)[65], rat anti-*D*E-Cadherin (1:1,000, DCAD2, DSHB)[79], rabbit anti-Rab5 (1:200; M. González Gaitán)[80], rabbit anti-Rab11 (1:1,000, D. F. Ready)[81], guinea pig anti-Spinster/Benchwarmer (1:100; G. W. Davis)[82], guinea pig anti-Hrs-FL (1:600; ref. 83).The samples were then incubated with Cy3- and/or Cy5-conjugated affinity purified donkey secondary antibodies (1:500; Jackson ImmunoResearch Laboratories). Images were captured using an LSM510 confocal microscope and Leica TCS SP5 confocal microscope. Images were processed with Amira 5.0.1 and Adobe PhotoShop 7.0.

Transmission electron microscopy (TEM). To identify the pIIa-pIIb cells, we used flies of the following genotype: *UAS–CD2::HRP; neur^{A101}-GAL4* (ref. 61). In this genotype the HRP-labelled cell membranes correspond to pIIa-pIIb at the 16–18 h APF time-point, as *neur^{A101}-GAL4* drives expression of the CD2::HRP in the SOP and its progeny. To identify the SOP progeny in *Arp3* mutant clones for TEM analysis, we examined the flies with the genotype *y w Ubx–FLP;UAS–-CD2::HRP; Arp3^{515FC} FRT80B neur^{A101}-GAL4/ arm-lacZ M(3) tub–GAL80 FRT80B* in which the CD2::HRP is activated only in *Arp3* mutant SOP progeny.

HRP label was visualized by TEM as described previously[84] except for the following modifications: the pupal thorax was dissected at 18 h APF. After amplification and visualization of the HRP signal under a dissecting microscope, the tissues were fixed[85] to preserve the actin filament structures. The tissues were then processed for TEM using microwave irradiation with PELCO BioWave equipped with PELCO Cold Spot and Vacuum System. Serial sections (60 nm) were cut and post-stained with Reynold's lead citrate, and examined with a JEOL transmission electron microscope (JEOL 1010). The serial sections were labelled on the basis of their depth from the first electron micrograph that shows the most apical portion of HRP labelled SOP microvilli.

Immunoelectron microscopy of phalloidin. To label actin, the pupal thorax was dissected at 18 h APF, fixed in 1% glutaraldehyde in 0.1M PB pH 7.2 for 1.5 h, permeabilized in 0.1% Triton PBS for 5 min, labelled with biotin-XX phalloidin (3 units; Invitrogen) in PBS for 30–35 min. Samples were then incubated in streptavidin-HRP in TNT buffer (1:100; Sigma). To develop enzyme activity, we used a procedure described previously[84].

Delta endocytosis and pulse-chase assay. The endocytosis and pulse-chase assays were modified from previous reports[86,87]. Pupae were partially dissected in Schneider's medium at 18 h APF by making an incision along the dorsal side, and the internal tissues were washed out. The 'empty' pupal case was incubated with the supernatant of monoclonal antibody mouse anti-Delta^{ECD} (1:10; C594.9B; DSHB)[72] for 15–20 min on ice in Schneider's medium supplemented with 25 μg ml^{-1} of 20-hydroxy-ecdysone (Sigma). The tissue was washed three times by medium changes. For the Delta pulse-chase assay the pupal cases were incubated at 25 °C for different time periods (0, 30 and 60 min) in Schneider's medium supplemented with 5 μg ml^{-1} of 20-hydroxy-ecdysone. For the endocytosis assay, the pupal cases were incubated in pre-warmed Schneider's medium supplemented with 5 μg ml^{-1} of 20-hydroxy-ecdysone at 34 °C in a water bath to inactivate the *shibire* gene in the negative control *shi^{ts1}*. After incubation at 25 °C (pulse-chase assay) or 34 °C (endocytosis assay), the pupal cases were fixed for 20 min with 4% formaldehyde in Schneider's medium supplemented with 5 μg ml^{-1} of 20-hydroxy-ecdysone. The normal immunostaining protocol was then followed.

The following antibodies were used in the experiments in the pulse-chase co-labelling experiments in the Supplementary Information: rabbit anti-Rab5 (1:200; M. González Gaitán)[80], rabbit anti-Rab11 (1:1,000, D. F. Ready)[81], guinea pig anti-Spinster/Benchwarmer (1:100; G. W. Davis)[82], guinea pig anti-Hrs-FL (1:600; ref. 83).

Statistical analysis. Measurements of total number of Delta vesicles that traffic to the ARS 1 h after chase, and measurements of the total number of Delta vesicles endocytosed were analysed using a Student's *t*-test (***P <0.0001. Measurements of the ARS area were quantified using the Measure function of the ImageJ software. The measurements were analysed using a Student's *t*-test (***P <0.0001). For TEM, measurements of total number of microvilli in SOP and epithelial cells were quantified using ImageJ. The measurements were analysed using a Student's *t*-test (P <0.05).

The measurement of Delta colocalization with Rab5 and Rab11 as well as the determination of Delta, Rab11 and Rab5 signal intensities were quantified using the labelvoxel and materialstatistics functions in Amira 5.0.1. The measurements were analysed using a Student's *t*-test (*P =0.01).

Western blotting. For the Delta western blots, 50 embryos of the appropriate genotypes were collected at 0–13 h AEL and 13–19 hAEL and lysed in ice-cold filtered RIPA buffer (150 mM NaCl, 1.0% NP-40, 0.5% deoxycholic acid, 0.1% SDS, and 50 mM Tris, pH 8.0) with complete protease inhibitor cocktail (Roche). Lysates were suspended in equal volume of 3× Laemmli sample buffer in the absence of reducing agents, and proteins were resolved by SDS–PAGE. Delta was detected on a western blot using anti-Delta (mAb C594.9B) ascites fluid at 1:10,000. HRP-conjugated goat anti-mouse IgG (Jackson ImmunoResearch) was used at 1:10,000 and the blots were developed using Western Lightning chemiluminescent substrate (PerkinElmer LAS).

57. Struhl, G. & Greenwald, I. Presenilin-mediated transmembrane cleavage is required for Notch signal transduction in *Drosophila*. *Proc. Natl Acad. Sci.USA* **98,** 229–234 (2001).
58. Hudson, A. M. & Cooley, L. A subset of dynamic actin rearrangements in *Drosophila* requires the Arp2/3 complex. *J. Cell Biol.* **156,** 677–687 (2002).
59. Ben-Yaacov, S., Le Borgne, R., Abramson, I., Schweisguth, F. & Schejter, E. D. Wasp, the *Drosophila* Wiskott-Aldrich syndrome gene homologue, is required for cell fate decisions mediated by Notch signaling. *J. Cell Biol.* **152,** 1–13 (2001).
60. Zallen, J. A. *et al.* SCAR is a primary regulator of Arp2/3-dependent morphological events in *Drosophila*. *J. Cell Biol.* **156,** 689–701 (2002).
61. Watts, R. J., Schuldiner, O., Perrino, J., Larsen, C. & Luo, L. Glia engulf degenerating axons during developmental axon pruning. *Curr. Biol.* **14,** 678–684 (2004).

DOI: 10.1038/ncb1888

62. Lai, E. C. & Rubin, G. M. neuralized functions cell-autonomously to regulate a subset of notch-dependent processes during adult *Drosophila* development. *Dev. Biol.* **231,** 217–233 (2001).
63. Frise, E., Knoblich, J. A., Younger-Shepherd, S., Jan, L. Y. & Jan, Y. N. The *Drosophila* Numb protein inhibits signaling of the Notch receptor during cell–cell interaction in sensory organ lineage. *Proc. Natl Acad. Sci. USA* **93,** 11925–11932 (1996).
64. Berdnik, D., Torok, T., Gonzalez-Gaitan, M. & Knoblich, J. A. The endocytic protein α-Adaptin is required for numb-mediated asymmetric cell division in *Drosophila*. *Dev. Cell* **3,** 221–231 (2002).
65. Lai, E. C., Deblandre, G. A., Kintner, C. & Rubin, G. M. *Drosophila* neuralized is a ubiquitin ligase that promotes the internalization and degradation of Delta. *Dev. Cell* **1,** 783–794 (2001).
66. Manning, L. & Doe, C. Q. Prospero distinguishes sibling cell fate without asymmetric localization in the *Drosophila* adult external sense organ lineage. *Development* **126,** 2063–2071 (1999).
67. Wang, W. & Struhl, G. *Drosophila* Epsin mediates a select endocytic pathway that DSL ligands must enter to activate Notch. *Development* **131,** 5367–5380 (2004).
68. Tien, A. C. *et al.* Ero1L, a thiol oxidase, is required for Notch signaling through cysteine bridge formation of the Lin12-Notch repeats in *Drosophila melanogaster*. *J. Cell Biol.* **182,** 1113–1125 (2008).
69. Blochlinger, K., Bodmer, R., Jan, L. Y. & Jan, Y. N. Patterns of expression of cut, a protein required for external sensory organ development in wild-type and cut mutant *Drosophila* embryos. *Genes Dev.* **4,** 1322–1331 (1990).
70. Robinow, S. & White, K. Characterization and spatial distribution of the ELAV protein during *Drosophila melanogaster* development. *J. Neurobiol.* **22,** 443–461 (1991).
71. Nolo, R., Abbott, L. A. & Bellen, H. J. Senseless, a Zn finger transcription factor, is necessary and sufficient for sensory organ development in *Drosophila*. *Cell* **102,** 349–362 (2000).
72. Fehon, R. G. *et al.* Molecular interactions between the protein products of the neurogenic loci Notch and Delta, two EGF-homologous genes in *Drosophila*. *Cell* **61,** 523–534 (1990).
73. Parks, A. L., Klueg, K. M., Stout, J. R. & Muskavitch, M. A. Ligand endocytosis drives receptor dissociation and activation in the Notch pathway. *Development* **127,** 1373–1385 (2000).
74. Patel, N. H., Snow, P. M. & Goodman, C. S. Characterization and cloning of fasciclin III: a glycoprotein expressed on a subset of neurons and axon pathways in *Drosophila*. *Cell* **48,** 975–988 (1987).
75. Yip, M. L., Lamka, M. L. & Lipshitz, H. D. Control of germ-band retraction in *Drosophila* by the zinc-finger protein HINDSIGHT. *Development* **124,** 2129–2141 (1997).
76. Woods, D. F. & Bryant, P. J. The discs-large tumor suppressor gene of *Drosophila* encodes a guanylate kinase homolog localized at septate junctions. *Cell* **66,** 451–464 (1991).
77. Morgan, N. S., Heintzelman, M. B. & Mooseker, M. S. Characterization of myosin-IA and myosin-IB, two unconventional myosins associated with the *Drosophila* brush border cytoskeleton. *Dev. Biol.* **172,** 51–71 (1995).
78. Rhyu, M. S., Jan, L. Y. & Jan, Y. N. Asymmetric distribution of numb protein during division of the sensory organ precursor cell confers distinct fates to daughter cells. *Cell* **76,** 477–491 (1994).
79. Oda, H., Uemura, T., Harada, Y., Iwai, Y. & Takeichi, M. A *Drosophila* homolog of cadherin associated with armadillo and essential for embryonic cell–cell adhesion. *Dev. Biol.* **165,** 716–726 (1994).
80. Wucherpfennig, T., Wilsch-Brauninger, M. & Gonzalez-Gaitan, M. Role of *Drosophila* Rab5 during endosomal trafficking at the synapse and evoked neurotransmitter release. *J. Cell Biol.* **161,** 609–624 (2003).
81. Dollar, G., Struckhoff, E., Michaud, J. & Cohen, R. S. Rab11 polarization of the *Drosophila* oocyte: a novel link between membrane trafficking, microtubule organization, and oskar mRNA localization and translation. *Development* **129,** 517–526 (2002).
82. Sweeney, S. T. & Davis, G. W. Unrestricted synaptic growth in spinster-a late endosomal protein implicated in TGF-β-mediated synaptic growth regulation. *Neuron* **36,** 403–416 (2002).
83. Lloyd, T. E. *et al.* Hrs regulates endosome membrane invagination and tyrosine kinase receptor signaling in *Drosophila*. *Cell* **108,** 261–269 (2002).
84. Larsen, C. W., Hirst, E., Alexandre, C. & Vincent, J. P. Segment boundary formation in *Drosophila* embryos. *Development* **130,** 5625–5635 (2003).
85. Maupin, P. & Pollard, T. D. Improved preservation and staining of HeLa cell actin filaments, clathrin-coated membranes, and other cytoplasmic structures by tannic acid-glutaraldehyde-saponin fixation. *J. Cell Biol.* **96,** 51–62 (1983).
86. Le Borgne, R. & Schweisguth, F. Unequal segregation of Neuralized biases Notch activation during asymmetric cell division. *Dev. Cell* **5,** 139–148 (2003).
87. Emery, G. *et al.* Asymmetric Rab 11 endosomes regulate Delta recycling and specify cell fate in the *Drosophila* nervous system. *Cell* **122,** 763–773 (2005).

nature cell biology

DOI: 10.1038/ncb1888

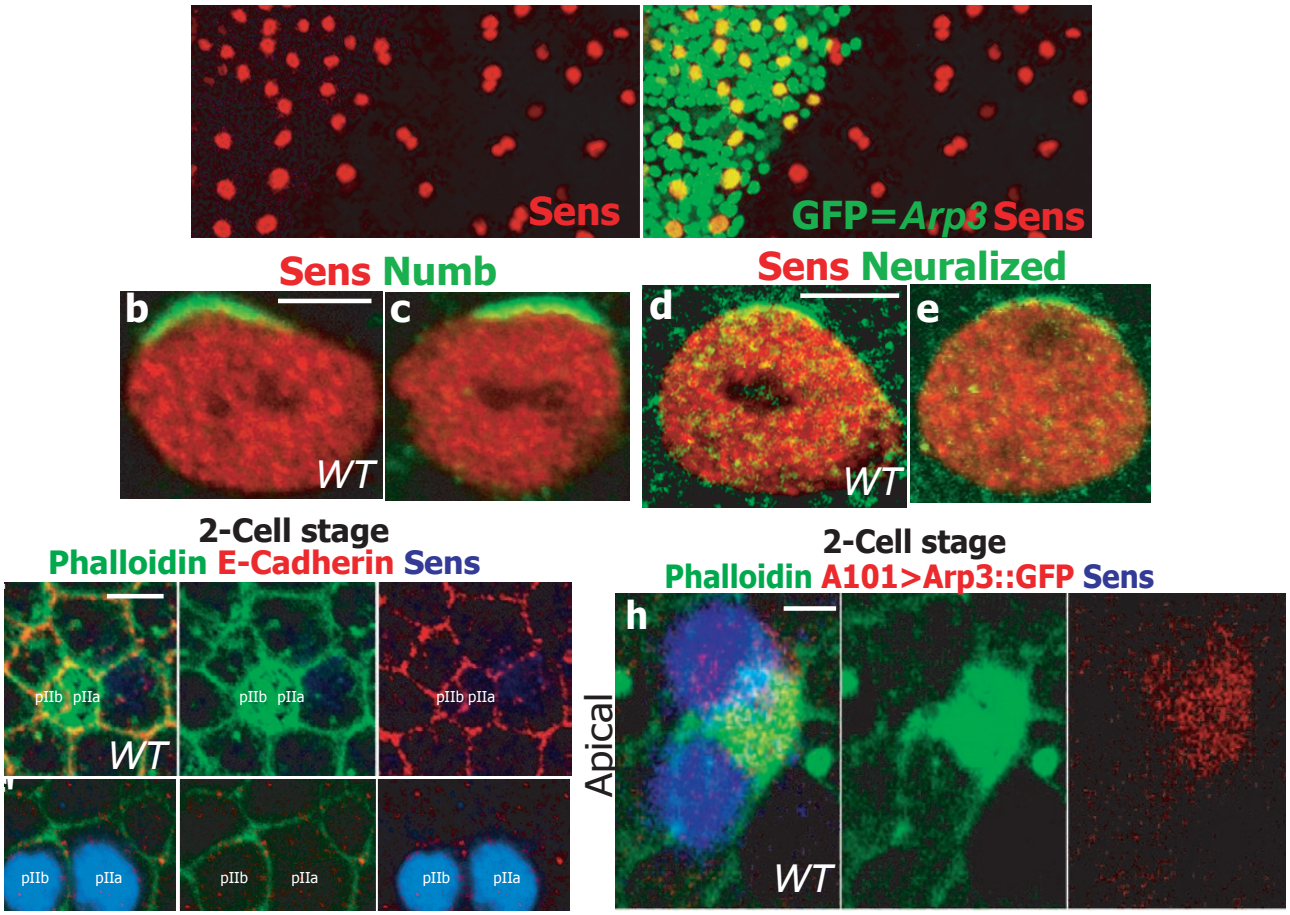

Figure S1 (**a** -**a'**) The SOPs are correctly specified in *Arp3*: (**a**) A projection of confocal sections along the XY-axis of a pupal notum at 17:30hr APF harboring *Arp3* clones marked by the presence of nuclear GFP (green) and immunostained for Sens (red) which marks the SOP and its progeny pIIa-pIIb. Note that SOPs are correctly specified in the mutant clones (green). (**b** -**e**) The segregation of asymmetric fate determinants is normal in *Arp3* mutant SOP: (**b** -**e**) Images showing a single confocal section along the XY-axis of a dividing SOP at 17:30hr APF of a *WT* or an *Arp3* pupal notum stained for asymmetric cell fate determinants (green) and Sens (red). Anterior side of the dividing SOP is oriented upwards in all these images. (**b**, **c**) Numb (green) segregates into the anterior side of the dividing SOP in both *WT* (**b**) and *Arp3* mutant clones (**c**), so that it is inherited into the anterior pIIb daughter. (**d**, **e**) Neuralized (green) segregates into the anterior side of the dividing SOP in both *WT* (d) and *Arp3* mutant clones (**e**), so that it is inherited into the anterior pIIb daughter. (**f** -**g'**) The ARS is formed only in the 2-cell stage: (**f**, **f'**) A confocal image of a single optical section along the XY-axis shows that the ARS forms above the pIIa-pIIb at the 2-cell stage. (**f**) *WT* pupal notum immunostained with phalloidin (green) reveals an apical (0.5 μm) actin enrichment, and this F-actin structure co-localizes with the apical stalk of the pIIa-pIIb cells marked by E-Cad (red). (**f'**) A basal section (~6 μm) of the sample shows the nuclei of the pIIa-pIIb cells marked with Sens (blue). (g, g') A confocal section along the XY-axis, showing immunostaining of *WT* pupal notum at the 1-cell stage with Sens (blue), phalloidin (green) and E-Cad (red). (**g**) The apical section (0.5 μm) reveals that the ARS has not yet formed at 1-cell stage. (**g'**) A basal section (6 μm) shows that the SOP, marked by Sens (blue) has not yet divided. F-actin (phalloidin–green) marks the cell membrane of the epithelial cells and SOP. (**h** -**h"**) Arp3 co-localizes with the ARS: (**h** -**h"**) Confocal images of a single optical section along the XY-axis (**h** -**h'**) and XZ-axis (**h"**) of pupal notum in which *UAS-Arp3-GFP* is expressed under the control of a *neuralized-GAL4* driver *A101-GAL4>Arp3::GFP* (red), immunostained with Sens (blue) and phalloidin (green) at the 2-cell stage. Scale bar: 10 μm in (a), 5 μm in (**f**- **g'**) and 2.5 μm in (**b**, **d**, **h**-**h"**).

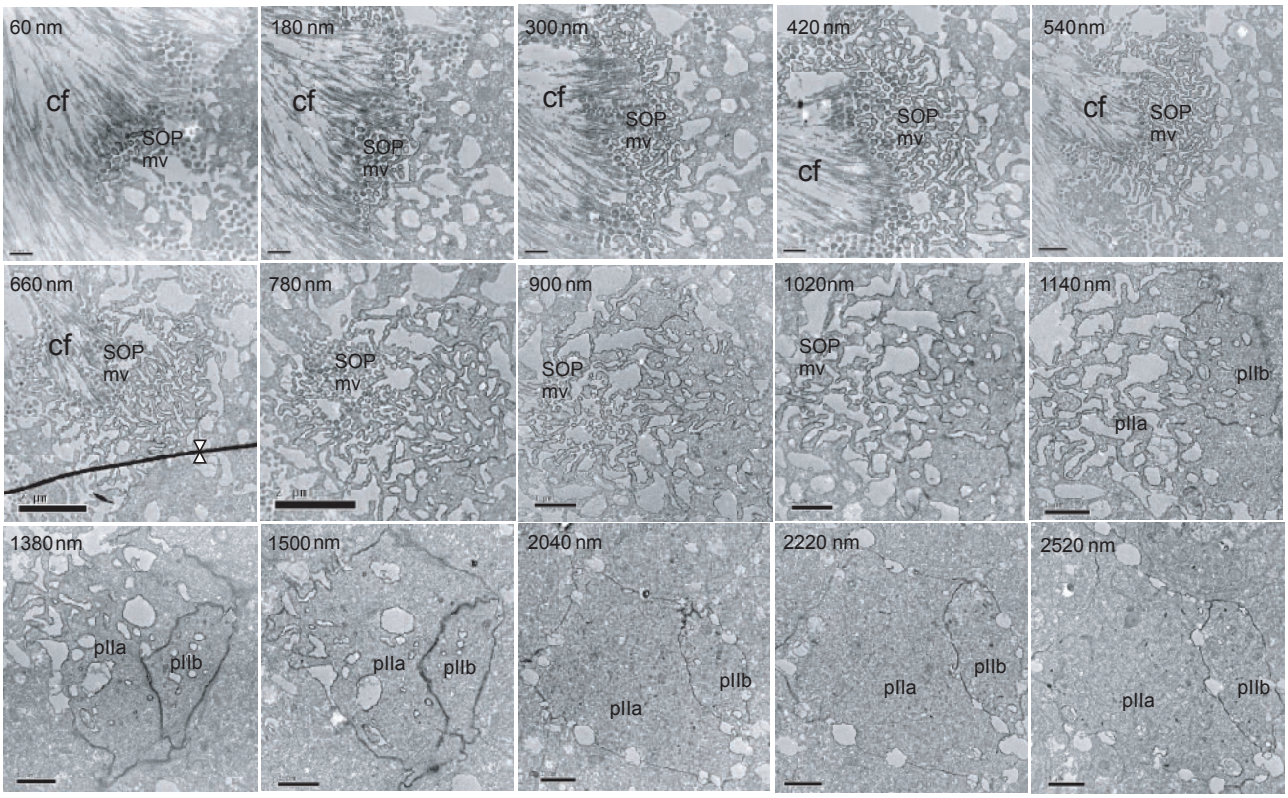

Figure S2 Transmission electron micrographs reveal the presence of finger-like projections on the apical surface of the pIIa-pIIb cells: Serial TEM micrographs of apical cross sections of pIIa-pIIb cells starting at 60 nm of the apical end through 2520 nm (basal end). Serial sections reveal the presence of numerous cross sections of finger-like projections, microvilli (mv) from 60 nm through 1020 nm. Sections from 1500 to 2520 nm show cell membrane outlines of pIIa-pIIb. The chitin fiber (cf) which assembles at the plasma membrane is a part of the apical extracellular matrix (cuticle). The dark line across 660nm with the double arrowhead is a section fold artifact.

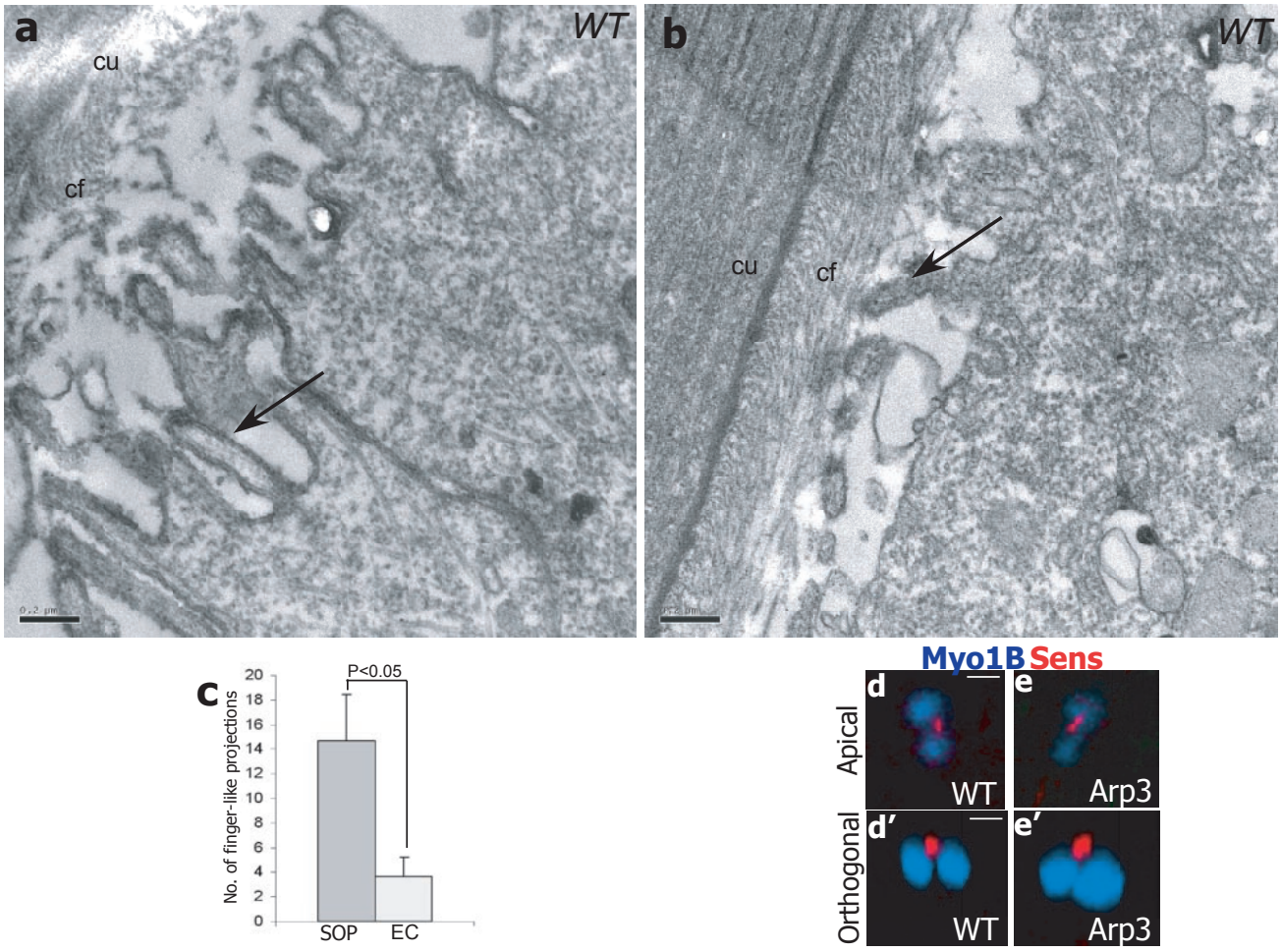

Figure S3 (**a** –**c**) The number of finger-like projections in pIIa-pIIb is significantly higher compared to those on epidermal cells: (**a**) TEM image along the XZ-axis of an SOP and (**b**) Epidermal cells at the 2-cell stage (**c**) A bar graph representing quantification of the number of finger-like projections in the epidermal cells versus the pIIa-pIIb cells. Three *WT* pIIa-pIIb pairs and six *WT* epidermal cells were used for this quantification. Arrows point to the finger-like projections. (**d** -**e'**) Microvilli marker Myo1B is correctly localized in *Arp3* mutant SOP progeny: (**d** -**e'**) Confocal images of single optical sections along the XY-axis (**d**, **e**) and the XZ-axis (**d'**, **e'**) depict immunostainings of *WT* (**d**, **d'**) and *Arp3* (**e**, **e'**) SOP progeny at the 2-cell stage, stained for Myo1B (red) and Sens (blue). Error bars indicate the SEM. Abbreviations: cuticle (cu), chitin fiber (cf). Scale bar: 0.2 µm in (**a**, **b**) and 5 µm in (**d**, **d'**).

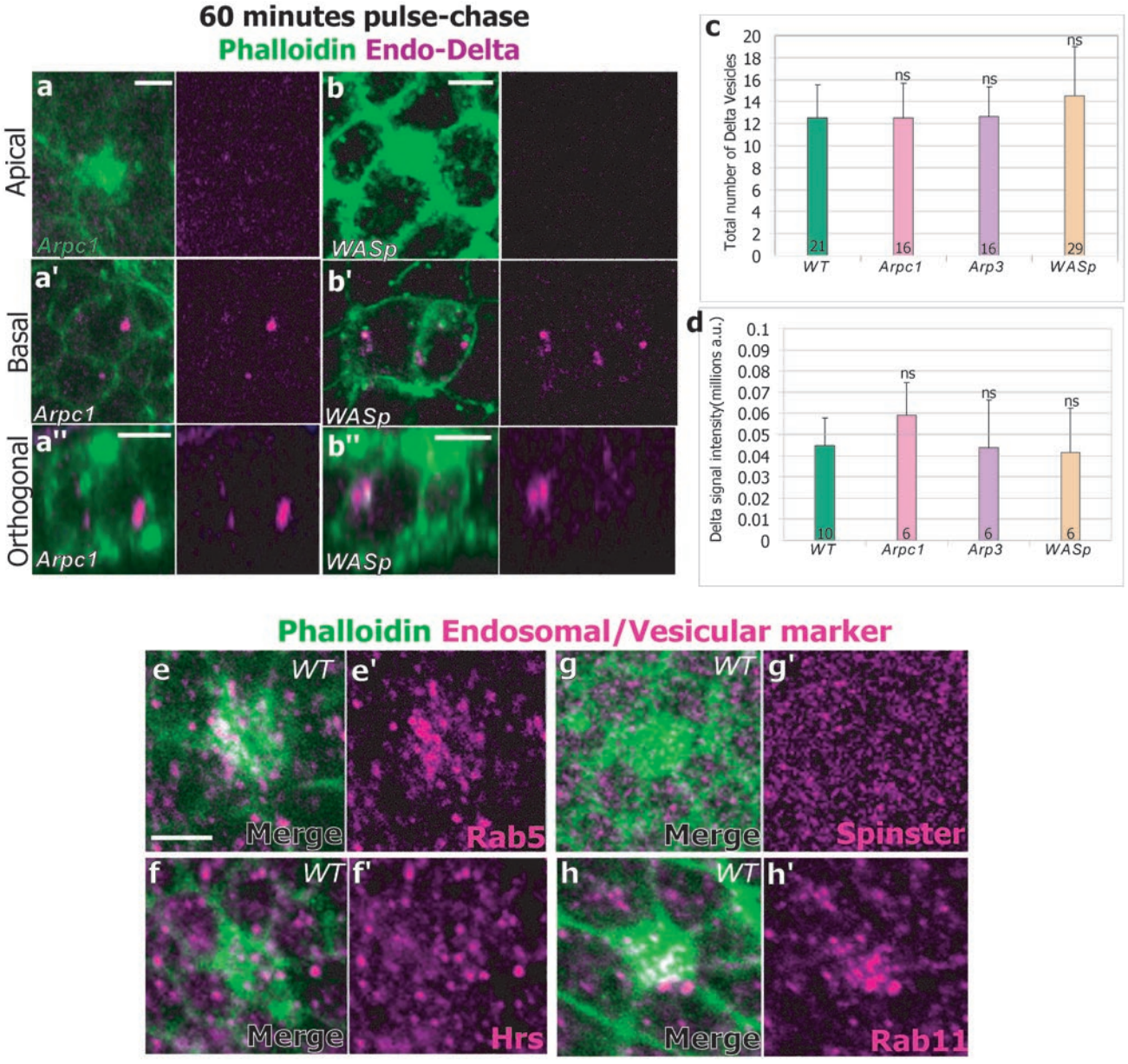

Figure S4 (**a**- **d**) Trafficking of endocytosed Delta traffics apically to the ARS after 60mins chase is compromised in *Arp2/3* and *WASp* mutants: (**a** -**b"**) Confocal images show a single section along the XY-axis (**a**, **a'**, **b**, **b'**) and XZ-axis (**a"**, **b"**) of SOP progeny at the 2-cell stage in *Arpc1* (**a**-**a"**) and *WASp* (**b**-**b"**) mutant during a 60 mins pulse-chase trafficking assay of internalized Delta–anti-Dl^{ECD} vesicles (magenta) with respect to the ARS stained by phalloidin (green). (**c**) A bar graph representing a quantification of the total number of internalized Delta vesicles which are present in the SOP progeny 60 mins after endocytosis. (**d**) A bar graph representing a quantification of the signal intensity of Delta immunostaining in the SOP progeny at 60 min chase. The number of SOP progeny (pIIa-pIIb) quantified per genotype is indicated in the bars. (**e –f'**) Early and recycling endosomes are enriched on the apical region of the ARS during fate specification: (**e** -**f'**) Confocal images of single Z-sections show immunostaining of ARS with phalloidin (green) and endosomal/vesicular markers (magenta) in *WT* pupal nota at the 2-cell stage. (**e**, **e'**) Rab5 (magenta) which marks the early endosome is enriched on the ARS (green). (**f**, **f'**) A subset of late endosomes marked by Hrs (magenta) do not show enrichment with respect to the ARS (green). (**g**, **g'**) The lysosomes marked by Spinster/ Benchwarmer (magenta) do not show enrichment relative to the ARS (green). (**e**, **e'**) Rab11 (magenta) which marks the recycling endosome is enriched with respect to the ARS (green). ns = not statistically significant. Error bars indicate SEM. Scale bar: **5** µm in (**a**, **b**, **a"**, **b"**) and 3.5 µm in (**e**).

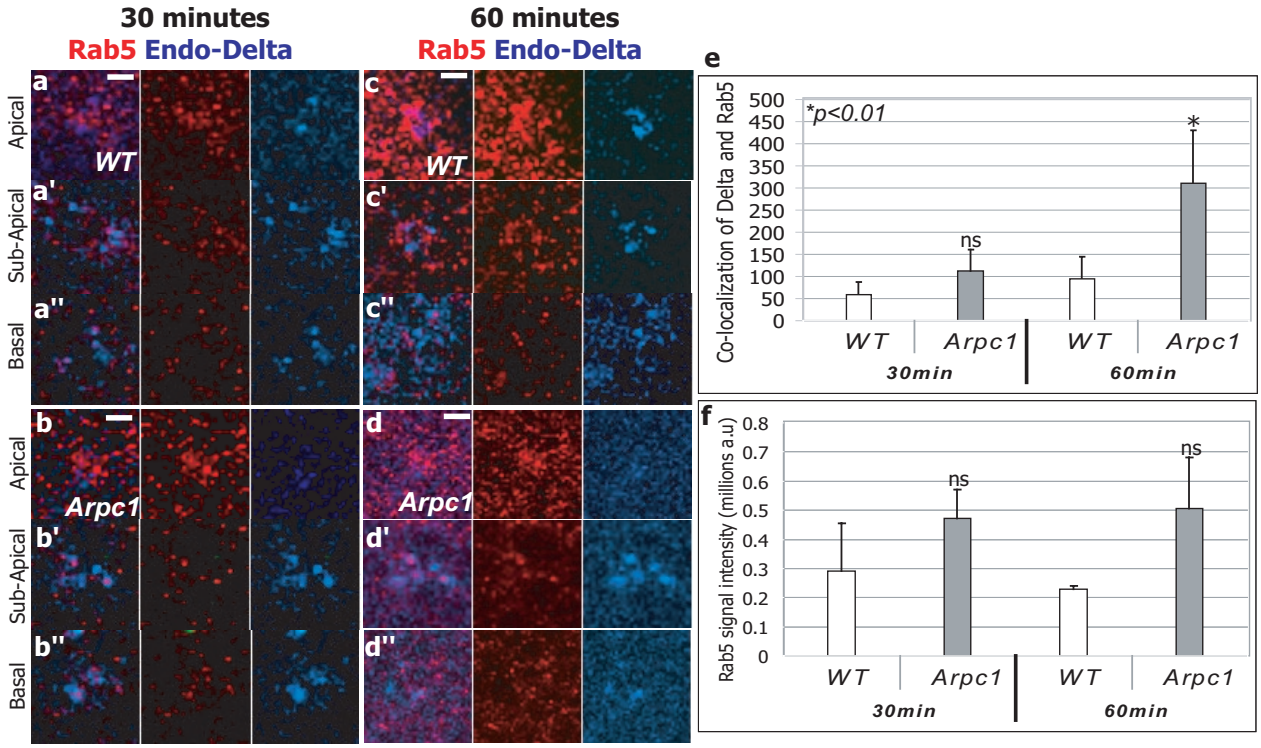

Figure S5 Pulse-chase trafficking of Delta with respect to the early endosomes (EE): Confocal images of single optical sections (**a**-**d"**) of SOP progeny at the 2-cell stage in *WT* (**a**-**a"**, **c**-**c"**) and *Arpc1* (**b**-**b"**, **d**-**d"**) after 30 mins (a-b") and 60 mins (c-**d"**) pulse-chase trafficking assays of internalized Delta–anti-DI^{ECD} (blue) with respect to the EE stained for Rab5 (red). (**a**-**d**) Apical sections (~0.5 µm) into the sample. (**a'**-**d'**) Sub-apical sections (~3 µm) into the sample. (**a"**-**d"**) Basal sections (~6 µm) into the sample. (**e**) A bar graph depicting co-localization intensity of Delta and Rab5 vesicles in arbitary units (a.u.). The measurements of signal intensities were analysed using a Student's t-test;*, p=0.01. Seven SOP progeny pairs were quantified per time point per genotype. (**f**) A bar graph depicting signal intensity of Rab5 vesicles in arbitary units (a.u.). The measurements of signal intensities were analysed using a Student's t-test;*, p=0.01. Seven SOP progeny pairs were quantified per time point per genotype. Abbreviation: ns = not statistically significant. Error bars indicate SEM. Scale bar: 3.5 µm.

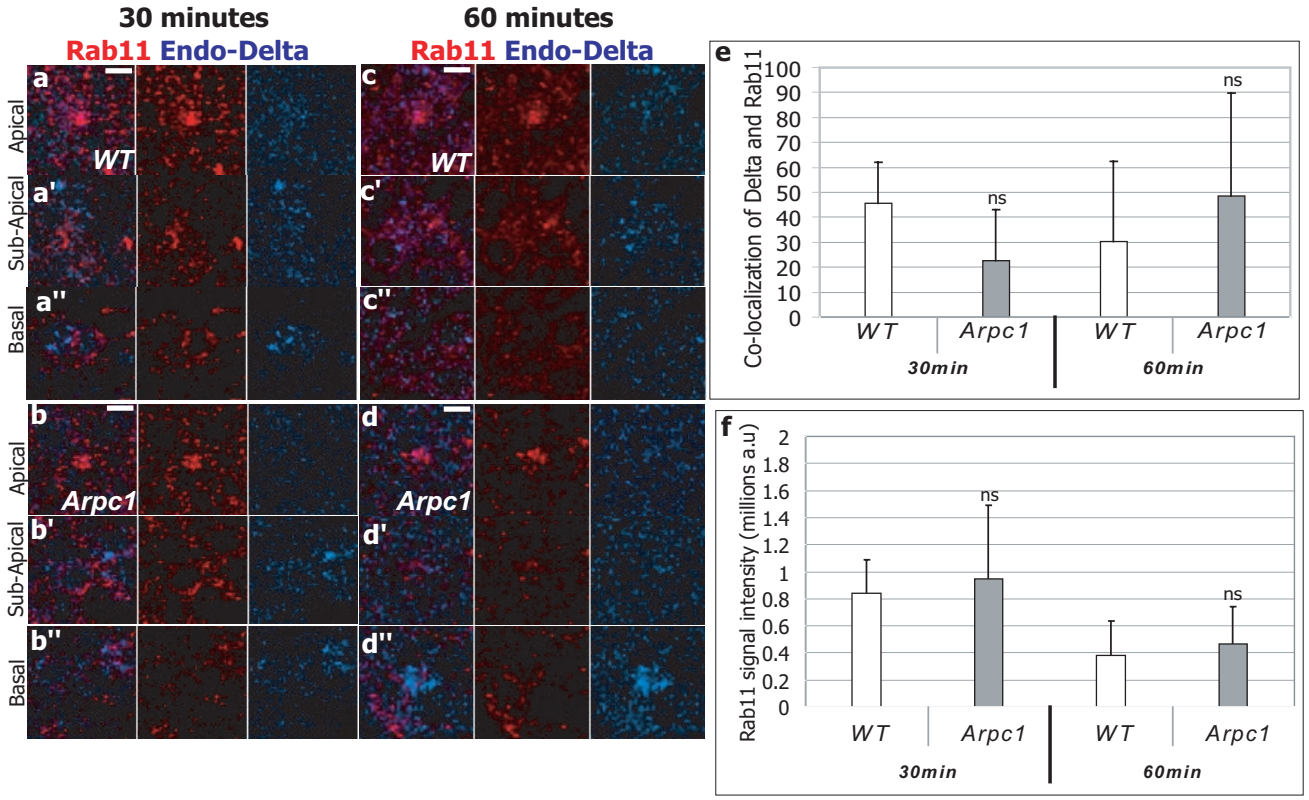

Figure S6 Pulse-chase trafficking of Delta with respect to the recycling endosomes (RE): Confocal images of single optical sections (**a**-**d”**) of SOP progeny at the 2-cell stage in *WT* (**a**-**a”**, **c**-**c”**) and *Arpc1* (**b**-**b”**, **d**-**d”**) after 30 mins (**a**-**b”**) and 60 mins (**c**-**d”**) pulse-chase trafficking assays of internalized Delta–anti-DI^{ECD} vesicles (blue) with respect to the RE stained for Rab11 (red). (**a**-**d**) Apical sections (~0.5 µm) into the sample. (**a’**-**d’**) Sub-apical sections (~3 µm) into the sample. (**a”**-**d”**) Basal sections (~6 µm) into the sample. (**e**) A bar graph depicting co-localization intensity of Delta and Rab11 vesicles in arbitrary units (a.u.). The measurements of signal intensities were analysed using a Student’s t-test;*, p=0.01. Seven SOP progeny pairs were quantified per time point per genotype. (**f**) A bar graph depicting signal intensity of Rab11 vesicles in arbitrary units (a.u.). The measurements of signal intensities were analysed using a Student’s t-test;*, p=0.01. Seven SOP progeny pairs were quantified per time point per genotype. Abbreviation: ns = not statistically significant. Error bars indicate SEM. Scale bar: 3.5 µm.

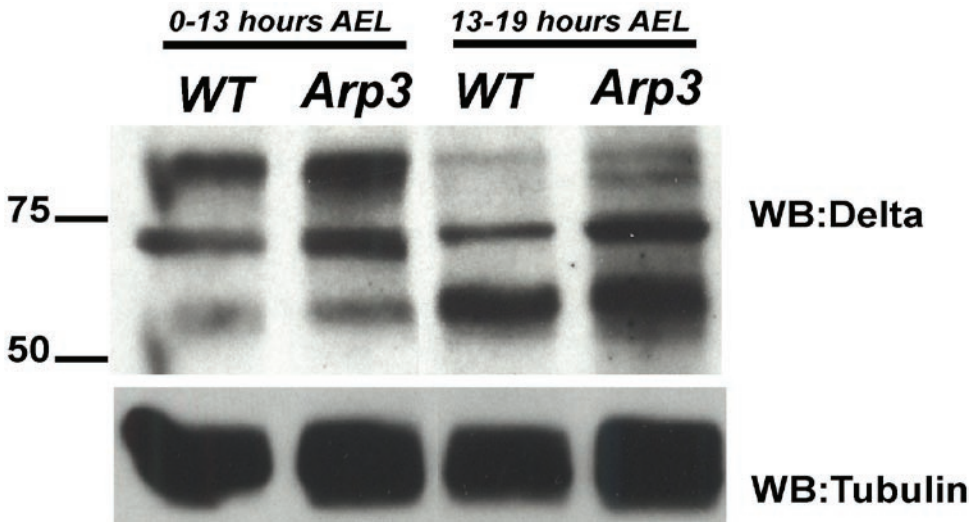

Figure S7 The processing of Delta in *Arp3* mutant embryos is unaffected: Western blotting analysis of *WT* and *Arp3* embryo lysates at 0-13hr AEL and 13-19hr AEL probed with mouse anti-Delta ascites fluid. At 0-13hr AEL note the presence of a 98 kDa band in *WT* and *Arp3* lanes. The Delta S isoform (68 kDa, is present at 0-13hr AEL but is weaker compared to the 98 kDa band. At 13-19hr AEL the 98 kDa band is much reduced in *WT* and *Arp3*. The Delta S isoform (68 kDa, arrow) is highly enriched at the 13-19 hr AEL time point in both *WT* and *Arp3* mutant. In the *Arp3* lane we sometimes observe a doublet at 98 kDa at 13-19hr AEL, but not consistently in various independent trials of the experiment.

Supplementary material:

Results:

Early and recycling endosomes are enriched on the apical region of the ARS during fate specification:

It has been proposed that Delta must be endocytosed and targeted to a specific endosomal compartment to become activated[1], possibly through a Rab11-positive recycling endosomal compartment[2, 3]. Based on our data, the ARS may have a role in these trafficking events. We therefore examined the co-localization of different endosomal compartments with respect to the ARS during cell fate specification. Immunostaining with endosomal and vesicular compartment markers including Rab5 (early endosomes, EE)[4], Rab11 (recycling endosomes, RE)[5], Hrs (late endosomes, LE)[6] and Spinster (lysosomes)[7, 8] revealed that EE and RE are enriched apically where they co-localize with the microvillar region of the ARS in the pIIa-pIIb at the 2-cell stage (Supplementary Fig. 4 e, e', h, h'). However, the LE and lysosomes are not enriched with respect to the ARS (Supplementary Fig. 4 g, g', f, f'). We find the localization of these endosomal and vesicular compartments are similar to *WT* in *Arp3, Arpc1* mutant pIIa-pIIb cells (data not shown).

Endosomal trafficking of Delta through the early endosomes (EE) and recycling endosomes (RE) during pIIa-pIIb fate specification:

To examine if Delta trafficking through the EE and RE is altered in mutants of the Arp2/3 complex, we performed pulse chase assays at 30 mins and 60 mins after

internalization (Supplementary Fig. 5, 6). We focused on these compartments as they were enriched on the ARS at the 2-cell stage (Supplementary Fig. 4 e, e', h, h'). With regard to the Rab5-positive EE compartment we find that there is no statistically significant difference of Delta co-localization with this compartment between *WT* and mutant at 30 mins post-internalization (Supplementary Fig. 5 a-b'', e). However, after 60 mins chase there seems to be a borderline significant increase in Delta vesicle co-localization to the Rab5 compartment (p=0.01, student's two-tailed test) in *Arpc1* mutants compared to *WT* (Supplementary Fig. 5 c-d'', e). We also assayed if the abundance of the EE is altered in the *Arpc1* mutant by quantifying the signal intensity of Rab5 immuno-staining in the *Arpc1* mutant pIIa-pIIb cells, 30 min and 60 mins after internalization, and we find that there is no significant difference (Supplementary Fig. 5 f).

Furthermore, we found that there is not a statistically significant difference of Delta trafficking with respect to the Rab11-positive RE at both 30 mins and 60 mins post internalization (Supplementary Fig. 6 a-d'', e). The distribution and abundance of the Rab11 compartment itself remains largely unaffected in the *Arpc1* mutants (Supplementary Fig. 6 f). In addition, when the pI cell divides, Emery et al (2005) have reported that Rab11 localizes asymmetrically to the pIIb cell[3]. We found that this asymmetric distribution of Rab11 to the pIIb compartment is unaffected in dividing pIs of *Arp3* mutants (data not shown).

Our hypothesis based on these results is that the primary defect in *Arp2/3* mutants is their inability to traffic Delta to the apical region of the ARS, and we consider this increased co-localization of Delta to the Rab5 compartment as a

secondary defect that seems to occur when the Delta vesicles do not arrive at their expected destination. The reason we favor this hypothesis is that the inability of Delta to cluster around the ARS and traffic apically seems to be a highly significant (Fig. 8g) defect as compared to a subtle increase in Delta co-localization to the Rab5 positive compartment (Supplementary Fig. 5e).

Delta processing is unaffected in *Arp3* mutants:

Wang and Struhl[1] have suggested that the internalization of Delta leads to a proteolytic cleavage in an unknown compartment. *Drosophila* full-length Delta (~98 kDa) is proteolytically processed into three different isoforms *in vivo*[9] and the short isoform Delta S (~68 kDa) may correspond to the activated form[1, 9]. During early stages of embryogenesis (0-6 hours after egg laying, hr AEL) the Delta S isoform is not generated[45]. At later developmental stages (13-24hr AEL) full-length Delta is much reduced, but the Delta S isoform is far more abundant[45]. To assay if lack of Arp2/3 function alters Delta processing we prepared lysates from *WT*, *Arp3* and *Arpc1* zygotic mutant embryos at two different developmental time periods, 0-13hr AEL and 13-19hr AEL, for western blot analysis. We find that processing of Delta is largely unaltered in *Arp3* embryos (Supplementary Fig. 7), suggesting that the processing of Delta may not depend on Arp2/3 function.

nature cell biology

CPAP is a cell-cycle regulated protein that controls centriole length

Chieh-Ju C. Tang[1], Ru-Huei Fu[1,3], Kuo-Sheng Wu[1,2], Wen-Bin Hsu[1] and Tang K. Tang[1,4]

Centriole duplication involves the growing of a procentriole (progeny centriole) next to the proximal end of each pre-existing centriole (parental centriole). The molecular mechanisms that regulate procentriole elongation remain obscure. We show here that expression of the centriolar protein CPAP (centrosomal P4.1-associated protein) is carefully regulated during the cell cycle, with the protein being degraded in late mitosis. Depletion of CPAP inhibited centrosome duplication, whereas excess CPAP induced the formation of elongated procentriole-like structures (PLSs), which contain stable microtubules and several centriolar proteins. Ultrastructural analysis revealed that these structures are similar to procentrioles with elongated microtubules. Overexpression of a CPAP mutant (CPAP-377EE) that does not bind to tubulin dimers significantly inhibited the formation of CPAP-induced PLSs. Together, these results suggest that CPAP is a new regulator of centriole length and its intrinsic tubulin-dimer binding activity is required for procentriole elongation.

The centrosome is the primary microtubule-organizing centre (MTOC), which is composed of two centrioles surrounded by pericentriolar material. The main function of the centrosome is to organize dynamic arrays of microtubules within cells[1,2]. In vertebrates, centrioles usually comprise cylindrical arrays of triplet microtubules with a nine-fold symmetry (~500 nm in length and ~200 nm in diameter)[3].

Centriole duplication involves the growing of procentrioles orthogonally to each of the two parental centrioles[4,5]. These two new procentrioles begin to grow during late S/G2 phase and reach their full length during the following cell cycle[6]. Recent studies have identified at least five centrosome-associated proteins (SPD-2, ZYG-1/Plk4, SAS-5, SAS-6 and SAS-4) that are essential for centrosome duplication in *Caenorhabditis elegans*[7–12] and *Drosophila melanogaster*[13–15]. At the initial stage of procentriole assembly in *C. elegans*, SPD-2 is required for the centriolar localization of ZYG-1 before recruitment of SAS-5, SAS-6 and later SAS-4 to the centrioles[16,17]. SAS-5 and SAS-6 are two coiled-coil proteins essential for the formation and elongation of the central tube, whereas SAS-4 seems to be required for the assembly of microtubules onto the periphery of the central tube[17]. Human homologues of SPD-2, ZYG-1, SAS-4 and SAS-6 have been identified as Cep192 (ref. 18), Plk4/Sak[13,19], CPAP[20] and hSAS-6 (ref. 9), respectively. Using short interfering RNA (siRNA) and immunoelectron microscopy approaches, a putative centriole assembly pathway in human cells has been proposed[21]. After activation of Plk4 on the surface of a parental centriole, hSAS-6, CPAP, Cep135 and γ-tubulin are rapidly recruited to a procentriole formation site[21]. Yet, whether these proteins are recruited at exactly the same time or how these proteins cooperate to initiate procentriole elongation is not clear.

To address these questions systematically, we first performed a comparative analysis of the protein expression pattern between CPAP and hSAS-6 (a known cell-cycle regulated centriole protein)[22] in synchronized cells. HeLa cells were released from a double thymidine block and analysed by western blotting (Fig. 1a). CPAP levels increased gradually from early S phase until mitosis (Fig. 1a; ~0–8 h). As cells exited mitosis and entered early G1 phase, both hSAS-6 and CPAP levels decreased significantly (Fig. 1a; ~8–12 h). Similar effects were also observed for two control proteins, Cyclin B1 and APC-Cdh1 (Fig. 1a, b), the levels of which are known to decrease during late anaphase and G1 (ref. 23). Centrobin, a known procentriole protein[24], showed no cell-cycle regulated expression pattern (Fig. 1a). The cell-cycle regulated pattern of CPAP was further confirmed in nocodazole-synchronized cells (Fig. 1b). Nocodazole is a microtubule-depolymerizing agent that arrests cells in G2/M phase. Both CPAP and hSAS-6 levels decreased significantly when cells exited mitosis (Fig. 1b; ~0–4 h). Together, our findings show that CPAP is a cell-cycle regulated protein.

The anaphase-promoting complex or cyclosome (APC/C) is an E3 ubiquitin ligase that assembles polyubiquitin chains on substrate proteins and targets them for destruction by the 26S proteasome. The APC/C is active during mitosis and in the G1 phase (ref. 23). Our observation that CPAP levels were significantly decreased in late mitosis raised the possibility that the APC/C–26S proteasome system may be involved in CPAP degradation. Consistently, HeLa cells synchronized at G2/M phase with nocodazole failed to show CPAP and cyclin B1 (a known 26S proteasome

[1]Institute of Biomedical Sciences, Academia Sinica, Taipei 11529, Taiwan. [2]Institute of Biochemistry and Molecular Biology, National Yang Ming University, Taipei 11221, Taiwan. [3]Current address: Graduate Institute of Immunology, China Medical University, Taichung 40402, Taiwan.
[4]Correspondence should be addressed to: T.K.T. (e-mail: tktang@ibms.sinica.edu.tw)

Received 19 March 2009; accepted 11 May 2009; published online 7 June 2009; DOI: 10.1038/ncb1889

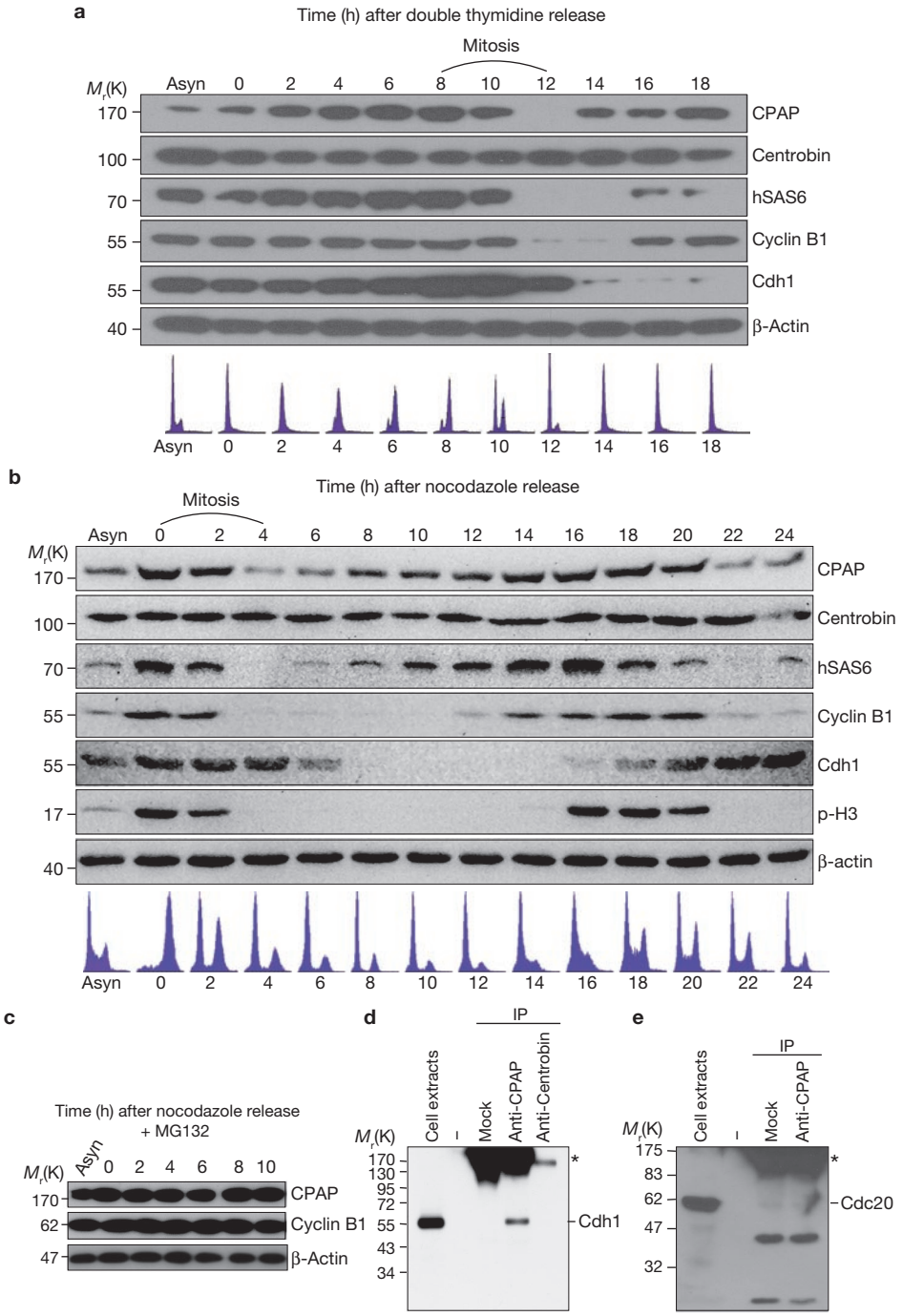

Figure 1 CPAP protein levels are cell-cycle regulated. (**a**, **b**) HeLa cells released from a double thymidine block (**a**) or nocodazole treatment (**b**) were analysed at the indicated times by immunoblotting using indicated antibodies (top) or by FACS (bottom; Asyn: asynchronized). In panel **a**, faint bands for CPAP (12 h after double thymidine release) and hSAS-6 (12 h and 14 h after double thymidine release) can be detected after longer exposure, reflecting their low expression levels at these times. (**c**) MG132, a 26S proteasome inhibitor, inhibits CPAP degradation during mitotic exit. HeLa cells were arrested at G2/M by nocodazole treatment and then released into fresh medium containing MG132 (20 μM). Lysates prepared at the indicated times after release were analysed by immunoblotting using the indicated antibodies. In **a**–**c**, β-actin was used as a loading control and asychronized cell lysates were loaded in the left-hand columns. (**d**, **e**) CPAP interacts with the APC/C–Cdh1 complex (**d**), but not with the APC/C–Cdc20 complex (**e**). HeLa cell lysates were first immunoprecipitated (IP) with antibodies against CPAP, centrobin (as a control) or a non-relevant normal mouse immunoglobulin, IgG (Mock). The immunoprecipitated protein complexes were then analysed by immunoblotting with an anti-Cdh1 (**d**) or anti-Cdc20 (**e**) antibody. Asterisks represent intact immunoglobulins in a non-reducing condition (see Methods). Full scans of western blots in **a**, **b** and **c** are shown in Supplementary Information, Fig. S8.

substrate) degradation in the presence of the proteasome inhibitor MG132 (Fig. 1c). In contrast, CPAP levels decreased significantly when cells exited mitosis in the absence of MG132 (Fig. 1b).

APC/C is activated by several cofactors during specific periods of the cell cycle. The best known cofactors are Cdc20 (activated during metaphase) and Cdh1 (activated during late anaphase and the G1phase)[23].

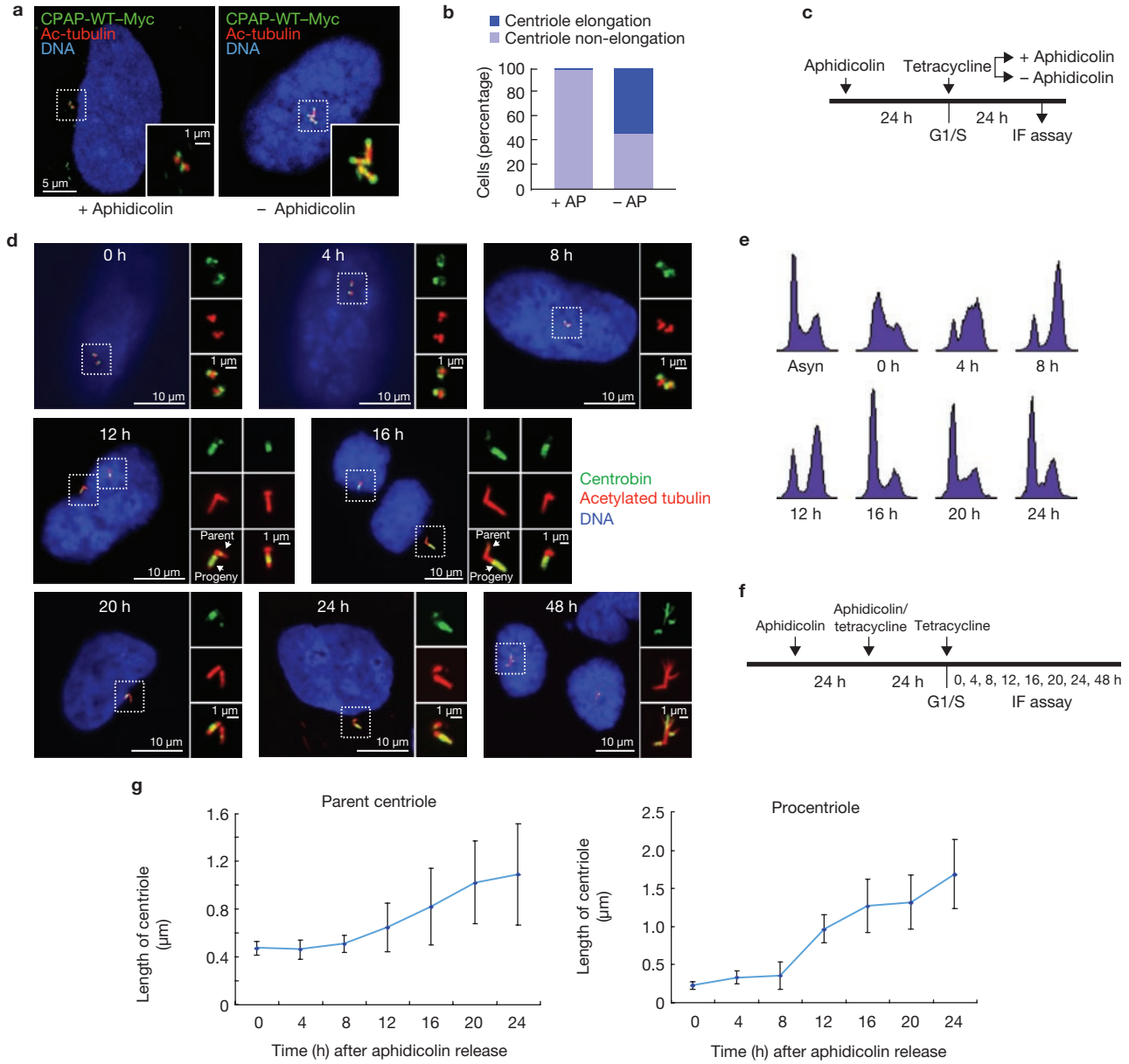

Figure 2 Excess CPAP induced the formation of PLSs. (**a**, **b**) CPAP-induced filaments occured after the G1 phase. U2OS-based CPAP-wildtype–Myc (WT) inducible cells were treated as shown in **c**. At 24 h after tetracycline induction, cells were either left untreated (– AP; right) or treated with aphidicolin (+ AP; left), co-stained with antibodies against Myc (green) and acetylated tubulin (Ac-tubulin; red), and analysed by immunofluorescence confocal microscopy (**a**). DNA was counterstained with DAPI (blue). The percentage of cells with elongated centrioles or non-elongated centrioles in the presence or absence of aphidicolin (1.6 μg ml^{-1}) are shown **b**. (**c**) A protocol to analyse CPAP-induced filaments after the G1 phase. (**d**–**g**) The timing of CPAP-induced filament growth during the cell cycle is shown. CPAP-wildtype–Myc-inducible cells were treated as described in **f**. At the indicated times after tetracycline induction cells were analysed by immunofluorescence confocal microscopy (**d**) using antibodies against acetylated tubulin (red) and centrobin (green), and by FACS (**e**). The lengths of centrioles (labelled with acetylated tubulin) were quantified at the indicated times (**g**; $n = 27$ centrioles). Error bars represent mean ± s.d. The procentrioles were primarily marked by centrobin staining.

Our coimmunoprecipitation experiments showed that only Cdh1 (Fig. 1d), but not Cdc20 (Fig. 1e), was detected in complexes precipitated by an anti-CPAP antibody, suggesting that CPAP is a target of APC/C–Cdh1, which recognizes either a KEN-box or a D-box motif in substrates[25,26]. There are seven putative D boxes (D1–D7) and two putative KEN boxes (K1 and K2) in CPAP (Supplementary Information, Fig. S1a). Our deletion mapping and site-directed mutagenesis studies indicate that the first KEN box (K1) and the fourth D box (D4) have essential roles in regulating CPAP degradation during mitotic exit (Supplementary Information, Fig. S1). The notion that CPAP is a target of APC/C–Cdh1 is further strengthened by the findings that CPAP is directly associated with Cdh1 (Supplementary Information, Fig. S2a–c) and is ubiquitylated *in vivo* (Supplementary Information, Fig. S2d–f). Taken together, our results indicate that during mitotic exit CPAP is recognized by the APC/C–Cdh1 system, which targets it for degradation by the 26S proteasome.

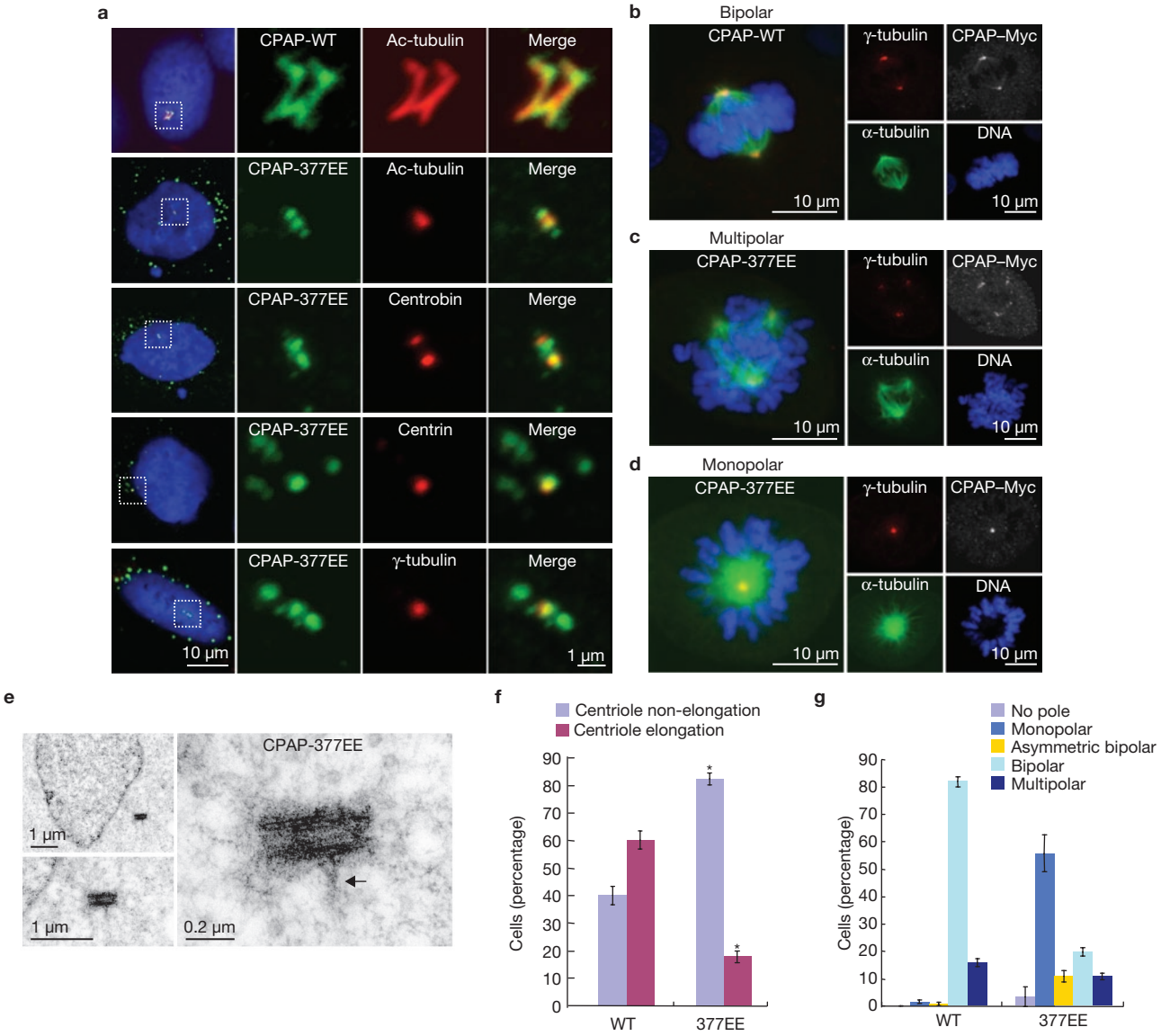

Figure 3 The CPAP-377EE mutant inhibits CPAP-induced PLSs and induces several abnormal mitotic phenotypes. (**a**) CPAP-wildtype–Myc (CPAP-WT) or CPAP-377EE–Myc cells were synchronized at the G1/S stage by treatment with aphidicolin (1.6 μg ml^{-1}) for one day. At 48 h after tetracycline induction without aphidicolin, cells were fixed and stained with the indicated antibodies and analysed by immunofluorescence confocal microscopy (Ac tubulin: acetylated tubulin). CPAP-wildtype–Myc and CPAP-377EE–Myc were detected by an anti-Myc antibody. DNA was counterstained with DAPI. (**b**–**d**) CPAP-wildtype–Myc (**b**) and CPAP-377EE–Myc (**c**, **d**) were induced by treatment with tetracycline (1 μg ml^{-1}) for three days. After fixation (without cold treatment and pre-extraction), the cells were stained with the indicated antibodies. Both normal bipolar (**b**) and abnormal mitotic phenotypes, including multipolar (**c**) and monopolar (**d**) spindles were shown. (**e**) CPAP-377EE–Myc-inducible cells were treated with tetracycline and analysed by electron microscopy as described in the Methods. Electron microscopy images with variable magnifications are shown. The distal end of parental centriole is readily identified by the presence of pericentriolar appendages (arrow). (**f**) The percentage of elongated or non-elongated centrioles induced by excess CPAP-wild type or CPAP-377EE is shown. Error bars represent mean ± s.d. of 200 cells from three experiments. Statistically significant changes (Student's *t*-test) from the respective controls are marked with asterisks (*$P < 0.0001$). (**g**) The percentage of various abnormal mitotic phenotypes is shown. Error bars represent mean ± s.d., $n = 100$ in triplicate.

We next investigated the potential biological functions of CPAP by depleting or overexpressing CPAP in cells. Depletion significantly suppressed centriole amplification in both Plk4-activated (Supplementary Information, Fig. S3aii, b)[21] and hydroxyurea-treated cells (Supplementary Information, Fig. S3dii, e). In the former case, such effects were effectively rescued by expression of wild-type siRNA-resistant CPAP (Supplementary Information, Fig. S3aiii, b), suggesting that CPAP is required for centriole duplication. On the other hand, when green fluorescent protein (GFP)–CPAP-wild-type constructs were transiently transfected into U2OS cells a small portion of transfected cells (~5%) had microtubule-based filamentous structures that seemed to extend from the end of the centriole (Supplementary Information, Fig. S4b), although most of the transfectants formed GFP–CPAP aggregates in the cytosol (Supplementary Information, Fig. S4a). These long microtubule-based filaments could also be detected in GFP–CPAP-transfected mouse embryonic fibroblasts (MEFs; Supplementary Information, Fig. S4c).

The phenotype of CPAP-induced filaments has also been observed by other research groups[27,28].

As overexpression of exogenous CPAP usually resulted in the formation of aggregated spots in the cytosol, hindering the observation of CPAP-induced filaments, we generated U2OS-derived stable transfectants that expressed full-length CPAP-wild type–Myc under tetracycline control. We first determined the cell-cycle stage in which these microtubule-based CPAP filaments are induced. The cell transfectants (clone WT-5) were synchronized with aphidicolin to arrest cells at the G1/S phase (Fig. 2c). Cells were then treated with tetracycline (with or without aphidicolin) for 24 h and analysed by confocal fluorescence microscopy (Fig. 2a) using an antibody against acetylated tubulin, which commonly marks stabilized microtubules rather than dynamic cytoplasmic microtubule networks. Very few elongated CPAP-induced filaments (1/201 cells) were observed in aphidicolin-treated cells (Fig. 2a, b). In the absence of aphidicolin, 121 out of 226 (54%) cells possessed these filaments (Fig. 2a, b). These results imply that CPAP-induced filaments form after the G1 phase.

To more closely examine the timing of these CPAP-induced filaments, we analysed WT-5 clone cells using FACS (fluorescence-activated cell sorting; Fig. 2e) and confocal fluorescence microscopy (Fig. 2d) with antibodies against acetylated tubulin and centrobin (a known procentriole marker) according to the protocol outlined in Fig. 2f. A biphasic growth pattern was commonly observed in these CPAP-induced filaments during the cell cycle. The lengths of these acetylated tubulin-labelled filaments gradually increased, starting at S phase (0–8 h after tetracycline induction, without aphidicolin; Fig. 2g) before rapid growth during G2 and M phases (Fig. 2g; ~8–12 h). Interestingly, the growth of these filaments could even be extended into the next G1/S phase (Fig. 2g; ~16–24 h). The average length of these acetylated tubulin filaments ranged from 0.5 μm (0 h) to 1.1 μm (24 h) in parental centrioles and from 0.2 μm (0 h) to 1.7 μm (24 h) in procentrioles (Fig. 2g). Surprisingly, CPAP-wild type–Myc may also induce these acetylated tubulin filaments to assemble from the parental centrioles (negative centrobin staining; Fig. 2d; 16 h), and a branched elongated filament was frequently observed after longer CPAP-wild type–Myc induction (Fig. 2d; 48 h). Similar results were also observed in CPAP-K1D4m mutant clones that are resistant to Cdh1-dependent degradation (Supplementary Information, Fig. S5). The quantity of the acetylated tubulin filaments induced by CPAP-K1D4m (~70%) was significantly higher than that induced by CPAP-wild type (~52%) and the filaments were longer with more branched structures, suggesting that the degradation-resistant CPAP-K1D4m mutant is prone to initiating these microtubule-based filaments.

A common feature of CPAP-induced filaments is that they contain acetylated tubulin. We took advantage of this to examine the incorporation of several known centriolar proteins, including CP110 (ref. 21), hSAS-6 (ref. 22), centrobin[24] and centrin[29]. Our immunofluorescence microscopy data (Supplementary Information, Fig. S6a–h) and electron microscopy analysis (Supplementary Information, Fig. S6j–k) show a normal incorporation of these centriolar proteins into CPAP-induced filaments, which resemble centriolar structures with elongated microtubules. Thus, these filaments are tentatively designated as PLSs, reflecting their similarity to typical centrioles. Together, these results support the notion that excess CPAP can induce centriole elongation possibly through the assembly of centriolar microtubules during centriole biogenesis.

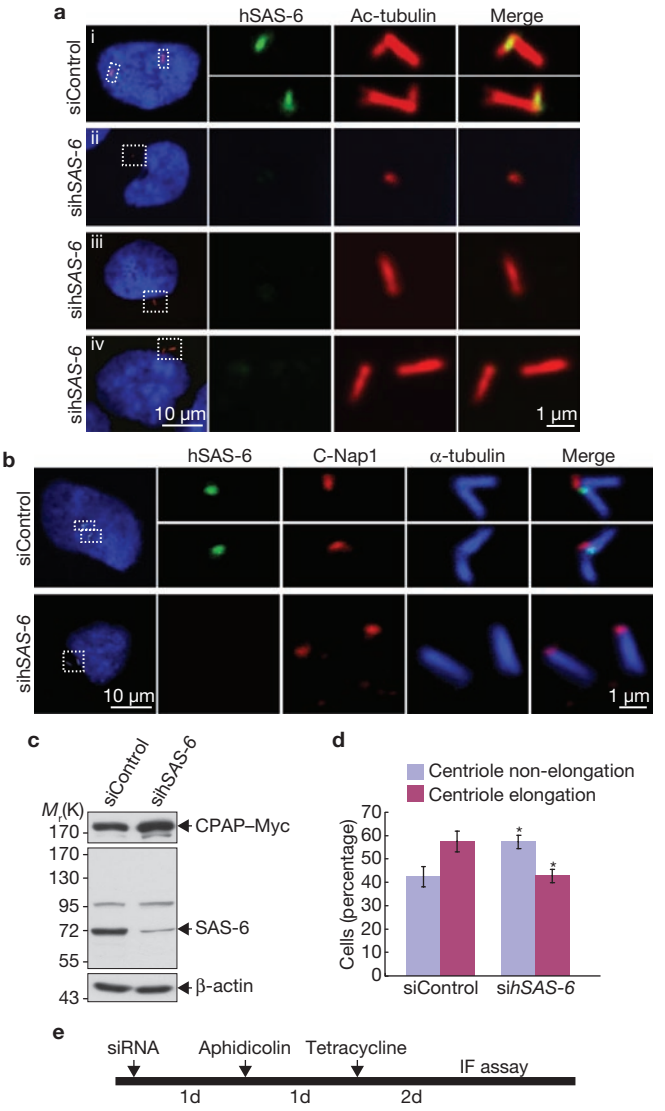

Figure 4 Depletion of *hSAS-6* specifically inhibits the formation of CPAP-induced PLSs derived from procentrioles. (**a**–**c**) CPAP–wildtype–Myc-inducible cells were transfected with siRNA duplexes targeting *hSAS-6* (si*hSAS-6*) or siRNA control duplexes (siControl), as described in **e**. Two days after tetracycline induction, cells were analysed by immunofluorescence confocal microscopy using the indicated antibodies (**a**, **b**; Ac: acetylated) or by immunoblotting (**c**). The α–tubulin signal in **b** was detected with an FITC (fluorescein isothiocyanate)-conjugated anti-tubulin antibody, whereas C-Nap1 and hSAS-6 were detected by Alexa568-conjugated anti-mouse and Alexa-647 conjugated anti-rabbit antibodies, respectively. DNA was counterstained with DAPI. (**d**) The percentages of elongated or non-elongated centrioles after siRNA treatment are shown. Error bars represent mean ± s.d. of 100 cells from four experiments. Statistically significant changes (Student's *t*-test) from the respective controls are marked with asterisks (*$P = 0.0013$). (**e**) A protocol to analyse the formation of CPAP-induced PLSs by hSAS-6 depletion. Full scans of western blots in **c** are shown in Supplementary Information, Fig. S8.

We next considered what the molecular mechanism is that controls the assembly of centriolar microtubules during centriole elongation. We reported previously that CPAP carries a polypeptide domain that binds to a tubulin heterodimer[30], and mutations (KR377EE) that alter the charge property of this domain significantly inhibit its binding to a tubulin dimer[31]. Thus, we generated CPAP-377EE–Myc-inducible cell lines under

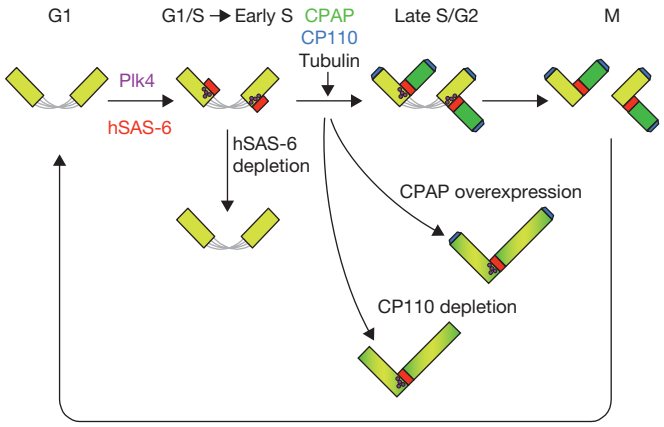

Figure 5 Model showing the role of CPAP in regulating centriole length during centriole biogenesis in human cells. hSAS-6 (red) is absent in the G1 phase and is first detected in early S phase[21,22]. After activation of Plk4 (purple) on the surface of the parental centriole[21], hSAS-6 is recruited to a site in an asymmetric position next to the proximal end of the centriole[22]. CPAP (green) accumulates gradually during the S and G2 phases and promotes the assembly of centriolar microtubules possibly through its intrinsic tubulin-dimer binding activity during procentriole elongation. CP110 targets to the growing end of centriole during centriole biogenesis. When cells exit mitosis, both CPAP and hSAS-6 (ref. 22) are degraded by the 26S proteosome in an APC/C–Cdh1-dependent pathway. Excess CPAP induces centriole elongation and hSAS-6-depletion inhibits the growth of CPAP-induced PLSs from procentrioles. Furthermore, depletion of CP110 (Supplementary Information, Fig. S7d) seems to induce centriole elongation from both parental and nascent centrioles, suggesting that CPAP and CP110 may have opposing roles in controlling centriole length.

tetracycline control to test whether tubulin-dimer binding activity is critical for this process. Our results showed that CPAP-induced PLSs were significantly reduced in the CPAP-377EE mutant (< 20%) when compared with CPAP-wild type (~58%; Fig. 3f). The inhibition of CPAP-induced PLSs was further demonstrated by co-staining of CPAP-377EE–Myc with acetylated tubulin and several centrosomal proteins, including centrin, centrobin and γ–tubulin (Fig. 3a). Surprisingly, excess CPAP-377EE also induced several abnormal mitotic phenotypes, including monopolar (~55%; Fig. 3d), multipolar (~11%; Fig. 3c), asymmetric bipolar (~11%; data not shown) and no-pole (~3%; data not shown). The most common phenotype (monopolar) observed in CPAP-377EE-inducible cells can be explained by inhibition of centriole duplication through the blocking of procentriole formation, as a single parental centriole with distal appendages was frequently detected by our electron microscopy analysis (Fig. 3e). Furthermore, we observed that depletion of CPAP impairs centriole amplification in Plk4-activated cells (Supplementary Information, Fig. S3aii) and such effects can be effectively reversed by expression of siRNA-resistant CPAP–wild type (Supplementary Information, Fig. S3aiii, b), but only weakly by siRNA-resistant CPAP-377EE mutant (Supplementary Information, Fig. S3aiv, b). Collectively, these results indicate that the tubulin-dimer binding activity of CPAP is required for the assembly of centriolar microtubules during centriole elongation.

Our results show that hSAS-6 localizes to the proximal end of CPAP-induced filaments (Supplementary Information, Fig. S6e) and that its depletion inhibits normal procentriole formation[21,22], suggesting that the correct recruitment of hSAS-6 to the base of the procentriole is required to initiate CPAP-induced PLSs. To test this possibility, we analysed the formation of these CPAP-induced PLSs in the presence of *hSAS-6* siRNA (si*hSAS-6*). Depletion of *hSAS-6* significantly reduced hSAS-6 protein expression (Fig. 4c) but had only minimal effects on the formation of CPAP-wild-type-induced PLSs (centriole elongation; Fig. 4d), which was reduced to 43% from 58% in control siRNA-treated cells (Fig. 4d). However, careful examination showed that most si*hSAS-6*-depleted cells contained no elongated filaments (Fig. 4aii; ~57%), whereas a few contained either a single elongated filament (Fig. 4aiii; ~30%) or two separated elongated filaments (Fig. 4aiv; ~13%). These elongated filaments seemed to be derived from the parental centrioles that showed no, or very weak, hSAS-6 (Fig. 4aiii–iv) and centrobin (data not shown) staining. To verify this, we co-stained *hSAS-6*-depleted cells with α–tubulin and C-Nap1 (a protein that normally marks the proximal end of parental centrioles)[32]. C-Nap1 signals were commonly detected at the base of CPAP-induced filaments (Fig. 4b). Thus, *hSAS-6* depletion mostly affects the CPAP-induced PLSs growing from newly formed procentrioles, but seems to have little effect on the growth of pre-existing parental centrioles. This observation further strengthens the notion that hSAS-6 is required for CPAP-dependent procentriole formation. Taken together, our results suggest that CPAP induces the assembly of centriolar microtubules after the recruitment of hSAS-6 to the proximal end of the procentriole.

The key findings from this study and from information derived from other reports suggest a model of how CPAP regulates centriole length (Fig. 5). After the activation of Plk4 on the proximal end of the parental centriole[21], hSAS-6 is recruited to a primitive site located at the base of nascent procentrioles in early S phase[21,22]. This hSAS-6-containing site may possibly serve as a scaffold on which CPAP assembles nine triplet microtubules during procentriole formation. This structure may be related to the central tube in *C. elegans*[17] or the cartwheel in *Chlamydomonas reinhardtii*[33]. The presence of an appropriate amount of CPAP is essential for controlling procentriole length during S/G2 phase and after mitotic exit, as overexpression of CPAP-wild type or a non-degradable CPAP-K1D4 mutant resulted in the elevation of CPAP levels and induced longer centrioles. Furthermore, our previous results have shown that CPAP carries both a tubulin-dimer-binding and a microtubule-binding domain and possesses the ability to destabilize microtubules[30,31]. Interestingly, the mutation CPAP-377EE, which disrupts the tubulin-dimer-binding activity of CPAP[31], significantly inhibits the formation of CPAP-induced PLSs (Fig. 3a). Thus, a possible explanation for procentriole elongation is that the microtubule-destabilizing activity of CPAP is at first inhibited by uncharacterized cellular factors in S/G2-phase cells. CPAP then promotes the assembly of centriolar microtubules by its tubulin-dimer-binding activity and stabilizes the polymerized centriolar microtubules by its microtubule-binding activity. This model remains to be further tested.

Finally, CP110 has been reported to be associated with the growing distal ends of centrioles[21] and depletion of CP110 promotes the formation of primary cilia in proliferating U2OS cells[34]. Interestingly, our preliminary data show that CP110 depletion can also induce microtubule-based filaments extending from both parental and progeny centrioles (Supplementary Information, Fig. S7d), with a structure similar to that of PLSs induced by CPAP overexpression. These results imply that CP110 may serve as a negative regulator in controlling centriole length (Fig. 5). Currently, it is not clear how CPAP works coordinately with CP110 to control centriole length and whether the elongated structures induced by CPAP overexpression resemble genuine primary cilia. Further molecular analyses of elongated filaments induced by

CPAP overexpression or CP110 depletion are required to resolve this issue. In conclusion, we provide the first line of evidence to show that CPAP is a new regulator of centriole length and that CPAP levels are carefully regulated during the cell cycle to ensure the correct length of duplicated centrioles. □

*Note added in proof: during the writing of this manuscript, two related papers were published (*Curr. Biol., *doi:10.1016/j.cub.2009.05.016 and* Curr. Biol., *doi:10.1016/j.cub.2009.05.018).*

METHODS

Methods and any associated references are available in the online version of the paper at http://www.nature.com/naturecellbiology/.

Note: Supplementary Information is available on the Nature Cell Biology website.

ACKNOWLEDGEMENTS

We thank J. L. Wang and W.-H. Lee for their helpful comments and discussion, and Y.-N. Lin, J.-Y. Shau, Y. Chang, S.-P. Lee, C.-P. Lin and C.-M. Chang for their technical support. This work was supported by a grant from the National Science Council (NSC-97-2321-B-001-011) and from the Institute of Biomedical Science.

AUTHOR CONTRIBUTIONS

C-J. C. T. conducted the experiments and helped with data analysis; R-H. F. and W-B. H. performed the cell-cycle work; K-S.W. assisted with electron microscopy analysis and T.K.T. planned and supervised the project and data analyses.

COMPETING FINANCIAL INTERESTS

The authors declare no competing financial interests.

Published online at http://www.nature.com/naturecellbiology/
Reprints and permissions information is available online at http://npg.nature.com/reprintsandpermissions/

1. Bornens, M. Centrosome composition and microtubule anchoring mechanisms. *Curr. Opin. Cell Biol.* **14,** 25–34 (2002).
2. Job, D., Valiron, O. & Oakley, B. Microtubule nucleation. *Curr. Opin. Cell Biol.* **15,** 111–117 (2003).
3. Delattre, M. & Gonczy, P. The arithmetic of centrosome biogenesis. *J. Cell Sci.* **117,** 1619–1630 (2004).
4. Nigg, E. A. Centrosome duplication: of rules and licenses. *Trends Cell Biol.* **17,** 215–221 (2007).
5. Strnad, P. & Gonczy, P. Mechanisms of procentriole formation. *Trends Cell Biol.* **18,** 389–396 (2008).
6. Azimzadeh, J. & Bornens, M. Structure and duplication of the centrosome. *J. Cell Sci.* **120,** 2139–2142 (2007).
7. Kemp, C. A., Kopish, K. R., Zipperlen, P., Ahringer, J. & O'Connell, K. F. Centrosome maturation and duplication in *C. elegans* require the coiled-coil protein SPD-2. *Dev. Cell* **6,** 511–523 (2004).
8. Kirkham, M., Muller-Reichert, T., Oegema, K., Grill, S. & Hyman, A. A. SAS-4 is a *C. elegans* centriolar protein that controls centrosome size. *Cell* **112,** 575–587 (2003).
9. Leidel, S., Delattre, M., Cerutti, L., Baumer, K. & Gonczy, P. SAS-6 defines a protein family required for centrosome duplication in *C. elegans* and in human cells. *Nature Cell Biol.* **7,** 115–125 (2005).
10. Leidel, S. & Gonczy, P. SAS-4 is essential for centrosome duplication in *C. elegans* and is recruited to daughter centrioles once per cell cycle. *Dev. Cell* **4,** 431–439 (2003).
11. O'Connell, K. F. *et al.* The *C. elegans zyg-1* gene encodes a regulator of centrosome duplication with distinct maternal and paternal roles in the embryo. *Cell* **105,** 547–558 (2001).
12. Pelletier, L. *et al.* The *Caenorhabditis elegans* centrosomal protein SPD-2 is required for both pericentriolar material recruitment and centriole duplication. *Curr. Biol.* **14,** 863–873 (2004).
13. Bettencourt-Dias, M. *et al.* SAK/PLK4 is required for centriole duplication and flagella development. *Curr. Biol.* **15,** 2199–2207 (2005).
14. Peel, N., Stevens, N. R., Basto, R. & Raff, J. W. Overexpressing centriole-replication proteins *in vivo* induces centriole overduplication and *de novo* formation. *Curr. Biol.* **17,** 834–843 (2007).
15. Rodrigues-Martins, A. *et al.* DSAS-6 organizes a tube-like centriole precursor, and its absence suggests modularity in centriole assembly. *Curr. Biol.* **17,** 1465–1472 (2007).
16. Delattre, M., Canard, C. & Gonczy, P. Sequential protein recruitment in *C. elegans* centriole formation. *Curr. Biol.* **16,** 1844–1849 (2006).
17. Pelletier, L., O'Toole, E., Schwager, A., Hyman, A. A. & Muller-Reichert, T. Centriole assembly in *Caenorhabditis elegans*. *Nature* **444,** 619–623 (2006).
18. Andersen, J. S. *et al.* Proteomic characterization of the human centrosome by protein correlation profiling. *Nature* **426,** 570–574 (2003).
19. Habedanck, R., Stierhof, Y. D., Wilkinson, C. J. & Nigg, E. A. The Polo kinase Plk4 functions in centriole duplication. *Nature Cell Biol.* **7,** 1140–1146 (2005).
20. Hung., L. Y., Tang, C. J. & Tang, T. K. Protein 4.1 R.-135 interacts with a novel centrosomal protein (CPAP) which is associated with the γ-tubulin complex. *Mol. Cell Biol.* **20,** 7813–7825 (2000).
21. Kleylein-Sohn, J. *et al.* Plk4-induced centriole biogenesis in human cells. *Dev. Cell* **13,** 190–202 (2007).
22. Strnad, P. *et al.* Regulated HsSAS-6 levels ensure formation of a single procentriole per centriole during the centrosome duplication cycle. *Dev. Cell* **13,** 203–213 (2007).
23. Peters, J. M. The anaphase promoting complex/cyclosome: a machine designed to destroy. *Nature Rev. Mol. Cell Biol.* **7,** 644–656 (2006).
24. Zou, C. *et al.* Centrobin: a novel daughter centriole-associated protein that is required for centriole duplication. *J. Cell Biol.* **171,** 437–445 (2005).
25. Burton, J. L. & Solomon, M. J. D box and KEN box motifs in budding yeast Hsl1p are required for APC-mediated degradation and direct binding to Cdc20p and Cdh1p. *Genes Dev.* **15,** 2381–2395 (2001).
26. Pfleger, C. M. & Kirschner, M. W. The KEN box: an APC recognition signal distinct from the D box targeted by Cdh1. *Genes Dev.* **14,** 655–665 (2000).
27. Schmidt, T. I. *et al.* Control of centriole length by CPAP and CP110. *Curr. Biol.* (in the press).
28. Kohlmaier, G. *et al.* Overly long centrioles and defective cell division upon excess of the SAS-4-related protein CPAP. *Curr. Biol.* (in the press).
29. Paoletti, A., Moudjou, M., Paintrand, M., Salisbury, J. L. & Bornens, M. Most of centrin in animal cells is not centrosome-associated and centrosomal centrin is confined to the distal lumen of centrioles. *J. Cell Sci.* **109 Pt 13**, 3089–3102 (1996).
30. Hung., L. Y., Chen, H. L., Chang, C. W., Li, B. R. & Tang, T. K. Identification of a novel microtubule-destabilizing motif in CPAP that binds to tubulin heterodimers and inhibits microtubule assembly. *Mol. Biol. Cell* **15,** 2697–2706 (2004).
31. Hsu, W. B. *et al.* Functional characterization of the microtubule-binding and -destabilizing domains of CPAP and d-SAS-4. *Exp. Cell Res.* **314,** 2591–2602 (2008).
32. Fry, A. M. *et al.* C-Nap1, a novel centrosomal coiled-coil protein and candidate substrate of the cell cycle-regulated protein kinase Nek2. *J. Cell Biol.* **141,** 1563–1574 (1998).
33. Nakazawa, Y., Hiraki, M., Kamiya, R. & Hirono, M. SAS-6 is a cartwheel protein that establishes the 9-fold symmetry of the centriole. *Curr. Biol.* **17,** 2169–2174 (2007).
34. Spektor, A., Tsang, W. Y., Khoo, D. & Dynlacht, B. D. Cep97 and CP110 suppress a cilia assembly program. *Cell* **130,** 678–690 (2007).

DOI: 10.1038/ncb1889

METHODS

Plasmid construction and antibodies. Plasmids encoding hSAS-6, His-Cdh1 and haemagglutinin (HA)–ubiquitin were provided by P. Gonczy (Swiss Institute for Experimental Cancer Research), Z.-F. Chang (Institute of Biochemistry and Molecular Biology, National Taiwan University) and D. Bohmann (Department of Biomedical Genetics, University of Rochester, NY), respectively. The cDNA encoding full-length CPAP, CPAP fragments or various CPAP mutants were cloned in-frame into a pEGFP-C1 (BD Biosciences Clontech) or pcDNA4/TO/Myc–His-A (Invitrogen) vector. For siRNA-resistant CPAP plasmid construction, the nucleotides targeted by siRNA within the full-length wild-type CPAP in the pcDNA4/TO/Myc–His-A vector (5'-AGAAUUAGCUCGAAUAGAAUU-3') were partially replaced without changing the amino-acid sequence (5'-GGAGCUGGCCCGGAUCGAGUU-3') using the QuickChange kit (Stratagene). All mutant clones including siRNA-resistant CPAP in the pcDNA4/TO/Myc–His-A vector were generated by site-directed mutagenesis using the QuickChange kit as described previously[31]. The resultant plasmids were sequence confirmed. The cDNA constructs described above were used for transient transfection or generation of tetracycline-inducible lines.

The anti-centrobin polyclonal antibody was initially provided by Q. Gao (Department of Medicine, Evanston Northwestern Healthcare Research Institute, Northwestern University, IL) and later generated by ourselves as described below. Rabbit polyclonal antibodies were raised against glutathione *S*-transferase (GST)–centrobin (amino-acids 443–626), GST-SAS-6 (amino-acids 1–489), GST–centrin 2 (amino-acids 1–173) and GST–CP110 (amino-acids 561–955). The antibodies were affinity purified using GST recombinant proteins immobilized on PVDF membranes as described previously[20]. The CPAP antibody was generated as described previously[20,35]. Other commercially available antibodies used in this study include: anti-Cdc20 (1:1000 dilution), anti-Cdh1 (1:2000 dilution) and anti-pericentrin (1:2000 dilution; all from Abcam); anti-β-actin (1:5000 dilution), anti-α-tubulin (1:200 diution; DM1a), anti-γ-tubulin (1:1000 dilution; GTU88) and anti-acetylated tubulin (1:500 dilution; all from Sigma-Aldrich); anti-cyclin B1 (1:2000 dilution) and anti-ubiquitin (1:500 dilution; Santa Cruz. Biotechnology); anti-HA (1:5000 dilution; Covance Research Products Inc.); anti-Myc (1:200 dilution; 4A6, Upstate Biotechnology or 1: 200 diution NB600-336, Novus Biologicals Inc); anti-C-Nap1 (1:500 dilution; BD Bioscience) and anti-His (1:1000 dilution; Serotec).

Cell culture and transfection. MEFs (P1) were provided by Y.-T. Yan (Institute of Biomedical Sciences, Academia Sinica, Taipei, Taiwan). U2OS, HeLa, 293T cells or MEFs were maintained in Dulbecco's modified Eagle's medium supplemented with fetal calf serum (10%). Cells were transiently transfected with various cDNA constructs by Lipofectamine 2000 as described previously[30]. MEFs were transfected with GFP–CPAP by electroporation using a nucleofector according to the manufacturer's instructions (Amaxa). To generate tetracycline-inducible clones, cDNAs encoding full-length CPAP, CPAP-K1D4m and CPAP-377EE were subcloned into pcDNA4/TO/Myc–His-A (Invitrogen), which is under the control of the CMV promoter and two tetracycline operator 2 (TetO2) sites. The tetracycline-inducible cell lines expressing various Myc-tagged CPAP constructs were generated by transfection of U2OS-T-REx cells that stably express the tetracycline repressor TetR. U2OS-T-REx cells were generated by transfection with pcDNA6/TR encoding TetR. Stable transfectants were selected and established according to the manufacturer's instructions (Invitrogen). CPAP–Myc expression was induced by the addition of tetracycline (1 μg ml^{-1}).

Cell synchronization, FACS and immunoblotting analysis. To analyse endogenous CPAP and hSAS-6 during the cell cycle, HeLa cells were synchronized at the G1/S stage by a double thymidine block. Briefly, cells were incubated with thymidine (2 mM) for 15 h before transfer into fresh medium for 12 h, and were then incubated again in thymidine (2 mM) for another 15 h. In another synchronization experiment, cells were arrested at the G2/M phase by incubation with nocodazole (200 ng ml^{-1}) for 16 h. After release into the fresh medium, the synchronized cells were collected at different times for immunoblotting or FACS (FACScan, BD Biosciences) analysis. U2OS or U2OS-T-REx-inducible cells were synchronized at the G1/S phase transition by aphidicolin (1.6 μg ml^{-1}).

To study the effects of the 26S proteasome, cells were arrested at the G2/M phase transition by nocodazole treatment for 16 h and released into fresh medium containing MG132 (20 μM; Sigma-Aldrich), a 26S proteasome inhibitor. The cell lysates were collected at various times and analysed by immunoblotting as described previously[20].

Immunoprecipitation, ubiquitylation and GST pulldown assays. To investigate whether mitotic CPAP is associated with Cdh1 or Cdc20, nocodazole-treated HeLa cells (2 h after release) were lysed in RIPA buffer (50 mM Tris-HCl at pH 8.0, 150 mM NaCl, 1% NP40, 1% sodium deoxycholate, 20 mM glycerophosphate, 1 mM PMSF, 0.3 mM Na_3VO_4, 1 μg μl^{-1} leupeptin, 1 μg μl^{-1} pepstatin and 1 μg μl^{-1} aprotinin) for 30 min at 4 °C. After centrifugation, cell lysates were immunoprecipitated with an anti-CPAP or anti-centrobin antibody or mouse immunoglobulin IgG as a control. The immunoprecipitates were resuspended in 1× SDS sample buffer (50 mM Tris-HCl at pH 6.8, 2% SDS, 10% glycerol and 0.1% bromophenol blue) in the absence of 2-mercaptoethanol. Samples in Fig. 1d, e were separated by SDS–PAGE (10%; without boiling to prevent the breakage of the disulfide bonds of IgG) and analysed by immunoblotting using an anti-Cdh1 or anti-Cdc20 antibody.

For GST pulldown assays, 293T cells were transiently transfected with or without a His-tagged Cdh1 cDNA construct. After transfection, cells were lysed in RIPA buffer as described above. The cell lysates were incubated with equal amounts of various GST–CPAP-truncated proteins, which had previously been affinity purified and immobilized on glutathione–agarose beads (Sigma-Aldrich). After incubation, the beads were subsequently washed and analysed by western blotting.

For ubiquitylation assays, 293T cells were transiently transfected with or without CPAP-wild type–Myc and HA–ubiquitin constructs. Seven hours after transfection, the cells were incubated with MG132 (20 μM) or nocodazole (200 ng ml^{-1}) for another 14 h. After incubation, the cell lysates were subjected to immunoprecipitation with an anti-Myc or anti-CPAP antibody, followed by immunoblotting with antibodies against HA or ubiquitin. In some experiments, the blot was stripped and reprobed with an anti-CPAP or anti-Myc antibody to examine the levels of endogenous and exogenous CPAP-wild type–Myc.

Immunofluorescence confocal microscopy and electron microscopy analysis. Cells on coverslips were cold-treated for 1 h at 4 °C before pre-extracting the cells with Triton X-100 (0.5%) in PBS for 1 min and then fixed in methanol at –20 °C for another 10 min as described previously[21]. After blocking with normal goat serum (10%) in PBS, the fixed cells were incubated with the indicated primary antibodies. After washing with PBST (PBS containing 0.1% Tween 20), cells were incubated with Alexa 568 conjugated anti-mouse or Alexa 488 conjugated anti-rabbit antibodies (Invitrogen) as described previously[30]. DNA was counterstained with DAPI (4, 6-diamidino-2-phenylindole). The samples were observed using a LSM 510 META confocal system (ZEISS) or a MRC 2100 system (Bio-Rad Laboratories).

For electron microscopy, cells were fixed in glutaraldehyde (2.5%) for 1 h. The fixed cells were washed three times with Hepes buffer (20 mM Hepes at pH 7.4), post-fixed in osmium tetroxide (2%) for 1 h, dehydrated with serial ethanol and embedded in LR white resin. Thin sections were cut (80 nm), picked up on grids and stained with uranyl acetate and lead citrate. The samples were examined with a Tecnai G2 Spirit Twin electron microscope (FEI Company).

siRNA-mediated protein depletion. The sequences of siRNA duplex oligonucelotides used for hSAS-6 (ref. 9), CP110 (ref. 34) and CPAP are listed below. All siRNAs and a non-targeting siRNA control (D-001810-10-20) were from Dharmacon Research Inc. Transfections were performed using Lipofectamine 2000. hSAS-6: 5'-GCACGUUAAUCAGCUACAAUU-3', CP110: 5'-AAGCAGCAUGAGUAUGCCAGUUU-3', CPAP: 5'-AGAAUUAGCUCGAAUAGAAUU-3'.

35. Chen, C. Y., Olayioye, M. A., Lindeman, G. J. & Tang, T. K. CPAP interacts with 14-3-3 in a cell cycle-dependent manner. *Biochem. Biophys. Res. Commun.* **342,** 1203–1210 (2006).

nature cell biology

DOI: 10.1038/ncb1889

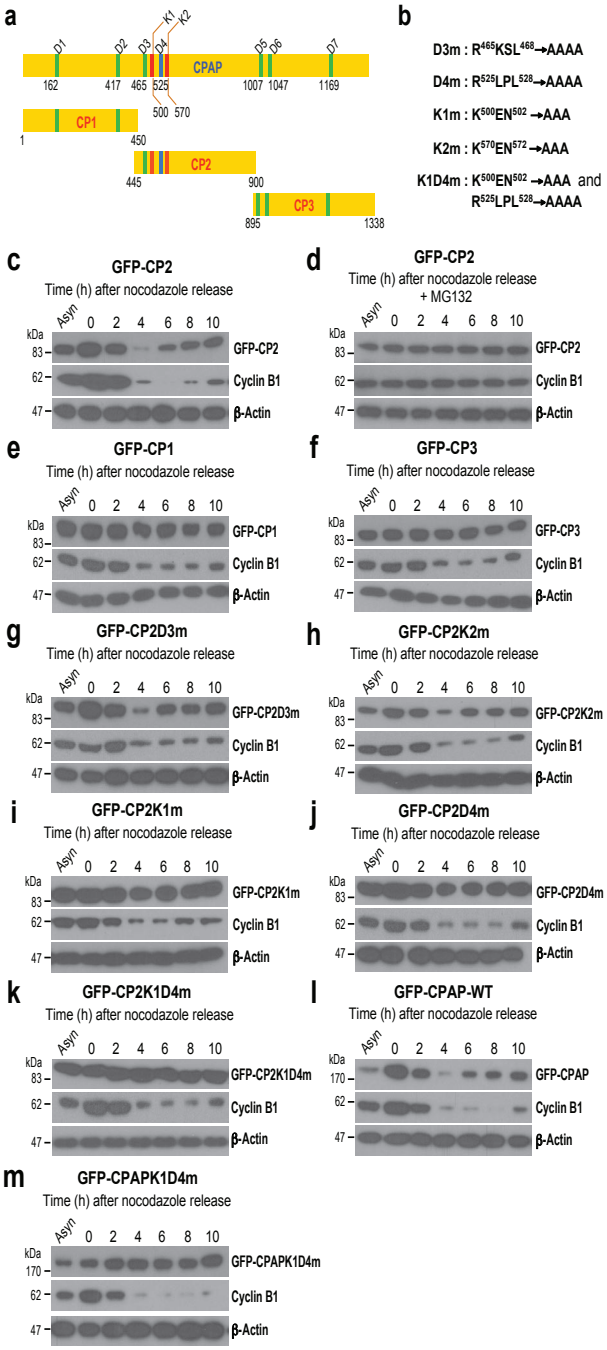

Figure S1 CPAP degradation is dependent on both a KEN-box (K1) and a D-box (D4). (**a**) A schematic presentation of CPAP denoting seven putative D boxes (D1-D7) and two putative KEN boxes (K1-K2). Three subregions (CP1, CP2 and CP3) of CPAP that carries various D boxes or KEN boxes are depicted. The numbers on the bottom of the scheme denote the amino acid number at which the consensus sequence starts in relation to the start codon. (**b**) A summary of various mutants that carries the mutations in D-box (D3m and D4m), KEN-box (K1m and K2m), or both (K1D4m). HeLa cells were transfected with various GFP-tagged CPAP constructs: GFP-CP2 (**c**), GFP-CP2 (+MG132; **d**), GFP-CP1 (**e**), GFP-CP3 (**f**), GFP-CP2D3m (**g**), GFP-CP2K2m (**h**), GFP-CP2K1m (**i**), GFP-CP2D4m (**j**), GFP-CP2K1D4m (**k**), GFP-tagged full-length CPAP-WT (**l**), or GFP-tagged full-length GFP-CPAPK1D4m (**m**). Twenty-four hours after transfection, the cells were treated with 200 ng/ml nocodazole (NZ) for 16 hr. The lysates prepared from NZ-release cells at indicated time points were analyzed by immunoblotting using indicated antibodies.

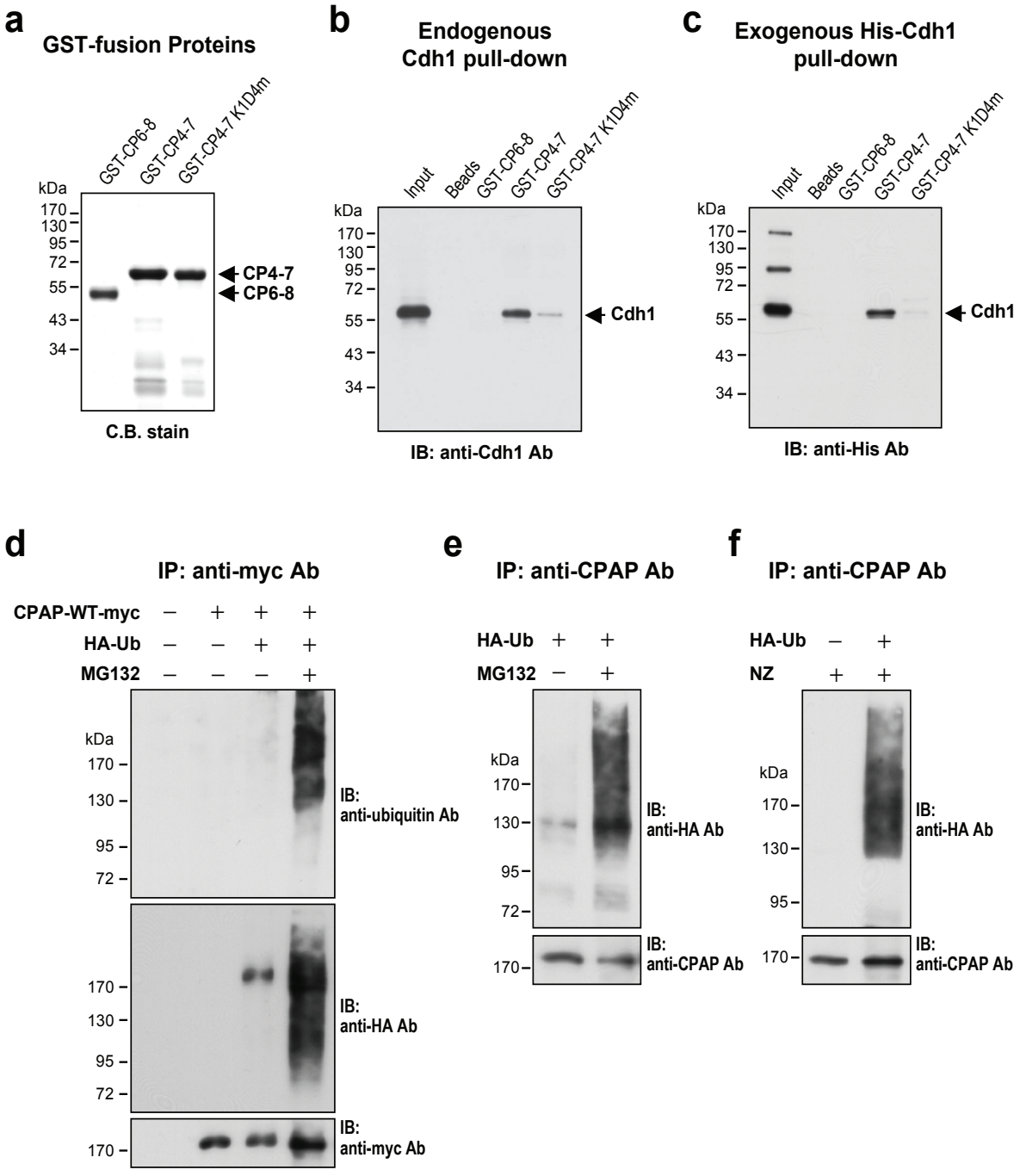

Figure S2 CPAP is directly associated with Cdh1 and is ubiquitinated *in vivo*. (**a**-**c**) CPAP is directly associated with Cdh1. (**a**) Various GST-CPAP truncated proteins (WT or mutant) used for GST pull-down assays were affinity purified and stained with Coomassie blue (C.B.). Equal amounts of various GST-CPAP truncated proteins were used to pull-down endogenous Cdh1 (**b**) or exogenously expressed His-tagged Cdh1 (**c**) from 293T lysates. The pull-down complexes were resolved by SDS-PAGE and analyzed by immunoblotting using anti-Cdh1 (**b**) or anti-His (**c**) antibody. GST-CP4-7 (residues 423-758) that carries K1 and D4 boxes can directly pull-down Cdh1, while the mutant (GST-CP4-7K1D4m) show a significant decrease of Cdh1 binding. (**d**-**f**) CPAP is ubiquitinated *in vivo*. 293T cells were co-transfected with HA-ubiquitin and CPAP-WT-myc constructs in presence or absence of MG132 (**d**). The cell lysates were first immunoprecipitated with anti-myc antibody and then immunoblotted with anti-ubiquitin, anti-HA, or anti-myc antibodies (**d**). In (**e** and **f**), 293T cells were transfected with HA-ubiquitin. Seven hours after transfection, the cells were treated with MG132 (**e**) or NZ (**f**) for another 14 hours. The cell lysates were immunoprecipitated with anti-CPAP antibody and then immunoblotted with anti-HA or anti-CPAP antibodies.

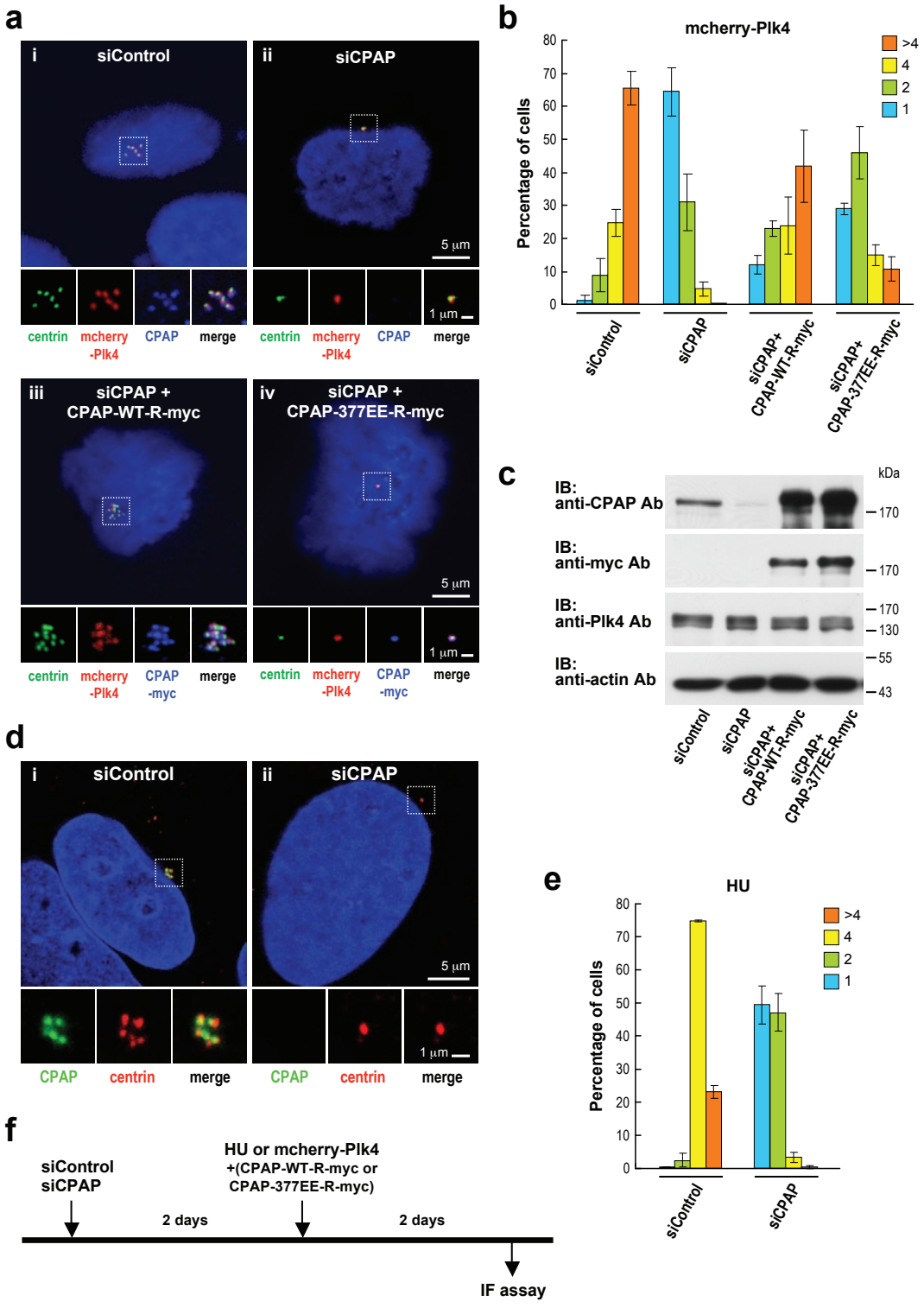

Figure S3 CPAP depletion inhibits centriole duplication and siRNA rescue experiments. U2OS cells were transfected with control siRNA or siRNA directed against CPAP for 2 days, followed by mcherry-Plk4 transfection (**a**-**c**) or by the addition of hydroxyurea (HU, 16 mM) (**d** and **e**) for another two days. In siRNA rescue experiments, siRNA-resistant CPAP-WT-R-myc (**a**-iii) or CPAP-377EE-R-myc mutant (**a**-iv) were cotransfected with mcherry-Plk4 for another two days (**f**). The cells were then processed for immunofluorescence confocal microscopy. Histogram illustrating the percentages of cells showing centriole numbers (counted by centrin staining; n=100 in triplicate) in HU-treated (**e**) or in mcherry-Plk4/siRNA-resistant CPAP co-transfected cells (**b**) in the presence of siControl or siCPAP duplexes. U2OS cells treated in (**b**) were analyzed by immunoblotting using indicated antibodies (**c**). (**f**) A schematic figure showing the timing and the procedures of siRNA treated cells.

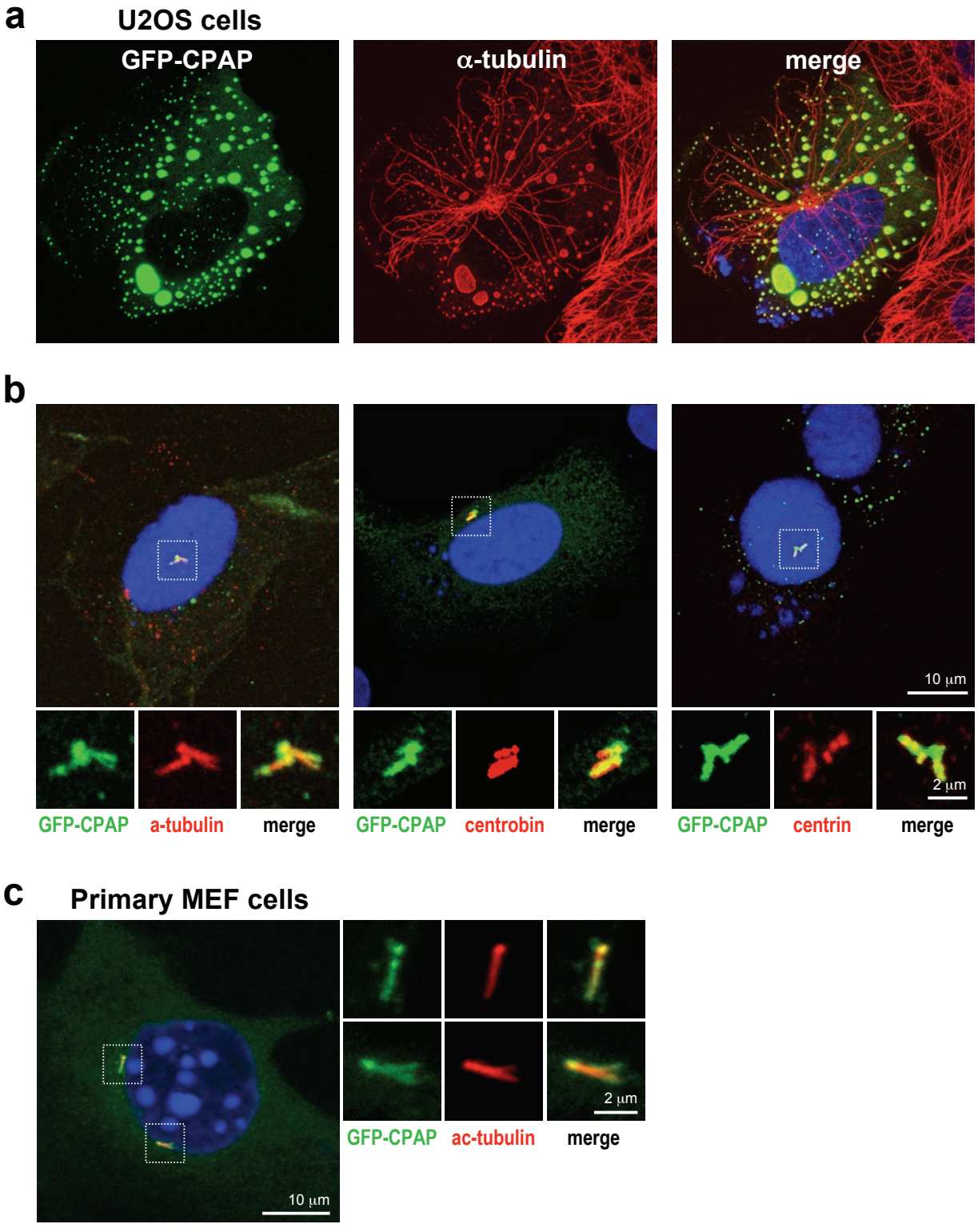

Figure S4 Transiently expressed GFP-CPAP induces the growing of microtubule-based filaments in primary and cancer cell lines. U2OS (**a** and **b**) cells or MEFs (mouse embryonic fibroblasts; **c**) were transiently transfected with GFP-CPAP. Twenty-nine hours after transfection, cells were fixed and stained with indicated antibodies. The GFP-CPAP proteins were directly observed by a confocal fluorescent microscope. DNA was counterstained with DAPI. High-level (**a**) or low-level (**b**) expression of GFP-CPAP in U2OS cells. (**c**) Low-level expression of GFP-CPAP in primary MEF cells.

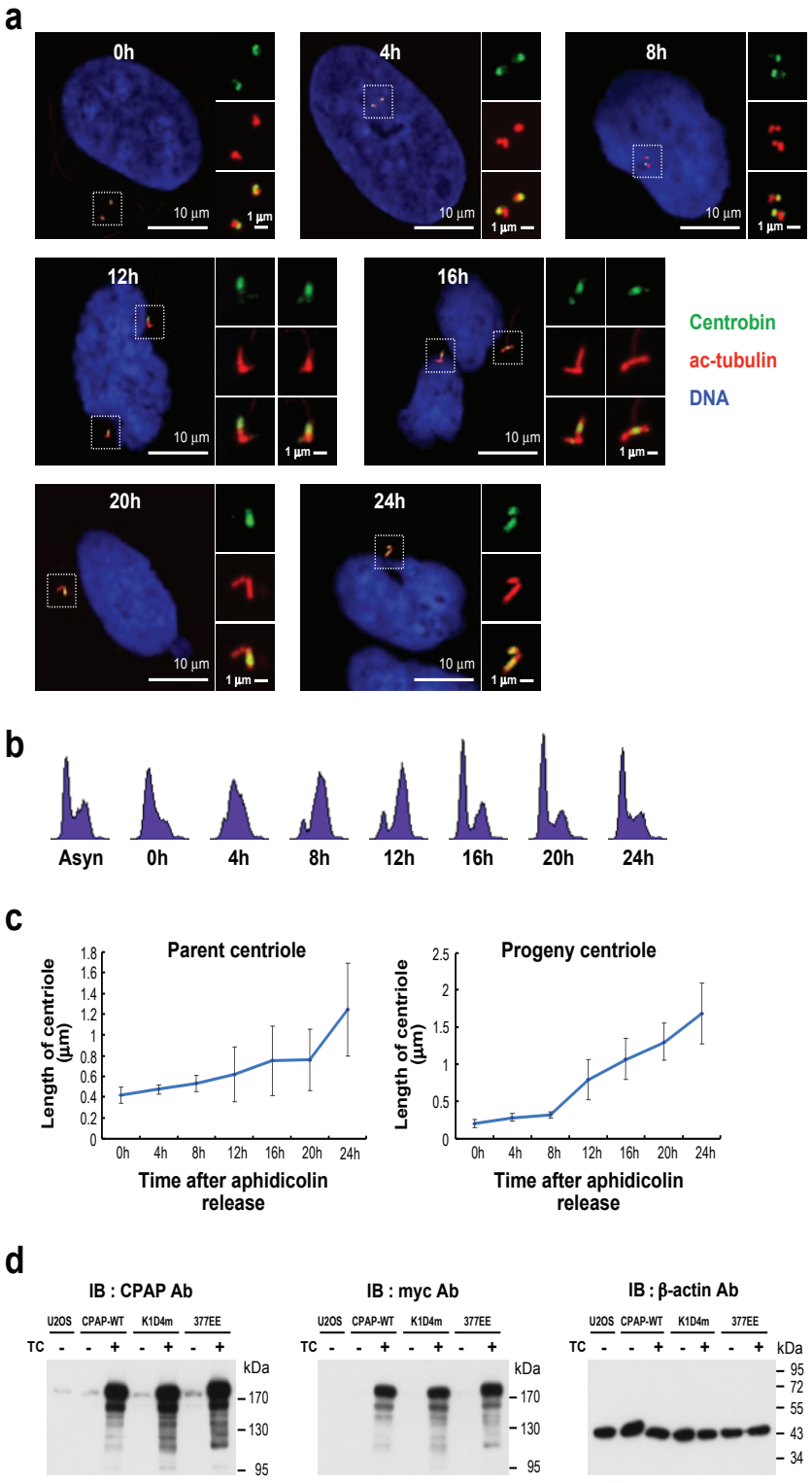

Figure S5 Excess CPAP-K1D4m-myc also induced the microtubule-based filaments. The CPAP-K1D4m-myc inducible cells were treated according to a protocol described in Fig. 2f. At the indicated time points after TC-induction, the cells were analyzed by FACS (**b**) and by immunofluorescence confocal microscopy (**a**) using the antibodies against acetylated tubulin (red) and centrobin (green). The centriole length (labeled with acetylated tubulin) was quantified (at each time point, n=25), and the results are shown in (**c**). Error bars represent mean +/- s.d.. The progeny centrioles were primarily marked by centrobin staining. Comparative analysis of the expression levels of endogenous CPAP and exogenously expressed CPAP-WT and its mutants are shown in (**d**). CPAP-WT-myc, CPAP-K1D4m-myc, and CPAP-377EE-myc inducible cells were treated with tetracycline. Twenty-four hours after tetracycline (TC) induction, cells were processed for immunoblot analysis with indicated antibodies.

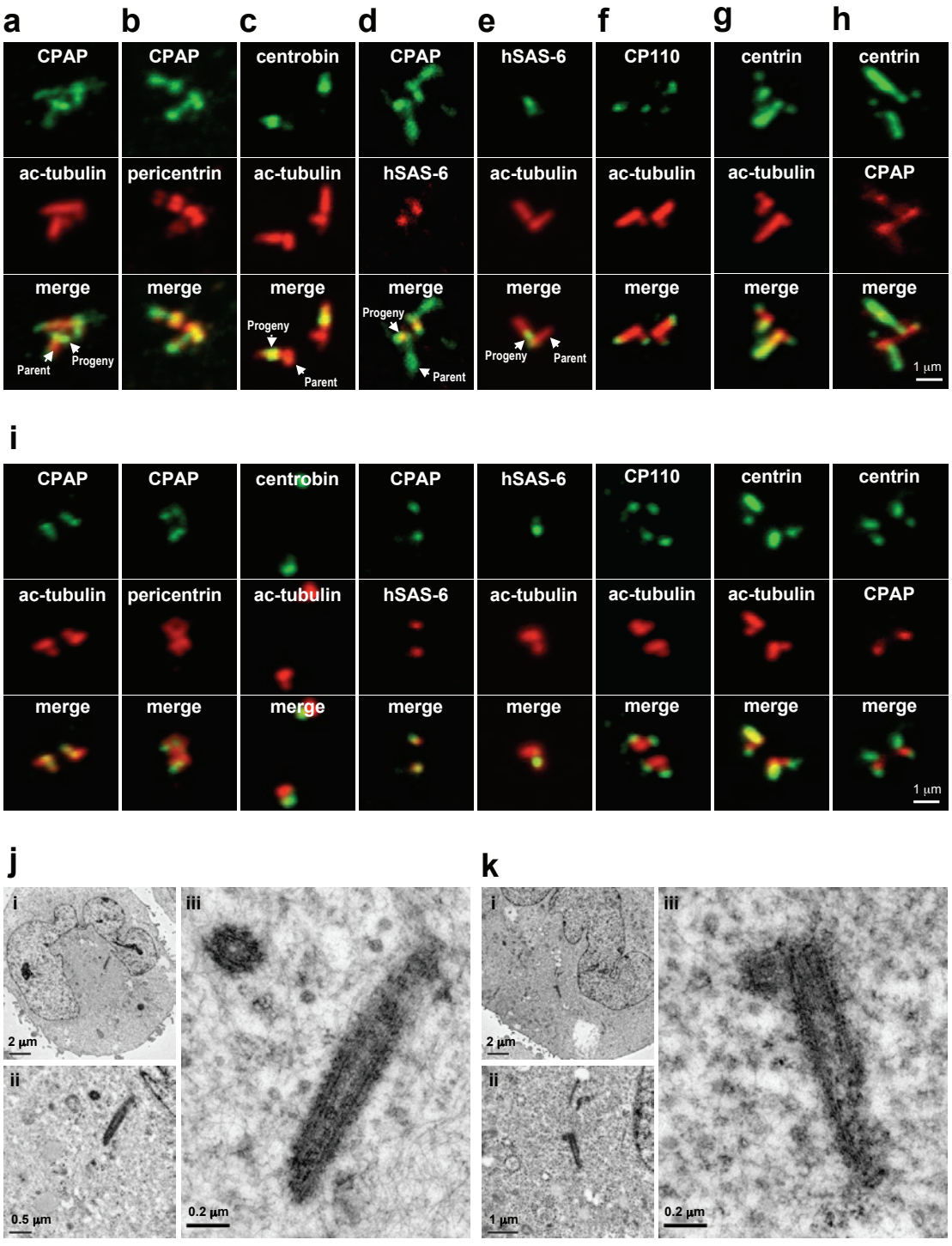

Figure S6 Localization of several centrosomal proteins in CPAP-induced PLSs. The CPAP-WT-myc (**a**-**h**) or CPAP-K1D4m-myc (**j** and **k**) inducible cells were treated with tetracycline for two days. After tetracycline induction, the cells were fixed and analyzed by immunofluorescence confocal microscopy (**a**-**h**) with indicated antibodies or by electron microscopy (**j** and **k**). Two sets of EM photos with variable magnification are shown in (**j** and **k**). The cells in a-h are not in the same cell-cycle stage. (**i**) A comparison of the localization of several centrosomal proteins in normal centrioles. CPAP-WT-myc non-inducible cells (in the absence of tetracycline) were fixed, stained with indicated antibodies, and analyzed by immunofluorescence confocal microscopy (**i**). The cells in (**i**) are not in the same cell-cycle stage. The DNA was counterstained by DAPI.

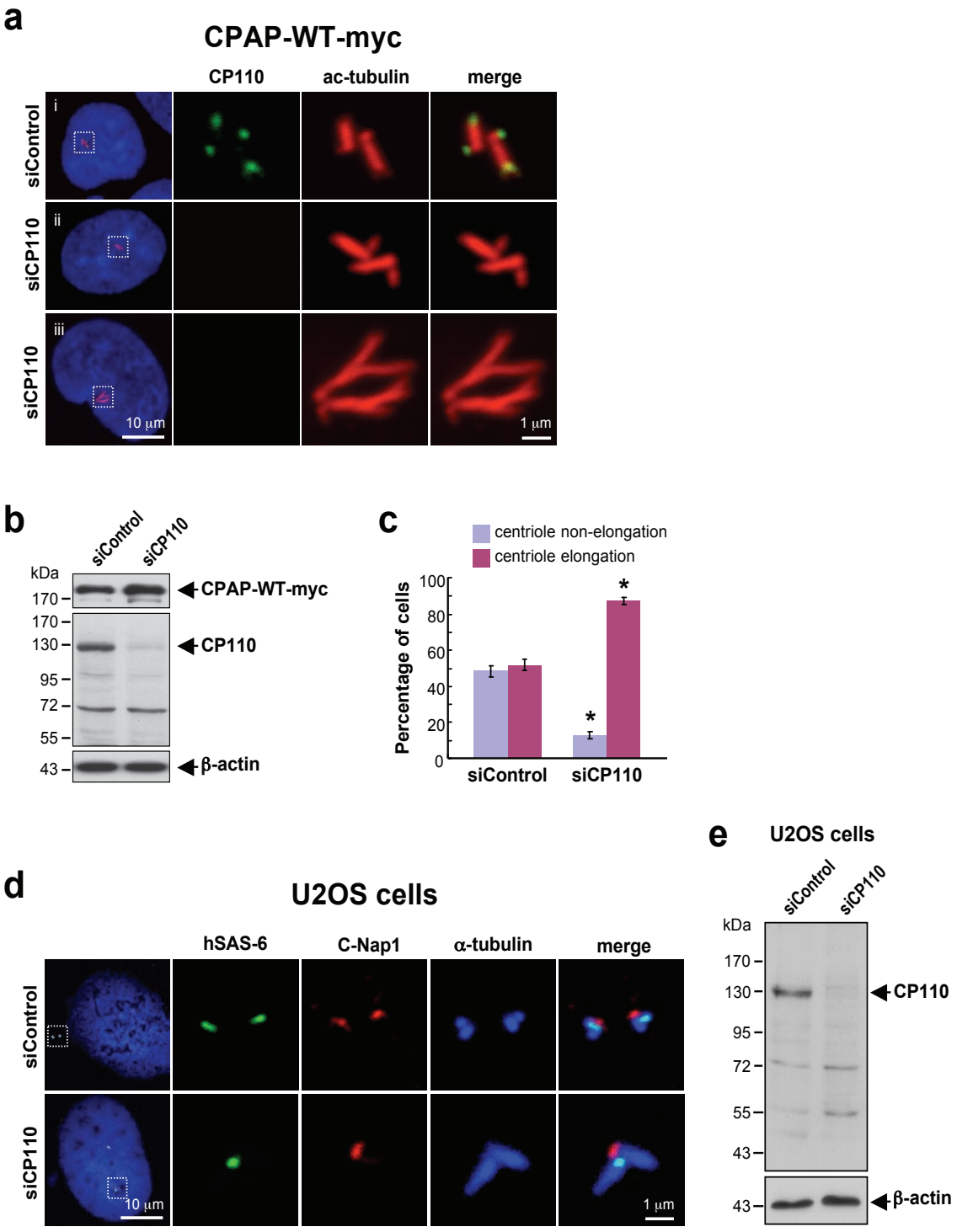

Figure S7 Depletion of CP110 promotes the formation of CPAP-induced PLSs and induces elongated microtubular filaments. (**a**-**c**) CPAP-WT-myc inducible cells were transfected with siRNA duplexes targeting to CP110 or siControl duplexes as described in Fig. 4e. After TC induction, cells were processed for immunofluorescence confocal microscopy with indicated antibodies (**a**), or immunoblotting (**b**). The percentages of elongated or non-elongated centrioles after siRNA treatment are shown in (**c**). Error Bars represent mean +/- s.d. of 208 cells in three experiments. Statistically significant changes (Student's *t*-test) to the respective controls are marked with asterisks ($*P < 0.0001$). (**d**-**e**) U2OS cells were depleted CP110 as described above, three days after siRNA treatment, cells were processed for immunofluorescence confocal microscopy with indicated antibodies (anti-hSAS6 to mark progeny centrioles and anti-C-Nap 1 to mark parental centrioles) (**d**), or immunoblotting (**e**). The alpha-tubulin signal in (**d**) was detected by a FITC-conjugated anti-tubulin antibody.

Fig.1a

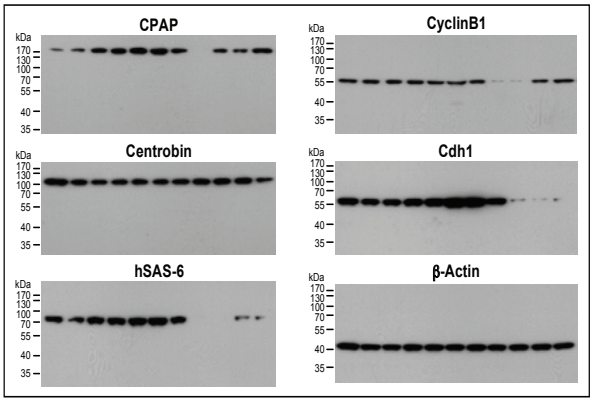

Fig.1b

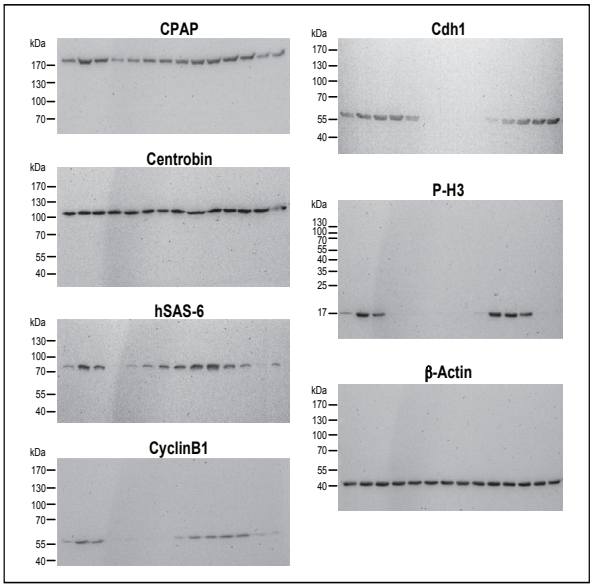

Fig.1c

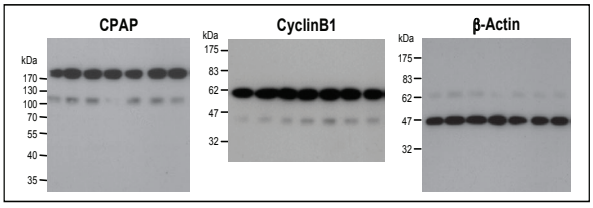

Fig.4c

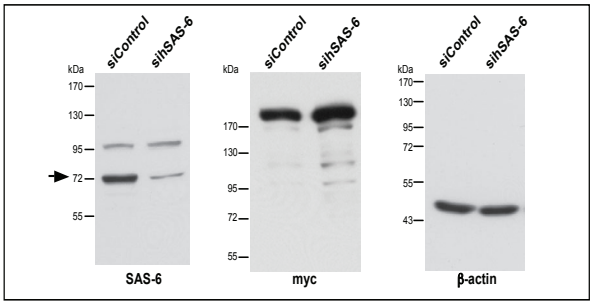

Figure S8 Full scans of western blot data

CPAP is a cell-cycle regulated protein that controls centriole length

Chieh-Ju C. Tang[1], Ru-Huei Fu[1,*], Kuo-Sheng Wu[2], Wen-Bin Hsu[1], and Tang K. Tang[1,#]

Supplementary Texts (1-5)

1) Degradation of CPAP is dependent on both a KEN-box and a D-box

We have identified seven putative D boxes (D1-D7) and two putative KEN-boxes (K1 and K2) in CPAP (Fig. S1a). To determine which region containing these putative recognition motifs can mediate protein degradation, we constructed GFP-tagged N-terminal (CP1: residues 1-450), middle-portion (CP2: residues 445-900), and C-terminal (CP3: residues 895-1338) fragments of CPAP and transfected into HeLa cells. The cells were synchronized at G2/M by NZ treatment and then released into fresh medium at indicated time points. Our results showed that GFP-CP2 and cyclin B1 were rapidly degraded when cells exited mitosis (4h after NZ release; Fig. S1c) and MG132 significantly inhibited their degradation (Fig. S1d). In contrast, the levels of GFP-CP1 (Fig. S1e) and GFP-CP3 (Fig. S1f) remained constant after NZ release, suggesting that the putative D-boxes in the CP1 (D1 and D2) and CP3 (D5-D7) fragments are not involved in CPAP degradation (Fig. S1a).

The CP2 fragment contains two putative D-boxes (D3 and D4) and two putative KEN-boxes (K1 and K2). To examine which motif in CP2 is essential for protein degradation, we mutated each of the four motifs in GFP-CP2 to AAAA or AAA amino acids (GFP-CP2D3m, GFP-CP2D4m, GFP-CP2K1m, and GFP-CP2K2m; Fig. S1b). As shown in Figure S1, both D3m (GFP-CP2D3m; Fig. S1g) and K2m (GFP-CP2K2m; Fig. S1h) mutants reveal similar protein degradation patterns as that of wild-type GFP-CP2 (Fig. S1c). In contrast, K1m (GFP-CP2K1m; Fig. S1i) and D4m (GFP-CP2D4m; Fig. S1j) levels remained constant as cells progressed through and exited from mitosis. To further confirm the essential role of these motifs, we generated a double mutant for K1D4m (GFP-CP2K1D4m). Our results showed that GFP-CP2K1D4m is able to resist protein degradation when cells exit mitosis (Fig. S1k). A similar resistance pattern was also observed in the full-length GFP-CPAP construct that carries K1D4m (Fig. S1m). Together, we concluded that the first KEN-box (K1) and the fourth D-box (D4) play essential roles that regulate CPAP degradation during mitotic exit.

2). CPAP is directly associated with Cdh1 and is ubiquitinated *in vivo*

To further examine whether there is a direct association between CPAP and Cdh1, we performed GST pull-down assays (Fig. S2a-c). GST-CP4-7 (a GST-tagged CPAP fragment; residues 423-758), which carries the first KEN-box (K1) and the fourth D-box (D4), can directly pull-down both endogenous Cdh1 (Fig. S2b) and exogenously expressed His-tagged Cdh1 (Fig. S2c). In contrast, GST-CP6-8 (a GST-tagged CPAP fragment; residues 608-850) that excludes all putative KEN- or D-boxes in CPAP did not pull-down Cdh1. Furthermore, the K1D4 mutant (GST-CP4-7K1D4m) that disrupted the Cdh1 recognition sites significantly reduced its binding to Cdh1 (Figs. S2b and S2c).

To determine whether CPAP is subject to ubiquitination, 293T cells were transfected with HA-ubiquitin and CPAP-WT-myc constructs in presence or absence of MG132. Lysates prepared from transfected cells were first immunoprecipitated with anti-myc antibody prior to immunoblot analysis using anti-HA, anti-ubiquitin, or anti-myc antibody (Fig. S2d). Ladders of high molecular weight ubiquitin conjugates were detected in the immunoprecipitated CPAP-WT-myc complexes in the presence of MG132, but these ladders were significantly reduced in the absence of MG132 (Fig. S2d). To verify that endogenous CPAP is indeed ubiquitinated *in vivo*, we transfected HA-ubiquitin into 293T cells with or without MG132 treatment. Endogenous CPAP was immunoprecipitated by an anti-CPAP antibody prior to immunoblot analysis. As shown in Figure S2e, endogenous CPAP is significantly ubiquitinated in presence of MG132. A similar result was also observed in nocodazole (NZ)-treated cells arrested in G2/M stage (Fig. S2f), suggesting that CPAP is ubiquitinated during mitosis. Taken together, our results indicate a direct association between CPAP and Cdh1 and CPAP undergoes ubiquitination *in vivo*.

3). CPAP with its intact tubulin-dimer binding activity is required for centriole duplication in human cells

Previous studies have shown that overexpression of Plk4[21] or a prolonged S phase due to hydroxy urea (HU)[24] arrest are capable of triggering centriole amplification in human cells. To examine the function of CPAP in centriole duplication, we depleted human CPAP by siRNA in mcherry-Plk4-transfected or HU-treated U2OS cells. As centrin represents an excellent marker for centriole formation in human cells, we used an anti-centrin antibody to monitor centriole duplication in these cells.

U2OS cells were first transfected with CPAP siRNA or control siRNA (Fig. S3). Forty-eight hours after transfection, the cells were then transfected with mcherry-Plk4 construct (Fig. S3a-c) or exposed to HU (Fig. S3d-e) for another two days. The cells

were fixed and analyzed by confocal fluorescence microscopy. As shown in Fig. S3a, centriole amplification (>4 centrioles; Fig. S3a-i) was clearly observed in approximately ~65% of the siControl of Plk4-transfected cells (Fig. S3b). In contrast, most CPAP-depleted cells (siCPAP) contained either one (Fig. S3a-ii; ~64% in Fig. S3b) or two centrioles (~31% in Fig. S3b) in Plk4-transfected cells and only few of them (<1%) had >4 centrioles (Fig. S3b), which is consistent with previous findings[21]. A similar effect was also observed in HU-treated cells (Fig. S3d and 3e). Interestingly, the Plk4-induced centriole amplification can be effectively rescued by an siRNA-resistant *CPAP-WT-myc* transgene (Fig. S3a-iii and S3b). Centriole amplification (>4 centrioles) in siRNA-resistant *CPAP-WT-myc* treated cells was recovered to ~42% as compared to ~65% in the siControl of Plk4-induced cells (Fig. S3b). In contrast, the siRNA-resistant CPAP-377EE mutant (Fig. S3a-iv) with deficiency in its tubulin-dimer binding activity revealed a low degree of recovery (~10% in S3b). Taken together, our findings indicate that CPAP with its intact tubulin-dimer binding activity is required for centriole duplication.

4). The incorporation of several key centriolar proteins into the CPAP-induced filaments and EM analysis

CPAP-induced filaments contain ac-tubulin. We examined the localization of several known centriolar proteins in these CPAP-induced filaments. As shown in Fig.S6a, CPAP is mainly detected at the proximal end, the distal end, and along the ac-tubulin-labeled filaments of these structures. A significant amount of CPAP-WT was also detected at the "parental" centrioles. This observation was further evidenced by co-staining with pericentrin, an integral component of the centrosome that localized around the centrioles. The dumbbell-like staining patterns were frequently observed in these CPAP-induced filaments with their proximal ends embedding into the regions surrounded by pericentrin (Fig. S6b).

Interestingly, these CPAP-induced filaments appear to be extended from both the parental centriole and the newly growing progeny centriole, which are decorated by centrobin staining (Fig. S6c). To investigate this further, we compared the localization of CPAP-WT-myc to that of hSAS-6, a well-established centriolar protein localized to the proximal end of the procentriole[22]. Figure S6d showed that CPAP-WT-myc signals were present at the elongated filaments derived from both parental and progeny centrioles. However, the hSAS-6 signal was only detected at the base of newly formed procentriole, suggesting that these filaments were assembled from the sites containing hSAS-6. Further analysis of co-distribution of hSAS-6 and ac-tubulin in these CPAP-induced filaments confirmed this finding (Fig. S6e). We have also analyzed the co-distribution of ac-tubulin with CP110 (Fig. S6f), a protein

associated with the growing distal tips of centrioles[21]. CP110 was correctly targeted to the growing ends of elongated filaments derived from both the parental and the nascent procentrioles (Fig. S6f). Centrin[29] was reported to be localized at the distal part of centrioles, and in some cases along the entire centrioles. Analysis of the co-staining patterns of centrin with ac-tubulin (Fig. S6g) is consistent with this finding and CPAP shows a partial colocalization with centrin (Fig. S6h). For comparison, control samples with normal-size centrioles are also shown for each antibody (Fig. S6i).

To further examine whether these CPAP (WT or K1D4m)-induced filaments reveal a canonical structure with elongated procentriole that has nine-fold symmetry, we analyzed this structure by electron microscopy (EM). Clearly, CPAP-K1D4m (2 days after TC induction) can induce elongated MT-based filaments with ~1.4 μm in length and ~0.2 μm in diameter (Fig. S6j). Another EM photo (Fig. S6k) showed a similar pattern, but with a nascent "procentriole" stemming from the base of the elongated "parental" centriole (produced by the previous round of cell cycle). Similar results were also observed in CPAP-WT-induced filaments (data not shown). Together, our EM analysis and the correct incorporation of several known centriolar proteins support the notion that excess CPAP can induce centriole elongation possibly through the assembly of centriolar microtubules during centriole biogenesis.

5). CP110 depletion promotes the assembly of CPAP-induced PLSs and induces elongated filaments

CP110 was recently reported to be associated with the growing distal ends of both parental and progeny centrioles[21], implying that CP110 may participate in centriole elongation. To examine whether CP110 affects the formation of CPAP-induced procentriole-like structures, we depleted CP110 by siRNA and analyzed the formation of CPAP-WT-induced PLSs (Fig. S7). In contrast to that of sihSAS-6 (Fig. 4), depletion of CP110 significantly increased the formation of CPAP-WT-induced PLSs to ~87% in comparison to siControl cells (~52%) (Fig. S7c). Interestingly, depletion of CP110 did not alter the growing of CPAP-induced PLSs from both parental and nascent centrioles (Fig. S7a-ii). However, we did observe a number of extremely long filaments (>2μm) with branched structures emanating from centrioles (Fig. S7a-iii) in some cell populations (< 20%).

Furthermore, we had found that in U2OS cells, CP110 depletion alone (Fig. S7d and S7e) appears to induce microtubule-based filaments extending from both parental (C-Nap1 staining, Fig. S7d, lower panel) and nascent procentrioles (hSAS-6 staining, Fig. S7d, lower panel), a pattern similar to that in CPAP-overexpressing cells (Fig. S6a-h). The frequency of these elongated filaments is about 20% (19/102) in

CP110-depleted U2OS cells. Taken together, these results imply that CP110 and CPAP may possibly play antagonistic roles in controlling centriole length. The underlying mechanism of how these two proteins cooperate to regulate microtubular extensions from centrioles is currently not clear. Future experiments are required to resolve this puzzle.

nature cell biology

Chromosome congression in the absence of kinetochore fibres

Shang Cai[1], Christopher B. O'Connell[3], Alexey Khodjakov[3] and Claire E. Walczak[2,4]

Proper chromosome congression (the process of aligning chromosomes on the spindle) contributes to accurate and faithful chromosome segregation. It is widely accepted that congression requires kinetochore fibres (K-fibres), microtubule bundles that extend from the kinetochores to spindle poles[1,2]. Here, we demonstrate that chromosomes in human cells co-depleted of HSET (human kinesin-14)[3,4] and hNuf2 (human Ndc80/Hec1-complex component)[5] can congress to the metaphase plate in the absence of K-fibres. However, the chromosomes are not stably maintained at the metaphase plate under these conditions. Chromosome congression in HSET + hNuf2 co-depleted cells required the plus-end directed motor CENP-E (centromere protein E; kinesin-7 family member)[6], which has been implicated in the gliding of mono-oriented kinetochores alongside adjacent K-fibres[7]. Thus, proper end-on attachment of kinetochores to microtubules is not necessary for chromosome congression. Instead, our data support the idea that congression allows unattached chromosomes to move to the middle of the spindle where they have a higher probability of establishing connections with both spindle poles. These bi-oriented connections are also used to maintain stable chromosome alignment at the spindle equator.

The assembly of a functional mitotic spindle involves the process of chromosome congression, which positions all chromosomes in the equatorial plane of the spindle. Congression is evolutionary conserved and enhances the fidelity of chromosome segregation[8]. Despite its importance, the molecular mechanisms that govern chromosome congression remain poorly understood. In the classic model, chromosomes move toward the spindle equator as a result of their bi-orientation, an arrangement where chromosomes are connected to both spindle poles[9]. In this scheme, congression requires K-fibres, which attach to the kinetochore of a chromosome in an end-on manner[1,2,10]. However, chromosome congression is also driven by the gliding of kinetochores alongside K-fibres of other already bi-oriented chromosomes, a process dependent on the plus-end-directed microtubule motor CENP-E, and one that does not require bi-oriented end-on kinetochore attachments to K-fibres[7]. It is not clear which of the two congression mechanisms is used by the majority of chromosomes in a typical mammalian cell.

We sought to address the question of whether chromosomes can congress efficiently under conditions that make proper end-on kinetochore attachment and formation of K-fibres impossible. Perturbation of the Ndc80/Hec1 complex, which is essential for microtubule–kinetochore attachment, severely disrupts K-fibre formation and chromosome alignment[5,11]. However, chromosomes are still capable of movement, presumably through lateral interactions between kinetochores and microtubules[11]. This prompted us to seek a condition in which we could restore efficient chromosome congression in the absence of end-on chromosome attachments.

To disrupt the Ndc80/Hec1 complex we used siRNA against the gene for the Ndc80 component hNuf2 (ref. 11). As expected, depletion of hNuf2 disrupted K-fibres and caused a significant increase in the percentage of cells with severely misaligned chromosomes (Fig. 1a, b)[5]. We hypothesized that forces driving chromosome congression are inhibited by minus-end-directed microtubule motors that produce poleward-directed forces. In the absence of K-fibres, contributions of these minus-end-directed forces might become overwhelming and cause chromosome scattering. Therefore, we tested whether inactivation of both HSET and cytoplasmic dynein (the two major minus-end-directed microtubule motors involved in spindle function)[2,12,13] restores proper chromosome alignment in Nuf2-depleted cells.

The frequency of cells with aligned chromosomes was significantly higher on co-depletion of hNuf2 and HSET than on depletion of hNuf2 alone (Fig. 1a, b), although not as high as in control cells. This result was observed with multiple *HSET* RNAi oligonucleotides (Supplementary Information, Fig. S1a, b). Western blotting analysis showed that the both the Hec1 component of the Ndc80 complex and HSET were efficiently knocked down in our experiments (Fig. 1c). Perturbation of kinetochore-bound dynein by knockdown of the dynein-targeting protein ZW10 (zeste-white 10; ref. 14) also partially restored chromosome alignment in hNuf2-knockdown cells, although this treatment was much less efficient than HSET knockdown (Supplementary Information, Fig. S1c, d).

[1]Biochemistry Program and [2]Medical Sciences Program, Indiana University, Myers Hall 262, 915 East 3rd Street, Bloomington, IN 47405, USA. [3]Division of Molecular Medicine, Wadsworth Center, New York State Department of Health, Albany, NY 12201,USA.
[4]Correspondence should be addressed to C.W. (e-mail: cwalczak@indiana.edu)

Received 12 February 2009; accepted 17 March 2009; published online 14 June 2009; DOI: 10.1038/ncb1890

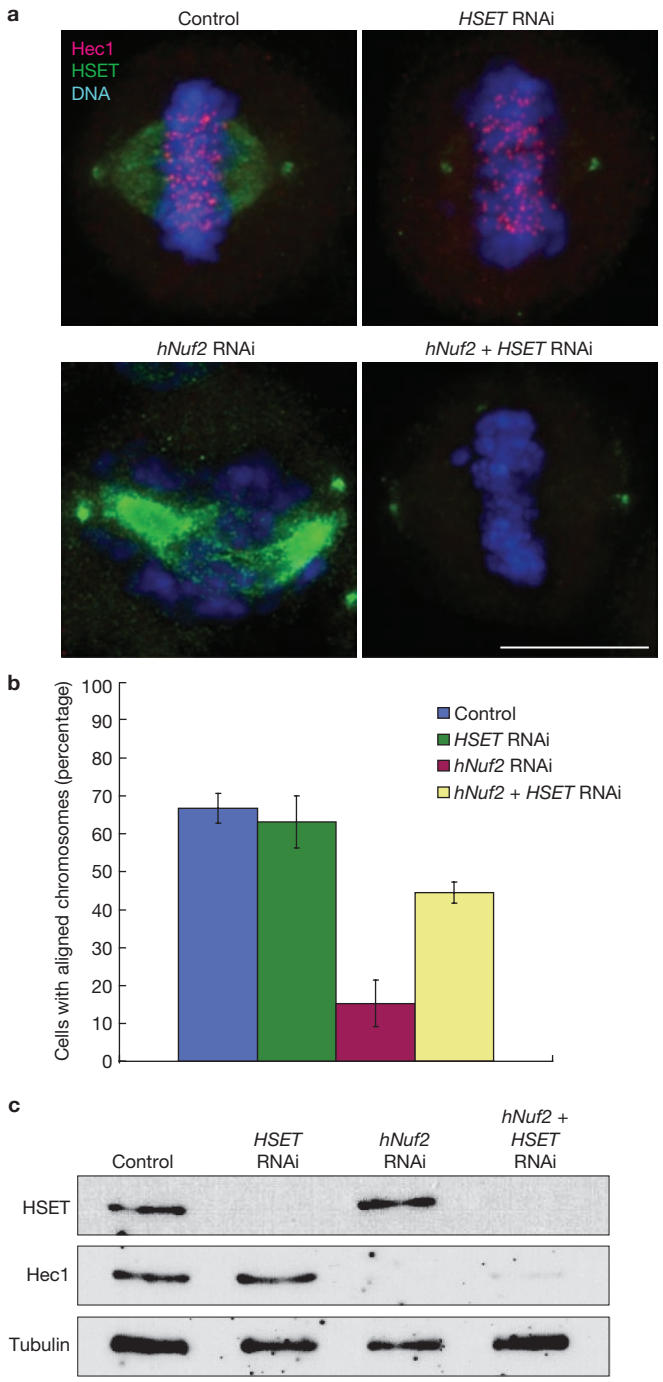

Figure 1 Chromosomes can align in cells lacking K-fibres. (**a**) HeLa cells transfected with luciferase control RNAi (Control), *hNuf2* RNAi, or *hNuf2* + *HSET* RNAi were stained to visualise HSET (green) Hec1 (red) and DNA (blue). Scale bar, 10 μm. (**b**) The average percentages of prometaphase and metaphase cells with aligned chromosomes are shown. Data are mean ± s.d. from three independent experiments, ~100 mitotic cells were scored per experiment. The differences between all the pairs are significant ($P < 0.05$). (**c**) Samples from each knockdown were analysed by western blotting and probed with antibodies to HSET, Hec1 and tubulin.

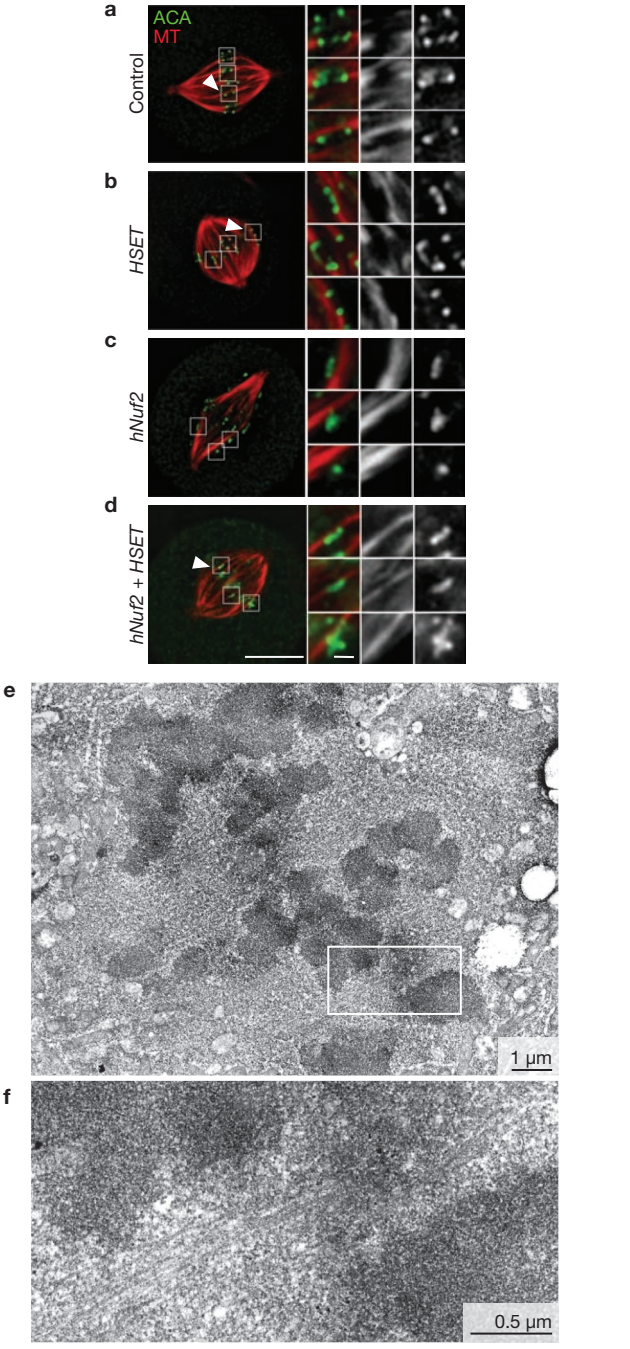

Figure 2 Kinetochores laterally bind stabilized microtubule bundles in the absence of K-fibres. (**a**–**d**) HeLa cells transfected with control (**a**), *HSET* (**b**), *hNuf2* (**c**), or *hNuf2* + *HSET* (**d**) RNAi were treated with $CaCl_2$ (0.2 mM) to depolymerise highly dynamic microtubules, and stained to visualise microtubules (MT; red), kinetochores (ACA, anti-centromere antibody; green) and DNA (blue). Scale bar, 10 μm for whole spindle images (left) or 1 μm for insets (right). Arrowheads indicate a microtubule bundle that transverses the spindle equator without making an end-on attachment to a kinetochore. (**e**) Correlative light/serial section electron microscopy was performed on *hNuf2* + *HSET* RNAi cells. The image is a low magnification view of a cell, showing the spindle equator region. (**f**) Higher magnification view of the region boxed in panel **e**. Note the bundle of microtubules bypassing the chromosomes.

We next tested whether restoration of the chromosome alignment observed in the *hNuf2* + *HSET* RNAi cells was due to regeneration of the K-fibres. It has been reported that the number of microtubules in a K-fibre is correlated with the amount of residual Ndc80 complex present on the kinetochore[11]. We quantified the amount of Hec1 that remained on kinetochores after knockdown, using immunofluorescence[11], and found that Hec1 levels on kinetochores were similar in *hNuf2* RNAi- and

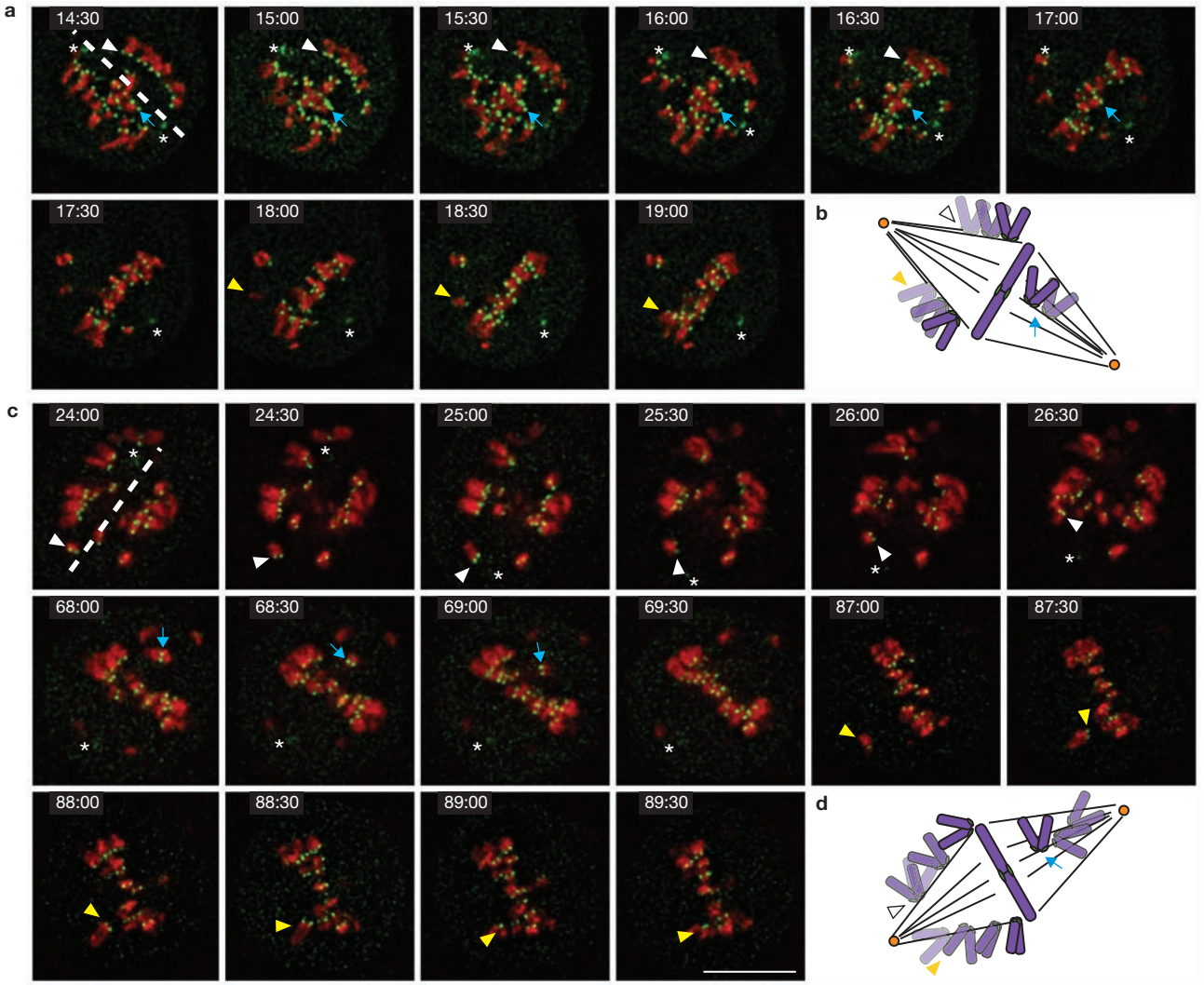

Figure 3 In the absence of K-fibres, kinetochores congress with alternating kinetochores leading. (**a**–**d**) Triple-labelled HeLa cells (GFP–CENP-A + GFP–γ-tubulin + mCherry–H2B) treated with control luciferase (**a**) or *hNuf2* + *HSET* (**c**) RNAi were imaged at 30 s intervals starting from nuclear envelope breakdown until telophase, and analysed for kinetochore orientation during congression. Time is marked in the upper left of each panel, asterisks mark the position of spindle poles and the arrows and arrowheads mark the individual kinetochore pairs schematised in **b** and **d**. Scale bar, 10 μm. Note that the arrowheads that reflect the orientation of the kinetochore pairs in the control cells do not change much over time, whereas the arrowheads in the *hNuf2* + *HSET* RNAi cell change orientation dramatically with time.

hNuf2 + *HSET* RNAi-transfected cells (Supplementary Information, Fig. S2a), suggesting that any residual kinetochore remnants that could mediate transient microtubule attachments were similar in both cell types, despite the dramatically different levels of chromosome alignment. As an alternative means to assess the presence of K-fibre microtubules, we examined the localization of the protein HURP (hepatoma upregulated protein), which is normally enriched towards the plus-ends of K-fibre microtubules[15,16]. In control cells, HURP was localized to the K-fibres, whereas in *hNuf2* and *hNuf2* + *HSET* RNAi cells HURP staining was diminished (Supplementary Information, Fig. S2b). These data suggest that K-fibres are not restored after simultaneous knockdown of *HSET* and *hNuf2*.

As proper end-on amphitelic attachments of microtubules are required for generating tension across the centromere, we compared inter-kinetochore distances between K-fibre-intact (control) and K-fibre-deficient (*hNuf2* + *HSET* RNAi) cells (Supplementary Information, Fig. S2c–e). These analyses were conducted in a HeLa cell line expressing GFP–CENP-A to mark kinetochores and GFP–γ-tubulin to mark centrosomes. During the pseudo-metaphase state, inter-kinetochore distances in *hNuf2* + *HSET* RNAi cells were, on average, 40% lower than in control cells (Supplementary Information, Fig. S2d). These results are consistent with previous reports on hNuf2-depleted cells[5], and similar to those obtained from cells treated with nocodazole (microtubule depolymeriser); they show that the centromeres in *hNuf2* + *HSET* RNAi cells are not under tension. Furthermore, live-cell analyses of individual kinetochore pairs revealed that the inter-kinetochore distance in *hNuf2* + *HSET* RNAi cells (8/10 cells) remained nearly constant over time, whereas in control cells the distance between sister kinetochores showed periodic fluctuations (4/4 cells; Supplementary Information, Fig. S2e and Movie 1). This was consistent with the narrower inter-kinetochore distance distribution range in *hNuf2* + *HSET* RNAi cells versus control cells (Supplementary Information, Fig. S2d).

Similarly to previous studies, we also found that kinetochores in *hNuf2* RNAi cells showed brief erratic movements[11]. These movements persisted in *hNuf2* + *HSET* RNAi cells (Supplementary Information, Fig. S2f–h). Together, our results strongly support the idea that chromosomes in *hNuf2* + *HSET* RNAi cells fail to establish the amphitelic attachments necessary to generate centromere tension.

To reveal the nature of interaction between chromosomes and microtubules in *hNuf2* + *HSET* RNAi cells, we used $CaCl_2$ to depolymerise highly dynamic microtubules so that stable microtubules of the spindle could be clearly observed. In both control and *HSET* RNAi cells, all aligned chromosomes established amphitelic attachments with K-fibres extending from each sister kinetochore towards the corresponding spindle pole (Fig. 2a, b). In contrast, in both *hNuf2* and *hNuf2* + *HSET* RNAi cells most of the kinetochores were laterally associated with microtubule bundles that traversed the centre of the spindle (Fig. 2c, d). We occasionally detected kinetochores in control cells that were not only connected to the K-fibres, but were also laterally bound to continuous microtubule bundles extending from each half spindle through the spindle midzone (Fig. 2a, arrowhead), suggesting that these bundles are probably also present in control cells. In contrast, in *hNuf2* and *hNuf2* + *HSET* RNAi cells, these bundles were prominently visible and microtubule bundles that terminated at the kinetochore were rarely detected.

To gain further insight into the interaction of chromosomes with microtubules, we performed serial-section electron microscopy on *hNuf2* + *HSET* RNAi cells (Fig. 2e, f). Cells were first followed by time-lapse light microscopy to monitor chromosome alignment, and then fixed and embedded for electron microscopy analyses (Supplementary Information, Fig. S3). Consistent with published data on Nuf2-depleted cells[11], electron microscopy revealed no typical tri-laminar kinetochores in any of the sections analysed (> 100) in *hNuf2* + *HSET* RNAi cells. We occasionally observed microtubule bundles that were traversing the central part of the spindle and were laterally associated with chromosomes (Fig. 2e, f). However, we never found evidence of microtubule bundles terminating at the chromosomes. During classic congression, chromosomes exhibit extended linear motion from the vicinity of the spindle pole toward the equator[7,17]. To examine whether this characteristic movement is preserved in *hNuf2* + *HSET* RNAi cells, we used time-lapse imaging in HeLa cells triple-labelled for kinetochores (GFP–CENP-A), centrosomes (γ-tubulin–GFP) and chromosomes (mCherry–H2B). Cells were imaged at 30 s intervals on a spinning-disk confocal microscope, from prophase to telophase (Fig. 3). Of the 21 *hNuf2* + *HSET* RNAi cells imaged, 11 cells aligned their chromosomes, consistent with the frequency of chromosome alignment in our in fixed–cell analyses (Fig. 1b). Although sustained velocities of individual chromosome movements were similar between control and *hNuf2* + *HSET* RNAi cells (1.5 ± 0.5 μm min^{-1}, $n = 6$ and 1.6 ± 0.3 μm min^{-1}, $n = 6$, respectively; Supplementary Information, Fig. S4), overall formation of the metaphase plate took significantly longer in cells co-depleted of *hNuf2* and *HSET*. Furthermore, only 2 of the *hNuf2* + *HSET* RNAi cells exited mitosis during our imaging period of ~2 h. In contrast, all control cells ($n = 9$) progressed through mitosis with normal timing, similarly to previous reports[16,18] (Supplementary Information, Movie 2). Thus, our imaging conditions did not impede normal mitotic progression. These results show that although chromosomes maintain the ability to congress when K-fibres are severely disrupted, the efficiency of this process is reduced.

Analysis of individual chromosome movements revealed characteristic differences between chromosome congression in control versus

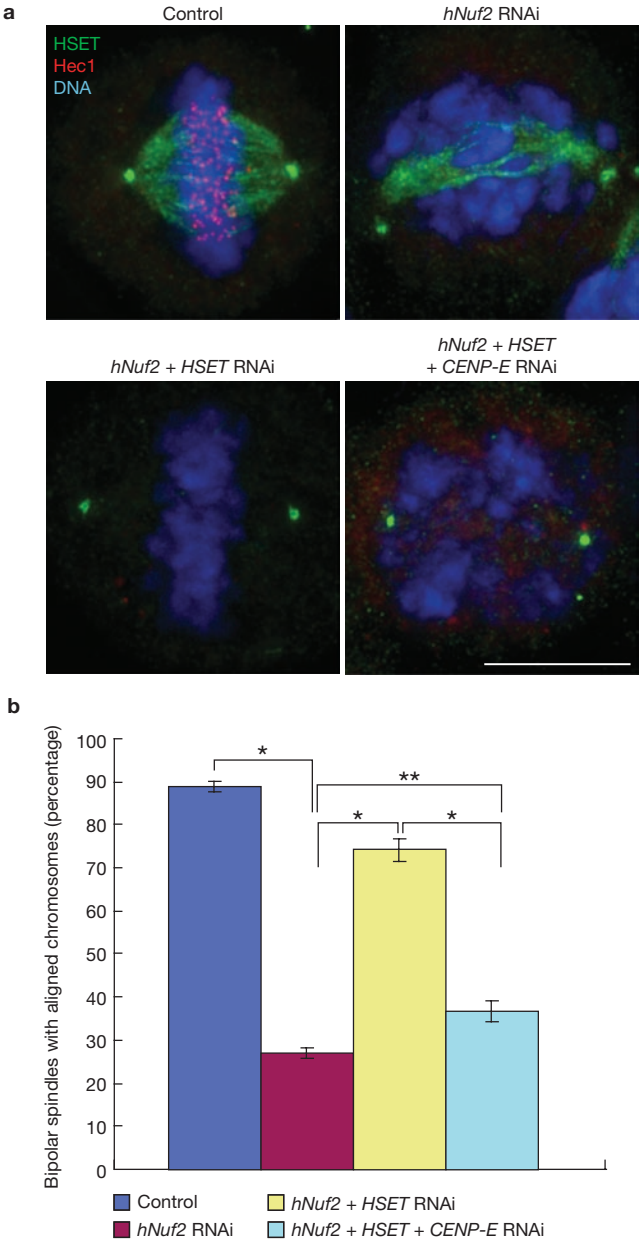

Figure 4 Chromosome congression in cells with disrupted K-fibres is dependent on CENP-E. (**a**) Cells in which *hNuf2*, *HSET* and *CENP-E* were knocked down were stained to visualize HSET (green), Hec1 (red) and DNA (blue). Luciferase RNAi was used as a control. Scale bar, 10 μm. (**b**) Quantification of the percentage of bipolar spindles with aligned chromosomes from the four different RNAi conditions. Data are mean ± s.d. from three independent experiments, ~300 total cells were scored per RNAi condition, * $P < 0.05$, ** $P = 0.45$.

hNuf2 + *HSET* RNAi cells. In control cells, one of the sister kinetochores continuously led the way during congression, and the orientation of the sister kinetochores with respect to the spindle axis remained constant. (Fig. 3a, b; Supplementary Information, Movie 2). In contrast, sister kinetochores tumbled frequently during congression in *hNuf2* + *HSET* RNAi cells. It was not unusual for sister kinetochores to transiently orientate perpendicular to the spindle axis (Fig. 3c, d; Supplementary Information, Movie 2). This behaviour suggests that in the absence of end-on attachments, congressing kinetochores do not maintain stable association

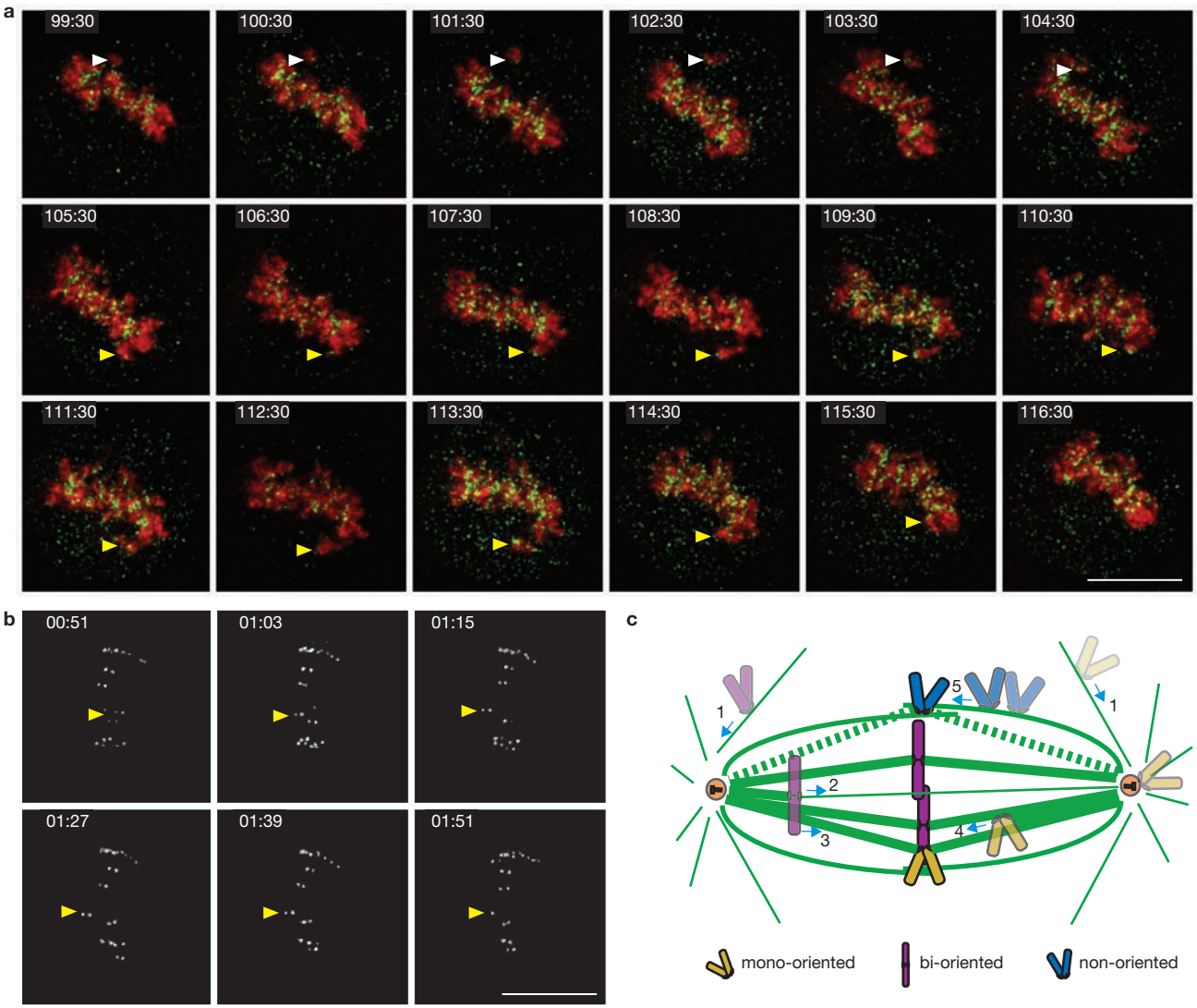

Figure 5 K-fibres are needed to maintain chromosome alignment. (**a**) Triple-labelled (GFP–CENP-A + GFP–γ-tubulin + mCherry–H2B) *hNuf2* + *HSET* RNAi HeLa cells were analysed for chromosome movement at 30 s intervals after congression. Times are shown in the upper left of each panel. White and yellow arrowheads point to two distinct, unstable chromosomes that move off, and then congress back to, the metaphase plate. (**b**) Kinetochore movements were tracked in cells with disrupted K-fibres at 3 s intervals during congression in *hNuf2* + *HSET* RNAi cells. The yellow arrowheads correspond to a chromosome that displays a rapid movement away from, and back towards, the metaphase plate. (**c**) Model depicting the different pathways by which chromosomes congress to the metaphase plate (k-fibres, green). The thick straight lines indicate the K-fibres of the bi-oriented chromosomes. The dashed lines indicate the K-fibres that will eventually form after the chromosome congresses to the metaphase plate. Chromosome 1 (purple) shows rapid lateral movement towards the spindle pole and then becomes bi-oriented and congresses through activities at its kinetochore (2) or its chromosome arms (3). Alternatively, chromosome 1 (light yellow) can congress through the mono-oriented pathway (4). Our data suggest that chromosomes (blue) do not need to be specifically oriented, but are able to congress on any stabilized microtubule bundle (5). Scale bars, 10 μm in **a** and **b**.

with microtubules. Instead, congression in *hNuf2* + *HSET* RNAi cells is driven by both sister kinetochores, which intermittently switch between leading and trailing positions. Overall, these findings strongly support a model in which chromosome congression occurs by gliding of unattached kinetochores alongside microtubule bundles[7]. Because this type of congression has been reported to require the activity of the plus-end kinesin CENP-E[7], we sought to investigate whether this protein is required for chromosome alignment in *hNuf2* + *HSET* RNAi cells.

Immunofluorescence analysis of CENP-E showed that neither *hNuf2* RNAi nor *hNuf2* + *HSET* RNAi affected CENP-E localization to kinetochores (Supplementary Information, Fig. S5a, b). Depletion of CENP-E in *hNuf2* + *HSET* RNAi cells caused a decrease in the percentage of cells with aligned chromosomes down to the levels found in *hNuf2* RNAi cells (Fig. 4b). This result strongly suggests that congression in *hNuf2* + *HSET* RNAi cells is driven by the activity of CENP-E.

Our findings that chromosome congression occurs in the absence of end-on kinetochore attachments to K-fibres led us to speculate that the forces that drive chromosome congression may be distinct from those that maintain chromosomes at the metaphase plate. To test this idea, we compared post-congression behaviour of chromosomes in control and *hNuf2* + *HSET* RNAi cells. Unlike in control cells, chromosomes in *hNuf2* + *HSET* RNAi cells were not stably maintained at the metaphase

plate, but showed rapid, periodic movements towards one of the spindle poles, followed by a slower return to the spindle equator (Fig. 5a b; Supplementary Information, Movies 3–4). The speed of the poleward excursions (~10 μm min^{-1}) was similar to that of the rapid poleward movement observed in chromosomes during the capture of astral microtubules[19]. It is noteworthy that fast dynein-dependent chromosome movements have been reported previously in cells with a disrupted Ndc80 complex[20]. To address whether the post-congression poleward excursions were also dynein-dependent, we knocked down ZW10 in *hNuf2* + *HSET* RNAi cells and then followed the behaviour of chromosomes near the metaphase plate. Whereas 77% of the *hNuf2* + *HSET* RNAi cells showed rapid poleward excursions (23/30 cells), only 36% of the the *hNuf2* + *HSET* + *zw10* triple-knockdown cells (13/36 cells) showed this type of movement. This difference suggests that dynein drives the movement of chromosomes off the metaphase plate.

From the standpoint of the classic 'search and capture' hypothesis[21], the attachment of sister kinetochores to the spindle occurs independently from one another. This results in chromosome mono-orientation — the movement of a chromosome towards one spindle pole (Fig. 5c). There, the chromosome remains until its sister kinetochore captures microtubules that emanate from the distal spindle pole. Only then will the chromosome congress and become stably positioned near the spindle equator. A conceptual difficulty with this mechanism is that the probability of capturing microtubules that emanate from the centrosome decreases dramatically as the distance between the centrosome and the kinetochore increases[22]. Our data provide an explanation for how cells can overcome this difficulty by revealing that chromosomes have the ability to congress to the spindle equator in the absence of end-on microtubule attachments. We favour the idea that congression is not a consequence of chromosome bi-orientation, but rather is a means to maximize the efficiency of kinetochore attachment by bringing the chromosome to the area with the highest concentration of microtubule plus-ends. Although congression of unattached kinetochores alongside the K-fibre of another chromosome has been observed previously[4], our data reveal for the first time that this mechanism is sufficient to achieve congression of all chromosomes in human cells in a reasonable time frame. Furthermore, we demonstrate that congression through CENP-E-mediated kinetochore gliding can occur along any microtubule bundle and does not require the trailing kinetochore to be attached (Fig. 5c).

Under normal conditions, only a limited number of chromosomes seem to show mono-orientation and congression through microtubule gliding[6,7,23]. This is probably because there are multiple pathways that achieve chromosome congression. In the presence of K-fibres, mono-oriented chromosomes have a large number of adjacent K-fibres available to glide on. However, the 'search and capture' hypothesis predicts that almost all chromosomes must transiently become bi-oriented and live-cell microscopy reveals that most chromosomes rapidly achieve stable bi-orientation during normal mitosis. Our data suggest that the fast bi-orientation can be achieved because unattached chromosomes are positioned near the spindle equator through CENP-E-mediated forces. Accordingly, the number of mono-oriented chromosomes increases in cells on inhibition of CENP-E[7,23–25].

An intriguing question is why CENP-E-mediated forces fail to support chromosome congression in cells with disrupted Ndc80/Hec-1 complex and normal HSET activity. One possibility is that HSET provides a pole-directed force that inhibits CENP-E activity. This pole-directed force would need to be indirect because we found no evidence of HSET association with chromosome arms or kinetochores. Another possibility is that chromosome congression requires stabilized microtubule bundles, thus mechanisms governing microtubule stability are critical to the congression process. In this light, we found that HSET has an important role in spindle assembly through its microtubule cross-linking activity[3,4]. We propose that inactivation of HSET results in an increase in the number of stabilized microtubule bundles in the central spindle. These bundles could provide the tracks for congressing chromosomes that glide in a CENP-E-mediated manner, indicating that CENP-E may have a more active role in chromosome congression than previously thought. □

METHODS

Methods and any associated references are available in the online version of the paper at http://www.nature.com/naturecellbiology/.

Note: Supplementary Information is available on the Nature Cell Biology website.

ACKNOWLEDGEMENTS

We thank S. Ems-McClung and J. Powers for discussions and critical comments on the manuscript, G. Fang for HURP antibodies, D. Compton for HSET constructs, B. Sullivan for the GFP–CENP A construct and T. Yen for the CENP-E antibody. S.C. is grateful to members of the Marine Biological Laboratory Physiology course for instruction in imaging and many thoughtful discussions. The Indiana University Bloomington Light Microscopy Imaging Center and Wadsworth Center's electron microscopy Core facility provided microscopy resources. This work was supported by NIH grants (GM59618) to C.E.W. and (GM59363) A.K; C.B.O. was supported by a Kirschstein-National Research Service Award post-doctoral fellowship (GM077911).

AUTHOR CONTRIBUTIONS

S.C. performed most of the experiments, analysed the data and prepared the initial draft of the manuscript; C.O. performed electron microscopy analyses and C.E.W. and A.K. in conjunction with S.C. and C.O. designed the experiments, interpreted the data, edited the manuscript and prepared the final data for publication.

COMPETING FINANCIAL INTERESTS

The authors declare no competing financial interests.

Published online at http://www.nature.com/naturecellbiology/.
Reprints and permissions information is available online at http://npg.nature.com/reprintsandpermissions/.

1. Maiato, H., DeLuca, J., Salmon, E. D. & Earnshaw, W. C. The dynamic kinetochore–microtubule interface. *J. Cell Sci.***117,** 5461–5477 (2004).
2. Walczak, C. E. & Heald, R. Mechanisms of mitotic spindle assembly and function. *Int. Rev Cytol.* **265,** 111–158 (2008).
3. Cai, S., Weaver, L. N., Ems-McClung, S. C. & Walczak, C. E. Kinesin-14 family proteins HSET/XCTK2 control spindle length by cross-linking and sliding microtubules. *Mol. Biol. Cell* **20,** 1348–1359 (2009).
4. Manning, A. L. & Compton, D. A. Mechanisms of spindle-pole organization are influenced by kinetochore activity in mammalian cells. *Curr. Biol.* **17,** 260–265 (2007).
5. DeLuca, J. G., Moree, B., Hickey, J. M., Kilmartin, J. V. & Salmon, E. D. hNuf2 inhibition blocks stable kinetochore–microtubule attachment and induces mitotic cell death in HeLa cells. *J. Cell Biol.* **159,** 549–555 (2002).
6. Wood, K. W., Sakowicz, R., Goldstein, L. S. & Cleveland, D. W. CENP-E is a plus end-directed kinetochore motor required for metaphase chromosome alignment. *Cell* **91,** 357–366 (1997).
7. Kapoor, T. M. *et al.* Chromosomes can congress to the metaphase plate before biorientation. *Science* **311,** 388–391 (2006).
8. Nicklas, R. B. & Arana, P. Evolution and the meaning of metaphase. *J Cell Sci* **102 (Pt 4),** 681–690 (1992).
9. Rieder, C. L. & Salmon, E. D. The vertebrate cell kinetochore and its roles during mitosis. *Trends Cell Biol.* **8,** 310–318 (1998).
10. Maiato, H. & Sunkel, C. E. Kinetochore-microtubule interactions during cell division. *Chromosome Res.* **12,** 585–597 (2004).
11. DeLuca, J. G. *et al.* Hec1 and nuf2 are core components of the kinetochore outer plate essential for organizing microtubule attachment sites. *Mol. Biol. Cell* **16,** 519–531 (2005).
12. Heald, R. & Walczak, C. E. in *The Kinetochore: From Molecular Discoveries to Cancer Therapy* (eds. De Wulf, P. & Earnshaw, W. C.) 231–268 (Springer Science and Business Media, 2009).
13. Scholey, J. M., Brust-Mascher, I. & Mogilner, A. Cell division. *Nature* **422,** 746–752 (2003).

14. Starr, D. A., Williams, B. C., Hays, T. S. & Goldberg, M. L. ZW10 helps recruit dynactin and dynein to the kinetochore. *J. Cell Biol.* **142,** 763–774 (1998).
15. Sillje, H. H., Nagel, S., Korner, R. & Nigg, E. A. HURP is a Ran-importin β-regulated protein that stabilizes kinetochore microtubules in the vicinity of chromosomes. *Curr. Biol.* **16,** 731–742 (2006).
16. Wong, J. & Fang, G. HURP controls spindle dynamics to promote proper interkinetochore tension and efficient kinetochore capture. *J. Cell Biol.* **173,** 879–891 (2006).
17. Skibbens, R. V., Skeen, V. P. & Salmon, E. D. Directional instability of kinetochore motility during chromosome congression and segregation in mitotic newt lung cells: a push-pull mechanism. *J. Cell Biol.* **122,** 859–875 (1993).
18. Bomont, P., Maddox, P., Shah, J. V., Desai, A. B. & Cleveland, D. W. Unstable microtubule capture at kinetochores depleted of the centromere-associated protein CENP.-F. *EMBO J.* **24,** 3927–3939 (2005).
19. Rieder, C. L. & Alexander, S. P. Kinetochores are transported poleward along a single astral microtubule during chromosome attachment to the spindle in newt lung cells. *J. Cell Biol.* **110,** 81–95 (1990).
20. Vorozhko, V. V., Emanuele, M. J., Kallio, M. J., Stukenberg, P. T. & Gorbsky, G. J. Multiple mechanisms of chromosome movement in vertebrate cells mediated through the Ndc80 complex and dynein/dynactin. *Chromosoma* **117,** 169–179 (2008).
21. Kirschner, M. W. & Mitchison, T. Microtubule dynamics. *Nature* **324,** 621 (1986).
22. Wollman, R. *et al.* Efficient chromosome capture requires a bias in the 'search-and-capture' process during mitotic-spindle assembly. *Curr. Biol.* **15,** 828–832 (2005).
23. McEwen, B. F. *et al.* CENP-E is essential for reliable bioriented spindle attachment, but chromosome alignment can be achieved via redundant mechanisms in mammalian cells. *Mol. Biol. Cell* **12,** 2776–2789 (2001).
24. Putkey, F. R. *et al.* Unstable kinetochore-microtubule capture and chromosomal instability following deletion of CENP.-E. *Dev. Cell* **3,** 351–365 (2002).
25. Weaver, B. A. *et al.* Centromere-associated protein-E is essential for the mammalian mitotic checkpoint to prevent aneuploidy due to single chromosome loss. *J. Cell Biol.***162,** 551–563 (2003).

METHODS

Cloning and antibody preparation. The *HSET* cDNA (genebank ID: 68299768) was a gift from D. Compton (Dartmouth Medical School, NH, USA). The cDNA encoding the non-motor domain of HSET (N-terminal, 304 amino acids) was subcloned into pGEX1 and p6HGFP-B with restriction enzymes *Bam*HI and *Eco*RI to generate GST- and 6-His–GFP-tagged fusion proteins, respectively. The cDNA for H2B was cloned from PtK2 cell RNA by RT-PCR (PCR with reverse transcription). pmCherry-C1 was created by replacing the EGFP sequence from pEGFP-C1 with mCherry. PtK-H2B cDNA was subsequently cloned into pmCherry-C1 to generate pmCherry-H2B. All resulting clones were verified by sequencing.

GST–HSET(amino-acids 2–304) was expressed in *E. coli* BL21(DE3) cells, and affinity purified with gluthione sepharose 4B (Amersham Biosciences) as described previously[26], followed by gel filtration on a Superose 12 column (GE Healthcare). His-GFP–HSET(2–304) was expressed, purified and cross-linked to Affi-Gel 10 (Bio-Rad) as described previously for antibody affinity purification[27]. Antibodies to the non-motor domain of HSET were generated by immunising a rabbit (Covance Research Products) with GST–HSET(2–304) protein that was first treated with 0.5% gluteraldehyde for 45 min and then quenched with a trace of sodium borohydride for 5 min at room temperature. HSET-specific antibodies were then affinity purified using a His-GFP–HSET(2–304) affinity column as described previously[27].

Cell culture and generation of stable cell lines. HeLa cells were cultured in Opti-MEM (Invitrogen), supplemented with 10% fetal bovine serum (Gibco) and penicillin/streptomycin (Gibco) at 37 °C and with 5% CO_2. To make the stable cell lines, pEGFP–HSET, pEGFP–CENP-A (a gift from B. Sullivan, Univeristy of Wisconsin-Madison, USA), γ-tubulin–pEGFP and/or pmCherry–H2B were individually or sequentially introduced into HeLa cells using calcium phosphate transfection[28] in the presence of Geneticin (2 mg ml^{-1}; Gibco). Transfected cells were re-plated at a density of 1,000 cells per plate, on 10 cm plates, and grown for 7–10 days with daily changes in media until each colony had ~200 cells. A single colony was isolated by using a pipette tip and examining the colony under a inverted fluorescence microscope, transferred to a new dish and maintained in Opti-MEM containing Geneticin (1 mg ml^{-1}).

Immunofluorescence and western blotting analysis. HeLa cells were fixed in -20 °C methanol for 5 min at room temperature and rehydrated in Tris (20 mM at pH 7.5) and NaCl (TBS; 150 mM) with Triton X-100 (TBS-Tx; 0.1%) for 2 min. Cells were blocked in Abdil (TBS, 1% bovine serum albumin, 0.1% Triton X-100 and 0.1% sodium azide) for 1 h at room temperature or overnight at 4 °C. Cells were stained with antibodies against HSET (2.5 μg μl^{-1}), Hec1 (1 μg μl^{-1}; Novus Biologicals), CENP-E (1:500 dilution; a gift from T. Yen, Fox Chase Cancer Center, PA, USA), ACA (1:100 dilution; Antibodies Incorporated) or α-tubulin DM1α (1:1,000 dilution; Sigma-Aldrich) and diluted in Abdil for 1 h at room temperature. Cells were subsequently stained with a 1:50 dilution of donkey anti-rabbit Alexa Fluor 488, donkey anti-mouse TexasRed (Jackson ImmunoResearch), or donkey anti-human Cy5 (Jackson ImmunoResearch). To visualize DNA, fixed cells were stained with Hoechst (2 μg ml^{-1}; Sigma-Aldrich) in TBS-TX. For HURP staining, cells were fixed with 4% formaldehyde in PHEM (25 mM HEPES, 10 mM EGTA, 60 mM PIPES and 2 mM MgCl2 at pH 6.9) and then stained with anti-HURP antibodies (1:200 dilution; a gift from G. Fang, Genentech, CA, USA). For p150 staining, cells were first permeabilized with 0.3% Triton X-100 in PHEM buffer at room temperature for 3 min, followed by fixation with 4% formaldehyde in the same buffer and then stained with a P150 antibody (1:200 dilution; BD Biosciences). For K-fibre visualization, HeLa cells were treated for 2 min at room temperature with $CaCl_2$ (0.2 mM) in PIPES (100 mM at pH 6.8), $MgCl_2$ (1 mM) and 0.1% Triton X-100, followed by fixation in the same buffer supplemented with 3.7% formaldehyde, for 20 min at room temperature. For western blotting analysis, HeLa cells were collected and lysed in sample buffer (125 mM Tris-HCl at pH 6.8, 4% SDS, 20% glycerol and 4% mercaptoethanol) at 3,000 cells per μl. From each sample 15,000 cells were loaded on a 7.5% SDS–PAGE gel, and transferred to Protran nitrocellulose (Schleicher and Schuell). Blots were then probed with DM1α (1:10,000 dilution), anti-HSET (2.5 μg μl^{-1}) or Hec1 (1 μg μl^{-1}) and detected with SuperSignal West Pico enhanced chemiluminescence.

RNAi. HeLa cells, at 4×10^4 cells per well, were plated into each well of a 6-well culture dish, arrested with thymidine (2 mM) for 20 h and then released into fresh media. At 2 h after release from the thymidine block, the following oligonucleotides were transfected into HeLa cells using oligofectamine (Invitrogen): luciferase RNAi negative control #2 (200 nM; Dharmacon), *HSET* RNAi for the coding region (200 nM; 5'-UCA GAA GCA GCC CUG UCA A-3'), *HSET* 3'UTR-1 RNAi (300 nM; 5'-GUG UCC CUA UGU CUA UGU A-3'), *HSET* 3'UTR-2 RNAi (200 nM; 5'-CAU GUC CCA GGG CUA UCA AAU-3'), *hNuf2* RNAi[3] (200 nM; 5'-AAG CAT GCC GTG AAA CGT ATA-3') or *zw10* RNAi[29] (200 nM; 5'-UGA UCA AUG UGC UGU UCA A-3'). When comparing knockdown of multiple proteins, an equivalent amount of luciferase negative control oligonucleotide was co-transfected with the specific oligonucleotide, such that the total amount of oligonucleotide transfected was identical for each well. At 24 h after transfection, cells were blocked with thymidine (2 mM) for 19 h to synchronize the cells and then released for ~11–12 h to allow cells to progress to late G2 phase. The cells were then processed for immunofluorescence or for western blotting analysis. For time-lapse imaging of living cells, we used the same protocol except that cells were plated onto 22×22-mm coverslips in 60-mm dishes. For the *CENP-E* knockdown assays, *CENP-E* RNAi oligonucleotide[7] (200 nM; 5'-AAG GCU ACA AUG GUA CUA UAU-3') was transfected into HeLa cells 24 h after *HSET* and *hNuf2* RNAi transfection. After an additional 24 h cells were processed for immunofluorescence .

Electron microscopy. GFP–CENP-A + GFP–γ-tubulin + mCherry–H2B HeLa cells were grown on electron-microscopy-grade gridded coverslips and then transfected with *hNuf2* + *HSET* siRNAs as described above. At 48 h post-transfection, cells were imaged on a Nikon spinning-disk confocal microscope to monitor kinetochore movement. Mitotic cells showing a clear phenotype (aligned chromosomes but shortened inter-kinetochore distances, kinetochore orientation changes and rapid movement towards spindle poles) were fixed with 2.5% glutaraldehyde in PBS (137 mM NaCl, 2.7 mM KCl, 10 mM Na_2HPO_4, 2 mM KH_2PO_4 at pH 7.2) for 30 min and post-fixed in OsO_4 (1%) according to standard protocols[30]. Cells of interest were re-located on the gridded coverslips and then serially sectioned (100-nm thickness). Images were collected on a Zeiss 910 microscope operated at 100 KV.

Imaging and data analysis. Fixed cells were imaged using a Nikon Eclipse 90i equipped with a ×100 apochromatic PLAN objective (NA 1.4) and a CoolSnap HQ CCD camera (Photometrics). The camera and filters were controlled by Metamorph (Molecular Devices). Image stacks were collected at 0.5-μm steps through the whole cell volume and then deconvolved using Autodeblur (Autoquant Imaging) for 10–20 iterations. For time-lapse imaging of living cells, RNAi-treated HeLa cells were blocked at G1/S phase with thymidine as described above, and then released into fresh Opti-MEM (Invitrogen). At 11–12 h after release, coverslips were placed into a Rose chamber with imaging medium (Opti-MEM, 20 mM Hepes at pH 7.7 and 30 U ml^{-1} Oxyrase) and covered with mineral oil. Cells were imaged at 37 °C on a Yokagawa spinning-disk CSU-10 mounted on a Nikon TE2000 microscope equipped with a 100X objective (apochromatic PLAN, NA1.4). Images were captured on a Roper Cascade II EM-CCD camera set at 3700 gain with 100-ms exposures for each channel at three *z*-axis sections of 0.5 μm. For experiments analysing mitotic progression, we used 30-s time intervals for approximately 2 h total imaging time. For experiments to measure kinetochore motility, we captured images from three focal planes at 3–5-s intervals for a total of 5 min.

To determine the percentage of cells with aligned or unaligned chromosomes, fixed cells were counted at 54 h post-transfection. The average percentage of cells with aligned or unaligned chromosomes was determined from three independent experiments with the *HSET* cDNA oligonucleotide in which 100 mitotic cells were counted per experiment. A cell was scored as having unaligned chromosomes when most chromosomes were scattered throughout the spindle region. A cell was scored as having aligned chromosomes if most chromosomes were tightly aligned at the metaphase plate. In addition, three independent experiments were performed for each of the two 3'UTR oligonucleotides. For each experiment, the average percentage of cells is graphed as the mean ± sd from three experiments.

The oscillatory behaviour of kinetochores and the inter-kinetochore distances were determined from transfection of the GFP–CENP-A + GFP–γ-tubulin HeLa

DOI: 10.1038/ncb1890

cell line with luciferase control oligonucleotide or the *hNuf2* and *HSET* oligonucleotides. For each movie, a randomly selected frame was analysed for the inter-kinetochore distance. A total of 27 kinetochores from four control cells and 54 kinetochores from eight *hNuf2* + *HSET* RNAi cells were measured. The average distance ± the s.d. is reported. To analyse the oscillation patterns, we tracked a single kinetochore pair over a defined period of time and plotted the inter-kinetochore distance versus time. The erratic kinetochore motility was manually tracked by identifying the centre of GFP–CENP-A dots using Image J as described previously[11]. The positional data of the kinetochore at each time point were plotted with Excel. The kymographs that represent chromosome motility during congression were assembled frame by frame from the movies of mitotic progression (30-s time interval) by drawing a rectangular box along their movement trajectory toward the metaphase plate.

The analysis of HURP staining was carried out with Metamorph 'line scan' function using a 30-pixel-width box along the spindle pole–pole axis. The gray scale data were plotted using Excel. The fluorescence intensity of Hec1 on the kinetochore was quantified from 300 kinetochores of 30 cells from three independent experiments, as reported previously[11].

Two-tailed Student's t-tests were performed where indicated in the text using Excel. Significance was considered when $P < 0.05$.

26. Ems-McClung, S. C., Zheng, Y. & Walczak, C. E. Importin α/β and Ran–GTP regulate XCTK2 microtubule binding through a bipartite nuclear localization signal. *Mol. Biol. Cell* **15,** 46–57 (2004).
27. Walczak, C. E., Verma, S. & Mitchison, T. J. XCTK2: a kinesin-related protein that promotes mitotic spindle assembly in *Xenopus laevis* egg extracts. *J. Cell Biol.* **136,** 859–870 (1997).
28. Rodriguez, A. & Flemington, E. K. Transfection-mediated cell-cycle signaling: considerations for transient transfection-based cell-cycle studies. *Anal. Biochem.* **272,** 171–181 (1999).
29. Yang, Z., Tulu, U. S., Wadsworth, P. & Rieder, C. L. Kinetochore dynein is required for chromosome motion and congression independent of the spindle checkpoint. *Curr. Biol.* **17,** 973–980 (2007).
30. Rieder, C. L. & Cassels, G. Correlative light and electron microscopy of mitotic cells in monolayer cultures. *Methods Cell Biol.* **61,** 297–315 (1999).

nature cell biology

DOI: 10.1038/ncb1890

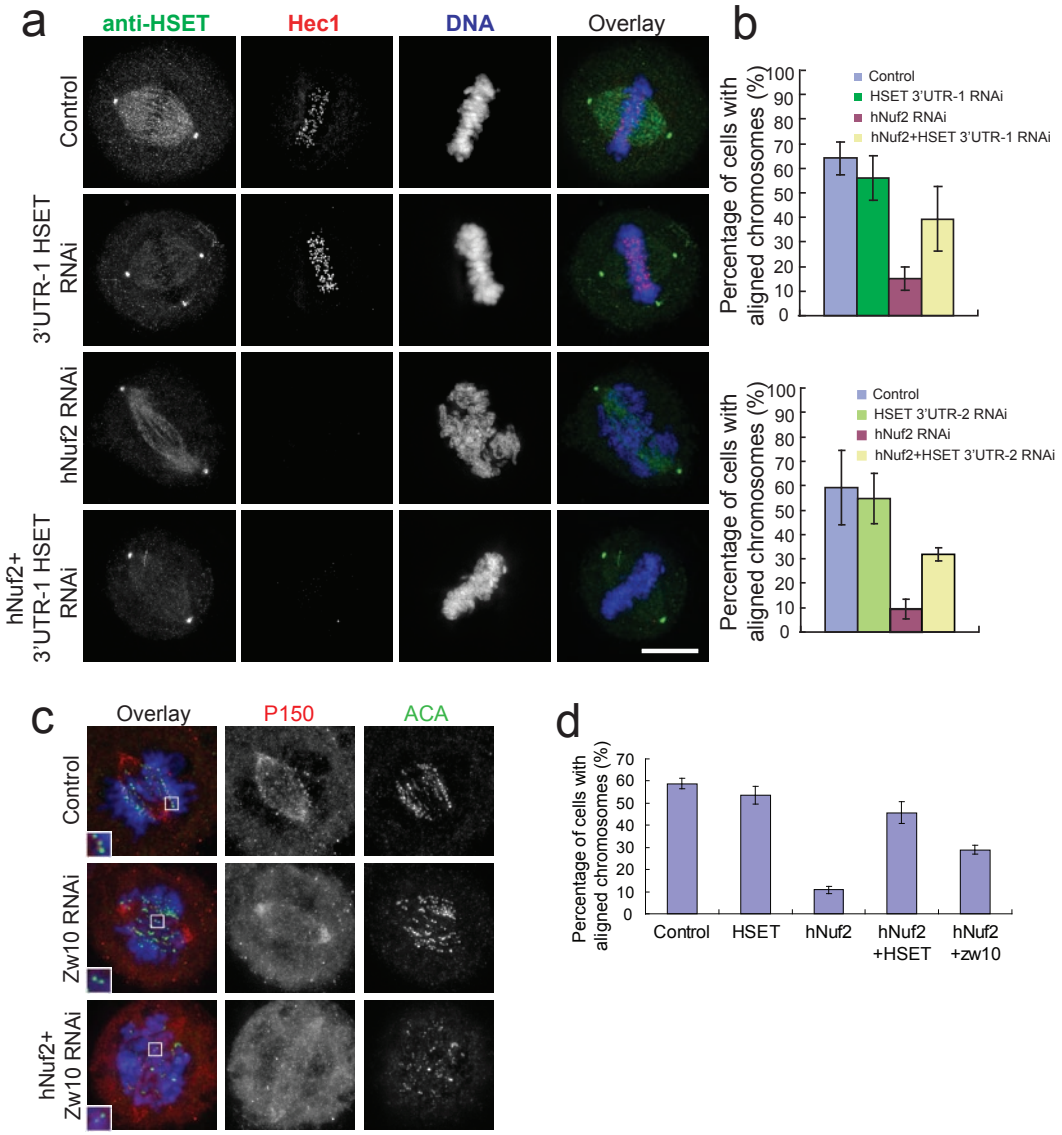

Figure S1 Perturbation of HSET or kinetochore dynein partially restores the chromosome congression in K-fibre disrupted spindles. **(a)** Cells transfected with an oligo raised against the 3' UTR of HSET (HSET-3'UTR-1) alone or in combination with an oligo against hNuf2 were stained to visualise HSET (green), Hec1 (red) and DNA (blue). Scale bar, 10 μm. **(b)** Quantification of the percentage of cells with aligned chromosomes in prometaphase/metaphase cells for two independent HSET 3'UTR oligos from four independent experiments where ~100 mitotic cells were scored per experiment. The mean percentage ± s.d of cells with aligned chromosomes is graphed for HSET 3'UTR-1 oligo (top) and HSET 3'UTR-2 oligo (bottom). The differences between the mean of control versus hNuf2 RNAi, hNuf2 RNAi versus hNuf2+HSET RNAi and control versus hNuf2+HSET RNAi are significant ($p<0.05$). **(c)** Cells in which HSET, hNuf2, and zw10 were knocked down were then stained to visualise the dynein-associated protein P150 (red), kinetochores (green), and DNA (blue). Note that P150 staining decreases as chromosomes become aligned on the metaphase plate so equivalent prometaphase stage cells are shown for each condition. (**d**) Quantification of the percentage of cells with aligned chromosomes in control, HSET RNAi, hNuf2 RNAi, hNuf2+HSET RNAi and hNuf2+zw10 RNAi. Three independent experiments and approximately 300 total cells were scored per RNAi condition. The differences between the mean percentages of control versus hNuf2 RNAi, hNuf2+HSET RNAi, hNuf2+zw10 RNAi are all significant ($p<0.05$). The difference between hNuf2+HSET RNAi and hNuf2+zw10 RNAi is also significant ($p<0.01$).

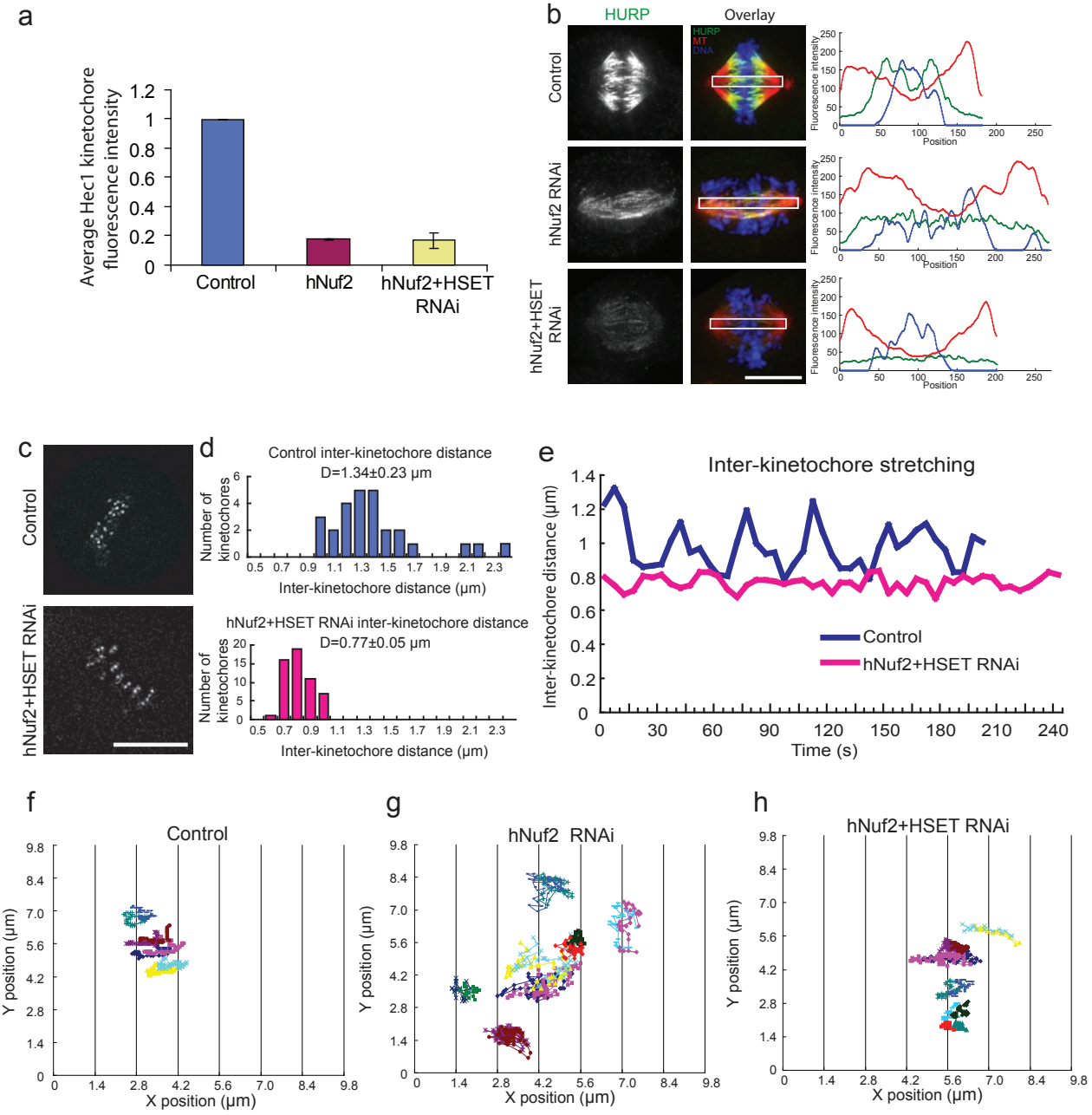

Figure S2 K-fibres have been severely disrupted after hNuf2+HSET knockdown. (**a**) Quantification of Hec1 fluorescence intensity on kinetochores in control, hNuf2 RNAi and hNuf2+HSET RNAi cells. Fluorescence intensities were measured from ~300 kinetochores total in 30 cells for each RNAi condition from three independent experiments. Fluorescence intensity was normalised to control, and the average intensity ± S.E.M. was reported in the graph. (**b**) Cells from control, hNuf2 RNAi, or hNuf2+HSET RNAi were stained to visualise MTs (red), HURP (green), DNA (blue). A 30 pixel wide box was scanned along the spindle axis, and the fluorescence intensity for each channel is plotted in the corresponding graph. (**c**) Luciferase control or hNuf2+HSET RNAi in GFP-CENP-A and GFP-gamma-tubulin expressing HeLa cells. Scale bar, 10 µm. **(d)** The distribution of inter-kinetochore distances measured is graphed for 27 kinetochores in four control cells (top) or 54 kinetochores in eight hNuf2+HSET RNAi cells (bottom). The mean distance (D) +/- SD is reported for each series of measurements. The difference between control and hNuf2+HSET RNAi is significant. ($p<0.05$) **(e)** Representative graph of the inter-kinetochore stretching versus time in a control (blue) and hNuf2+HSET RNAi cell (red) is plotted. **(f-g)** Control cells (f), hNuf2 RNAi cells (**g**), or hNuf2+HSET RNAi cells (**h**) were imaged using GFP-CENP A/GFP-gamma-tubulin/mcherry-H2B cell line on the spinning disk microscope at 5 sec time intervals for a period of 5 min. Kinetochore movements were manually tracked using Image J. The positions of each individual kinetochore were plotted on X and Y axes where each colour indicates the movement of an individual kinetochore.

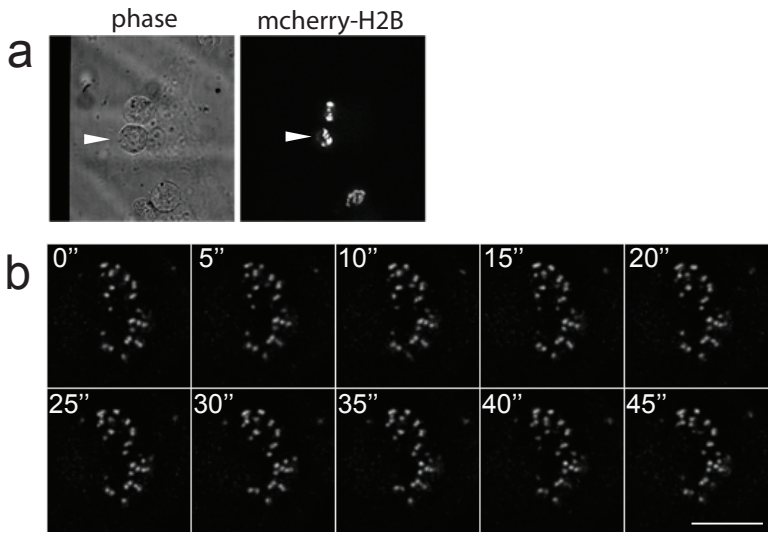

Figure S3 Analysis of Cells prior to Electron Microscopy. (**a**) hNuf2+HSET RNAi was performed in the GFP-CENP-A/GFP-gamma-tubulin/mcherry-H2B cell line. Pseudo-metaphase cells were selected by looking for cells with aligned chromosomes (as judged by mcherry-H2B fluorescence) by light microscopy. (**b**) Selected cells were imaged every 5 sec to monitor kinetochore motility. Cells showing short inter-kinetochore distance, impaired kinetochore stretching, or kinetochore orientation perturbation were fixed and processed for EM. The cell shown in this figure is a cell with short inter-kinetochore distance and severely impaired kinetochore stretching.

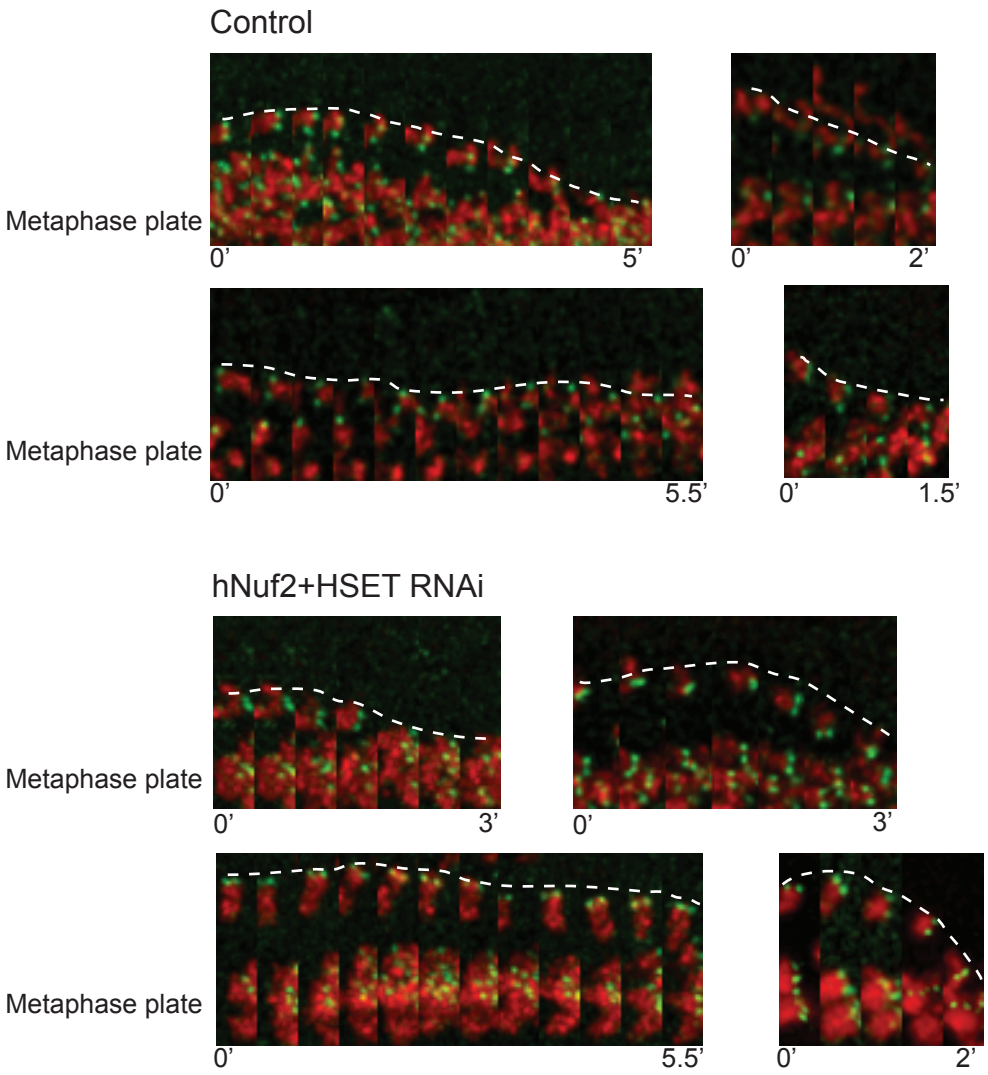

Figure S4 Kymograph of kinetochore movement during congression. Kinetochore motility was manually tracked using Image J. Kymographs were assembled from four separate image slices acquired at 30 s intervals for either control or hNuf2+HSET RNAi knockdown. A dashed line was drawn in each panel to show the trace of the kinetochore. Note that the kinetochore pairs were turning around during congression in double knockdown cells.

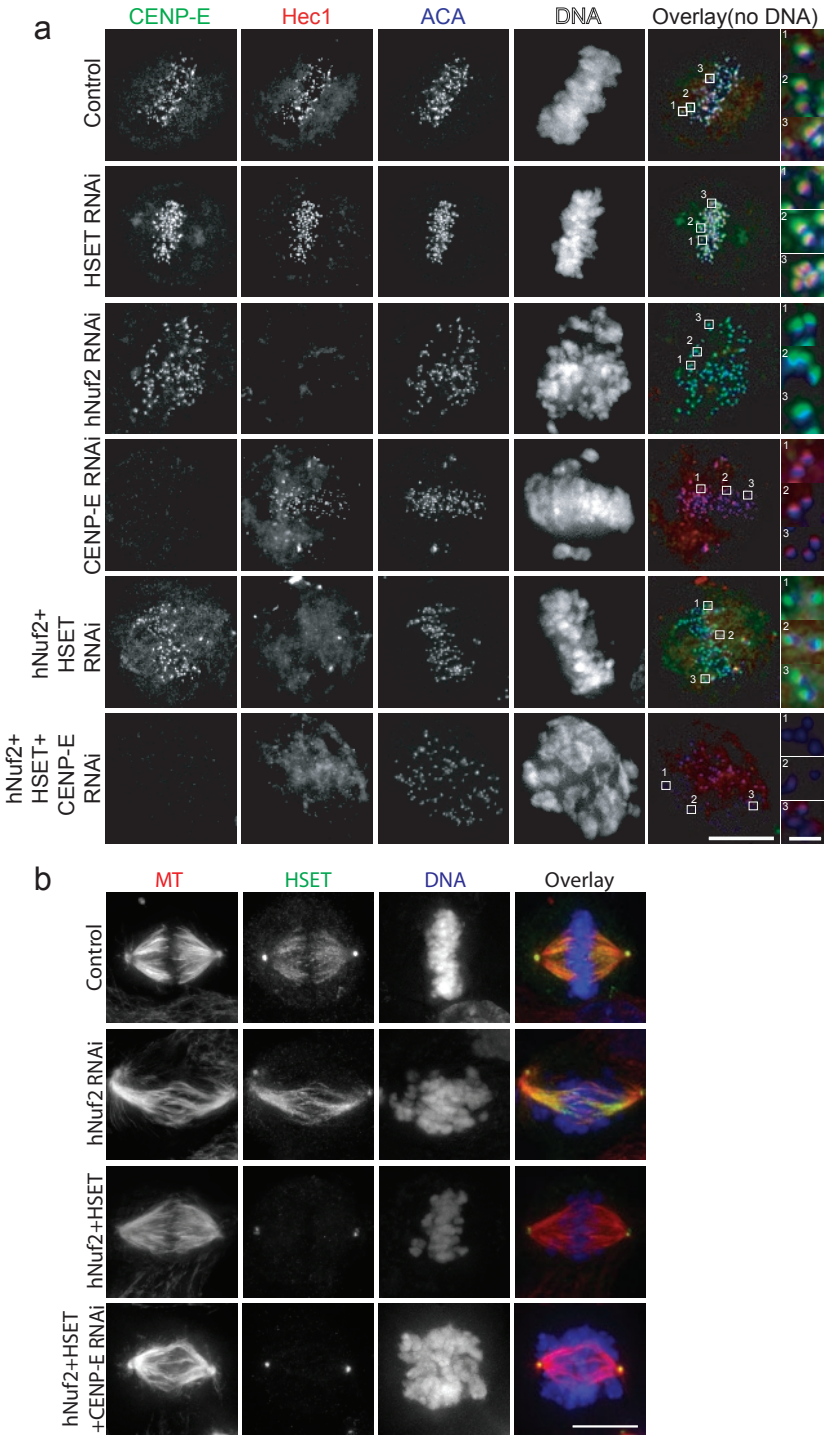

Figure S5 hNuf2 and HSET RNAi do not disrupt the localisation of CENP-E at the kinetochore. (**a**) Cells transfected with siRNAs to HSET, hNuf2, CENP-E or a combination were stained to visualise CENP-E (green), Hec1 (red), kinetochores (ACA, blue) and chromosomes (white). Note that the overlay does not include the DNA channel. The insets show the relative staining of CENP-E, Hec1 and ACA at individual kinetochore pairs. (**b**) Cells transfected with siRNAs to HSET, hNuf2, CENP-E or a combination as described in the methods section were stained to visualise HSET (green), MTs (red), chromosome (blue). Scale bar, 10 μm.

Supplementary Movie Legends

Movie S1 Kinetochores do not exhibit inter-kinetochore stretching in hNuf2+HSET RNAi cells. GFP-CENP-A and γ-tubulin-GFP expressing cells were imaged on a spinning disk confocal miscroscope equipped with a 100X objective (Apochromatic PLAN NA 1.4) and a Roper Cascade II EM-CCD camera camera. Images were acquired in three Z-axis sections (0.5 μm steps) using 100 ms exposure times and 5 s intervals for about 5 min. Image stacks were then deconvolved using Autodeblur and assembled as movies in MetaMorph with a playback speed of 15 frames per s. Note that the inter-kinetochore distance in the hNuf2+HSET RNAi cells is shorter than that in control cells and was relatively constant over time relative to control cells. Also note that the orientation of the kinetochores in the hNuf2+HSET RNAi cells is not always parallel to the spindle pole axis.

Movie S2 Mitotic progression is slowed in hNuf2+HSET RNAi cells. GFP-CENP-A, γ-tubulin-GFP, and mcherry-H2B expressing cells were imaged from nuclear envelope breakdown at 30 s time intervals for approximately 2 h on a spinning disc confocal miscroscope using a 100X objective (Apochromatic PLAN NA 1.4), 100 ms exposure time, three 0.5 μm Z stacks. Images were deconvolved using Autodeblur, and movies were assembled in MetaMorph and played back at 15 frames per s. The timestamp is in the top left corner of each movie. Notice that the cells treated with hNuf2+HSET RNAi had an extended congression time in comparison to control cells. In control cells, kinetochore pairs maintained a parallel orientation to the spindle axis over time. In contrast, some hNuf2+HSET RNAi kinetochore pairs changed their orientation frequently. Note also that hNuf2+HSET RNAi cells did not stably maintain their chromosomes at the metaphase plate.

Movie S3 Chromosomes are not stably maintained at the metaphase plate in the absence of K-fibres. Luciferase control RNAi and hNuf2+HSET RNAi cells expressing GFP-CENP-A ,GFP-γ-tubulin and mcherry-H2B were imaged after congression on a spinning disk confocal miscroscope equipped with a 100X objective (Apochromatic PLAN NA 1.4) and a Roper Cascade II EM-CCD camera. Images were acquired in three Z-axis sections (0.5 μm steps) using 100 ms exposure times and 30 s intervals for about 75 min. Image stacks were then deconvolved using Autodeblur and assembled as movies in MetaMorph with a playback speed of 15 frames per s.

Movie S4 Kinetochore pairs undergo quick excursions away from the metaphase plate in the absence of K-fibres. Luciferase control RNAi and hNuf2+HSET RNAi cells expressing GFP-CENP-A, GFP-γ-tubulin and mcherry-H2B were imaged after congression on a spinning disk confocal miscroscope equipped with a 100X objective (Apochromatic PLAN NA 1.4) and a Roper Cascade II EM-CCD camera. Images were acquired in three Z-axis sections (0.5 μm steps) using 100 ms exposure times for each channel and 5 s intervals for about 5 min. Image stacks were then deconvolved using Autodeblur and assembled as movies in MetaMorph with a playback speed of 15 frames per s. Note that in the hNuf2+HSET RNAi congressed kinetochore pairs underwent fast poleward excursions (~10 μm/min) and then moved back to the metaphase plate. Only the GFP channel is shown.

nature cell biology

Lateral microtubule bundles promote chromosome alignment during acentrosomal oocyte meiosis

Sarah M. Wignall[1,2,3] and Anne M. Villeneuve[1,2,3]

Although centrosomes serve to organize microtubules in most cell types, oocyte spindles form and mediate meiotic chromosome segregation in their absence. Here, we used high-resolution imaging of both bipolar and experimentally generated monopolar spindles in *Caenorhabditis elegans* to reveal a surprising organization of microtubules and chromosomes within acentrosomal structures. We found that homologous chromosome pairs (bivalents) are surrounded by microtubule bundles running along their sides, whereas microtubule density is extremely low at chromosome ends despite a high concentration of kinetochore proteins at those regions. Furthermore, we found that the chromokinesin KLP-19 (kinesin-like protein 19) is targeted to a ring around the centre of each bivalent and provides a polar ejection force that is required for congression. Together, these observations create a new picture of chromosome–microtubule association in acentrosomal spindles and reveal a mechanism by which metaphase alignment can be achieved using this organization. Specifically, we propose that ensheathment by lateral microtubule bundles places spatial constraints on the chromosomes, thereby promoting biorientation, and that localized motors mediate movement along these bundles, thereby promoting alignment.

In mitotically dividing cells, duplicated centrosomes are used as structural cues to define and organize the spindle poles. These centrosomes nucleate microtubules that capture the sister kinetochores of each chromosome, facilitating chromosome biorientation and congression[1]. In contrast, during meiosis in female animals the centrosomes are degraded before the meiotic divisions, and therefore oocyte spindles form in their absence. How these spindles are organized and the mechanisms by which chromosomes become bioriented and align are poorly understood. We used *C. elegans* oocyte meiosis as an *in vivo* model for investigating these mechanisms.

In the course of an RNAi (RNA-mediated interference) screen designed to identify factors involved in the assembly of the oocyte spindle (Supplementary Information, Fig. S1), we identified two proteins required for acentrosomal spindle bipolarity. Depletion of either KLP-18 (kinesin-like protein of the kinesin-12 family) or a new protein, C28C12.2 (which we named *me*iotic *sp*indle 1, or MESP-1), resulted in the formation of aster-like microtubule arrays (Figs 1a, 2a); we demonstrated that these asters were monopolar spindles by using an antibody against ASPM-1 (abnormal spindle and primary microcephaly) as a pole marker (Fig. 1b; Supplementary Information, Fig. S2). The ability to induce monopolar acentrosomal spindles *in vivo* represents a powerful experimental tool, as analogous approaches have proven valuable for investigating the function of centrosome-containing spindles[2–4]. In this study, we exploited this tool to probe acentrosomal spindle organization.

High-resolution imaging of monopolar oocyte spindles uncovered a notable and unexpected feature of chromosome–microtubule organization. Specifically, live imaging of green fluorescent protein (GFP)–tubulin and GFP–histone revealed that robust microtubule bundles run along the sides of and surround each of the six bivalents, whereas microtubule density is extremely low at the ends of the chromosomes (Fig. 2a). This organization was especially evident when examining a *z*-stack of images and focusing on the focal planes immediately surrounding each bivalent (Supplementary Information, Movie 1). Although it is possible that a relatively small number of microtubules contact the bivalent ends, by quantifying pixel intensities we measured up to a 60-fold higher density in the ensheathing microtubule bundles compared with the region adjacent to the bivalent end (Supplementary Information, Fig. S3). This notable difference indicates that lateral microtubule bundles ensheathing the chromosomes are a predominant feature of acentrosomal spindle organization. The same organization was observed in meiosis II monopolar spindles, which contain 12 individual chromosomes since homologues separate in meisosis I but a polar body does not form (Fig. 1b)[5]. Importantly, chromosomes on monopolar spindles were oriented such that their long axes were parallel to the microtubule bundles (Supplementary Information, Fig. S4A). This organization results in an arrangement in which homologues (in meiosis I) or sister chromatids (in meiosis II) are pointed in opposite directions, apparently constrained by the microtubule bundles that ensheath them.

Although these features of spindle organization were first detected in monopolar spindles, they were also observed in bipolar oocyte spindles. Prometaphase and metaphase spindles were imaged live using a

[1]Department of Developmental Biology and [2]Department of Genetics, Stanford University School of Medicine, 279 Campus Drive, Stanford, CA 94305, USA.
[3]Correspondence should be addressed to S.M.W. or A.M.V. (e-mails: swignall@stanford.edu; villen@cmgm.stanford.edu)

Received 19 January 2009; accepted 23 March 2009; published online 14 June 2009; DOI: 10.1038/ncb1891

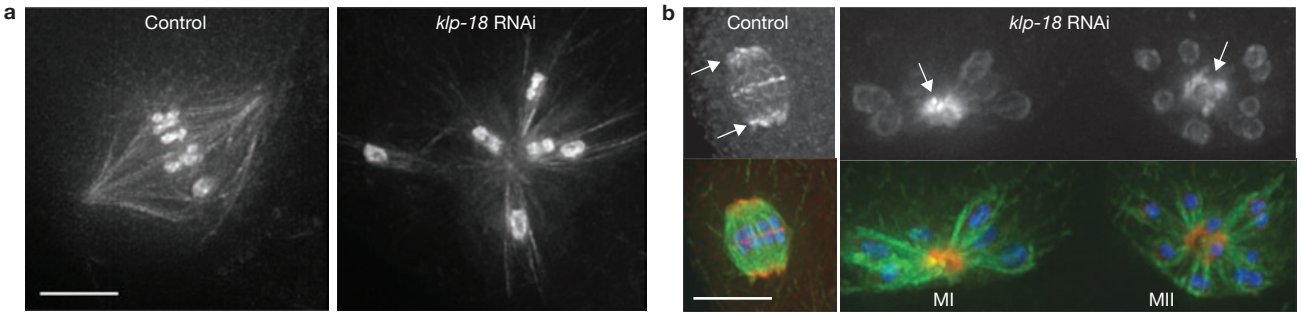

Figure 1 KLP-18 and MESP-1 are required for the bipolarity of acentrosomal oocyte meiotic spindles. (**a**) Microtubule arrays formed in live worms expressing GFP–tubulin and GFP–histone. Left panel shows a bipolar spindle formed during oocyte meiosis in a control worm. Right panel shows an astral microtubule array formed in a *klp-18* RNAi embryo. (**b**) Images of fixed oocyte spindles stained for tubulin (green), DNA (blue) and a spindle pole marker, ASPM-1 (red). ASPM-1 (top) concentrates at the poles of the control oocyte spindle (arrows, left) and marks the centres of the microtubule asters formed after *klp-18* RNAi (arrows, right) in both meiosis I (MI) and meiosis II (MII). An additional signal from the ASPM-1 antibody is also seen associated with chromosomes, but this staining is not depleted by *aspm-1* RNAi (Supplementary Information, Fig. S2). Scale bars, 5 μm.

C. elegans strain expressing GFP–tubulin and mCherry–histone (Fig. 2b; Supplementary Information, Movie 2), and also in fixed embryos (Fig. 2c). In both cases, we observed microtubule bundles ensheathing the chromosomes and a dearth of microtubule density at chromosome ends. These findings indicate that lateral associations of microtubules with chromosomes predominate in *C. elegans* acentrosomal oocyte spindles during prometaphase and metaphase. Interestingly, parallel microtubule bundles also surrounded the chromosomes at earlier stages, before a bipolar spindle was apparent (data not shown). This observation indicates that ensheathment by microtubule bundles can constrain chromosome orientation as spindles are forming, so that when bundles align in the plane of the spindle to establish bipolarity, the chromosomes will naturally biorient (here, biorientation refers to an arrangement where chromosomes are oriented axially on the spindle such that the homologues, in meiosis I, or sister chromatids, in meiosis II, are pointing towards opposite spindle poles)[6]. Thus, laterally associated microtubule bundles could serve both as a major mode of chromosome association with the spindle and as a mechanism for placing spatial constraints on the chromosomes that facilitate biorientation.

Imaging of *C. elegans* holocentric kinetochores during oocyte meiosis revealed an abundance of kinetochore proteins surrounding the ends of the bivalents[7,8] in regions where microtubule density was very low (Fig. 2d). In contrast, centrosome-containing male meiotic spindles had regions of high microtubule density immediately adjacent to the kinetochores at chromosome ends during prometaphase and metaphase (Fig. 2e; Supplementary Information, Fig. S5), suggesting that kinetochore–microtubule interactions are abundant during these stages in spermatocyte meiosis. Furthermore, whereas oocyte spindles had regions of high microtubule density extending across their centres (23/23 spindles), we found a paucity of microtubule density at the centres of spermatocyte spindles (Fig. 2e; Supplementary Information, Fig. S5; 27/28 spindles), which is consistent with a substantial fraction of microtubules terminating at the chromosomes. These contrasting results suggest that acentrosomal and centrosome-containing meiotic spindles differ with respect to the predominant mode of chromosome association with spindle microtubules. Additionally, the marked difference in microtubule density adjacent to kinetochores suggests that a substantial portion of the kinetochore material on oocyte bivalents may not support microtubule attachments during chromosome congression.

These findings raised the question of how chromosomes align on acentrosomal spindles, as classic congression models emphasize a contribution from forces provided by dynamic microtubules embedded in kinetochores[1]. Given the low density of microtubules at chromosome ends, we hypothesized that chromokinesins (which also contribute to congression during mitosis)[9] might provide a driving force to move chromosomes along lateral microtubule bundles. We focused on KLP-19, as it provides a polar ejection force to push chromosomes towards the metaphase plate during mitosis and localizes to the mid-bivalent (where homologues are connected by chiasmata) during meiosis I (ref. 10). High-resolution imaging of KLP-19 on prometaphase/metaphase oocyte spindles revealed that it forms a ring around the centre of each bivalent (in meiosis I) and around the sister chromatid interface (in meiosis II; Fig. 3a and data not shown). As these domains ultimately align at the metaphase plate, localization of KLP-19 to a ring around these regions makes it a good candidate for promoting congression through interaction with the microtubule bundles surrounding the chromosomes. To assess effects on chromosome alignment, we used a *C. elegans* strain containing a temperature-sensitive mutation affecting the anaphase promoting complex (APC) to enrich for metaphase I spindles. Although RNAi-induced KLP-19 depletion did not prevent ensheathment of bivalents by microtubule bundles or cause chromosome orientation defects (Fig. S4b), we observed severe defects in metaphase alignment (Fig. 4a), indicating a role for this chromokinesin in congression. Furthermore, depletion of KLP-19 on monopolar oocyte spindles (generated by KLP-18 depletion) caused the bivalents to be found closer to the centre of each aster (Fig. 4b), indicating that KLP-19 provides a polar ejection force that moves chromosomes towards microtubule plus-ends. These findings support the hypothesis that KLP-19 contributes to congression on acentrosomal spindles by providing a polar ejection force to move chromosomes along lateral microtubule bundles towards the metaphase plate.

Given that chromokinesins associate broadly with non-kinetochore chromatin during mitosis[9,10], our finding that KLP-19 is concentrated in a mid-bivalent ring during meiosis led us to speculate that the targeting of KLP-19 to this location may be important for its activity or regulation. As the chromosome passenger complex (CPC) localizes to the mid-bivalent (meiosis I) and the sister chromatid interface (meiosis II)[11–15], we assessed the relationship between this complex and KLP-19. The CPC consists of the AIR-2 (aurora/IpI1-related kinase), ICP-1

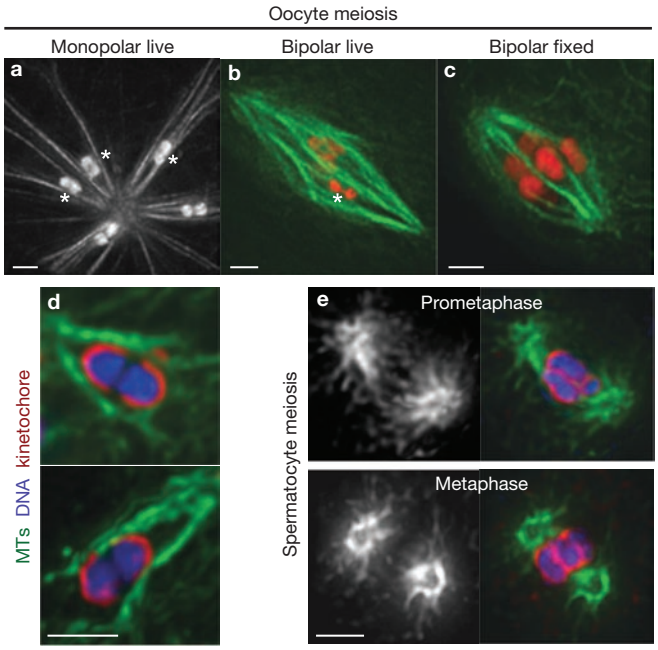

Figure 2 Chromosomes are ensheathed by lateral microtubule bundles in acentrosomal spindles. (**a**–**c**) Images are partial projections of 3D stacks that highlight the nature of the interactions between microtubules and individual bivalents: specifically, microtubule bundles associate laterally with the bivalents and microtubule density is low near bivalent ends. When multiple chromosomes are displayed in the same image, asterisks mark bivalents where this organization is most evident. (**a**) Monopolar spindle formed following *mesp-1* RNAi, imaged in a live worm expressing GFP–tubulin and GFP–histone. (**b**) Live image of a bipolar oocyte meiotic spindle in a worm expressing GFP–tubulin (green) and mCherry–histone (red). (**c**) Image of a bipolar oocyte spindle fixed and stained for DNA (Hoechst; red) and tubulin (green). (**d**) Close-up images of bivalents in monopolar spindles formed after *klp-18* RNAi, stained for tubulin (green; MTs, microtubules), DNA (blue) and the kinetochore protein KNL-3 (red). Kinetochore proteins form cup-like structures around the bivalents[7,8]. Microtubule density is low at the ends of the bivalents, despite concentrated kinetochore proteins in those regions. (**e**) Prometaphase (top) and metaphase (bottom) centrosome-containing spindles formed during spermatocyte meiosis. Images on the right show DNA (Hoechst; blue), tubulin (green) and KNL-3 (red); tubulin alone is shown on the left. In contrast to oocyte meiosis, high microtubule density is observed adjacent to kinetochores at chromosome ends, and microtubule density is low at the spindles centres. Scale bars, 2 μm.

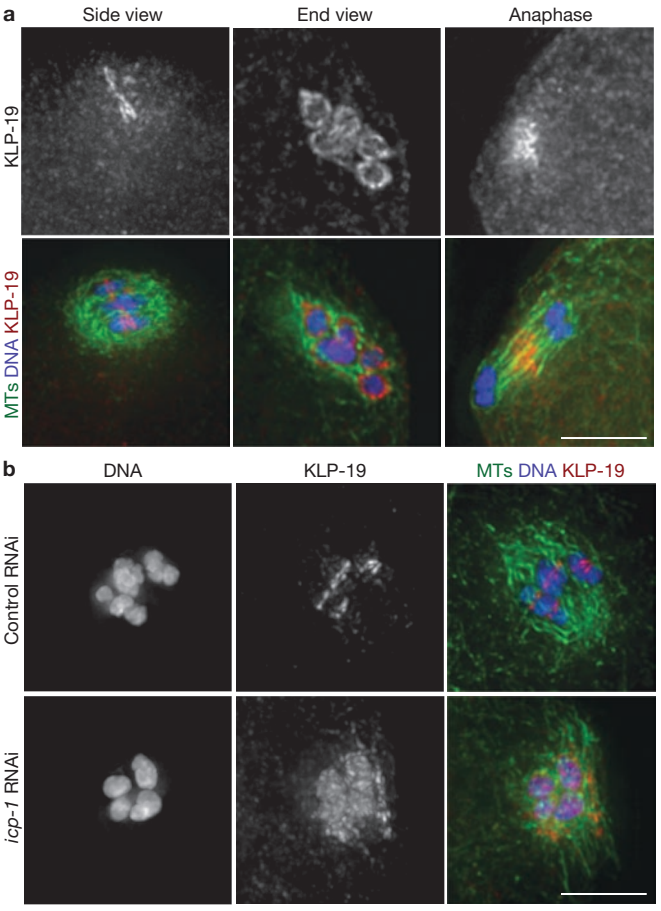

Figure 3 Localization of the chromokinesin KLP-19 to a ring at the mid-bivalent is regulated by the chromosome passenger complex. All images show oocyte spindles stained for tubulin (green; MTs, microtubules), DNA (blue) and KLP-19 (red). (**a**) Imaging of KLP-19 localization during wild-type oocyte meiosis. Left panel is a side view of a metaphase I spindle, showing KLP-19 concentrated at the mid-bivalent. Middle panel is an end view of a prometaphase I spindle, showing that KLP-19 forms rings around the chromosomes. Right panel is a side view of an anaphase I spindle, showing that KLP-19 is no longer associated with chromosomes and instead is localized to the central spindle. (**b**) KLP-19 localization is disrupted following depletion of the chromosome passenger complex component ICP-1. Whereas KLP-19 is concentrated at the mid-bivalent following control RNAi, KLP-19 spreads all over the chromosomes and partially onto the spindle following *icp-1* RNAi. Scale bars, 5 μm.

(INCENP), BIR-1 (baculovirus inhibitory repeat family member) and CSC-1 (chromosome segregation and cytokinesis defective). Similarly to KLP-19, CPC proteins localize to a ring around the centre of the chromosomes during prometaphase/metaphase of meiosis I and II (Supplementary Information, Fig. S6A, B; M. Schvarzstein and A.M.V., unpublished data). Moreover, KLP-19 relocalized to the central spindle during anaphase I and II (Fig. 3a and data not shown), as has been shown previously for the CPC. To determine whether KLP-19 localization is CPC-dependent, we depleted ICP-1 using RNAi, which causes the removal of AIR-2 (ref. 16; Supplementary Information, Fig. S6C) and other CPC components[15] from chromosomes. Under these conditions, KLP-19 spread all over the chromosomes and partially onto the spindle (Fig. 3b) and we observed severe chromosome congression defects, similar to those elicited by *klp-19* RNAi (Fig. 4a). These results indicate that the CPC is required to restrict KLP-19 to the rings around meiotic chromosomes. Furthermore, although it is possible that the CPC contributes to chromosome alignment in other ways, these findings are consistent with the hypothesis that concentration of KLP-19 into this ring configuration is required for proper congression.

Taken together, our data support a model in which chromosome congression on the *C. elegans* acentrosomal oocyte spindle is driven primarily by movement of chromosomes along laterally associated microtubule bundles. In this model (Fig. 5), ensheathment of chromosomes by microtubule bundles imposes spatial constraints that result in biorientation. Additionally, plus-end directed motors targeted to the mid-bivalent during meiosis I (or to the sister-chromatid interface during meiosis II) interact with antiparallel microtubule bundles in the spindle. In principle, metaphase alignment could be achieved in this context primarily by attaining a balance of anti-poleward forces driving chromosomes towards the plus ends of these overlapping

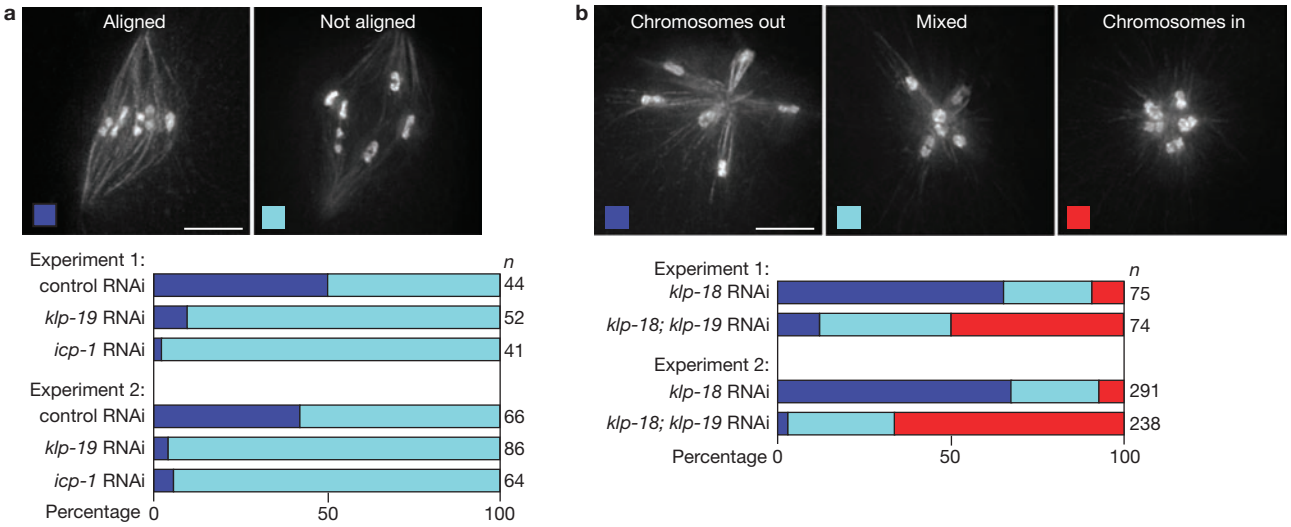

Figure 4 KLP-19 provides a polar ejection force to position meiotic chromosomes. (**a**) Chromosome alignment was quantified in worms expressing GFP–tubulin and GFP–histone and in which meiosis was arrested at metaphase I. Images show examples of oocyte spindles with aligned (left) and unaligned (right) chromosomes. Stacked bar graphs depict the percentages of bipolar spindles examined that had the indicated configuration of chromosomes. *klp-19* RNAi and *icp-1* RNAi cause an increase in spindles with unaligned chromosomes ($P > 0.0001$, determined using the Fisher exact test). (**b**) The positions of chromosomes on monopolar spindles were quantified in worms expressing GFP–tubulin and GFP–histone, which were arrested at metaphase of meiosis I. Images show examples of monopolar spindles with all of the chromosomes out (left), all in (right) or with a mixed population (middle). Stacked bar graphs depict percentages of monopolar spindles with the indicated configuration of chromosomes. KLP-19 depletion results in an increase in structures where the chromosomes are found closer to the centre of the asters ($P > 0.0001$, determined using the Chi Square test). Scale bars, 5 μm.

bundles. However, it is likely that opposing poleward forces also operate at this stage, as chromosomes are not ejected from monopolar spindles (where microtubule plus-ends are oriented towards the outside). Given the predominance of lateral microtubule–chromosome associations in acentrosomal spindles, we suggest that such poleward forces may also be mediated through lateral interactions.

Several features of the proposed mechanisms by which lateral microtubule interactions promote chromosome alignment during oocyte meiosis are quite distinct from the ways in which lateral associations aid biorientation and congression during mitosis. During mitotic prometaphase in yeast[17] and vertebrate cells[18–20], kinetochores initially associate with the lateral surfaces of microtubules and these associations can then be converted into end-on attachments. Additionally, when a chromosome is mono-oriented in mammalian cells, movement of the chromosome towards the metaphase plate along the sides of microtubules can promote capture of the unattached kinetochore by microtubules emanating from the opposite pole, resulting in biorientation[21]. In contrast, acentrosomal spindles must form and achieve biorientation and congression in the absence of pre-defined spindle poles; therefore a 'search and capture' strategy is not thought to be used[1]. Instead, we propose that lateral associations play several roles that together promote chromosome alignment. First, ensheathment of chromosomes between parallel microtubule bundles promotes biorientation by constraining the orientation of meiotic chromosomes such that homologous chromosomes (in meiosis I), or sister chromatids (in meiosis II), point in opposite directions, even in the context of monopolar spindles (where bipolar tension is not applied to the bivalents). Furthermore, targeting of motors involved in congression to the domains where cohesion will be released during the meiotic divisions ensures that these regions will be aligned on the metaphase plate, thereby promoting accurate chromosome segregation. An important feature of this model, distinguishing it from models involving centrosome-containing spindles, is that it requires neither capture of kinetochores by microtubule ends, nor forces generated by microtubules associated with chromosome ends, to achieve chromosome biorientation or congression.

Although our model provides a mechanism by which chromosomes can orient and align without a requirement for kinetochore–microtubule end attachments, it is possible that kinetochore proteins located on the sides of the bivalent do contribute to the ensheathment of chromosomes by lateral microtubule bundles. Consistent with this possibility, depletion of kinetochore components during oocyte meiosis causes defects in bivalent orientation (J. Dumont and A. Desai, personal communication). However, a potential involvement of kinetochore proteins in mediating lateral associations is compatible with our model, as such interactions could promote chromosome ensheathment and orientation even in the absence of spindle bipolarity.

The view of chromosome–microtubule organization that has emerged from our analysis of *C. elegans* oocyte meiosis is likely to be relevant for acentrosomal spindles in general. Images of wild-type and mutant oocyte spindles in *Drosophila melanogaster* are consistent with the possibility that their bivalents are also encased by laterally associated microtubule bundles[22–25]. Moreover, features of our model may help explain the previous intriguing observation that in mouse oocytes, both substantial congression and biorientation of bivalents occur several hours before the establishment of detectable end-on microtubule–kinetochore associations[26,27]. Although it had been assumed that biorientation in this context was mediated by unstable microtubule associations in the vicinity of kinetochores, in light of our current findings we suggest an alternative view. Specifically, we envision that bivalents in mouse oocytes may be similarly ensheathed by lateral microtubule bundles and that this may enable congression and biorientation of bivalents (without requiring

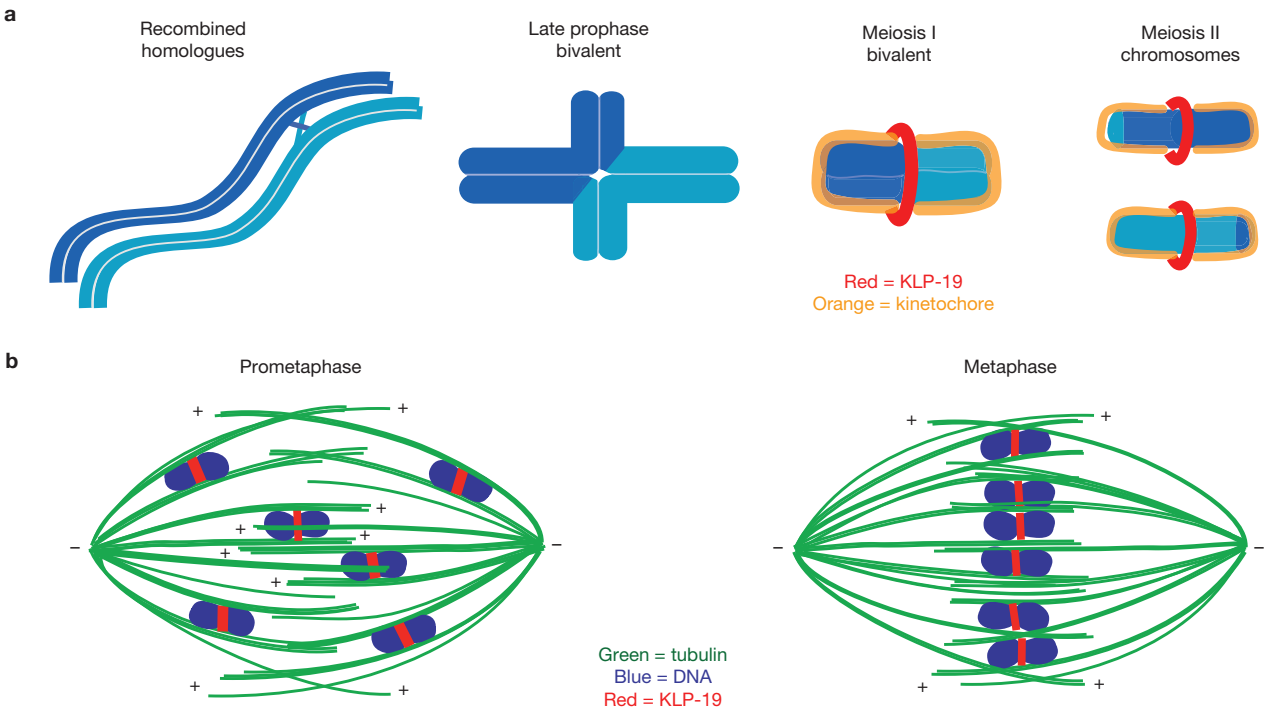

Figure 5 Model of chromosome organization and congression on acentrosomal spindles. (**a**) Schematic of chromosome organization during *C. elegans* meiosis. A pair of homologous chromosomes is depicted in light and dark blue. During mid prophase, a single crossover recombination event occurs between parallel-aligned homologues (far left). During late prophase, the chromosomes condense and reorganize into a cruciform bivalent structure in which the homologues are linked by a chiasma, a structure resulting from the crossover in combination with sister chromatid cohesion (middle-left); as the crossover usually occurs at an off-centre position, the bivalent contains long and short arms. Before the initiation of the meiotic divisions, the bivalent condenses further (making the short arms difficult to distinguish) and the holocentric kinetochore (orange) forms around each half of the bivalent (middle-right). By prometaphase, KLP-19 (red) forms a ring around the centre of the bivalent. In meiosis II, the homologues are separate (far right). The kinetochore forms around each sister chromatid, and KLP-19 forms a ring at the interface between the sisters. (**b**) Model of chromosome congression on acentrosomal spindles. Parallel microtubule bundles ensheath meiotic chromosomes, promoting biorientation. KLP-19 (red) forms a ring around these chromosomes and provides a force to move them along lateral microtubule bundles towards microtubule plus ends. Chromosomes align at the metaphase plate by achieving a balance of forces resulting from lateral associations of chromosomes with overlapping antiparallel microtubule bundles associated with opposite spindle poles. The regions of the chromosomes around which KLP-19 forms a ring during prometaphase and metaphase are the domains where sister chromatid cohesion will be released at the corresponding meiotic division. This localization of congression-promoting motors ensures that these chromosomal domains will be aligned on the metaphase plate, thereby promoting homologue segregation (at anaphase I) or sister chromatid segregation (at anaphase II).

kinetochore–microtubule end attachments), as described in our proposed model (Fig. 5).

During meiosis in mouse oocytes, kinetochores eventually interact with microtubule ends and form kinetochore fibres just before the metaphase to anaphase transition[26]. It is possible that such end-on interactions are also established in *C. elegans* oocytes and could provide a poleward force to drive anaphase A. Alternatively, chromosome segregation could be accomplished by chromosome movement along laterally associated microtubule bundles, using the proposed poleward force that opposes KLP-19 during prometaphase. Under either scenario, we suggest that removal of KLP-19 (and regulatory factors such as the CPC) from chromosomes at anaphase may contribute to their separation to the spindle poles by relieving the forces that push them to the metaphase plate.

In addition to providing a new view of how chromosome congression is achieved on acentrosomal spindles, our studies identified two proteins (KLP-18 and MESP-1) required for spindle bipolarity. Although the Kinesin-12 family motor KLP-18 is known to be required for oocyte spindle assembly[5], our high-resolution analysis allowed us to ascribe a specific role for this protein in the establishment and/or maintenance of bipolarity. This finding is intriguing given previous work in *Xenopus laevis* egg extracts. While addition of a dominant-negative form of *Xenopus* Kinesin-12 to extracts caused bipolarity defects[28], immunodepletion did not significantly affect spindle assembly[29,30], leading to confusion about the function of this motor. In light of our findings, we speculate that Kinesin-12 motors may have a conserved role in promoting bipolarity, but that their contributions may be masked in some organisms by Kinesin-5 (which functions in bipolarity establishment and maintenance)[31]. Intriguingly, recent *Xenopus* experiments have revealed conditions where spindle bipolarity can be achieved in the absence of Kinesin-5 function[32,33]; it will be interesting to test whether Kinesin-12 provides this activity. Thus, analysis of spindle assembly in *C. elegans* (an organism where Kinesin-5 does not dominate)[34] provided an opportunity to identify new factors promoting bipolarity and we expect that future studies of these proteins will shed light on how bipolarity is established in the absence of centrosomes. Moreover, the ability to induce the formation of monopolar acentrosomal spindles will be a valuable tool for future studies of chromosome dynamics during oocyte meiosis. □

METHODS

Methods and any associated references are available in the online version of the paper at http://www.nature.com/naturecellbiology/.

Note: Supplementary Information is available on the Nature Cell Biology website.

ACKNOWLEDGEMENTS

We thank members of the Villeneuve laboratory for support and discussions, R. Heald, V. Indjeian and M. Schvarzstein for comments on the manuscript, J. Monen, P. Maddox and members of the Desai and Oegema laboratories for technical advice, J. Dumont and A. Desai for sharing data before publication, and J. Audhya, B. Bowerman, A. Desai, B. Meyer, J. Powers and J. Schumacher for reagents. Additionally, some strains used in this work were provided by the Caenorhabditis Genetics Center, which is funded by the NIH National Center for Research Resources (NCRR). This work was supported by an NIH grant (RO1 GM53804) to A.M.V.; S.M.W. was a Damon Runyon Fellow supported by the Damon Runyon Cancer Research Foundation (DRG-#1827-04) and is currently a Special Fellow of the Leukemia and Lymphoma Society.

AUTHOR CONTRIBUTIONS

All experimental data and figures were generated by S.M.W., who also had primary responsibility for experimental design, data analysis and manuscript writing. A.M.V. contributed to experimental design, data analysis and manuscript writing.

COMPETING FINANCIAL INTERESTS

The authors declare no competing financial interests.

Published online at http://www.nature.com/naturecellbiology/.
Reprints and permissions information is available online at http://npg.nature.com/reprintsandpermissions/.

1. Walczak, C. E. & Heald, R. Mechanisms of mitotic spindle assembly and function. *Int. Rev. Cytol.* **265,** 111–158 (2008).
2. Kapoor, T. M., Mayer, T. U., Coughlin, M. L. & Mitchison, T. J. Probing spindle assembly mechanisms with monastrol, a small molecule inhibitor of the mitotic kinesin, Eg5. *J. Cell Biol.* **150,** 975–988 (2000).
3. Canman, J. C. *et al.* Determining the position of the cell division plane. *Nature* **424,** 1074–1078 (2003).
4. Lampson, M. A., Renduchitala, K., Khodjakov, A. & Kapoor, T. M. Correcting improper chromosome-spindle attachments during cell division. *Nature Cell Biol.* **6,** 232–237 (2004).
5. Segbert, C. *et al.* KLP-18, a Klp2 kinesin, is required for assembly of acentrosomal meiotic spindles in Caenorhabditis elegans. *Mol. Biol. Cell* **14,** 4458–4469 (2003).
6. Albertson, D. G. & Thomson, J. N. Segregation of holocentric chromosomes at meiosis in the nematode, *Caenorhabditis elegans*. *Chromosome Res.* **1,** 15–26 (1993).
7. Howe, M., McDonald, K. L., Albertson, D. G. & Meyer, B. J. HIM-10 is required for kinetochore structure and function on *Caenorhabditis elegans* holocentric chromosomes. *J. Cell Biol.* **153,** 1227–1238 (2001).
8. Monen, J., Maddox, P. S., Hyndman, F., Oegema, K. & Desai, A. Differential role of CENP-A in the segregation of holocentric *C. elegans* chromosomes during meiosis and mitosis. *Nature Cell Biol.* **7,** 1248–1255 (2005).
9. Mazumdar, M. & Misteli, T. Chromokinesins: multitalented players in mitosis. *Trends Cell Biol.* **15,** 349–355 (2005).
10. Powers, J. *et al.* Loss of KLP-19 polar ejection force causes misorientation and missegregation of holocentric chromosomes. *J. Cell Biol.* **166,** 991–1001 (2004).
11. Schumacher, J. M., Golden, A. & Donovan, P. J. AIR-2: An Aurora/Ipl1-related protein kinase associated with chromosomes and midbody microtubules is required for polar body extrusion and cytokinesis in *Caenorhabditis elegans* embryos. *J. Cell Biol.* **143,** 1635–1646 (1998).
12. Speliotes, E. K., Uren, A., Vaux, D. & Horvitz, H. R. The survivin-like *C. elegans* BIR-1 protein acts with the Aurora-like kinase AIR-2 to affect chromosomes and the spindle midzone. *Mol. Cell* **6,** 211–223 (2000).
13. Rogers, E., Bishop, J. D., Waddle, J. A., Schumacher, J. M. & Lin, R. The aurora kinase AIR-2 functions in the release of chromosome cohesion in *Caenorhabditis elegans* meiosis. *J. Cell Biol.* **157,** 219–229 (2002).
14. Kaitna, S., Pasierbek, P., Jantsch, M., Loidl, J. & Glotzer, M. The aurora B kinase AIR-2 regulates kinetochores during mitosis and is required for separation of homologous Chromosomes during meiosis. *Curr. Biol.* **12,** 798–812 (2002).
15. Romano, A. *et al.* CSC-1: a subunit of the Aurora B kinase complex that binds to the survivin-like protein BIR-1 and the incenp-like protein ICP-1. *J. Cell Biol.* **161,** 229–236 (2003).
16. Kaitna, S., Mendoza, M., Jantsch-Plunger, V. & Glotzer, M. Incenp and an aurora-like kinase form a complex essential for chromosome segregation and efficient completion of cytokinesis. *Curr. Biol.* **10,** 1172–1181 (2000).
17. Tanaka, K. *et al.* Molecular mechanisms of kinetochore capture by spindle microtubules. *Nature* **434,** 987–994 (2005).
18. Rieder, C. L. & Alexander, S. P. Kinetochores are transported poleward along a single astral microtubule during chromosome attachment to the spindle in newt lung cells. *J. Cell Biol.* **110,** 81–95 (1990).
19. Hayden, J. H., Bowser, S. S. & Rieder, C. L. Kinetochores capture astral microtubules during chromosome attachment to the mitotic spindle: direct visualization in live newt lung cells. *J. Cell Biol.* **111,** 1039–1045 (1990).
20. Merdes, A. & De Mey, J. The mechanism of kinetochore-spindle attachment and polewards movement analyzed in PtK2 cells at the prophase-prometaphase transition. *Eur. J. Cell Biol.* **53,** 313–325 (1990).
21. Kapoor, T. M. *et al.* Chromosomes can congress to the metaphase plate before biorientation. *Science* **311,** 388–391 (2006).
22. Skold, H. N., Komma, D. J. & Endow, S. A. Assembly pathway of the anastral *Drosophila* oocyte meiosis I spindle. *J. Cell Sci.* **118,** 1745–1755 (2005).
23. Cullen, C. F., Brittle, A. L., Ito, T. & Ohkura, H. The conserved kinase NHK-1 is essential for mitotic progression and unifying acentrosomal meiotic spindles in *Drosophila melanogaster*. *J. Cell Biol.* **171,** 593–602 (2005).
24. Jang, J. K., Rahman, T. & McKim, K. S. The kinesinlike protein Subito contributes to central spindle assembly and organization of the meiotic spindle in *Drosophila* oocytes. *Mol. Biol. Cell* **16,** 4684–4694 (2005).
25. Jang, J. K., Rahman, T., Kober, V. S., Cesario, J. & McKim, K. S. Misregulation of the kinesin-like protein Subito induces meiotic spindle formation in the absence of chromosomes and centrosomes. *Genetics* **177,** 267–280 (2007).
26. Brunet, *S. et al.* Kinetochore fibers are not involved in the formation of the first meiotic spindle in mouse oocytes, but control the exit from the first meiotic M phase. *J. Cell Biol.* **146,** 1–12 (1999).
27. Schuh, M. & Ellenberg, J. Self-organization of MTOCs replaces centrosome function during acentrosomal spindle assembly in live mouse oocytes. *Cell* **130,** 484–498 (2007).
28. Boleti, H., Karsenti, E. & Vernos, I. Xklp2, a novel *Xenopus* centrosomal kinesin-like protein required for centrosome separation during mitosis. *Cell* **84,** 49–59 (1996).
29. Walczak, C. E., Vernos, I., Mitchison, T. J., Karsenti, E. & Heald, R. A model for the proposed roles of different microtubule-based motor proteins in establishing spindle bipolarity. *Curr. Biol.* **8,** 903–913 (1998).
30. Wittmann, T., Wilm, M., Karsenti, E. & Vernos, I. TPX2, A novel *Xenopus* MAP involved in spindle pole organization. *J. Cell Biol.* **149,** 1405–1418 (2000).
31. Kashina, A. S., Rogers, G. C. & Scholey, J. M. The bimC family of kinesins: essential bipolar mitotic motors driving centrosome separation. *Biochim. Biophys. Acta* **1357,** 257–271 (1997).
32. Mitchison, T. *J. et al.* Roles of polymerization dynamics, opposed motors, and a tensile element in governing the length of *Xenopus* extract meiotic spindles. *Mol. Biol. Cell* **16,** 3064–3076 (2005).
33. Yang, *G. et al.* Architectural dynamics of the meiotic spindle revealed by single-fluorophore imaging. *Nature Cell Biol.* **9,** 1233–1242 (2007).
34. Bishop, J. D., Han, Z. & Schumacher, J. M. The *Caenorhabditis elegans* Aurora B kinase AIR-2 phosphorylates and is required for the localization of a BimC kinesin to meiotic and mitotic spindles. *Mol. Biol. Cell* **16,** 742–756 (2005).

METHODS

Strains. In this study, 'wild-type' refers to N2 (Bristol) worms, while 'control' refers to control RNAi worms. For most experiments, integrated lines expressing GFP–tubulin; GFP–histone (strain EU1067; a gift from B. Bowerman, University of Oregon, USA) or GFP–tubulin; mCherry–histone (strain OD57; a gift from Jon Audhya, University of California San Diego, USA)[35] were used. *emb-27(g48)* worms obtained from the *C. elegans* Genetics Center were crossed with EU1067 to create the strain AV335 *emb-27(g48)II; unc-119(ed3) ruIs32[unc-119(+) pie-1^{promoter}::gfp-H2B]III; ruIs57[[unc-119(+) pie-1^{promoter}::gfp–tubulin]*; these worms were used for all experiments requiring APC-arrest. Metaphase I-arrest was achieved by increasing the temperature of adult AV335 worms from 20 °C to 25 °C for 5–7 h before imaging.

RNAi. Individual RNAi clones picked from an RNAi feeding library[36,37] were used to inoculate Luria broth + ampicillin (100 μg ml^{-1}) for overnight cultures. These saturated cultures were used to seed nematode growth media (NGM) plates containing ampicillin (100 μg ml^{-1}) and IPTG (isopropyl-β-D-thiogalactopyranoside;1 mM). Plates were left at room temperature overnight to induce double-stranded RNA formation. The next day, L1 worms synchronized by bleaching were plated and grown to adulthood at 15 °C for five days. Control plates were seeded with bacteria containing an empty feeding library vector (L4440).

Immunofluorescence. Immunofluorescence was performed as described previously[8,38], using a fixation time of 30 min in methanol at –20°C. Primary antibodies used were: mouse anti-α-tubulin (DM1α; 1:500 dilution; Sigma), rabbit anti-KLP-19 (1:4000 dilution; ref. 10), rabbit anti-AIR-2 (1:250 dilution; ref. 11), rabbit anti-KNL-3 (1:4000 dilution; ref. 39), rat anti-HIM-10 (1:500 dilution; ref. 7) and rabbit anti-ASPM-1 (1:4000 dilution). The anti-ASPM-1 antibody (a gift from A. Desai, University of California San Diego, USA) was raised and affinity purified against amino-acids 9–165. Secondary antibodies used were: Alexa Fluor 488-conjugated goat anti-mouse and Alexa Fluor 555-conjugated goat anti-rabbit antibodies (both at a 1:400 dilution).

High-resolution imaging. For live imaging, GFP- or mCherry-expressing worms were mounted on Multitest slides (MP Biomedicals). Each worm was picked onto a drop of M9 buffer containing tricaine (0.1%) and tetramisole[40] (0.01%), a coverslip was laid on top and the slide was imaged immediately. Deltavision deconvolution microscopy with a 100× objective was used for both live and fixed imaging. Image stacks were obtained at 0.2 μm *z*-steps for fixed samples and 0.3 μm for live imaging, deconvolved and projected for presentation. Except where noted, images are full projections of data stacks encompassing the entire meiotic spindle. In some cases, partial projections are displayed to highlight particular features of spindle organization. Movies show individual *z*-sections displayed at two sections per second. Control and RNAi worms were processed in parallel and image exposure times were kept constant within each experiment.

To quantitatively compare the fluorescence intensities of microtubules ensheathing the chromosomes with fluorescence adjacent to the bivalent ends, individual pixel intensities within a 4×33–34 pixel area spanning the ensheathing microtubule bundles in the vicinity of the bivalent ends were determined and plotted using softWoRx software (Applied Precision; Supplementary Information, Fig. S3). Pixel intensities in the domains outside the ensheathing microtubule bundles were averaged for each image, and these average values were then subtracted from the dataset. These subtracted values were used to calculate ratios between the peak intensity of each ensheathing bundle and the region of minimum intensity between the bundles.

Quantification. For quantification of bivalent orientation, worms expressing GFP–histone and GFP–tubulin were fixed in ethanol by picking worms onto a slide, adding ethanol (100%) and letting the ethanol evaporate (this ethanol step was performed three times before adding mounting media). This fixation preserved GFP fluorescence and allowed high-resolution images to be acquired. For monopolar spindles (generated by *klp-18* RNAi), chromosome orientation was determined by tracing a line from the centre of each aster through the midpoint of each bivalent. A second line was then drawn mirroring the long axis of each bivalent, and the angle between the two lines was measured (Supplementary Information, Fig. S4). For bipolar spindles, bivalents were classified either as oriented or not oriented; bivalents were considered to be oriented if their long axes were parallel with the spindle axis.

For quantification of RNAi phenotypes, APC-arrested worms expressing GFP–histone and GFP–tubulin were mounted live and visualized using a 63× objective with a Zeiss Axioplan II microscope. Although the APC-arrest conditions yielded a row of embryos arrested at metaphase I, only the most recently fertilized embryo from each gonad arm (the +1 embryo, next to the spermatheca) was analysed to avoid the possibility of problems introduced by prolonged arrest. For quantitation of chromosome congression, only embryos that had assembled bipolar spindles were considered. A subset of +1 embryos in both control and experimental worms had disorganized microtubule arrays, presumably reflecting earlier stages of spindle assembly. For *klp-19* RNAi, the fractions of embryos in this excluded class were similar to control worms in both experiments (experiment 1: control 51.1%, *klp-19* RNAi 48%, $P = 0.77$; experiment 2: control 29%, *klp-19* RNAi 25.9%, $P = 0.64$). However, *icp-1* RNAi embryos showed an increase in disorganized arrays, possibly reflecting additional roles for ICP-1 (experiment 1: control 51.1%, *icp-1* RNAi 61.7%, $P = 0.15$; experiment 2: control 29%, *icp-1* RNAi 52.9%, $P = 0.0004$). In experiments assessing chromosome positions on monopolar spindles, all +1 embryos in both control (*klp-18* RNAi) and experimental (*klp-18* RNAi; *klp-19* RNAi) worms showed clear aster-like monopolar spindles, suggesting that monopolar spindles form immediately after initiation of the meiotic divisions.

35. McNally, K., Audhya, A., Oegema, K. & McNally, F. J. Katanin controls mitotic and meiotic spindle length. *J. Cell Biol.* **175,** 881–891 (2006).
36. Fraser, A. *G. et al.* Functional genomic analysis of *C. elegans* chromosome I by systematic RNA interference. *Nature* **408,** 325–330 (2000).
37. Kamath, R. S. *et al.* Systematic functional analysis of the *Caenorhabditis elegans* genome using RNAi. *Nature* **421,** 231–237 (2003).
38. Oegema, K., Desai, A., Rybina, *S.*, Kirkham, M. & Hyman, A. A. Functional analysis of kinetochore assembly in *Caenorhabditis elegans*. *J. Cell Biol.* **153,** 1209–1226 (2001).
39. Cheeseman, I. M. *et al.* A conserved protein network controls assembly of the outer kinetochore and its ability to sustain tension. *Genes Dev.* **18,** 2255–2268 (2004).
40. McCarter, J., Bartlett, B., Dang, T. & Schedl, T. On the control of oocyte meiotic maturation and ovulation in *Caenorhabditis elegans*. *Dev. Biol.* **205,** 111–128 (1999).

nature cell biology

DOI: 10.1038/ncb1891

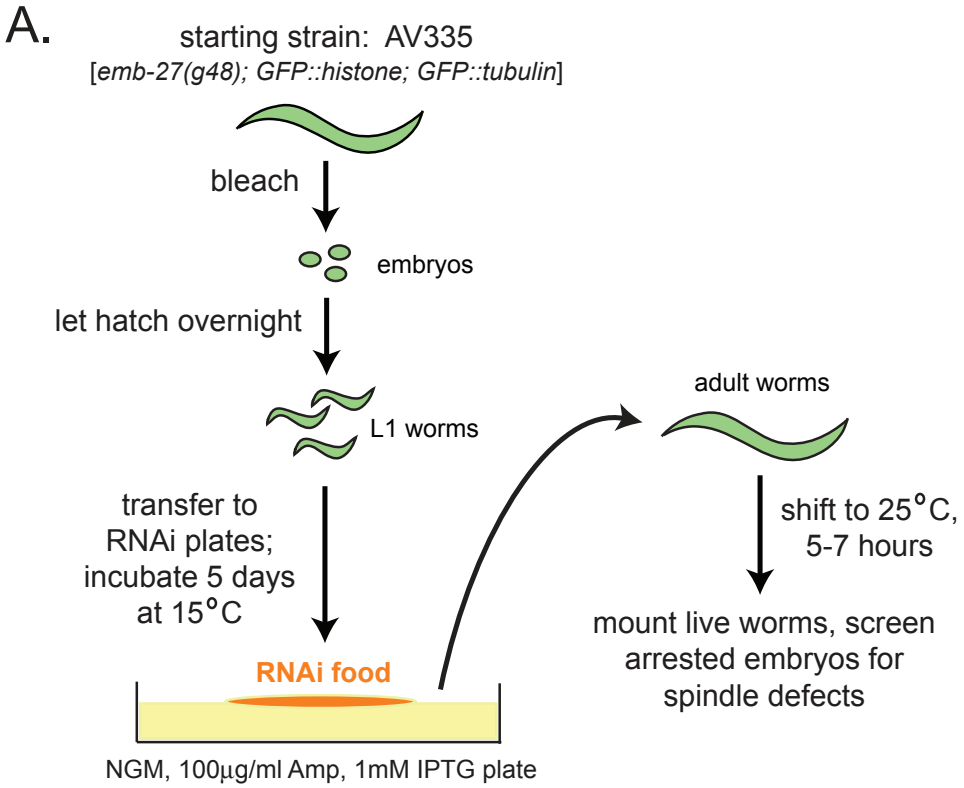

Figure S1 Design and implementation of the RNAi screen. (**a**) Gravid adult worms expressing GFP::tubulin and GFP::histone and containing a temperature-sensitive mutation affecting the Anaphase Promoting Complex (*emb-27ts*) were bleached to release embryos. These embryos were allowed to hatch overnight to synchronize L1-stage worms, which were then transferred to RNAi plates and incubated for 5 days at 15°C. Gravid adult worms from these plates were then shifted to 25°C for 5-7 hours to induce the APC arrest, resulting in embryos arrested at metaphase I. Live worms were then mounted for microscopy and visually screened for defects in the organization of the oocyte spindle. (**b**) Examples of normal and abnormal spindles observed in the primary screen. Metaphase I-arrested embryos expressing GFP::tubulin and GFP::histone in control (left) and *klp-18(RNAi)* (right) worms. The most recently arrested embryo (+1) was screened for defects in spindle morphology. In the control, a bipolar spindle with chromosomes aligned at the metaphase plate is clearly visible in the +1 embryo. In the *klp-18(RNAi)* worm, microtubules are found in abnormal aster-like structures (rather than bipolar spindles). Spindles in +2 embryos often appeared to have collapsed due to the prolonged arrest and were therefore excluded from analysis. Following the primary screen, candidates were rescreened without the APC arrest using high-resolution imaging (Fig. 1).

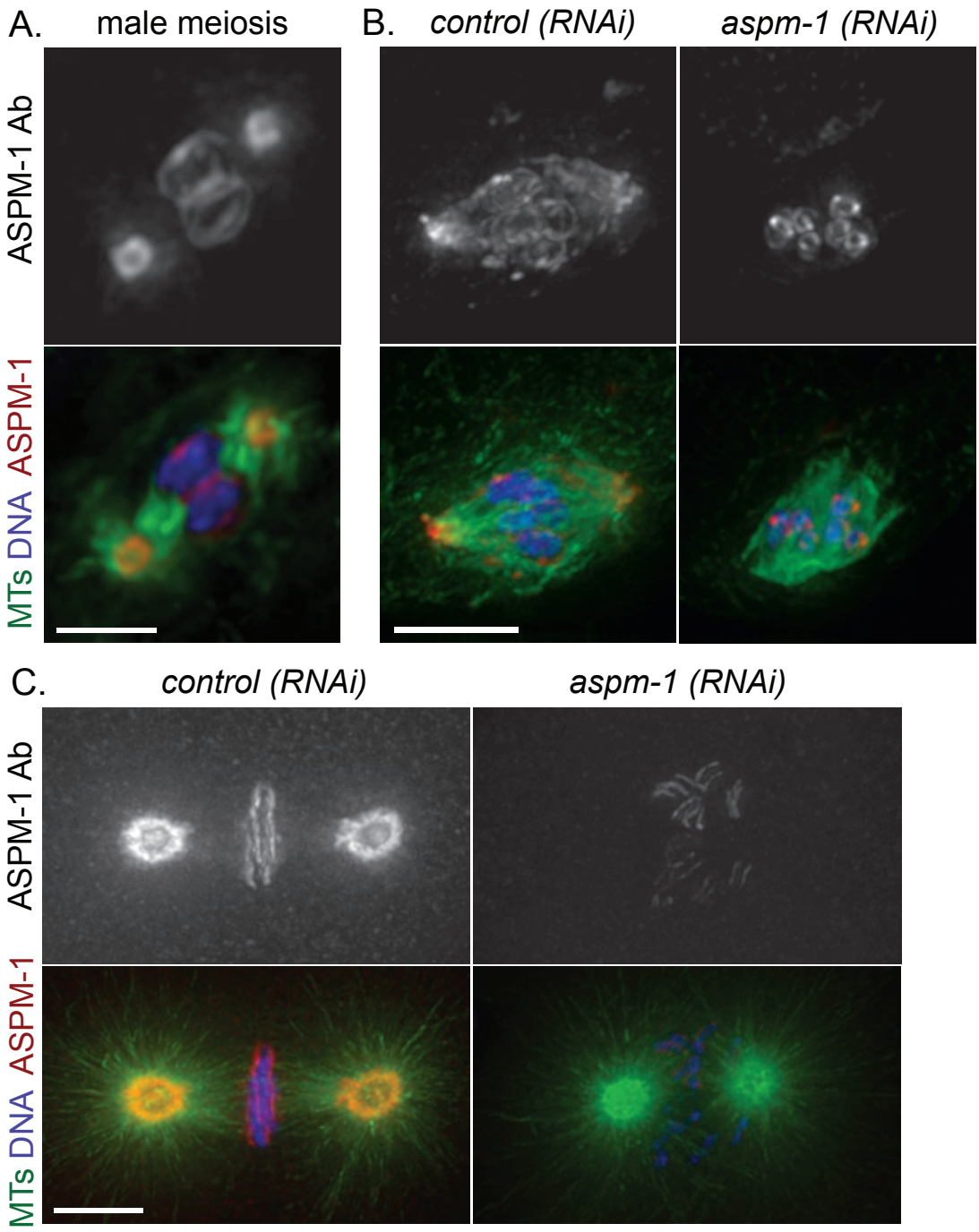

Figure S2 ASPM-1 localizes to the poles of both centrosomal and acentrosomal spindles. (**a-c**) Worms stained with Hoechst (blue), α-tubulin antibodies (green) and an antibody raised against ASPM-1 (red). The ASPM-1 antibody stains spindle poles as well as kinetochores and mid-bivalents in male spermatocyte and oocyte meiosis (**a**, **b**), and spindle poles as well as kinetochores in mitotic one-cell stage embryos (**c**). We find that *aspm-1(RNAi)* disrupts oocyte meiotic spindle organization (**b**, right) and that the ASPM-1 antibody does not stain the disorganized poles. However, residual staining at kinetochores and mid-bivalents was not eliminated, indicating that it may not correspond to ASPM-1. The fact that defined poles lacking ASPM-1 staining are present in mitotic spindles following *aspm-1(RNAi)* (**c**) indicates that pole staining is ASPM-1–dependent. The *aspm-1(RNAi)* image shown in **c** is an earlier stage embryo than the control, chosen to highlight the residual staining at individual kinetochores. Scale bar, 2 μm (**a**); 5 μm (**b**,**c**).

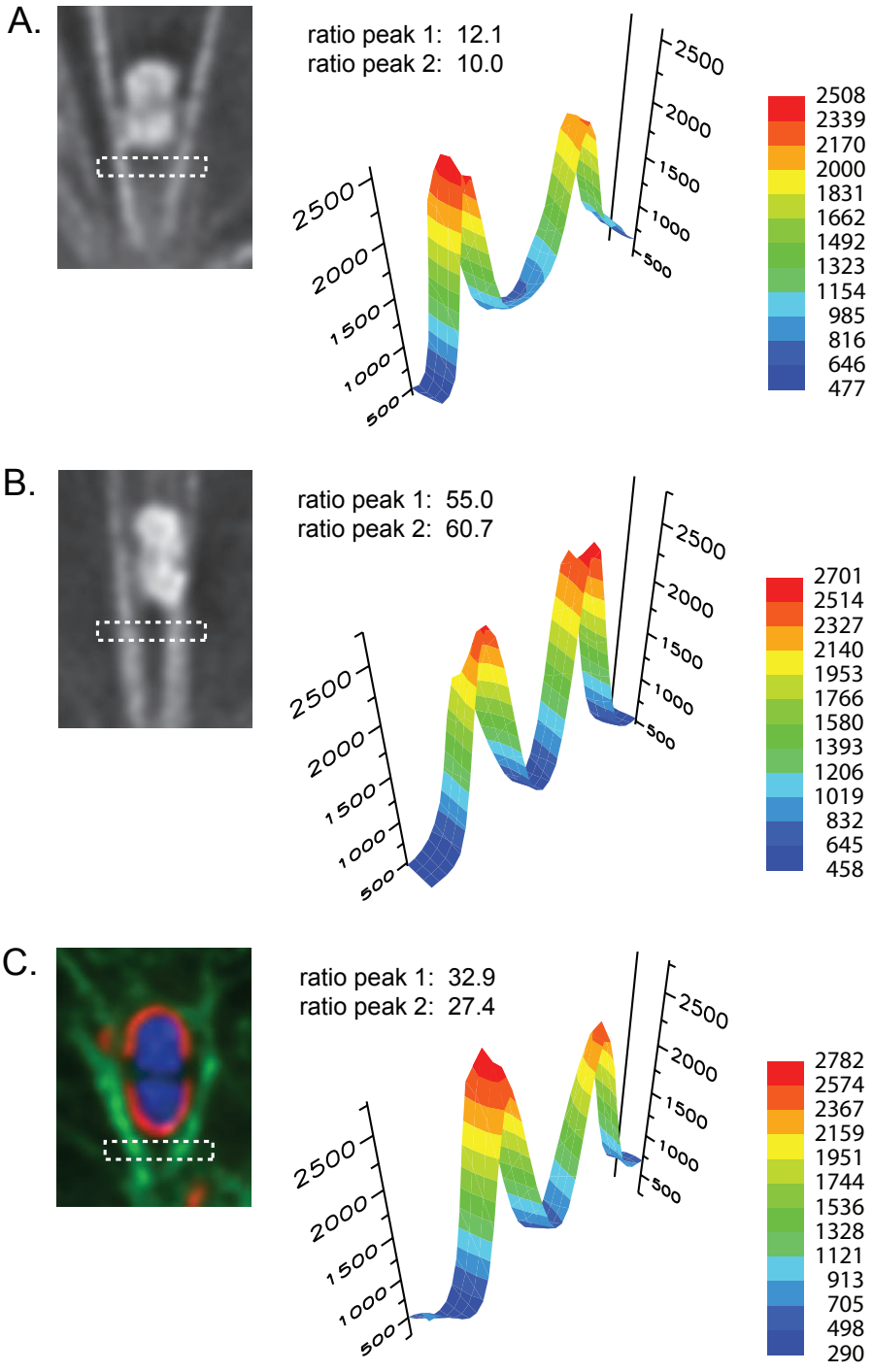

Figure S3 Microtubule density at chromosome ends is substantially lower than in the lateral microtubule bundles. (**a-c**) Assessment of relative microtubule density in the vicinity of three different chromosomes on monopolar spindles. Pixel intensities were measured within a 4 pixel by 33-34 pixel area (white boxes shown on the images at left); graphical representations of these data are shown on the right. Images depicted and analyzed are single sections selected from high-resolution image stacks (in **a-b,** the analyzed chromosomes are from the monopolar spindle shown in Fig. 2A; **c** is taken from one of the images shown in Fig. 2D). The ratios between the peak intensities and the region of minimum intensity between the bundles (adjacent to the chromosome end) are shown above each graph. Peak 1 corresponds to the peak on the left of each graph; peak 2 is on the right. Ratios were calculated following subtraction of the average pixel intensity values for domains outside the ensheathing microtubule bundles. In part **c**, only the microtubule channel (displayed in green) was analyzed.

A.

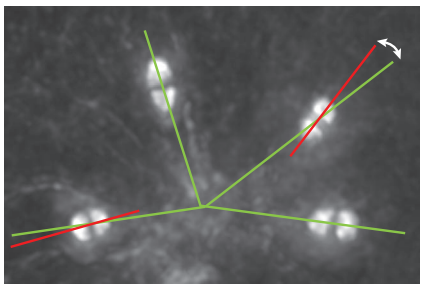

green line:
drawn from center of aster through bivalent midpoint

red line:
long axis of bivalent

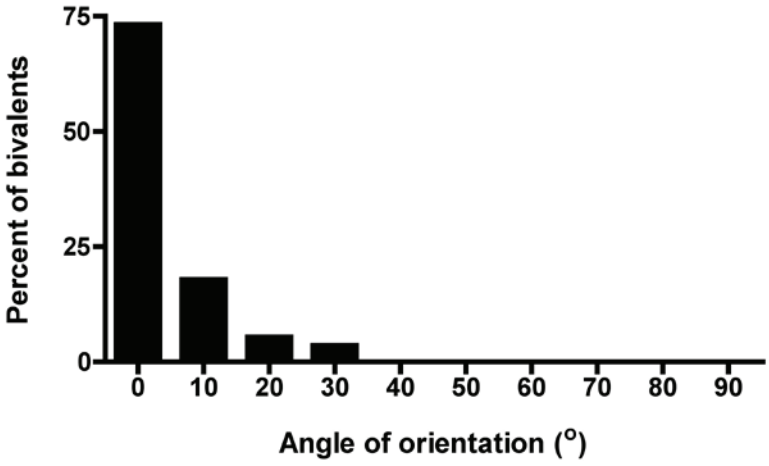

B.

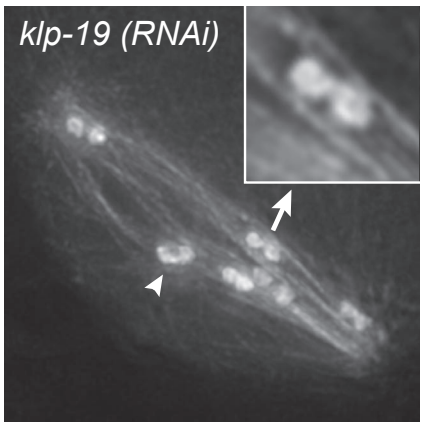

	total chr scored	# oriented
vec (RNAi)	102	101
klp-19 (RNAi)	125	122

Figure S4 Bivalent orientation on monopolar (**a**) and bipolar (**b**) oocyte spindles. Images show GFP::tubulin and GFP::histone. (**a**) Bivalent orientation was assessed by drawing a line from the center of the aster through the midpoint of the bivalent (green line) and measuring the angle between that line and the long axis of the bivalent (red line). These angles were then binned with values rounded to the nearest 10 and graphed. Most bivalents were found oriented parallel to the microtubule bundles ensheathing them. (**b**) Microtubule bundles still ensheath chromosomes (inset) and bivalent orientation is not disrupted following KLP-19 depletion. For quantification, chromosomes were classified as oriented if they were found parallel to the spindle axis. The image shows an example of a spindle formed following *klp-19(RNAi)*, where five chromosomes are oriented and one (arrowhead) is not.

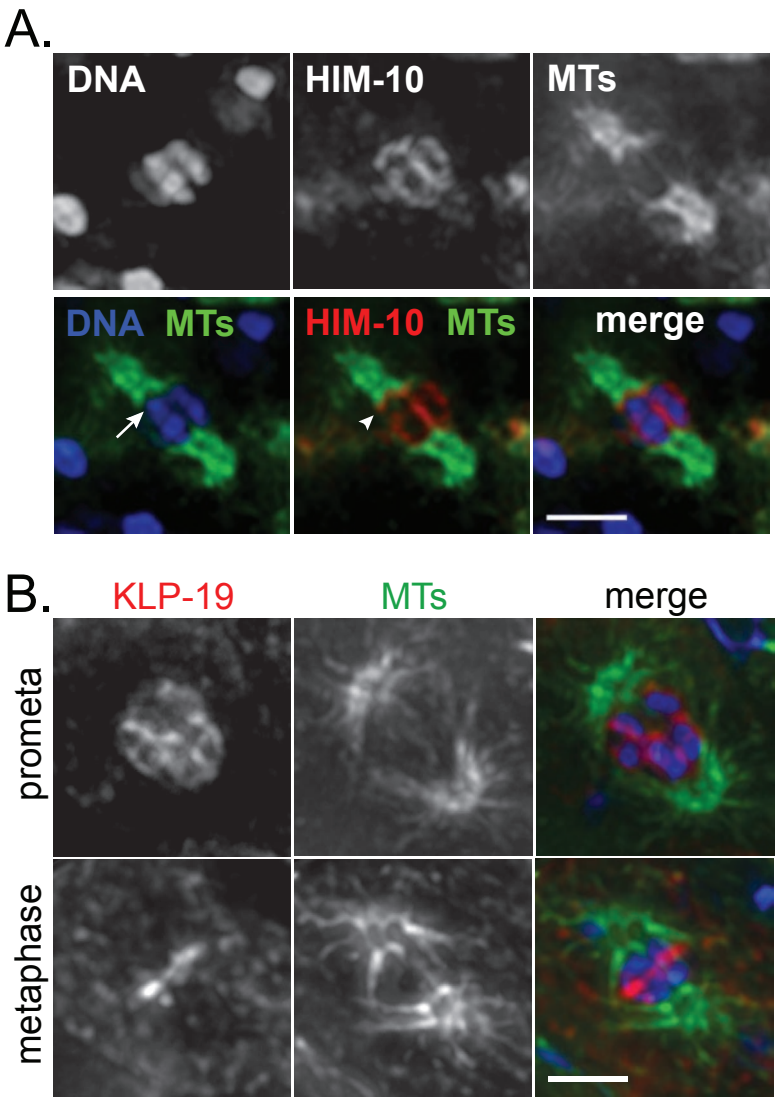

Figure S5 Organization of centrosome-containing male meiotic spindles. Spermatocytes stained for DNA (blue), tubulin (green) and HIM-10 (red in **a**) or KLP-19 (red in **b**). (**a**) HIM-10 marks the kinetochore. Single channel images are shown, in addition to different combinations of merged images. The kinetochore forms a cup-like structure around the ends of meiotic bivalents, and regions of high microtubule density are seen immediately adjacent to the kinetochore staining at bivalent ends (arrowhead). In the image of the microtubules and DNA, a gap is observed (arrow) where the kinetochore is located. (**b**) KLP-19 localizes to chromosomes during spermatocyte meiosis. In prometaphase spermatocytes, KLP-19 is localized broadly over the chromosomes; at metaphase, KLP-19 is enriched at the midbivalent. In all spermatocytes (**a**-**b**), microtubule density appears low in the center of the spindle, where the chromosomes are located, suggesting that a substantial fraction of microtubules may terminate at the chromosomes. Scale bars, 2 μm.

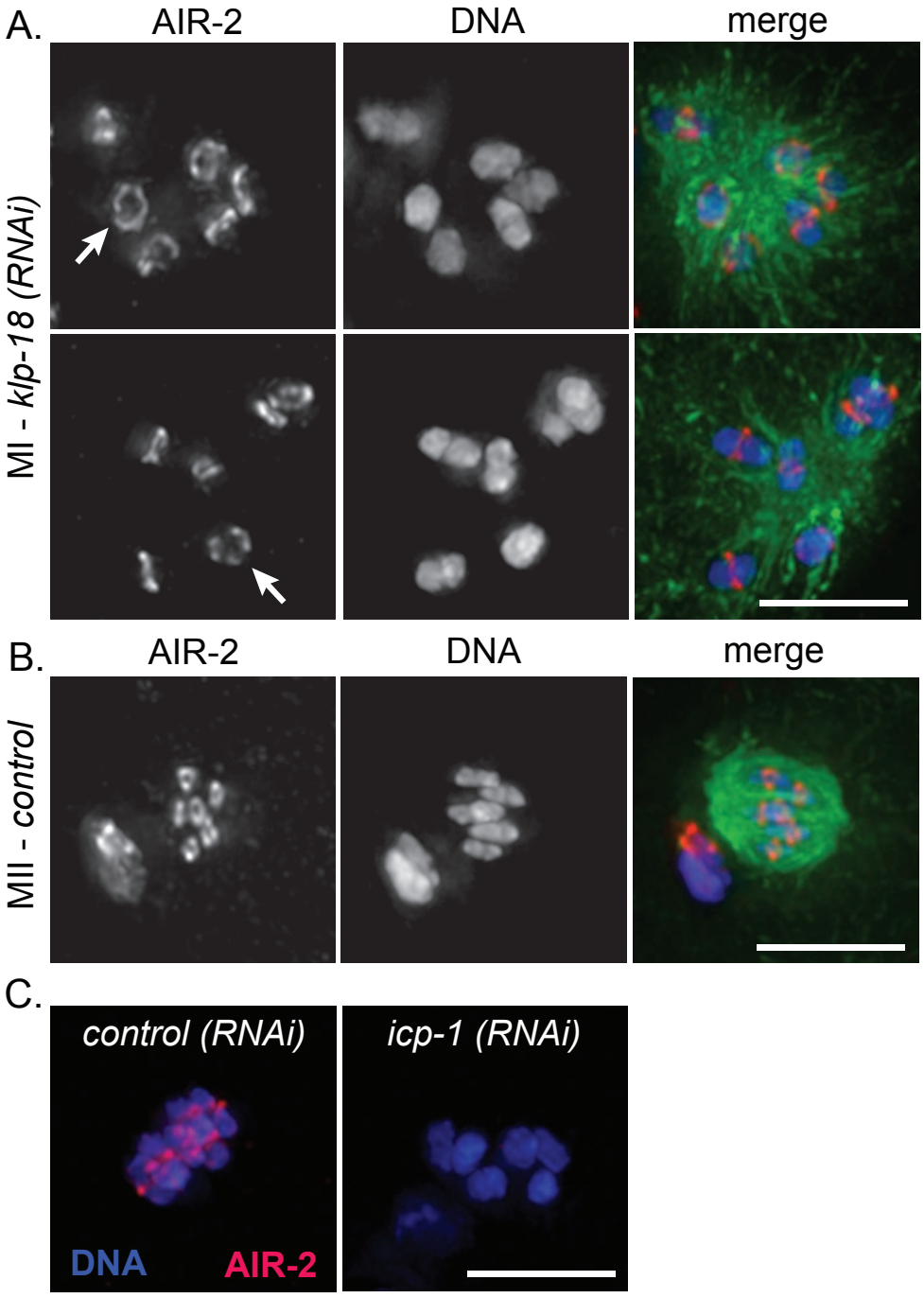

Figure S6 AIR-2 localizes to a ring around meiotic chromosomes. (**a, b**) Structures stained for Aurora B kinase AIR-2 (red), DNA (blue), and tubulin (green), in Meiosis I (**a**) and Meiosis II (**b**). Shown in **a** are monopolar spindles from *klp-18(RNAi)* worms, since the bivalents are spread out and some are positioned to reveal the AIR-2 ring (arrows). In **b**, the control metaphase II spindle is tilted, so the AIR-2 rings are visible. (**c**) Oocyte spindles stained for AIR-2 (red) and DNA (blue). *icp-1(RNAi)* (right) causes removal of AIR-2 from the chromosomes. Scale bars, 5 μm.

Supplementary Movie Legends

Movie S1 Full Z-stack of the image projection displayed in Figure 2A, showing lateral microtubule bundles ensheathing the chromosomes in a monopolar spindle, imaged using a strain expressing GFP::histone and GFP::tubulin. Image stacks were obtained at 0.3 μm Z steps. Images are displayed at 2 frames per second.

Movie S2 Full Z-stack of the image projection displayed in Figure 2B, showing lateral microtubule bundles ensheathing the chromosomes in a bipolar spindle, imaged using a strain expressing mCherry::histone (red) and GFP::tubulin (green). Image stacks were obtained at 0.3 μm Z steps. Images are displayed at 2 frames per second.

Supplementary Information

Design and implementation of a targeted RNAi screen for genes involved in acentrosomal spindle assembly

We sought to identify proteins required for acentrosomal spindle assembly by performing a targeted RNAi-based screen for defects in oocyte spindle formation in *C. elegans*. Our screening strain contained transgenes expressing GFP::tubulin and GFP::histone to allow visualization of microtubules and chromosomes in live worms. The screening strain also contained a temperature-sensitive mutation affecting the anaphase promoting complex (APC), which was used to enrich for spindles arrested at metaphase of meiosis I[1] [strain AV335 (*emb-27(g48)II; unc-119(ed3) ruIs32[unc-119(+) pie-1::GFP::H2B]III; ruIs57[unc-119(+) pie-1::GFP::tubulin]*)]. Approximately 800 genes that were previously annotated as embryonic lethal in a genome-wide screen[2] were chosen to be tested in our targeted screen, as this class contained two genes, *mei-1* and *mei-2*, previously shown to be required for normal organization of the oocyte spindle[3-5].

A schematic of the RNAi screen is shown in Figure S1A. Individual clones selected from an RNAi feeding library[2, 6] were used to inoculate 3 ml overnight LB/100 μg/ml Amp cultures. These saturated cultures were then used to seed NGM plates containing 100 μg/ml Amp and 1 mM IPTG; plates were left at room temperature overnight to induce dsRNA formation. The next day, L1 worms (synchronized by bleaching adults[7] and then letting the embryos hatch overnight on a plate without food) were put on the RNAi plates, and the worms were grown to adulthood by placing the plates at 15°C for 5 days.

Prior to screening worms for spindle defects, the RNAi plates were shifted to 25°C for 5-7 hours to arrest embryos in metaphase of meiosis I. Live worms were then mounted on a slide and their fertilized embryos were screened (using the 63X objective of a Zeiss Axioplan II microscope) for defects in oocyte meiotic spindle organization. Although the APC arrest induced a row of embryos arrested at metaphase I, only the most recently arrested embryos were analyzed to avoid potential problems associated with prolonged arrest. This primary screen successfully identified *mei-1* and *mei-2* as genes required for proper spindle morphology, validating the rationale for the screen. Candidates from the primary screen are being rescreened to confirm perturbation of spindle organization and to better define the nature of the spindle defects elicited by RNAi. Rescreening is being conducted using high-resolution Deltavision deconvolution imaging in the absence of the APC arrest.

In the primary screen stage, we identified two candidates (*klp-18* and C28C12.2) for which RNAi caused the formation of abnormal aster-like structures (Fig. S1B). For both of these genes, high-resolution imaging at the rescreening stage and subsequent immunofluorescence analysis demonstrated that the aster-like structures elicited by RNAi were monopolar spindles (Fig. 1). KLP-18 was known to be required for normal oocyte spindle formation[8], but previous analysis had not revealed the organization of the aberrant structures that formed following KLP-18 depletion. Our high-resolution imaging allowed us to ascribe a specific role for this protein in promoting spindle bipolarity. Since C28C12.2 is a novel gene, we named it *mesp-1* (meiotic spindle 1). MESP-1 is a member of a rapidly evolving protein family whose members exhibit high sequence divergence within the *Caenorhabditis* genus and that includes multiple paralogues in other *Caenorhabditis* species. MESP-1 does not contain any recognized predicted functional domains.

Supplementary References

1. Golden, A. et al. Metaphase to anaphase (mat) transition-defective mutants in Caenorhabditis elegans. *J Cell Biol* **151**, 1469-82 (2000).
2. Kamath, R. S. et al. Systematic functional analysis of the Caenorhabditis elegans genome using RNAi. *Nature* **421**, 231-7 (2003).
3. Mains, P. E., Kemphues, K. J., Sprunger, S. A., Sulston, I. A. & Wood, W. B. Mutations affecting the meiotic and mitotic divisions of the early Caenorhabditis elegans embryo. *Genetics* **126**, 593-605 (1990).
4. Clark-Maguire, S. & Mains, P. E. mei-1, a gene required for meiotic spindle formation in Caenorhabditis elegans, is a member of a family of ATPases. *Genetics* **136**, 533-46 (1994).
5. Srayko, M., Buster, D. W., Bazirgan, O. A., McNally, F. J. & Mains, P. E. MEI-1/MEI-2 katanin-like microtubule severing activity is required for Caenorhabditis elegans meiosis. *Genes Dev* **14**, 1072-84 (2000).
6. Fraser, A. G. et al. Functional genomic analysis of C. elegans chromosome I by systematic RNA interference. *Nature* **408**, 325-30 (2000).
7. Stiernagle, T. Maintenance of C. elegans. *WormBook*, 1-11 (2006).
8. Segbert, C. et al. KLP-18, a Klp2 kinesin, is required for assembly of acentrosomal meiotic spindles in Caenorhabditis elegans. *Mol Biol Cell* **14**, 4458-69 (2003).

nature cell biology

OsHAL3 mediates a new pathway in the light-regulated growth of rice

Shi-Yong Sun[1,4], Dai-Yin Chao[1,4], Xin-Min Li[1], Min Shi[1], Ji-Ping Gao[1], Mei-Zhen Zhu[1], Hong-Quan Yang[1], Sheng Luan[2,3] and Hong-Xuan Lin[1,2,5]

Plants show distinct morphologies in different light conditions through a process called photomorphogenesis. A predominant feature of photomorphogenesis is the reduced growth of seedlings under light conditions compared with darkness. For this adaptive event, the most well-known molecular mechanism involves photoreceptor-mediated inhibition of cell elongation[1–4]. However, it is not known whether additional pathways exist. Here, we describe a newly discovered pathway of light-modulated plant growth mediated by the halotolerance protein HAL3, a flavin mononucleotide (FMN)-binding protein involved in cell division[5–8]. We found that light, especially blue light, suppresses growth of rice seedlings by reducing the activity of *Oryza sativa* (Os) HAL3. Both *in vitro* and *in vivo* studies showed that OsHAL3 is structurally inactivated by light through photo-oxidation and by direct interaction with photons. In addition, the transcriptional expression of *OsHAL3* is synergistically regulated by different light conditions. Further investigation suggested that OsHAL3 promotes cell division by recruiting a ubiquitin system, rather than by its 4'-phosphopantothenoylcysteine (PPC) decarboxylase activity. Our results uncover a new mechanism for light-regulated plant growth, namely, light not only inhibits cell elongation but also suppresses cell division through HAL3 and E3 ubiquitin ligase. This study thus brings new insights into our understanding of plant photomorphogenesis.

HAL3 (also known as SIS2) is a highly conserved flavoprotein present in fungi, plants and animals[5–11]. It functions in G1/S transition of the cell cycle, halotolerance (through enhancing Na^+/K^+ homeostasis) and cell integrity in yeast[5,6,12–14]. Studies in *Arabidopsis thaliana* and tobacco have demonstrated that the salt tolerance of HAL3 is conserved during the cell cycle[8,10]. Unlike *Arabidopsis* and tobacco, which contain at least two *HAL3*-like genes, the rice *O. sativa* genome has only a single copy of the *OsHAL3* gene. Overexpression of *OsHAL3* in rice (Fig. 1a, b) produced a consistent phenotype of increased seedling growth under normal light/dark cycles (Fig. 1c, d) and enhanced salt tolerance and Na^+/K^+ homeostasis (Supplementary Information, Fig. S1). Further investigation showed that the root meristematic zone and root cap in the *OsHAL3* overexpression lines were longer than those of the vector control lines (Supplementary Information, Fig. S2a, b) and had more cells (Supplementary Information, Fig. S2e, f). In contrast, cell sizes did not seem to change (Supplementary Information, Fig. S2c, d g). These data demonstrate that the enhanced growth is manifested as an accelerated cell division and therefore supports the role of HAL3 in promoting the cell cycle.

Interestingly, *OsHAL3*-overexpression lines exposed to different light conditions showed a variety of phenotypes. *OsHAL3*-overexpressing plants grew faster than wild-type plants under normal white light/dark cycles (Fig. 1c) or blue light/dark cycles (Fig. 1d). However, such a growth-enhancing effect was not observed under continuous white light (Fig. 1f), blue light (Fig. 1g), darkness (Fig. 1h) or far-red light (Fig. 1i). A weak phenotype was observed under continuous red light conditions (Fig. 1e). These data suggest that OsHAL3-promoted growth is regulated by different light regimes.

To address how light regulates OsHAL3, we examined OsHAL3 activity under different light conditions by determining its structure. On the basis of the crystal structure, the active form of HAL3 is a homotrimer[15]. The conservation of residues involved in trimer formation and FMN binding (Fig. 2a) suggests that the active form of OsHAL3 is also a trimer. Consistently, yeast two-hybrid experiments detected a physical interaction between OsHAL3 monomers (Fig. 2b). Interestingly, a strong interaction was observed in darkness (Fig. 2b), but not in light, especially blue light (Fig. 2b). This indicates that blue light inhibits formation or induces dissociation of OsHAL3 trimers. In contrast with OsHAL3, the interaction between CRY1, a blue light receptor[16], and its amino-terminal (CNT) was not affected by light (Fig. 2b)[17]. We further confirmed the light-mediated dissociation of OsHAL3 *in vivo* using a chemical cross-linking experiment. No detectable OsHAL3 trimer was

[1]National Key Laboratory of Plant Molecular Genetics, Shanghai Institute of Plant Physiology and Ecology, and [2]SIBS-UC Berkeley Center for Molecular Life Sciences, Shanghai Institutes for Biological Sciences (SIBS), Chinese Academy of Sciences, 300 Fenglin Road, Shanghai 200032, China. [3]Department of Plant and Microbial Biology, University of California, Berkeley, CA 94720, USA.
[4]These authors contributed equally to this work.
[5]Correspondence should be addressed to H.X.L. (e-mail: hxlin@sibs.ac.cn)

Received 30 January 2009; accepted 13 April 2009; published online 21 June 2009; DOI: 10.1038/ncb1892

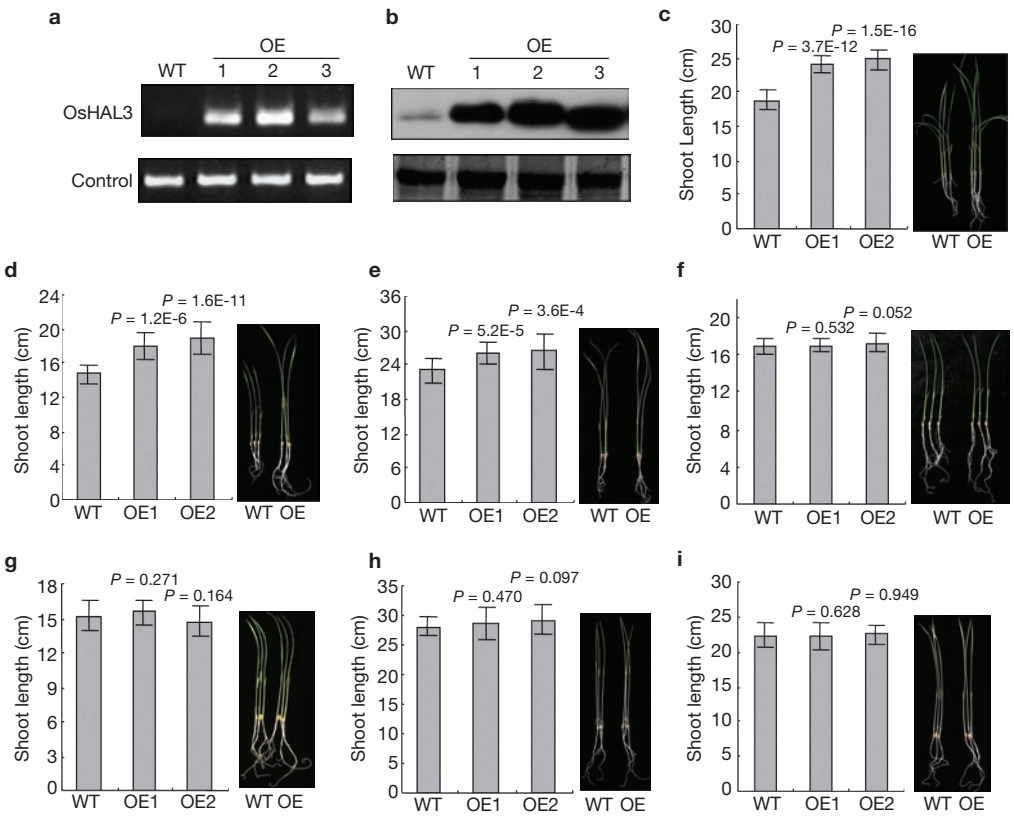

Figure 1 The enhanced growth rate enabled by *OsHAL3* overexpression is regulated by light. *OsHAL3* overexpression in *Zhonghua 11* was observed at the transcriptional level (**a**) and protein level (**b**). *Actin* was used as a control for RT-PCR (**a**) and Rubisco was used as a control for immunoblotting (**b**). See Supplementary Information, Fig. S3 for full scans of western blots in **b**. (**c**–**i**) Phenotypes of OsHAL3 overexpression lines under different light conditions. Wild type and *OsHAL3*-overexpressing seedlings were grown under different light regimes, including white light/darkness cycles (**c**), blue light/darkness cycles (**d**), continuous red light (**e**), continuous white light (**f**), continuous blue light (**g**), continuous darkness (**h**) and continuous far-red light (**i**). Shoot lengths were measured after 12 days of seedling growth. Photographs of seedlings exposed to each condition are shown on the right. WT, wild type; OE, overexpression line. Data are mean ± s.d. ($n \geq 20$, see Supplementary Information, Table S2). The corresponding *P* values were determined using Student's *t*-test (two tailed) comparing data from the wild type with that from transgenic lines.

observed when rice seedlings were grown under continuous blue light (Fig. 2c), whereas 35.9% of OsHAL3 was in the trimer formation in darkness (trimer : monomer ratio was 0.56:1; Fig. 2c). The trimer : monomer ratio decreased to 0.49:1 after exposing the seedlings to blue light for only 15 min, and it further decreased to 0.21:1 after 90 min (Fig. 2c). These data suggest that the OsHAL3 trimer dissociates rapidly on blue light illumination.

A previous study showed that an oxidative environment facilitates the dissociation of HAL3, suggesting that the maintenance of the HAL3 trimer requires the reduced FMN ligand[18]. Given that light produces reactive oxygen species in plants cells, it is reasonable to propose that photo-oxidation may have caused the trimer disassembly in rice seedlings. This hypothesis is supported by the dissociation of the OsHAL3 trimer by blue, red and far-red light. However, blue light is the stronger inducer of OsHAL3 dissociation. This may suggest that blue light is more closely involved in the trimer disruption (Fig. 2b), because $FMNH_2$ directly absorbs blue but not red or far-red light (Fig. 2d). Alternatively, dissociation may be mediated by blue light photoreceptors.

Structural analysis indicates that the FMN group may be required for trimer formation of HAL3 (ref. 15). To test if OsHAL3 requires its ligand for its trimer formation, we produced a mutant of OsHAL3 in which the amino-acid residues 106 to 109 Ser-Ala-Asn-Thr, which contribute to FMN–HAL3 association[15], were changed to Pro-Pro-Tyr-Pro (OsHAL3^{PPYP}; Fig. 2a). The mutations eliminated the absorption ability of OsHAL3 in the UV-A and visible light spectra (Fig. 2d), indicating that the mutant lacks FMN binding. Yeast two-hybrid experiments further demonstrated that the mutant could not form a trimer, even in darkness (Fig. 2e). Together with the previous study[15], our results indicate that $FMNH_2$ mediates the trimer formation of HAL3. To test if $FMNH_2$ directly absorbs photons that cause trimer dissociation, we performed GST (glutathione *S*-transferase) pulldown assays using GST–OsHAL3 and MBP (maltose binding protein)–OsHAL3 fusion proteins purified from *Escherichia coli*. We detected co-purification or interaction of GST–OsHAL3 and MBP–OsHAL3 in the dark but not under blue light (Fig. 2f). Inhibition of OsHAL3 protein interaction by blue light in this system involves only photons and OsHAL3, implying that blue light directly triggers dissociation of OsHAL3 in plant cells after absorbtion by FMNH2.

Light-mediated dissociation of the OsHAL3 active form (trimer) explains why OsHAL3-overexpressing seedlings showed enhanced growth under light/dark cycles but not under continuous blue or white light. However, the underlying cause of the growth phenotypes in continuous darkness and far-red light was unclear. To address this issue we investigated the expression pattern of OsHAL3.

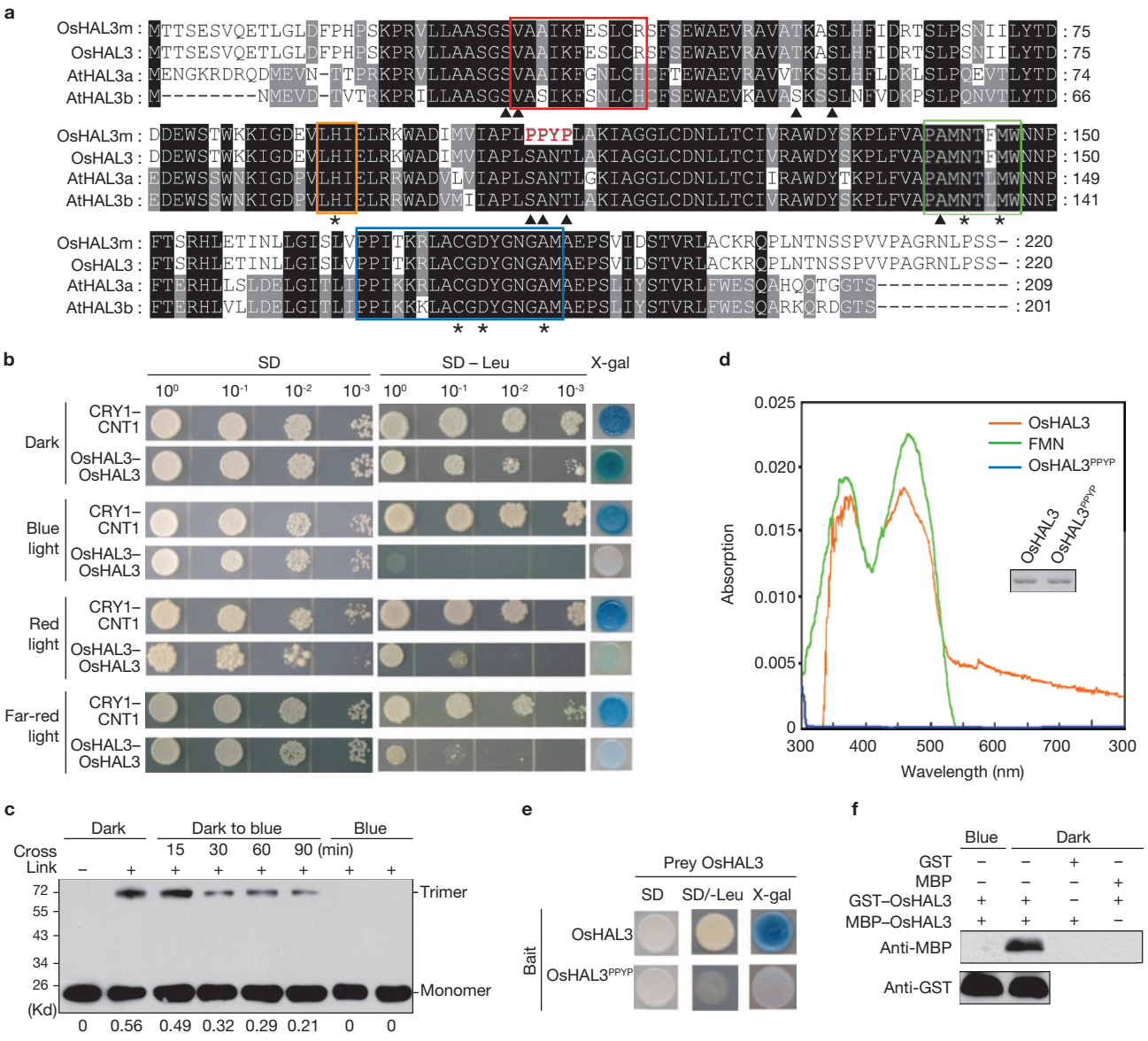

Figure 2 Light-mediated OsHAL3 trimer dissociation. (**a**) Sequence alignment of OsHAL3 with AtHAL3a and AtHAL3b. Triangles indicate protein residues that contribute to hydrogen bond formation between OsHAL3 and FMN. Asterisks and boxes show conserved residues and motifs required for PPC decarboxylase activity. OsHAL3m (OsHAL3^{PPYP}) mutations are shown in red. (**b**) Yeast two-hybrid experiment to test the OsHAL3–OsHAL3 and CRY1–CNT1 interactions under various light conditions. OsHAL3 and OsCRY1 were separately constructed into bait and prey vectors, and transformed into the yeast strain EGY48. Transformed yeast was diluted and dropped onto synthetic dropout (SD) media, leucine-negative (– Leu) SD media or X-gal media. Transformants were tested under the light conditions indicated. (**c**) Cross-linking experiments were used to test trimer dissociation of OsHAL3 *in vivo* under blue light. Proteins were extracted from two-week-old *OsHAL3*-overexpressing rice seedlings grown under continuous blue light (Blue), in darkness (Dark), or transferred from darkness to blue light (Dark to blue) with (+) or without (–) cross-linking by 1% formaldehyde. The ratio of trimers : monomers is shown below each lane. (**d**) Absorption spectra of OsHAL3 (orange line), OsHAL3m (blue line) and FMN (green line). Protein loading controls are shown on the right panel. (**e**) Yeast two-hybridization experiment to test for the interaction between OsHAL3 and OsHAL3^{PPYP}. The experiment was performed as described in **b**, and interactions were tested in darkness. (**f**) GST-pulldown of OsHAL3. Prokaryotic expressed proteins were mixed and incubated with GST beads under blue light or darkness as indicated. Washes were also performed under the corresponding conditions. Immunoblotting with an MBP antibody was used to detect the interactions between GST–OsHAL3 and MBP–OsHAL3. A GST antibody was used to show the loading and binding control. See Supplementary Information, Fig. S3 for full scans of western blots in **c** and **f**.

Using an *OsHAL3* promoter GUS (β-glucuronidase) reporter strategy, we found that *OsHAL3* is predominantly expressed in all the meristems of rice plants (Fig. 3a–f), but only weakly expressed in some differentiating tissues (Fig. 3c, g–i). Interestingly, GUS expression was strong in the tip of coleoptiles during elongation (Fig. 3h), but disappeared on leaf emergence (Fig. 3c), which may indicate an adaptive and light-regulated mode of *OsHAL3* expression. These data again suggest that HAL3 functions in promoting plant cell division, a similar function to that of its yeast homologue[5,13].

Consistent with our observation, studies in *Arabidopsis* (At) also show that *AtHAL3a* is highly expressed in seed embryos[8] and meristem tissues such as root tip, callus and shoot apex[19,20]. In addition, *AtHAL3a*

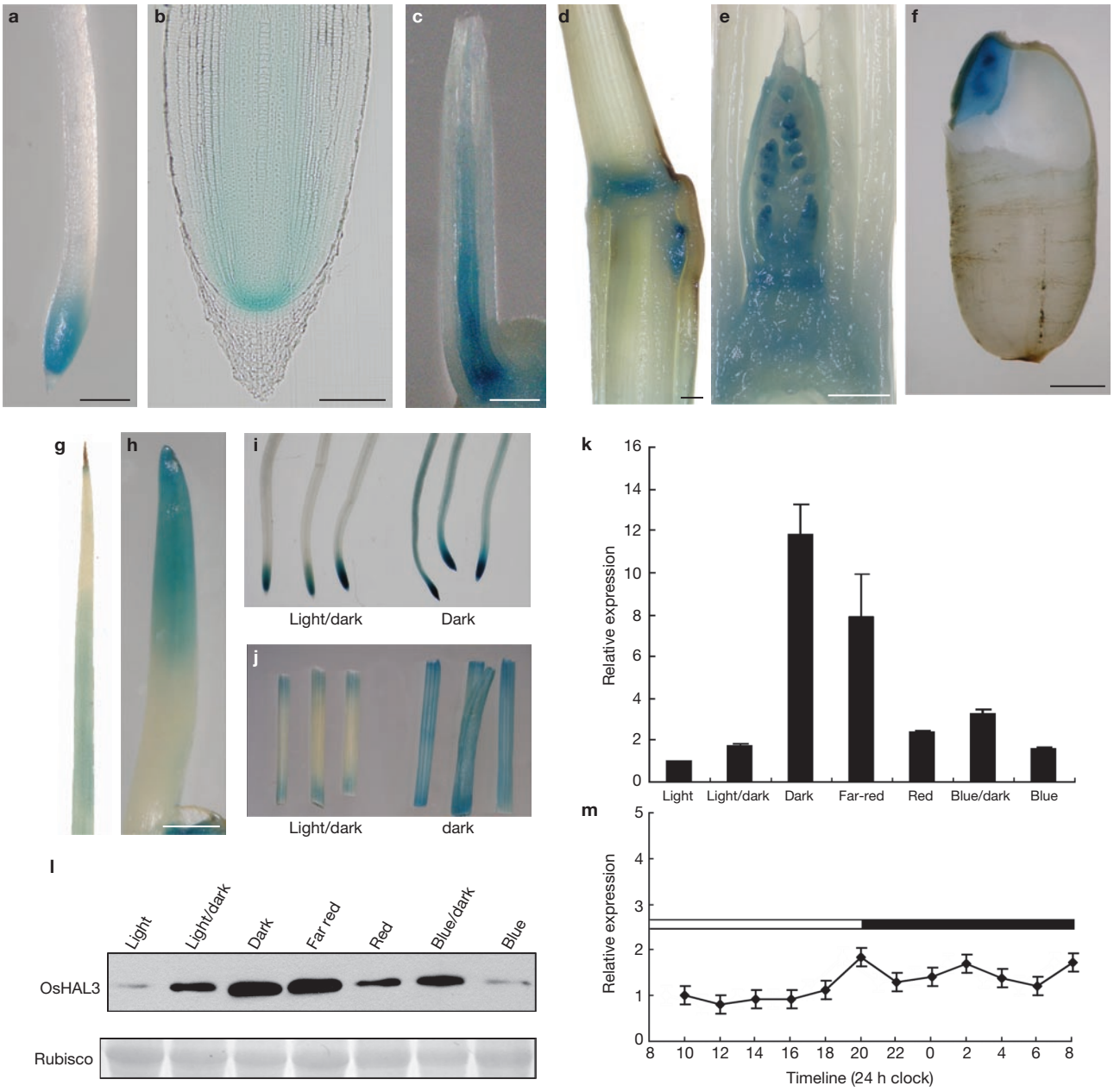

Figure 3 Expression pattern of *OsHAL3*. (**a**–**j**) *OsHAL3* promoter-GUS expression pattern in transgenic rice plants. (**i**–**j**)The expression of *OsHAL3* is shown by GUS staining in the root meristematic zone (**a**, **b**), shoot apical meristem (**c**), intercalary meristem (**d**), floral meristem (**e**), embryo (**f**), the tip of the coleoptile before true leaf emergence (**h**) and in young leaf blades, which show weak expression (**g**), under light/dark conditions. *OsHAL3* expression in root (**i**) and leaf sheath (**j**) under continuous darkness and light/dark cycles, as indicated, are also shown by GUS staining. Specimens in **a**–**f**, **h** and **i**–**j** were stained for 2 h, and those in **g** were stained overnight. Scale bars, 1 mm in **a**, **c**–**f** and **h**; 100 μm in **b**. (**k**–**m**) *OsHAL3* transcripts and its protein accumulation in rice seedlings under different light conditions, as indicated, were assessed by real-time RT-PCR (**k**) and immunoblotting (**l**). Relative expression values were plotted relative to expression under continuous white light, which was set as a baseline equal to 1. *Actin* was used as a control for real-time RT-PCR and Rubisco as a loading control for immunoblotting. Data are mean ± s.d. ($n = 4$). See Supplementary Information, Fig. S3 for full scans of western blots in **l**. (**m**) Expression pattern of *OsHAL3* during a light/dark cycle. Relative expression values were plotted relative to the expression level at 10:00 am, which was set as a baseline equal to 1. The open bar and shaded bar indicate the light and dark period, respectively. The timeline, in hours, is shown on the *x*-axis. Data are mean ± s.d. ($n = 4$).

can be induced by 6-benzyl adenine (6-BA), an artificial cytokinin that promotes plant cell division[19]. Relevantly to our study, previous research has indicated that protein levels of both AtHAL3a and AtHAL3b are regulated by light[20].

Next, we examined expression patterns of *OsHAL3* under various light conditions and found that *OsHAL3* was expressed at a much higher level in darkness than under normal light/dark cycles (Fig. 3i, j). Real-time reverse transcription (RT)-PCR and immunoblot experiments revealed high levels of *OsHAL3* transcripts and OsHAL3 protein in the dark or far-red light, but significantly lower levels in blue, red or white light (Fig. 3k, l). *OsHAL3* transcript levels were also low under white light/dark or blue light/dark cycles (Fig. 3k, l), and varied little during a diurnal cycle (Fig. 3m).

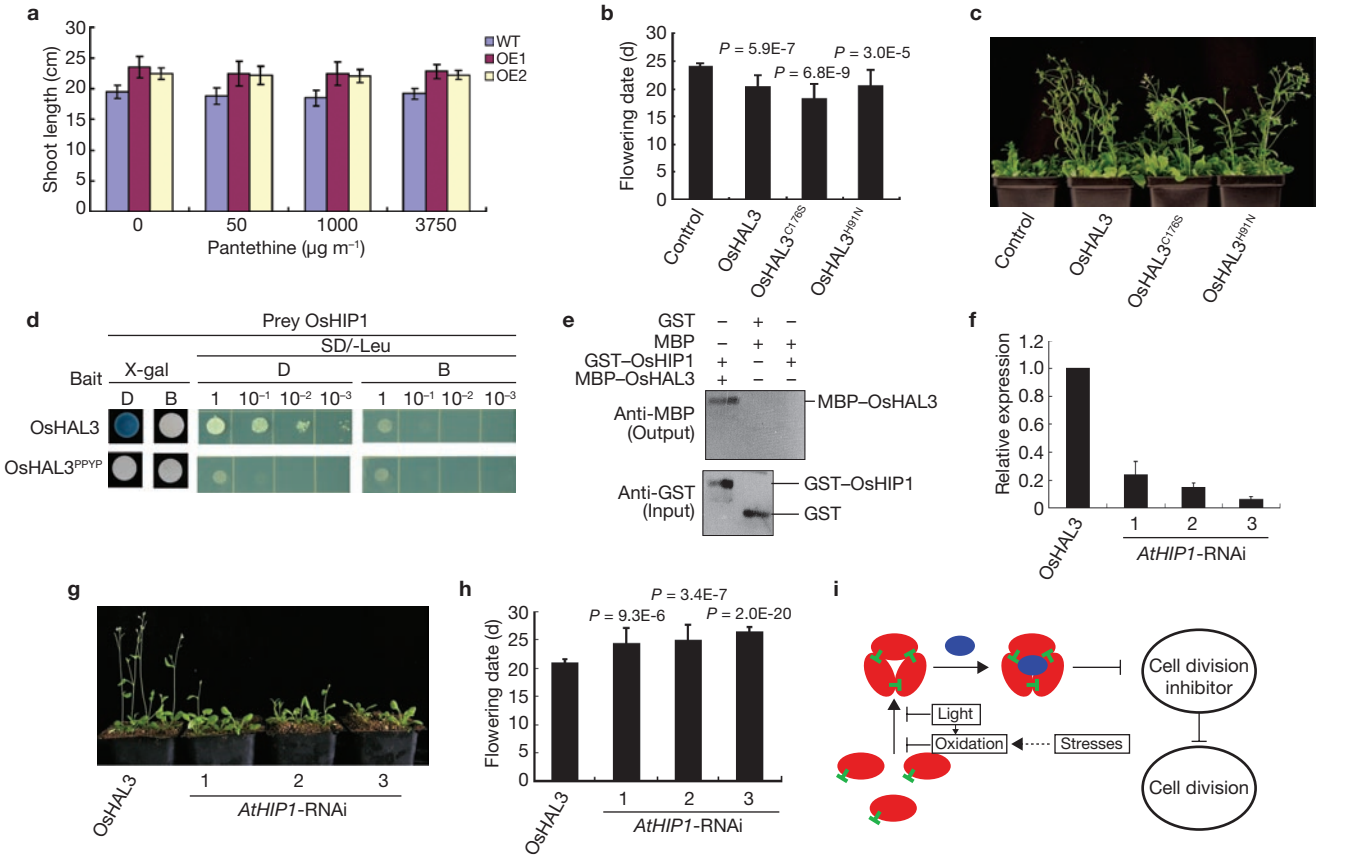

Figure 4 OsHAL3 function in growth regulation may involve ubiquitin-dependent proteolysis but independent from its PPC decarboxylase activity. (**a**) Pantethine complementation assay. Wild type and various OsHAL3-overexpression lines were germinated and grown in rice culture solutions with pantethine as indicated. Seedling length was measured 2 weeks after germination. (**b**, **c**) Flowering time of *Arabidopsis* lines overexpressing OsHAL3 or its mutants as indicated. Flowering time (**b**) was recorded by scoring the number of days from sowing to the time when flower buds were visible at the centre of the rosette. The image (**c**) was taken 25 d after seed germination. Control, empty vector. (**d**, **e**) The interaction between OsHAL3 and OsHIP1 was tested by yeast two-hybrid (**d**) and pulldown assays (**e**). The yeast two-hybrids were tested in different mediums and under a variety of light conditions as indicated. Pulldown assays were performed in darkness for binding and in weak light for washing and elution. GST and MBP were used as controls. D, darkness; B, blue light. See Supplementary Information, Fig. S3 for full scans of western blots in **e**. (**f**–**h**) RNAi-mediated knockdown of *AtHIP1* in an *Arabidopsis* line overexpressing *OsHAL3*. The *AtHIP1* transcript levels in the empty vector control and *AtHIP1* RNAi lines in the *OsHAL3* overexpression background were detected by quantitative RT-PCR (**f**). The image (**g**) was taken 25 d after germination, and the flowering time (**h**) was calculated as for **b**. OsHAL3 indicates an *OsHAL3* overexpression line transformed by an empty control vector; AtHIP-RNAi (1-3) indicates *OsHAL3* overexpression lines transformed by AtHIP-RNAi construct. (**i**) A model for the HAL3 pathway. Red ellipses represent the HAL3 monomer, blue ellipses represent HIP1 and the green 'T' blocks represent FMN. The dashed arrow indicates the predicted pathway, the solid arrows and lines indicate the pathway directly supported by this study. Data for histograms in **a**, **b**, **f** and **h** are mean ± s.d. ($n = 20$ in **a** and $n \geq 10$ in **b** and **h**, see Supplementary Information, Table S2; $n = 5$ in **f**). *P* values in **b** and **h** were determined using Student's *t*-test (two tailed) comparing data with that from control lines

The expression pattern of the *OsHAL3* gene provides an interpretation for the phenotypes of the overexpression lines under darkness and far-red light. Dark and far-red light may be sufficient for the full function of the highly expressed native OsHAL3, and as a result, further enhancement of growth was not observed in the overexpression transgenic plants under these light regimes. However, under a normal light/dark cycle, the OsHAL3 overexpressed lines grow faster than the wild type because the OsHAL3 protein level is lower than a threshold level, increasing the growth rate in the dark period.

Collectively, our results indicate that HAL3 may be involved in a pathway of light-regulated plant growth that is distinct from the photoreceptor-mediated ones. In addition to the photoreceptor-mediated inhibition of cell elongation, light (especially blue light) also inhibits cell division through inactivating photosensitive HAL3. To further support this conclusion, we attempted to examine the phenotypes of loss-of-function mutants of the *OsHAL3* gene. However, we were not able to obtain such mutant lines possibly owing to lethality caused by the suppression of *OsHAL3* expression (data not shown), consistent with the finding that its homologues in *Arabidopsis* are essential genes probably due to their requirement in cell division[21].

In yeast, HAL3 functions through its direct inhibition of PPz1 (refs 6, 13, 22), a type 1 phosphatase[22], suggesting a role in signalling pathways. Although HAL3 function is thought to be conserved between yeast and plants[15], some studies have revealed divergences between different homologues. AtHAL3 has been found to function as a PPC decarboxylase[9,18,21,23,24] with His 90 and Cys 175 (equivalent to His 91 and Cys 176 of OsHAL3) being required for the PPC decarboxylase activity of AtHAL3a (refs 18, 23, 24). Yet, a mutation of His 378 (equivalent to His 90 of AtHAL3a) did not affect functions of ScHAL3 in yeast, and ScHAL3 does not contain a residue analogous to Cys 175 in AtHAL3a (ref. 25). These data suggest that HAL3s may have several independent functions.

Accordingly, the involvement of ScHAL3 in independent pathways has been suggested[26,27].

A recent report indicated that OsHAL3 can serve as a PPC decarboxylase[11]. However, it was not known if the PPC decarboxylase activity of OsHAL3 is associated with its role in cell division. Pantethine has been shown to complement loss of PPC decarboxylase function of HAL3 in *Arabidopsis*[21]. We treated rice medium with different levels of pantethine and found it had no effect on rice seedling growth (Fig. 4a). In addition, the difference in growth rate between overexpressing and wild-type lines was not affected by pantethine (Fig. 4a), suggesting that the PPC decarboxylase activity of HAL3 is not associated with its role in cell division.

To perform further functional analysis of OsHAL3, we decided to test the feasibility of using *Arabidopsis* as a model system. *Arabidopsis* plants overexpressing *OsHAL3* also showed a faster growth rate phenotype (an earlier flowering time; Fig. 4b, c), similar to that of plants overexpressing *AtHAL3* (ref. 8), suggesting a conservation of the HAL3 function in *Arabidopsis* and rice. We constructed two mutant proteins of OsHAL3, $OsHAL3^{H91N}$ and $OsHAL3^{C176S}$, with point mutations at residues required for PPC decarboxylase activity but not for trimer formation[11,18,23,24]. These mutant proteins, like the wild-type OsHAL3 protein, enhanced the growth of *Arabidopsis* plants when overexpressed in transgenic lines (Fig. 4b, c). This result supports the conclusion from the pantethine experiment, that HAL3 function in cell division is independent from its PPC decarboxylase activity.

We therefore tested the possibility that HAL3 functions as a regulatory component in cell division, like the yeast homologue, by interacting with other signalling proteins. Using a yeast two-hybrid screening, we identified several OsHAL3-interacting proteins (OsHIP). One of them, OsHIP1 a protein with a RING-finger motif with similarity to E3 ligase (gene accession No. AK071468), was used for further analysis. In addition to the results obtained from the yeast two-hybrid screen (Fig. 4d), pulldown assays also confirmed that OsHAL3 interacts with OsHIP1 (Fig. 4e). Interestingly, we found that this interaction, like the formation of OsHAL3, was also suppressed by blue light (Fig. 4d), suggesting that it may require the trimer formation of OsHAL3. Consistently, the OsHAL3 mutant $OsHAL3^{PPYP}$, which was shown to lack the capability to form trimers, could not recruit OsHIP1 even in darkness (Fig. 4d). These data suggest that the OsHAL3–OsHIP1 interaction may be functionally relevant and that OsHAL3 regulates the cell cycle through a ubiquitin-related pathway mediated by OsHIP1.

As OsHAL3 functions similarly in *Arabidopsis*, we used *Arabidopsis* as a model to detect whether HIP1 is involved in cell division. The gene *At4g34040* encodes the *Arabidopsis* homologue with highest similarity to OsHIP1 and is named *AtHIP1* in this study. We knocked down *AtHIP1* expression in the *OsHAL3*-overexpression *Arabidopsis* line (Fig. 4f), and found that a reduced level of AtHIP1 led to suppression of the *OsHAL3*-overexpression phenotype (Fig. 4g, h). This is consistent with the idea that AtHIP1 functions downstream of OsHAL3 and is required for HAL3-mediated cell division. Using the data from this and previous studies, we proposed a model for HAL3 function in plant development (Fig. 4i). Trimerization of OsHAL3 recruits and activates HIP1, which leads to the degradation of cell cycle suppressor(s), resulting in an enhancement of cell division and plant growth. Light, especially blue light, suppresses this process by inactivating HAL3. This model describes a previously unrecognized pathway for light-regulated plant growth, which is in addition to the classic photoreceptor-mediated inhibition of cell elongation[1–4].

Furthermore, this finding also provides new perspectives for understanding stress-induced cell-cycle arrest in diverse organisms. Many stress conditions lead to the formation of reactive oxygen speices (ROS) that may inactivate HAL3, thereby inhibiting cell division. This may account for one mechanism of salt toxicity in plants as high salt-induced ROS may inactivate HAL3, leading to inhibited growth. In line with this idea, our data show that overexpression of *OsHAL3* enhanced salt tolerance in transgenic rice plants. Other abiotic stress conditions such as drought, low temperature and high light all elicit production of ROS that could affect the function of HAL3 in the regulation of cell division. Similar features could be conserved in other organisms, including yeast to human where HAL3 function appears to be highly conserved[9]. □

METHODS

Methods and any associated references are available in the online version of the paper at http://www.nature.com/naturecellbiology/.

Accession codes. Genbank: *OsHAL3*, FJ809894.

Note: Supplementary Information is available on the Nature Cell Biology website.

ACKNOWLEDGEMENTS

We thank Q.-H. Yao for providing a rice cDNA library and T. G. Sors for revising the manuscript. This work was supported by grants from the Ministry of Science and Technology of China (2006CB100100 and 2006AA10A102), the Chinese Academy of Sciences (KSCX2-YW-N-011), the National Natural Science Foundation of China (30730058 and 30821004), the Ministry of Agriculture of China (2009EX08009-0678) and the Shanghai Science and Technology Development Fund.

AUTHOR CONTRIBUTIONS

H.X.L., D.Y.C and S.Y.S. designed the experiments; H.Q.Y. designed some experiments; S.Y.S. and D.Y.C. performed most of the experiments; H.X.L., X.M.L., S.M., J.P.G. and M.Z.Z. performed some of the experiments; H.X.L. conceived and supervised the work and D.Y.C, H.X.L. and S. L. wrote the manuscript.

COMPETING FINANCIAL INTERESTS

The authors declare no competing financial interests.

Published online at http://www.nature.com/naturecellbiology/.
Reprints and permissions information is available online at http://npg.nature.com/reprintsandpermissions/.

1. Arnim, A. & Deng, X. W. Light control of seedling development. *Annu. Rev. Plant Physiol. Plant Mol. Biol.* **47,** 215–243 (1996).
2. Lin, C. & Shalitin, D. Cryptochrome structure and signal transduction. *Annu. Rev. Plant Biol.* **54,** 469–496 (2003).
3. Rockwell, N. C., Su, Y. S. & Lagarias, J. C. Phytochrome structure and signaling mechanisms. *Annu. Rev. Plant Biol.* 57**,** 837–858 (2006).
4. J., Lau, O. S. & Deng, X. W. Light-regulated transcriptional networks in higher plants. *Nature Rev. Genet.* **8,** 217–230 (2007).
5. Di Como, C. J., Bose, R. & Arndt, K. T. Overexpression of *SIS2*, which contains an extremely acidic region, increases the expression of *SWI4*, *CLN1* and *CLN2* in sit4 mutants. *Genetics* **139,** 95–107 (1995).
6. Ferrando, A., Kron, S. J., Rios, G., Fink, G. R. & Serrano, R. Regulation of cation transport in *Saccharomyces cerevisiae* by the salt tolerance gene *HAL3*. *Mol. Cell Biol.* **15,** 5470–5481 (1995).
7. Rodriguez, P. L., Ali, R. & Serrano R. CtCdc55p and CtHa13p: two putative regulatory proteins from *Candida tropicalis* with long acidic domains. *Yeast* **12**, 1321–1329 (1996).
8. Espinosa-Ruiz, A., Belles, J. M., Serrano, R. & Culianez-Macla, F. A. *Arabidopsis thaliana* AtHAL3: a flavoprotein related to salt and osmotic tolerance and plant growth. *Plant J.* **20,** 529–539 (1999).
9. Kupke, T., Hernández-Acosta, P. & Culiáñez-Macià, F. A. 4'-phosphopantetheine and coenzyme A biosynthesis in plants. *J. Biol. Chem.* 278, 38229–38237 (2003).
10. Yonamine, I. *et al.* Overexpression of *NtHAL3* genes confers increased levels of proline biosynthesis and the enhancement of salt tolerance in cultured tobacco cells. *J. Exp. Bot.* **55,** 387–395 (2004).
11. Zhang, N., Wang, X. & Chen, J. Role of OsHAL3 protein, a putative 4'-phosphopantothenoylcysteine decarboxylase in rice. *Biochemistry* **74,** 61–67 (2009).
12. Rios, G., Ferrando, A. & Serrano, R. Mechanisms of salt tolerance conferred by overexpression of the *HAL1* gene in *Saccharomyces cerevisiae*. *Yeast* **13,** 515-528 (1997).

13. Clotet, J., Gari, E., Aldea, M. & Arino, J. The yeast ser/thr phosphatases sit4 and ppz1 play opposite roles in regulation of the cell cycle. *Mol, Cell Biol,* **19**, 2408–2415 (1999).
14. Y., Mulet, J. M., Ariño, J. & Serrano, R. The Ppz protein phosphatases are key regulators of K^+ and pH homeostasis: implications for salt tolerance, cell wall integrity and cell cycle progression. *EMBO J.* **21,** 920–929 (2002).
15. Albert, A. *et al.* The X-ray structure of the FMN-binding protein AtHal3 provides the structural basis for the activity of a regulatory subunit involved in signal transduction. *Structure* **8,** 961–969 (2000).
16. Lin, C. *et al.* Association of flavin adenine dinucleotide with the *Arabidopsis* blue light receptor CRY1. *Science* **269,** 968–970 (1995).
17. Sang, Y. *et al*. N-terminal domain-mediated homodimerization is required for photoreceptor activity of *Arabidopsis* Cryptochrome 1. *Plant Cell* **17**, 1569–1584 (2005).
18. Hernandez-Acosta, P., Schmid, D. G., Jung, G., Culianez-Macia, F. A. & Kupke, T. Molecular characterization of the *Arabidopsis thaliana* flavoprotein AtHAL3a reveals the general reaction mechanism of 4'-phosphopantothenoylcysteine decarboxylases. *J. Biol. Chem.* **277**, 20490-20498 (2002).
19. Zimmermann, P., Hirsch-Hoffmann, M., Hennig, L. & Gruissem, W. GENEVESTIGATOR. *Arabidopsis* Microarray Database and Analysis Toolbox. *Plant Physiol.* **136,** 2621–2632 (2004).
20. Baerenfaller, K. *et al*. Genome-scale proteomics reveals *Arabidopsis thaliana* gene models and proteome dynamics. *Science* **320,** 938–941 (2008).
21. Rubio, S. *et al*. An *Arabidopsis* mutant impaired in coenzyme A biosynthesis is sugar dependent for seedling establishment. *Plant Physiol.* **140,** 830-843 (2006).
22. de Nadal, E. *et al*. The yeast halotolerance determinant Hal3p is an inhibitory subunit of the Ppz1p Ser/Thr protein phosphatase. *Proc. Natl. Acad. Sci. USA* **95**, 7357–7362 (1998).
23. Kupke, T., Hernandez-Acosta, P., Steinbacher, S. & Culianez-Macia, F. A. *Arabidopsis thaliana* flavoprotein AtHAL3a catalyzes the decarboxylation of 4'-Phosphopantothenoylcysteine to 4'-phosphopantetheine, a key step in coenzyme A biosynthesis. *J. Biol.Chem.* **276,** 19190–19196 (2001).
24. Steinbacher, S. *et al*. Crystal structure of the plant PPC decarboxylase AtHAL3a complexed with an ene-thiol reaction intermediate. *J. Mol. Biol.* **327**, 193–202 (2003).
25. Munoz, I. *et al*. Functional characterization of the yeast Ppz1 phosphatase inhibitory subunit Hal3: a mutagenesis study. *J. Biol. Chem.* **279,** 42619-42627 (2004).
26. Ruiz, A. *et al*. Functional characterization of the *Saccharomyces cerevisiae* VHS3 gene: a regulatory subunit of the Ppz1 protein phosphatase with novel, phosphatase-unrelated functions. *J. Biol. Chem.* **279,** 34421–34430 (2004).
27. Muñoz, I. *et al*. Functional characterization of the yeast Ppz1 phosphatase inhibitory subunit Hal3: a mutagenesis study. *J. Biol. Chem.* **279,** 42619-42627 (2004).

DOI: 10.1038/ncb1892

METHODS

Plant material and growth conditions. All rice (*Oryza sativa*) plants used in this study were, or were derived from, the *japonica* variety *Zhonghua11*. The plants were cultivated in Yoshida's liquid culture solution under different conditions, including various light regimes specified as: continuous darkness (26 °C), white light (240 μmol m^{-2} s^{-1}, 26 °C), blue light (30 μmol m^{-2} s^{-1}, 26 °C), red light (50 μmol m^{-2} s^{-1}, 26 °C), far-red light (50 μmol m^{-2} s^{-1}, 26 °C); white light (240 μmol m^{-2} s^{-1}, 26 °C)/darkness (26 °C) cycle, and blue light (30 μmol m^{-2} s^{-1}, 26 °C)/darkness (26 °C) cycle. The light sources were the same as described previously[17,28]. Seedling length was measured on day 12 after seed germination.

OsHAL3 antibody and western blotting. A rabbit was immunized with more than 5 mg of purified His–OsHAL3 protein at three-week intervals. OsHAL3 antibodies were purified from the crude rabbit antiserum using MBP–OsHAL3 fusion protein as described previously[29]. Subsequent protein extraction and immunoblotting were performed as described previously[17].

Cross-linking assay. We performed cross-linking assays as described previously[17] with some modifications. Briefly, rice seedlings were ground to a powder in liquid nitrogen and were immediately incubated in PBSM buffer (1.76 mM KH_2PO_4, 10 mM Na_2HPO_4, 136 mM NaCl, 2.6 mM KCl, 5 mM $MgCl_2$ and 10% glycerol) containing 1% formaldehyde under vacuum for 30 min. The cross-linking reactions were quenched by addition of Tris-HCl at pH 7.5 to a final concentration of 0.25 M for 5 min. After brief centrifugation, the supernatant was removed and the pellet collected. Proteins were extracted from the pellet and examined by immunoblotting.

Pulldown assays. The purified fusion proteins (MBP–OsHAL3, GST–OsHAL3 and GST–OsHIP1) and control peptides (MBP and GST) were equilibrated in phosphate buffered saline at 4 °C overnight in dialysis bags. The two equilibrated fusion proteins were incubated with GST-sepharose beads in GST-pulldown buffer and exposed to blue light (30 μmol m^{-2} s^{-1}) for 30 min. For blue light treatment, the incubation was continued for another 60 min in blue light (30 μmol m^{-2} s^{-1}). For the darkness condition, the incubated mixture was transferred into darkness for 60 min. After washing five times under blue light or darkness, the beads were suspended in 30 μl of 1×SDS loading buffer and boiled for 3 min. After brief centrifugation, the supernatant was collected and subjected to immunoblotting analysis.

Reverse transcription and real-time PCR. Total RNA was extracted from 12-day-old rice seedlings using TRIzol reagent. First strand cDNA was synthesized using Promega's reverse transcription system (Promega). Real-time PCR was performed using an SYBR green method[30] on Rotor-gene 3000 (Corbett Research). The primers used for *OsHAL3*, *AtHIP1* and the *actin* control are listed in Supplementary Information, Table S1.

Pantethine treatment. Pantethine treatment was performed as described previous[21]. Bis[N-pantothenylamidoethyl] disulfide (pantethine, Sigma P2125) was added into the rice culture solution to final concentrations of 50 μg ml^{-1}, 1,000 μg ml^{-1} or 3,750 μg ml^{-1}, respectively. Germinated rice seedlings were transferred into the culture solutions with or without pathethine and their growth (seedling length) was measured 12 days after growing under the light/dark conditions.

Rice and *Arabidopsis* transformation. Full-length *OsHAL3* was amplified using primers introduced at restriction sites (see Supplementary Information, Table S1). The PCR-amplified fragment was then cloned into a pGEM-Teasy vector (Clontech), and then subcloned into a plant overexpression vector pHB[28]. For *OsHAL3* promoter-GUS analysis, a 1.5-kb promoter region upstream of the initial codon was also amplified by PCR from *Zhonghua 11* (ZH11) genomic DNA (Primers are shown in Supplementary Information, Table S1). The promoter fragment together with a GUS reporter gene was subcloned into the binary vector pCAMBIA1300. The two constructs and pHB and pCAMBIA1300 empty vectors were transformed into ZH11 using an Agrobacterium-mediated method[31]. The OsHAL3 overexpression vector was also transformed into *Arabidopsis* ecotype of Col-0 by the floral dip method. GUS histochemical staining was performed as described previously[32].

For *AtHIP1* RNAi, a 342 bp fragment was amplified by RT-PCR using specific primers with designed *Kpn*I and *Pst*I restriction sites (primers are shown in Supplementary Information, Table S1), and inserted into sense RNAi vector p1300-RS[33]. And the RNAi vector was transformed into an OsHAL3-overexpression *Arabidopsis* line by the floral dip method.

Construction of OsHAL3 mutants. The OsHAL3 mutants were obtained by site-directed mutagenesis. The mutants were produced by amplifying a pTA2 vector inserted with *OsHAL3*, using primers designed with mutated nucleotides (see Supplementary Information, Table S1). The PCR products were digested with *Dpn*I and then transformed into *E. coli* strain DH5α. After sequencing of the transformants, the mutated sequences of OsHAL3 were subcloned into corresponding vectors. $OsHAL3^{PPYP}$ was inserted into a pET-32a in frame and $OsHAL3^{H91N}$ and $OsHAL3^{C176S}$ were cloned into pHB for *Arabidopsis* transformation.

Yeast two-hybridization. Yeast two-hybridization was performed using the LexA system (Clontech). A PCR-amplified *OsHAL3* fragment was cloned in frame into *Eco*RI and *Bam*HI sites of pLexA to form the bait construct (primers are shown in Supplementary Information, Table S1). The bait construct was digested with *Eco*RI and *Sal*I. The fragment containing *OsHAL3* was collected and inserted into the *Eco*RI and *Xho*I sites of pJG4-5 to form the prey construct. The *OsHAL3* mutant was generated from pBluescript SK-*OsHAL3* using primers listed in Supplementary Information, Table S1. The *OsHAL3* mutant fragment was inserted into *Eco*RI and *Bam*HI sites of pLexA to form the bait construct for the $OsHAL3^{PPYP}$ mutant. The bait and prey constructs together with a reporter vector were transformed into yeast strain EGY48 according to the manufacturer's instructions for the Matchmaker LexA twohybrid system (Clontech). The bait and prey constructs for CRY1 and CRY1 N-terminal domain (CNT1) was made as described previously[17]. The transformants were grown on different mediums at 30 °C in darkness, blue light (30 μmol m^{-2} s^{-1}), red light (50 μmol m^{-2} s^{-1}) or far-red light (50 μmol m^{-2} s^{-1}).

For protein interaction screens, the OsHAL3 bait construct, the reporter vector and a rice cDNA library constructed on the prey vector pPC86 were co-transformed into EGY48 cells. Screening was performed in darkness. The sequences of gene encoding putative OsHAL3 interacting proteins were obtained through a combination of PCR and plasmid rescue of Bacteria (sequencing primers are shown in Supplementary Information, Table S1). The positive interactions were confirmed by tests of transformants only with preys and transformants with re-transformed prey and bait.

Prokaryotic expression and purification of fusion proteins. *OsHAL3* fragment was amplified using specific primers (Supplementary Information, Table S1) and digested with *Eco*RI and *Xho*I. The digestion fragment was inserted in frame into pET32a. For expression of MBP-OsHAL3 and GST-OsHAL3 fusion proteins, an *OsHAL3* fragment was re-digested from pET32a-OsHAL3 construction with *Eco*RI and *Sal*I and inserted into pMAL and pGEX. For the GST–OsHIP1 fusion protein, the *OsHIP1* gene was cloned by RT-PCR using specific primers (Supplementary Information, Table S1) with designed restriction sites (*Eco*RI and *Sal*I). Then the fragment was recombined into pGEX through *Eco*RI and *Sal*I sites to form the expression vector for GST–OsHIP1. Bacteria strain BL21 (DE3) was transformed with these constructs to produce His–OsHAL3, MBP–OsHAL3, GST–OsHAL3 and GST–OsHIP1 fusion proteins. MBP–OsHAL3, GST–OsHAL3 and GST–OsHIP1 were induced by 1 mM IPTG (isopropyl-β-D-thiogalactoside) for 48 h at 12 °C to extract active fusion proteins and His–OsHAL3 was induced for 5 h at 37 °C for extracting denatured fusion proteins. The cultured bacteria cells were lysed with a refrigerant plunger and the fusion proteins were purified in a Ni-column (QIAGEN company), amylose column with maltose (New England Biolabs) and glutathione Sepharose (Amersham) according the manufacturers' instructions.

28 Mao, J., Zhang, Y. C., Sang, Y., Li, Q. H. & Yang, H. Q. A role for *Arabidopsis* cryptochromes and COP1 in the regulation of stomatal opening. *Proc. Natl. Acad. Sci. USA* **102,** 12270–12275 (2005).

29 Osterlund, M. T., Hardtke, C. S., Wei, N. & Deng, X. W. Targeted destabilization of HY5 during light-regulated development of *Arabidopsis*. *Nature* **405,** 462–466 (2000).

30 Karsai, A., Muller, S., Platz, S. & Hauser, M. T. Evaluation of a homemade SYBR green I reaction mixture for real-time PCR quantification of gene expression. *Biotechniques* **32,** 790–796 (2002).

31 Hiei, Y. *et al.* Efficient transformation of rice (*Oryza sativa L.*) mediated by Agrobacterium and sequence analysis of the boundaries of the T-DNA. *Plant J* **6,** 271–282 (1994).

32 Lagarde, D. *et al.* Tissue-specific expression of *Arabidopsis AKT1* gene is consistent with a role in K^+ nutrition. *Plant J* **9,** 195–203 (1996).

33 Mei, C., Zhou, X. & Yang, Y. Use of RNA interference to dissect defense signaling pathways in rice plants. In *Methods in Molecular Biology: Plant-Pathogen Interactions* Vol. **354,** (Ed. P. Ronald) 161–171 (Humana Press, 2007).

nature cell biology

DOI: 10.1038/ncb1892

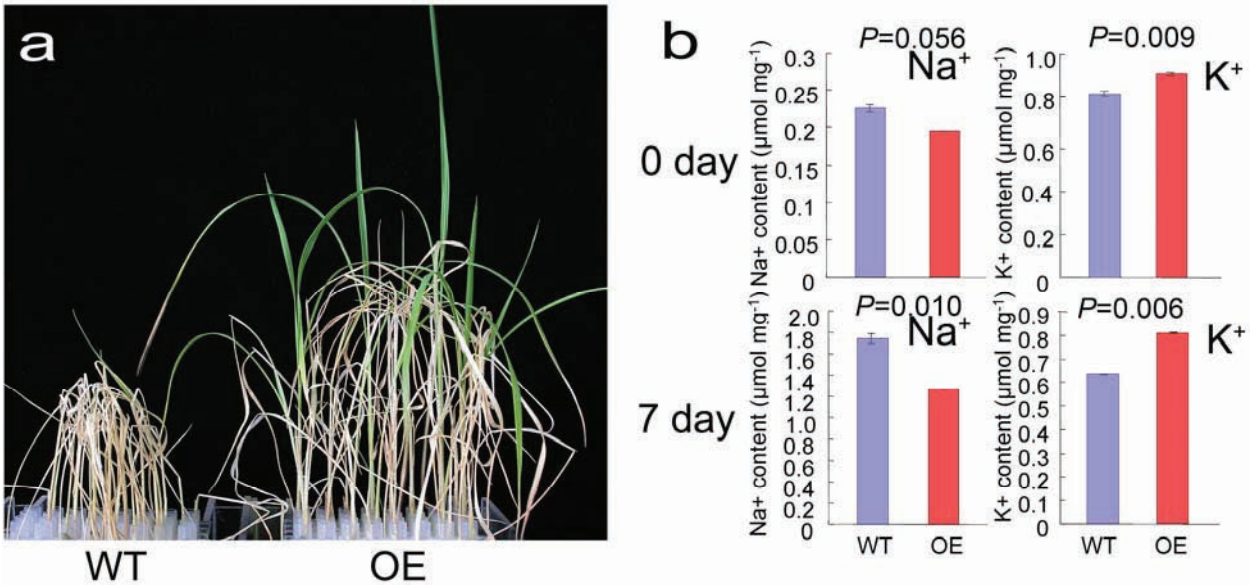

Figure S1 Overexpression of *OsHAL3* enhanced rice salt tolerance. **a**, Phenotype of wild type (WT) and *OsHAL3* overexpression (OE) lines after treated with 120 mM NaCl for 25 days. **b**, Sodium and potassium content in seedlings of wild type (WT) and *OsHAL3* overexpression (OE) lines before (upper) and after salt treatment (lower) for 7 days.

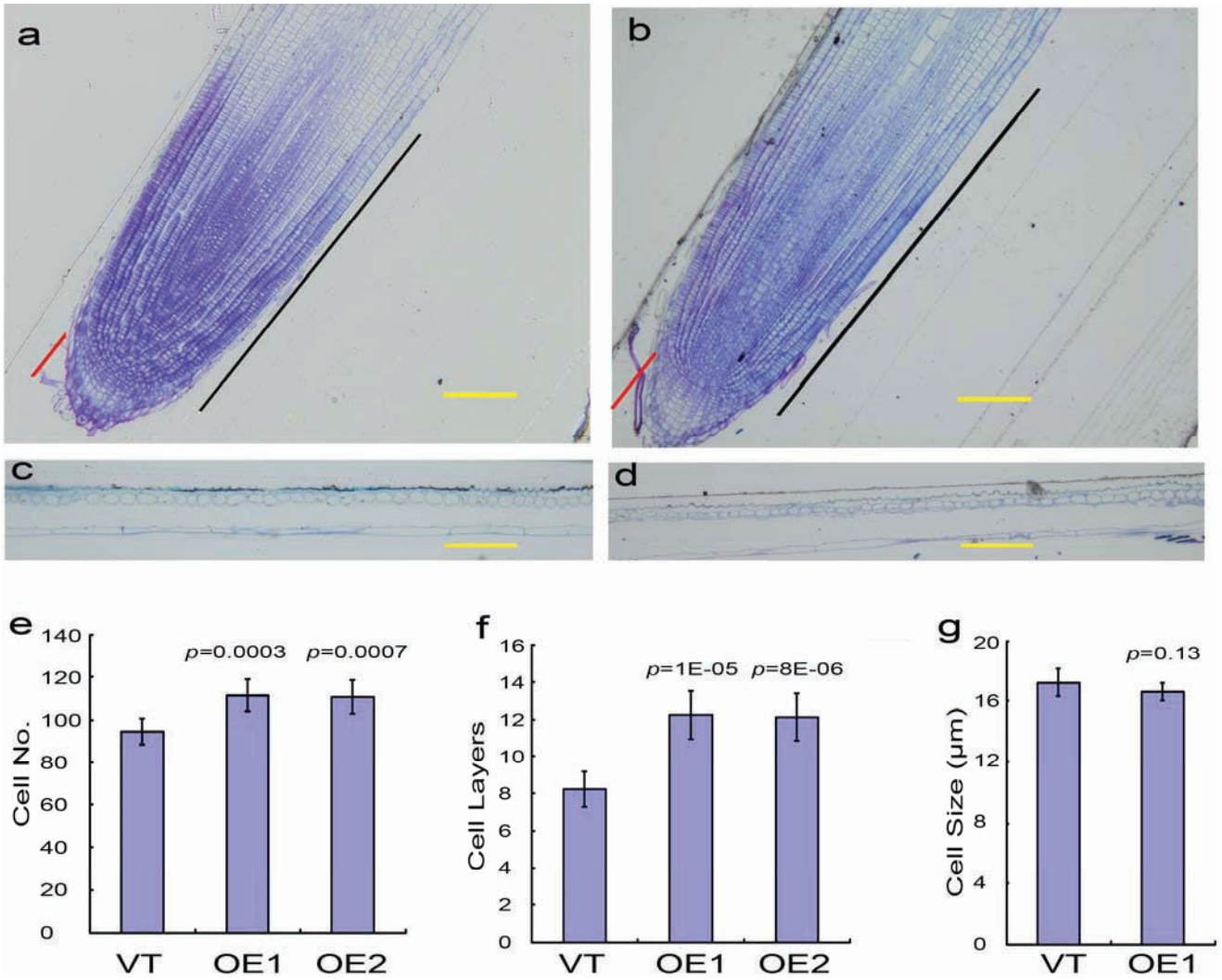

Figure S2 Cell biological analysis of *OsHAL3* overexpression lines. a-d, Tissue sections of root tips (a, b) and sheathes (c, d) of vector control line (a, c) and *OsHAL3* overexpression lines (b, d). Black bars show root meristematic zones, and red bars show root cap zones. The yellow lines with same length are scale bars representing 100 μm. **e**, Epidermal cell numbers in root meristematic zones. **f,** Cell layers of root caps. **g**, Epidermal cell size in sheath. VT, Vector control line; OE, *OsHAL3* overexpression lines. Data are shown in (e-g) as means ± s.d. (n=9 in (e, f) and n=6 in (g)). P values were generated by a student t-test compared data from empty vector control and transgene lines, and indicated correspondingly.

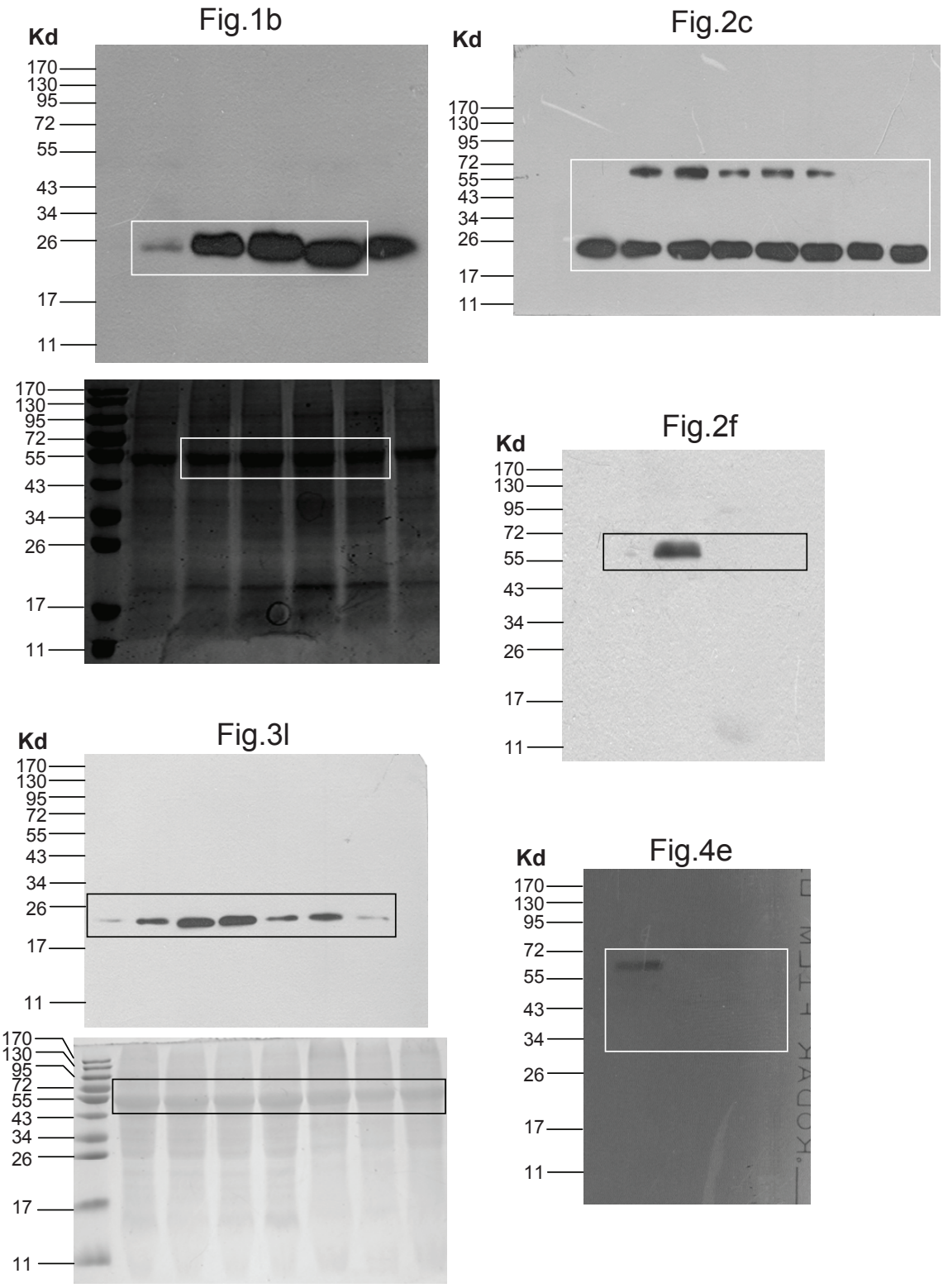

Figure S3 Full scans of western blots. Rectangles delimit cropped areas used in the indicated figures.

Table S1. The primers for OsHAL3 molecular analysis.

Name	Primer sequence	Purpose
CH3946U	5'CCGCGAATTCATGACTACATCAGAGTCAG3'	Bait and prey construction for y2h of OsHAL3
CH3946-1L	5'CCGCGGATCCGCTAGATGGGAGGTTTCTG3'	Bait and prey construction for y2h of OsHAL3
PET3946U	5'CCGCGAATTCATGACTACATCAGAGTCAG3'	prokaryotic expression for OsHAL3 fusion proteins
PET3946L	5'CCGCCTCGAGCGCTAGATGGGAGGTTTCTG3'	prokaryotic expression for OsHAL3 fusion protein
RTHAL3aU	5'CACCAGCAATCTTAGCTAG3'	RT-PCR
RTHAL3aL	5'ATGACTACATCAGAGTCAG3'	RT-PCR
Actin-U	5' TCCATCTTGGCATCTCTCAG 3'	RT-PCR and Real-time RT-PCR
Actin-L	5' GTACCCGCATCAGGCATCTG 3'	RT-PCR and Real-time RT-PCR
OsHal3YS	5'TGATAGAACGTCTCTGCCTAGCA3'	Real-time RT-PCR
OsHal3YA2	5'ATACCTAGCAGGTTGATTGTCTCA3'	Real-time RT-PCR
C3946-1U	5'CGGGATCCATGACTACATCAGAGTCAG3'	Overexpression vector construction of OsHAL3
C3946-1L	5'CGAGCTCTCAGCTAGATGGGAGGTTTC3'	Overexpression vector construction of OsHAL3
P3946U	5'ACGCGTCGACCACCTCAGTACTTCACCTGTAC3'	Cloning of promoter of OsHAL3
P3946-1L	5'AAAACTGCAGGCGAGCATAGGAGCTCAGTG3'	Cloning of promoter of OsHAL3
MA4a-S	5'GATTGCGCCATTACCACCTTATCCCCTGGCTAAGATTG3'	Producing mutant of OsHAL3-PPYP
MA4a-A	5'CAATCTTAGCCAGGGGATAAGGTGGTAATGGCGCAATC3'	Producing mutant of OsHAL3-PPYP
C176S1	5'CATTACCAAAAGGCTGGCCTcTGGTGATTATGGTAATGGTGC3'	Producing mutant of OsHAL3-C176S
C176S2	5'GCACCATTACCATAATCACCAgAGGCCAGCCTTTTGGTAATG3'	Producing mutant of OsHAL3-C176S
H91N1	5'TAGGGGATGAAGTTTTGaACATTGAACTGCGAAAATGGG3'	Producing mutant of OsHAL3-H91N
H91N2	5' CCCATTTTCGCAGTTCAATGTtCAAAACTTCATCCCCTA3'	Producing mutant of OsHAL3-H91N
TLB1	5'AGCGTCAATTTGTTTACACCAC3'	Screening T-DNA mutant of *oshal3*
HR1	5'CTTCATCCCCTATCTTCTTCCA3'	Screening T-DNA mutant of *oshal3*
HalF	5'GCCCATTTTCGCAGTTCAAT3'	Screening T-DNA mutant of *oshal3*
HalR	5'GAGTCTCCGCCTCTTCCCGT3'	Screening T-DNA mutant of *oshal3*
Ppc86U	5'GCGTATAACGCGTTTGGAATC3'	For sequencing candidate cDNA fragments conding OsHAL3 interacting proteins
Ppc86L	5'CGTAAAATTTCTGGCAAGGTAGAC3'	For sequencing candidate cDNA fragments conding OsHAL3 interacting proteins

Table S2. The plant number in Figures 1 and 4.

	Fig. 1c	**Fig. 1d**	**Fig. 1e**	**Fig. 1f**	**Fig. 1g**	**Fig. 1h**	**Fig. 1i**
WT	20	24	21	35	32	20	24
OE1	20	21	21	27	22	20	22
OE2	22	22	20	34	24	21	24

Fig. 4b	VT	OsHAL3	OsHAL3-C176S	OsHAL3-H91N
	17	10	10	10
Fig. 4h	OsHAL3	AtHIP1-RNAi-1	AtHIP1-RNAi-2	AtHIP1-RNAi-3
	21	16	20	15

nature cell biology

Increasing organismal healthspan by enhancing mitochondrial protein quality control

Karin Luce[1] and Heinz D. Osiewacz[1,2]

Degradation of damaged proteins by members of the protein quality control system is of fundamental importance in maintaining cellular homeostasis. In mitochondria, organelles which both generate and are targets of reactive oxygen species (ROS), a number of membrane bound and soluble proteases are essential components of this system. Here we describe the regulation of *Podospora anserina* LON (PaLON) levels, an AAA+ family serine protease localized in the matrix fraction of mitochondria. Constitutive overexpression of *PaLon* results in transgenic strains of the fungal ageing model *P. anserina* showing increased ATP-dependent serine protease activity. These strains display lower levels of carbonylated (aconitase) and carboxymethylated proteins, reduced secretion of hydrogen peroxide and a higher resistance against exogenous oxidative stress. Moreover, they are characterized by an extended lifespan without impairment of vital functions such as respiration, growth and fertility. The reported genetic manipulation proved to be a successful intervention in organismal ageing and it led to an increase in the healthy lifespan, the healthspan, of *P. anserina*.

Ageing of organisms is controlled by a complex network of molecular pathways in which mitochondria play a central role[1,2]. Although essential for the efficient generation of adenosine triphosphate (ATP), these organelles are at the same time the main source of ROS, compounds which are causally linked to the progressive accumulation of molecular damage ultimately leading to cellular dysfunction and death[3,4]. Consequently, either scavenging ROS or reducing their generation can lead to lifespan extension[5,6]. Another strategy to counteract the harmful consequences of ROS is the induction of molecular pathways involved in repair and degradation of damaged molecules.

Our investigations aimed at improving the efficacy of the cellular machinery controlling the degradation of damaged proteins. We concentrated on mitochondria in which the soluble serine protease LON, is active. In addition to its ATP-dependent protease function, LON is involved in maintaining mitochondrial DNA integrity and, as a molecular chaperone, is involved in the control of protein complex assembly[7,8]. Knockout of *Pim1*, the gene coding for the yeast homologue of LON, leads to respiration deficiency[8]. In human lung fibroblasts, the downregulation of *Lon* has been reported to impair mitochondrial structure and function and cause cell death[9].

We investigated the role of LON in *P. anserina*, an experimentally tractable, short-lived *in vivo* system with a well defined mitochondrial etiology of ageing[10]. Computer analysis identified one gene, *PaLon*, in the *P. anserina* genome that encoded a putative LON homologue. The deduced amino-acid sequence corresponds to a protein monomer with a relative molecular mass of 122,000 (M_r 122K) that has the characteristic domains highly conserved from bacteria to humans (Supplementary Information, Fig. S1). Use of a polyclonal peptide antibody showed PaLON to be localized in the mitochondrial cell fraction (Supplementary Information, Fig. S2).

Although it is thought that LON is a critical component of the mitochondrial protein quality control system, relevant for development and ageing, the data is inconsistent. For instance, in rat liver mitochondria it has been shown that LON activity decreases during ageing, whereas in rat heart mitochondria its activity increases. In mice muscle cells, transcription and protein levels drop in aged cells. Interestingly, this effect can be abolished by calorie restriction[11]. These differences in age-dependent regulation may result from tissue-specific differences in the level of damaged proteins and from interactions of different cells and tissues in multicellular systems. We therefore investigated an age-related role of LON in *P. anserina* in which — due to its simple organization — such complications do not exist. Real-time (rt) PCR experiments revealed a 2.9-fold increase in *PaLon* transcript levels in senescent versus juvenile cultures (Fig.1a; Supplementary Information, Fig. S3a). Unexpectedly, neither PaLON abundance (Fig. 1b) nor ATP-dependent protease activity (Fig. 1c; Supplementary Information, Fig. S3b), which can be inhibited by the serine protease inhibitor pefabloc, was found to change significantly in the matrix fraction of mitochondria during the ageing of wild-type cultures. Although we currently cannot conclusively explain these discrepancies, they may result from age-related impairments of translation efficacy and/or the capacity to transport proteins from cytoplasm into mitochondria.

[1]Johann Wolfgang Goethe University, Faculty for Biosciences and Cluster of Excellence Macromolecular Complexes, Institute of Molecular Biosciences, Max-von-Laue-Strasse 9, 60438 Frankfurt, Germany.
[2]Correspondence should be addressed to H.D.O. (e-mail: osiewacz@bio.uni-frankfurt.de)

Received 18 September 2008; accepted 19 March 2009; published online 21 June 2009; DOI: 10.1038/ncb1893

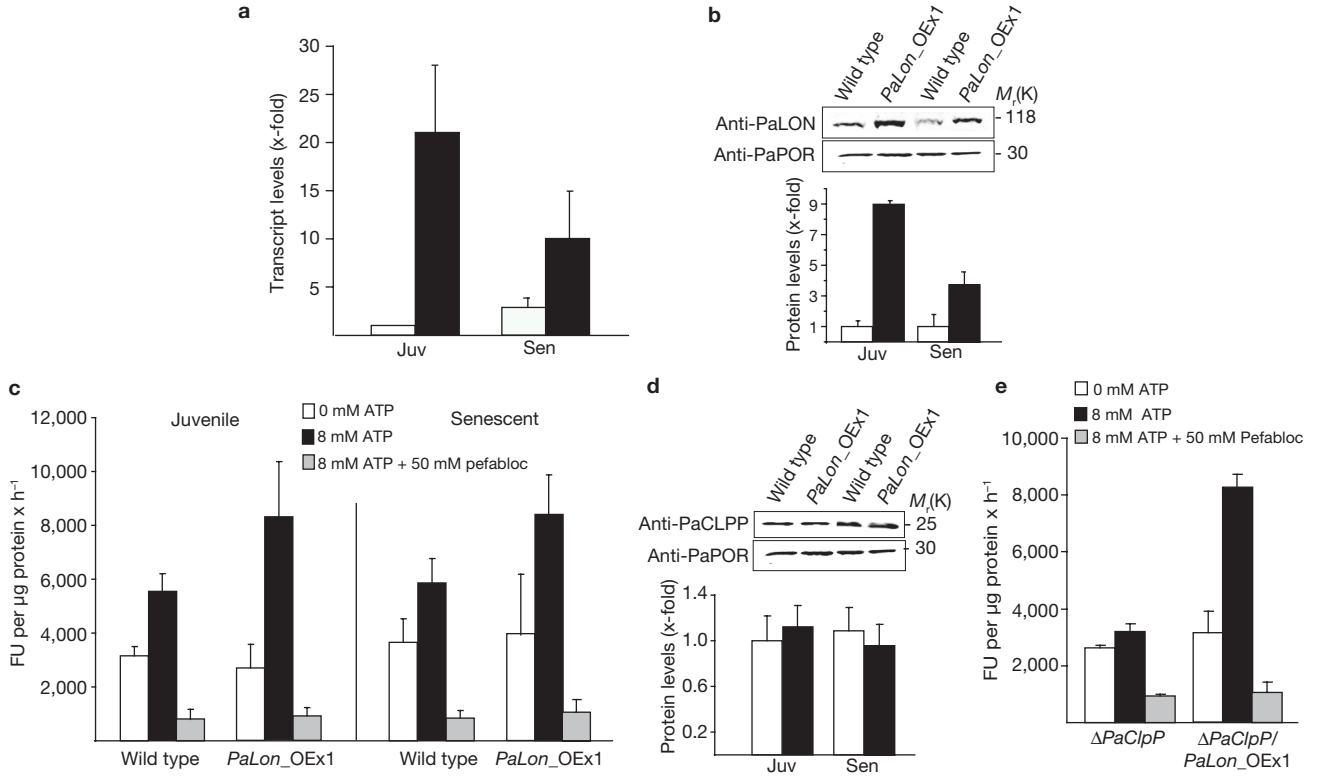

Figure 1 Overexpression of *PaLon* encoding the LON protease of *P. anserina*. (**a**) Relative transcription of *PaLon* in juvenile (Juv; 1; $n = 8$) and senescent (Sen; 2.88 ± 0.84; $n = 8$; $P = 1.8E\text{-}4$) wild-type strains (white bars) and juvenile (21.04 ± 6.73; $n = 6$; $P = 2.0E\text{-}4$) and senescent (10.03 ± 4.81; $n = 5$; $P = 7.9E\text{-}3$) *PaLon*-overexpression strains (black bars;). Data are mean ± s.d. from three independent experiments. (**b**) Protein level of PaLON visualized by western blotting analysis and densitometrically analysed using mitochondrial protein extracts from juvenile (1.0 ± 0.32; $n = 5$) and senescent (1 ± 0.77; $n = 5$; $P = 0.27$) wild-type strains (white bars) and juvenile (8.9 ± 0.17; $n = 5$; $P = 2.0E\text{-}4$) and senescent (3.7 ± 0.79; $n = 5$; $P = 6.2E\text{-}3$) *PaLon*_OEx1 strains (black bars). The predicted sizes of the proteins are shown (top). Porin was used as a loading control for quantification. Data are mean ± s.d. from three independent experiments. (**c**) Protease activity in soluble mitochondrial protein extracts from juvenile ($n = 4$) and senescent ($n = 4$) wild-type strains and juvenile ($n = 4$) and senescent ($n = 4$) *PaLon*_OEx1 strains in the absence of ATP, presence of ATP (8 mM) and presence of ATP + pefabloc (8 mM and 50 mM, respectively). Data are mean ± s.d. from six independent experiments. FU, fluorescence units (**d**) Protein abundance of PaCLPP in mitochondria of juvenile (1 ± 0.22; $n = 4$) and senescent (1.09 ± 0.20; $n = 4$; $P = 0.61$) wild-type strains (white bars) and juvenile (1.12 ± 0.19; $n = 4$; $P = 0.63$) and senescent (0.96 ± 0.18; $n = 4$; $P = 0.63$). *PaLon*_OEx1 strains (black bars) Porin was used as loading control for quantification. Data are mean ± s.d. from three independent experiments. (**e**) Protease activity in the soluble mitochondrial protein fraction of juvenile Δ*PaClpP* ($n = 4$) and Δ*PaClpP*/*PaLon*_OEx1 ($n = 4$) strains in the absence of ATP, presence of ATP (8 mM) and presence of ATP + pefabloc (8 mM and 50 mM, respectively). Data are mean ± s.d. from six independent experiments. *P* values were determined by two tailed Wilcoxon test.

To experimentally elucidate the potential role of PaLON in ageing and lifespan control, we set out to generate *P. anserina* strains with increased PaLON abundance. Stable secondary transformants containing the open reading frame of *PaLon* under the control of the constitutive strong metallothioneine (PaMT1) promoter integrated into chromosomal DNA[12] were selected. Compared with the juvenile wild-type strain, the *PaLon*-overexpressing strain showed increased *PaLon* transcript and protein levels as well as increased ATP-dependent protease activity in both juvenile and senescent cultures. Although transcript levels were 21-fold higher in juvenile and 10-fold higher in senescent samples (Fig. 1a), PaLON abundance was found to be 8.9-fold higher in senescent and 3.7-fold higher in juvenile samples (Fig. 1b). The reduction in transcript levels and protein abundance observed in senescent strains may result from general impairments in *PaLon*-expression and/or increased RNA and protein degradation, respectively. Notably, the ATP-dependent protease activity was increased about 1.5-fold in both juvenile and senescent cultures of *PaLon*-overexpressing strains (Fig. 1c). Since it is probable that the active protease in *P. anserina*, as in other systems (for example, yeast and humans), is a homo-oligomer (that is, a heptamer ring-like structure), and as at least one other ATP-dependent mitochondrial protease, CLPP, may contribute to the measured protease activity, the observed activity values in the *PaLon*-overexpressing strain seem to be realistic. The detection of a putative *P. anserina* CLPP protein, PaCLPP, as a second serine protease in immunoblots of mitochondrial matrix proteins strongly supports this conclusion. Notably, the abundance of PaCLPP does not change significantly during ageing of either the wild-type or the *PaLon*-overexpressing strain (Fig. 1d). A newly generated *PaClpP*-deletion strain (Supplementary Information, Fig. S4) showed ATP-dependent protease activity that was 44% lower than that of the wild type (Fig. 1c, e). Finally, we determined the ATP-dependent protease activity in the Δ*PaClpP*/*PaLon*_OEx1 double mutant (Supplementary Information, Fig. S4) and found a 2.6-fold higher activity level than in the *PaClpP*-deletion

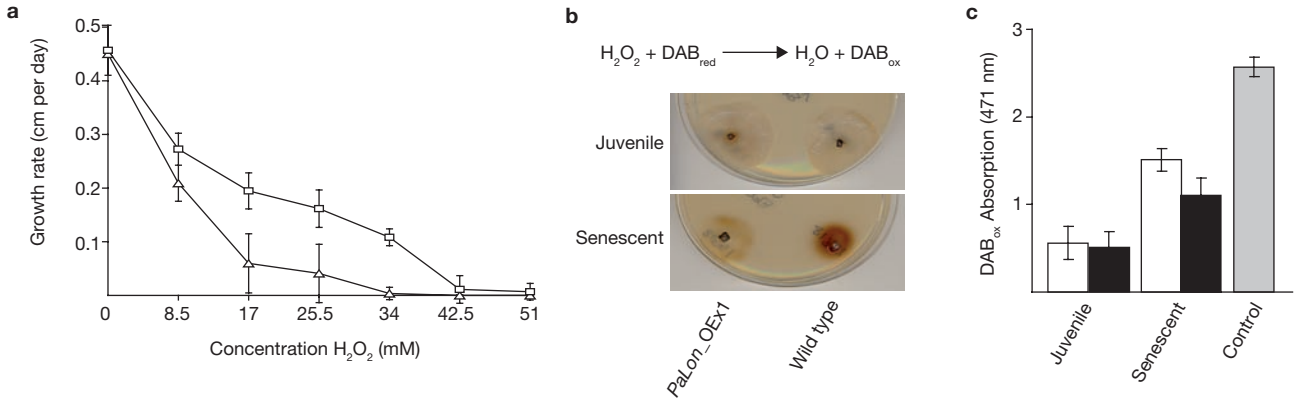

Figure 2 Analysis of oxidative stress tolerance and the release of hydrogen peroxide by strains overexpressing *PaLon*. (**a**) Growth rate of wild-type (triangles; $n = 11$) and *PaLon*_OEx1 (squares; $n = 12$) strains on standard media with 0 mM ($P = 0.98$), 8.5 mM ($P = 8.03E-5$), 17 mM ($P = 4.7E-5$), 25.5 mM ($P = 4.0E-5$), 34 mM ($P = 2.5E-5$), 42.5 mM ($P = 0.98$) and 51 mM ($P = 0.97$) H_2O_2. (**b**) Determination of H_2O_2 amounts in juvenile and senescent wild-type and *PaLon* OEx1 strains ($n = 8$) by DAB staining. (**c**) Quantification of oxidized DAB as a measure of H_2O_2 release by juvenile wild-type (white bar) and *PaLon*_OEx1 (black bar) strains ($n = 8$; $P = 0.97$) and senescent wild-type (white bar) ($n = 8$; $P = 1.6E-4$) and *PaLon*_OEx1 (black bar) strains ($n = 8$; $P = 7.0E-3$). H_2O_2 (0.02%) was added to the DAB solution as a positive control (Control). *P* values were determined by two tailed Wilcoxon test.

strain (Fig. 1e). Collectively, these data support the conclusion that the identified increase in ATP-dependent protease activity in the *PaLon*_OEx1 strain results from overexpression of *PaLon* and that about half of the activity in the wild-type strain is derived from PaLON and half from PaCLPP. Furthermore, as PaCLPP protease is not produced in the Δ*PaClpP/ PaLon*_OEx1 double mutant, the increase in ATP-dependent protease activity identified in this strain represents PaLON-specific serine protease activity in the mitochondrial matrix.

In a subsequent series of experiments we investigated the impact of increased *PaLon* expression on fungal cultures. First, we compared the resistance of transgenic and wild-type strains against exogenous oxidative stress (Fig. 2a). Strains overexpressing *PaLon* were found to grow better on H_2O_2-supplemented medium than wild-type strains. This increase in stress tolerance may be the result of reduced endogenous oxidative stress in the *PaLon*_OEx1 strain. To investigate this possibility, we compared the release of H_2O_2 in juvenile and senescent wild-type and *PaLon*_OEx1 strains using a histochemical assay[13] and observed an increase of H_2O_2 release during ageing in both strains (Fig. 2b, c). Significantly, this age-related increase was more pronounced in the wild-type (2.7-fold) than in the mutant strain (2.1-fold).

Next, we investigated whether the increase in stress tolerance and the reduction in H_2O_2 release observed in the *PaLon*-overexpressing strain correspond to a reduction in the endogenous load of damaged proteins. Using a monoclonal antibody, which detects proteins containing carboxymethylated lysine (CML)[14], we identified, for the first time, an age-dependent increase of this oxidative post-translational modification in *P. anserina* (Fig. 3a). The increase was much stronger in senescent strains of the wild-type than in the transgenic strain. In other systems, this type of protein modification, which is related to the formation of advanced glycation end products (AGE), is known to accumulate during ageing[15]. In contrast to the strong increase in carboxymethylated proteins during ageing in the wild type, we were unable to demonstrate such a strong increase in carbonylation, the most commonly investigated oxidative protein modification, using western blotting (Oxy Blot) of proteins fractionated on 1D SDS polyacrylamide gels (SDS–PAGE). However, when compared with juvenile and senescent cultures of the wild-type, the corresponding cultures of *PaLon*-overexpressing strain showed ~50% reduction in carbonylated proteins (Fig. 3b, c). This may be because during ageing it is not the bulk of proteins that become oxidatively damaged, but only a specific set of proteins. To address this possibility, we compared 2D SDS–PAGE-fractionated mitochondrial proteins from juvenile and senescent wild-type and *PaLon*-overexpressing strains. Some marked differences were identified in both the pattern (Fig. 3d) and abundance (Fig. 3e; Anti-ACO) of carbonylated proteins. Specifically, an age-related increase in carbonylation of mitochondrial aconitase isoforms in both wild-type and mutant strains was observed in immunoblots. Significantly, the fraction of carbonylated aconitase (Fig. 3e; Anti-DNP) and the total abundance of aconitase were reduced in *PaLon*-overexpressing strains (Fig. 3e; Coomassie). The latter was even more evident on 1D immunoblots (Fig. 3f). Interestingly, aconitase activity was almost identical in the wild-type and the *PaLon*-overexpressing strains (Fig. 3g). As the carbonylated form of this Krebs-cycle protein has been found to be a substrate of LON in human cell cultures[16], we hypothesise that this also holds true in *P. anserina* and that the damaged protein is more efficiently degraded in *PaLon*-overexpressing strains. In contrast, in the wild-type strain a substantial fraction of aconitase seems to be damaged and inactive.

Next, after having demonstrated an age-related increase in *Lon* transcript levels and protein modification, we addressed the question of whether there is an effect on transcriptional control of *PaLon* through calorie restriction, an experimental regime known from other systems to slow down protein oxidation[17]. When middle-aged cultures of *P. anserina* wild-type strains were grown on standard medium and under calorie restriction, no effect on *PaLon* transcription was observed (Supplementary Information, Fig. S5).

We next investigated the impact of *PaLon* overexpression on the lifespan and fitness of *P. anserina*. Remarkably, the *PaLon*-overexpression strain showed a 67% increase in mean lifespan when

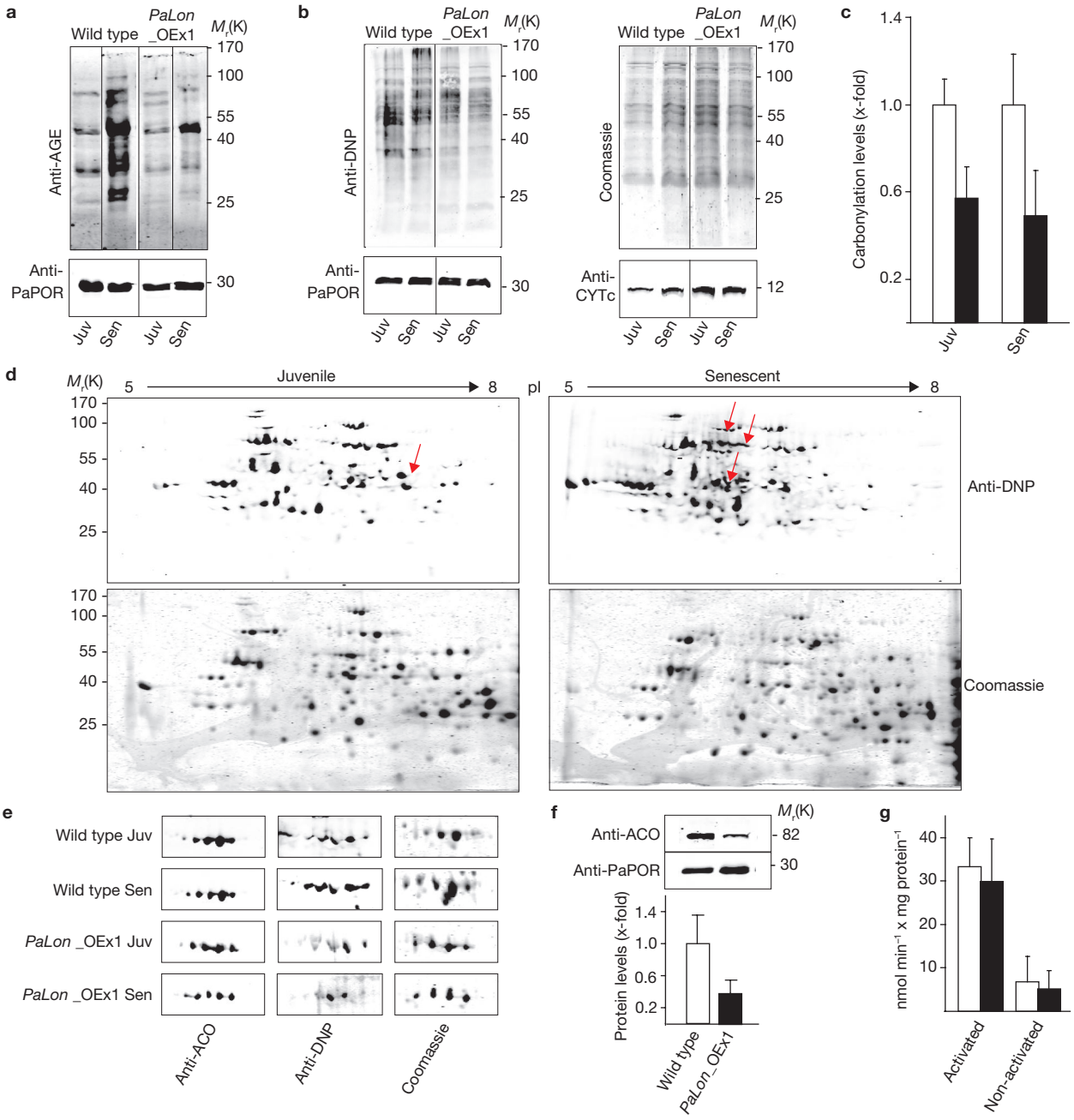

Figure 3 Analysis of oxidative protein damage and degradation of oxidized proteins in strains overexpressing *PaLon*. (**a**) Representative western blot of carboxymethylated mitochondrial proteins (Anti-AGE) from three independent juvenile (Juv) and senescent (Sen) wild-type and *PaLon*_OEx1 strains. Porin was used as a loading control. (**b**) Representative western blot of protein carbonyls (Anti-DNP) in mitochondria of juvenile and senescent wild-type and *PaLon*_OEx1 strains (left). The indicated antibodies were used. Migration of the protein marker is shown on the right. Porin, cytochrome c and the coomassie-stained membranes were used as loading controls. (**c**) Densitometric analysis of protein carbonyls in mitochondria of juvenile (1.0 ± 0.11; $n = 4$) and senescent (1 ± 0.23; $n = 4$; $P = 0.39$) wild-type (white bars) and juvenile (0.57 ± 0.15; $n = 4$; $P = 8.0E-5$) and senescent (0.49 ± 0.21; $n = 4$; $P = 7.7E-2$) *PaLon*_OEx1 (black bars) strains. Data are mean ± s.d. from three independent experiments. Porin was used for quantification. (**d**) Determination of carbonylated proteins in mitochondria of juvenile ($n = 3$) and senescent ($n = 3$) wild-type strains by 2D western blot analysis. Coomassie-stained 2D gels were used as a loading control. Migration of a protein marker is shown on the left. Red arrows mark some examples of carbonylated proteins with increased or decreased abundance in juvenile versus senescent samples. pI, isoelectric point. (**e**) Coomassie-stained 2D gels and 2D western blot analysis of total aconitase protein levels (Anti-ACO) and carbonylated aconitase (Anti-DNP) in juvenile and senescent wild-type and *PaLon*_OEx1 strains. See Supplementary Information Fig. S10 for full scans. (**f**) Representative western blot analysis (top) and densitometric evaluation (bottom) of mitochondrial aconitase in juvenile wild-type (1 ± 0.36; $n = 4$) and *PaLon*_OEx1 (0.39 ± 0.17; $n = 4$) strains ($P = 2.0E-4$). The antibodies used are indicated on the left (top), predicted sizes of the proteins are shown on the right (top). Porin was used as loading control for quantification. Data are mean ± s.d. from three independent experiments. (**g**) Aconitase activity in activated (33.34 ± 6.7; $n = 4$) and non-activated (6.83 ± 5.8; $n = 4$; $P = 2.9E-2$) juvenile wild-type strains (white bars) and activated (29.89 ± 9.8; $n = 4$; $P = 0.57$) and non-activated (5.14 ± 4.3; $n = 4$; $P = 2.9E-2$) juvenile *PaLon*_OEx1 (black bars) strains. Data are the mean ± s.d. from two independent measurements. *P* values were determined by two tailed Wilcoxon test.

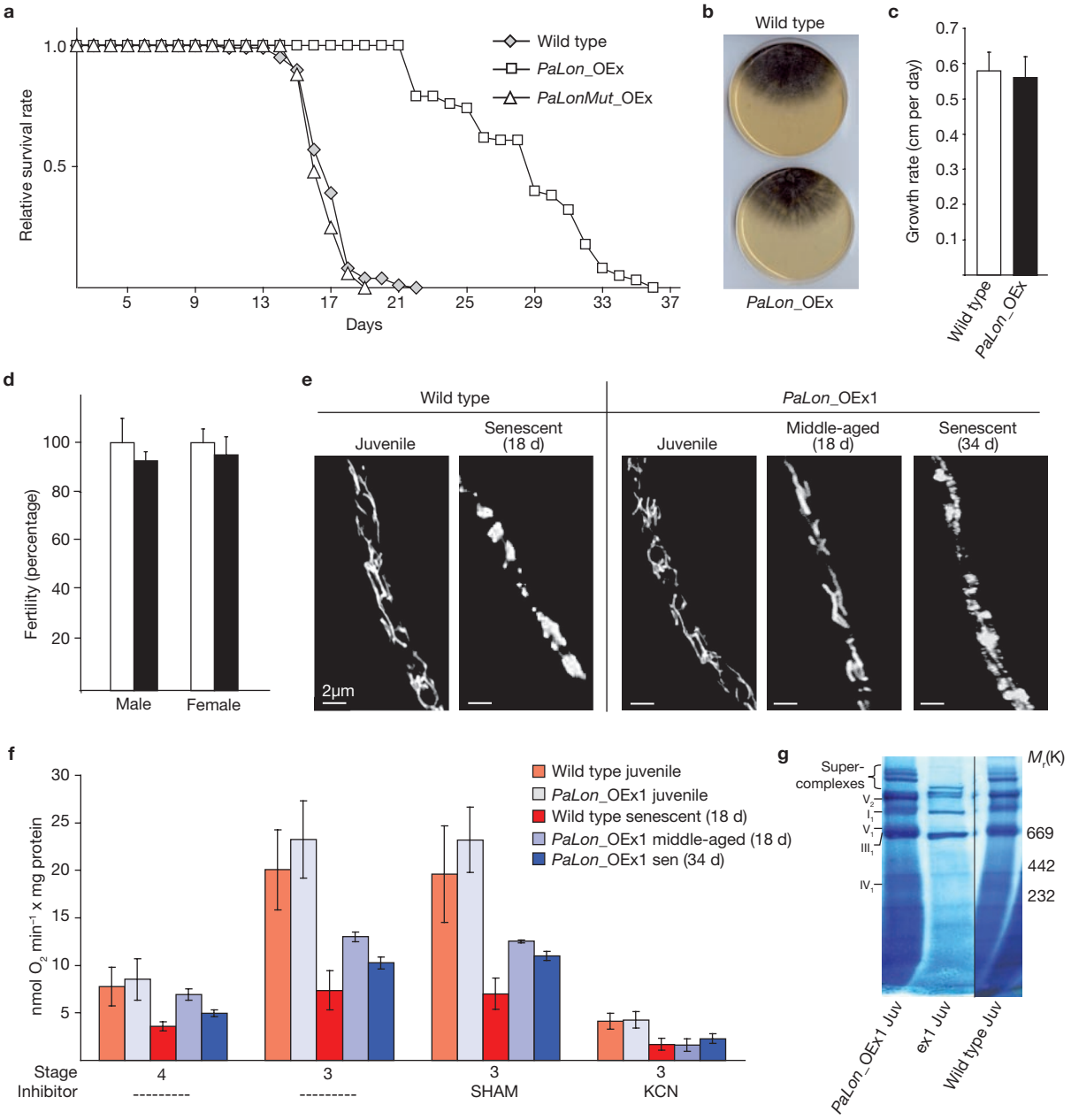

Figure 4 Phenotypic and molecular comparisons of independent wild-type and *PaLon*_OEx strains. (**a**) Mean lifespan of wild-type (14.94 ± 1.6; $n = 80$), *PaLon*_OEx (25.88 ± 4.3; $n = 80$; $P = 6.0E\text{-}25$) and *PaLonMut*_OEx1 (14.41 ± 1.2; $n = 32$; $P = 0.4E\text{-}1$) isolates. The monokaryotic ascospores of the *PaLon*_OEx strains were derived from three independent primary transformants (*PaLon*_OEx1-3) with one additional copy of *PaLon*. (**b**) Morphologies of representative middle-aged wild-type and *PaLon*_OEx cultures on agar plates. (**c**) Growth rate of the strains in **b** (wild type, 0.58 ± 0.05, $n = 80$; *PaLon*_OEx, 0.56 ± 0.06, $n = 80$) grown on synthetic PASM media ($P = 0.99$). (**d**) Male and female fertility of wild-type (white bars; male, 100 ± 9.8, $n = 8$; female, 100 ± 5.5, $n = 8$) and *PaLon*_OEx1 (black bars; male, 92.7 ± 3.7, $n = 8$; female, 95.1 ± 7.3, $n = 8$) isolates (male, $P = 2.3E\text{-}2$; female, $P = 1.7E\text{-}1$). (**e**) Representative images of mitochondria (Mitotracker Red, CMX-ROS) from juvenile and senescent (18 d) wild-type ($n = 6$) and juvenile, middle-aged (18 d) and senescent (34 d) *PaLon*_OEx1 ($n = 6$) strains. Scale bars, 2 µm. (**f**) Oxygen consumption in a buffer containing pyruvate (20 mM) and malate (5 mM). Respiration was measured in untreated (stage 4) mitochondria and those supplemented with ADP (300 µM; stage 3) in the absence or presence of the inhibitors SHAM (AOX inhibitor) or KCN (COX inhibitor). Mitochondria of juvenile ($n = 4$) and senescent (18 d; $n = 4$) wild-type strains and juvenile ($n = 4$), middle-aged (18 d; $n = 4$; Stage 4, $P = 7.9E\text{-}3$; stage 3, $P = 5.9E\text{-}3$) and senescent (34 d; $n = 4$; Stage 4, $P = 7.9E\text{-}2$; stage 3, $P = 2.7E\text{-}3$) mutant *PaLon*_OEx1 strains were analysed. The senescent wild-type was used as reference for statistical analysis. Data are mean ± s.d. from six measurements. (**g**) Coomassie-stained BN–PAGE with mitochondrial proteins of juvenile *PaLon*_OEx1, ex1 and wild-type strains. Migration of the native protein marker used is shown on the right, assigned respiratory chain complexes are indicated on the left.

compared with the wild type. In contrast, overexpression of a proteolytic inactive variant of *PaLon* (*PaLonMut*_OEx1) in which the catalytic Ser 992 is replaced by Ala (Supplementary Information, Figs S1, S6, S7) did not increase lifespan (Fig. 4a), verifying the conclusion that the increase in lifespan of the *PaLon*_OEx1 strain results from the enhanced PaLON-protease activity.

Mycelial morphology and pigmentation are not impaired in the *PaLon*_OEx1 strain (Fig. 4b, c). Moreover, the growth rate is not reduced (Fig. 4c) and male and female fertility are not affected (Fig. 4d). In contrast to many previously described long-lived strains of *P. anserina*, fitness of the newly generated strain thus appears not to be impaired. Also, at the cellular level, we did not observe any change in mitochondrial morphology. Juvenile and middle-aged cultures of *PaLon*-overexpressing strains showed the same healthy tubular mitochondria as the juvenile wild type, whereas senescent mitochondria from both strains had a fragmented mitochondrial morphology[18] (Fig. 4e). All these characteristics also hold true for the strain *PaLonMut*_OEx1 overexpressing a mutated copy of *PaLon* (data not shown).

Ageing of *P. anserina* is known to have a strong mitochondrial etiology. A hallmark of wild-type ageing is the age-related reorganization of the mitochondrial DNA (mtDNA)[19]. Increased mtDNA integrity is often found in long-lived strains. Moreover, several long-lived strains are characterized by a switch from standard cytochrome oxidase (COX)-dependent respiration to an alternative type of respiration, resulting in a reduction in both ROS and ATP generation. In corresponding mutants, longevity is accompanied by impairments in growth and fertility[20–22]. We consequently assessed these mitochondrial characteristics in the *PaLon*-overexpressing strain. Similarly to the wild-type, this strain predominantly respires through cyanide-sensitive COX. In both strains, oxygen consumption in stage 3 (malate, pyruvate and ADP) is strongly inhibited by potassium cyanide (Fig. 4f). In contrast, inhibition of the alternative oxidase (AOX) by salicyl hydroxamic acid (SHAM) did not result in significant changes in oxygen consumption, demonstrating that *PaAox* is not induced. Interestingly, middle-aged and senescent samples of the *PaLon*-overexpressing strain respire more efficiently than the corresponding samples of the wild-type. These differences were statistically significant (Fig. 4 legend). One reason may be that in *PaLon*_OEx1strains the respiratory chain complexes are less damaged and more active than in the aged wild-type strain.

Next, we biochemically analysed the respiratory chain in the transgenic strain using blue-native gel electrophoresis (BN–PAGE). In contrast to mitochondria of the long-lived mutant ex1, mitochondria of wild-type and *PaLon*_OEx1 strains do not exclusively respire through AOX, and they show identical Coomassie-stained protein patterns, indicating that they have the same overall respiratory chain composition (Fig. 4g). In-gel activity staining of complex I, IV and V revealed no significant differences between the *PaLon*_OEx1 and wild-type strains (Supplementary Information, Fig. S8), whereas the mutant strain ex1 showed clear differences from the others, with no complex IV activity.

Finally, we investigated the stability of mtDNA in more detail. Recently, in human cell cultures, it was shown that LON binds to the promoter region of mtDNA and is involved in mtDNA maintenance[7]. We therefore asked whether or not *PaLon* overexpression affects the typical age–related mtDNA reorganization in the wild-type *P. anserina* strain. No change in the type or the degree of mtDNA reorganization was observed (Supplementary Information, Fig. S9). Thus, it is possible that apart from mediating indirect effects, by increasing protease activity, increased PaLON abundance may also function more directly on mtDNA stability and consequently on the remodelling capacity of the system, thereby affecting life- and healthspans of *PaLon*-overexpressing strains. However, the direct interaction of PaLON with mtDNA, as a protein component of the mitochondrial nucleotide of *P. anserina,* remains to be demonstrated.

For the first time, we demonstrate a beneficial effect of increasing LON protease abundance on stress resistance and organism ageing. These data provide mechanistic clues suggesting that increased degradation of damaged mitochondrial proteins leads to a reduction of endogenous oxidative stress, an increased tolerance to exogenous oxidative stress and an increased lifespan. In addition, other consequences of increased PaLON abundance, including improved remodelling and chaperone functions may contribute to the described effects in transgenic strains. Our work complements previous studies in which downregulation or deletion of genes coding for human LON and the yeast homologue PIM1 were found to induce negative effects[8,9,23]. Significantly, in *P. anserina*, the constitutive overexpression of *PaLon* results in a marked extension in lifespan without impairing fitness; thus it is an example of a successful intervention into the ageing process at the organism level that results in an increased healthspan. It is now a challenge to develop strategies for related interventions in other systems and to elucidate the role of the different components of the mitochondrial quality control system and the interactions of individual components. □

METHODS

Methods and any associated references are available in the online version of the paper at http://www.nature.com/naturecellbiology/.

Note: Supplementary Information is available on the Nature Cell Biology website.

ACKNOWLEDGEMENTS

We thank R. Lill and B. Friguet for the antibodies used in this study. H.D.O. was supported by a grant from the Deutsche Forschungsgemeinschaft. Part of the work of H.D.O. was supported by the European Commission (FP6-518230; Proteomage).

AUTHOR CONTRIBUTIONS

K.L. and H.D.O. designed the experiments, analysed data and wrote the manuscript; H.D.O. supervised the work and K.L. performed the experiments.

COMPETING FINANCIAL INTERESTS

The authors declare no competing financial interests.

Published online at http://www.nature.com/naturecellbiology/
Reprints and permissions information is available online at http://npg.nature.com/reprintsandpermissions/

1. Osiewacz, H. D. & Hermanns, J. The role of mitochondrial DNA rearrangements in aging and human diseases. *Aging (Milano.)* **4,** 273–286 (1992).
2. Wallace, D. C. A mitochondrial paradigm of metabolic and degenerative diseases, aging, and cancer: a dawn for evolutionary medicine. *Annu. Rev. Genet.* **39,** 359–407 (2005).
3. Harman, D. Aging: a theory based on free radical and radiation chemistry. *J. Gerontol.* **11,** 298–300 (1956).
4. Finkel, T. & Holbrook, N. J. Oxidants, oxidative stress and the biology of ageing. *Nature* **408,** 239–247 (2000).
5. Gredilla, R., Grief, J. & Osiewacz, H. D. Mitochondrial free radical generation and lifespan control in the fungal aging model *Podospora anserina*. *Exp. Gerontol.* **41,** 439–447 (2006).
6. Schriner, S. E. *et al.* Extension of murine life span by overexpression of catalase targeted to mitochondria. *Science* **308,** 1909–1911 (2005).
7. Lu, B. *et al.* Roles for the human ATP-dependent Lon protease in mitochondrial DNA maintenance. *J. Biol. Chem.* **282,** 17363–17374 (2007).
8. Suzuki, C. K., Suda, K., Wang, N. & Schatz, G. Requirement for the yeast gene LON in intramitochondrial proteolysis and maintenance of respiration. *Science* **264,** 891 (1994).
9. Bota, D. A., Ngo, J. K. & Davies, K. J. Downregulation of the human Lon protease impairs mitochondrial structure and function and causes cell death. *Free Radic. Biol. Med.* **38,** 665–677 (2005).

10. Osiewacz, H. D. Genes, mitochondria and aging in filamentous fungi. *Ageing Res. Rev.* **1,** 425–442 (2002).
11. Bulteau, A. L., Szweda, L. I. & Friguet, B. Mitochondrial protein oxidation and degradation in response to oxidative stress and aging. *Exp. Gerontol.* **41,** 653–657 (2006).
12. Osiewacz, H. D., Skaletz, A. & Esser, K. Integrative transformation of the ascomycete *Podospora anserina*: identification of the mating-type locus on chromosome VII of electrophoretically separated chromosomes. *Appl. Microbiol. Biotechnol.* **35,** 38–45 (1991).
13. Scheckhuber, C. Q. *et al.* Reducing mitochondrial fission results in increased life span and fitness of two fungal ageing models. *Nature Cell Biol.* **9,** 99–105 (2007).
14. Ikeda, K. *et al.* N (epsilon)-(carboxymethyl)lysine protein adduct is a major immunological epitope in proteins modified with advanced glycation end products of the Maillard reaction. *Biochemistry* **35,** 8075–8083 (1996).
15. Bakala, H. *et al.* Changes in rat liver mitochondria with aging. Lon protease-like reactivity and N(epsilon)-carboxymethyllysine accumulation in the matrix. *Eur. J. Biochem.* **270,** 2295–2302 (2003).
16. Bota, D. A. & Davies, K. J. Lon protease preferentially degrades oxidized mitochondrial aconitase by an ATP-stimulated mechanism. *Nature Cell Biol.* **4,** 674–680 (2002).
17. Reverter-Branch, Cabiscol, E., Tamarit, J. & Ros, J. Oxidative damage to specific proteins in replicative and chronological-aged *Saccharomyces cerevisiae*: common targets and prevention by calorie restriction. *J. Biol. Chem.* **279,** 31983–31989 (2004).
18. Scheckhuber, C. Q., Rödel, E. & Wüstehube, J. Regulation of mitochondrial dynamics--characterization of fusion and fission genes in the ascomycete *Podospora anserina*. *Biotechnol. J.* **3,** 781–790 (2008).
19. Osiewacz, H. D. & Borghouts, C. Mitochondrial oxidative stress and aging in the filamentous fungus *Podospora anserina*. *Ann. NYAcad. Sci.* **908,** 31–39 (2000).
20. Borghouts, C., Kimpel, E. & Osiewacz, H. D. Mitochondrial DNA rearrangements of *Podospora anserina* are under the control of the nuclear gene grisea. *Proc. Natl. Acad. Sci. U SA* **94,** 10768–10773 (1997).
21. Dufour, E., Boulay, J., Rincheval, V. & Sainsard-Chanet, A. A causal link between respiration and senescence in *Podospora anserina*. *Proc. Natl. Acad. Sci. USA* **97,** 4138–4143 (2000).
22. Stumpferl, S. W., Stephan, O. & Osiewacz, H. D. Impact of a disruption of a pathway delivering copper to mitochondria on *Podospora anserina* metabolism and life span. *Eukaryot. Cell* **3,** 200–211 (2004).
23. van Dyck L., Neupert, W. & Langer, T. The ATP-dependent PIM1 protease is required for the expression of intron-containing genes in mitochondria. *Genes Dev.* **12,** 1515–1524 (1998).

METHODS

***P. anserina* strains and cultivation.** *P. anserina* wild-type strain 's' (ref. 24); long-lived mutant ex1 (ref. 25); the *PaLon*_OEx1 strain overexpressing *PaLon*; the *PaLonMut*_OEx1 strain expressing a proteolytically inactive variant of PaLON; the Δ*PaClpP* strain deleted of *PaClpP*, which encodes the *P. anserina* CLPP protease and Δ*PaClpP/PaLon*_OEx1 a *PaClpP* deletion strain overexpressing *PaLon* are all in the genetic background of wild-type strain 's', and were used in this study. Strains were grown on standard cornmeal agar (BMM) at 27 °C. For incubation of strains with H_2O_2, mycelia were grown on BMM standard plates with different H_2O_2 concentrations (0–50 mM) for five days, in the dark. Growth rates were assigned daily and calculated as growth rates per day.

Cloning procedures and generation of *P. anserina* mutants. To overexpress *PaLon* in *P. anserina,* the open reading frame of *PaLon* was amplified by PCR using the primers *Lonfor* (5'-AAAGATCTATGCTGCCGCGACAGC-3') and *Lonrev* (5'-GGTCTAGACTAATCACTCTCCTCC-3'), introducing *Bgl*II and *Xba*I restriction sites (underlined), respectively. The amplicon was cloned into the pEX backbone (*Bam*HI / *Xba*I digested) under the control of a strong constitutive promoter (metallothionein promoter), resulting in the plasmid pEX-Lon-hph. This plasmid was used to transform *P. anserina* wild-type protoplasts. Transformants were selected on hygromycin-resistance (hph) and analysed by Southern blot analysis. Strains containing one extra copy of *PaLo*n were named *PaLon*_OEx.

To overexpress a catalytically inactive variant of PaLON, point mutations were introduced into the open reading frame of *PaLon*, encoding a serine essential for protease activity at the position 992. Therefore, the gene was amplified by PCR in two parts. The 5' part of the gene was amplified using the primers *Lonfor* (5'-AAAGATCTATGCTGCCGCGACAGC-3'), introducing a *Bgl*II restriction site (underlined), and *LonMutrev* (5'-TGCACCGCCCCCTCAGGCACATGCACATGA-3'). The 3' part was amplified using the primers *LonMutfor* (5'-GAAGGATGGGCCGGCAGCGGGGATCACGAT-3'), introducing the point mutations (underlined), and *Lonrev* (5'-GGTCTAGACTAATCACTCTCCTCC-3'), introducing an *Xba*I restriction site (underlined). The 5' fragment was digested with *Bgl*II and the 3' fragment with *Xba*I. The plasmid pExMtterhph, constructed by cloning the *Xba*I/*Hind*III-digested metallothionein terminator into the *Xba*I/*Hind*III-digested plasmid pExMthph[26], was digested with *BamH*I and *Xba*I. In a three-fragment ligation, the plasmid pEX-PaLon_Mut was constructed and the identity of the point mutations and the construct were verified by sequencing. The plasmid was used to transform *P. anserina* wild-type protoplasts. Transformants were selected on the basis of hygromycin-resistance (hph) and analysed by Southern blotting. Strains containing one copy of the mutated *PaLo*n gene were named *PaLonMut*_OEx.

The generation of a *PaClpP*-deletion strain was performed as described previously [27]. Briefly, small flanking regions of the *PaLon* gene were amplified using the 5'-flank primers *ClpPKO5'KpnIfor* (5'-AAGGTACCGACCTCTGCCGAATCTTT-3') and *ClpPKO5'Hind*III*rev* (5'-GCAAGCTTGATAGCGTATCGATATGT-3'), and the 3'-flank oligonucleotides *ClpPKO3'Bcu*I*for* (5'-GCACTAGTGCGTTCTAGTTGTACGAA-3') and *ClpPKO3'Not*I*rev* (5'-AAGCGGCCGCTCCAGACTGCTACCGTAT-3'). The introduced restriction sites are underlined. The 5' fragment was digested with *Kpn*I and *Hin*dIII and the 3' fragment was digested with *Bcu*I and *Not*I. The plasmid pKO4 was used for ligation. It was generated from a *Pst*I digestion and religation of pKO3, a knockout plasmid described previously[27]. pKO4 lacks several duplicate restriction sites (for example, *Hin*dIII) which are present in pKO3, thereby facilitating cloning of the flanks of the gene to be replaced. The plasmid pKO4 was digested with all four restriction enzymes (*Kpn*I, *Hin*dIII, *Bcu*I and *Not*I) and a four fragment ligation was performed, resulting in the plasmid pPaClpPKO, containing both fragments flanking a phleomycin and blasticidin resistance cassette genes for fungal and bacterial selection. The resistance cassette with the flanking regions was excised by restriction with *Not*I and *Kpn*I and transformed into the *Escherichia coli* KS272 strain, containing the plasmid pKOBEG[28], and the cosmid 25B12 (ref. 29) bearing the *PaClpP* gene. Homologous recombination between the flanks of the resistance cassette and cosmid 25B12 leads to generation of cosmid ΔClpP-25B12, containing the phleomycin–blasticidin cassette with large flanking genomic regions. The cosmid was used to transform protoplasts of the *P. anserina* wild-type strain 's'. Transformants were selected by growth on phleomycin-containing medium and successful deletion of *PaClpP* was verified by Southern blot analysis. Positive strains, lacking the *PaClpP* gene and harbouring the phleomycin gene instead, were termed Δ*PaClpP*.

To construct a Δ*PaClpP/PaLon*_OEx1 double mutant, a monokaryotic Δ*PaClpP* isolate was crossed with a monokaryotic *PaLon*_OEx1 mutant strain. Meiotic offspring bearing the double mutation were identified by testing the growth of mycelia germinated on phleomycin- and hygromycin-containing medium. The successful generation of the Δ*PaClpP/PaLon*_OEx1 double mutant was verified by Southern blotting analysis. Isolation of genomic DNA, digestion and Southern blotting analysis were performed as described previously[13].

Isolation of RNA and real-time (rt) PCR. RNA was isolated using RNeasy Plant isolation Kit (QIAGEN) according to the manufacturer's instructions. Reverse transcription was performed using iScript cDNA Synthesis Kit (Bio-Rad). Expression analysis of *PaLon* was performed by quantitative rtPCR analysis in a MyiQ rtPCR thermal cycler (Bio-Rad) using IQ SYBR Green Supermix (Bio-Rad). *PaLon* was amplified using primers *RealLonfor* (5'-AGGCCGGTGAGTTGGTATTC-3') and *RealLonrev* (5'-CTCCTTGTTCTCAGCCACCA-3'). For normalization, *PaPorin* was amplified as an internal reference using primers *porin-rt-for* (5'-TCTCCTCCGGCAGCCTTG-3') and *porin-rt-rev* (5'-GAGGGTGTCGGCAAGTTC-3'). The efficiency (E) of the primer pairs was calculated based on rtPCR with a dilution series of cDNA, according to the equation $E = 10^{[-1/Slope]}$. Using the efficiency and the crossing point deviation, it was possible to determine the expression ratio (R) relative to the *PaPorin* expression. The relative expression ratio was calculated; the expression level in standard cultures (juvenile wild-type) was set to one and quantified as described[30].

Western blotting and densitometry analysis. Total cell lysates[31], mitochondrial proteins and post-mitochondrial fractions[5] from *P. anserina* strains were isolated as described. For oxy blotting analysis, mitochondria were isolated in the present of dithiothreitol (50 mM). Proteins were fractionated by SDS–PAGE (8–16% separating gels) according to standard protocols. After electrophoresis, proteins were transferred to PVDF membranes (ImmobiLON-FL, Millipore). Blocking, antibody incubation and washing steps were performed according to the Odyssey Western Blot analysis handbook (Licor). Primary antibodies were raised against a PaLON specific synthetic peptide ([H]-CDKIGRGYQGDPS-[OH]; Sigma) corresponding to AA 677-688, a PaCLPP specific synthetic peptide ([Ac]-CGTMLSADAKEGKH-[OH]; New England Peptide) corresponding to AA 242-254, and the PaPORIN (anti-PaPOR) full length protein (New England Peptide). Antibodies against yeast aconitase (anti-ACO) and yeast cytochrome c (anti-CYTc) were provided by R. Lill (Institute für Zytobiologie, Philipps Universität Marburg, Germany), those against human CLPP protease (anti-HsCLPP) by B. Friguet (Laboratoire de Biologie et Biochimie Cellulaire du Vieillissement, Université Paris, France). The β-actin (anti-β-ACT) antibody was purchased from Abcam (ab8224) and the anti-AGE antibody from Trans Genic Inc. (clone 6D12). Immunoblot detection of carbonyl groups in proteins (anti-DNP) was performed with the OxyBlot™ protein oxidation detection kit (Chemicon) according to the manufacturer's instructions. In all analyses, secondary antibodies conjugated with IRDye CW800 or IRDye 680 (1:15.000; Licor) were used. The Odyssey infrared scanner (Licor) was used for detection and quantification was performed according to the manufacturer's software (Odyssey Application Software 2.1.12) and handbook.

Two-dimensional Oxy blot analysis. To identify carbonyl groups in proteins after oxidative modification, 2D Oxy blot analysis was performed. Derivatization of proteins was performed as described previously[32]. Mitochondrial proteins (300 μg) were derivatized with four volumes of a 2 N HCl solution, containing 2.4-Dinitrophenylhydrazine (10 mM). After 30 min of incubation at 4 °C, proteins were precipitated with tricarboxylic acid (TCA; 15% final concentration). After centrifugation, proteins were washed three times with ethanol/ethylacetat (1:1) and subsequently dried. Protein samples were resuspended in IEF buffer (7 M urea, 2 M thiourea, 0.4% dithiothreitol, 2% CHAPS and 0.5% ampholytes at pH 3–10). For the first dimension, protein (100 μg) was applied to IEF strips (7 cm, pH 5-8; Bio-Rad). Isoelectric focusing was performed at 250 V for 15 min, at 250 to 4000 V ramp for 2 h, and 4000 V for 5 h, at 20 °C. For the second dimension, IEF strips were equilibrated for 10 min in Tris base (45 mM at pH 8.8) containing urea (6 M), SDS (2%), glycerol (30%) and dithiothreitol (2%), and then re-equilibrated for 10 min in the same buffer containing iodoacetamide (2.5%) in place of dithiothreitol. Subsequently, the strips were placed on SDS separating polyacrylamide gels (10%), overlaid with agarose (0.5%), and gels were run at 200 V for 1 h. After electrophoresis, proteins were transferred to PVDF

DOI: 10.1038/ncb1893

membranes (ImmobiLON-FL, Millipore) for blotting with appropriate antibodies and handled as described above. As a loading control, 2D gels were Coomassie stained after electrophoresis.

LON protease activity measurements. For determination of LON protease activity, mitochondria were isolated. After sonication and subsequent centrifugation, soluble matrix proteins were separated from membrane proteins. To measure protease activity, a protease fluorescent detection kit (Sigma) was used according to the manufacturer's instructions. FITC-Casein substrate (20 µl), soluble matrix proteins (10 µl) and 20 µl incubation buffer (20 mM sodium phosphate and 150 mM sodium chloride at pH 7.6) were incubated for 1 h at 37 °C in the dark, in the presence or absence of ATP (8 mM). As a control, pefabloc (50 mM; Roth), a serine protease inhibitor, was added. TCA (150 µl, 0.6 N) was added and the samples were incubated for 30 min at 37 °C in the dark. After centrifugation (10000*g*, 4 °C, 10 min) the supernatant (10 µl) and 1 ml assay buffer (500 mM Tris buffer at pH 8.5) were mixed. The sample was transferred (300 µl per well)to a black 96-well micro-titer plate (Nunc). The fluorescence intensity (FU) was recorded at 535 nm (emission) after excitation at 485 nm in a multiplate reader (Saphire 2, TECAN) and calculated per mg protein^{-1} and h (FU/ hour^{-1}, mg protein^{-1}).

Aconitase-activity measurements. To measure aconitase activity, soluble matrix proteins (300–500 µg) in Tris (100 mM at pH 7.4), were used. Activation of aconitase in the samples was performed in the presence of $FeNH_4SO_4$ (24 µM) and L-cysteine (2.3 mM) for 1 h at 4 °C. Aconitase activity was measured using activated and non-activated samples, by converting citrate into α-ketoglutarate and concomitantly reducing NAD[33]. The buffer contained Tris (50 mM at pH 7.4), citrate sodium (0.1 mM), $MnSO_4$ (2 mM), NAD^+ (0.27 mM) and isocitrate dehydrogenase (0.21 U). The formation of NADH was monitored for 20 min at 27 °C and 340 nm in a multiplate reader (Saphire2, TECAN). Aconitase activity was calculated as U mg^{-1} protein^{-1} min^{-1}.

H_2O_2 release from *P. anserina* colonies. This was performed as described previously[13]. Mycelia were grown on plates containing synthetic PASM media for 2–3 days in the dark and afterwards flooded with a solution containing diaminobenzidine (2.5 mM; DAB) and horseradish peroxidase (0.02 mg ml^{-1}; Sigma). Released H_2O_2 oxidises DAB forming a brown precipitate on the plate. This precipitate can be measured photometrically. After 1 h incubation at 27 °C in the dark, the solution was poured off and the plates incubated again for 2 h at 27 °C in the dark. A scanner (Hewlett Packard) was used for documentation. For quantification of H_2O_2release, a 3 × 3 mm piece of mycelia was incubated in DAB solution (300 µl) for 3 h at 27 °C in the dark. The absorption of the supernatant was subsequently recorded at 471 nm in a multiplate reader (Saphire 2, TECAN).

***P. anserina* lifespan, growth rate and fertility analysis.** Mononucleate ascospores were isolated from independent crosses of wild-type strain 's', *PaLon*_OEx1-3, and *PaLonMut*_OEx1 and germinated on BMM supplemented with ammonium acetate (60 mM). Lifespan measurements were performed in race tubes on synthetic PASM media[34] as described previously[22]. Growth was measured until the isolate stopped growing. The elapsed time until this point was recorded as the lifespan of the corresponding isolate and the growth of the isolates was counted as cm per day. Male and female fertility measurements of wild-type and *PaLon* overexpression strains were performed as described previously[13]. The number of spermatia (male gametes) and perithecia of the wild type were calculated as 100%.

Oxygen consumption measurements. Respiration of *P. anserina* mitochondria was determined with a Clark-type electrode (Rank Bros.) as described previously[5]. To distinguish between COX and AOX-dependent respiration, potassium cyanide (KCN; 2.2 mM) and salicylhydroxamic acid (SHAM; 4 mM) were used as inhibitors.

Blue-native gel electrophoresis (BN-PAGE). Mitochondria from *P. anserina* strains were processed as described previously[35] using a digitonin/protein ratio of 4 g/g. Protein (150 µg) was solubilized and loaded on each lane. Linear 4–13% gradient gels overlaid with a 3.5% stacking gel were used. Gels were stained with Coomassie Blue and the complexes were assigned as described previously[36]. Alternatively, activity staining of complex I, IV and V in BN-PAGE was performed as described previously[37,38].

Visualization of *P. anserina* mitochondria. Growth of mycelia and confocal laser scanning microscopy of *P. anserina* mitochondria were performed as described previously[13].

Statistical analysis. Comparisons between different samples were statistically analysed with Wilcoxon test, two-tailed. The minimum level of statistical significance was set at $P < 5.0$ E-2 for all analyses. All data shown are the mean ± s.d.

24. Esser, K. *Podospora anserina. Handbook of Genetics* (ed. R. C. King) 531–551 (Plenum Press, 1974).
25. Kück, U. *et al.* The onset of senescence is affected by DNA rearrangements of a discontinuous mitochondrial gene in *Podospora anserina. Curr. Genet.* **9,** 373–382 (1985).
26. Kunstmann, B. & Osiewacz, H. D. Over-expression of an S-adenosylmethionine-dependent methyltransferase leads to an extended lifespan of *Podospora anserina* without impairments in vital functions. *Aging Cell* **7,** 651–662 (2008).
27. Hamann, A., Krause, K., Werner, A. & Osiewacz, H. D. A two-step protocol for efficient deletion of genes in the filamentous ascomycete *Podospora anserina. Curr. Genet.* **48,** 270–275 (2005).
28. Chaveroche, M. K., Ghigo, J. M. & d'Enfert, C. A rapid method for efficient gene replacement in the filamentous fungus *Aspergillus nidulans. Nucleic Acids Res.* **28,** E97 (2000).
29. Osiewacz, H. D. A versatile shuttle cosmid vector for the efficient construction of genomic libraries and for the cloning of fungal genes. *Curr. Genet.* **26,** 87–90 (1994).
30. Pfaffl, M. W. A new mathematical model for relative quantification in real-time RT-PCR. *Nucleic Acids Res.* **29,** e45 (2001).
31. Borghouts, C., Werner, A., Elthon, T. & Osiewacz, H. D. Copper-modulated gene expression and senescence in the filamentous fungus *Podospora anserina. Mol. Cell Biol.* **21,** 390–399 (2001).
32. Levine, R. L., Williams, J. A., Stadtman, E. R. & Shacter, E. Carbonyl assays for determination of oxidatively modified proteins. *Methods Enzymol.* **233,** 346–357 (1994).
33. Nulton-Persson, A. C. & Szweda, L. I. Modulation of mitochondrial function by hydrogen peroxide. *J. Biol. Chem.* **276,** 23357–23361 (2001).
34. Hamann, A., Brust, D. & Osiewacz, H. D. Deletion of putative apoptosis factors leads to lifespan extension in the fungal ageing model *Podospora anserina. Mol. Microbiol.* **65,** 948–958 (2007).
35. Schägger, H. & Pfeiffer, K. Supercomplexes in the respiratory chains of yeast and mammalian mitochondria. *EMBO J.* **19,** 1777–1783 (2000).
36. Krause, F. *et al.* Supramolecular organization of cytochrome c oxidase- and alternative oxidase-dependent respiratory chains in the filamentous fungus *Podospora anserina. J. Biol. Chem.* **279,** 26453–26461 (2004).
37. Jung, C., Higgins, C. M. & Xu, Z. Measuring the quantity and activity of mitochondrial electron transport chain complexes in tissues of central nervous system using blue native polyacrylamide gel electrophoresis. *Anal. Biochem.* **286,** 214–223 (2000).
38. Nijtmans, L. G., Henderson, N. S. & Holt, I. J. Blue Native electrophoresis to study mitochondrial and other protein complexes. *Methods* **26,** 327–334 (2002).

nature cell biology

DOI: 10.1038/ncb1893

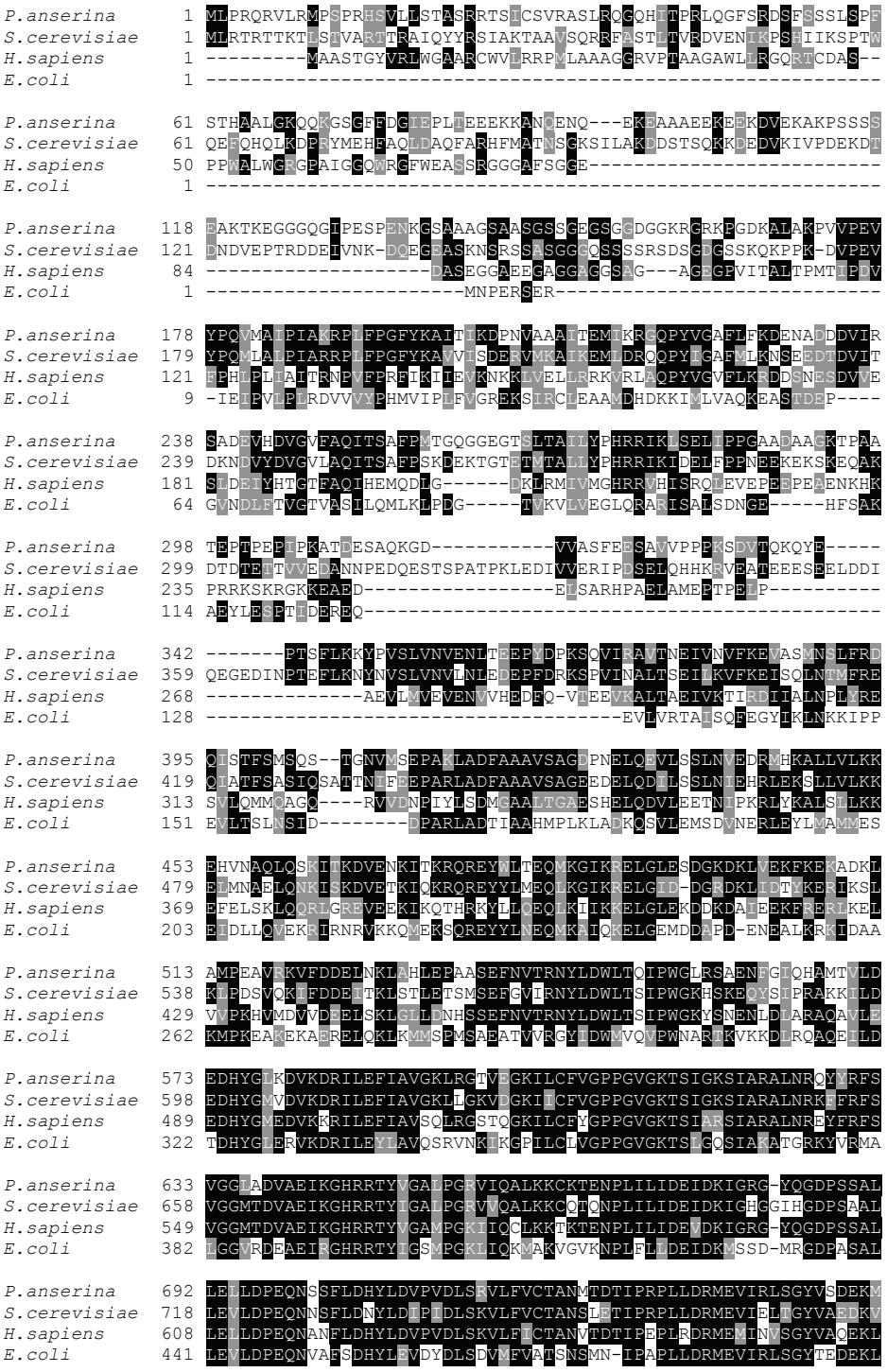

Figure S1 *In silico* identification of a LON protease in *P. anserina*. Alignment of the LON protease amino acid sequences from selected eukaryotes and prokaryotes. *P. anserina* (Pa_3_4170; accession number of the *P. anserina* sequencing consortium: http://www.genoscope.cns.fr/externe/English/Projets/Projet_GA/GA.html); *S. cerevisiae* (Accession No. P36775, SwissProt); *H. sapiens* (Accession No. P36776, SwissProt); *E. coli* (Accession No. P0A9M0, SwissProt). Identical amino acids in all species are indicated by a black background, similar amino acids are shaded in grey. The proteolytic active serine at position 992 is highlighted.

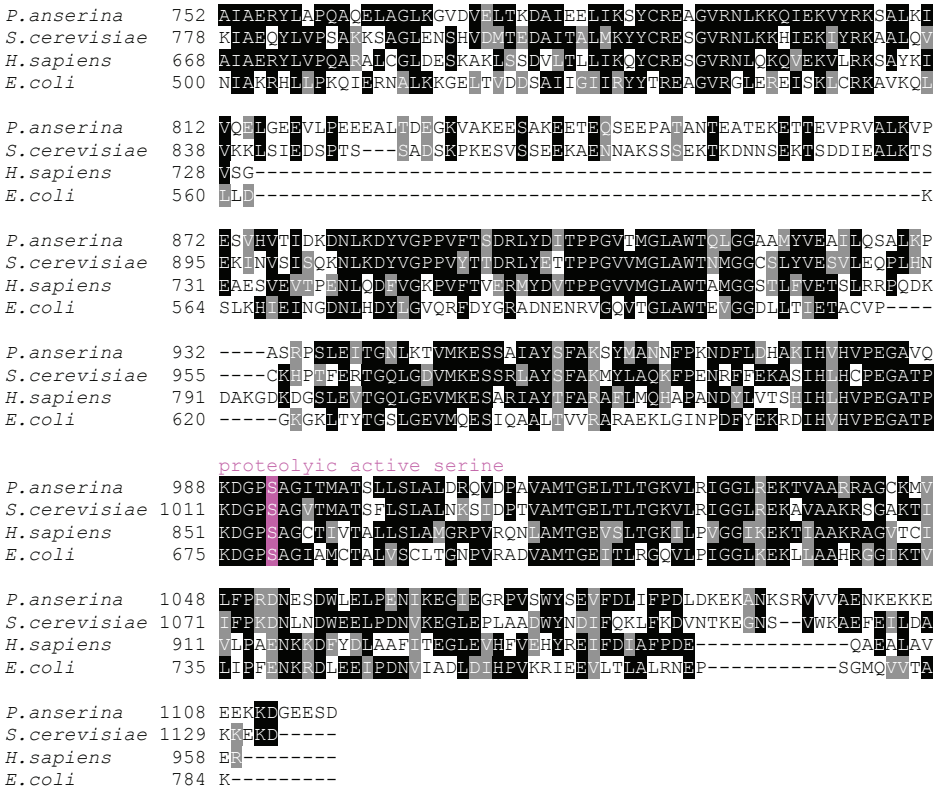

Figure S1 continued

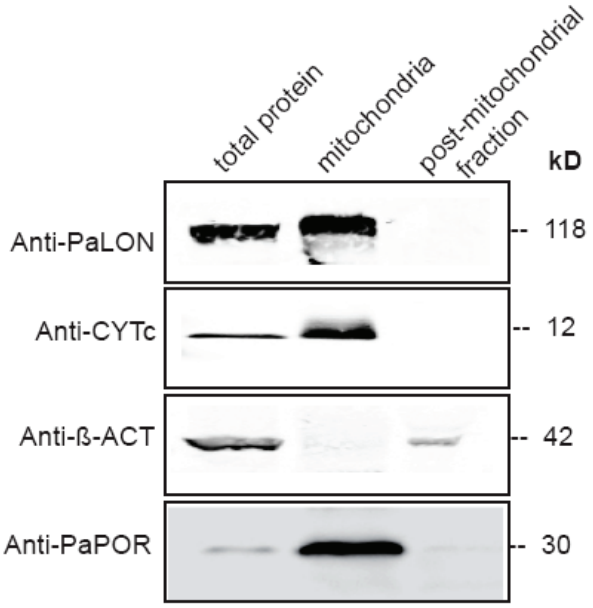

Figure S2 Localisation of *P. anserina* LON protease in mitochondria. Western Blot analysis of total cell lysate (total protein), mitochondria and the post-mitochondrial fraction from the *P. anserina* wild-type strain "s". Antibodies against cytochrome c (Anti-CYTc) and porin (Anti-PaPOR) were used as mitochondrial markers, while an antibody against ß-actin (Anti-ß-ACT) was used as cytoplasmic marker. The predicted sizes of the proteins are shown on the right. The size of PaLON (118 kDa) corresponds to the predicted size of the imported protein which lacks the processed mitochondrial targeting sequence. Anti-PaLON is a polyclonal rabbit antibody generated against a polypeptide of the *P. anserina* LON protease.

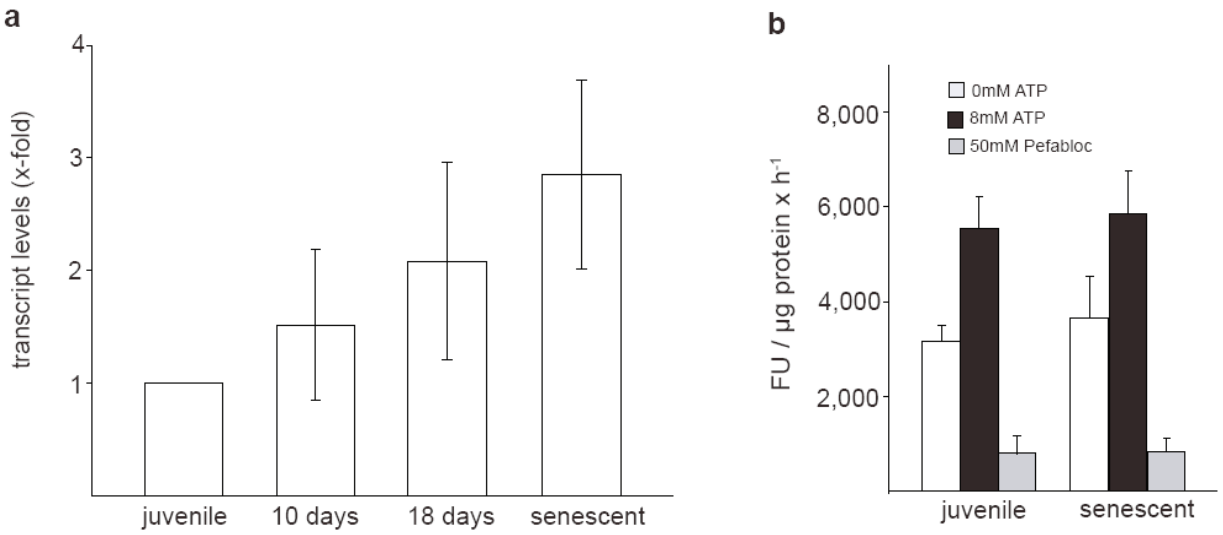

Figure S3 Regulation of *P. anserina* LON protease during ageing. **a,** relative transcription of *PaLon* in juvenile (1; n=8), 10 days (1.4; n=5; Wilcoxon test, two-tailed, P = 0.5), 18 days old (1.9; n=4; Wilcoxon test, two-tailed, P = 5.9E-2) and senescent (2.75±0.787; n=8; Wilcoxon test, two-tailed, P = 2.0E-4) wild-type strain "s", showing a steady increase in transcription during ageing. **b,** protease activity in juvenile (n=4) and senescent (n=4) soluble mitochondrial proteins in the absence of ATP (P = 0.569; white), in the presence of 8 mM ATP (black) and in the presence of 8 mM ATP + 50 mM Pefabloc (grey) illustrating that activity in the wild-type strain is not increased during ageing. Data are the mean ± s.d. from six independent experiments.

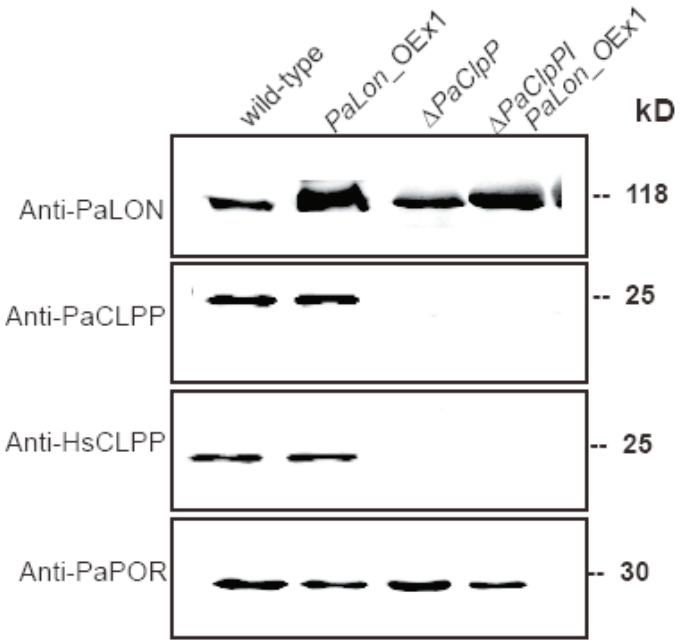

Figure S4 Identification of strains with manipulated amounts of PaLON and/or PaCLPP protein. Western Blot analysis of mitochondrial protein extracts from *P. anserina* wild-type, *PaLon*_OEx1, *ΔPaClpP* and *ΔPaClpP*/*PaLon*_OEx1 strains. In the *ΔPaClpP* strain, the CLPP protein is missing, while the abundance of PaLON protein is similar to those in the wild-type. In the *ΔPaClpP*/*PaLon*_OEx1 double-mutant, PaLON protein amounts are increased like in PaLon_OEx1 mutant. In this strain no CLPP protein can be detected. Antibodies used are represented on the left, predicted sizes of the proteins are shown on the right.

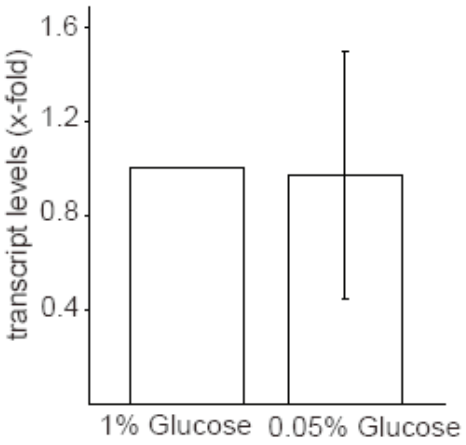

Figure S5 Expression of *PaLon* does not change during calorie restriction. Relative expression of *PaLon* in middle-aged wild-type strain "s", grown under normal (1 % Glucose) (1; n=5) and calorie restricted conditions (0.05 % Glucose) (0.97±0.53; n=5) (Wilcoxon test, two-tailed, P = 0.19). Expression of the wild-type on 1 % Glucose was set to one.

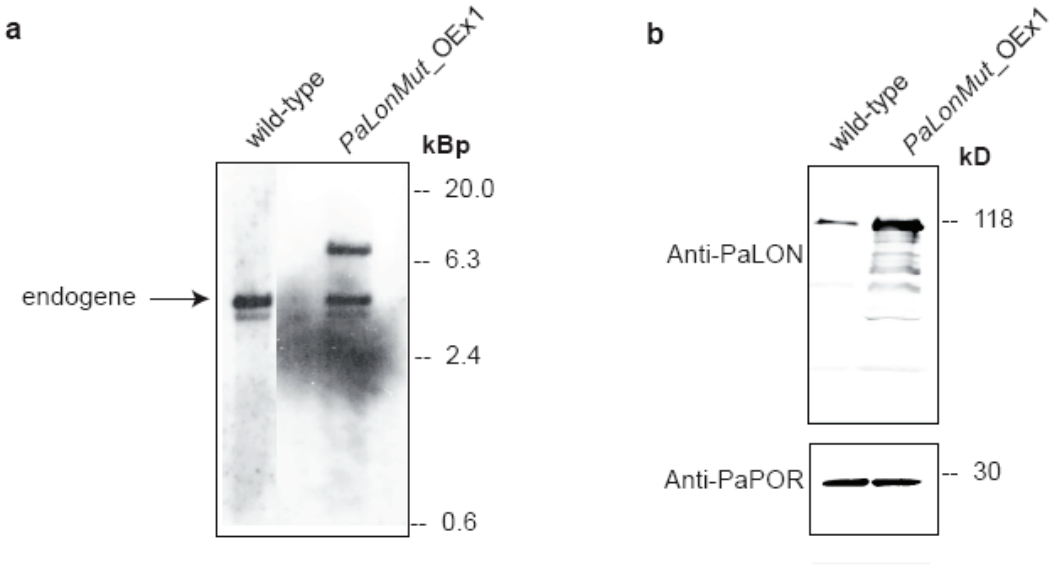

Figure S6 Over-expression of a mutated *PaLon* gene coding for a proteolytically inactive variant of PaLON in *P. anserina*. **a,** Southern Blot analysis of total DNA from wild-type and *PaLonMut*_OEx1 strain digested with *BamHI*. The DNA was hybridised with a probe corresponding to the *PaLon* gene. While both strains contain one copy of the endogene (wild-type copy of *PaLon*), an additional copy is present in strain *PaLonMut*_OEx1. This copy results from the integration of a plasmid into the genome of *P. anserina* which contains a *PaLon* gene encoding a proteolytic inactive LON protein. **b,** Western Blot analysis of mitochondria from *P. anserina* wild-type and *PaLonMut*_OEx1 strains, supporting the successful over-expression of *PaLonMut* in the *PaLonMut*_OEx1 mutant. Used antibodies are indicated on the left, predicted sizes of the proteins are shown on the right. Porin was used as loading control.

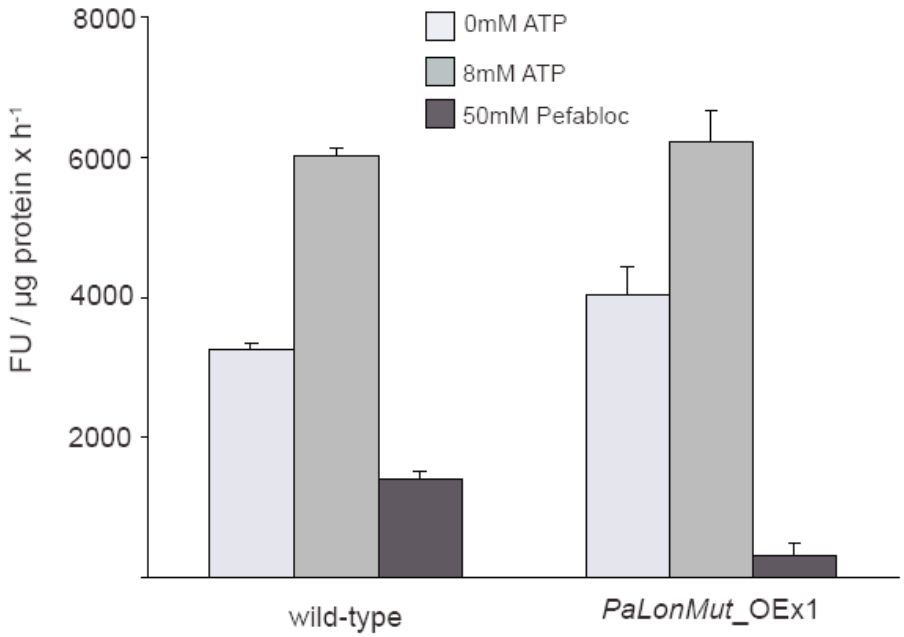

Figure S7 Comparison of protease activity in wild-type (n=4) and *PaLonMut_*OEx1 (n=4) strains of *P. anserina*. Soluble mitochondrial proteins were measured in the absence of ATP, in presence of 8 mM ATP and in the presence of 8 mM ATP + 50 mM Pefabloc, demonstrating that increased abundance of a catalytically inactive version of PaLON (S992A) does not increase proteolytic activity. Data are the mean ± s.d. from two independent measurements.

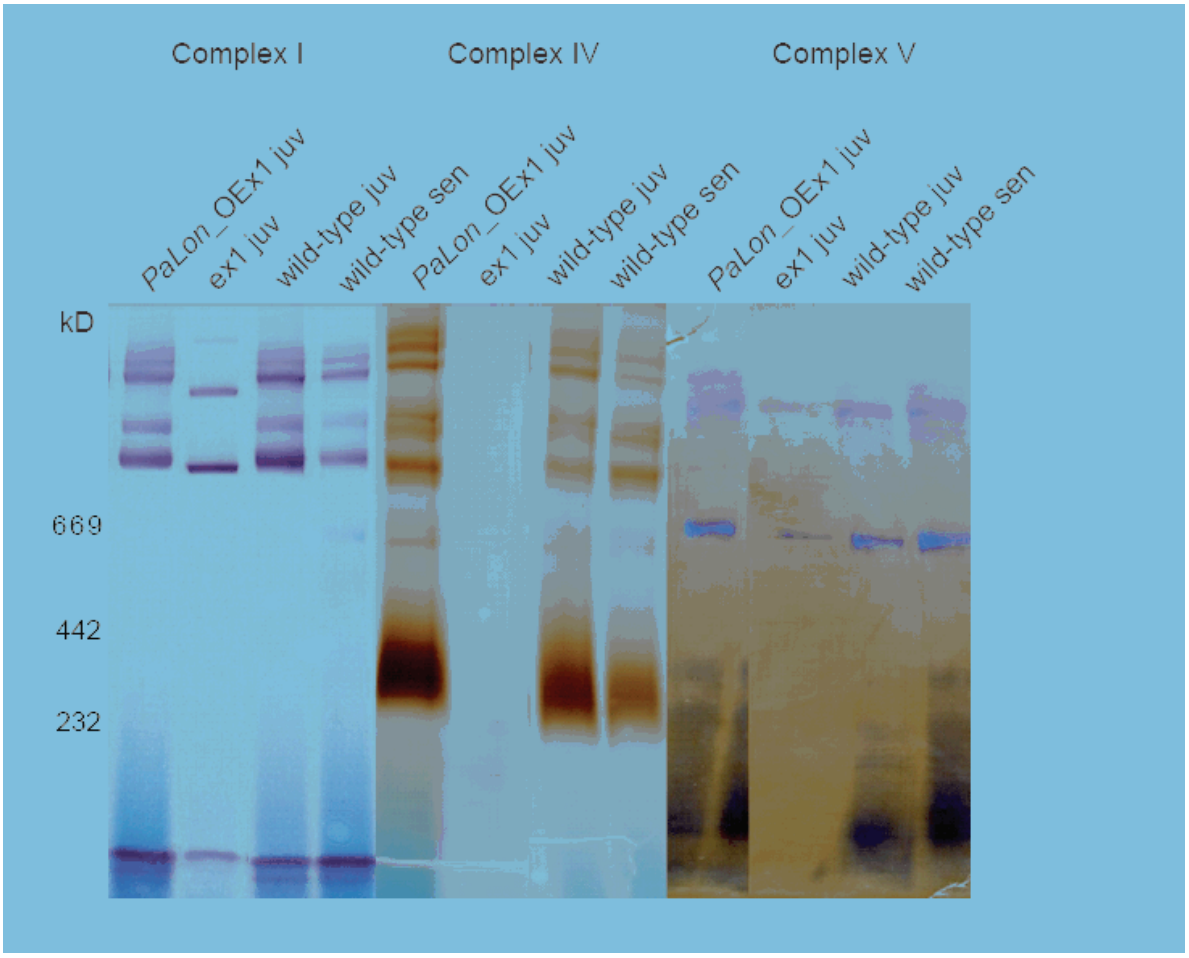

Figure S8 Activity of the respiratory chain complexes. Complex I, IV and V activity stained in blue native poly acrylamid gels of *PaLon*_OEx1 (Lane 1), Ex1 (Lane 2), juvenile (Lane 3) and senescent (Lane 4) wild-type mitochondria. The activities of the investigated complexes of the *PaLon*_OEx1 strain are comparable to those in the wild-type, while mutant ex1 is characterised by complex IV deficiency.

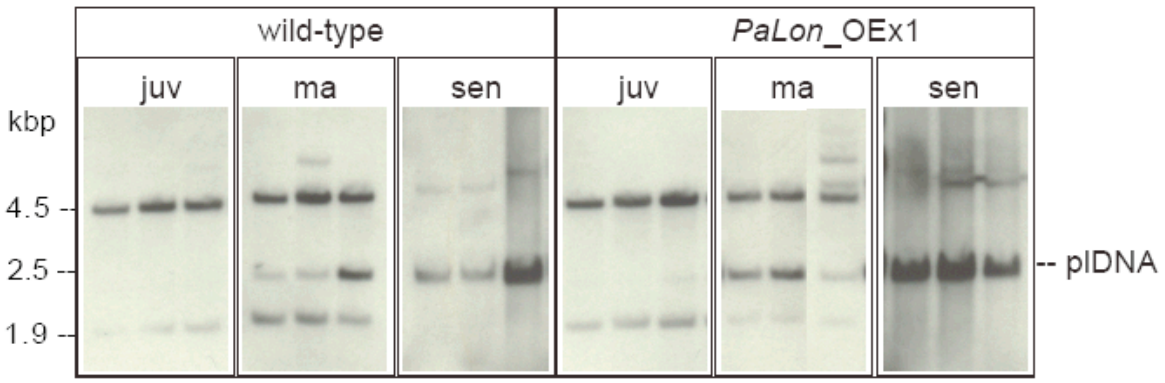

Figure S9 MtDNA stability of juvenile (juv), middle-aged (ma) and senescent (sen) wild-type and *PaLonMut*_OEx1 strains. Detection of plDNA, a 2.5 kbp circular DNA species derived from the first intron of the gene coding for cytochrome c oxidase subunit I (COXI). This circular plDNA which is linearised by *Bgl*II is a biomarker of senescence in wild-type strains *of P. anserina*.

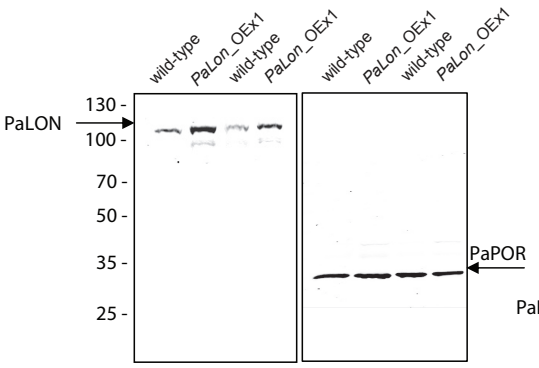

Fig. 1b

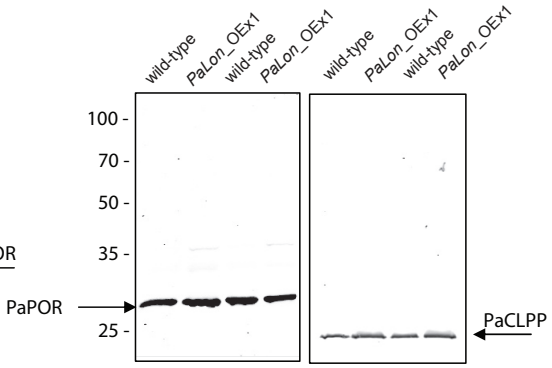

Fig. 1d

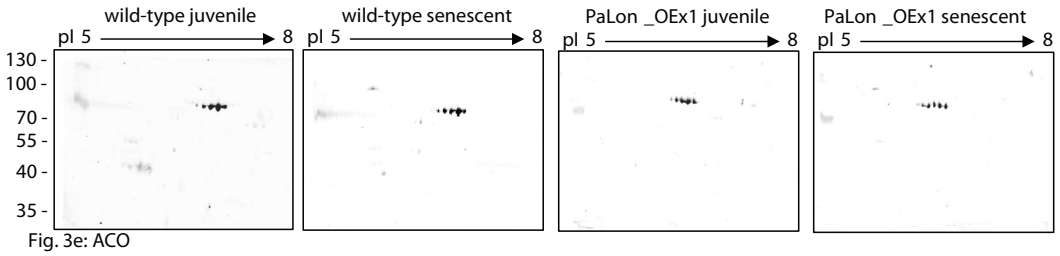

Fig. 3e: ACO

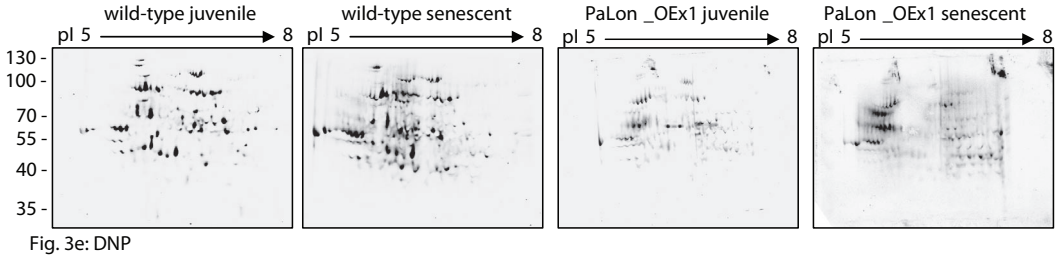

Fig. 3e: DNP

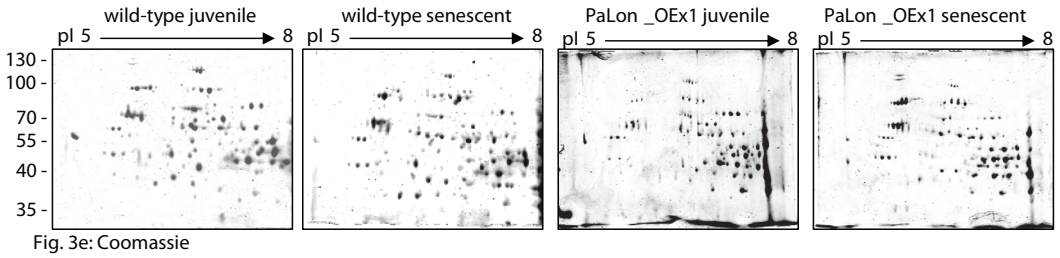

Fig. 3e: Coomassie

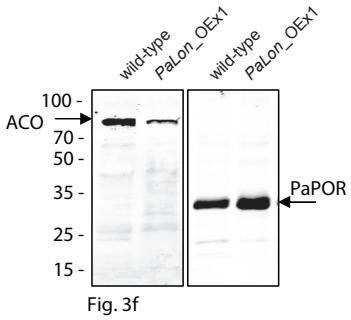

Fig. 3f

Figure S10 Full scans of key Western blots presented in the manuscript

nature cell biology

Cell shape changes indicate a role for extrinsic tensile forces in *Drosophila* germ-band extension

Lucy C. Butler[1,7], Guy B. Blanchard[1,7], Alexandre J. Kabla[2], Nicola J. Lawrence[3], David P. Welchman[4], L. Mahadevan[5,6], Richard J. Adams[1] and Benedicte Sanson[1,8]

***Drosophila* germ-band extension (GBE) is an example of the convergence and extension movements that elongate and narrow embryonic tissues. To understand the collective cell behaviours underlying tissue morphogenesis, we have continuously quantified cell intercalation and cell shape change during GBE. We show that the fast, early phase of GBE depends on cell shape change in addition to cell intercalation. In antero-posterior patterning mutants such as those for the gap gene *Krüppel*, defective polarized cell intercalation is compensated for by an increase in antero-posterior cell elongation, such that the initial rate of extension remains the same. Spatio-temporal patterns of cell behaviours indicate that an antero-posterior tensile force deforms the germ band, causing the cells to change shape passively. The rate of antero-posterior cell elongation is reduced in *twist* mutant embryos, which lack mesoderm. We propose that cell shape change contributing to germ-band extension is a passive response to mechanical forces caused by the invaginating mesoderm.**

Convergence and extension movements remodel tissues during the morphogenesis of many embryos and organs, including vertebrate axis elongation[1–4]. During *Drosophila* gastrulation, the embryo trunk (the germ band) elongates in the antero-posterior (AP) axis and narrows in the dorso-ventral (DV) axis[5]. Polarized cell intercalation, which requires AP patterning, contributes to GBE[6–9]. However, the relative importance of cell intercalation versus other possible cell behaviours[10] has not been explained. Here we quantify the contribution of cell intercalation and cell shape change to tissue deformation in wild-type and mutant embryos.

We recorded the movement of up to 700 cells at 30-s intervals during GBE, imaging the ventral side of live *Drosophila* embryos (Fig. 1a). Cell outlines were labelled with *Drosophila* E–Cadherin–GFP[11], and cell movements were tracked and quantified with a theory and algorithms presented elsewhere[12] (Fig. 1a′, a′). To quantify local tissue deformation, domains defined by a central cell surrounded by a corona of neighbouring cells were followed over 2-min windows[12]. We quantified how fast each of these domains changed dimensions along the AP and the DV axes of the embryo ('total' strain rates). Next we quantified the average rates of shape change for cells belonging to each domain ('cell shape' strain rates). Finally, the strain rates attributable to cell intercalation were derived for each domain by subtracting the 'cell shape' strain rates from the 'total' strain rates (on the basis of the relationship total strain rate = cell shape strain rate + cell intercalation strain rate, defined in ref. 12). A strength of this method is that it provides a continuous measure of cell intercalation that encompasses every type of cell intercalation described so far in the germ band[6,7]. This measure also includes subtler cell intercalation movements that do not necessarily lead to cell neighbour exchange but nonetheless contribute to tissue deformation (Supplementary Information, Movie 1).

GBE proceeds rapidly for about 30 min (the fast phase), then continues at a slower rate for a further 90 min (the slow phase)[8,13]. GBE has been shown to require cell intercalation, but it is not clear why the extension rate is biphasic[6–10]. To understand this, we analysed five movies of wild-type embryos during the first 50 min of GBE. We confirmed that cell intercalation contributed to extension throughout the period analysed (Fig. 1b, c). However, we also found that cell shape change contributed to the first 30 min of GBE, with the peak contribution of cell shape change, at about 10 min, coinciding with the peak rate of tissue extension (Fig. 1b). Over these first 30 min, cell shape change contributed about one-third of total tissue deformation, identifying cell shape as a novel and significant contributor to GBE (Fig. 1c). We conclude that this additional contribution of cell shape change explains the higher rate of extension that distinguishes the fast phase from the slow phase.

Mutants in which AP patterning is defective, such as those for the gap gene *Krüppel*, do not extend their germ bands fully[6–9]. However, in all AP patterning mutants examined, normal tissue extension occurs initially, even though polarized cell intercalation is defective[8]. To understand this apparent contradiction we analysed five movies of *Krüppel*$^-$ embryos and found that in the

[1]Department of Physiology, Development and Neuroscience, University of Cambridge, Downing Street, Cambridge CB2 3DY, UK. [2]Engineering Department, University of Cambridge, Trumpington Street, Cambridge CB2 1PZ, UK. [3]Gurdon Institute, University of Cambridge, Tennis Court Road, Cambridge CB2 1QN, UK. [4]Global Health Institute, École Polytechnique Fédérale de Lausanne, CH-1015 Lausanne, Switzerland. [5]School of Engineering and Applied Sciences, Harvard University, Cambridge, Massachusetts 02138, USA. [6]Department of Systems Biology, Harvard Medical School, Boston, Massachusetts 02115, USA.
[7]These two authors contributed equally to the work.
[8]Correspondence should be addressed to B.S. (e-mail: bs251@cam.ac.uk)

Received 9 February 2009; accepted 28 April 2009; published online 7 June 2009; DOI:10.1038/ncb1894

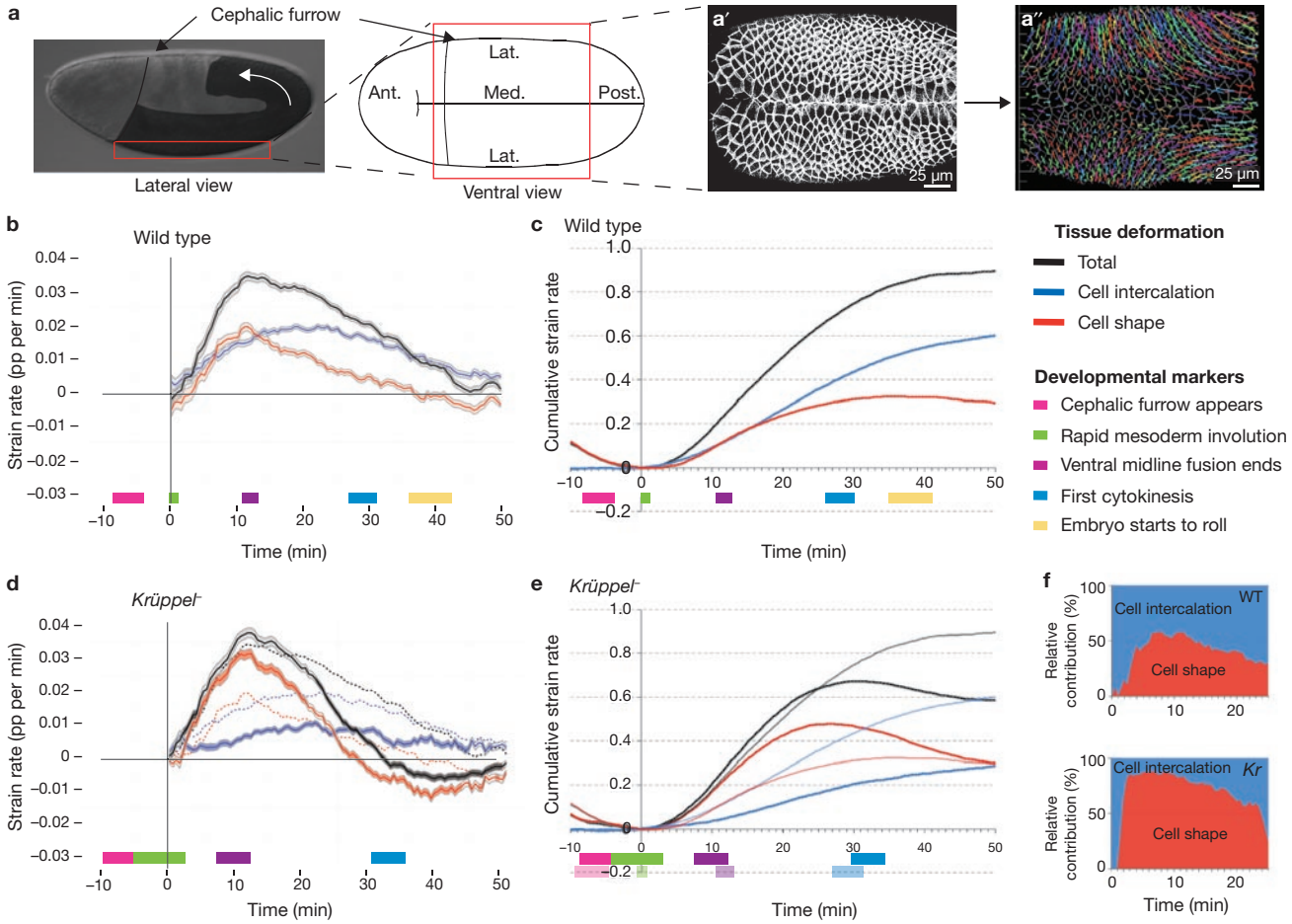

Figure 1 Relative contribution of cell shape change and cell intercalation to germ-band extension in wild-type and *Krüppel*⁻ embryos. (**a**) Lateral view of a *Drosophila* embryo: the extending germ band is shaded (anterior to the left, dorsal uppermost). The red box indicates the stack of optical sections taken by confocal imaging, which corresponds to the ventral field of view shown in the adjacent panel. The left-hand side of the field of view is positioned with the cephalic furrow as a landmark. (**a′**) Corresponding movie frame showing a projection of confocal sections through the cell apices labelled with *DEcadGFP* (Methods). The midline bisecting the embryo is the closing furrow through which the mesoderm has invaginated. (**a″**) Tracked movie frame showing the cell lineages (tracks), cell centroids (endpoints of tracks) and cell outlines recorded by the tracking software. (**b**) Summary of deformation (strain) rates in the AP axis for five wild-type embryos, showing total, cell intercalation and cell shape strain rates (see key). A strain rate is the ratio of the change in length to the original length, divided by the time interval, with units of proportion (pp) per minute. The lines show the mean strain rates for all five embryos, and the ribbon width represents the average standard error within a data set. The timing of developmental landmarks is shown for the five embryos recorded. (**c**) Cumulative representation of the same data, accumulating from $t = 0$. (**d**) Tissue deformation in the AP axis for five homozygous *Krüppel*⁻ embryos. Dotted lines show the wild-type data for comparison. The shaded sections of the ribbons indicate when a given cell behaviour in the mutant was significantly different from the equivalent at that time in the wild type ($P < 0.05$). (**e**) Cumulative representation of the same data; for comparison, wild-type curves are shown as a lighter coloured line, and wild-type developmental landmarks as lighter coloured boxes on the same graph. (**f**) Relative instantaneous contribution of cell shape changes and cell intercalation to extension in wild-type (WT) and *Krüppel*⁻ (*Kr*) mutant embryos, for the first 25 min of germ-band extension, which corresponds to the period when the total extension rate is the same in both genotypes.

first 25 min of GBE, although the rate of cell intercalation was decreased, the rate of cell shape change was increased (Fig. 1d). This increased rate of cell shape change compensated fully for the loss of cell intercalation, resulting in an initial rate of tissue extension indistinguishable from that of the wild type (Fig. 1e), with cell shape change now accounting for most of the tissue extension (Fig. 1f). We found a similar compensation when analysing two other AP patterning mutants: a mutant in the pair-rule gene *even-skipped* (*eve*), and a double mutant in the gap genes *knirps* and *hunchback* (*kni hb*) (Supplementary Information, Fig. 3). Because these analyses were conducted for the whole field of view, we confirmed them by examining the ectodermal cell population alone (Fig. 2a). In the mutant ectoderms, cell intercalation rates were either reduced (*eve* and *kr* mutants) or abolished (*kni hb*), whereas cell shape change was systematically increased compared with that of the wild type (Fig. 2b–d). Increased cell shape change therefore explains the maintenance of an initial rapid rate of tissue extension in AP mutants with defective cell intercalation[8].

Our results indicate that an unidentified mechanism independent of AP patterning or polarized cell intercalation causes cell shape change in the germ band. Cell shape change could be cell-autonomously controlled by a genetic program acting independently of AP patterning. However, this would not explain why cell shape change increases when polarized cell intercalation decreases in AP-patterning mutants. A more plausible scenario is that in both wild-type and AP mutants, an external force is acting on the germ-band cells, causing them to change shape passively in response to tension[14]. We propose that autonomous polarized cell intercalation relaxes the stress imposed on the germ-band tissue by this external

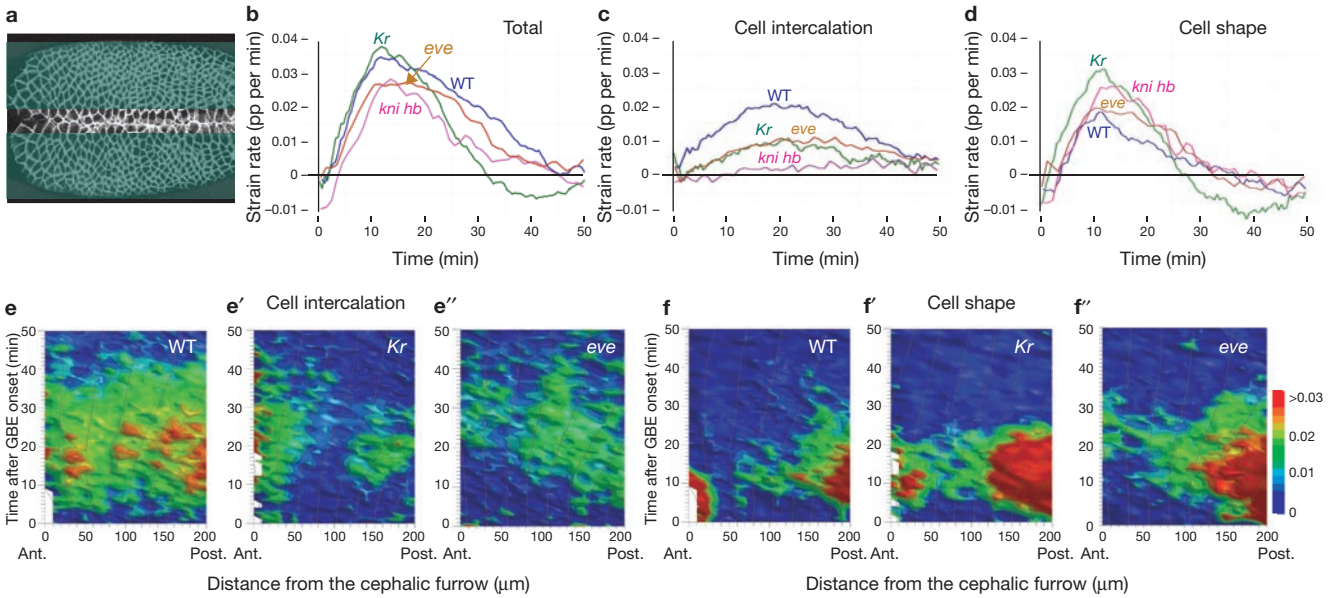

Figure 2 Spatio-temporal analysis of cell behaviours in the ectoderm of wild-type and AP patterning mutant embryos. (**a**) The field of view that we analyse contains a mixture of ectodermal cells (laterally) and mesectodermal cells (at the ventral midline). The ectodermal cells (shaded areas) were selected for further analysis. (**b**–**d**) Comparison of the strain rates in the AP axis for total tissue (**b**), cell intercalation (**c**) and cell shape (**d**), for the wild type (WT) and three AP patterning mutants, *even-skipped* (*eve*), *Krüppel* (*Kr*) and *knirps hunchback* (*kni hb*). Lines show the mean strain rate (pp, proportion) for the ectodermal cells for five embryos (WT, *Kr* and *eve*) or a single embryo for *kni hb*. (**e**–**e**′) Strain rates for cell intercalation contributing to tissue extension in WT (**e**), *Kr*$^-$ (**e**′) and *eve*$^-$ (**e**′′) embryos (average for five embryos of each genotype), represented as a function of the cell's position along the AP axis. Strain rates are colour-coded in accordance with the scale shown (note that any values below 0 are coded blue, and any above 0.03 are coded red). Cell position is given in micrometres from the anterior cephalic furrow (or corresponding position for *eve*$^-$), which separates head from trunk tissue (see Fig. 1a). The tissue is moving with respect to the cephalic furrow as it extends in the AP axis, and the overlaid black lines follow this translation of the tissue over time. The data are shown here for the ectodermal cell population only. (**f**–**f**′′) Similar analysis for cell shape strain rates.

force. In AP-patterning mutant embryos, this dissipation is decreased because cell intercalation is defective, and cell shape change increases.

To investigate this further, we looked at variations in cell behaviour along the AP axis in the ectoderm of wild-type and AP-patterning mutant embryos (Fig. 2e–f′′). Cell intercalation rates were mostly uniform along this axis in wild-type embryos (Fig. 2e). In *kni hb* embryos, which lack AP patterning in the trunk, cell intercalation was abolished throughout the field of view, as expected (Supplementary Information, Fig. 3g). In *Krüppel*$^-$ embryos, cell intercalation was abolished in a central region, and decreased elsewhere (Fig. 2e′). This pattern is consistent with a loss of cell intercalation where *Krüppel* is normally expressed, and a weaker trunk-wide effect, perhaps due to mis-expression of pair-rule genes in the *Krüppel*$^-$ mutant. Planar polarization of myosin II is associated with polarized cell intercalation in the germ band[6,7,9]. Consistent with this was our observation that myosin II concentration at the apical cell cortex was decreased in the ventral ectoderm of *Krüppel*$^-$ mutant embryos (data not shown). Note that we did not detect a difference in myosin II localization between the central and posterior domain to explain the observed difference in cell intercalation rates (Fig. 2e′). In *even-skipped*$^-$ embryos, cell intercalation was decreased uniformly along the length of the trunk (Fig. 2e′), which is consistent with *eve* expression in seven closely spaced stripes.

The pattern of cell shape change in wild-type embryos was graded along the AP axis, increasing from the centre towards the posterior end of the embryo between 5 and 20 min of GBE (Fig. 2f). There was also a shorter pulse of cell elongation at the anterior end for the first 15 min of GBE, which was also present in *Krüppel* embryos (Fig. 2f′) but absent from *even-skipped*$^-$ embryos (Fig. 2f′). This suggests that anterior cell elongation is a consequence of cephalic furrow formation, which is defective in *eve* mutants[15] (Supplementary Information, Fig. 3a). In both *Krüppel*$^-$ and *even-skipped* mutants (and also in *kni hb* mutants; Supplementary Information, Fig. 3h), the central to posterior gradient of cell elongation was maintained but the rate of cell shape change was increased (Fig. 2f′, f′′). The presence of a gradient of AP cell elongation in wild-type and all AP mutants examined supports the idea that cell shape change is a passive response to the same extrinsic force.

This extrinsic force could be an AP pulling force or a DV pushing force. To investigate this, we examined the posterior domain of the germ band in *Krüppel*$^-$ mutants, a region with strong deformation (Fig. 3a–c). If cells deform passively in response to mechanical forces, they should behave qualitatively like a passive cellular material such as a foam, in which shape reflects stress[16]. Accordingly, different signatures are expected for pulls or pushes: if the tissue experiences a pull in one direction, it will tend to contract in the other two axes, leading to an increase in the cell projected area. Conversely if the tissue is compressed (for instance in the DV axis), cell area is expected to decrease. We found an increase in apical cell area as cells elongated in the posterior tissue of *Krüppel*$^-$ embryos (Fig. 3d, d′; see also Fig. 3e), suggesting that AP cell elongation in this domain results from an AP pull rather than a DV compression.

The analyses of cell shape and cell area also showed that, 10 min after GBE initiation, cells in wild-type embryos acquired an isometric apical shape that they maintained for the remainder of GBE (Fig. 3d, e). In *Krüppel*$^-$ mutants, however, cell shapes were briefly isometric at about 10 min then became elongated in the AP axis (Fig. 3d′, e). We propose that in wild-type embryos, autonomous polarized cell intercalation relaxes the stress imposed externally on the germ band, allowing stretched cells to return to isometric shapes. In *Krüppel*$^-$ embryos, the

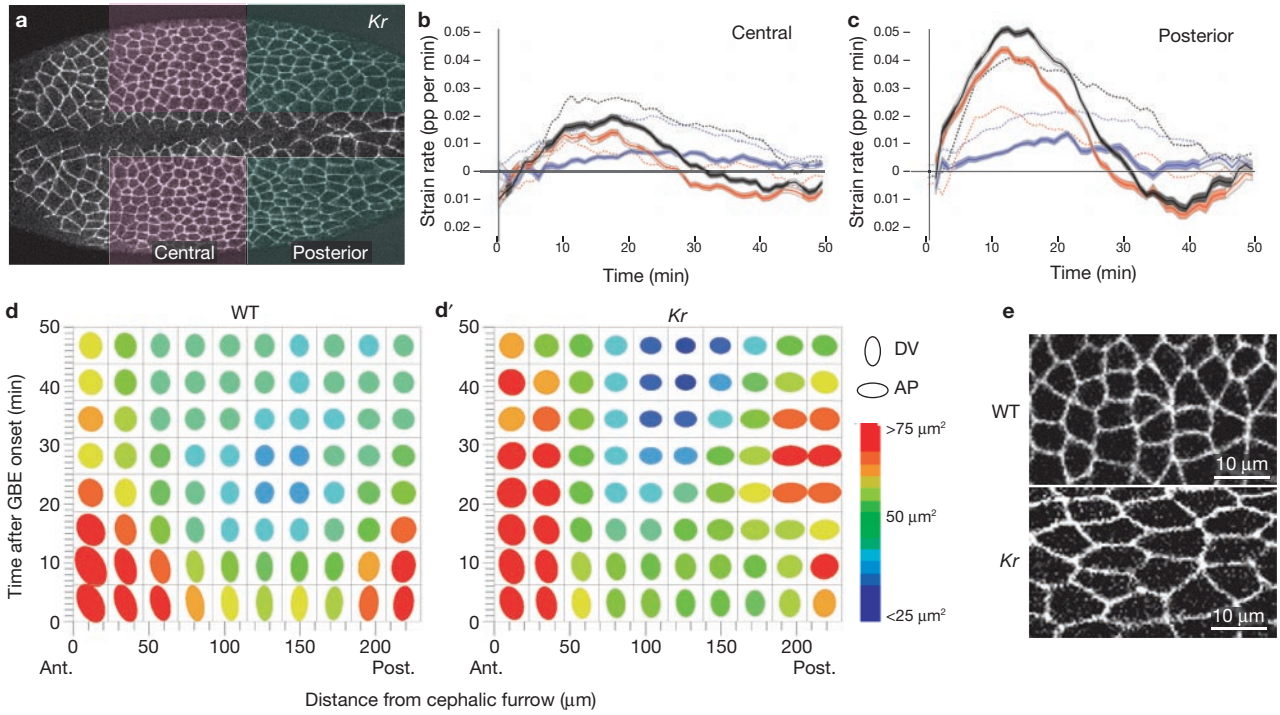

Figure 3 Spatio-temporal analysis of cell shape and cell area change in the ectoderm of wild-type and *Krüppel*⁻ embryos. (**a**) The central and posterior ectodermal cell populations (shaded areas) were analysed separately (see also Supplementary Information, Fig. 3i, j). (**b**, **c**) Strain rates in the AP axis for total (black), cell intercalation (blue) and cell shape (red), for the central (**b**) and posterior (**c**) populations of ectodermal cells in wild-type (WT) and *Krüppel*⁻ embryos (pp, proportion). Wild-type is shown as dotted lines and *Krüppel*⁻ as a ribbon, with ribbon shading indicating a significant difference between the two genotypes ($P < 0.05$). (**d**, **d**′) Representation of the average cell shape, cell area (quantified by colour coded scale) and cell orientation (see key), in accordance with the cell's position along the AP axis (cell positions are given in μm from cephalic furrow) and time. Note that ectodermal cells only are analysed in wild-type (**d**) and *Krüppel*⁻ (**d**′) embryos. After 10 min of GBE, the WT germ-band cells acquire an isotropic shape and maintain it, whereas the cells elongate in the AP orientation in *Krüppel*⁻ mutants, especially at the posterior, where cell area is also greatest at this time. (**e**) Close-up of movie frames of WT and *Krüppel*⁻ embryos at mid-extension in the posterior domain, showing that whereas WT cells retain an isotropic shape, mutant cells are visibly elongated in the AP axis.

decrease in polarized intercalation caused by the defect in AP patterning upsets this balance, and cells stretch passively in the AP axis in response to tension. When this tension ceases, at about 25 min into GBE, the cells contract back for another 25 min, suggesting that the tissue relaxes as in an elastic response (Fig. 3c; see also Fig. 1d).

Other morphogenetic movements happening concurrently with GBE are good candidates for causing an AP tensile force. The sharp increase in the rate of cell shape change at the beginning of GBE overlaps with mesoderm invagination (Fig. 1b, d). Because *twist* is required for mesoderm specification and invagination[5,17–19], we analysed five movies of *twist*⁻ mutant embryos (Fig. 4). Mesoderm invagination causes the cells on both sides of the furrow to become elongated towards the midline[5,11,20,21] (see also Fig. 3d, d′). The peak of cell elongation in the DV axis, which was lost as expected in *twist*⁻ mutants (Fig. 4a′; see also Fig. 4f), was tightly temporally correlated with the onset of GBE (Fig. 4a; Supplementary Information, Fig. 1). Moreover, in *twist*⁻ embryos, in which mesoderm invagination failed, the rates of both cell shape and cell intercalation strains in the AP axis were decreased in the first 20 min of GBE (Fig. 4b, c), even though *twist*⁻ mutants ultimately extended their germ bands as far as those in the wild type[8] (Supplementary Information, Fig. 2). This indicates that *twist* is required for the fast rate of extension at the beginning of GBE. In contrast to the wild type, small, non-invaginated 'mesodermal' cells are present in the field of view in *twist*⁻ mutants. To compare the same population of cells in *twist*⁻ mutants and the wild type, we analysed the ectodermal cell population alone and confirmed these results (Fig. 2a; Supplementary Information, Fig. 4a, b). Given that ectodermal cells do not express *twist*, this demonstrates an indirect (non-cell-autonomous) requirement for *twist* in the fast phase of GBE.

Cell intercalation in *twist*⁻ mutants was decreased almost uniformly along the AP axis (Fig. 4d), but cell shape change was not (Fig. 4e). The anterior pulse of cell elongation was maintained, as expected because *twist* mutants have normal cephalic furrows, but the steep gradient of cell shape change towards the posterior was substantially reduced. Thus, *twist* is required non cell-autonomously for cell shape change that is patterned in the AP axis. Because *twist* is not known to regulate AP patterning[5,22,23], this suggests that the gradient of cell shape change and the AP tensile force depends on the invaginating mesoderm itself. Moreover, ectodermal cells in *twist*⁻ embryos maintained an isometric shape throughout extension despite decreased cell intercalation (Fig. 4f), which is consistent with the hypothesis that the tensile force is attenuated in this mutant.

The non-invaginated 'mesodermal' cells in *twist* mutants could act as a brake and decrease an AP tensile force generated by morphogenetic movements elsewhere in the embryo. Alternatively, the invaginating mesoderm could be the direct cause of the AP tensile force deforming the germ band in the fast phase. Note that AP cell elongation in wild-type and AP-patterning mutant embryos might also result from a relaxation of the ectoderm stretched along the DV axis during mesoderm invagination. However, tissue relaxation is unlikely to explain the observed

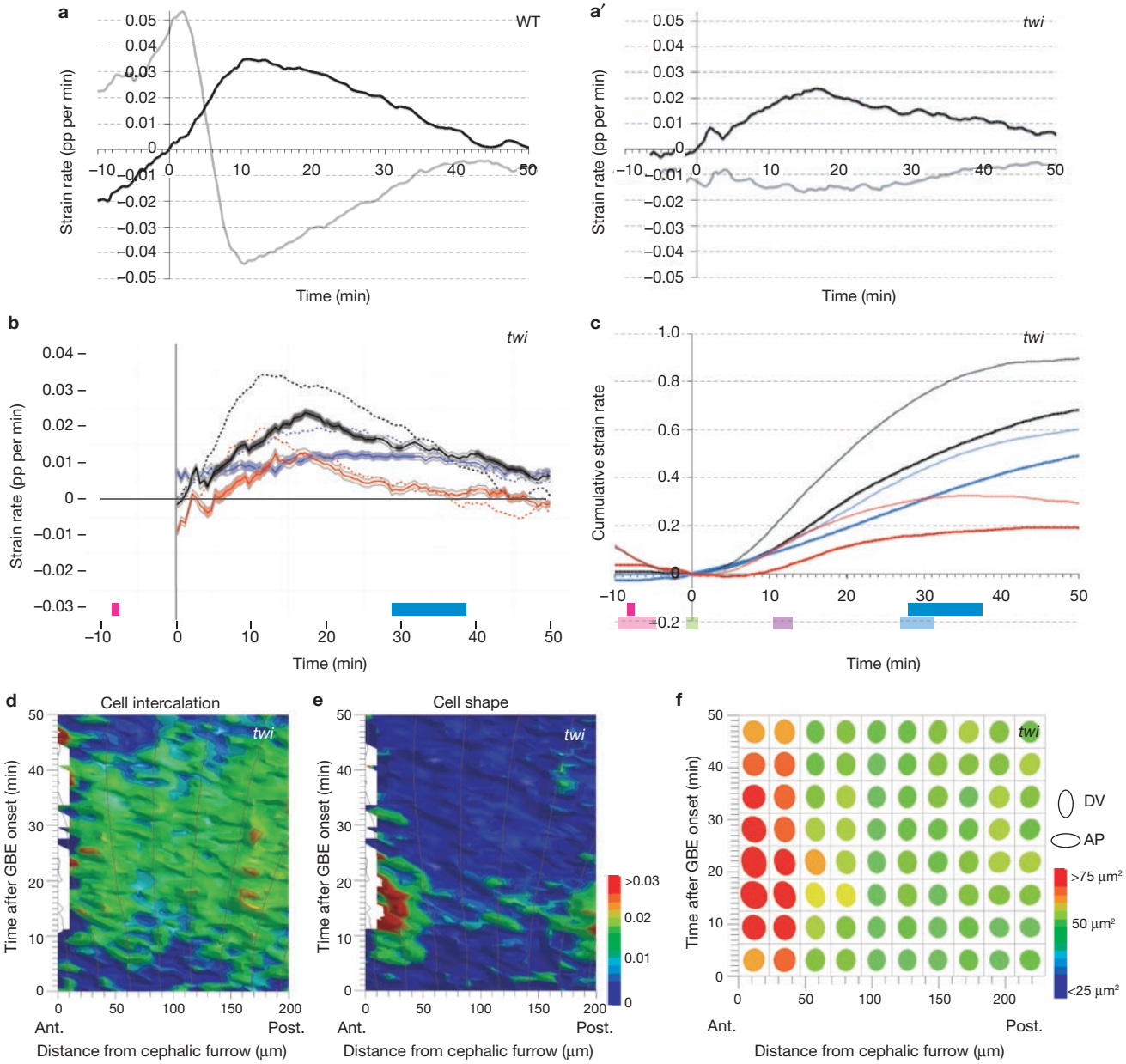

Figure 4 Relationship between mesoderm invagination and germ-band extension. (**a**) Tissue deformation in the DV axis (convergence, grey) and the AP axis (extension, black) in wild-type (WT) embryos. The tissue deformation peak in the DV axis at the onset of germ-band extension corresponds to the ventrolateral tissue stretching in the DV axis in response to mesoderm invagination (pp, proportion). (**a′**) As expected, this peak of DV stretching is absent in *twist*⁻ (*twi*) embryos. (**b**) Tissue deformation in the AP axis for five homozygous *twist*⁻ embryos in which there is no mesodermal invagination (total strain rate in black, cell shape in red, cell intercalation in blue). Dotted lines show the wild-type data for comparison. Ribbon shading indicates a significant difference between mutant and wild type ($P < 0.05$). (**c**) Cumulative representation of the same data, with lighter colours for corresponding wild-type data. (**d**) Strain rates for cell intercalation contributing to tissue extension in *twist*⁻ embryos are represented as a function of the cell's position along the AP axis. (**e**) Similar analysis for cell shape strain rates. (**f**) Representation of averages for cell shape, area and orientation, along the AP axis and throughout germ-band extension for *twist*⁻ embryos.

increase in cell area and cell elongation in the posterior of the germ band, suggesting that an AP tensile force predominates here.

Aside from mesoderm invagination, three other morphogenetic movements could conceivably produce the force deforming the germ band: cephalic furrow formation, posterior midgut invagination and amnioserosa cell elongation. Although cephalic furrow formation is correlated with the pulse of cell elongation in the anterior domain (Fig. 2f–f′′), the central-to-posterior gradient of cell elongation is intact in *eve* mutants, which do not have cephalic furrows. Posterior midgut invagination, which initiates on the dorsal posterior side, could pull the ectodermal tissue around the posterior of the embryo[5]. However, analysis of extension rates in a *folded gastrulation* (*fog*) mutant, which blocks the formation of posterior midgut invagination[19], shows that tissue deformation, cell intercalation and cell shape change are indistinguishable from those in the wild type during the first 20 min of extension (Supplementary Information, Fig. 5). Finally,

DV elongation of the amnioserosa cells on the dorsal side[24] could push the ectodermal tissue towards the midline. However, cell area measurements suggest that AP tension rather than DV compression explains cell deformation in the posterior domain (see Fig. 3d′, e). Given the above, we propose that mesoderm invagination is the main source of AP tensile force.

In support of a direct role for the invaginating mesoderm, we found that the germ band extends fastest close to the midline during the fast phase, suggesting an axial pull (Supplementary Information, Fig. 4c, d). A possible mechanism is that, once invaginated, the mesoderm undergoes convergence and extension (through an AP-patterning-independent mechanism), elongating the tube in the AP axis. This convergence and extension of the mesoderm (which is consistent with earlier observations[5,19]) could drag the midline cells and adjacent ectodermal tissue, as reported for amphibian gastrulation[14,25].

In summary, we have found, in contrast to what was previously thought[6,8,13], that cell shape change contributes significantly to the fast phase of germ-band extension. Whereas cell intercalation during GBE requires AP patterning[6–9], cell shape change is under the control of DV patterning, because it is decreased in *twist*$^{-}$ mutants. Our analysis of cell shape change and cell intercalation shows that at the beginning of the fast phase, the decrease in cell intercalation in AP mutants is compensated for by an increase in AP cell elongation such that the overall rate of tissue extension can initially remain the same. These findings parallel our earlier observations on notochord extension in zebrafish[1], another tissue previously thought to extend as a sole consequence of active convergence. In both studies, quantitative analyses reveal redundancy in the forces extending the body axis, highlighting the robustness of convergence and extension movements.

We propose that cell shape change is a passive response to an AP tensile force resulting from convergence and extension of the internalizing mesoderm. Intriguingly, in addition to a decrease in the rate of cell shape change, the rate of intercalation is decreased by about 30% in the first 25 min of GBE in *twist*$^{-}$ mutants (Fig. 4b, c; Supplementary Information, Fig. 4a), even though the AP patterning system on which the polarized exchange of cell neighbours depends is not affected in *twist*$^{-}$ mutants[5,8]. One possible explanation is that the AP tensile force that normally stretches the ectodermal cells also increases the rate of polarized cell intercalation. Stretching cells in the AP axis could make it mechanically favourable for cell junctions to shorten in the orthogonal DV axis, as suggested previously[26,27]. DV junction shortening is the first step leading to cell neighbour exchange in the germ band[6,7]. Thus, our analysis provides an opportunity to explore how the autonomous cell behaviours described previously[6–9] interact with mechanical forces generated by morphogenetic movements[14]. □

METHODS

Methods and any associated references are available in the online version of the paper at http://www.nature.com/naturecellbiology/

Note: Supplementary Information is available on the Nature Cell Biology website.

ACKNOWLEDGEMENTS

We thank Claire Lye, Bruno Monier and Daniel St Johnston for comments on the manuscript and discussions. We thank the Bloomington Drosophila Stock Centre for fly strains. This work was supported by a Human Frontier Science Program grant to B.S., a Wellcome Trust studentship to L.C.B., a Medical Research Council grant to R.J.A. and a Harvard–National Science Foundation Materials Research Science and Engineering Center award to M.L.

AUTHOR CONTRIBUTIONS

This project grew from a close collaboration between the groups of B.S. and R.J.A. L.C.B. performed the experiments and analysed the data with G.B.B., R.J.A. and B.S. N.J.L. performed the initial experiments and developed the time-lapse methods. D.P.W. contributed to experiments and manuscript preparation. Strain rate analyses were developed by G.B.B., A.J.K., R.J.A. and L.M., building on a tracking and quantification framework of G.B.B. and R.J.A. B.S. and L.C.B. designed the *Drosophila* experiments and prepared the manuscript. All authors contributed to data interpretation and editing of the manuscript.

COMPETING FINANCIAL INTERESTS

The authors declare that they have no competing financial interests.

Published online at http://www.nature.com/naturecellbiology
Reprints and permissions information is available online at http://npg.nature.com/reprintsandpermissions/

1. Glickman, N. S., Kimmel, C. B., Jones, M. A. & Adams, R. J. Shaping the zebrafish notochord. *Development* **130,** 873–887 (2003).
2. Keller, R. Mechanisms of elongation in embryogenesis. *Development* **133,** 2291–2302 (2006).
3. Solnica-Krezel, L. Conserved patterns of cell movements during vertebrate gastrulation. *Curr. Biol.* **15**, R213–R228 (2005).
4. Munro, E. M. & Odell, G. M. Polarized basolateral cell motility underlies invagination and convergent extension of the ascidian notochord. *Development* **129,** 13–24 (2002).
5. Costa, M., Sweeton, D. & Wieschaus, E. Gastrulation in *Drosophila*: Cellular mechanisms of morphogenetic movements in *The development of Drosophila melanogaster* (eds. Bate, M. & Martinez-Arias, A.) 425–465 (Cold Spring Harbor Laboratory Press, 1993).
6. Bertet, C., Sulak, L. & Lecuit, T. Myosin-dependent junction remodelling controls planar cell intercalation and axis elongation. *Nature* **429,** 667–671 (2004).
7. Blankenship, J. T., Backovic, S. T., Sanny, J. S., Weitz, O. & Zallen, J. A. Multicellular rosette formation links planar cell polarity to tissue morphogenesis. *Dev. Cell* **11,** 459–470 (2006).
8. Irvine, K. D. & Wieschaus, E. Cell intercalation during *Drosophila* germband extension and its regulation by pair-rule segmentation genes. *Development* **120,** 827–841 (1994).
9. Zallen, J. A. & Wieschaus, E. Patterned gene expression directs bipolar planar polarity in *Drosophila*. *Dev. Cell* **6,** 343–355 (2004).
10. da Silva, S. M. & Vincent, J. P. Oriented cell divisions in the extending germband of *Drosophila*. *Development* **134,** 3049–3054 (2007).
11. Oda, H. & Tsukita, S. Real-time imaging of cell–cell adherens junctions reveals that *Drosophila* mesoderm invagination begins with two phases of apical constriction of cells. *J. Cell Sci.* **114,** 493–501 (2001).
12. Blanchard, G. B. *et al.* Tissue tectonics: morphogenetic strain rates, cell shape change and intercalation. *Nature Methods* **6,** 458–464 (2009).
13. Hartenstein, V. & Campos-Ortega, J. A. Fate-mapping in wild-type *Drosophila melanogaster*. 1. The spatio-temporal pattern of embryonic cell divisions. *Roux' Arch. Dev. Biol.* **194,** 181–195 (1985).
14. Keller, R., Shook, D. & Skoglund, P. The forces that shape embryos: physical aspects of convergent extension by cell intercalation. *Phys. Biol.* **5,** 15007 (2008).
15. Vincent, A., Blankenship, J. T. & Wieschaus, E. Integration of the head and trunk segmentation systems controls cephalic furrow formation in *Drosophila*. *Development* **124,** 3747–3754 (1997).
16. Weaire, D. & Hutzler, S. *The Physics of Foams* (Oxford Univ. Press, 2001).
17. Leptin, M. & Grunewald, B. Cell shape changes during gastrulation in *Drosophila*. *Development* **110,** 73–84 (1990).
18. Seher, T. C., Narasimha, M., Vogelsang, E. & Leptin, M. Analysis and reconstitution of the genetic cascade controlling early mesoderm morphogenesis in the *Drosophila* embryo. *Mech. Dev.* **124,** 167–179 (2007).
19. Sweeton, D., Parks, S., Costa, M. & Wieschaus, E. Gastrulation in *Drosophila*: the formation of the ventral furrow and posterior midgut invaginations. *Development* **112,** 775–789 (1991).
20. Kam, Z., Minden, J. S., Agard, D. A., Sedat, J. W. & Leptin, M. *Drosophila* gastrulation: analysis of cell shape changes in living embryos by three-dimensional fluorescence microscopy. *Development* **112,** 365–370 (1991).
21. Pouille, P. A. & Farge, E. Hydrodynamic simulation of multicellular embryo invagination. *Phys. Biol.* **5,** 15005 (2008).
22. Leptin, M. *twist* and *snail* as positive and negative regulators during *Drosophila* mesoderm development. *Genes Dev.* **5,** 1568–1576 (1991).
23. Thisse, B., Stoetzel, C., Gorostiza-Thisse, C. & Perrin-Schmitt, F. Sequence of the *twist* gene and nuclear localization of its protein in endomesodermal cells of early *Drosophila* embryos. *EMBO J.* **7,** 2175–2183 (1988).
24. Pope, K. L. & Harris, T. J. Control of cell flattening and junctional remodeling during squamous epithelial morphogenesis in *Drosophila*. *Development* **135,** 2227–2238 (2008).
25. Keller, R., Shih, J. & Sater, A. The cellular basis of the convergence and extension of the *Xenopus* neural plate. *Dev. Dyn.* **193,** 199–217 (1992).
26. Keller, R. E. & Trinkaus, J. P. Rearrangement of enveloping layer cells without disruption of the epithelial permeability barrier as a factor in *Fundulus* epiboly. *Dev. Biol.* **120,** 12–24 (1987).
27. Weliky, M. & Oster, G. The mechanical basis of cell rearrangement. I. Epithelial morphogenesis during *Fundulus* epiboly. *Development* **109,** 373–386 (1990).

METHODS

Fly strains. Apical cell membranes were labelled with *ubi–DE–Cadherin–GFP* (abbreviated as *DEcadGFP*), a fusion between DE–Cadherin and GFP[11]. We used the null mutant alleles *eve[3], Kr[1]*, *kni[10]hb[4]*, *twist[1]* and *fog[S4]*. To label cells in these mutant backgrounds, we made the recombinant chromosomes *eve[3]DEcadGFP*, *Kr[1]DEcadGFP* and *twist[1]DEcadGFP* and the balanced stocks *DEcadGFP; kni[10]hb[4]* and *fog[S4]; DEcadGFP*.

Movie acquisition. Embryos at the end of cellularization were mounted on O_2-permeable membrane (Sartorius) and covered in Voltalef oil (Attachem). The embryo to be imaged was rolled to have the ventral side in the field of view, and the stage was rotated to capture the equivalent field of view for each embryo, with the cephalic furrow just visible to the left and the ventral furrow bisecting the field of view horizontally (Fig. 1a′). The tissue that undergoes polarized intercalation at gastrulation is the ventrolateral ectoderm, and this tissue is about 40 cell diameters long in the AP axis, and 20–23 cell diameters wide in the DV axis at the beginning of GBE[13]. Our field of view captures 12–15 cell diameters on each side of the invaginated mesoderm (midline) at the onset of GBE (Fig. 1a′; see also Supplementary Information, Movies 2–4). This corresponds to the ventralmost 60% of the ventrolateral ectoderm on each side of the midline. Homozygous mutant embryos were identified by the absence of GFP expression from the balancer chromosome *CyOKrGal4UASGFP*[28] and by their phenotypes. Note that *twist*-null mutants show variable mesoderm invagination defects that range from very shallow furrows to almost wild-type-like deep furrows[18]. To ensure a consistent phenotype, we analysed five *twi* mutant embryos exhibiting the most severe of these phenotypes. Movies were recorded at 20.5 ± 1 °C, measured with a high-resolution thermometer (Checktemp1). Time points were taken every 30 s on a MRC1024 Bio-Rad confocal microscope coupled to an upright Nikon Eclipse E800 microscope (with a 40× oil-immersion Plan/Fluor objective, numerical aperture 1.3). For each time point, a z-stack of ten optical slices separated by 1 μm were taken, starting from the apical surface of the cells (Supplementary Information, Movies 2–4). After each movie, embryos were left to develop, to check that they survived normally until the end of embryogenesis. For mutant embryos, the cuticle was mounted in Hoyer's medium to verify that it showed the expected phenotype.

Movie tracking. The confocal *Z*-stacks were converted into stacks of curved two-dimensional representations, the outermost of which followed the surface of the embryo. The section giving the clearest view of cell apices was selected for tracking. Tracking software identifies cells and links them in an iterative process using a watershedding algorithm[12]. For each cell at each time point, the program stores the coordinates of the centroid and also those of a polygon describing the cell, as well as information about the cell lineage (Supplementary Information, Movies 5–7).

Movie analysis. Using the relative movement of cell centroids, the strain rate for a small domain of tissue composed of one corona of cell neighbours is calculated for each cell and for each 2-min interval (corresponding to four movie frames)[12] (Supplementary Information, Movies 8–10). A direct measure of cell shape change is calculated by first approximating each cell from this small region to an ellipse, then finding the strain rates that best map a cell's elliptical shape as it evolves over time (Supplementary Information, Movies 11–13). The difference between the total strain rate and cell shape strain rate is attributed to cell intercalation[12] (Supplementary Information, Movies 14–16). These strain rates are then projected onto the embryonic axes, AP and DV. Cell area change is calculated as the mean of the AP and DV cell shape strain rates.

Intragenotype movie synchronization. Within the same genotype, movies were synchronized in most cases by making a quantitative comparison, using a given threshold of proportional change per minute for instantaneous proportional extension in the AP axis. We use a synchronization threshold of 0.01 for wild-type and *Krüppel*$^-$ and 0.005 for *twist*$^-$ embryos (which have a lower initial rate of extension). For *even-skipped*$^-$ embryos, we made a qualitative comparison, using the peaks of extension and convergence to synchronize the movies.

Intergenotype movie synchronization. Average strain rate curves weighted by planar cell area were calculated for each genotype. Genotypes were then synchronized using the zero time of average instantaneous extension in the AP axis. Note that, in contrast with mutant embryos analysed in this study, most wild-type embryos rolled on their sides during filming, about 40 min after the onset of germ-band extension (see Fig. 1b). Thus, the field of view in wild-type embryos incorporated progressively more lateral cells from this point onwards than in the mutants analysed.

Statistical validation. To test for evidence of differences between data derived from different embryos, we constructed a mixed-effects model[29] using R software[30]. We estimated the *P* value associated with a fixed effect of differences between genotypes, allowing for random effects contributed by differences between embryos within a given genotype. Error ribbons show the typical standard error for data from one embryo, averaged across all embryos of that group[31]. Sections of ribbons are shaded when $P < 0.05$, signifying evidence for a difference between genotypes.

28. Casso, D., Ramirez-Weber, F. A. & Kornberg, T. B. GFP-tagged balancer chromosomes for *Drosophila melanogaster*. *Mech. Dev.* **88,** 229–232 (1999).
29. Pinheiro, J. C. & Bates, D. M. *Mixed-effects Models in S and S-PLUS* (Springer, 2000).
30. R Research Development Team. *R: A language and environment for statistical computing*. (R Foundation for Statistical Computing, 2008).
31. Wickham, H. ggplot2: an implementation of the grammar of graphics. *R package version 0.8.1* (Springer, 2008).

nature cell biology

DOI: 10.1038/ncb1894

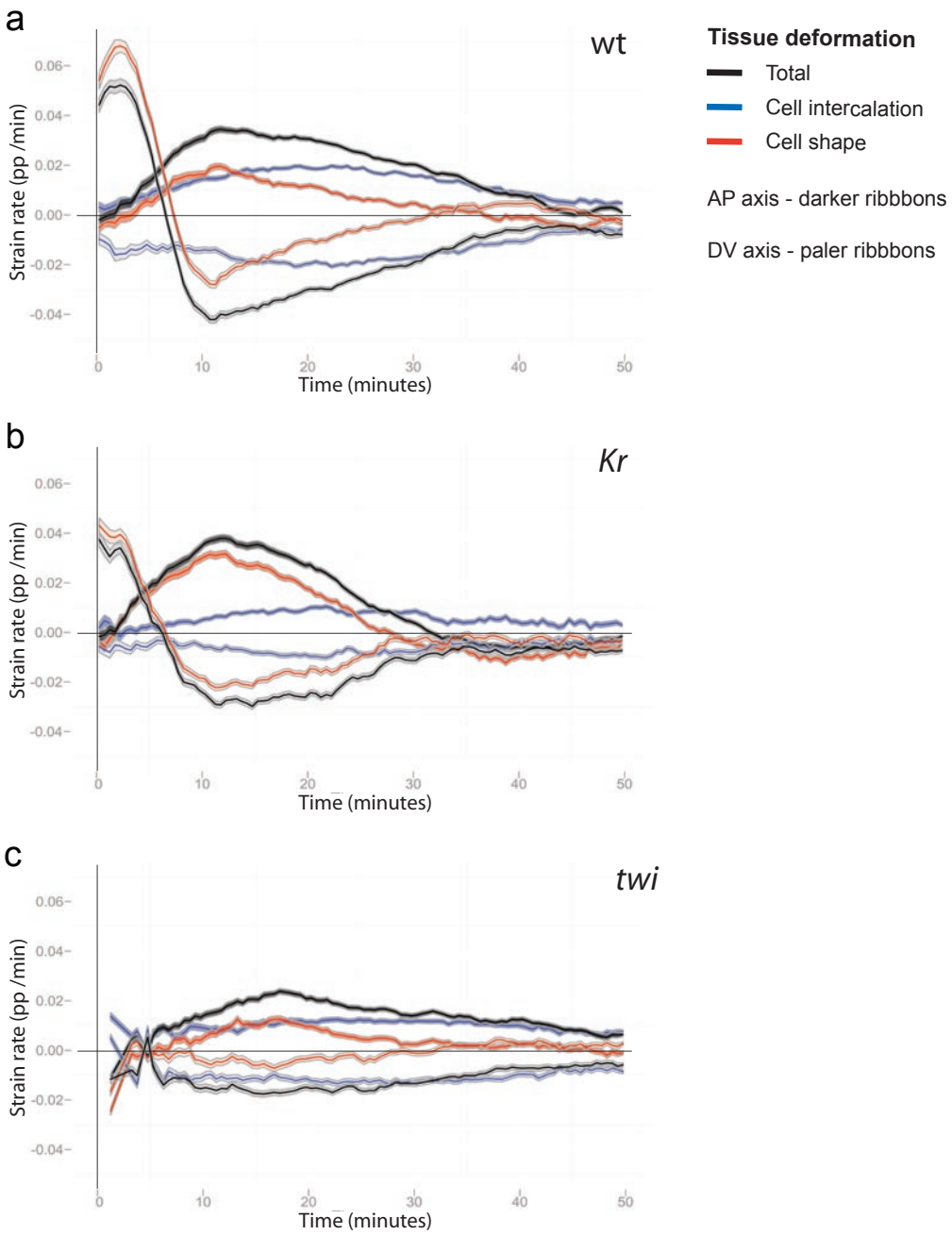

Figure S1 Tissue deformation in the AP and DV embryonic axes for wild-type, *Kruppel-* and *twist-* embryos. Contrarily to the deformation in the AP axis (extension), most deformation in the DV axis is negative (convergence), except for a peak of cell shape changes caused by mesoderm invagination which overlaps with the first 10 minutes of germ-band extension. Consistent with this, the peak of positive tissue deformation in DV is present in wild-type and *Kruppel-* embryos (**A**, **B**), but not in *twist-* embryos (**C**). The ribbons for AP axis deformations are shaded, whereas those for DV axis deformations are not.

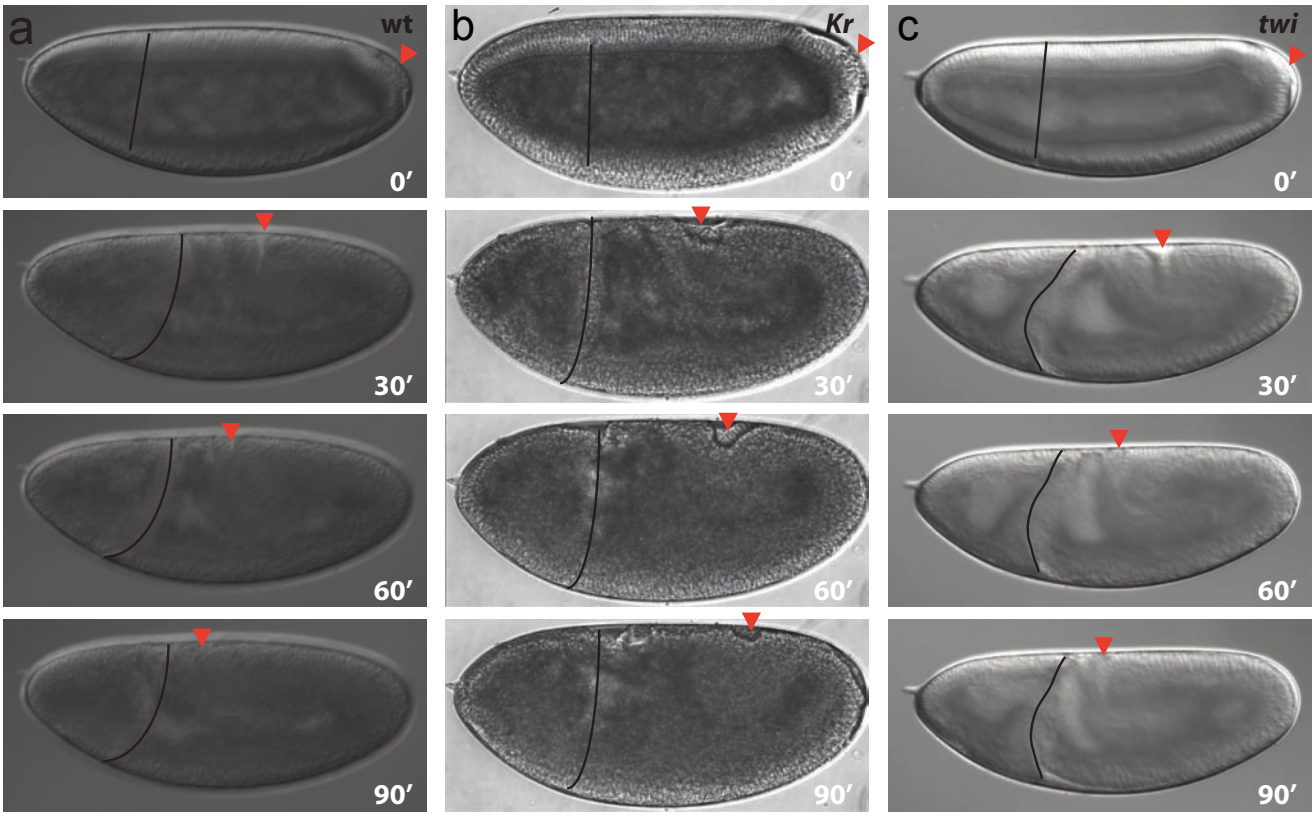

Figure S2 Germ-band extension in wild-type, *Kruppel-* and *twist-* embryos. Frames of movies collected under Nomarski optics, showing lateral views of embryos from wild-type, *Krüppel-* and *twist-* embryos (anterior to the left, dorsal uppermost). The red arrow labels the position of the extending end of the germ-band (thus the extent of GBE), while the black line shows the position of the cephalic furrow. Whereas wild-type and *twist-* embryos have almost completely extended their germ-band after 90 minutes, *Krüppel-* embryos fail to complete extension. Note that the extension which remains in *Kruppel-* embryos takes place within the first 30 minutes of GBE.

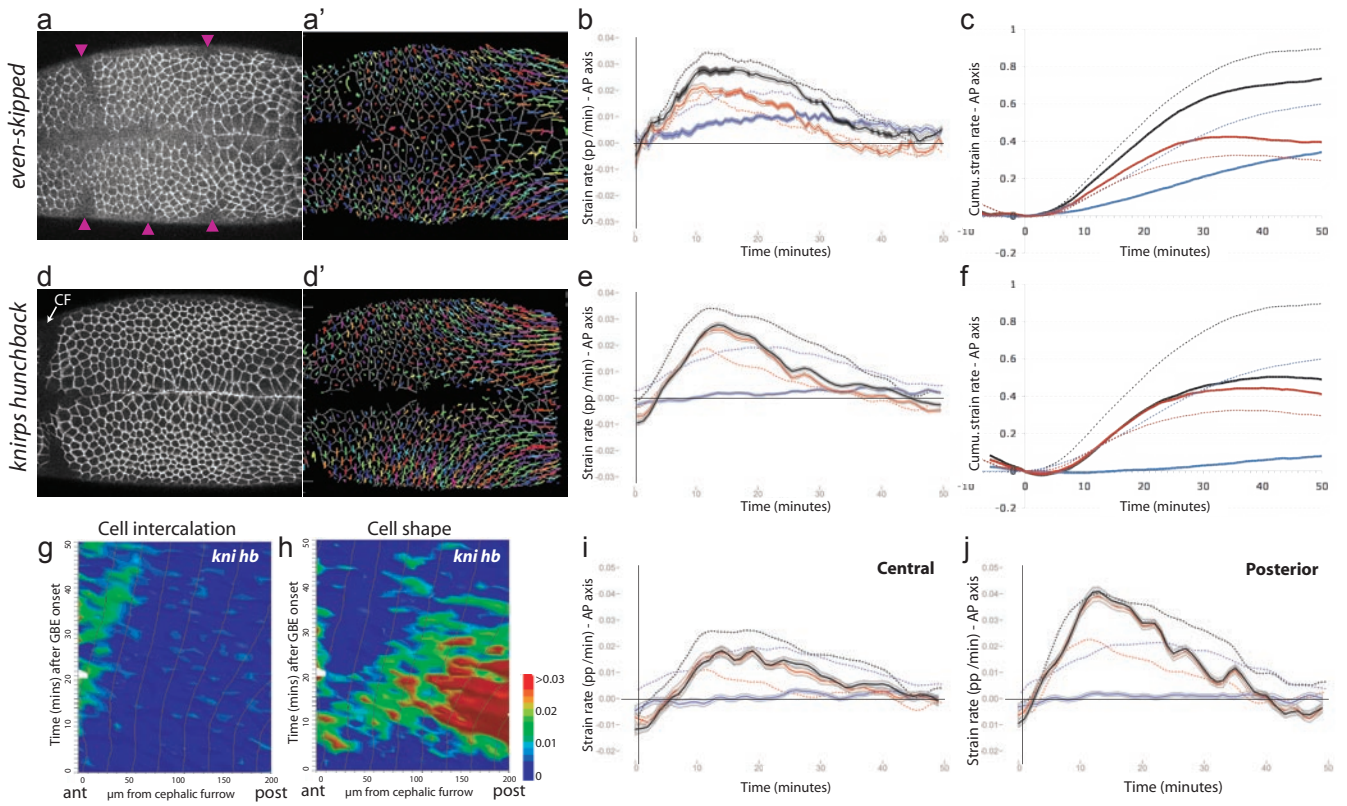

Figure S3 Relative contribution of cell shape change and cell intercalation to germ-band extension in *even-skipped* **and** *knirps hunchback* mutant embryos. **(A**-**C**) Analysis of *even-skipped* (*eve*) mutant embryos**.** (**A**) Movie frame showing a projection of confocal sections through the cell apices labelled with *DEcadGFP* for a typical *eve* mutant embryo. *eve* mutants do not form a cephalic furrow (compare with D), but shallow folds form in the epithelium (arrowheads). A') Corresponding tracked movie frame, showing the cell lineages, cell centroids and cell outlines recorded by the tracking software. (**B**) Summary of tissue in the AP axis for 5 *eve* embryos, showing total (black), cell intercalation (blue) and cell shape (red) strain rates. Dotted lines show the wild-type data for comparison. The shaded sections of the ribbons indicate when a given cell behaviour in the mutant is significantly different from the equivalent at that time in wild-type ($p<0.05$). (**C**) Cumulative representation of the same data, accumulating from t=0. (**D**-**J**) Analysis of a single *knirps hunchback* (*kni hb*) mutant embryo. (**D**) Movie frame showing a projection of confocal sections through the cell apices labelled with *DEcadGFP*. The cephalic furrow (CF) is indicated with an arrow. (**D'**) Corresponding tracked movie frame. (**E**) Summary of tissue deformation in the AP axis for one *kni hb* embryo, showing total (black), cell intercalation (blue) and cell shape (red) strain rates. Dotted lines show the wild-type data for comparison. The statistical model used can not be applied to a sample size with a single embryo, hence ribbons are not colour-coded. (**F**) Cumulative representation of the same data, accumulating from t=0. (**G**, **H**) Strain rates for cell intercalation and cell shape contributing to tissue extension, in a *kni hb* embryo represented as a function of the cell's position along the AP axis. Strain rates are colour coded according to the scale shown (note that any values below 0 will be coded blue, while any above 0.03 will be coded red). (**I**, **J**) Strain rates in the AP axis for total (black), cell intercalation (blue) and cell shape (red), for the central and posterior populations of ectodermal cells in wild-type and a *kni hb* embryo. Wild-type is shown as dotted lines and *kni hb* as a ribbon.

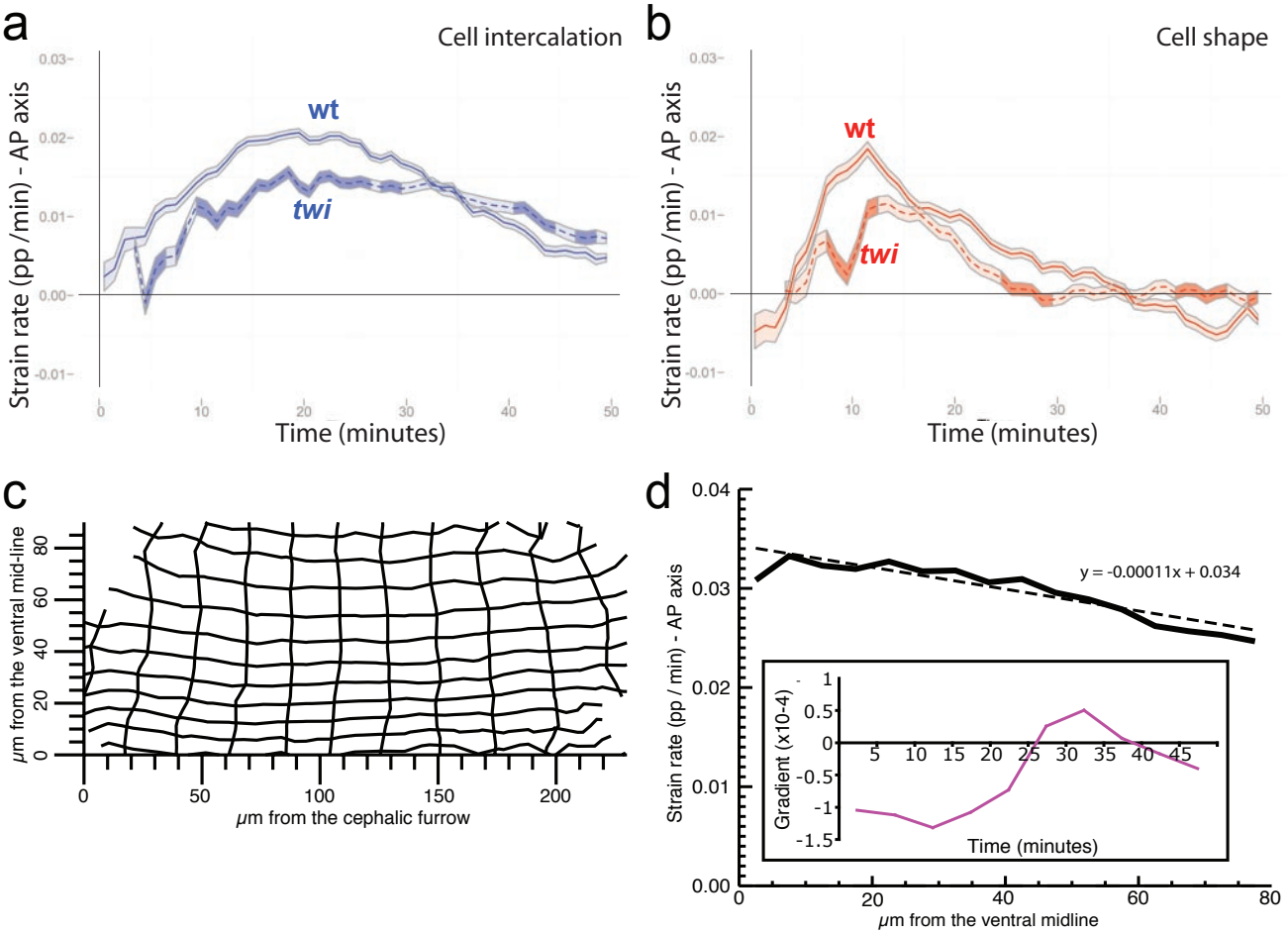

Figure S4 Further analysis on *twist* mutant embryos. (**A**) Rate of cell intercalation in ectodermal cells for *twist*- embryos compared to wild-type. Ribbon shading indicates a significant difference between mutant and wild-type ($p<0.05$). (**B**) Similar analysis for the rate of cell shape changes. (**C**-**D**) Quantification of the difference in the rate of tissue extension between the midline and lateral ectoderm. (**C**) Representation of the tissue stretching occurring between 5 and 25 minutes of germ-band extension in wild-type embryos with respect to the two embryonic axes. For the AP axis, positions are given in µm from the cephalic furrow, which is located at the anterior edge of the field of view. For the DV axis, cell positions are given in µm from the midline that bisects the embryo (see Fig 1A, (**A'**). The tissue extends more axially (close to the midline) than laterally (away from the midline), as shown by the spacing between the vertical lines in the deformation grid: these are more widely spaced closer to the midline. (**D**) Rate of tissue deformation in wild-type embryos summarised over the same period (5 to 25 minutes of germ-band extension), as a function of cells position along the DV axis. This confirms that there is a gradient of deformation, with rate of deformation being highest for tissue close to the midline (black curve with best fit function shown as a dotted line). The inset shows the time evolution of this gradient: the gradient's slope is negative between 5 and 25 minutes, as shown in the above curve. This is the period of GBE when there is an axial bias in tissue deformation. At 25 minutes, this bias ceases, and then reverses, showing that between 25 and 40 minutes, the lateral tissue is now deforming faster than the midline tissue.

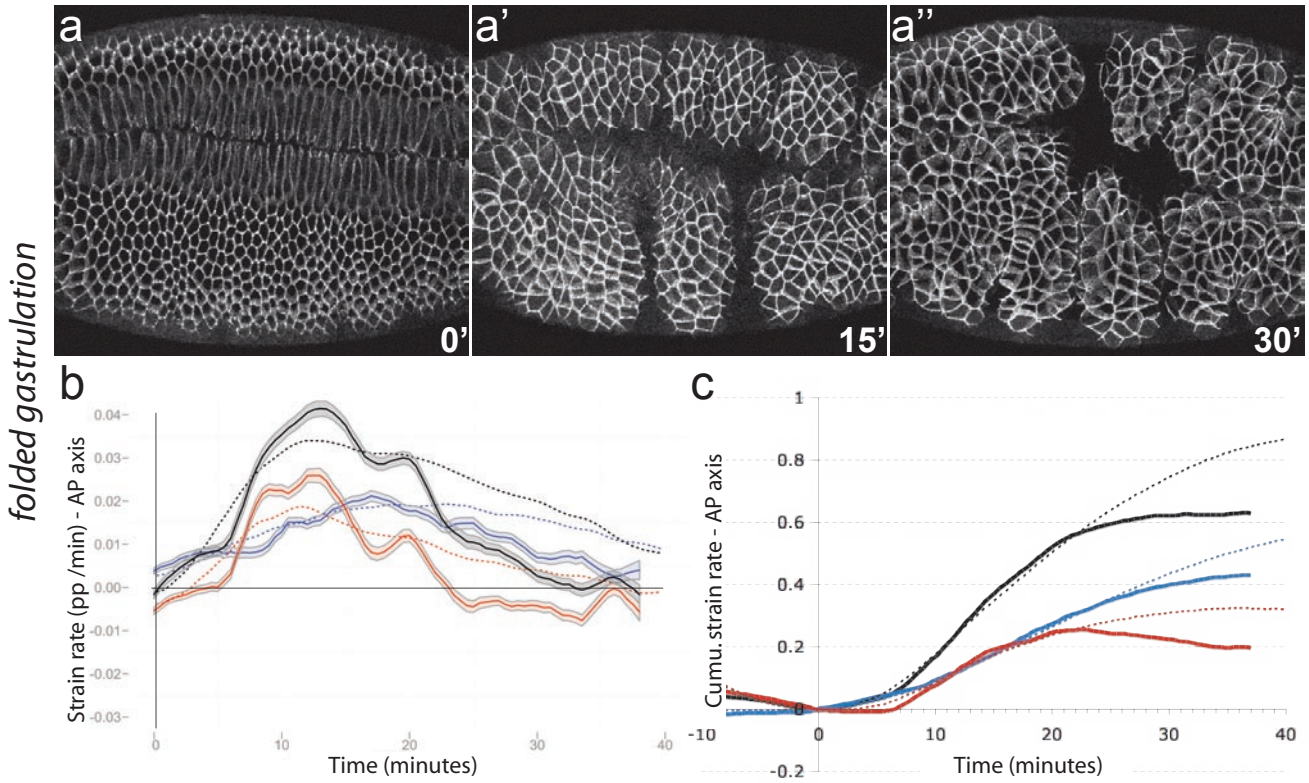

Figure S5 Analysis of a *folded gastrulation* mutant. (**A-A"**) Movie frames showing the ventral side of a *folded gastrulation* mutant embryo. When germ-band extension starts (panel 0 minute), the embryo looks similar to a wild-type embryo. As the germ-band extends, folds form progressively perpendicular to the ventral mid-line, and the embryo starts to twist. The block in posterior midgut invagination, which forces the extending germ-band to buckle, causes this concertinaed phenotype. (**B**) Summary of tissue deformation in the AP axis for this embryo, showing total (black), cell intercalation (blue) and cell shape (red) strain rates. Ribbons are not colour-coded, since we cannot apply the statistical model to a sample size with a single embryo. Dotted lines show the wild-type data for comparison. (**C**) Cumulative representation of the same data, accumulating from t=0. Curves starts to deviate from wild-type (dotted lines) at around 20 minutes, when deformation curves are not comparable to those in wild-type embryos because *fog* embryos start twisting.

Supplementary Movies Legends

Movie S1 Camera lucida cartoon of a small patch of extending lateral tissue, based on frames from a DECad-GFP confocal movie. This movie illustrates the complexity of the cell behaviours occurring during germ-band extension.

Movie S2 Confocal DECad-GFP movie for a representative wild-type embryo.

Movie S3 Confocal DECad-GFP movie for a representative *Kruppel-* embryo

Movie S4 Confocal DECad-GFP movie for a representative *twist-*embryo

Movie S5 Tracked movie for the wild-type embryo. Multicoloured tracks represent the trajectory of the centre of each cell over the previous 8 time-points (4 minutes).

Movie S6 Tracked movie for the *Kruppel-* embryo. Multicoloured tracks represent the trajectory of the centre of each cell over the previous 8 time-points (4 minutes).

Movie S7 Tracked movie for the *twist-* embryo. Multicoloured tracks represent the trajectory of the centre of each cell over the previous 8 time-points (4 minutes).

Movie S8 Tissue deformation movie for the corresponding wild-type embryo. The positive strain rate vectors (indicating extension) are shown in blue, while the negative strain rate vectors (indicating convergence) are in red.

Movie S9 Tissue deformation movie for the corresponding *Kruppel-* embryo. The positive strain rate vectors (indicating extension) are shown in blue, while the negative strain rate vectors (indicating convergence) are in red.

Movie S10 Tissue deformation movie for the corresponding *twist-* embryo. The positive strain rate vectors (indicating extension) are shown in blue, while the negative strain rate vectors (indicating convergence) are in red.

Movie S11 Cell shape deformation movie for the corresponding wild-type embryo

Movie S12: Cell shape deformation movie for the corresponding *Kruppel-* embryo

Movie S13 Cell shape deformation movie for the corresponding *twist-* embryo

Movie S14 Cell intercalation deformation movie for the corresponding wild-type embryo

Movie S15 Cell intercalation deformation movie for the corresponding *Kruppel-* embryo

Movie S16 Cell intercalation deformation movie for the corresponding *twist-* embryo

nature cell biology

BRIT1/MCPH1 links chromatin remodelling to DNA damage response

Guang Peng[1], Eun-Kyoung Yim[1], Hui Dai[1], Andrew P. Jackson[2], Ineke van der Burgt[3], Mei-Ren Pan[1], Ruozhen Hu[1], Kaiyi Li[4] and Shiaw-Yih Lin[1,5]

To detect and repair damaged DNA, DNA-damage-response proteins need to overcome the barrier of condensed chromatin to gain access to DNA lesions[1]. ATP-dependent chromatin remodelling is one of the fundamental mechanisms used by cells to relax chromatin in DNA repair[2,3]. However, the mechanism mediating their recruitment to DNA lesions remains largely unknown. BRIT1 (also known as MCPH1) is an early DNA-damage-response protein that is mutated in human primary microcephaly[4–8]. Here we report a previously unknown function of BRIT1 as a regulator of the ATP-dependent chromatin remodelling complex SWI–SNF in DNA repair. After damage to DNA, BRIT1 increases its interaction with SWI–SNF through ATM/ATR-dependent phosphorylation on the BAF170 subunit. This increase in binding affinity provides a means by which SWI–SNF can be specifically recruited to and maintained at DNA lesions. Loss of BRIT1 causes impaired chromatin relaxation as a result of decreased association of SWI–SNF with chromatin. This explains the decreased recruitment of repair proteins to DNA lesions and the reduced efficiency of repair in BRIT1-deficient cells, resulting in impaired cell survival after DNA damage. Our findings therefore identify BRIT1 as a key molecule that links chromatin remodelling with response to DNA damage in the control of DNA repair, and its dysfunction contributes to human disease.

BRIT1 (BRCT-repeat inhibitor of hTERT expression) was initially identified as a transcriptional repressor of human telomerase reverse transcriptase (hTERT)[4]. Its sequence was later matched to that of a disease gene called *microcephalin* (*MCPH1*)[7]. In humans, loss-of-function mutations in *BRIT1* cause primary microcephaly (MCPH), which is inherited in an autosomal recessive pattern and characterized by a decrease in brain size to one-third of normal size[7,8]. BRIT1 contains three BRCT domains and functions as an early DNA-damage-response protein[5,6]. In addition, dysfunction of BRIT1 impairs the recruitment of DNA damage signalling proteins to DNA lesions[5]. However, it is still unknown how the dysfunction of BRIT1 in DNA damage response leads to MCPH.

To answer this question, we systematically identified the binding partners of BRIT1, among which we found five core subunits of the human SWI–SNF complex: BRG1–BRM, BAF170, BAF155 and SNF5 (ref. 9) (Fig. 1a). SWI–SNF is an ATP-dependent chromatin-remodelling complex that uses ATP hydrolysis to alter chromatin structure[10]. The validation of our mass spectrometry result is shown in Fig. 1b and in Supplementary Information, Fig. S1a.

To further characterize the interaction between BRIT1 and SWI–SNF, we first sought to identify the subunit(**s**) of the SWI–SNF complex that mediated this interaction with BRIT1. Depletion of BAF170 abolished this interaction completely. Depletion of BAF155 also resulted in a loss of interaction between BRG1–BRM and BRIT1, and significantly decreased the interaction between BAF170–SNF5 and BRIT1 (Fig. 1c). In contrast, the two catalytic subunits, BRG1 and BRM, and also SNF5, were not necessary for interaction between BRIT1 and SWI–SNF (Supplementary Information, Fig. S1b–e). In addition, endogenous SNF5 can pull down other subunits of SWI–SNF in BAF155-deficient or BAF170-deficient cells, excluding the possibility of an unstable SWI–SNF complex resulting from a deficiency in BAF155 or BAF177 (Supplementary Information, Fig. S2f). Our data therefore showed that the core subunits BAF170 and BAF155 mediate interaction between BRIT1 and SWI–SNF. Next we analysed the critical regions that mediated these interactions. An amino-terminal region of BRIT1 was required for its interaction with SWI–SNF (Fig. 1d). We also confirmed the direct binding of this region with SWI–SNF with a glutathione *S*-transferase (GST) pull-down assay, which was not affected by treatment with λ-phosphatase (Fig. 1e), indicating that interaction between BRIT1 and SWI–SNF is not dependent on phosphorylation in the absence of DNA damage. When we analysed a series of deletion mutants of BAF155 (ref. 11) and BAF170, a conserved SANT domain of BAF155 (residues 595–839) and a region of BAF170 (residues 571–645) were required for their binding to BRIT1 (Supplementary Information, Fig. S1g, h). Taken together, our data clearly establish an interaction between BRIT1 and the SWI–SNF complex, probably mediated through the N-terminal region of BRIT1 and the specific domains of the BAF170 and BAF155 subunits of SWI–SNF.

[1]Department of Systems Biology, Unit 950, The University of Texas M. D. Anderson Cancer Center, Houston, Texas 77054, USA. [2]MRC Human Genetics Unit, Western General Hospital, Edinburgh EH4 2XU, UK. [3]Department of Human Genetics, University Medical Center Nijmegen, PO Box 9101, Nijmegen, The Netherlands.
[4]Department of Surgery, Baylor College of Medicine, Houston, Texas 77030, USA.
[5]Correspondence should be addressed to S.-Y.L. (e-mail: sylin@mdanderson.org)

Received 27 January 2009; accepted 2 April 2009; published online 14 June 2009; DOI:10.1038/ncb1895

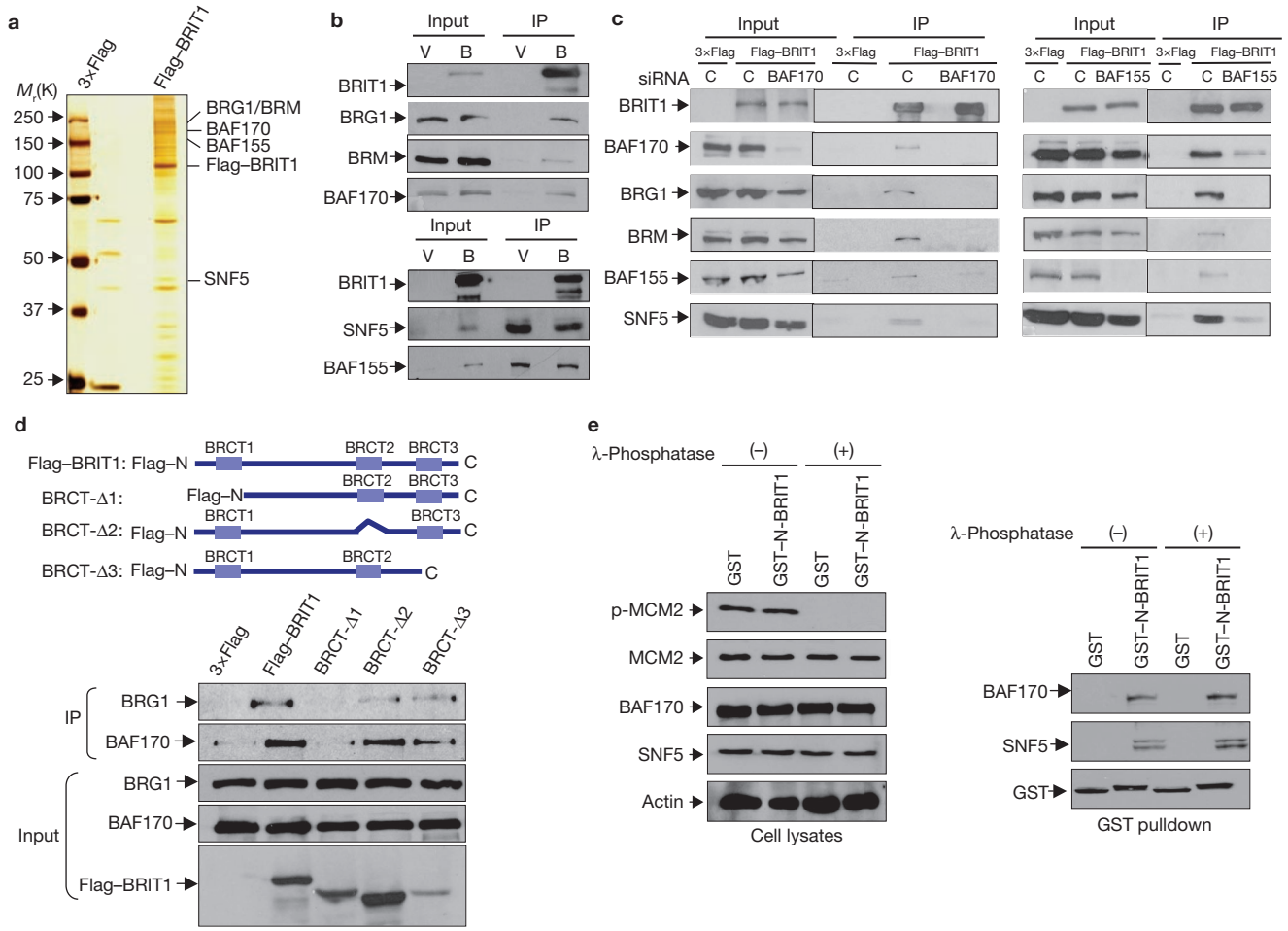

Figure 1 BRIT1 interacts with the SWI–SNF complex. (**a**) Silver staining of the BRIT1 complex separated by SDS–PAGE. The whole-cell extracts were prepared from U2OS cells transiently transfected with empty vector or Flag–BRIT1. Subunits of SWI–SNF are indicated. (**b**) Co-immunoprecipitation of SWI–SNF with BRIT1 analysed by western blotting from cells transfected with empty vector (V) or Flag–BRIT1 (B). IP, immunoprecipitation. (**c**) Interaction between BRIT1 and SWI–SNF dependent on BAF170 (left) and BAF155 (right). C, control siRNA. (**d**) N-terminal BRIT1 is required for interaction between BRIT1 and SWI–SNF. Top: schematic diagram of BRIT1 deletions. Bottom: co-immunoprecipitation of BAF170 with Flag–BRIT1 containing the indicated deletions. (**e**) SWI–SNF interacts specifically with the N-terminal of BRIT1 (N-BRIT1; residues 1–90) *in vitro*. Lysates of 293T cells were treated with or without λ-phosphatase, and incubated with purified GST or GST-tagged N-terminal BRIT1. MCM-2 phosphorylation (S40/41) was used as a positive control for effective phosphatase treatment. Full scans of blots are shown in Supplementary Information, Fig. S8.

Because BRIT1 is an early DNA-damage-response protein[5,6], we next examined whether the interaction between BRIT1 and SWI–SNF is responsive to DNA damage. The interaction was indeed enhanced 15 min after DNA damage with ionizing radiation (Fig. 2a). To gain mechanistic insights into this DNA damage-enhanced interaction between BRIT1 and SWI–SNF, we first determined whether the interaction is dependent on ATM (ataxia-telangiectasia mutated) and/or ATR (ATM and Rad3-related), two central kinases in the DNA-damage response network. No apparent change was observed when either ATM or ATR was depleted (Supplementary Information, Fig. S2a, b). However, deficiency in both ATM and ATR abolished the damage-enhanced interaction without affecting the basal binding affinity (Fig. 2b). These results suggest that ATM/ATR kinases are required for the DNA-damage-enhanced interaction between BRIT1 and SWI–SNF. ATM/ATR substrates have a common motif, S/TQ. We identified BAF170 (not BAF155) as a potential ATM/ATR substrate, which could be pulled down by phospho-S/TQ (p-S/TQ) antibody in an ATM/ATR-dependent manner (Fig. 2c). We then generated a series of mutations (serine/threonine residues to alanines) on BAF170 S/TQ sites and found that when S969 was mutated, there was a significant decrease in p-S/TQ antibody-binding affinity (Fig. 2d). The sequences around this site are very similar to those around BRCA1 (S1432), a known ATM/ATR target site[12] (Supplementary Information, Fig. S2c), which in fact allowed us to detect p-BAF170 (S969) with the antibody against p-BRCA1 (S1432), while the S969A mutant was not detected (Supplementary Information, Fig. S2c). The phosphorylation of this site was further confirmed by *in vitro* kinase assays (Fig. 2e).

To test the hypothesis that the phosphorylation of S969 by ATM/ATR after DNA damage may increase the binding of BRIT1 to SWI–SNF, we compared the binding affinity of BRIT1 for BAF170 and its S969A mutant, and found that the mutation of BAF170 on S969 blocked its DNA-damage-enhanced binding affinity for BRIT1 but not its basal binding affinity (Supplementary Information, Fig. S2d). We then reconstituted BAF170 expression with either the wild type or the S969A mutant construct in BAF170-depleted cells. Although the mutant BAF170 could restore the interaction between BRIT1 and SWI–SNF in the absence of

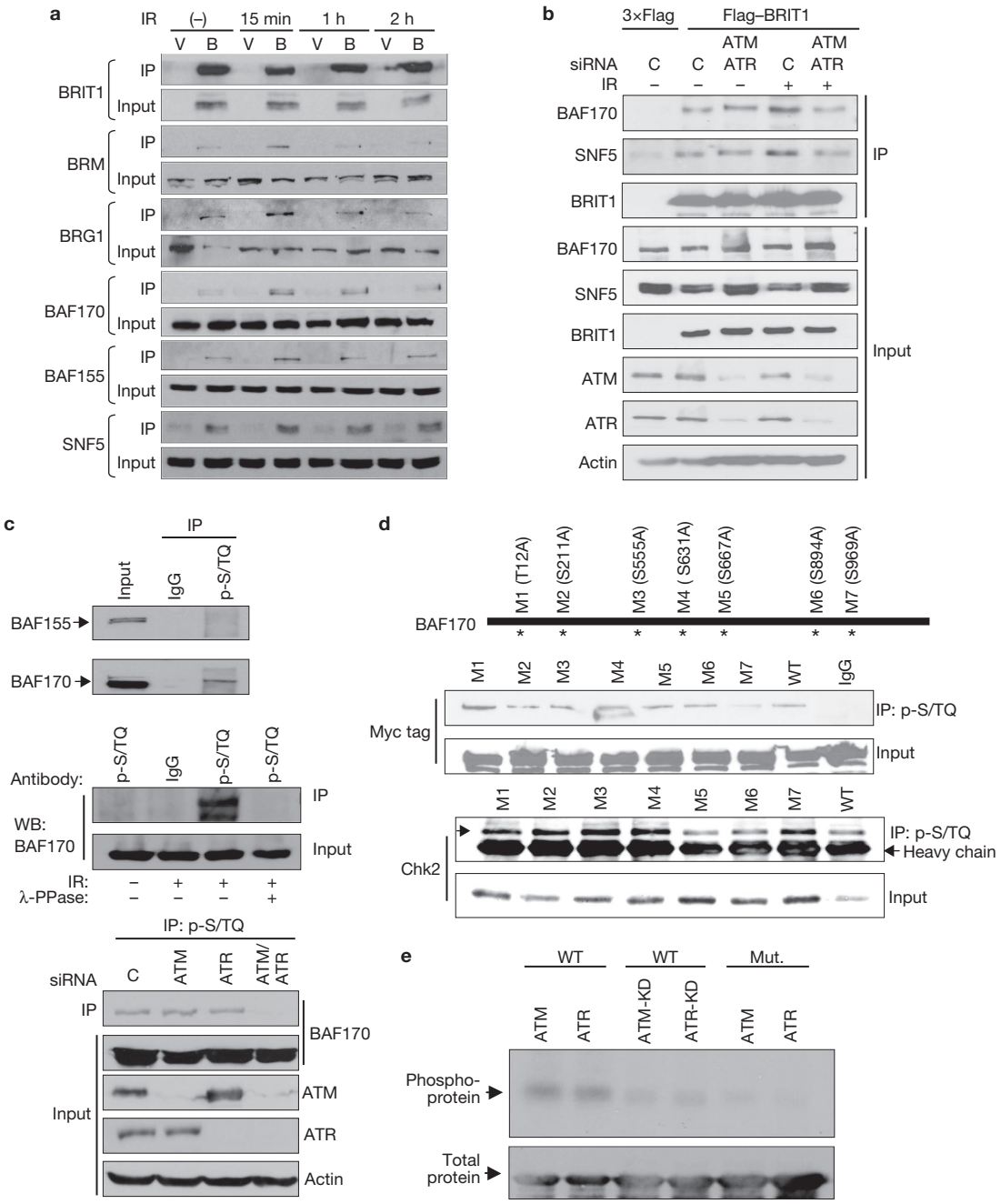

Figure 2 Interaction between BRIT1 and SWI–SNF is responsive to DNA damage. (**a**) Interaction between BRIT1 and SWI–SNF is enhanced in the presence of DNA damage signalling. Lysates were prepared from cells transfected with empty vector (V) or Flag–BRIT1 (B) at the indicated time points after exposure to ionizing radiation (IR; 10 Gy) and immunoprecipitated (IP). (**b**) DNA-damage-induced interaction between BRIT1 and SWI–SNF is dependent on ATM/ATR signalling. Cells were harvested 15 min after exposure to ionizing radiation (10 Gy). (**c**) BAF170 is a substrate candidate for ATM/ATR (top and middle) and its phosphorylation is dependent on the presence of ATM/ATR (bottom). WB, western blot. (**d**) The mutation in BAF170 (S969) suppressed the recognition of BAF170 by the p-S/TQ antibody after exposure to ionizing radiation. A series of mutations on BAF170 were generated to replace potential ATM/ATR target sites S/TQ to AQ. Chk2-pulldown by p-S/TQ was used as a positive control to show that the general binding activity of p-S/TQ to other ATM/ATR substrates was not affected in cells transfected with the M7 mutant. (**e**) BAF170 (S969) is phosphorylated *in vitro* by ATM/ATR kinase assay. The sequence around BAF170 (S969) was cloned into GST vector (WT) and the phospho-mutant (S969A) was made in this vector (Mut.). KD, kinase-dead mutant. Full scans of blots are shown in Supplementary Information, Fig. S8.

DNA damage, it failed to recover their DNA-damage-enhanced interaction. In contrast, wild-type BAF170 readily rescued both (Supplementary Information, Fig. S2e), suggesting that the enhanced interaction between BRIT1 and SWI–SNF in response to DNA damage is mediated through an ATM/ATR-dependent phosphorylation of BAF170.

Recent studies have demonstrated a role for ATP-dependent chromatin remodelling complexes in repairing DNA double-strand breaks (DSBs)[1–3] and in the maintenance of cell survival after DNA damage[13,14]. We have shown previously that BRIT1 deficiency leads to prolonged H2AX phosphorylation after DNA damage, indicating

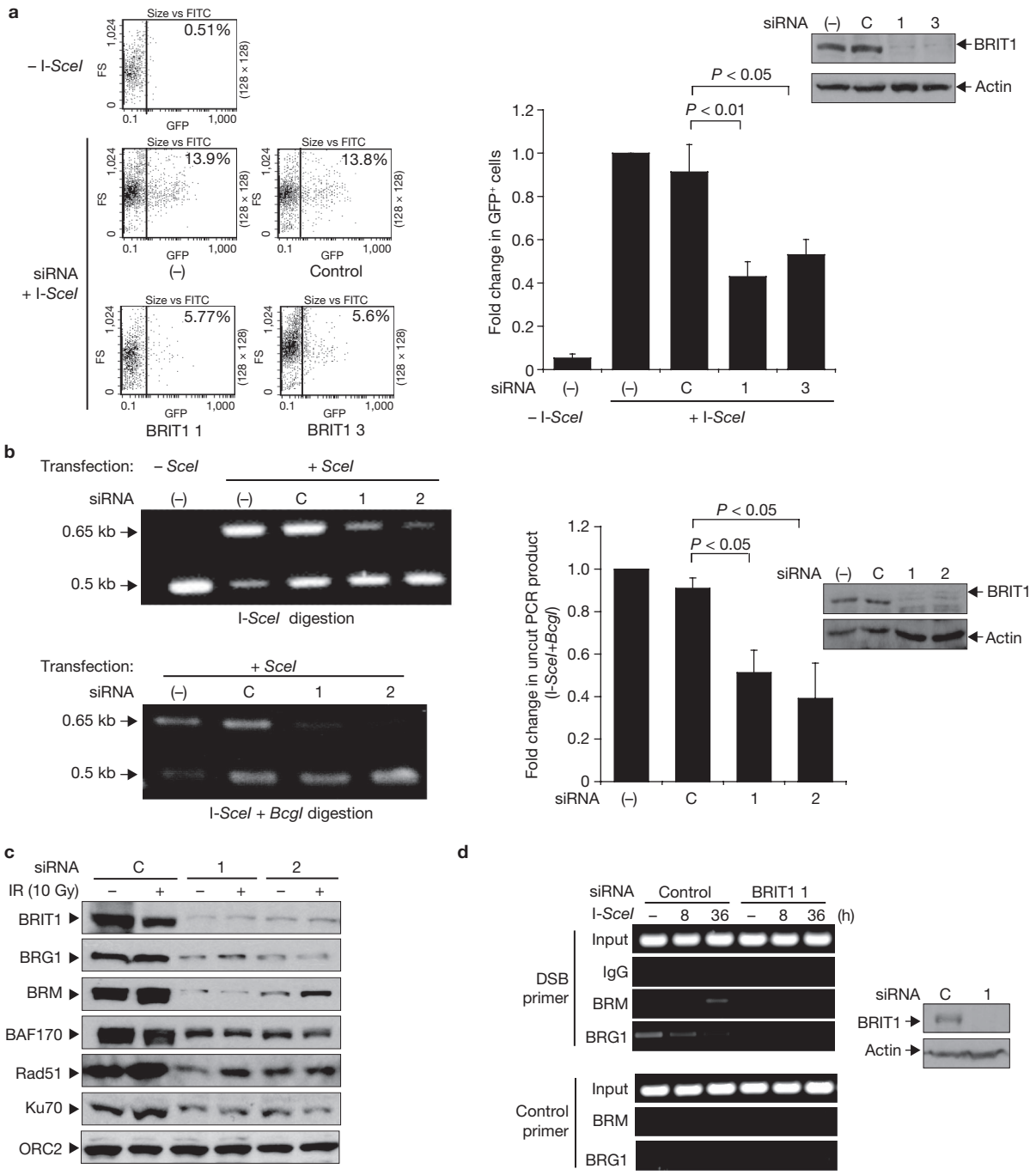

Figure 3 BRIT1 depletion impairs DNA DSB repair. (**a**) Defective HR repair in BRIT1-depleted-cells transfected with BRIT1 siRNA 1 (BRIT1 1) and siRNA 3 (BRIT1 3) on DSB induced by I-*Sce*I. Left: representative flow cytometry profile. Right: quantitative summary of at least three independent experiments. Each value is relative to the percentage of GFP$^+$ cells in I-*Sce*I-transfected cells without siRNA transfection, which was set to 1 and is shown as the mean and s.d. for three independent experiments; Student's *t*-test. (**b**) Defective NHEJ repair in BRIT1-depleted-cells transfected with BRIT1 siRNA 1 (1) and siRNA 2 (2) on DSB induced by I-*Sce*I. Left: representative image of PCR products digested by I-*Sce*I or I-*Sce*I + *Bcg*I. Right: quantification of NHEJ repair product (uncut by I-*Sce*I + *Bcg*I). The percentage of uncut products in cells without siRNA transfection was set at 1. Each value is shown as the mean and s.d. for three independent experiments; Student's *t*-test. Western blot analyses to demonstrate the effective BRIT1 knockdown are shown next to the graph. (**c**) Impaired recruitment of SWI–SNF and DNA repair proteins to chromatin in BRIT1-depleted cells (a time-course study and densitometry analyses are shown in Supplementary Information, Fig. S4a, b). Full scans of blots are shown in Supplementary Information, Fig. S8. (**d**) Impaired recruitment of SWI–SNF to the DNA damage site. Chromatin immunoprecipitation analyses were performed at the indicated time points after induction of DSB by I-*Sce*I transfection.

potentially impaired DNA repair[5]. We therefore tested whether the interaction between BRIT1 and SWI–SNF might function in repairing DSB.

First, we used neutral-pH comet assays to demonstrate that BRIT1 deficiency resulted in a significant defect in DSB repair (Supplementary Information, Fig. S3a, b). In mammalian cells, two

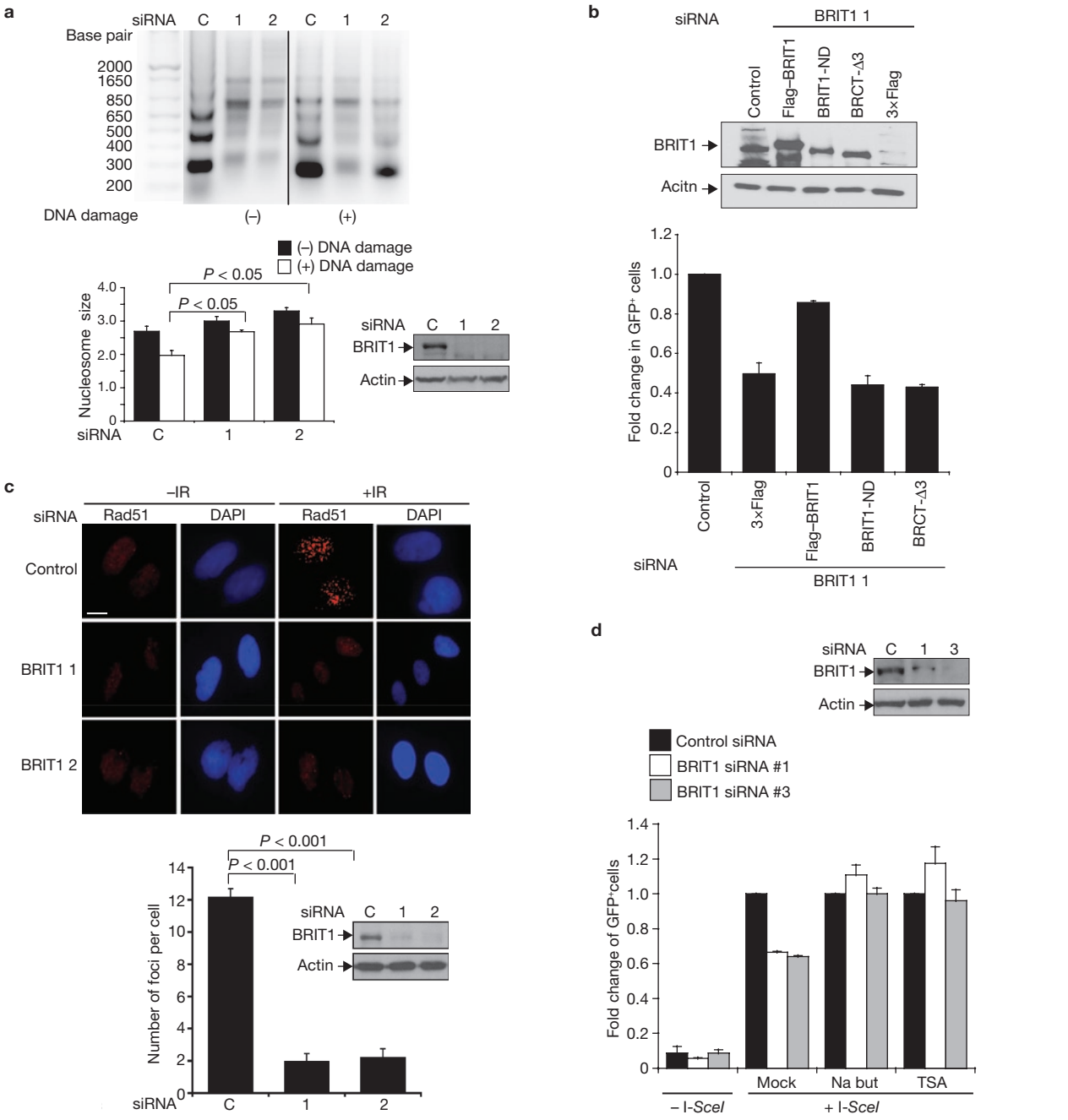

Figure 4 BRIT promotes the function of SWI–SNF. (**a**) Impaired chromatin relaxation analysed by MNase sensitivity assay. Cells were exposed to 4 Gy of ionizing radiation. Top: representative image. Bottom: quantification of average nucleosome size. Each value is shown as the mean and s.e.m. for three independent experiments; Student's *t*-test. (**b**) The function of BRIT1 in DNA repair is dependent on its interaction with SWI–SNF. BRIT1-deficient cells were reconstituted with the indicated plasmids. BRIT1 with N-terminal deletion (BRIT1-ND), which lacks its SWI–SNF interaction domain, was unable to rescue the defect of DNA repair to a similar extent to the BRIT1 BRCT-Δ3 mutant, which lost its activity to be recruited to DNA damage lesions. Each value is relative to the percentage of GFP$^+$ cells in I-*Sce*I-transfected cells with control siRNA transfection, which was set at 1, and is shown as the mean and s.d. for three independent experiments. Full scans of blots are shown in Supplementary Information, Fig. S8. (**c**) Requirement of BRIT1 for Rad51 foci formation. Top: representative immunostaining images. DAPI, 4,6-diamidino-2-phenylindole. Scale bar, 10 μm. Bottom: the bar graph is shown as the mean and s.d. for three independent experiments; Student's *t*-test. At least 50 cells were scored in each sample. (**d**) Restored HR repair in BRIT1-deficient cells in the presence of chromatin relaxation agents. Each value is relative to the percentage of GFP$^+$ cells without siRNA transfection, which was set at 1, and is shown as the mean and s.d. for three independent experiments. TSA, trichostatin A. Western blot analyses to demonstrate the effective BRIT1 knockdown are shown next to the graph.

conserved pathways are involved in DSB repair, namely homologous recombination (HR) and non-homologous end joining (NHEJ)[15,16]. To confirm the role of BRIT1 in DSB repair and to determine which repair pathway it acts in, we analysed BRIT1-deficient cells by using an HR repair analysis system[17] (Supplementary Information, Fig. S3c, d) and found that BRIT1 knockdown cells showed a significant decrease

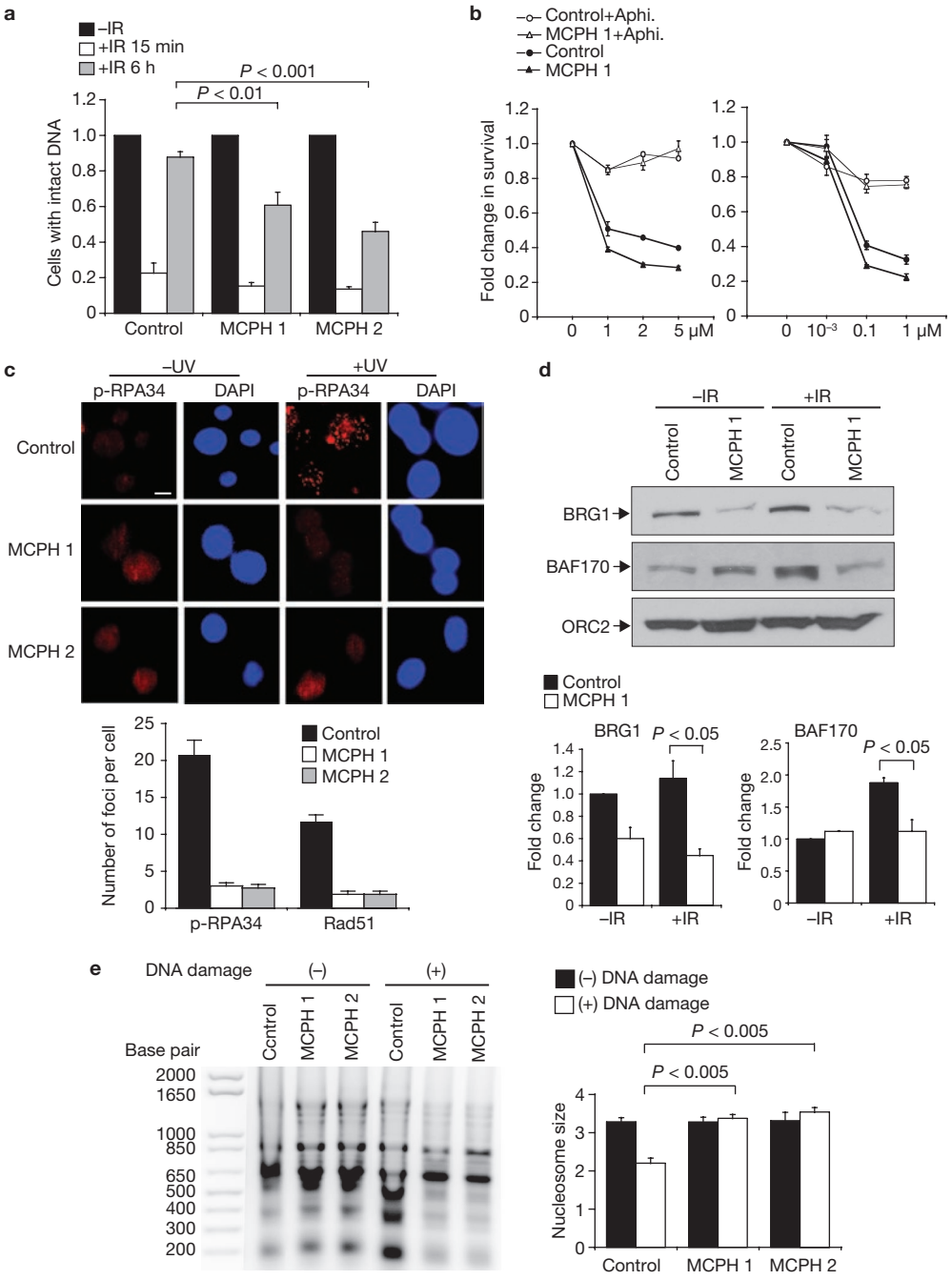

Figure 5 BRIT1 promotes DNA repair and chromatin relaxation in two human MCPH lymphoblastoid cell lines (MCPH 1 and MCPH 2). (**a**) Impaired DNA repair analysed by comet assay after exposure of cells to ionizing radiation. Percentage of cells with intact DNA (tail moment less than 2) in cells without exposure to ionizing radiation was set at 1. At least 100 cells were scored in each sample and each value is shown as the mean and s.e.m. for three independent experiments; Student's *t*-test. Representative images are shown in Supplementary Information, Fig. S7b. (**b**) Impaired cell survival in MCPH 1 cells exposed to DSB-inducing agents. Cells were pretreated with the DNA replication inhibitor aphidicolin (Aphi.) where indicated, and then treated with etoposide (left) or camptothecin (right). The graphs show the mean ± s.d. for three independent experiments. (**c**) Requirement of BRIT1 for foci formation of DNA repair proteins. Top: immunostaining of p-RPA foci. Scale bar, 10 μm. Bottom: quantification of p-RPA and Rad51 foci formation from three independent experiments; results are shown as means and s.d. At least 50 cells were scored in each sample for each experiment. (**d**) Decreased association of SWI–SNF with chromatin. Top: representative western blots. Bottom: densitometry analyses of indicated protein values normalized against ORC2. Each value is shown as the mean and s.d. for three independent experiments; Student's *t*-test. Full scans of blots are shown in Supplementary Information, Fig. S8. (**e**) Impaired chromatin relaxation analysed by MNase sensitivity assay. Cells were exposed to the DSB-inducing agent neocarzinostatin (400 ng ml^{-1}). Left: representative image. Right: quantification of average nucleosome size. Each value is shown as the mean and s.e.m. for three independent experiments; Student's *t*-test.

(40–60%) in HR-repaired GFP$^+$ cells, indicating defective HR repair (Fig. 3a). The decreased GFP signal was not due to effects on the cell cycle distribution, transfection efficiency or on the cutting efficiency of I-*Sce*I (Supplementary Information, Fig. S3e–g). An indirect decrease in HR repair, through decreased expression of BRCA1 by BRIT1 knockdown[18–20] was also excluded (Supplementary Information, Fig. S3h, i).

During the course of our studies, another study (ref. 21) also confirmed this new function of BRIT1 in HR repair.

In parallel, we used the method described in Supplementary Information, Fig. S3j, to analyse NHEJ repair[22] and found that NHEJ repair efficiency was also decreased by 50–60% in BRIT1 knockdown cells (Fig. 3b), an effect that was not reversed by ectopic expression of BRCA1, but by the ectopic expression of short interfering RNA (siRNA)-resistant BRIT1 (Supplementary Information, Fig. S3k). Taken together, our data reveal a critical function for BRIT1 in both HR and NHEJ repair.

HR and NHEJ are two distinct mechanisms for DSB repair. However, both mechanisms are confronted with DNA wrapped into highly condensed chromatin structure. Therefore, the involvement of BRIT1 in both HR and NHEJ could be explained by their relaxing chromatin structure to allow repair proteins access to DNA lesions. Such access could be provided by BRIT1 facilitating association of the SWI–SNF complex with chromatin and so promoting chromatin relaxation. In the first experiment to examine this possibility, we found that depletion of BRIT1 significantly decreased the amount of chromatin-associated BRG1, BRM, BAF170 and two key DNA repair proteins, Rad51 and Ku70 (refs 15, 16), but their total expression remained constant (Fig. 3c; Supplementary Information, Fig. S4a–c).

To examine whether SWI–SNF recruitment was altered specifically at sites of induced DSBs, chromatin immunoprecipitation assays were performed with the I-*Sce*I GFP system described in Supplementary Information, Fig. S3c. BRM and BRG1 are two catalytic subunits of the SWI–SNF complex. The recruitment of BRM after I-*Sce*I-induced DSB was abolished in BRIT1 knockdown cells (Fig. 3d). Both basal and damage-induced DNA localizations of BRG1 were also undetectable in BRIT1 knockdown cells (Fig. 3d). In contrast, depletion of individual SWI–SNF subunit affected neither the association of BRIT1 with chromatin nor its recruitment to the DNA damage loci (Supplementary Information, Fig. S4d), placing SWI–SNF functions downstream of BRIT1.

Because SWI–SNF relaxes chromatin and hence facilitates protein access to chromatin, we reasoned that impaired recruitment of SWI–SNF to chromatin in BRIT1-deficient cells might affect the state of chromatin relaxation and consequently the recruitment of the downstream DNA repair proteins to DNA lesions. To test this hypothesis, we assessed the extent of chromatin condensation by using a micrococcal nuclease (MNase) sensitivity assay, which provides a measure of chromatin compaction[1,23]. BRIT1 knockdown cells were less sensitive to digestion with MNase in both the absence and presence of DNA damage, indicating that chromatin structure is more compact in BRIT1-deficient cells (Fig. 4a; Supplementary Information, Fig. S7h). Impaired chromatin relaxation and defective HR repair were also observed consistently in SWI–SNF knockdown cells (Supplementary Information, Fig. S5d–f).

To show that the function of BRIT1 in chromatin relaxation and DNA repair is dependent on SWI–SNF, we made a small N-terminal deletion (residues 1–48) in BRIT1 (BRIT1-ND), which abolished its interaction with SWI–SNF but preserved its ability to form DNA-damage-induced foci (Supplementary Information, Fig. S5a, b). By reconstitution of wild-type BRIT1 or BRIT1-ND in BRIT1-deficient cells, we observed that, in contrast with the wild-type construct, BRIT1-ND was unable to restore the defects in chromatin relaxation and DNA repair in BRIT1 knockdown cells, a phenomenon similar to our observations in cells reconstituted with BRIT1 BRCT1-Δ3 (Fig. 4b; Supplementary Information, Fig. S5a). As a consequence, the cells reconstituted with BRIT1-ND still showed increased sensitivity to ionizing radiation (Supplementary Information, Fig. S5c). Because the BRIT1 BRCT-Δ3 mutant (containing only residues 1–752 of BRIT1) could not form DNA-damage-induced foci, it is not surprising that this mutant also failed to restore chromatin relaxation and DNA repair activity.

We also tested whether mutants of BAF155 or BAF170 lacking BRIT1-binding activity could exert dominant-negative effects to block a proper DNA damage response such as DNA damage repair (Supplementary Information, Fig. S5g–i). By sequence analysis, we found that BAF155 contained a highly hydrophobic sequence on its BRIT1-interacting domain (SANT), which has been reported to be essential for the function of the SANT domain[24]. This sequence is also conserved in the BRIT1-interacting domain of BAF170. We therefore replaced four consecutive leucine residues in BAF155 (residues 629–632) and BAF170 (residues 607–610) with arginine residues. These subtle mutations abolished their binding activity to BRIT1 without affecting their incorporation into the endogenous SWI–SNF complex. Overexpression of these mutants decreased the binding of BRIT1 to other SWI–SNF subunits and thus exerted dominant-negative effects that impaired HR repair in the cells. Taken together, these data further support the notion that dysfunction of SWI–SNF is the underlying mechanism responsible for impaired chromatin relaxation, HR repair and cell survival in BRIT1-deficient cells.

We next tested whether impaired chromatin relaxation would lead to defects in the recruitment of DNA repair proteins to DNA damage sites. The foci formation of Rad51 and phosphorylated replication protein A (p-RPA), key participants in DSB repair[15,25], was significantly decreased in BRIT1-depleted cells (Fig. 4c; Supplementary Information, Fig. S6a). The binding of p-RPA34 to chromatin was also impaired. However, treatment with chromatin relaxation agents reversed the effects of BRIT1 depletion on foci formation by RPA, RPA phosphorylation and binding of RPA to chromatin (Supplementary Information, Fig. S6a–d). Consistent with this notion, decreased HR repair efficiency in BRIT1 knockdown cells was reversed in the presence of chromatin relaxation agents (Fig. 4d), indicating that the impaired recruitment of DNA repair proteins is a direct consequence of impaired access to chromatin in BRIT1-deficient cells.

To confirm the physiological relevance of our findings, we examined lymphoblastoid cell lines (LCLs) from patients with MCPH by using homozygous loss-of-function mutations in *BRIT1* (Supplementary Information, Fig. S7a).

Comet assays demonstrated a significantly decreased DSB repair efficiency in BRIT1 LCLs (Fig. 5a; Supplementary Information, Fig. S7b). Consistent with this, BRIT1 LCLs also showed increased sensitivity to the topoisomerase inhibitors camptothecin and etoposide, which generate DSBs during S phase, a cell-cycle phase in which lesions are predominantly repaired by HR[26]. This increased sensitivity was consistent with DSB generation during S phase, because the effects were abrogated when cells were treated with the DNA replication inhibitor aphidicolin (Fig. 5b). In addition, increased sensitivity to ionizing-radiation-induced DNA damage was observed in BRIT1 LCLs arrested in G1, a cell-cycle phase that exclusively uses NHEJ to repair DSBs (Supplementary Information, Fig. S7c). Together, our data suggested that BRIT1 LCLs might have impaired cell survival as a result of generated DSBs being unrepaired because of defects in both HR and NHEJ repair. Furthermore, the formation of repair foci was also impaired in these cells, with significantly reduced recruitment of RPA and Rad51 (Fig. 5c). These results were further confirmed by our detection of a decreased association of DNA repair proteins to chromatin in patients' cells, whereas total protein levels were unaffected (Supplementary Information, Fig. S7d–f).

Binding of SWI–SNF to chromatin was also severely impaired in BRIT1 LCLs (Fig. 5d). Again, decreased binding of SWI–SNF to chromatin was not due to decreased total cellular protein levels (Supplementary Information, Fig. S7e). In keeping with our BRIT1 siRNA studies, BRIT1 LCLs did not undergo chromatin relaxation after DNA damage, unlike control LCLs. Control LCL chromatin showed increased sensitivity to MNase after neocarzinostatin-induced DNA damage, whereas the chromatin of BRIT1 LCLs remained more resistant to digestion with MNase (Fig. 5e; time course shown in Supplementary Information, Fig. S7h). Induction of chromatin relaxation also restored the damage-induced phosphorylation of RPA in BRIT1 LCLs (Supplementary Information, Fig. S7g). The defects in cell survival and in chromatin relaxation could be rescued by the introduction of wild-type Flag–BRIT1 into BRIT1-deficient LCLs, but not by the introduction of the BRCT-Δ1 mutant (containing residues 84–836 of BRIT1), which abrogated its SWI–SNF-binding activity (Supplementary Information, Fig. S7i–l). We also found a partial rescuing effect from the BRCT-Δ2 mutant (containing a deletion between residues 308–752), which might have been due to the requirement for the carboxy-terminal BRCT domain for other cellular functions[6]. Our findings in BRIT1 LCLs are therefore again consistent with a requirement for BRIT1 in the mediation of chromatin relaxation and the recruitment of DNA repair proteins to DNA lesions after damage to DNA.

Our results suggest a model for BRIT1 function: BRIT1 interacts with SWI–SNF through the core subunits BAF170 and BAF155. These interactions are enhanced in response to DNA damage through an ATM/ATR-dependent phosphorylation of BAF170. We suspect that BRIT1 is required for the recruitment and maintenance of SWI–SNF at DNA lesions by promoting chromatin relaxation and in turn facilitating the recruitment of DNA repair proteins to DNA lesions for efficient repair. A loss of BRIT1 would therefore lead to impaired chromatin relaxation and DNA DSB repair, which may contribute to the development of MCPH and cancer.

In addition, besides the recognition of histone modifications by the chromatin remodelling factors[2,3], our findings reveal a mechanism by which the SWI-SNF complex is recruited to DNA lesions without containing intrinsic specificity for a particular nuclear process[10,27,28]. Indeed, multiple mechanisms may be involved in regulating chromatin structure to cope with different stages of damage response and/or response to different types of DNA lesion and/or repair DNA lesions located in different regions of chromatin (euchromatin or heterochromatin)[1,23,29]. In addition, our studies reveal that post-translational modifications such as phosphorylation may serve as critical mechanisms in regulating the functions of SWI–SNF. It will therefore be of interest to determine the additional roles of phosphorylation on other SWI–SNF subunits in the DNA damage response[12] and dysfunction in the pathogenesis of human diseases[30,31]. □

METHODS

Methods and any associated references are available in the online version of the paper at http://www.nature.com/naturecellbiology/

Note: Supplementary Information is available on the Nature Cell Biology website.

ACKNOWLEDGEMENTS

We thank S. Rosenberg, X. Shen and F. Meric-Bernstam for critical reading of the manuscript; S. Deming for proofreading it; M. Jasin for reagents; E. Griffith for identifying the mutation in the MCPH no. 2 cell line; and the core facilities of the M. D. Anderson Cancer Center for mass spectrometry and fluorescence-activated cell sorting. This work was supported by a grant from the National Cancer Institute (R01CA112291) and an American Cancer Society Research Scholar Award to S.Y.L.

AUTHOR CONTRIBUTIONS

S.-Y.L. conceived the project. G.P. and S.-Y.L. designed the experiments and wrote the manuscript. G.P. performed the experimental studies with technical assistance from H.D., E.-K.Y., M.-R.P. and R.H. on immunofluorescent staining, subcloning and western blotting. G.P. and K.L. performed data analysis. A.P.J. and I.v.d.B. contributed molecularly characterized cell lines from patients with MCPH1. A.P.J. also provided thoughtful comments on the manuscript.

Published online at http://www.nature.com/naturecellbiology
Reprints and permissions information is available online at http://npg.nature.com/reprintsandpermissions/

1. Tsukuda, T., Fleming, A. B. & Nickoloff, M. A. Chromatin remodeling at a DNA double-strand break site in *Saccharomyces cerevisiae*. *Nature* **438,** 379–383 (2005).
2. Morrison, A. J. et al. IN80 and γ-H2AX interaction links ATP-dependent chromatin remodeling to DNA damage repair. *Cell* **119,** 767–775 (2004).
3. van Attikum, H., Fritsch, O., Hohn, B. & Gasser, S. M. Recruitment of the INO80 complex by H2A phosphorylation links ATP-dependent chromatin remodeling with DNA double-strand break repair. *Cell* **119,** 777–788 (2004).
4. Lin, S. Y. & Elledge, S. J. Multiple tumor suppressor pathways negatively regulate telomerase. *Cell* **113,** 881–889 (2003).
5. Rai, R. et al. BRIT1 regulates early DNA damage response, chromosomal integrity, and cancer. *Cancer Cell* **10,** 145–157 (2006).
6. Wood, J. L., Singh, N., Mer, G. & Chen, J. MCPH1 functions in an H2AX-dependent but MDC1-independent pathway in response to DNA damage. *J. Biol. Chem.* **282,** 35416–35423 (2007).
7. Jackson, A. P. et al. Identification of microcephalin, a protein implicated in determining the size of the human brain. *Am. J. Hum. Genet.* **71,** 136–142 (2002).
8. Alderton, G. K. et al. Regulation of mitotic entry by microcephalin and its overlap with ATR signalling. *Nature Cell Biol.* **8,** 725–733 (2006).
9. Phelan, M. L., Sif, S., Narlikar, G. J. & Kingston, R. E. Reconstitution of a core chromatin remodeling complex from SWI/SNF subunits. *Mol. Cell* **3,** 247–253 (1999).
10. Martens, J. A. & Winston, F. Recent advances in understanding chromatin remodeling by Swi/Snf complex. *Curr. Opin. Genet. Dev.* **13,** 136–142 (2003).
11. Chen, J. & Archer, T. K. Regulating SWI/SNF subunit levels via protein–protein interactions and proteasomal degradation: BAF155 and BAF170 limit expression of BAF57. *Mol. Cell. Biol.* **25,** 9016–9027 (2005).
12. Matsuoka, S. et al. ATM and ATR substrate analysis reveals extensive protein networks responsive to DNA damage. *Science* **316,** 1160–1166 (2007).
13. Chai, B., Huang, J., Cairns, B. R. & Laurent, B. C. Distinct roles for the RSC and Swi/Snf ATP-dependent chromatin remodelers in DNA double-strand break repair. *Genes Dev.* **19,** 1656–1661 (2005).
14. Park, J. H. et al. Mammalian SWI/SNF complexes facilitate DNA double-strand break repair by promoting γ-H2AX induction. *EMBO J.* **25,** 3986–3997 (2006).
15. Sung, P. & Klein, H. Mechanism of homologous recombination: mediators and helicases take on regulatory functions. *Nature Rev. Mol. Cell. Biol.* **7,** 739–750 (2006).
16. Lieber, M. R., Ma, Y., Pannicke, U. & Schwarz, K. Mechanism and regulation of human non-homologous DNA end-joining. *Nature Rev. Mol. Cell Biol.* **4,** 712–720 (2003).
17. Pierce, A. J., Johnson, R. D., Thompson, L. H. & Jasin, M. XRCC3 promotes homology-directed repair of DNA damage in mammalian cells. *Genes Dev.* **13,** 2633–2638 (1999).
18. Lin, S. Y., Rai, R., Li, K., Xu, Z. Y. & Elledge, S. J. BRIT1/MCPH1 is a DNA damage responsive protein that regulates the Brca1–Chk1 pathway, implicating checkpoint dysfunction in microcephaly. *Proc. Natl Acad. Sci. USA* **102,** 15105–15109 (2005).
19. Scully, R. & Livingston, D. M. In search of the tumour-suppressor functions of BRCA1 and BRCA2. *Nature* **408,** 429–432 (2000).
20. Xu, X., Lee, J. & Stern, D. F. Microcephalin is a DNA damage response protein involved in regulation of CHK1 and BRCA1. *J. Biol. Chem.* **279,** 34091–34094 (2004).
21. Wood, J. L., Liang Y., Li, K. & Chen, J. Microcephalin/MCPH1 associates with the Condensin II complex to function in homologous recombination repair. *J. Biol. Chem.* **283,** 29586–29592 (2008).
22. Nakanishi, K. et al. Human Fanconi anemia monoubiquitination pathway promotes homologous DNA repair. *Proc. Natl Acad. Sci. USA* **102,** 1110–1115 (2005).
23. Ziv, Y. et al. Chromatin relaxation in response to DNA double-strand breaks is modulated by a novel ATM-and KAP-1 dependent pathway. *Nature Cell Biol.* **8,** 870–876 (2006).
24. Boyer, L. A., Latek, R. R. & Peterson, C. L. The SANT domain: a unique histone-tail-binding module? *Nature Rev. Mol. Cell. Biol.* **5,** 1–6 (2004).
25. Zou, L. & Elledge, S. J. Sensing DNA damage through ATRIP recognition of RPA–ssDNA complexes. *Science* **300,** 1542–1548 (2003).
26. Sartori, A. A. et al. Human CtIP promotes DNA end resection. *Nature* **450,** 509–514 (2007).
27. Narlikar, G. J., Fan, H. & Kingston, R. E. Cooperation between complexes that regulate chromatin structure and transcription. *Cell* **108,** 475–487 (2002).
28. Peterson C. L. & Workman, J. L. Promoter targeting and chromatin remodeling by the SWI/SNF complex. *Curr. Opin. Genet. Dev.* **10,** 187–192 (2000).
29. Goodarzi, A. A. et al. ATM signaling facilitates repair of DNA double-strand breaks associated with heterochromatin. *Mol. Cell* **31,** 167–177 (2008).
30. Rass, U., Ahel, I. & West, S. C. Defective DNA repair and neurodegenerative disease. *Cell* **130,** 991–1004 (2007).
31. Roberts, C. W. M. & Orkin, S. H. The SWI/SNF complex: chromatin and cancer. *Nature Rev. Cancer* **4,** 133–142 (2004).

METHODS

Cell culture. U2OS and 293T cells were purchased from the American Type Culture Collection. The U2OS cells were maintained in McCoy's 5A medium supplemented with 10% fetal bovine serum (FBS). 293T cells were grown in DMEM medium with 10% FBS. Lymphoblastoid control cell line and two MCPH cell lines (MCPH 1 (C74G)[7] and MCPH 2 (G321C; A. P. Jackson and E. Griffith, personal communication)] were grown as a suspension culture in RPMI 1640 medium supplemented with 20% FBS.

Plasmids, small interfering RNAs (siRNAs), and transfection. siRNA 1, 2 and 3 sequences, control siRNAs, Flag–BRIT1, Flag–BRIT1 mutant resistant to siRNA 1, BRCA1 plasmids and the procedures for BRIT1 knockdown and ectopic expression of BRCA1–haemagglutinin, Flag–BRIT1 or deletion mutants of BRIT1 in BRIT1 knockdown cells were all as described previously[5,18]. On-target smart pool siRNAs against BAF170, BAF155, SNF5, ATM and ATR were purchased from Dharmacon Research. Short hairpin RNA (shRNA) vectors targeting BRG1 or BRM were purchased from Sigma. All RNA interference sequences can be found in Supplementary Methods. The deletions of BRIT1 were generated from Flag–BRIT1 plasmid by polymerase chain reaction (PCR), using primers with restriction sites and subcloned into N-terminal p3 × Flag–CMV plasmid in frame. A series of deletion mutants of BAF155 were provided by T. K. Archer (National Institutes of Health, North Carolina, USA)[12]. Flag-tagged ATM, ATR, ATM-KD (catalytic dead) and ATR-KD plasmids were provided by M. Kastan (St Jude Children's Research Hospital, Memphis, Tennessee, USA), K. Cimprich (Stanford University) and L. Zou (Harvard University). BAF170 was cloned from cDNA of HMEC cells (normal breast epithelial cells). The deletions of BAF170 were generated by PCR using primers with restriction sites and subcloned into pCMV/Myc/Nuc (Invitrogen). All the mutations described in the paper were generated by QuickChange II Site-Directed Mutagenesis Kit (Stratagene). Fragments containing BAF170 (S969) and BAF170 (S969A) were sub-cloned into pGEX vectors (GE Healthcare). Detailed cloning information is available from the authors on request. Plasmids were verified by DNA sequencing. Oligofectamine (Invitrogen) was used for all siRNA transfections, and FuGENE 6 (Roche) was used for all plasmid transfections, in accordance with the manufacturers' protocols. Transfection in LCLs was performed as described previously[8].

Affinity purification of BRIT1 protein complex. U2OS cells were transiently transfected with empty Flag plasmid or Flag–BRIT1 plasmid. After 48 h, whole-cell extracts were prepared with RIPA buffer (50 mM Tris-HCl pH 7.4, 1% Nonidet P40, 150 mM NaCl, 1 mM EDTA, 10% sodium deoxycholate, freshly added with 1 mM phenylmethylsulphonyl fluoride (PMSF), 1 mM Na_3VO_4 and 1 mM NaF) and immunoprecipitated with anti-Flag M2 affinity gel (Sigma) overnight. Bead-bound immunocomplexes were eluted with 3 × Flag peptide (Sigma) and subjected to SDS–PAGE. Silver staining was performed with a SilverSNA kit for mass spectrometry (Pierce). Specific bands were excised and digested, and the peptides were analysed by mass spectrometry at the M. D. Anderson Cancer Center Proteomic Facility.

Purification of GST fusion proteins and GST pulldown assay. Purification and GST pulldown methods were adapted from a previous publication[32]. BL21 bacteria containing indicated plasmids were allowed to grow for 6 h after the addition of isopropyl β-D-thiogalactoside. Cell pellets were resuspended in lysis buffer and sonicated. The supernatant was incubated overnight with glutathione-agarose beads at 4 °C. After washing, GST fusion proteins were eluted with glutathione. Then cell lysates (1 mg) were incubated with 2–5 μg of GST fusion protein and 40 μl of gluthatione-agarose beads in a total of 1 ml of RIPA buffer at 4 °C on a rotator for 2–4 h. After the beads had been washed three times with RIPA buffer, the protein was eluted for SDS–PAGE gel analysis.

***In vitro* ATM and ATR kinase assay.** Immunoprecipitations of ATM and ATR and the *in vitro* kinase assay were performed as described previously[33]. In brief, 293T cells were transfected with 8 μg of Flag-tagged ATM, ATR, ATM-KD and ATR-KD plasmids. Cell extracts were prepared in lysis buffer (50 mM Tris-HCl pH 7.5, 150 mM NaCl, 1% Tween 20, 0.3% Nonidet P40, 1 mM sodium fluoride, 1 mM Na_3VO_4, 1 mM PMSF, 50 mM glycerophosphate, 1 mM dithiothreitol, 1 mM EGTA, 10% glycerol and 1 × protease inhibitor mixture from Roche Molecular Biochemicals). Cleared supernatants were immunoprecipitated with anti-Flag M2 antibody (Sigma). After being washed five times with lysis buffer and kinase buffer (20 mM HEPES pH 7.5, 50 mM NaCl, 10 mM $MgCl_2$, 1 mM dithiothreitol, 10 mM $MnCl_2$), the immunoprecipitate was resuspended in 50 μl of kinase buffer containing 10 μCi of [γ-^{32}P]ATP, 10 μM ATP, 1 mM sodium fluoride, 1 mM Na_3VO_4, 20 mM glycerophosphate and 1 μg of GST fusion substrate. The kinase reaction was performed at 30 °C for 20 min and stopped by the addition of SDS sample buffer. Proteins were separated by SDS–PAGE and transferred to poly(vinylidene difluoride) membrane. Radiolabelled proteins were revealed by autoradiography.

Antibodies, immunoprecipitation, chromatin fractionation and western blot analysis. BRIT1, BRCA1, RPA34 and p-RPA34 antibodies were described previously[5,22]. Rabbit anti-SWI/SNF subunit antibodies (BRG1, BRM, BAF170, BAF155 and SNF5), MCM2 and p-MCM2 (Ser40/Ser41) were purchased from Bethyl Laboratory. Rabbit anti-Rad51 (Ab-1) antibody was purchased from Calbiochem. Mouse anti-Ku70 antibody was purchased from Novus. Control rabbit immunoglobulin G (IgG) and anti-ATR antibody were purchased from Santa Cruz. Anti-Mcy tag antibody, Chk1, p-Chk1 (Ser 345), Chk2, p-Chk2 (Ser 68), p-S/TQ antibodies and anti-ATM antibody were ordered from Cell Signaling. Immunoprecipitation with anti-Flag affinity beads was performed as described above. For reciprocal immunoprecipitation, whole-cell extracts were prepared in RIPA buffer as indicated above and pre-cleaned with Protein A/G plus-agarose beads (Santa Cruz). Cell extracts were then subjected to incubation for 2 h with antibodies against BRG1 or BRGM (2 μg) followed by incubation overnight with Protein A/G-agarose beads at 4 °C. The immunocomplex was eluted in loading buffer by being boiled for 5 min at 95 °C. The preparation of chromatin fractions and western blot analyses, including the conditions for RPA analysis, were performed as described previously[5,22]. For the chromatin fractions to analyse SWI/SNF and DNA repair proteins, cells were exposed to ionizing radiation (10 Gy), then harvested 2 and 5 h later, respectively. Densitometry analysis was performed with National Institutes of Health IMAGE software.

Chromatin immunoprecipitation (ChIP) assay. DSBs were induced in cells transfected with control siRNA or BRIT1 siRNA 1 by I-*Sce*I expression. At indicated time points, cells were crosslinked with formaldehyde and ChIPs were performed with an EZ ChIP kit (Upstate) in accordance with the manufacturer's instructions. Cellular lysates were subjected to five sets of sonication on wet ice with a 60 Sonic Dismembrator (Fisher Scientific). Each set consisted of 8 s of sonication separated by 1-min intervals on ice. BRG1 and BRM (10 μl) antibodies were used for immunoprecipitation. The ChIP primers used to analyse proteins binding at the site of DSBs were 5′-TACGGCAAGCTGACCCTGAA-3′ (sense) and 5′-GCCCATATATGGAGTTCCGC-3′ (antisense).

The primers used as a negative control on chromosome 12 were 5′-ATGGTTGCCACTGGGGATCT-3′ (sense) and 5′-TGCCAAAGCCTAGGGGAAGA-3′ (antisense).

Methods for the following assays are available in Supplementary Information: DNA repair assays (comet assay, HR repair analysis, NHEJ repair analysis), cell cycle analysis, MNase sensitivity assay, colony-forming assay, cell viability assay, and immunofluorescent staining for foci formation.

Statistical analysis. All statistical analysis was performed with a one-tailed Student's *t*-test.

32. Yu, X., Ghini, C. C., He, M., Mer, G. & Chen, J. The BRCT domain is a phospho-protein binding domain. *Science* **302,** 639–642 (2003).
33. Pandita, T. K. *et al.* Ionizing radiation activates the ATM kinase throughout the cell cycle. *Oncogene* **19,** 1386–1391 (2000).

nature cell biology

DOI: 10.1038/ncb1895

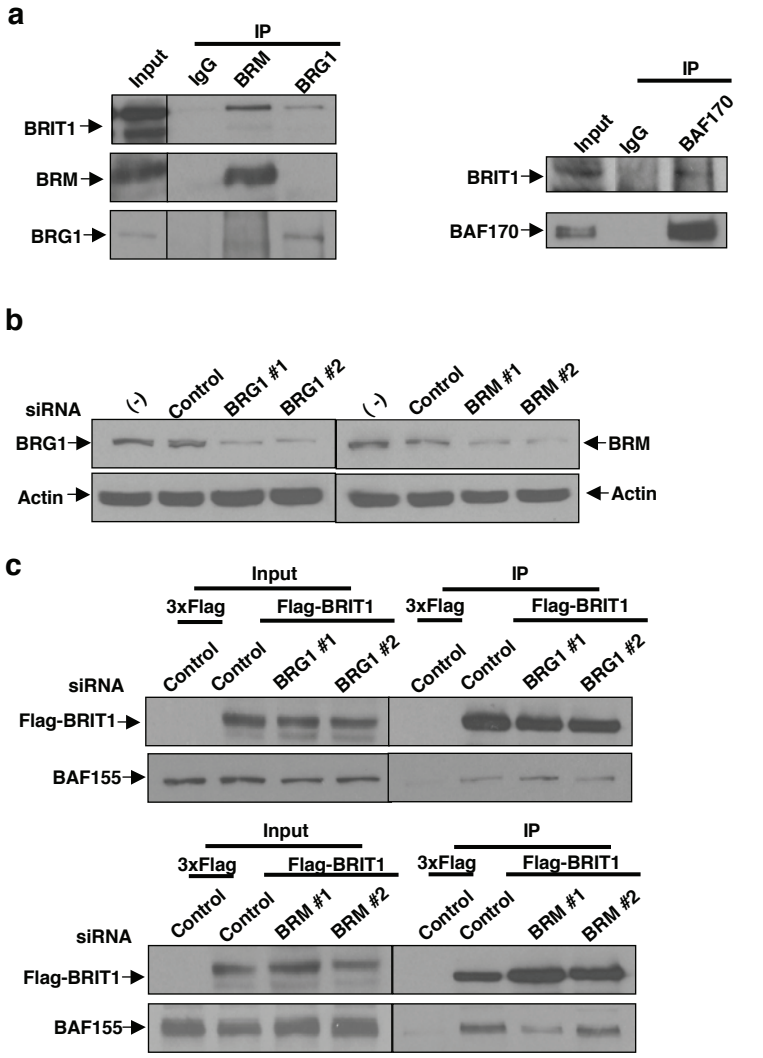

Figure S1 BRIT1 interacts with SWI/SNF. (**a**) Endogenous BRIT1 are co-immunoprecipitated with SWI/SNF subunits. The whole cell extracts were subjected to immunoprecipitation with control, anti-BRM, anti-BRG1 or BAF170 antibodies and then subjected to Western blot analysis with the indicated antibodies. (**b-e**) BRG1, BRM, and SNF5 subunits are not required for BRIT1-SWI/SNF interaction. (**b**) Western blot analysis for BRG1 and BRM knockdown in U2OS cells. (**c**) **and** (**d**) Cell extracts were prepared from BRG1/BRM knockdown cells and immunoprecipitated with Flag affinity beads. The BRIT1-SWI/SNF interaction was analyzed by Western blotting with the indicated antibodies. (**e**) SNF5 was knocked down in U2OS cells. Cell extracts were subjected to immunoprecipitation with Flag affinity beads, and BRIT1-SWI/SNF interaction was analyzed by Western blotting with the indicated antibodies. (**f**) Knockdown of BAF155 or BAF150 did not disrupt the SWI/SNF complex. Cells were depleted with BAF155 or BAF170 by siRNAs and immunoprecipitation were conducted using anti-SNF5 antibody. (**g-h**) Specific regions on BAF155 and BAF170 are required for their interactions with BRIT1. (**g**) The middle region (595-839aa) of BAF155 is required for BRIT1-SWI/SNF interaction. Flag-BRIT1 and a series of deletion mutants of BAF155 tagged with c-Myc were expressed in cells to assess their ability of interaction. Cell lysates were immunoprecipitated with Flag affinity beads and blotted with the indicated antibodies. (Top) Schematic diagram of deletions in BAF155. Conserved domains are indicated. (Bottom) Co-immunoprecipitation of BAF155-Myc with Flag-BRIT1. BRIT1 bound effectively to full-length BAF155 as well as the mutants with deletions (Δ2, Δ3, and Δ5), whereas it failed to associate with the mutants ((Δ1 and Δ4) with the deletion of middle region containing a conserved SANT domain. (**h**) N-terminal of BAF170 is implicated in BRIT1-SWI/SNF interaction. Flag-BRIT1 and deletion mutants of BAF170 tagged with c-Myc were expressed in cells to assess their ability of interaction. Cell lysates were immunoprecipitated with Flag affinity beads and blotted with the indicated antibodies. (Top) Schematic diagram of deletions in BAF170. Conserved domains are indicated. (Bottom) Co-immunoprecipitation of BAF170-Myc with Flag-BRIT1. BRIT1 bound effectively to full-length BAF170 as well as the mutants with deletions (Δ1-Δ4 and Δ6), whereas it failed to associate with the mutants (Δ5) lack of the N-terminal region.

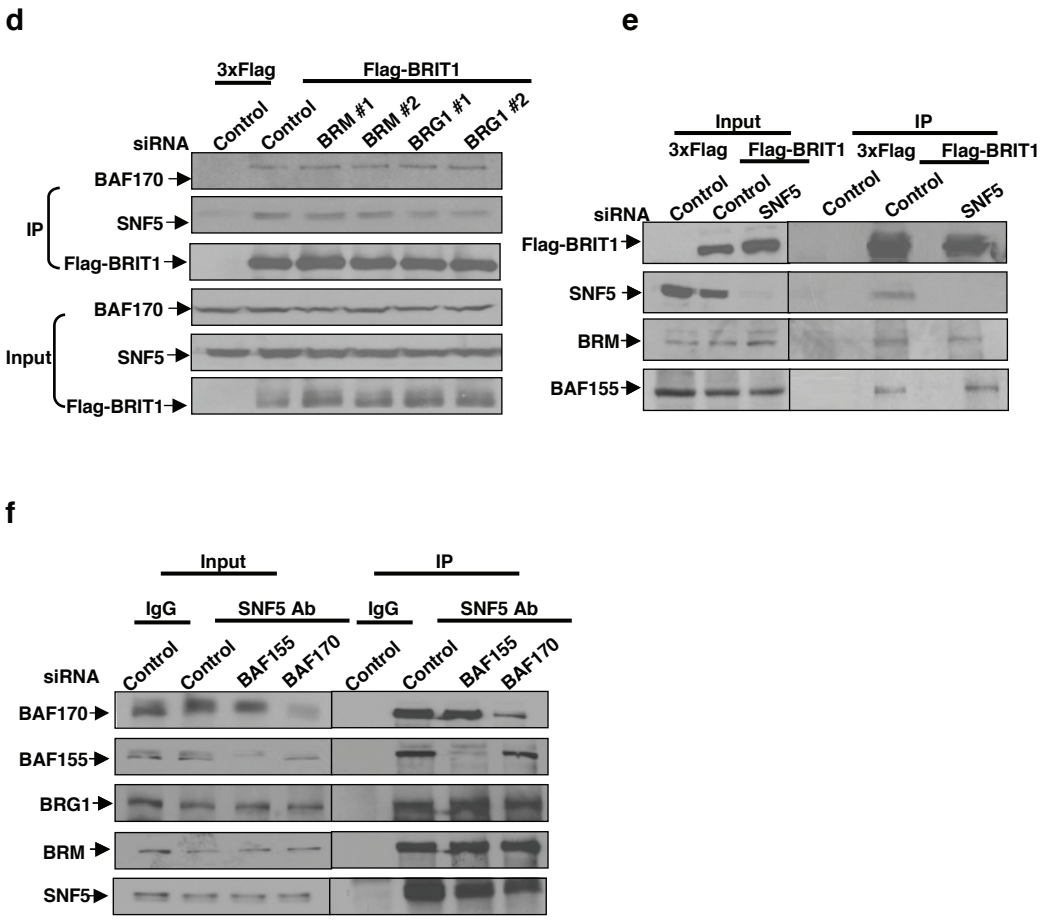

Figure S1 continued

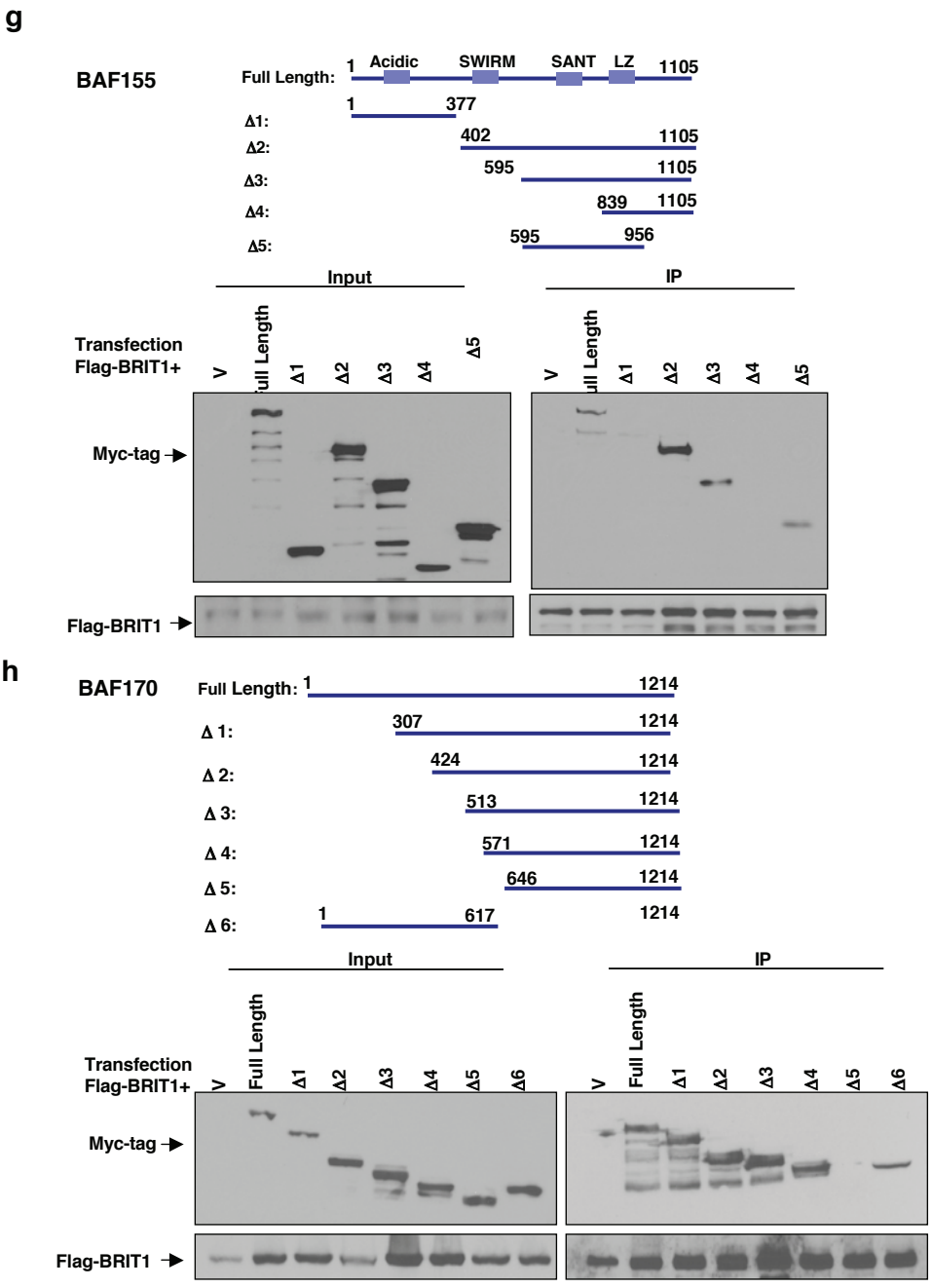

Figure S1 continued

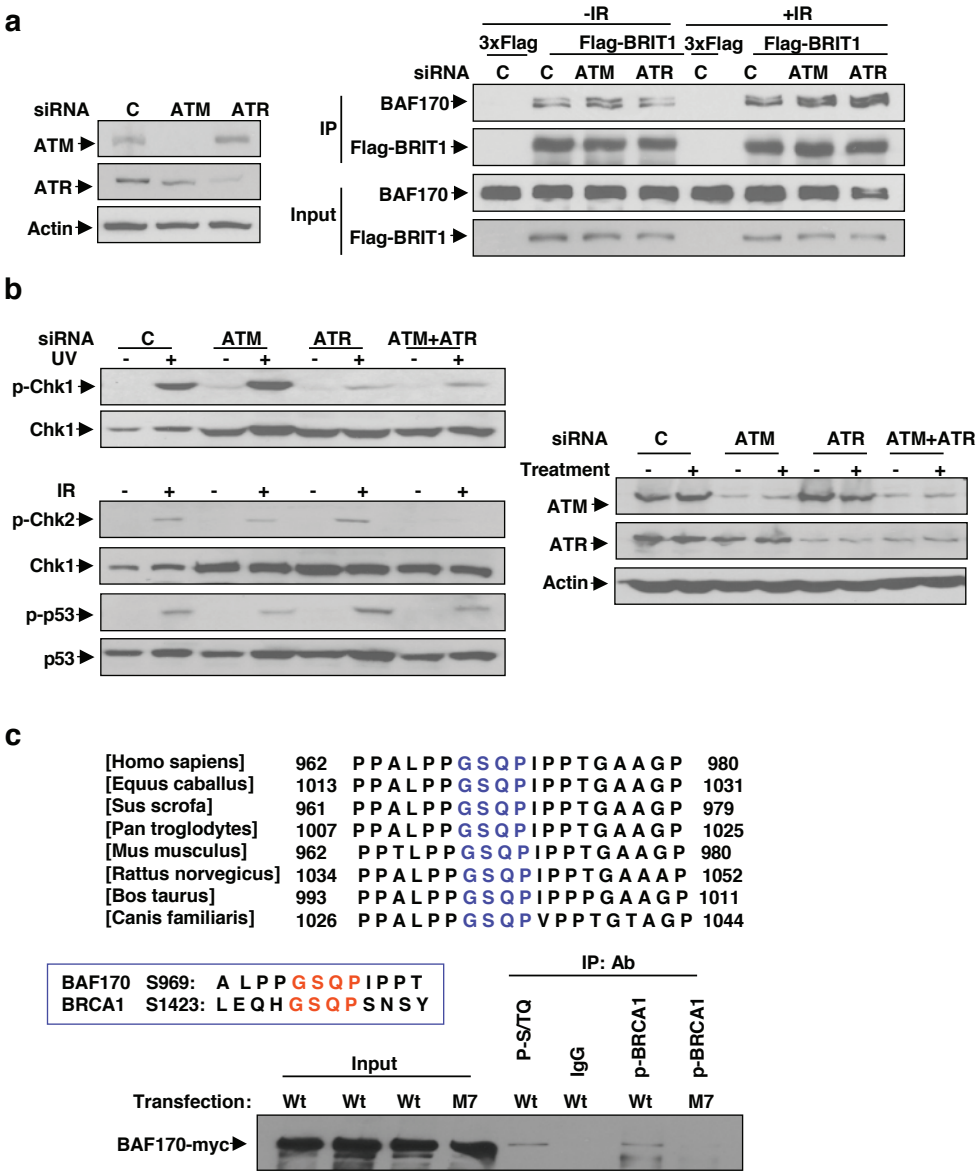

Figure S2 ATM/ATR-dependent phosphorylation of BAF170 mediates DNA damage-enhanced BRIT1-SWI/SNF interaction. (a) Depletion of either ATM or ATR does not affect BRIT1-SWI/SNF interaction. (Left) Cell lysates for immunoprecipiations. ATM or ATR was depleted by transient siRNA transfection. (Right) Immunoprecipitations by anti-Flag antibody and blotted with BAF170. Twenty-four hours after siRNA transfection, cells were transfected with empty Flag vector or Flag-BRIT1. Forty-eight hours later, cell lysates were prepared for immunoprecipitations. (b) Depletions of ATM, ATR or ATM+ATR in cells affected activation of their downstream effectors upon DNA damage signaling. 48 hrs after transfection, cells were exposed to UV (50 J) or IR (10 Gy), and 2 hrs later, cell lysates were extracted for Western blotting analysis to detect phosphorylation of Chk1, Chk2 or p53. (c) Recognition of BAF170 (S969) after IR by p-BRCA1 (S1423) antibody. (Top) Protein sequences around BAF170 (S969) are evolutionarily conserved and very similar to the sequences around BRCA1 (S1423). (Bottom) 293T cells were transfected with wild-type or S969A mutated (M7) BAF170. 48 hrs after transfection, cells were exposed to IR (10 Gy). 1 hr later, cell lysates were harvested and incubated with anti-p-SQ/TQ or anti-p-BRCA1 (S1423) antibody. Similar condition was also used for Fig. 2c and Fig. 2d. (d) The binding between BAF170 mutant M7 (S969A) and BRIT1 did not increase after IR. 293T cells were transfected with indicated plasmids. Immunoprecipitation was performed by anti-Flag M2 antibody and detected by anti-Myc-tag antibody on Western blot. (e) In BAF170 depleted cells, reconstitution of BAF170 mutant M7 (S969A) was unable to rescue IR-enhanced BRIT1-SWI/SNF interaction. (Left) The expression levels of endogenous and ectopic BAF-170 in the cell lysates. (Right) Endogenous SWI/SNF subunits associated with BRIT1 were detected by the indicated antibodies in immunoprecipitation assay. Cells were transfected with indicated plasmids and 5 hrs later, BAF170 was depleted by siRNA transfection. 48 hrs after the transfection, cells were harvested and immunoprecipiation was performed as above.

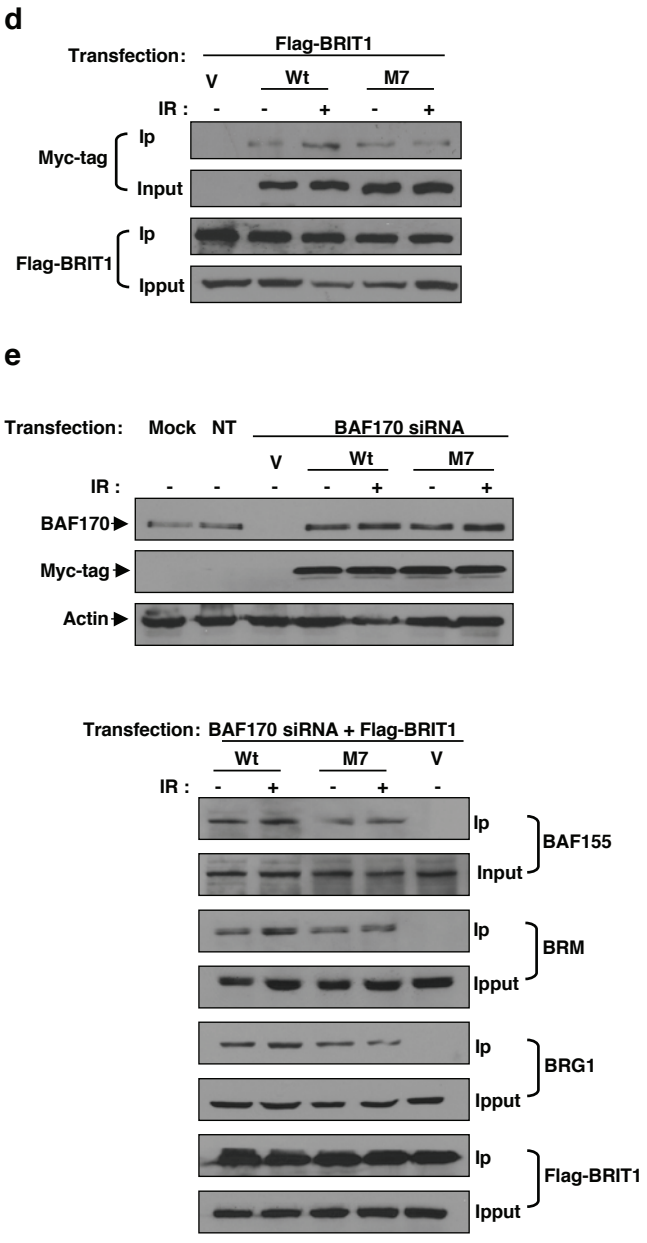

Figure S2 continued

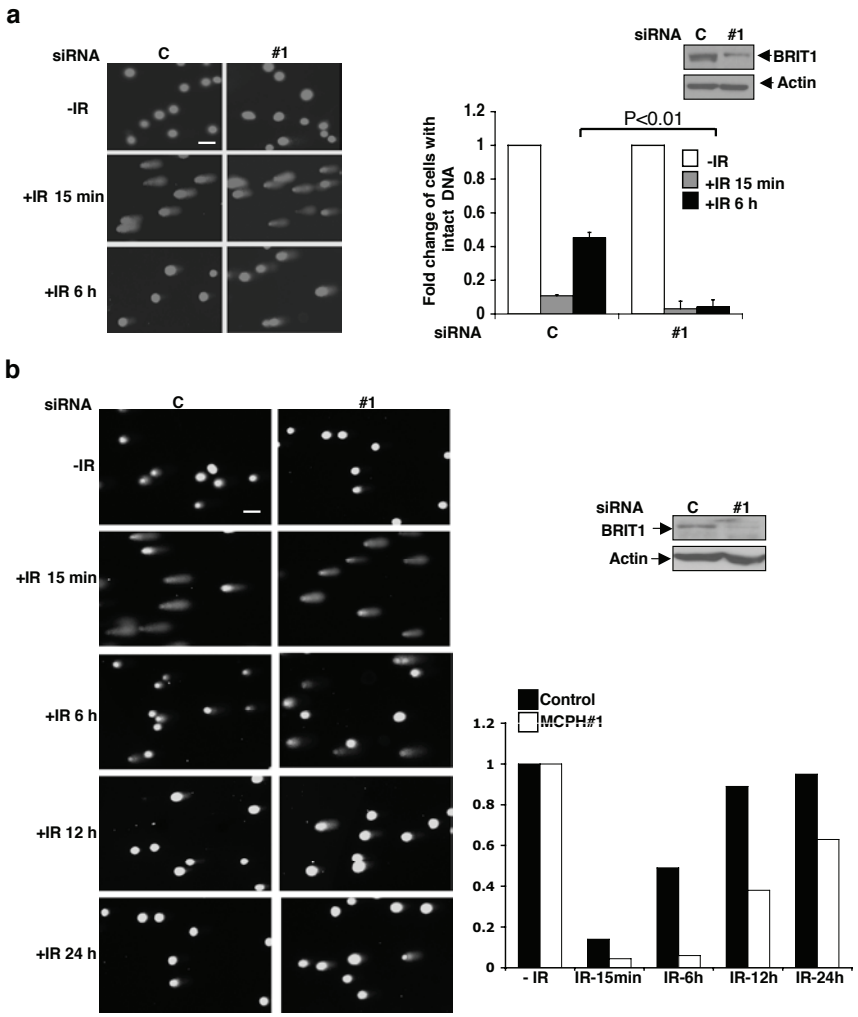

Figure S3 BRIT1 depletion impairs DNA DSB repair. **(a)** Comet analyses at the indicated time points after exposure of U2OS cells transfected with control siRNA (C) or BRIT1 siRNA#1 (#1) to ionizing radiation (IR). (Left) Representative images. Scale bar is 40 μM. (Right) Quantitative analysis of three independent experiments. Percentage of cells with intact DNA (tail moment less than 2) in cells without IR exposure was set as 1. At least 100 cells were scored in each sample and each value represents the mean ± SEM of three independent experiments; Student *t*-test. (**b**) (Left) Representative images of Comet analyses at the indicated time points after exposure of U2OS cells transfected with control or BRIT1 siRNA#1 to IR (10 Gy). Scale bar is 40 μM. (Right) Quantitative analysis of cells with intact DNA (defined as tail moment less than 2) in each sample. Western blotting analysis showed the effective BRIT1 knockdown in the cells (next to the graph). Student *t*-test. (**c-i**) HR repair analysis in BRIT1-depleted cells. (**c**) **and** (**d**) Generation of stable cell line for HR repair assay. (**c**) Schematic diagram of HR assay. The DR-GFP reporter substrate was integrated into cellular genomic DNA. SceGFP contains an I-SceI endonuclease site within the coding region, which abolishes GFP expression. iGFP is a truncated GFP, which contains homologous sequence for the SceGFP. Expression of I-SceI induces a single DSB in the genome. When this DSB is repaired by HR, the expression of GFP can be restored and analyzed by flow cytometry to indicate the efficiency of HR repair. A Southern probe was used to verify-single copy integration of the reporter. (**d**) Representative Southern blot of positive clone integrated with a single copy of reporter, which exhibited two specific bands after digestion with HindIII and probed with indicated Southern probe. (**e-i**) Impaired HR specifically results from the loss of BRIT1. (**e**) Cell-cycle profiles of cells that were analyzed for HR repair efficiency. (**f**) Transfection efficiency was monitored by using a control GFP-expression vector (pEGFP-C1) in indicated cells. (**g**) Cutting efficiency of I-SceI was detected by semi-quantitative PCR using a primer pair flanking the DSB site. BRIT1 knockdown cells exhibited a reduction in PCR products compared to control cells at 48 hs after I-SceI transfection owing to the lack of efficient DNA repair, but no differences in PCR products were apparent between BRIT1 knockdown and control cells at early time-points, suggesting similar cutting efficiency of I-SceI in BRIT1 knockdown and control cells. (**h and i**) Ectopic expression of siRNA-resistant BRIT1 but not BRCA1 rescued the impaired HR in BRIT1 knockdown cells. (**h**) Effect of ectopic expression of siRNA-resistant BRIT1 on HR repair in BRIT1-depleted cells. (Left) Quantitative summary of multiple experiments. Each value is relative to the percentage of GFP+ cells transfected with control siRNA, which was set as 1, and represents the mean ± SD of three independent experiments. (Right) Western blot analysis of lysates from the BRIT1 knockdown cells ectopically expressing siRNA-resistant BRIT1 mutant. (**i**) Effect of ectopic expression of BRCA1 on HR repair in BRIT1-depleted cells. (Left) Quantitative summary of multiple experiments. Each value is relative to the percentage of GFP+ cells transfected with control siRNA, which was set as 1, and represents the mean ± SD of three independent experiments. (Right) Western blot analysis of lysates from BRIT1 knockdown cells with overexpressing BRCA1. (**j-k**) NHEJ repair is impaired in BRIT1-depleted cells. (**j**) PCR strategy to analyze NHEJ repair at the DR-GFP locus. PCR products around the I-SceI-induced DSB site were amplified by the indicated primers and subjected to enzyme digestion with I-SceI or I-SceI and BcgI. The fragment resistant to I-SceI digestion consisted of repaired DSB products, which cause loss of the I-SceI restriction enzyme site. As HR repair replaces the I-SceI site with the BcgI site, the fragment resistant to both I-SceI and BcgI digestion represents DSB products repaired by NHEJ. NHEJ repair efficiency can be quantitated by the percentage of uncut DNA present in PCR products after I-SceI and BcgI digestion. (**k**) Analysis of NHEJ repair in BRIT1 knockdown cells with ectopically expressed BRIT1 resistant to siRNA#1 and BRCA1 (The efficiency of knockdown and ectopic expression was represented as in **h** and **i**.) The NHEJ repair deficiency was not reversed by ectopic expression of BRCA1, but was reversed by ectopic expression of siRNA-resistant BRIT1, confirming the specific role of BRIT1 in NHEJ repair.

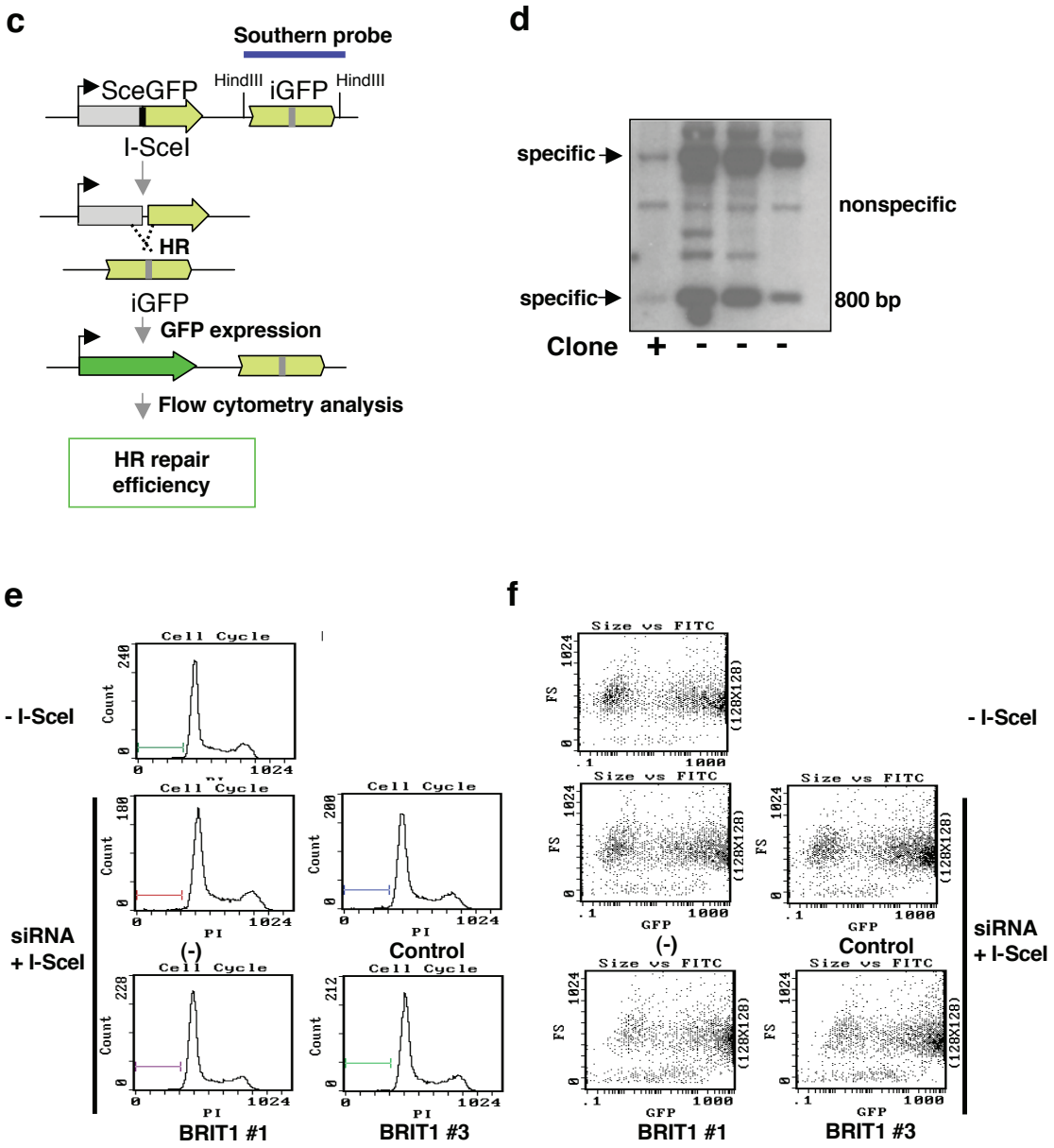

Figure S3 continued

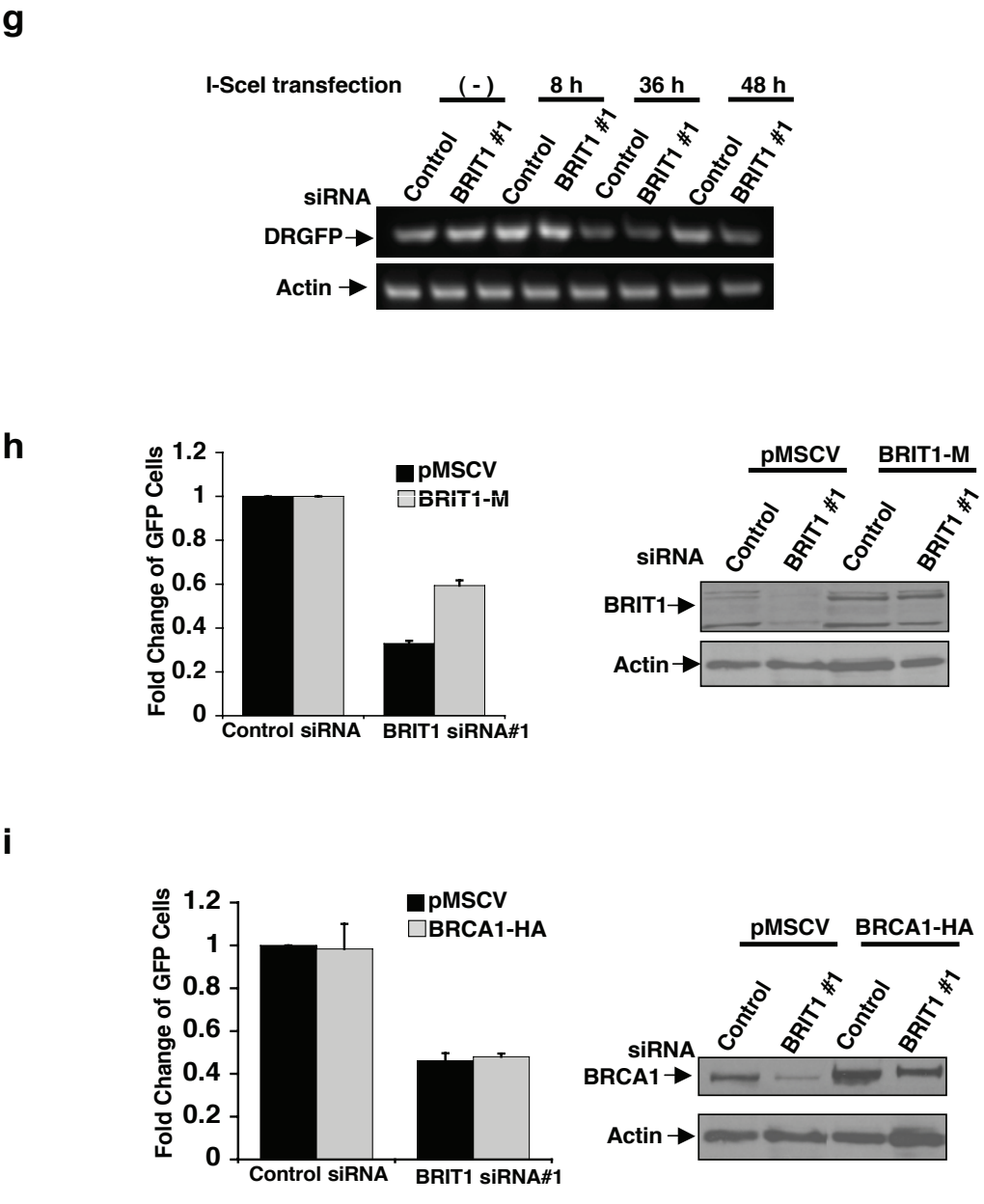

Figure S3 continued

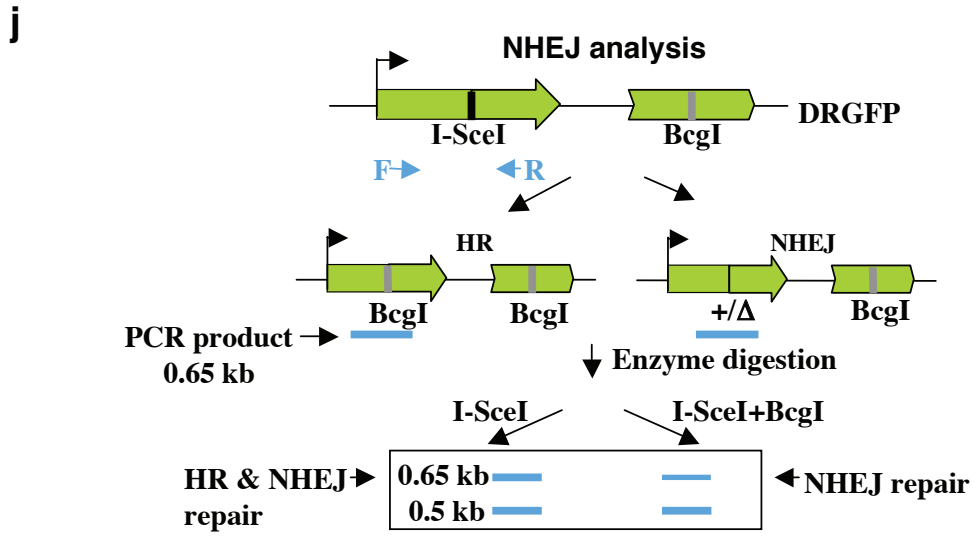

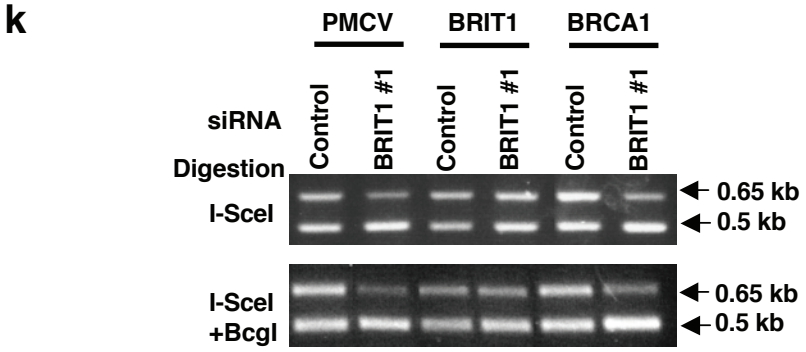

Figure S3 continued

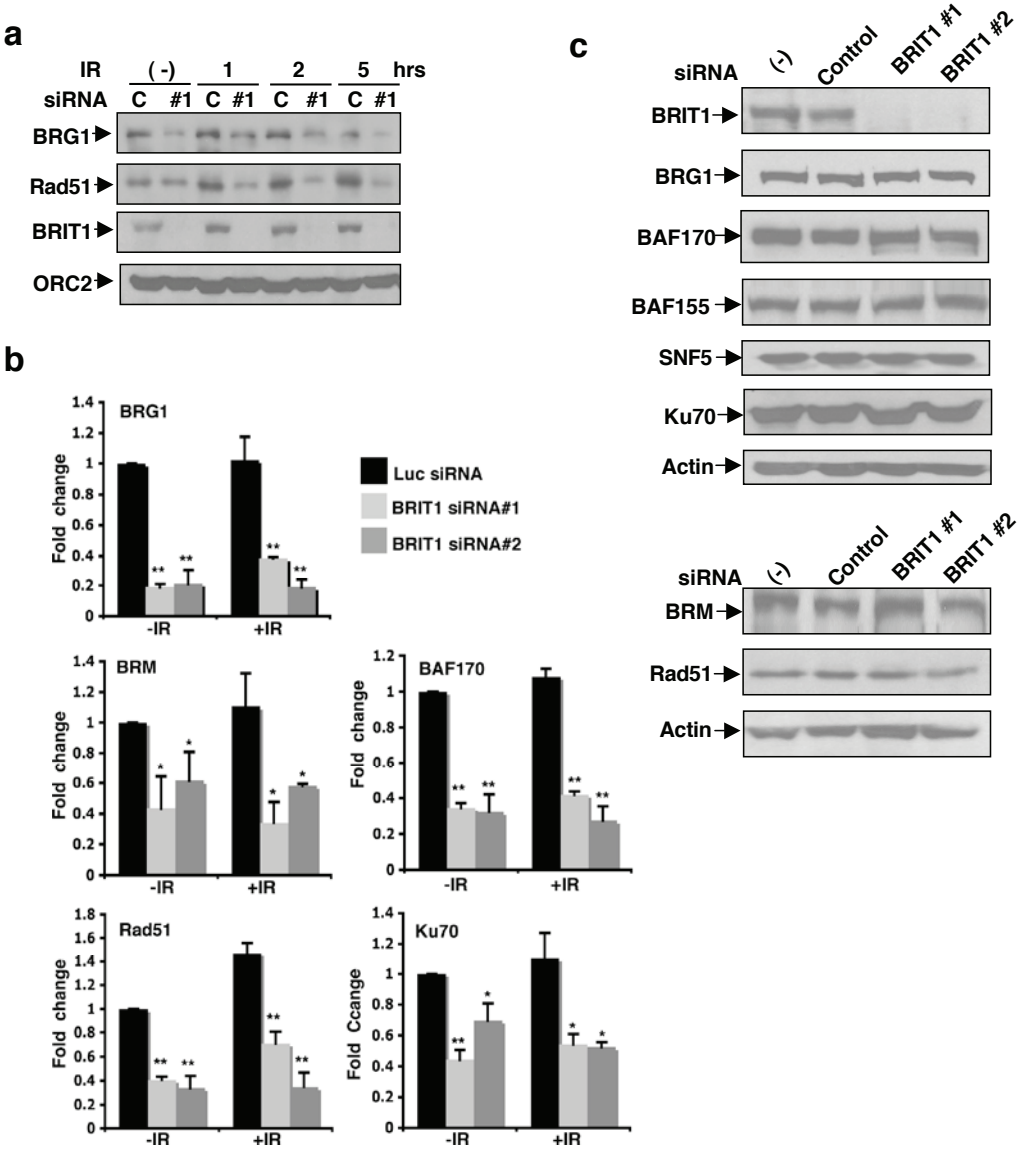

Figure S4 Recruitment of SWI/SNF and DNA repair proteins to chromatin is impaired in BRIT1-depleted cells. (**a**) Binding of BRG1 and Rad51 to chromatin was reduced in BRIT1-deficient cells. Cells transfected with the control or BRIT1 siRNA #1 were exposed to IR (10 Gy), and cell lysates were then prepared at indicated time points (**b**) Densitometry analyses (Western blots were shown in Fig. 3c) of indicated protein values normalized against ORC2. Each value represents the mean ± SD of three independent experiments (* P≤ 0.05; ** P≤ 0.01). Student *t*-test. (**c**) BRIT1 knockdown does not affect the expression of SWI/SNF and DNA repair proteins. U2OS cells were transfected with control or BRIT1 siRNA. Cell lysates were prepared 48 h after the transfection and subjected to Western blot analysis with the indicated antibodies. (**d**) Recruitments of BRIT1 to chromatin and DNA damage sites are SWI/SNF independent. (Top) Association of BRIT1 with chromatin in SWI/SNF knockdown cells. U2OS cells were transfected with siRNA or shRNA vectors to knockdown individual SWI/SNF subunit as indicated. Association of BRIT1 with chromatin was analyzed by chromatin fractionation assay 48 hr after transfection. (Bottom) BRIT1 Foci formation in SWI/SNF knockdown cells. Cells were treated with 10 Gy of IR after knockdown of each SWI/SNF subunit. One hour later, cells were fixed and stained with antibody to BRIT1. Nuclei were visualized by DAPI staining. Scale bar is 10 μM.

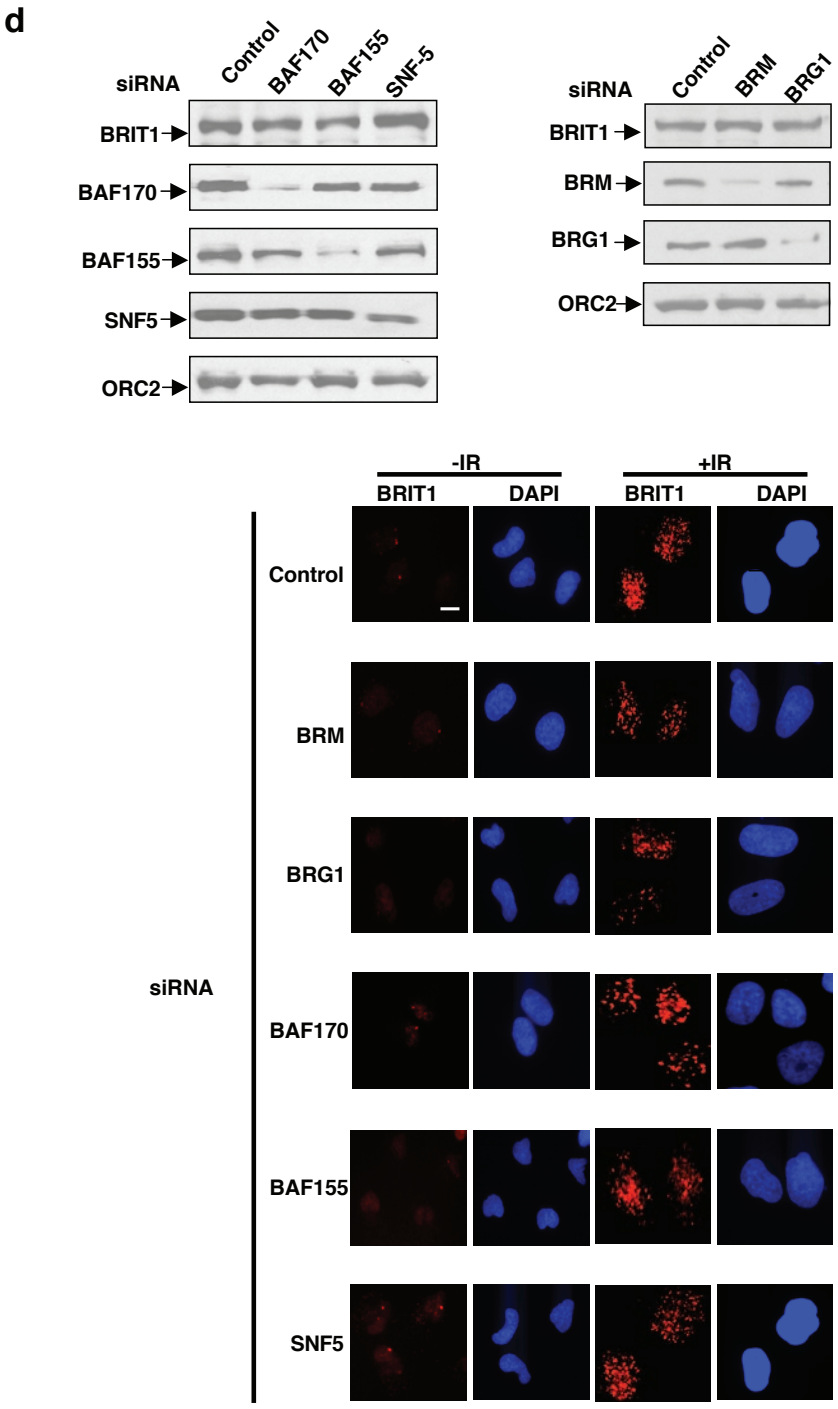

Figure S4 continued

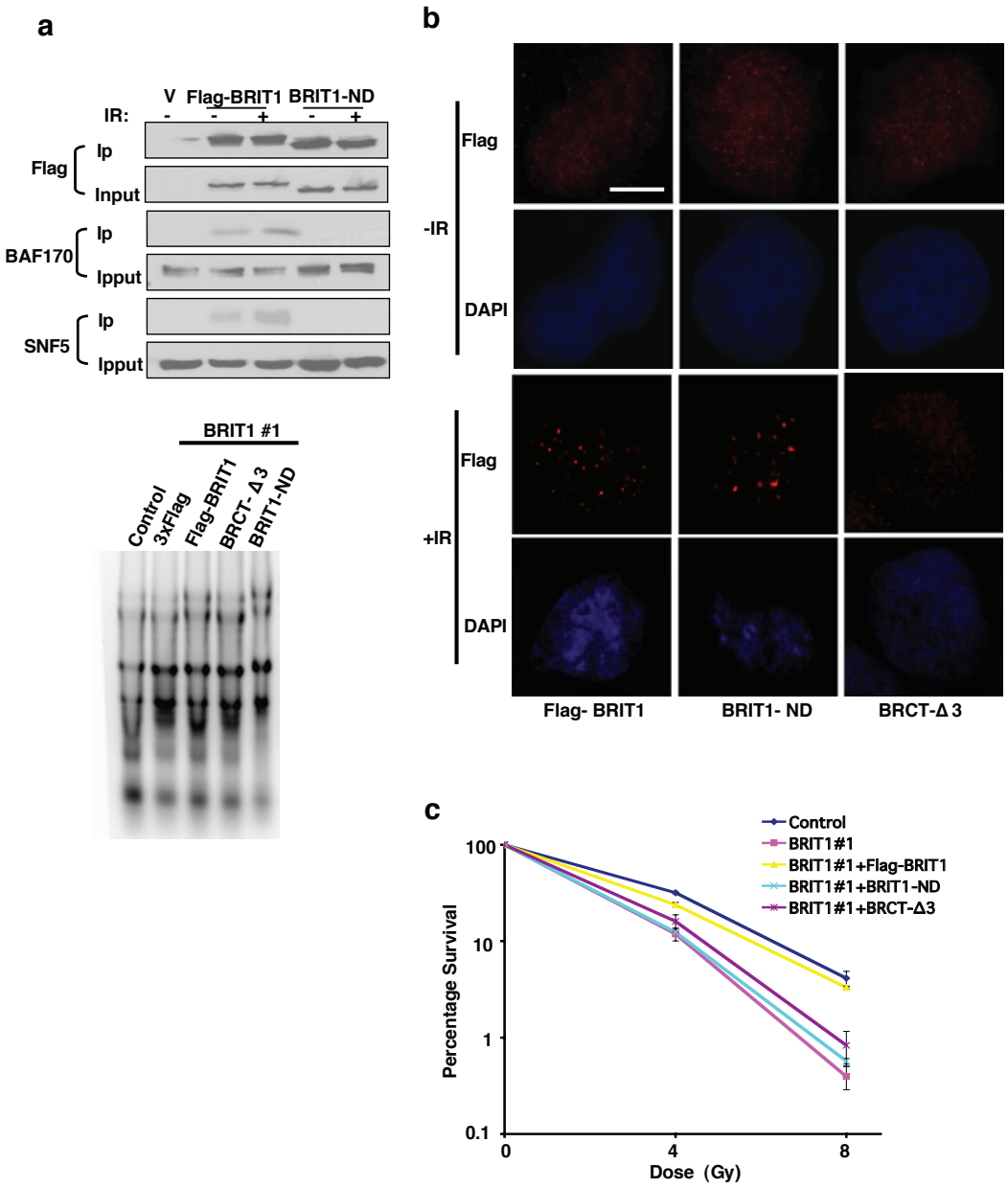

Figure S5 Impaired chromatin relaxation and HR repair in cells with dysfunction of SWI/SNF. (**a**) (Top) A small deletion on BRIT1 N-terminal region abolishes BRIT1-SWI/SNF interaction. Cells were transfected with indicated plasmids and treated with or without IR (10 Gy). 15 minutes after IR, immunoprecipitation was performed by anti-Flag M-2 beads. (Bottom) The function of BRIT1 in chromatin relaxation is dependent on its interaction with SWI/SNF. BRIT1 with N-terminal deletion (BRIT1-ND), which lacks its SWI/SNF interaction domain, was unable to rescue the defect of chromatin relaxation. (**b**) Foci formation of indicated Flag-tagged BRIT1 proteins detected by immunostaining with anti-Flag M2 antibody 1 hrs after IR (10 Gy). Scale bar is 10 μM. (**c**) BRIT1-ND-reconstituted cells were sensitive to IR. Indicated plasmids were transfected into U2OS cells and then treated with control or BRIT1 siRNAs. 2 days later, cells were plated at low density and exposed to IR. Colonies were counted 2 weeks later. The graph represents the mean ± SD of three independent experiments (**d**) Western blots for BRM and BAF155 knockdown efficiency. (**e**) Impaired chromatin relaxation analyzed by MNase sensitivity assay in BRM or BAF155 knockdown cells. (**f**) Impaired HR repair in BRM or BAF155 knockdown cells analyzed 48 hours after I-SceI transfection. Each value is relative to the percentage of GFP+ cells in I-SceI-transfected cells with control siRNA expression, which was set to 1 and represents the mean±SD of three independent experiments. Student *t*-test. (**g**) (Top) sequences indicating conserved hydrophobic sequences on BAF155 and BAF170. Mutations were made at corresponding sites to replace leucines to arginines. (Bottom) L4R mutants of BAF155 and BAF170 can be incorporated into endogenous SWI/SNF complex. 293T cells were transfected with indicated plasmids. 48 hrs later, immunoprecipitation was performed using anti-SNF5 antibody. (**h**) L4R mutants lack their binding activities to BRIT1 and can exert dominant-negative effects toward BRIT1-SWI/SNF interaction. Cells were co-transfected with Flag-BRIT1 and indicated plasmids. 48 hrs later, immunoprecipitation was performed using anti-Flag M2 beads. (**i**) Impaired HR repair in cells transfected with L4R mutants of BAF155 or BAF170 (Left) Western blots that showed ectopic expression of indicated plasmids. (Right) GFP analyses were performed 48 hours after I-SceI transfection. Each value is relative to the percentage of GFP+ cells in I-SceI-transfected cells with empty vector transfected, which was set to 1 and represents the mean±SD of three independent experiments.

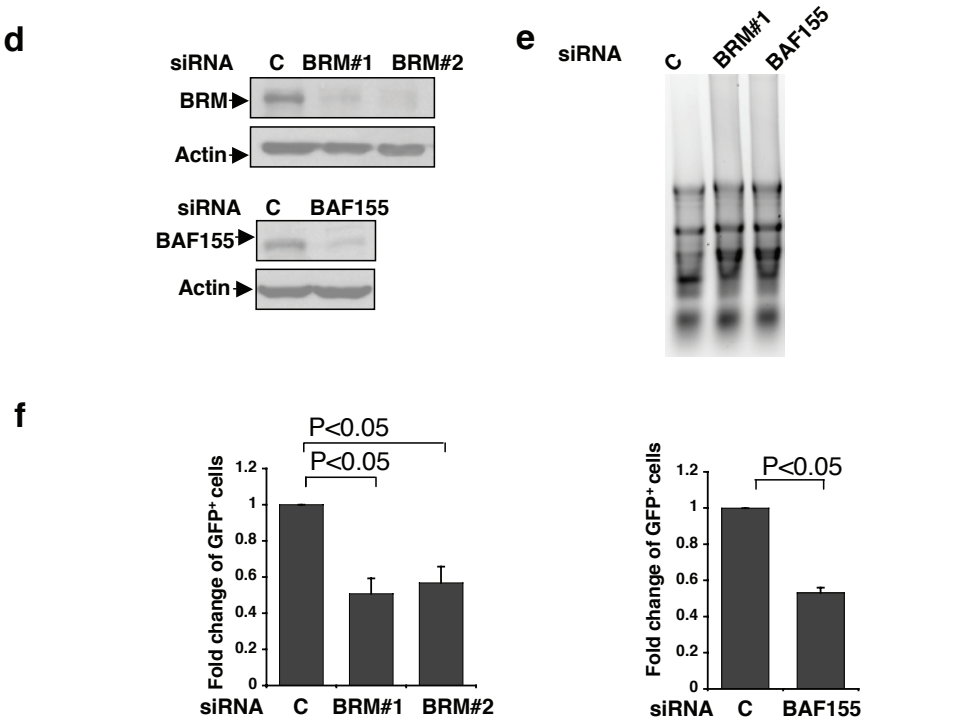

Figure S5 continued

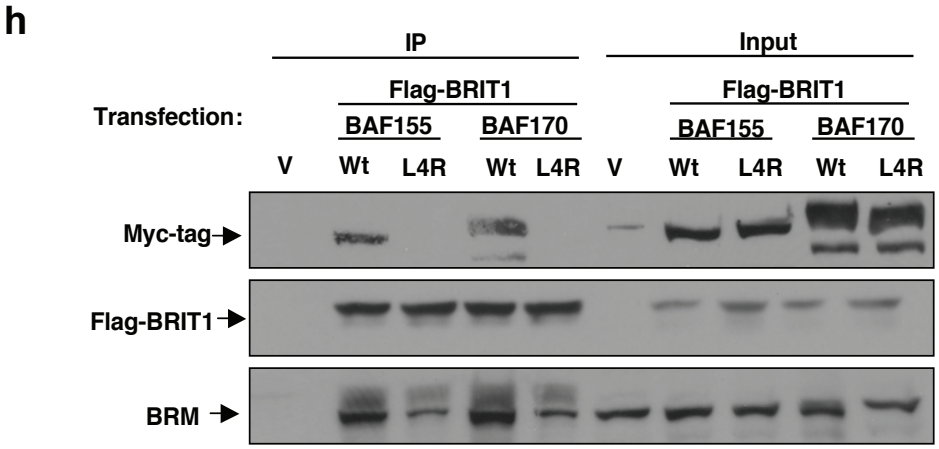

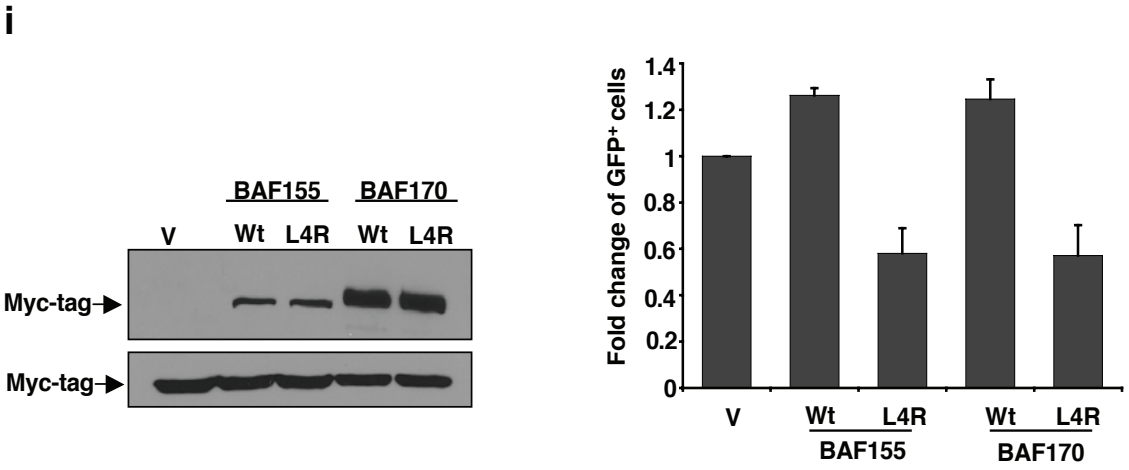

Figure S5 continued

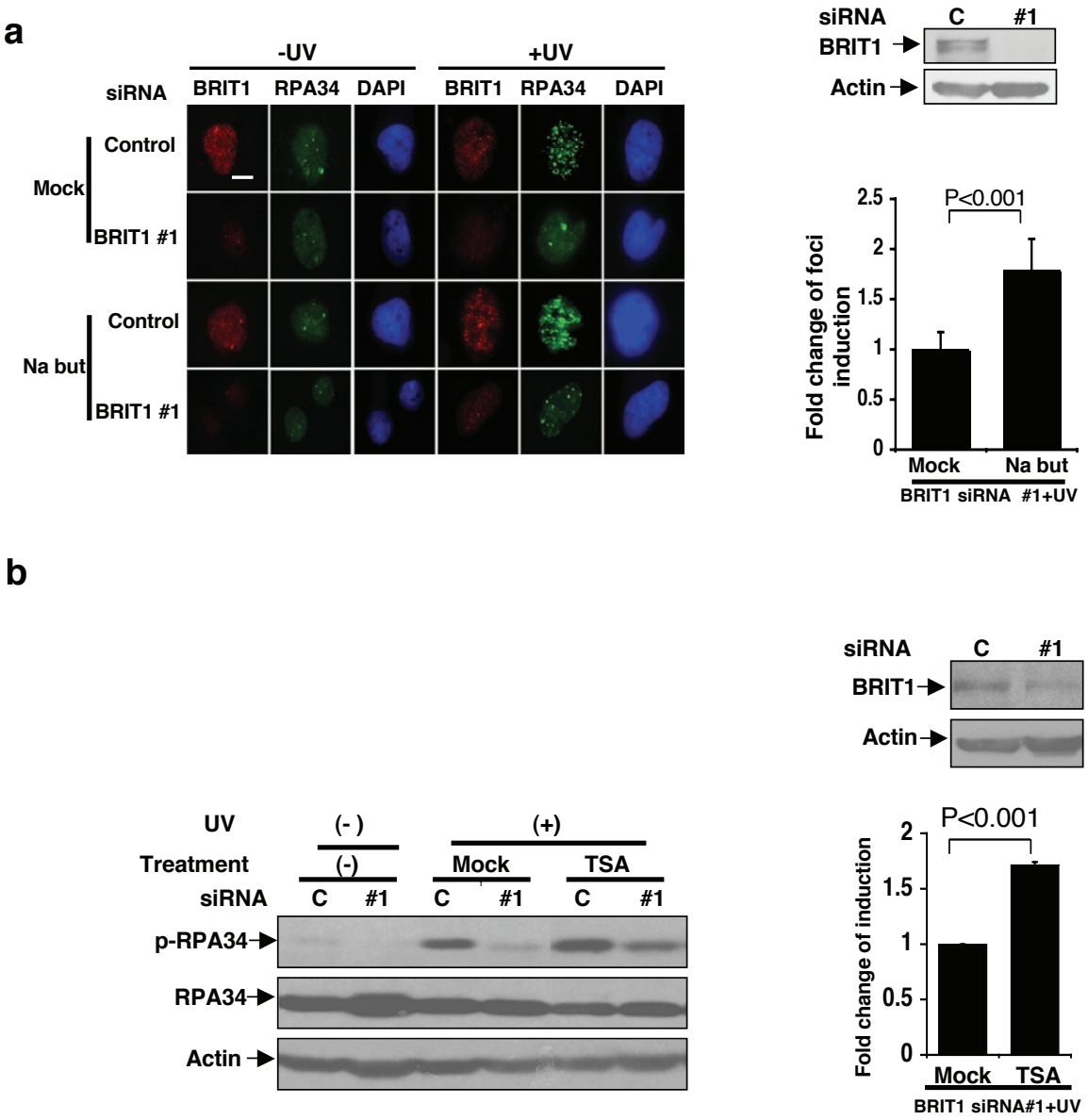

Figure S6 Chromatin relaxation agents improve activation of DNA repair protein RPA. Western blotting analysis showed the effective BRIT1 knockdown in the cells (shown above the graph in each panel). (**a**) RPA34 foci formation improved by sodium butyrate (Na but)-induced chromatin relaxation. (Left) Representative immunostaining images. Scale bar is 10 μM. (Right) Quantitative analysis of RPA34 foci induced in BRIT1 depleted-cells from multiple experiments. At least 50 cells were scored in each sample. The number of foci per cell without treatment was set as 1. (**b**) (Left) Representative Western blot for p-RPA after trichostatin A treatment. BRIT1 knockdown ells were exposed to 30 J/m^2 of UV irradiation in the presence or absence of trichostatin A (200 ng/mL). Cell lysates were prepared and subjected to Western blotting analysis 8 hr after irradiation. (Right) Densitometry analysis of p-RPA induction (mean ± SD) by trichostatin A in BRIT1 knockdown cells after irradiation from three independent experiments. (**c**) (Left) Representative Western blot for p-RPA after sodium butyrate treatment (5 mM). (Right) Densitometry analysis of p-RPA induction (mean ± SD) by sodium butyrate in BRIT1 knockdown cells after irradiation from three independent experiments. (**d**) (Left) Representative Western blot for chromatin-associated RPA after sodium butyrate treatment (5 mM). BRIT1 knockdown cells were treated with 50 J/m^2 of UV irradiation in the presence or absence of sodium butyrate (5 mM). Two hours after treatment, chromatin-enriched fractions were subjected to Western blot analysis. (Right) Densitometry analysis of induction of RPA binding to chromatin (mean ± SD) by sodium butyrate in BRIT1 knockdown cells after irradiation (from three independent experiments).

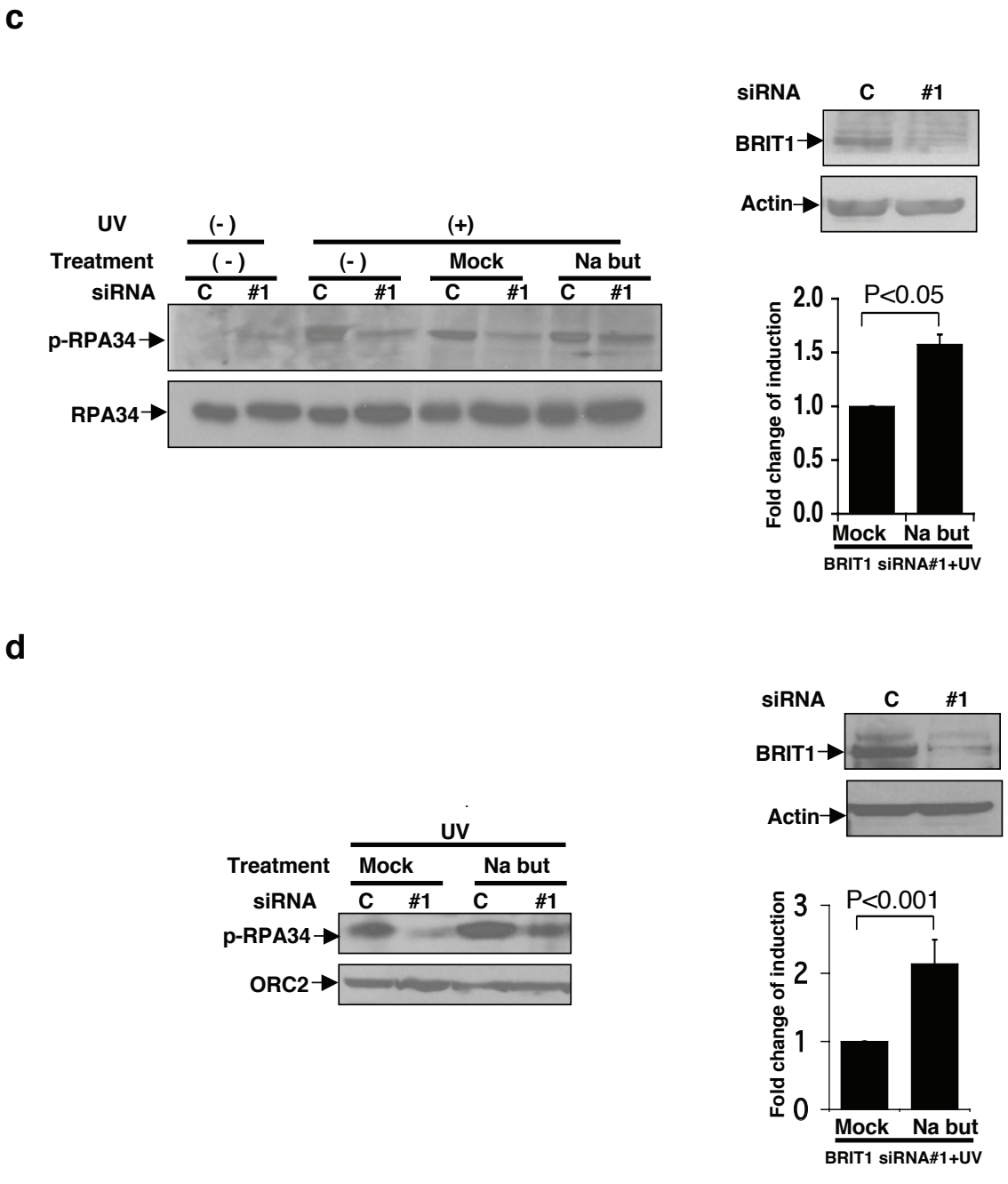

Figure S6 continued

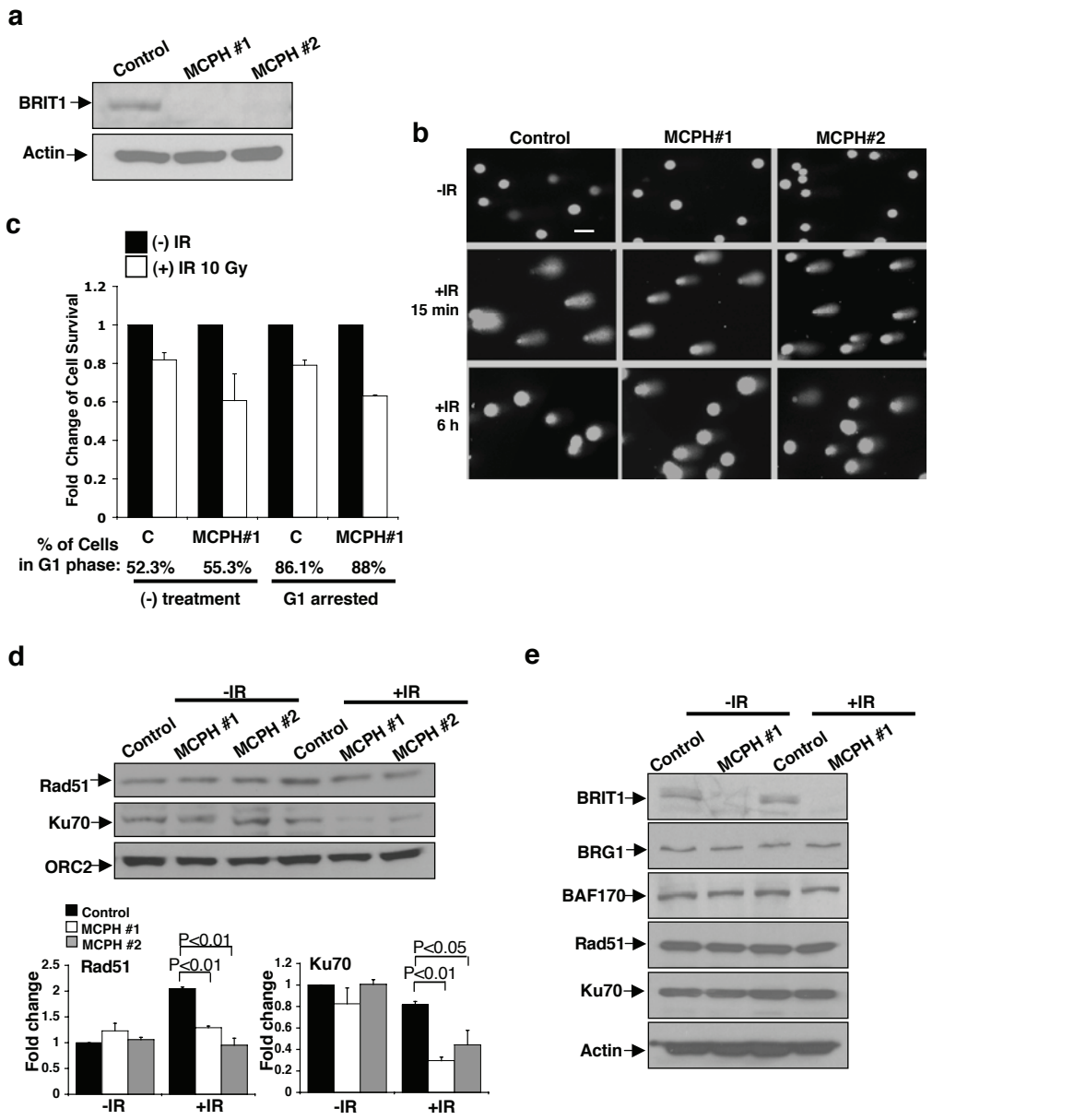

Figure S7 Impaired DNA repair in MCPH cells. (**a**) Deficiency of BRIT1 expression in human MCPH lymphoblastoid cell lines. Cell lysates were prepared from MCPH cells with BRIT1 mutations and subjected to Western blotting analysis for analysis of BRIT1 expression. (**b**) Representative images of Comet analyses for Fig. 5a. Scale bar is 40 μM. (**c**) Increased sensitivity to IR-induced DNA damage in G1-arrested BRIT1 LCLs. The percentage of cells in G1 phase was analyzed by flow cytometry and shown at the bottom of the graph. Arrested cells and non-synchronized cells were both exposed to IR (10 Gy). Cell survival was then measured 72 h after IR. Each value is relative to the percentage of survival cells in the control groups without IR exposure, which was set to 1 and represents the mean±SD of three independent experiments. (**d**) (Top) Impaired association of Rad51 and Ku70 with chromatin. MCPH cells were treated with 10 Gy IR. After 5 h, chromatin-enriched fractions were isolated. (Bottom) Densitometry analyses of Rad51 and Ku70 values normalized against ORC2. Each value represents the mean± SD of three independent experiments; Student *t*-test. (**e**) Deficiency of BRIT1 in MCPH cells does not affect expression of SWI/SNF and DNA repair proteins. Cell lysates were prepared from MCPH cells and subjected to Western blot analysis with the indicated antibodies. (**f-h**) Impaired RPA activation and chromatin relaxation in MCPH cells. **(f)** (Left) Impaired association of phosphorylated PRA with chromatin. MCPH cells were treated with 50 J/m^2 of UV irradiation. After 2 h, chromatin-enriched fractions were subjected to Western blotting with antibodies against p-RPA34. (Right) Densitometry analyses of p-RPA34 values normalized against ORC2. Each value represents the mean± SD of three independent experiments. (**g**) Chromatin relaxation improves phosphorylation of RPA in MCPH cells. (Left) Representative Western blot for p-RPA after trichostatin A treatment. Cells were treated as described in Supplementary Fig. 6b. (Right) Densitometry analysis of p-RPA induction (mean ± SD of three independent experiments) by trichostatin A in MCPH cells after irradiation from three independent experiments. (**h**) Time-course study of partial MNase digestion of chromatin obtained from U2OS cells (Left) or MCPH #1 cells (Right). (**i-l**) Wild-type BRIT1 but not BRCT-Δ1 rescues the defects of cell viability, DNA repair and chromatin relaxation in BRIT1 LCLs. (**i**) Western blots for the ectopic expression of indicated plasmids in LCLs. 24 h after first transfection, cells were retransfected with the plasmids and incubated for additional 48 h before processing. (**j**) Increased cell survival following the transfection with Flag-BRIT1. The percentage of cell survival was measured after exposure to 1 μM Etoposide to induce DNA damage. The bar graph represents mean ± SD of three independent experiments. (**k**) Recovered DNA repair efficiency following the transfection of Flag-BRIT1. Cells were exposed to IR (10 Gy). The repair efficiency was analyzed in each group by the percentage of cells with intact DNA (tail moment less than 2) 6 h after IR exposure. (**l**) Rescued the defect of chromatin relaxation following the transfection with Flag-BRIT1. Chromatin relaxation was measured by MNase sensitivity assay.

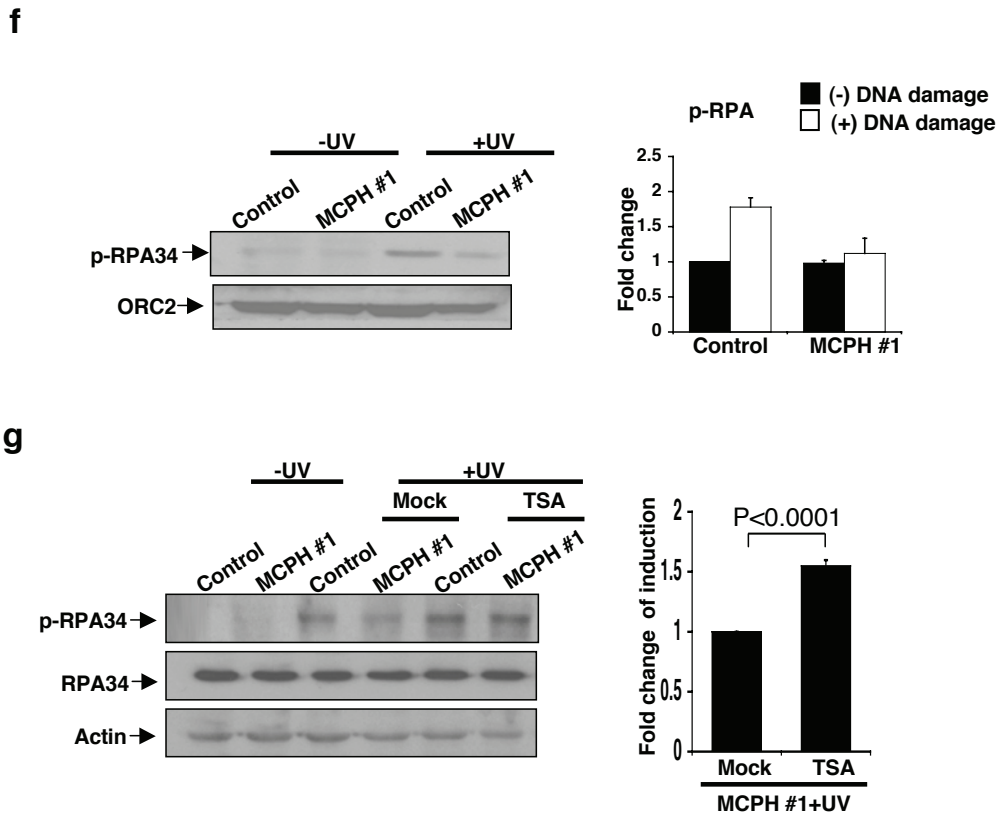

Figure S7 continued

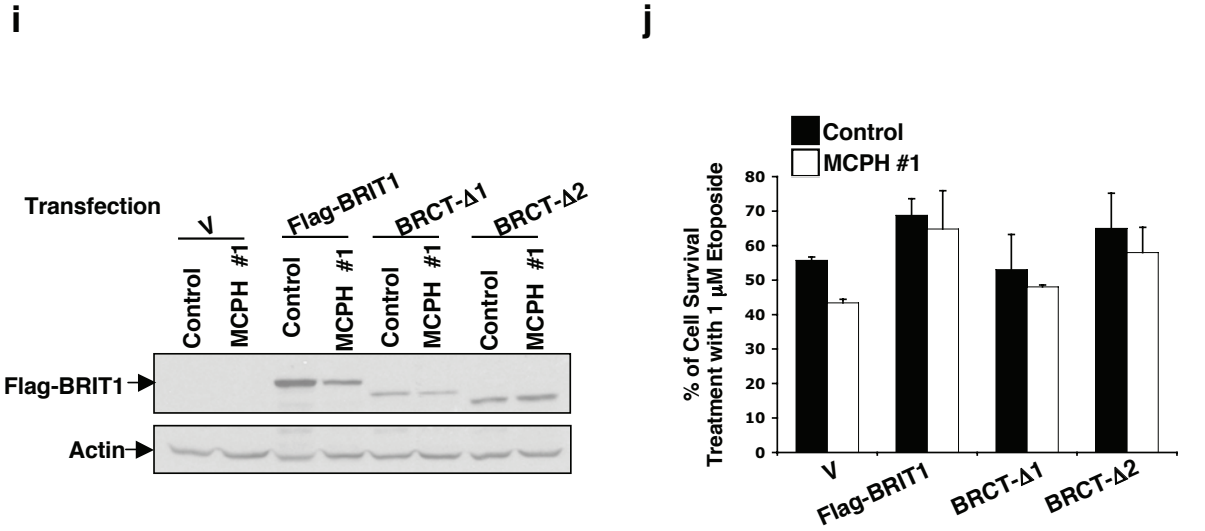

Figure S7 continued

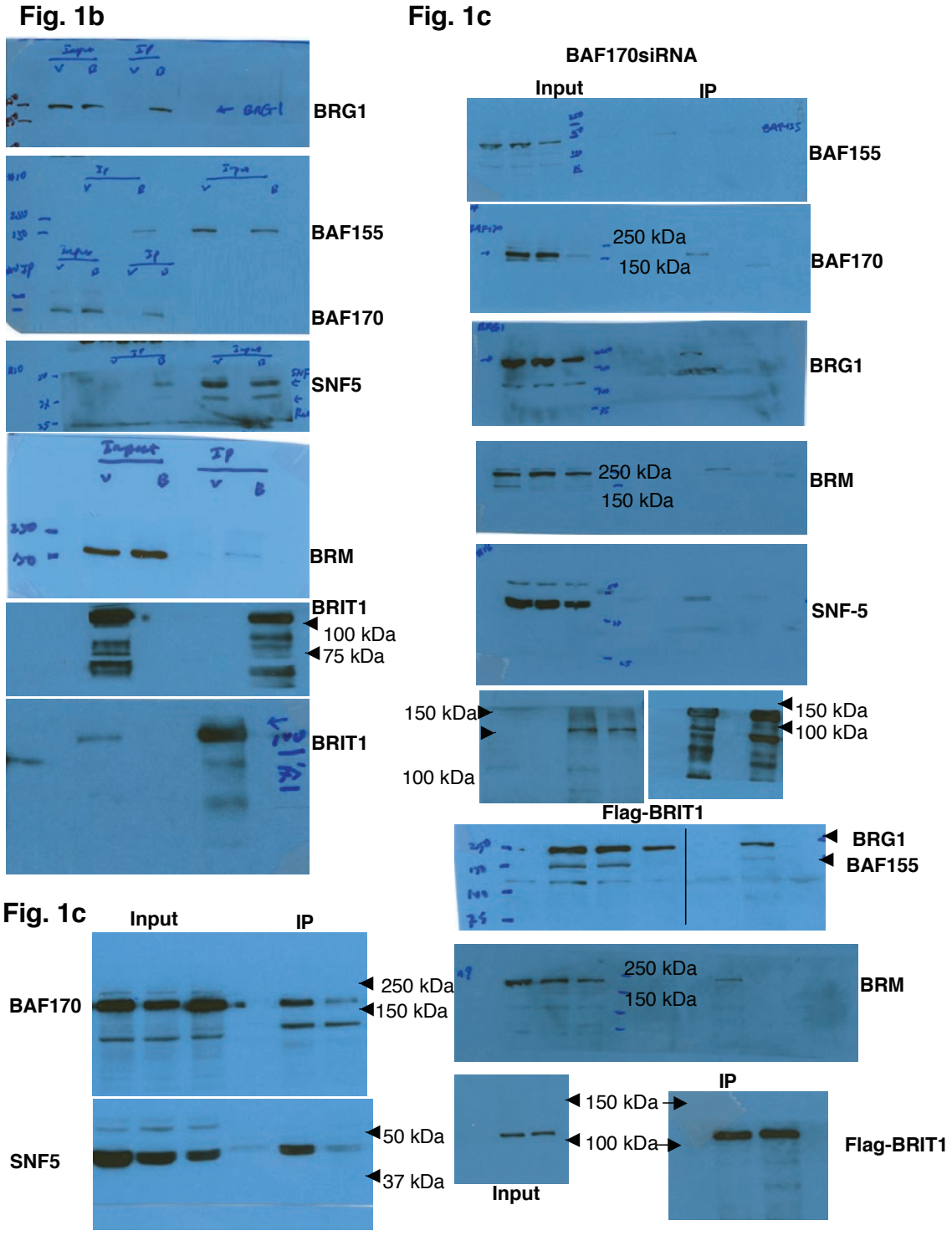

Figure S8 Full scans of key Western blots presented in the manuscript.

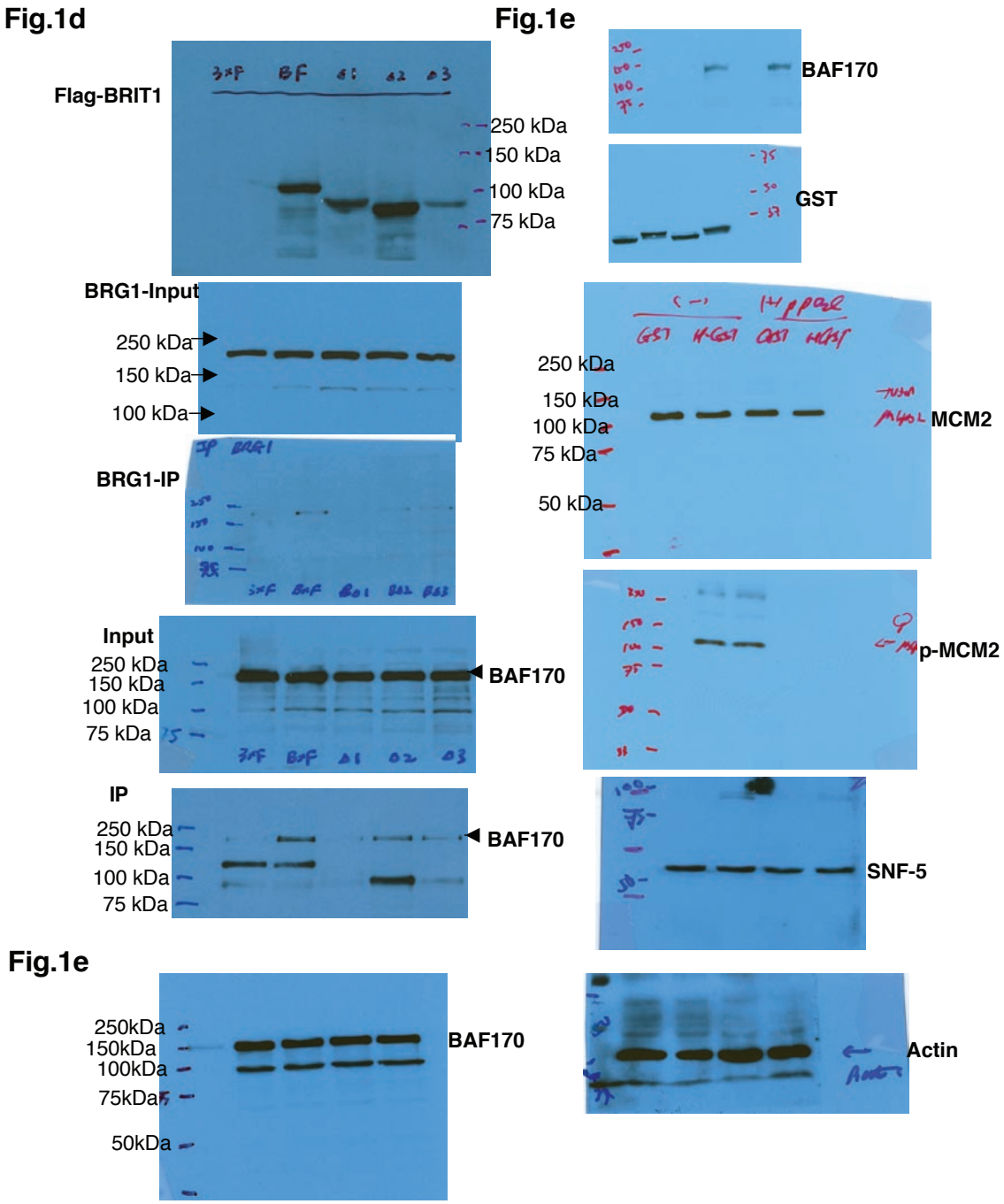

Figure S8 continued

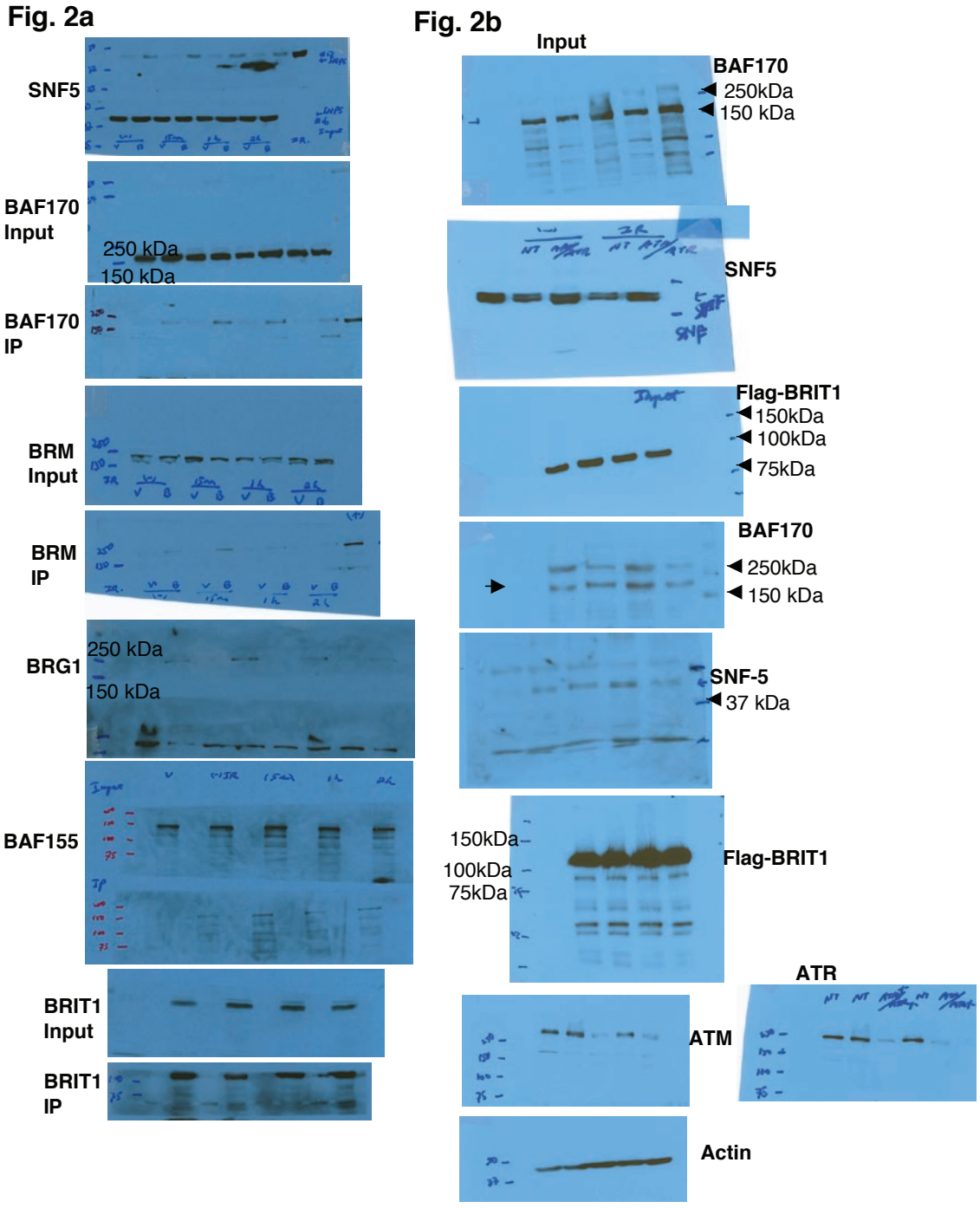

Figure S8 continued

Fig. 2c

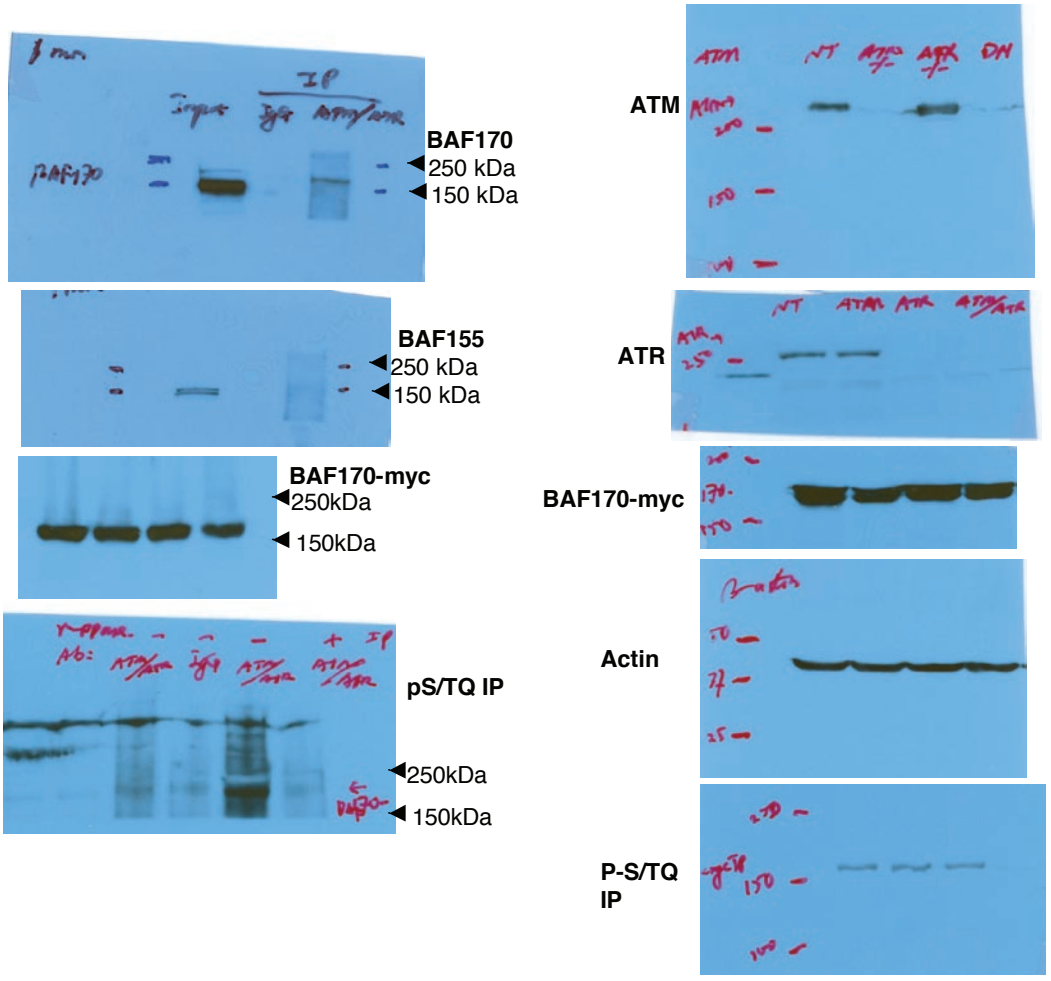

Fig. 2d

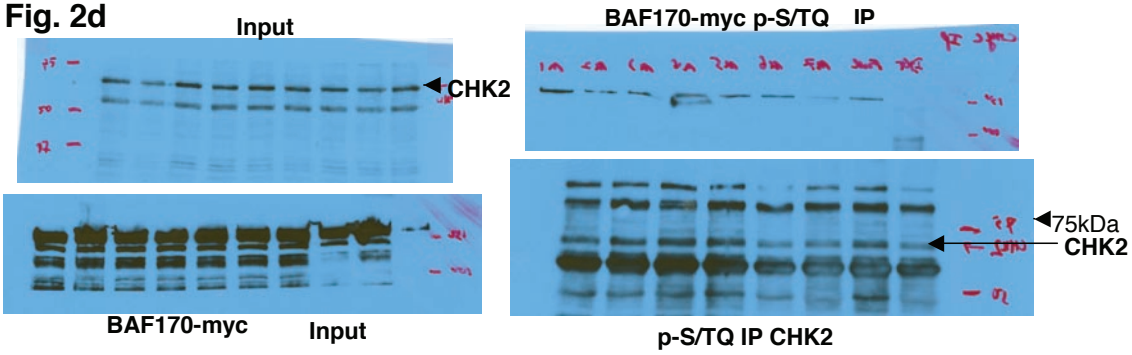

Figure S8 continued

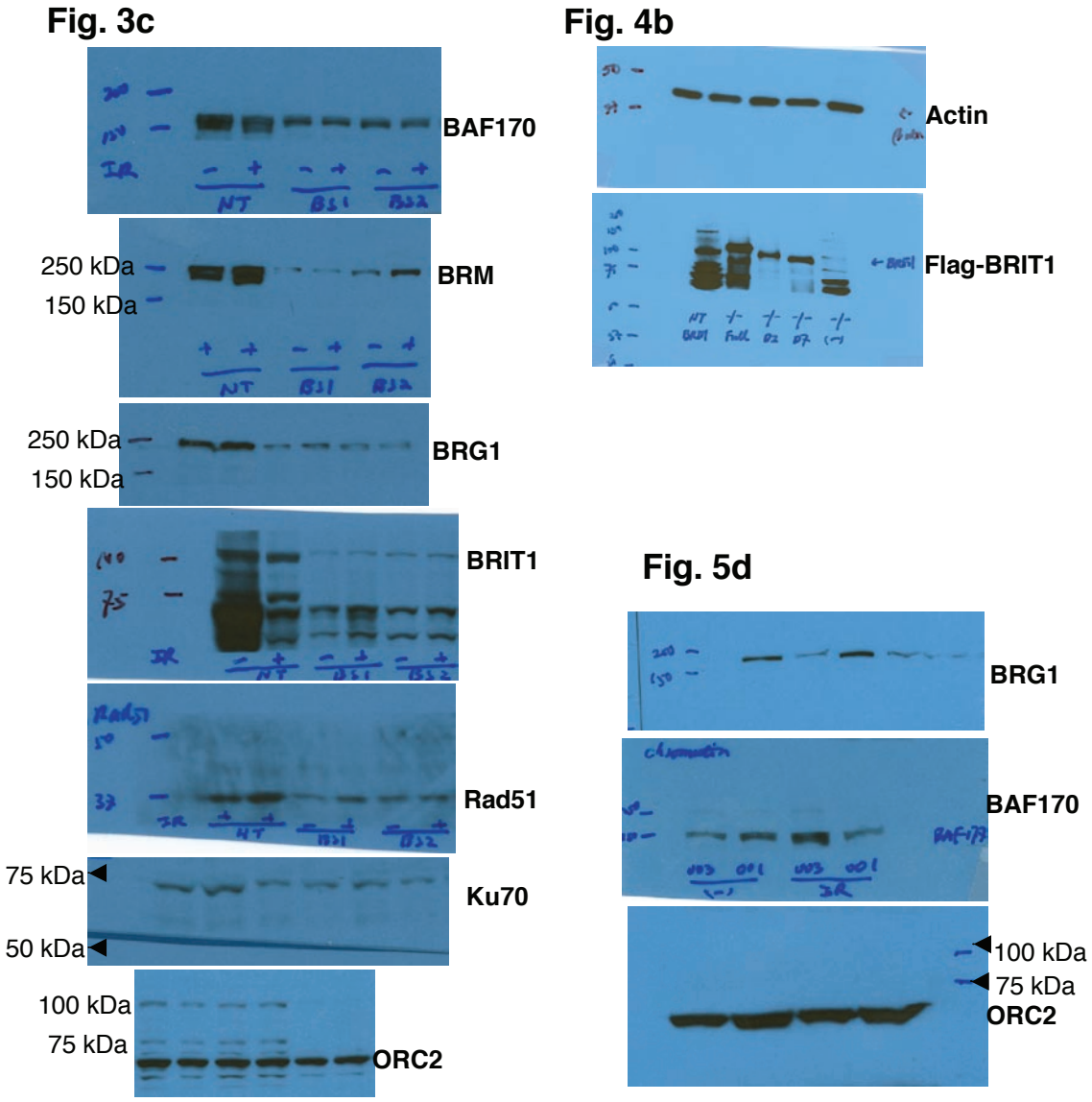

Figure S8 continued

Supplementary Information Methods:

The list of siRNAs and shRNAs sequences

Gene Name	Sequence	Catalog #
Non-Target shRNA	CCGGCAACAAGATGAAGAGCACCAACTCGAGTTGGTGCTCT TCATCTTGTTGTTTTT	Mission Non-target shRNA control vector SHC002 (Sigma)
BRG1	#1:CCGGCCCGTGGACTTCAAGAAGATACTCGAGTATCTTCTT GAAGTCCACGGGTTTTT	MISSION™ shRNA lentiviral plasmids SHGLY NM_003072 (Sigma)
	#2:CCGGCCGAGGTCTGATAGTGAAGAACTCGAGTTCTTCACT ATCAGACCTCGGTTTTT	
BRM	#1: CCGGCCAAACCTGTAGTGAGCGATTCTCGAGAATCGCTCACT ACAGGTTTGGTTTTT	MISSION™ shRNA lentiviral plasmids SHGLY-NM_003070 (Sigma)
	#2: CCGGCGGAATCTTAGCCGATGAAATCTCGAGATTTCATCGGC TAAGATTCCGTTTTT	
ATM	#1: GCAAAGCCCUAGUAACAUA	ON-TARGETplus SMARTpool L-003201 (Dharmacon)
	#2: GGUGUGAUCUUCAGUAUAU	
	#3: GAGAGGAGACAGCUUGUUA	
	#4: GAUGGGAGGCCUAGGAUUU	
ATR	#1: GAGAAAGGAUUGUAGACUA	ON-TARGETplus SMARTpool L-003202 (Dharmacon)
	#2: GCAACUCGCCUAACAGAUA	
	#3: CCACGAAUGUUAACUCUAU	
	#4: CCGCUAAUCUUCUAACAUU	
SNF5	#1: sense-GUGACGAUCUGGAUUUGAAUU antisense-PUUCAAAUCCAGAUCGUCACUU	SiGENOME ON-TARGETplus SMARTpool L-010536 (Dharmacon)
	#2: sense-GAAACUACCUCCGUAUGUUUU antisense-PAACAUACGGAGGUAGUUUCUU	
	#3: sense-GAUGACGCCUGAGAUGUUUUU antisense-PAAACAUCUCAGGCGUCAUCUU	
	#4: sense-GGCAGAAGCCCGUGAAGUUUU antisense-PAACUUCACGGGCUUCUGCCUU	
BAF155	#1: sense-GAGCAGACCAAUCACAUUAUU antisense-PUAAUGUGAUUGGUCUGCUCUU	SiGENOME ON-TARGETplus SMARTpool L-010813 (Dharmacon)
	#2: sense-GUACUGACAUUUACUCCAAUU antisense-PUUGGAGUAAAUGUCAGUACUU	
	#3: sense-GAACAUUUACGGAUGAGAAUU antisense-PUUCUCAUCCGUAAAUGUUCUU	
	#4: sense-CAACACCUGUACCCAAUAUUU antisense-PAUAUUGGGUACAGGUGUUGUU	
BAF170	#1: UCACUAAACUGCCGAUCAA	SiGENOME ON-TARGETplus SMARTpool L-008312 (Dharmacon)
	#2: GAGAAGCACUGGAGUAUCA	
	#3: GCUACUAUCCUGACAGUUA	
	#4: UAAGAAAGGUCCCUCAACA	
BRIT1	#1: AGGAAGUUGGAAGGAUCCAdTdT	Ordered from Dharmacon
	#2: CUCUCUGUGUGAAGCACCUdTdT	
Luciferase siRNA	UAAGGCUAUGAAGAGAUACdTdT	

ON-TARGETplus Non-targeting Pool (D-001810-10-20) was also purchased from Darmachon and used as the controls for smart pool knockdown.

Comet assay

Double-strand break (DSB) repair was analyzed by neutral comet assay using the Trevigen's Comet Assay kit (4250-050-K) according to the manufacturer's instruction. Cells were exposed to 10 Gy γ-irradiation (IR) and subjected to comet analysis at indicated time points. After staining with SYBR green, comet images were captured by fluorescence microscopy. Tail moments (percentage of DNA in tail x tail length) were quantitated for 100 cells/slide by using CometScore software (available through www.autocomet.com). The calculation method was previously described1. In cells not treated with IR, more than 95% of cells contained tail moments less than 2, which was set as the parameter for cells with intact DNA. In each sample, the percentage of cells with tail moment less than 2 at the different time points after IR exposure was calculated and represented the cells with intact DNA. In the bar graph, the percentage of cells with intact DNA in the cells without IR exposure was set as "1". The percentage of cells with intact DNA from different time points after IR exposure was then drawn relative to this control.

HR repair analysis

DR-GFP, pCAGGS and pCBASce plasmids were kindly provided by Dr. Maria Jasin from Memorial Sloan-Kettering Cancer Center (New York, NY). U2OS cells containing a single copy of the HR repair reporter substrate DR-GFP in a random locus were generated as previously described[2]. Positive clone integrated with a single copy of reporter exhibits two specific bands after digestion with HindIII and probed with

indicated Southern probe. GFP expressing plasmid (pEGFP-C1) was used for transfection efficiency control. pCAGGS was used in mock transfection. Twenty-four hours after BRIT1 siRNA transfection, cells were re-seeded and then the next day they were transfected with mock or pCBASce plasmids. Forty-eight hours later, flow cytometry analysis was performed to detect GFP positive cells using a FACScalibur apparatus with Cellquest software (Becton Dickinson, San Jose, CA) at the M. D. Anderson Cancer Center Flow Cytometry Facility. To induce chromatin relaxation, cells were incubated for 16 hr in sodium butyrate (5 mM) or trichostatin A (200 ng/mL) before analysis by flow cytometry.

NHEJ repair analysis and PCR analysis of I-SceI-induced DNA cutting

The genomic DNA of mock- or I-SceI-transfected cells was extracted. PCR using primers around the DSB site and enzyme digestion with I-SceI or I-SceI+BcgI were performed as previously described[3]. I-SceI and BcgI restriction enzymes were purchased from New England Biolabs. After gel electrophoresis, the intensity for the enzyme-resistant or enzyme-cleaved fragments was quantified using NIH IMAGE software. To assay the cutting efficiency of I-SceI in cells transfected with control or BRIT1 siRNA, genomic DNA was extracted at different time points after I-SceI transfection and adjusted to equal concentrations. Semi-quantitative PCR was carried out using the same primers for NHEJ analysis (30 cycles). Beta-actin primers (Applied biosystems) were used as an internal control (25 cycles). Cycle number was determined to generate PCR products in the range of linear amplification.

Cell cycle analysis

Cells from HR repair analysis were fixed in 70% cold ethanol (-20^{o}C) overnight. After washing with cold phosphate-buffered saline (PBS), cells were incubated in staining solution (10 μg/mL propidium iodide, 20 μg/mL RNAase A and 0.05% Triton X-100)). Cell cycle analysis was performed at the M. D. Anderson Cancer Center Flow Cytometry Facility. For fluorescence-activated cell sorter (FACS) analysis, the percentage of cells in each phase of the cell cycle was quantitated with Cellquest software (Becton-Dickinson) and ModFit software (Verity Software House Inc.)

Micrococcal nuclease (MNase) sensitivity assay

To induce DNA damage, U2OS cells were treated with 4 Gy IR. MCPH cell lines were treated with the DSB inducing agent neocarzinostatin (400 ng/mL) (Sigma) for 2 hr. Cells (2 x 10^6 for U2OS cells and 8 x10^6 for MCPH cells) were harvested by scrapping cells into lysis buffer (10 mM Tris/HCl pH8.0, 10 mM MgCl2, 1 mM DTT and 0.5% NP-40). Nuclei were pelleted and then digested with MNase at a concentration of 0.2 U/200 ul digestion buffer (15 mM Tris-HCl pH 7.4, 60 mM KCl, 15 mM NaCl, 0.25 M sucrose, 1 mM $CaCl_2$ and 0.5 mM DTT). Aliquots (50 μl) were prepared at 1 min, 2 min, and 5 min. Genomic DNA was purified and separated by electrophoresis in 1.2% agarose gel. Band intensity was determined using NIH IMAGE software. The average nucleosome size was calculated as described previously[4]. Briefly, intensity of each lane and intensity of individual band in each lane were obtained. Oligonucleosome average size was calculated as $\sum_{N1\text{-}Ni}(NiP_{Ni})$, where Ni is the oligonucleosome size (expressed as number of nucleosomes) and P_{Ni} is the fraction of that oligonucleosome out of the total scan

calculated as the ratio of specific band intensity to the intensity of the whole lane. Statistical significance of the difference in average oligonucleosome size between the control group and BRIT1 deficient groups were analyzed by Student's t-test.

Colony-forming assay

Transfection and colony-forming assay were performed as previously described[5]. Briefly, U2OS cells were transfected with indicated plasmids, and 5 h later were transfected with BRIT1 siRNA. Cells were exposed to IR two days after transfection, seeded at low density and left for 2 weeks to allow colonies to form. Colonies were stained with 2% methylene blue/50% ethanol and counted. Colonies containing 50 or more cells were counted.

Cell viability assay

The sensitivity of MCPH cells to DSB-inducing agents was analyzed using CellTiter 96 Aq_{ueous} One Solution Cell Proliferation Assay (MTS assay, Promega). Briefly, $1x10^4$ cells/well were seeded in a 96-well plate in a total volume of 100 μl in triplicate in each experiment. The next day, cells were treated with the DSB-inducing agent etoposide (Sigma) or camptothecin (Sigma) at indicated concentrations. To inhibit DNA replication, cells were pre-incubated with aphidicolin (Sigma) for 90 min before treatment with DSB-inducing agents. Seventy-two hours later, the number of surviving cells was assayed using MTS solution. G1 arrest in patient cells was induced as described previously[6]. Cell cycle arrest was confirmed by flow cytometry. Arrested cells and non-synchronized cells were exposed to IR (10 Gy). Cell viability assay was performed 72 h

after IR exposure. Plates were read at 490 nm and 650 nm (background) in a microplate reader (Molecular Devices). After subtraction of background, the cell viability was calculated as fold change relative to control cells.

Immunofluorescent staining for foci formation

For detection of DNA damage induced foci of p-RPA34 and RPA34, immunofluorescent staining was carried out essentially as described previously[7]. To detect Rad51 foci, cells were exposed to IR (10 Gy) and the staining was performed 5 h after IR as in the previous publication[32]. For MCPH cell lines, cells were subjected to the same procedures as cells grown on coverslips including cytoskeleton buffer, stripping buffer and fixing buffer. Then cells were spread onto the slides for the staining. Rabbit anti-Rad51 antibody (1:500) was used to detect Rad51 foci. Primary antibodies were incubated for 2 h at room temperature (RT) and secondary antibody rhodamine-conjugated goat anti-rabbit IgG was incubated for 1 h at RT. Slides were mounted in medium containing DAPI (Vector laboratories, Burlingame, CA) and analyzed under a fluorescence microscope. The number of foci per cell was scored for at least 50 cells per sample. For chromatin relaxation, cells were incubated in the presence of sodium butyrate (5 mM) after ultraviolet (UV) exposure before staining for p-RPA foci was performed.

Reference:

1. Murr, R. *et al*. Histone acetylation by Trrap-Tip60 modulates loading of repair proteins and repair of DNA double-strand breaks. *Nat. Cell. Biol.* **8**, 91-99 (2006).
2. Pierce, A. J., Johnson, R. D., Thompson, L. H. & Jasin, M. XRCC3 promotes homology-directed repair of DNA damage in mammalian cells. *Genes Dev.* **13**, 2633-2638 (1999).

3. Nakanishi, K. *et al*. Human Fanconi anemia monoubiquitination pathway promotes homologous DNA repair. *Proc. Natl. Acad. Sci. SA* **102**, 1110-1115 (2005).
4. Ziv, Y. *et al.* Chromatin relaxation in response to DNA double-strand breaks is modulated by a novel ATM-and KAP-1 dependent pathway. *Nat. Cell. Biol.* **8**, 870-876 (2006).
5. Lin, S.Y., Rai, R., Li, K., Xu, Z. Y. & Elledge, S. J. BRIT1/MCPH1 is a DNA damage responsive protein that regulates the Brca1-Chk1 pathway, implicating checkpoint dysfunction in microcephaly. *Proc. Natl. Acad. Sci. USA* **102**, 15105-15109 (2005).
6. Teraoka H., Mikoshiba M., Takase K., Yamamoto K. &Tsukada K. Reversible G1 arrest induced by dimethyl sulfoxide in human lymphoid cell line: dimethyl sulfoxide inhibits IL-6-induced Differentiation of SKW6-CL4 into IgM-Secreting plasma cells. *Experimental Cell Research* **222**, 218-224 (1996)
7. Rai, R. *et al*. BRIT1 regulates early DNA damage response, chromosomal integrity, and cancer. *Cancer Cell* **10**, 145-157 (2006).

nature cell biology

Epidermal growth factor-like domain 7 (EGFL7) modulates Notch signalling and affects neural stem cell renewal

Mirko H.H. Schmidt[1,2,3], Frank Bicker[2], Iva Nikolic[2], Jeannette Meister[2], Tanja Babuke[1], Srdjan Picuric[1], Werner Müller-Esterl[1], Karl H. Plate[2] & Ivan Dikic[1,3]

Epidermal growth factor-like domain 7 (EGFL7) is a secreted factor implicated in cellular responses such as cell migration and blood vessel formation; however the molecular mechanisms underlying the effects of EGFL7 are largely unknown. Here we have identified transmembrane receptors of the Notch family as EGFL7-binding molecules. Secreted EGFL7 binds to a region in Notch involved in ligand-mediated receptor activation, thus acting as an antagonist of Notch signalling. Expression of EGFL7 in neural stem cells (NSCs) *in vitro* decreased Notch-specific signalling and consequently, reduced proliferation and self-renewal of NSCs. Such altered Notch signalling caused a shift in the differentiation pattern of cultured NSCs towards an excess of neurons and oligodendrocytes. We identified neurons as a source of EGFL7 in the brain, suggesting that brain-derived EGFL7 acts as an endogenous antagonist of Notch signalling that regulates proliferation and differentiation of subventricular zone-derived adult NSCs.

The Notch signalling pathway governs metazoan development, as Notch receptors and their cognate ligands submit decisions of cell fates to neighbouring cells[1]. Their role in neural development and neurodegeneration has been well described[1,2]. The four known receptor precursors in vertebrates have a molecular mass of approximately 300,000 (M_r 300K) and share a common architecture[3–5], with multiple extracellular EGF-like repeats[6]. Of particular importance are repeats 11 and 12, as their binding to Notch ligands[7] of the Delta[8] or Jagged[9] type is crucial for receptor activation[10]. A degenerated EGF-like motif within these ligands termed DSL domain[11] is required for Notch activation[3,12]. Binding induces a series of cleavage events in Notch receptors mediated by ADAM metalloproteases and γ-secretase-presenilin[13,14]. Subsequently, Notch intracellular domains (NICD) translocate into the nucleus of the receptor-presenting cell[15] and associate with CBF1/RBP-Jk[16], converting this repressor into an activator of transcription. Eventually, gene repressors such as *Hes* and *Herp* are activated[17,18], causing downregulation of proneural genes[19] and inhibition of neuronal differentiation[17].

EGFL7, which has been described recently, is secreted by endothelial cells and is implicated in the regulation of blood vessel formation and cell migration[20–22]. The 30K molecule is expressed in actively proliferating vasculature but is absent from mature blood vessels[21]. EGFL7 is modularly assembled and consists of a signal sequence, followed by an Emilin-like domain (EMI) and two EGF-like domains (Fig. 1a). Many signalling cascades are involved in both angiogenesis and neural development[23]. Here we add to this emerging concept by providing evidence that EGFL7 interacts with receptors of the Notch family and acts as an antagonist of the Notch signalling pathway in cultured NSCs.

The extracellular domains of Notch1–4 were identified as EGFL7-interacting molecules in yeast two-hybrid screens using human EGFL7 without signal sequence as bait. Isolated Notch domains were back-transformed into yeast together with various EGFL7 constructs and tested for positive interactions by β-galactosidase assays (Fig. 1b). EMI and both EGF-like domains of EGFL7 were necessary and sufficient for Notch binding. As a control, the extracellular domain of Notch1 was split into two and screened against EGFL7. Only the amino-terminal half interacted with EGFL7 (Supplementary Information, Fig. S1a). Glutathione-S-transferase (GST) pulldown assays demonstrated that constructs containing EMI and/or EGF-like domains precipitated Notch1 to varying degrees (Fig. 1c). The isolated EMI domain was the most potent Notch1 interactor but binding was strengthened by EGF-like domains. Human low-density lipoprotein receptor (hLDLR) and rat Jagged1 (rtJag1), which were used as negative controls, did not interact with GST–EGFL7 (Supplementary Information, Fig. S1b).

Murine Notch1–4 receptors were expressed in HEK293 and tested for binding to co-expressed Flag- or V5-tagged human EGFL7. Notch

[1]Institute of Biochemistry II, Johann Wolfgang Goethe University School of Medicine, Theodor-Stern-Kai 7, D-60590 Frankfurt am Main, Germany. [2]Institute of Neurology, Johann Wolfgang Goethe University School of Medicine, Heinrich-Hoffmann-Str. 7, D-60528 Frankfurt am Main, Germany.
[3]Correspondence should be addressed to I.D. or M.H.H.S. (e-mail: Ivan.Dikic@biochem2.de; Mirko.Schmidt@kgu.de)

Received 26 November 2008; accepted 13 March 2009; published online 7 June 2009; DOI: 10.1038/ncb1896

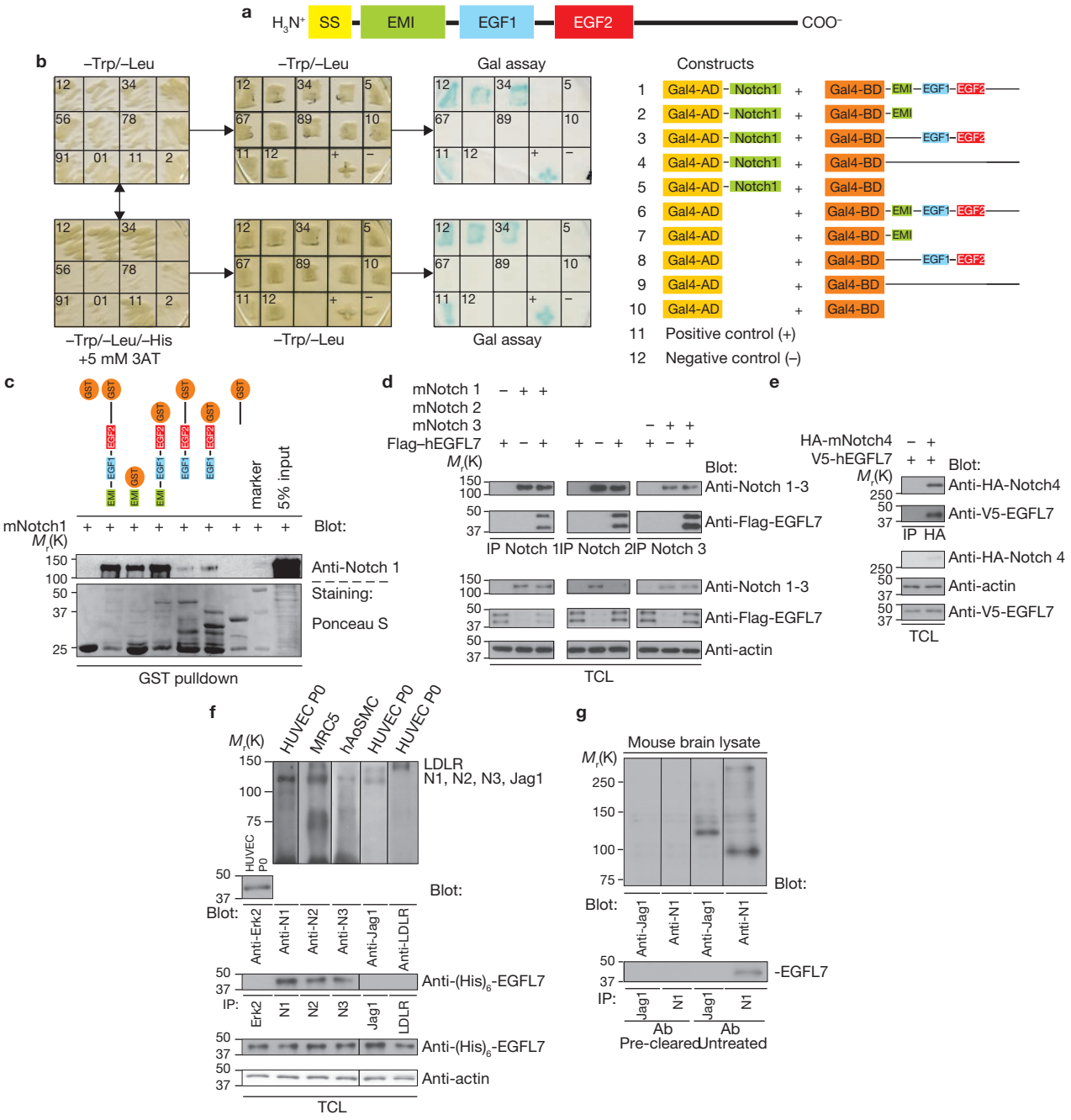

Figure 1 EGFL7 binds to Notch receptors. (**a**) Modular assembly of EGFL7. An N-terminal signal sequence (SS) targets the protein for secretion. It is followed by a cysteine-rich Emilin-like domain (EMI) and two EGF-like domains. The more C-terminal domain is Ca^{2+}-dependent. (**b**) Yeast two-hybrid screens identified the extracellular domains of Notch molecules as EGFL7-binding peptides. Transformation of various human EGFL7 constructs fused to Gal4-BD together with the fished Gal4-AD-Notch1 chimaeras revealed that full-length EGFL7 (1), the isolated EMI domain (2) and the EGF-like domains (3) bind to human Notch1, but the isolated C terminus of EGFL7 (4) does not. (**c**) Various EGFL7 constructs fused to GST were produced in bacteria and coupled to sepharose beads. Murine Notch1 was overexpressed in HEK293 cells, which were collected 48 h after transfection. GST–EGFL7 fusion proteins coupled to beads were added to the cell lysates and incubated over night at 4°C. Precipitates were analysed by immunoblotting. Full-length EGFL7 and a construct comprising EMI plus EGF-like domains bound Notch1 most strongly, followed by the isolated EMI domain and the EGF-like domains. (**d**) Murine Notch1, 2 and 3 constructs were co-expressed with Flag-tagged EGFL7 in HEK293 cells. Co-immunoprecipitation studies verified the Notch–EGFL7 interaction in a mammalian expression system. (**e**) V5-tagged EGFL7 interacted with murine Notch4 harbouring an HA tag within EGF-like domain 5, upon expression in HEK293 cells and immunoprecipitation by anti-HA antibody. (**f**) Recombinant (His)6 tagged EGFL7 (1 μg/ml) was applied to cell lines expressing significant levels of human Notch1, -2 or -3 (N1, N2, N3) in the absence of cross-linker. Cells were lysed and co-immunoprecipitation studies using Notch isoform-specific antibodies revealed an interaction of endogenous human Notch1, -2 and -3 with recombinant human EGFL7. Erk2-, Jagged1- and LDLR-immunoprecipitates did not contain EGFL7. Jagged1- and LDLR-immunoprecipitates were performed from the same lysates with a time-lag of a few days. Loading controls shown were run in parallel on the same gel. (**g**) Mouse brain lysates were prepared and used for Notch1 co-immunoprecipitation studies. After immunoprecipitatin of Notch1, endogenous EGFL7 was readily detectable, whereas immunoprecipitation of Jagged1 did not produce a signal. Pre-clearance of antibodies with 5 μg recombinant Notch1 or Jagged1 verified the specificity of the bands retrieved by immunoprecipitatin from brain lysates. Full scans of key western blots are shown in Supplementary Information, Fig. S8. HRP, horse radish peroxidase; TCL, total cell lysate.

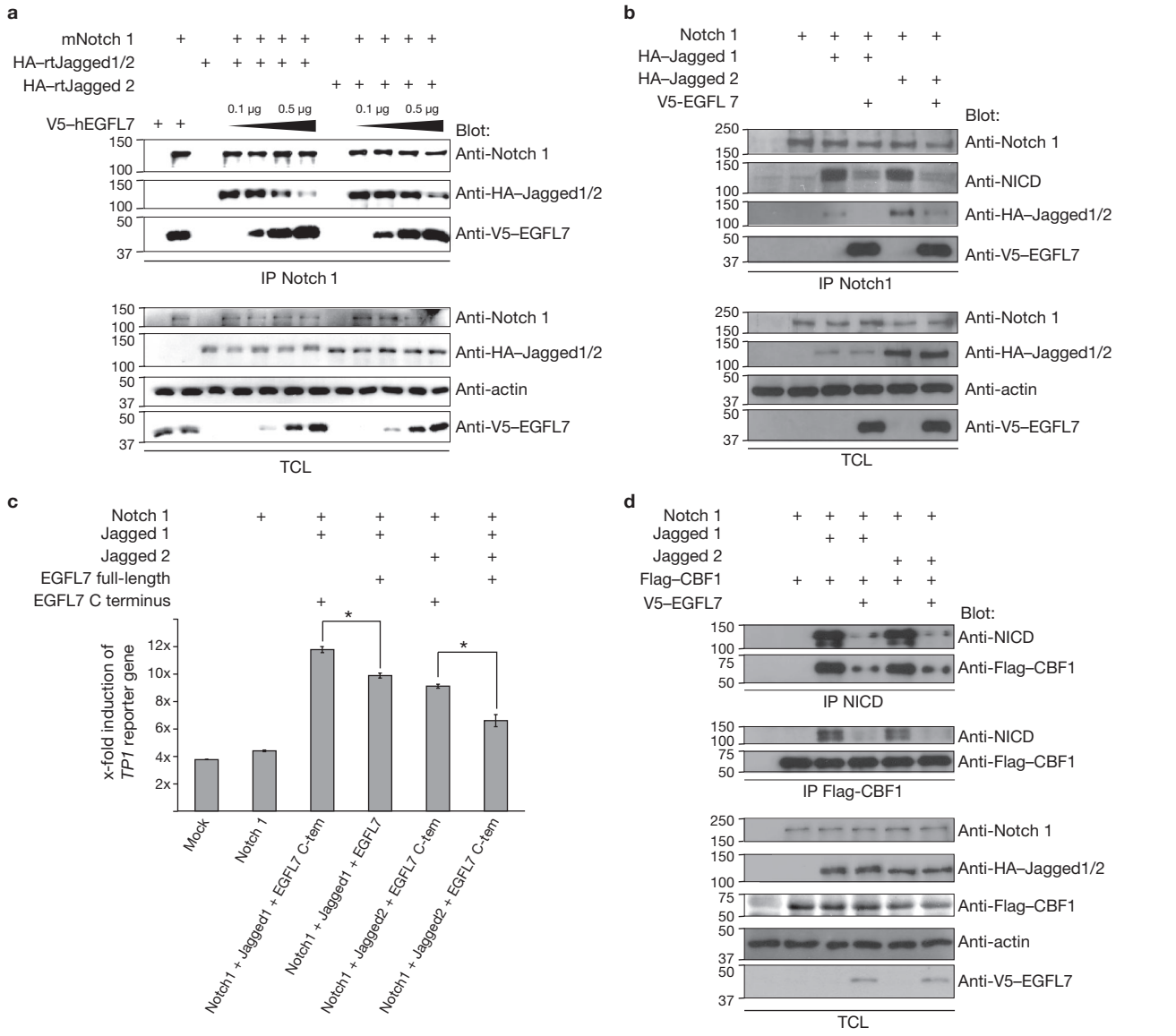

Figure 2 EGFL7 antagonizes canonical Notch1 signalling. (**a**) Co-expression of increasing amounts of human EGFL7 in HEK293 cells reduced the amounts of rat Jagged1/2 that co-immunoprecipitated with murine Notch1. (**b**) Under similar conditions co-expression of EGFL7 reduced the amount of murine Notch1 activated by rat Jagged1/2 by 72% and 84%, respectively. Results were quantified by densitometry after immunoblotting of activated Notch1 with a specific antibody recognizing a newly formed epitope exposed after cleavage of Notch1 by γ-secretase-presenilin (α-NICD). (**c**) This assay was repeated under co-expression of the TP1-firefly luciferase reporter and β-galactosidase for normalization purposes. Cells were collected 12 h after transfection. Comparing EGFL7 and a deletion mutant lacking EMI and EGF-like domains (EGFL7 C terminus), which cannot bind Notch1, we found that full-length human EGFL7 reduced rat Jagged1/2-induced murine Notch1 signalling (mean ± s.d., n = four independent experiments, $^*P < 0.001$). (**d**) Upon activation of Notch receptors, the C terminus is cleaved off and associates with CBF1 in the nucleus to form an active transcription factor complex. EGFL7 reduced the amount of active Notch1 and the transcriptional active Notch1–CBF1 complex, as shown by co-immunoprecipitation. Full scans of key western blots are shown in Supplementary Information, Fig. S8.

receptors were immunoprecipited using specific antibodies that had been tested previously for specificity (Supplementary Information, Fig. S1c). Detection of receptors and EGFL7 by immunoblotting using Flag or V5 tags revealed binding of EGFL7 to Notch1–4 (Fig. 1d, e). Increasing amounts of Notch1 precipitated increasing amounts of EGFL7 (Supplementary Information, Fig. S1d) and binding was retained on expression of EGFL7 and Notch1 in apposing cells (Supplementary Information, Fig. S1e). Control receptors containing varying numbers of EGF-like domains did not interact with EGFL7 (Supplementary Information, Fig. S1f).

The interaction strength between EGFL7 and Notch1 was quantified using hIgG-tagged Notch1-coated dishes incubated with increasing amounts of purified EGFL7, which was detected by anti-$(His)_6$ primary and HRP-coupled secondary antibodies. Conversion of the HRP-substrate TMB and measurement of absorbance at 370 nm gave a K_D of 28.57 nM for the Notch1–EGFL7 interaction (Supplementary Information, Fig. S1g).

Recombinant human EGFL7 (1 µg ml^{-1}) was added to the medium covering HEK293 cells transfected with Notch1–3. Cell surface proteins were crosslinked using DTSSP and biotinylated by sulpho-NHS-LC-biotin.

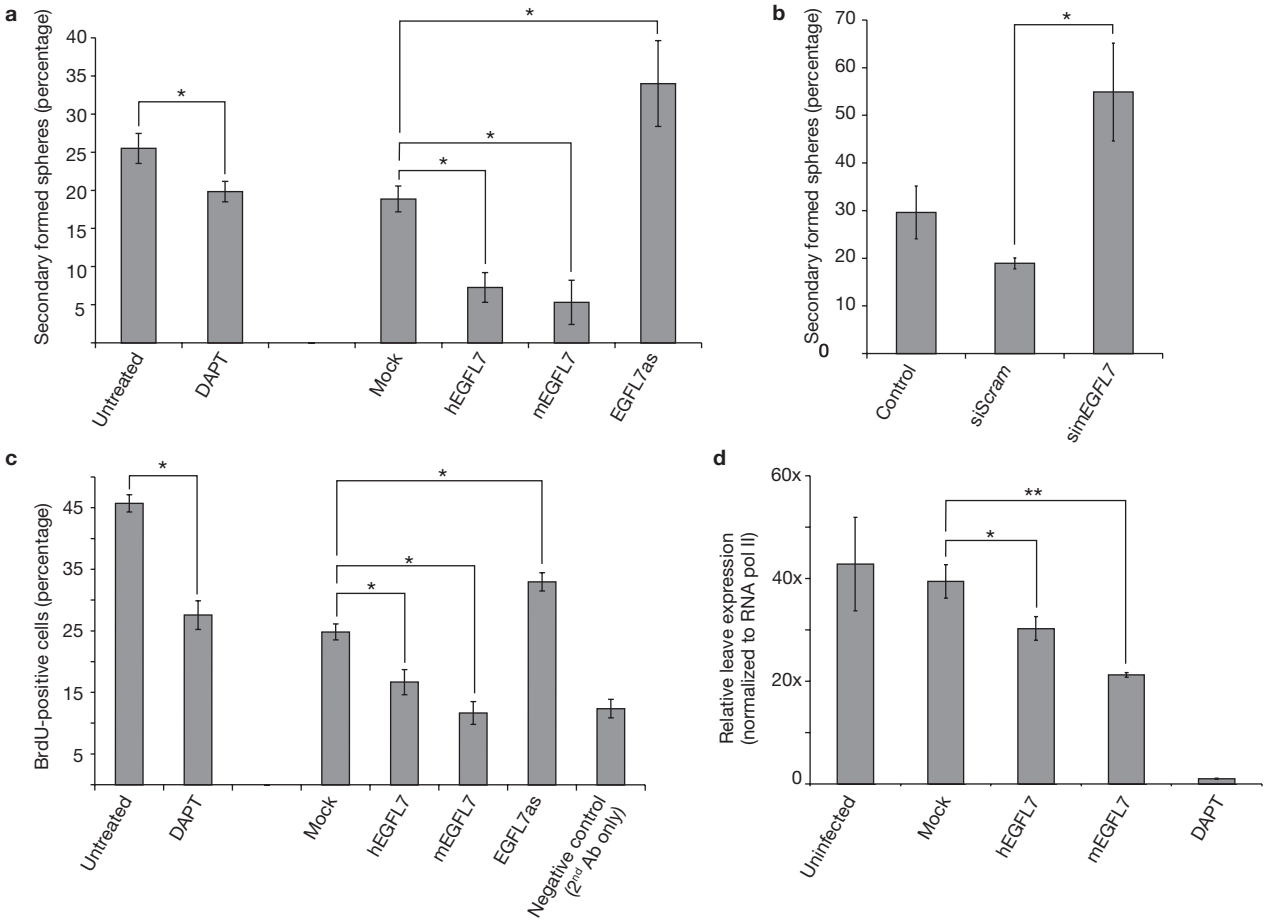

Figure 3 EGFL7 impairs NSC self-renewal. (**a**) Infection of neurospheres with adenovirus encoding human and mouse EGFL7, or application of DAPT (0.1 μM), a synthetic inhibitor of Notch processing and signalling, significantly decreased the self-renewal potential of NSC (mean ± s.d., n = three independent experiments, $^*P < 0.05$) as measured in secondary formed neurospheres. EGFL7 antisense increased NSC self-renewal, compared with mock (empty virus). (**b**) Application of murine *EGFL7*-specific siRNA increased the NSC self-renewal potential (mean ± s.d., n = three independent experiments, $^*P < 0.005$). (**c**) Measurement of BrdU incorporation by FACS revealed that the decreased NSC renewal was caused by a decreased proliferation rate (mean ± s.d., n = three independent experiments, $^*P < 0.001$). (**d**) Quantitative RT–PCR of the Notch activated gene product Hes5 of infected as well as DAPT-treated (1 μM) neurospheres revealed that EGFL7 and DAPT reduced the amount of Hes5 production (mean ± s.d., n = three independent experiments, $^*P < 0.05$, $^{**}P < 0.005$).

Post-lysis Notch receptor isoforms were immunoprecipitated in a first round using specific antibodies and were released from immunoprecipitation beads by acidic glycine buffer (pH 2.7). This supernatant underwent a second round of precipitation using streptavidin-coated beads. The purified cell surface Notch receptors bound to recombinant EGFL7, indicating that both molecules associated at the cellular surface (Supplementary Information, Fig. S2a).

To discriminate between mature and precursor EGFL7 we cloned a V5-tag N-terminal to the signal sequence of human EGFL7, which delayed processing and resulted in two bands of about 50K (immature form) and 37K (mature form) on expression in HEK293 cells (Supplementary Information, Fig. S2b). Surface-exposed Notch receptors were crosslinked with DTSSP as described above and cells were lysed in RIPA buffer to disrupt non-covalent interactions. Upon Notch immunoprecipitation, only the small form of EGFL7 was recovered, which we suggest to be the secreted form (Supplementary Information, Fig. S2c).

Cell surface binding of EGFL7 to Notch1 was further analysed by incubation of HEK293 cells permanently expressing Notch1 with recombinant $(His)_6$-tagged EGFL7 or Jagged1. Proteins binding to the cellular surface were detected by a combination of anti-$(His)_6$ primary and APC-conjugated anti-mIgG secondary antibodies. Complexes were visualized by FACS. EGFL7 and Jagged1 bound to the cell surface of Notch1-transfected HEK293 cells in a comparable manner (Supplementary Information, Fig. S2d). Binding to the cell surface was quantified using an HRP-conjugated secondary antibody. Conversion of the HRP-substrate TMB gave a K_D of 29.63 nM for EGFL7 and 47.26 nM for Jagged1 (Supplementary Information, Fig. S2e).

Endogenous Notch1, Jagged1 and hLDLR (from HUVECs), Notch2 (from MRC5) and Notch3 (from hAoSMC) were analysed for EGFL7 binding (Fig. 1f). Recombinant EGFL7 (1 μg ml^{-1}) was applied to cells; Erk2, Jagged1 and LDLR served as internal negative controls. Recombinant EGFL7 associated with only endogenous Notch1–3 in co-immunoprecipitations, as detected by immunoblotting (Fig. 1f). Furthermore, mouse brain-derived endogenous Notch1 specifically interacted with EGFL7 (Fig. 1g).

To map the interaction sites in both EGFL7 and Notch receptors, partial constructs of EGFL7 were fused with GFP and co-expressed

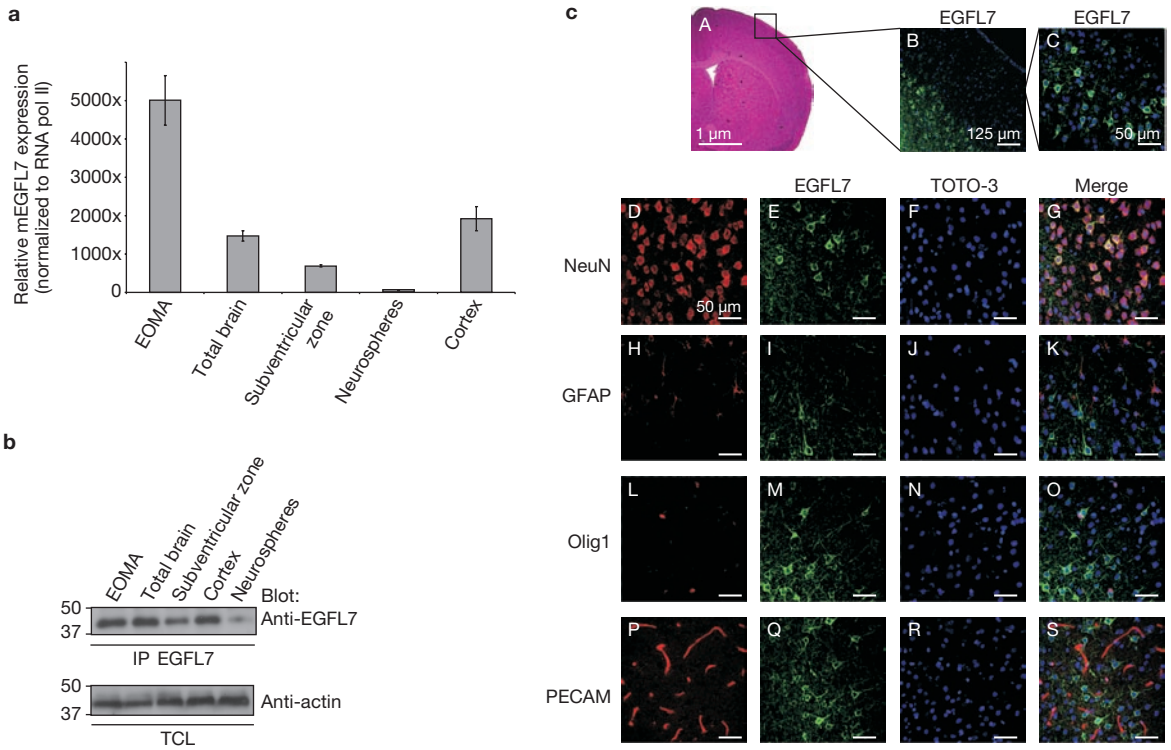

Figure 4 EGFL7 is expressed in a subtype of neurons in the adult mouse brain. (**a**) Quantitative RT–PCR of murine *EGFL7* in various regions of the mouse brain revealed that it is highly expressed in the cortex but is less expressed in the subventricular zone. In cultured neurospheres isolated from the subventricular zone, EGFL7 is expressed at low levels. (**b**) Endogenous EGFL7 was immunoprecipitated from various brain tissues and the local protein concentration was comparable to the amounts suggested by quantitative RT–PCR. Full scans of western blots are shown in Supplementary Information, Fig. S8. (**c**) Immunohistochemical staining of mouse brain sections (A) using an EGFL7-specific antibody revealed a high signal in a subset of cortical cells (B, C). Triple stainings were performed using cell-line-specific markers, such as the neuronal marker NeuN (D), the astrocyte marker GFAP (H), the oligodendrocyte marker Olig1 (L) or the endothelial marker PECAM (P) together with EGFL7 (E, I, M, Q). Cell nuclei were stained with TOTO-3 (F, J, N, R). Triple-positive cells were detected only in case of staining with the neuronal marker NeuN (G) but not with GFAP (K), Olig1 (O) or PECAM (S). The data suggest that neurons are the source of brain-derived EGFL7. Scale bars, 50 µm in panels D to S.

together with murine Notch1 in HEK293 cells (Supplementary Information, Fig. S3a). Co-immunoprecipitations revealed that constructs containing an EMI domain were able to interact strongly with Notch1. EGF-like domains alone bound weakly but supported binding of EMI to Notch1, indicating a binding triade of EMI and EGF-like domains. Deletion mutants of EGFL7 strengthened this conclusion (Supplementary Information, Fig.S3b). Similarly, EGF-like domain-containing regions of Notch1–4 were fused with GFP. Upon co-expression of these chimaeras with Flag-tagged EGFL7 in HEK293 cells and subsequent immunoprecipitation of the GFP-tagged Notch domains, a strong interaction with EGFL7 was observed (Supplementary Information, Fig. S3c).

Our data indicate that EGFL7 might compete with the binding of known ligands to Notch receptors. When Jagged1 or Jagged2 was co-expressed with Notch1 in HEK293 cells, EGFL7 effectively competed with this interface (Fig. 2a), an effect also seen in apposing cells transiently (Supplementary Information, Fig. S4a) or permanently (Supplementary Information, Fig. S4b) transfected with each construct. Ternary complexes between Notch1, Jagged1 and EGFL7 were not detected (Supplementary Information, Fig. S4c). This finding offers the possibility that EGFL7 modulates Notch signalling itself. The formation of NICD upon Jagged1 and Jagged2 binding to Notch1 was measured by immunoblotting and found to be decreased (Fig. 2b) by 72% (Jagged1) and 84% (Jagged2) in the presence of EGFL7. Similar data was obtained for HEK293 cells transfected with Notch1 and seeded on Jagged1-coated dishes in the presence of recombinant EGFL7 (Supplementary Information, Fig. S4d). Notch reporter gene assays based on *TP1* promoter-driven luciferase[24] showed that EGFL7 decreased Jagged1/Jagged2-induced Notch signalling by 30% (Fig. 2c). An EGFL7 construct lacking the Notch-binding triade (termed EGFL7 C terminus) served as a negative control. Similarly, coated Jagged1 showed reduced Notch signalling in the presence of EGFL7 (Supplementary Information, Fig. S4e, f). Finally, the amount of NICD in complex with its nuclear binding partner CBF1 was reduced by EGFL7 (Fig. 2d).

NSC self-renewal in neurosphere culture depends strictly on Notch1 and its ligand Jagged1 in preparation of NSCs from the subventricular zone[25]. Our data suggest an antagonistic effect of EGFL7 on Jagged1-induced Notch1 signalling. Mouse-derived neurospheres were infected using an adenovirus approach. Infected neurospheres expressed EGFL7 of human and mouse origin, whereas endogenous EGFL7 was ablated by almost 100% by expression of the antisense construct (Supplementary Information, Fig. S5a). Human and mouse EGFL7 reduced the number of secondary formed spheres by 64% or 74%, compared with mock (empty virus)-infected cells (Fig. 3a). Recombinant EGFL7 decreased NSC self-renewal by 67% under similar conditions (Supplementary Information, Fig. S5b). Infection with EGFL7 antisense raised the self-renewal potential of NSC by

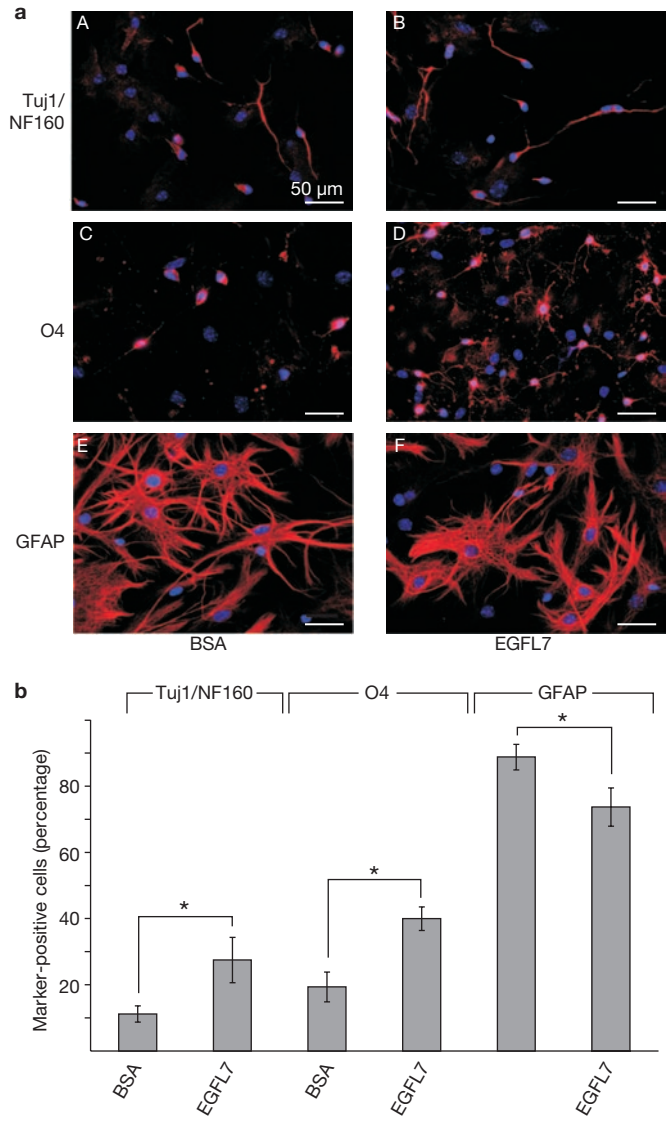

Figure 5 EGFL7 affects NSC differentiation. (**a**) Coverslips were coated with 10 μg ml^{-1} BSA (A, C, E) or EGFL7 (B, D, F). Two-day-old neurospheres were seeded on these coverslips and were allowed to differentiate for 12 days. Staining for neurons (Tuj1/NF160, A, B), oligodendrocytes (O4, C, D) and astrocytes (GFAP, E, F) suggested an increase in the amount of neurons (B) and differentiated oligodendrocytes (D) on EGFL7-coated coverslips, as compared with control (C). Scale bars, 50 μm in panels A to F. (**b**) Quantitative analysis of the total amount of individual cell types formed after differentiation revealed a statistically significant increase (mean ± s.d., $n = 15$ independent experiments, $^*P < 0.005$) in the amount of neurons and oligodendrocytes, as well as an equally significant decrease in the amount of astrocytes formed on EGFL7-coated coverslips.

79%, an effect also observed with a murine *EGFL7*-specific siRNA (Fig. 3b). The siRNA quality was checked by quantitative RT–PCR of *mEGFL7* (Supplementary Information, Fig. S5c). Treatment of neurospheres with the Notch silencer DAPT at concentrations of 0.1 μM and 100 μM resulted in decreases in the number of secondary formed spheres by 22% and 81% respectively (Supplementary Information, Fig. S5d). The latter value is comparable to the inhibitory effect produced by infection with EGFL7 (see above). To use a Notch-specific setting, we analysed NSC self-renewal after infection with adenovirus expressing the extracellular domains of human DLL4 (hDll4ec) as a dominant-negative form of this Notch ligand. Further, we expressed a fragment of MamL1, which interferes with NICD–CBF1 binding and specifically silences Notch-induced gene transcription[26]. Both constructs reduced NSC self-renewal similarly to EGFL7 (Supplementary Information, Fig. S5e). The decreased NSC self-renewal caused by infection with EGFL7 was fully reversible by NICD (Supplementary Information, Fig. 5f). Cell proliferation was measured by incorporation of BrdU and quantified by FACS. Clearly, EGFL7 and DAPT decreased cell proliferation, whereas antisense EGFL7 increased it (Fig. 3c), suggesting that Notch signalling is required to maintain NSC proliferation. Apoptosis of NSCs was not altered (Supplementary Information, Fig. S5g).

Endogenous EGFL7 expression was changed in NSCs by Notch signalling, as measured by quantitative RT–PCR (Supplementary Information, Fig. S5h). Inhibition of Notch signalling by DAPT increased EGFL7 expression more than fivefold, offering the possibility of a negative-feedback loop. This concept was further strengthened by quantification of mEGFL7 expression in neurospheres after inhibition of Notch signalling by hDll4ec and dominant-negative MamL1 (Supplementary Information, Fig. S5i), or increased Notch signalling by NICD (Supplementary Information, Fig. S5j).

To determine whether or not EGFL7 acted as an inhibitor of Notch1 signalling in NSCs, we analysed the specific Notch1 target gene *Hes5*. Quantitative RT–PCR of the *Hes5* gene product in NSCs infected with adenovirus or treated with DAPT (1 μM) revealed that mouse EGFL7 reduced *Hes5* transcription by 50% (Fig. 3d), whereas DAPT completely abrogated *Hes5* translation. Similarly, hDll4ec and the MamL1 fragment decreased *Hes5* transcription by an amount comparable to the effect of EGFL7 (Supplementary Information, Fig. S5k), whereas siRNA against mEGFL7 increased *Hes5* transcription (Supplementary Information, Fig. S5l). Soluble and coated EGFL7 affected Hes5 signalling in NSC to comparable degrees (Supplementary Information, Fig. S6a).

The observed effects of EGFL7 on NSCs prompted us to analyse expression of EGFL7 in the brain. Quantitative RT–PCR of murine EGFL7 revealed that mouse brain, especially the cortex, contained significant amounts of EGFL7 (Fig. 4a). In contrast, transcription of EGFL7 in the subventricular zone and cultured neurospheres was low. Immunoprecipitation of mEGFL7 from brain tissues confirmed our qRT–PCR findings (Fig. 4b). Immunohistochemical staining of mouse brain sections with an EGFL7-specific antibody identified EGFL7-positive cells in the cortex (Fig. 4c, panels B, C). EGFL7-positive cells were co-stained with the neuronal marker NeuN (Fig. 4c, panel G), the astrocyte marker GFAP (Fig. 4c, panel K), the oligodendrocyte marker Olig1 (Fig. 4c, panel O) and the blood vessel marker PECAM (Fig. 4c, panel S). Confocal microscopy identified only EGFL7 plus NeuN double-positive cells, indicating that neurons are the major source of EGFL7 in the cortex.

According to current models, Notch signalling favours differentiation of neural precursors into astrocytes[27,28]. To analyse differentiation effects of EGFL7 on NSCs, coverslips were coated with 10 μg ml^{-1} bovine serum albumin (BSA) or recombinant EGFL7. Neurospheres were allowed to differentiate on these coated coverslips, which were stained with neuronal (Tuj1/NF160), oligodendrocytal (O4) and astrocytal (GFAP) markers (Fig. 5a). An increase in the number of

neurons (Fig. 5a, panels A, B) and in the number and differentiation state of oligodendrocytes (Fig. 5a, panels C, D) were observed on EGFL7-coated coverslips. These changes were statistically significant ($P < 0.005$ s.d.; Fig. 5b). Infection of NSCs with adenovirus encoding EGFL7 caused a comparable effect, whereas infection with EGFL7 antisense had an opposing effect (Supplementary Information, Fig. S6b). Treatment of NSCs with DAPT increased the number of neurons and oligodendrocytes but decreased the amount of astrocytes (Supplementary Information, Fig. S6c). Differentiating NSCs produced significantly less *Hes5* in the presence of EGFL7 and DAPT (Supplementary Information, Fig. S6d). Moreover, EGFL7 affected PC12 cells, which produce the neuronal cell marker β-III tubulin in a Notch-dependent manner[29] when seeded on collagen[30]. EGFL7 induced neuronal marker expression in PC12 similarly to collagen (Supplementary Information, Fig. S6e). Analysis of *Hes5* expression in differentiated and non-differentiated NSCs by qRT–PCR showed that the gene was upregulated 8-fold in non-differentiated NSCs (Supplementary Information, Fig. S6f), whereas EGFL7 expression was 80-fold higher in differentiated NSCs (Supplementary Information, Fig. S6g). The antagonistic expression of EGFL7 and Hes5 in neurospheres indicates that EGFL7 may oppose Notch signalling during differentiation of NSC.

In the present study we have described EGFL7 (refs 20, 22) as an antagonist of Notch receptor-mediated signalling. EGFL7 is the first ever described naturally occurring, secreted, functional antagonist of Notch receptors. We were able to show that EGFL7 interacts with all four subtypes of Notch receptors. Triggering of Notch receptor signalling requires dissociation of the Notch heterodimer before proteolysis, which is promoted by ligand endocytosis[31,32]. The observed inhibition of Notch signalling by EGFL7 can thus be explained. As EGFL7 is a soluble protein, it cannot create mechanical forces and is not able to effectively separate the Notch heterodimer. Furthermore, EGFL7 competed with Notch ligands of the Jagged type, perhaps by binding to an overlapping region. This closely resembles the effects of soluble DSL ligands, which are not as potent as their corresponding membrane-integral ligands[33] in stimulating Notch and may act as antagonists[34]. However, inhibitory effects of EGFL7 seem specific for Jagged-type ligands, as preliminary data suggest selective binding of EGFL7 and Dll4 (Supplementary Information, Fig. S7).

Notch signalling determines the number of NSCs *in vitro* and *in vivo*[35] dependent on the interaction between Notch1 and Jagged1[25]. Consequently, EGFL7 as an antagonist of Jagged1 reduced the self-renewing capacity of NSCs and was mostly excluded from the subventricular zone *in vivo*. On mobilization of NSCs from the subventricular zone, cells could meet neuronal EGFL7 hotspots in the striatum that trigger differentiation rather than proliferation. Interestingly, as Notch1 signalling defines the differential outcome of stem cell populations[36] and favours gliogenesis over neurogenesis, repression of Notch signalling by seeding neurospheres on EGFL7-coated coverslips reversed this effect and NSCs differentiated into increasing numbers of neurons and oligodendrocytes at the expense of astrocytes. The most striking phenotype was observed for oligodendrocytes. Differentiation of oligodendrocytes depends on an intact Notch1–Jagged1 interface[37], and the effect of EGFL7 on NSC differentiation might be caused by the same mechanism underlying its negative effect on NSC self-renewal. Our hypothesis that EGFL7 has a specific role in mature neurons was supported by a recent study[38]. The group compiled a mouse transcriptome database of more than 20,000 genes at various postnatal ages between postnatal day 1 (P1) and P30. EGFL7 was among the top 4% of genes specifically upregulated in mature neurons between P1 and P30. Taken together, our work presents evidence that EGFL7 has a previously unrecognized role in the neural system by modulating Notch signalling in adult NSCs. □

METHODS

Methods and any associated references are available in the online version of the paper at http://www.nature.com/naturecellbiology/

Note: Supplementary Information is available on the Nature Cell Biology website.

ACKNOWLEDGEMENTS

We thank all our colleagues who provided constructs. Thanks to Julio Granados, Yonathan Lissanu Deribe and Koraljka Husnjak for initial help with the yeast two-hybrid system. Thanks to Verdon Taylor for helpful suggestions, Ruth von Laer for help with FACS analysis and Stefan Momma and David G. McEwan for comments on the manuscript. This work was financially supported by the DFG within the SFB Transregio 23, subproject A4 and the Excellence Cluster Cardiopulmonary System, by the Adolf Messer Foundation, by the Paul and Ursula Klein Foundation, and an EMBO long-term fellowship granted to M.H.H.S. (ALTF 2003-881).

AUTHOR CONTRIBUTIONS

M.H.H.S. and I.D. designed experiments, analysed data and wrote the manuscript; I.D. supervised biochemical research; M.H.H.S. performed biochemical experiments and supervised neural and vascular experiments; F.B. worked on neurospheres and did IHC; I.N. and J.M. did experiments on D114 and HUVEC; T.B. did qRT-PCR; S.P. worked on protein purification; W.M.E. created EGFL7 antibodies and supported biochemical experiments; K.H.P. helped with experiments in brain and vasculature and all authors discsussed the results and commented on the manuscript.

COMPETING INTERESTS

The authors declare that they have no competing financial interest.

Published online at http://www.nature.com/naturecellbiology/
Reprints and permissions information is available online at http://npg.nature.com/reprintsandpermissions/

1. Artavanis-Tsakonas, S., Rand, M. D. & Lake, R. J. Notch signaling: cell fate control and signal integration in development. *Science* **284,** 770–776 (1999).
2. Selkoe, D. & Kopan, R. Notch and Presenilin: regulated intramembrane proteolysis links development and degeneration. *Annu. Rev. Neurosci.* **26,** 565–597 (2003).
3. Weinmaster, G. The ins and outs of notch signaling. *Mol. Cell Neurosci.* **9,** 91–102 (1997).
4. Artavanis-Tsakonas, S., Matsuno, K. & Fortini, M. E. Notch signaling. *Science* **268,** 225–232 (1995).
5. Uyttendaele, H. *et al.* Notch4/int-3, a mammary proto-oncogene, is an endothelial cell-specific mammalian Notch gene. *Development* **122,** 2251–2259 (1996).
6. Weinmaster, G., Roberts, V. J. & Lemke, G. A homolog of *Drosophila* Notch expressed during mammalian development. *Development* **113,** 199–205 (1991).
7. Rebay, I. *et al.* Specific EGF repeats of Notch mediate interactions with Delta and Serrate: implications for Notch as a multifunctional receptor. *Cell* **67,** 687–699 (1991).
8. Muskavitch, M. A. Delta-notch signaling and *Drosophila* cell fate choice. *Dev. Biol.* **166,** 415–430 (1994).
9. Fleming, R. J., Scottgale, T. N., Diederich, R. J. & Artavanis-Tsakonas, S. The gene Serrate encodes a putative EGF-like transmembrane protein essential for proper ectodermal development in Drosophila melanogaster. *Genes Dev.* **4,** 2188–2201 (1990).
10. Ge, C., Liu, T., Hou, X. & Stanley, P. *In vivo* consequences of deleting EGF repeats 8–12 including the ligand binding domain of mouse Notch1. *BMC Dev. Biol.* **8,** 48 (2008).
11. Tax, F. E., Yeargers, J. J. & Thomas, J. H. Sequence of *C. elegans* lag-2 reveals a cell-signalling domain shared with Delta and Serrate of *Drosophila*. *Nature* **368,** 150–154 (1994).
12. Nichols, J. T., Miyamoto, A. & Weinmaster, G. Notch signaling—constantly on the move. *Traffic* **8,** 959–969 (2007).
13. Mumm, J. S. & Kopan, R. Notch signaling: from the outside in. *Dev. Biol.* **228,** 151–165 (2000).
14. Weinmaster, G. Notch signal transduction: a real rip and more. *Curr. Opin. Genet. Dev.* **10,** 363–369 (2000).
15. De Strooper, B. *et al.* A presenilin-1-dependent γ-secretase-like protease mediates release of Notch intracellular domain. *Nature* **398,** 518–522 (1999).

16. Honjo, T. The shortest path from the surface to the nucleus: RBP–J κ/Su(H) transcription factor. *Genes Cells* **1,** 1–9 (1996).
17. Kageyama, R. & Ohtsuka, T. The Notch–Hes pathway in mammalian neural development. *Cell Res.* **9,** 179–188 (1999).
18. Iso, T., Kedes, L. & Hamamori, Y. HES and HERP families: multiple effectors of the Notch signaling pathway. *J. Cell Physiol.* **194,** 237–255 (2003).
19. Bertrand, N., Castro, D. S. & Guillemot, F. Proneural genes and the specification of neural cell types. *Nature Rev. Neurosci.* **3,** 517–530 (2002).
20. Soncin, F. *et al.* VE-statin, an endothelial repressor of smooth muscle cell migration. *EMBO J.* **22,** 5700–5711 (2003).
21. Fitch, M. J., Campagnolo, L., Kuhnert, F. & Stuhlmann, H. Egfl7, a novel epidermal growth factor-domain gene expressed in endothelial cells. *Dev. Dyn.* **230,** 316–324 (2004).
22. Parker, L. H. *et al.* The endothelial-cell-derived secreted factor Egfl7 regulates vascular tube formation. *Nature* **428,** 754–758 (2004).
23. Carmeliet, P. & Tessier-Lavigne, M. Common mechanisms of nerve and blood vessel wiring. *Nature* **436,** 193–200 (2005).
24. Strobl, L. J. *et al.* Both Epstein-Barr viral nuclear antigen 2 (EBNA2) and activated Notch1 transactivate genes by interacting with the cellular protein RBP–Jκ. *Immunobiology* **198,** 299–306 (1997).
25. Nyfeler, Y. *et al.* Jagged1 signals in the postnatal subventricular zone are required for neural stem cell self-renewal. *EMBO J.* **24,** 3504–3515 (2005).
26. Weng, A. P. *et al.* Growth suppression of pre-T acute lymphoblastic leukemia cells by inhibition of notch signaling. *Mol. Cell Biol.* **23,** 655–664 (2003).
27. Louvi, A. & Artavanis-Tsakonas, S. Notch signalling in vertebrate neural development. *Nature Rev. Neurosci.* **7,** 93–102 (2006).
28. Yoon, K. & Gaiano, N. Notch signaling in the mammalian central nervous system: insights from mouse mutants. *Nature Neurosci.* **8,** 709–715 (2005).
29. Levy, O. A., Lah, J. J. & Levey, A. I. Notch signaling inhibits PC12 cell neurite outgrowth via RBP-J-dependent and -independent mechanisms. *Dev. Neurosci.* **24,** 79–88 (2002).
30. Ohuchi, T., Maruoka, S., Sakudo, A. & Arai, T. Assay-based quantitative analysis of PC12 cell differentiation. *J. Neurosci. Methods* **118,** 1–8 (2002).
31. Chitnis, A. Why is delta endocytosis required for effective activation of notch? *Dev. Dyn.* **235,** 886–894 (2006).
32. Le Borgne, R., Bardin, A. & Schweisguth, F. The roles of receptor and ligand endocytosis in regulating Notch signaling. *Development* **132,** 1751–1762 (2005).
33. Shimizu, K. *et al.* Integrity of intracellular domain of Notch ligand is indispensable for cleavage required for release of the Notch2 intracellular domain. *EMBO J.* **21,** 294–302 (2002).
34. Hicks, C. *et al.* A secreted Delta1-Fc fusion protein functions both as an activator and inhibitor of Notch1 signaling. *J. Neurosci. Res.* **68,** 655–667 (2002).
35. Androutsellis-Theotokis, A. *et al.* Notch signalling regulates stem cell numbers *in vitro* and *in vivo*. *Nature* **442,** 823–826 (2006).
36. Morrison, S. J. *et al.* Transient Notch activation initiates an irreversible switch from neurogenesis to gliogenesis by neural crest stem cells. *Cell* **101,** 499–510 (2000).
37. Wang, S. *et al.* Notch receptor activation inhibits oligodendrocyte differentiation. *Neuron* **21,** 63–75 (1998).
38. Cahoy, J. D. *et al.* A transcriptome database for astrocytes, neurons, and oligodendrocytes: a new resource for understanding brain development and function. *J. Neurosci.* **28,** 264–278 (2008).

METHODS

Protein expression, purification and further assays. Recombinant EGFL7 was purified from the total cell lysate of Sf9 cells infected with baculovirus (viral stock >10^8 pfu ml^{-1}) at a multiplicity of infection (MOI) of 5 in complete insect medium. Five days after infection, cells were lysed on ice in hypotonic buffer for 15 min. Lysates were loaded on 5 ml HisTrap FF columns loaded with Ni^{2+} ions that had previously been equilibrated with equilibration buffer (50 mM sodium phosphate (pH 8.0), 500 mM NaCl, 20 mM imidazole). The flow-through was collected and columns washed with 15 column volumes of equilibration buffer. Bound proteins were eluted with elution buffer (50 mM sodium phosphate (pH 8.0), 500 mM NaCl and 500 mM imidazole). Fractions containing recombinant EGFL7 were pooled and desalted by gel filtration on a Sephadex G75 column using an Äkta purifier chromatography system (GE Healthcare). The biological activity of the purified EGFL7 was tested by inhibition of PDGF-induced migration of human aortic smooth muscle cells in a modified Boyden chamber[20].

Secreted proteins from various cell types were precipitated from the supernatant by 10% trichloroacetic acid and 0.1% phosphotungstic acid. After an acetone wash, precipitates were analysed by immunoblotting. Extracellular crosslinking of proteins was performed using 3,3´-dithiobis sulphosuccinimidylpropionate (DTSSP, Pierce), a water-soluble, homobifunctional, thiol-cleavable and membrane-impermeable crosslinker, following the manufacturer's instructions. In brief, cells were incubated on ice with DTSSP (1 mM) for 30 min. The reaction was stopped with glycine (20 mM) for 15 min. After vigorous washing, cell surface biotinylation was performed using EZ-Link sulpho-NHS-LC-biotin (Pierce), according to the manufacturer's guidelines. In brief, cells were incubated on ice and EZ-Link sulpho-NHS-LC-Biotin in PBS (pH 8.0; 5 mM) was added to adherent cells for 2 h. The reaction was stopped with glycine (100 mM) for 15 min. Cells were lysed and used for immunoprecipitation studies (see below).

Pulldown assays. For immunoprecipitation studies, cells were lysed in ice-cold Triton X-100 lysis buffer (50 mM HEPES (pH 7.4), 150 mM NaCl, 1% Triton X-100, 10% glycerol, 1.5 mM $MgCl_2$, 1 mM EDTA, 1 mM EGTA, 1 mM sodium orthovanadate, 20 mM NaF, 1 mM PMSF, 10 μg ml^{-1} aprotinin, 2 μg ml^{-1} leupeptin, and 10 μM $ZnCl_2$) or RIPA buffer (lysis buffer containing 0.5% sodium deoxycholate and 0.1% sodium dodecyl sulphate). Lysates were cleared at 4 °C by centrifugation at 16,200*g* for 20 min and subsequently incubated with antibody for 2 h at 4 °C while rotating. Protein–antibody complexes were collected by incubation with protein A-agarose (Roche) for another 2 h followed by centrifugation and three washing steps with lysis buffer.

For GST pulldowns, HEK293 cells were transiently transfected with target protein-encoding plasmids and after 48 h lysed in Triton X-100 lysis buffer (see above). Lysates with adjusted protein concentrations, as determined by the micro BCA protein assay kit (Pierce), were incubated with equal amounts of GST proteins coupled to glutathione Sepharose 4B beads (GE Healthcare), and were incubated overnight at 4 °C under rotation. The next day, beads were precipitated, vigorously washed, boiled in sample buffer and analysed by western blotting.

For western blot analysis, all precipitates were boiled at 95 °C for 5 min in SDS-containing sample buffer, resolved by standard SDS–PAGE, blotted on nitrocellulose membranes and probed with the indicated antibodies. Antibody complexes were detected using horseradish peroxidase-conjugated secondary antibodies and ECL substrate (Santa Cruz Biotechnology).

Yeast two-hybrid system. Human EGFL7 lacking its signal sequence (termed EGFL7 full-length) and EGFL7 domains were cloned into the vector pYTH9 to create fusion proteins with the DNA-binding domain of the Gal4 transcription factor. EGFL7–pYTH9 was introduced into the yeast strain Y190 and screened against human fetal brain, spleen, thymus and kidney cDNA libraries (Clontech). Subdomains of EGFL7 in pYTH9 were transformed into Y190 together with putative binding partners identified by library screens in order to identify the corresponding binding sites within EGFL7.

Construction of adenoviral expression vectors. Adenoviral expression systems were created by cloning human and mouse EGFL7, a corresponding antisense structure, constitutively active murine Notch1 (amino acids 1739–2526) or dominant-negative human Dll4 (amino acids 1–528) and human MamL1 (amino acids 11–74) into the multiple cloning site of a modified version of the adenoviral transfer plasmid pDC515, provided by Andreas Simm (Martin Luther University, Germany) . This plasmid contains an IRES site plus EGFP (derived from pIRES2–EGFP, Clontech) 3´ to the MCS. EGFP served as an internal infection control for the purified recombinant adenoviruses. Infectious particles were created by co-transfection of pDC515–EGFL7 with the adenoviral packaging vector pBHGfrt(del)E1,3FLP into E1a-transformed HEK293 cells[39]. After 14–20 days infectious particles were collected. The titres of the adenoviral preparations were approximately one plaque-forming unit per 500 particles. Viruses were applied to NSCs at a concentration of 50 particles per cell.

Neurosphere cultures and assays. Primary cultures were prepared from the brain of adult C57bl6 mice (6–8 weeks old) by preparation of the lateral wall of the lateral ventricles. Tissue was dissociated in papain (0.8 mg ml^{-1}; Worthington) in Leibovitz´s L-15 medium containing 400 U DNaseI and 0.5 mM EDTA. Cells were centrifuged at 1,000*g* for 3 min, suspended in neurosphere medium (DMEM/Hams-F12 1:1 plus glutamax, B27 supplement, 10 mM HEPES (pH 7.4) and 2 mM L-glutamine) containing 20 ng ml^{-1} EGF, 20 ng ml^{-1} FGF, 100 U ml^{-1} penicillin and 100 μg ml^{-1} streptomycin and cultured in tissue culture dishes at 37 °C. Primary neurosphere cultures were collected 7–9 days after plating by centrifugation at 1,000*g* for 3 min. Spheres were suspended in Accutase in Dulbecco's PBS containing 0.5 mM EDTA (PAA), incubated for 10 min at 37 °C and gently triturated to aid dissociation. Cells were centrifuged, suspended in neurosphere medium supplemented as above, plated in tissue culture flasks and incubated at 37 °C and 5% CO_2. Secondary and proximate neurosphere cultures were split 5 days after plating. Subsequent assays were performed using cells up to passage five.

To determine the NSC self-renewal potential, neurosphere cultures were infected with adenovirus three days after passage. After two days, cells were dissociated, plated at clonal density (100 cells/cm^2 or 0.5 cells μl^{-1}, respectively) and the number of secondary formed neurospheres was determined after five days[40]. The proliferation capacity of neurospheres was analysed by measurement of BrdU incorporation. Two days after infection, freshly dissociated neurospheres were treated with 5-bromo-2-deoxyuridine (BrdU, 20 μg ml^{-1}) for 12 h. Cells were then dissociated, fixed for 20 min in 70% ethanol at –20 °C and stained with anti-BrdU antibody and Alexa568-conjugated goat anti-mouse IgG (Molecular Probes). BrdU incorporation was quantified by FACS analysis (FACSCalibur, BD). Similarly, apoptosis of neurosphere cells was determined by ELISA, measuring cytosolic fragmented DNA by the cell death detection kit (Roche), according to the manufacturer's instructions.

For differentiation assays, cells derived from freshly dissociated neurospheres were transferred to coverslips coated with 10 μg ml^{-1} BSA or EGFL7 by centrifugation at 1,000*g* for 3 min. Cells were then cultured for 12 days in neurosphere medium containing 1% FCS without addition of EGF and FGF. The cells were fixed in 4% paraformaldehyde for 10 min at room temperature and stained for lineage-specific markers using anti-GFAP (astrocytes), anti-β-III tubulin or anti-NF160 (neurons), and anti-O4 (oligodendrocytes) antibodies. The percentage of neurons, glia or oligodendrocytes was determined by counting 15 independent fields under a fluorescence microscope.

39. Bett, A. J., Haddara, W., Prevec, L. & Graham, F. L. An efficient and flexible system for construction of adenovirus vectors with insertions or deletions in early regions 1 and 3. *Proc. Natl Acad. Sci. USA* **91,** 8802–8806 (1994).
40. Singec, I. *et al*. Defining the actual sensitivity and specificity of the neurosphere assay in stem cell biology. *Nature Methods* **3,** 801–806 (2006).

nature cell biology

DOI: 10.1038/ncb1896

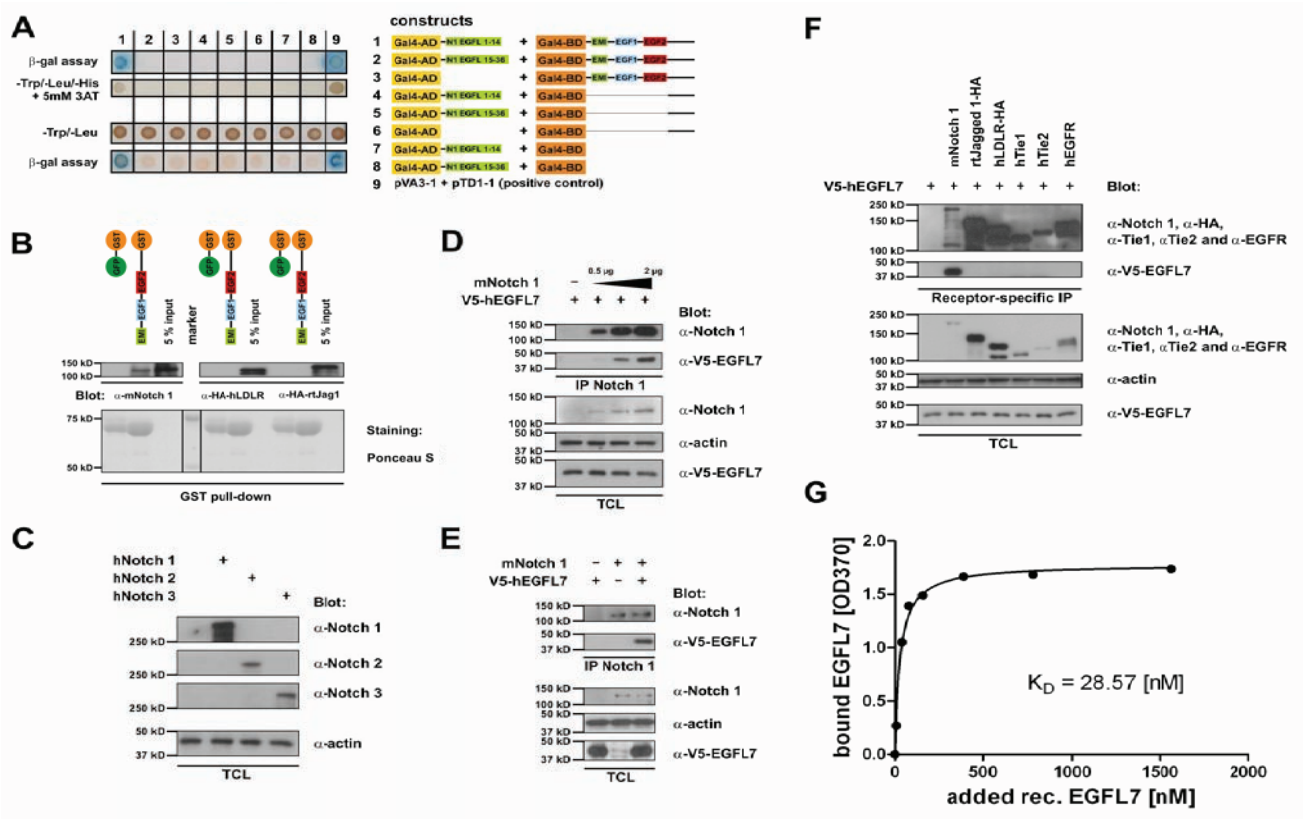

Figure S1 Addendum to EGFL7-Notch interaction. (**A**) The extracellular domains of human Notch1 comprising the EGF-like domains 1-14 or 15-36, respectively, were fused to Gal4-AD and screened against full-length EGFL7 or the isolated C terminus of EGFL7 in yeast two hybrid assays. Only the combination of Notch1 EGFL 1-14 and full-length EGFL7 yielded a positive signal (1), while all other combinations including the EGFL domains 15-36 of Notch1 failed to do so. pVA3-1 (murine p53 fused to Gal4-BD) and pTD1-1 (SV40 large T fused to Gal4-AD) served as positive interaction control. (**B**) Full-length EGFL7 or GFP fused to GST were produced in bacteria and coupled to glutathione sepharose 4B beads. Murine Notch1, human HA-tagged LDL receptor or rat HA-tagged Jagged1 were overexpressed in HEK293 cells, which were harvested 48h after transfection. GST fusion proteins coupled to beads were added to cell lysate and incubated at 4°C over night. Precipitates were analyzed by immunoblotting. Full-length EGFL7 bound murine Notch1 but not human LDLR or rat Jagged1 and the GFP-GST control did not bind any of the receptors. (**C**) The specificity of Notch antibodies used in Fig. 2 was checked by overexpression of human Notch1, -2 and -3 in HEK293 cells and subsequent immunoblotting with the respective antibodies. (**D**) Increasing amounts of murine Notch1 were co-expressed with V5-tagged human EGFL7 for 48h in HEK293 cells. Immunoprecipitation of Notch1 and blot for EGFL7 showed that increasing amounts of Notch1 co-precipitated increasing amounts of EGFL7. (**E**) Murine Notch1 and V5-tagged human EGFL7 were individually transfected into HEK293 cells that were harvested after 24h and mixed. After another 24h cells were harvested and co-immunoprecipitation experiments displayed binding of EGFL7 to Notch1. (**F**) Murine Notch1, HA-tagged rat Jagged1 and human LDLR as well as human Tie1, Tie2 or EGF receptor were co-expressed with V5-tagged human EGFL7 in HEK293 cells. Co-immunoprecipitation studies verified the Notch1-EGFL7 interaction and revealed the specificity of the interaction as none of the other receptors bound to EGFL7. Control receptors were chosen due to their various numbers of EGF-like domains. (**G**) Recombinant hIgG Fc-tagged rat Notch1 was coupled to 96 well dishes via α-hIgG antibody. Various amounts of recombinant, purified $(His)_6$-tagged EGFL7 were applied, followed by incubation with mouse α-$(His)_6$ primary and HRP-coupled goat α-mIgG secondary antibody. Conversion of the HRP-substrate TMB and determination of the absorbance at 370 nm in a microplate reader allowed us to create a binding curve. A K_D of 28.57 nM was determined for the Notch1-EGFL7 interaction by non-linear regression using GraphPad prism software version 5. TCL, total cell lysate

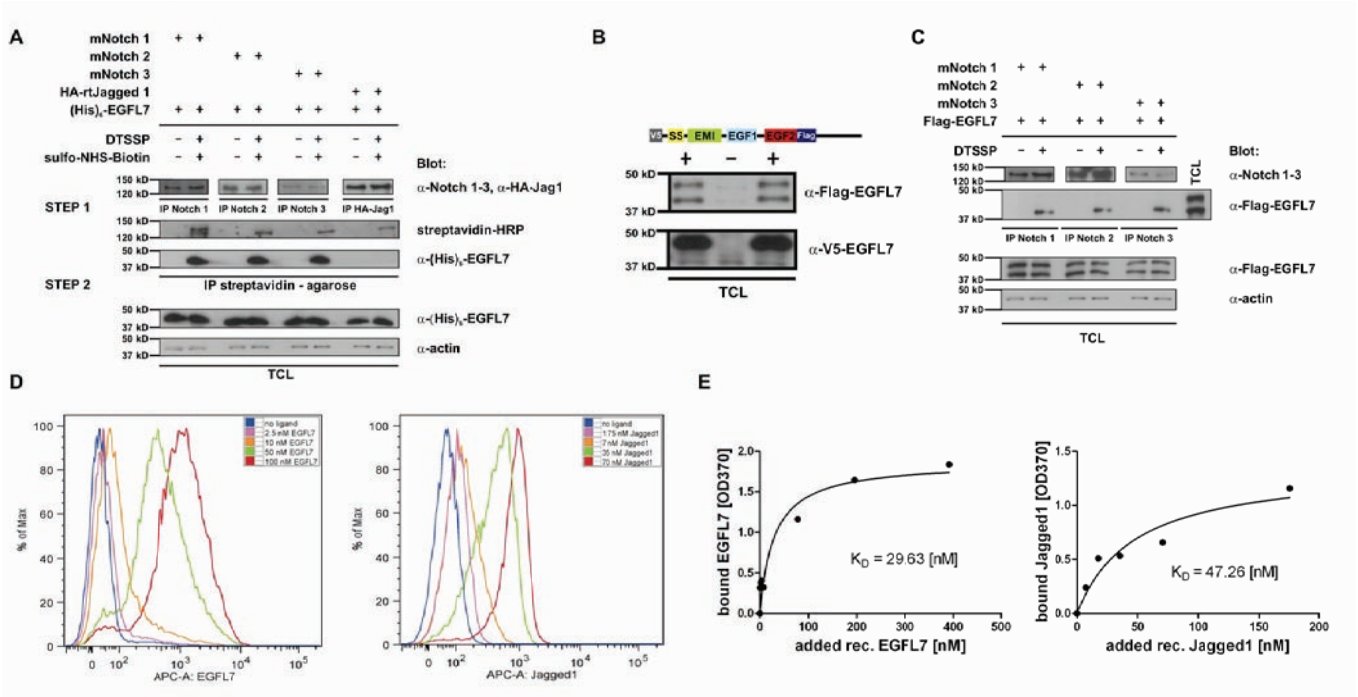

Figure S2 Secreted EGFL7 binds to Notch receptors at the cell surface. (**A**) Murine Notch1, -2 and -3 as well as HA-tagged rat Jagged1 were expressed in HEK293 cells. Recombinant, purified $(His)_6$-tagged human EGFL7 was applied to the cells at a concentration of 1 µg/ml 48h after transfection. Supernatant was removed and surface proteins cross-linked with the membrane-impermeable, thiol-cleavable cross-linker DTSSP for 30 min on ice. Subsequently, surface proteins were biotin-labelled for 2h on ice using sulfo-NHS-LC-Biotin. Cells were lysed and in step 1 complexes containing Notch1, -2, -3 or HA-Jagged1 were precipitated using specific antibodies. Proteins were released from immunoprecipitation beads using 20 mM glycine buffer (pH 2.7). In order to isolate the receptors from the Notch pool that were present on the plasma membrane during the time of the experiment, supernatants underwent precipitation with streptavidin-agarose beads in step 2. Within these complexes, $(His)_6$-tagged recombinant EGFL7 was detectable only after IP of Notch receptors as shown by immunoblot. Data indicate that recombinant human EGFL7 interacted with cell surface Notch1, -2 and -3 but not Jagged1. (**B**) An N-terminal V5- plus intramolecular Flag-tagged EGFL7 construct was expressed in HEK293 cells. This construct displayed delayed N-terminal processing and was detected as a bigger precursor form of 50 kD and a smaller, presumably mature, form of 37 kD. Only the bigger form, presumably the EGFL7 precursor, was V5-positiv, while both forms were Flag-positive. This allowed discrimination between the premature intracellular form and the processed, secreted form of EGFL7. (**C**) Murine Notch1, -2 and -3 and the EGFL7 construct were co-expressed in HEK293 cells. 48h after transfection supernatant was removed and surface proteins cross-linked with the membrane-impermeable, thiol-cleavable cross-linker DTSSP for 30 min on ice. Cells were lysed and complexes containing Notch1, -2 or -3 were precipitated using specific antibodies to Notch isoforms. Upon Western blotting and immunodetection of Flag-EGFL7 only the short form was detected. This data indicates that the processed form of EGFL7 binds to Notch1, -2 and -3 in the extracellular space. (**D**) Recombinant $(His)_6$-tagged EGFL7 or Jagged1 were loaded to the surface of HEK293 cells expressing Notch1 and detected by a combination of mouse α-$(His)_6$ primary and APC-conjugated α-mIgG secondary antibody. Visualisation by a FACS Canto II device displayed that increasing amounts of recombinant protein resulted in increasing amounts of APC-positive cells. Recombinant EGFL7 and Jagged1 displayed similar binding kinetics. (**E**) The previous experiment was quantified by replacement of the secondary antibody with an HRP-conjugated one. Application of various amounts of recombinant EGFL7 or Jagged1 carrying $(His)_6$ tags, conversion of the HRP-substrate TMB and determination of the absorbance at 370 nm in a microplate reader resulted in a binding curve that was analysed by non-linear regression using GraphPad prism software version 5. Recombinant EGFL7 bound with a K_D of 29.63 nM, recombinant Jagged1 with a K_D of 47.26 nM to the surface of living cells.

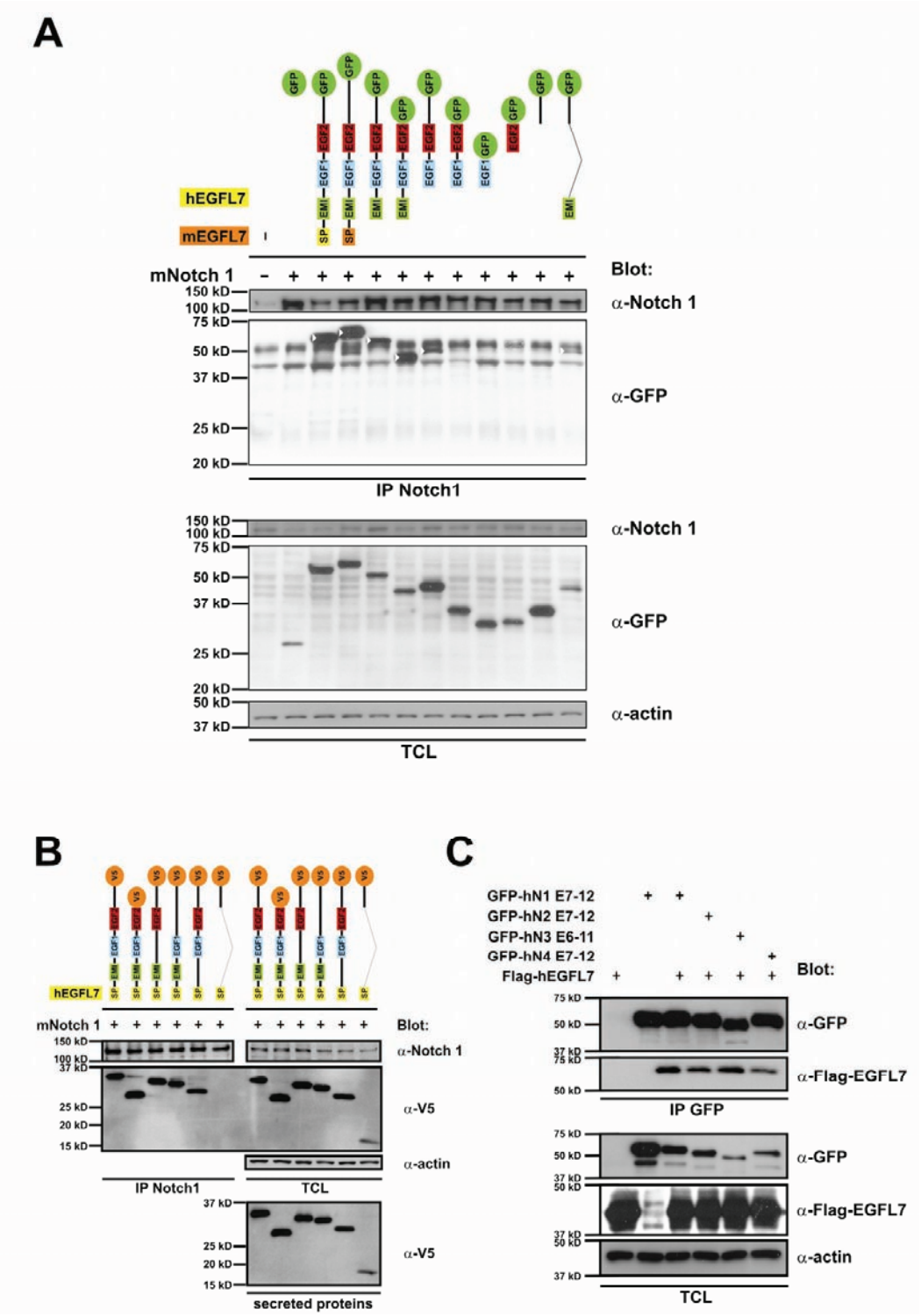

Figure S3 EGFL7 binds to Notch1 via its EMI and EGF-like domains. (**A**) Various human and one mouse EGFL7 construct were C-terminally tagged with GFP. These constructs were co-expressed with murine Notch1 in HEK293 cells and harvested after 48h. Detection of GFP-EGFL7 chimeras that co-immunoprecipitated with Notch1 (white triangles) revealed that all constructs harbouring an EMI domain strongly interacted with Notch1 (lane 3-6 and lane 12). EGF-like domains supported the binding of EMI (lane 3-6) and each other (lane 7) but did not individually associate with Notch1 (lane 9+10). This indicates that a binding triade of EMI and the two EGF-like domains mediated the interaction between EGFL7 and Notch1. (**B**) In HEK293 cells, Notch1 co-immunoprecipitation studies using EGFL7 deletion mutants indicated that a loss of binding can only be achieved upon deletion of the EMI and both EGF-like domains. Secretion of the deletion mutants was not impaired. (**C**) GFP fusion products of a set of EGF-like domains including the DSL binding sites of human Notch1, -2, -3 and -4 were co-expressed with Flag-tagged human EGFL7 in HEK293 cells. Co-immunoprecipitation studies revealed that EGFL7 binds close to the activation site of all four human Notch isoforms (N1-N4). E denotes the respective EGF-like domains of Notch receptors analyzed.

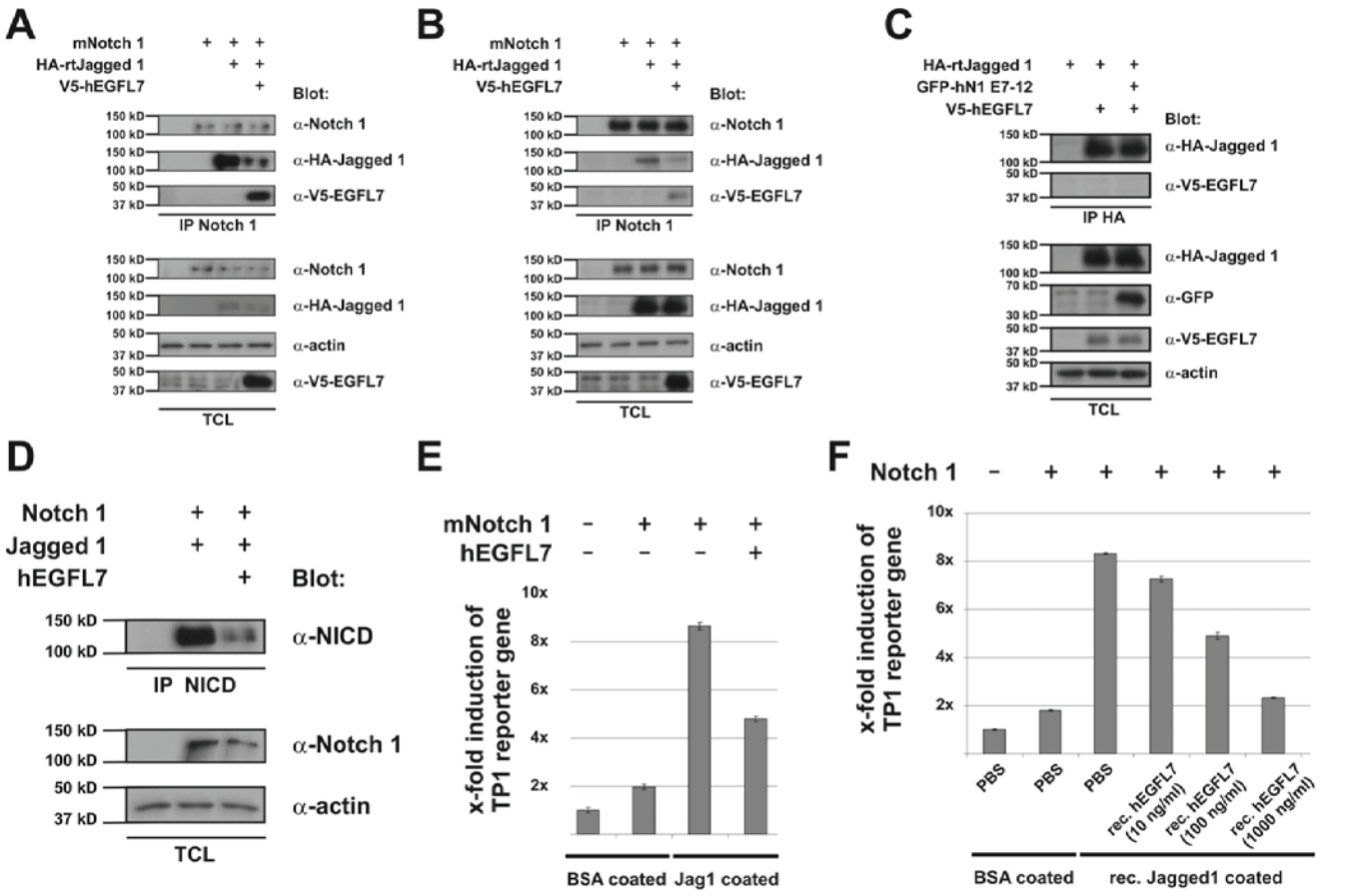

Figure S4 Addendum to EGFL7 antagonizes canonical Notch1 signalling. (**A**) Murine Notch1, HA-tagged Jagged1 and V5-tagged human EGFL7 were individually transfected into HEK293 cells that were harvested after 24h and mixed. After another 24h cells were lysed and co-immunoprecipitation experiments displayed interference of EGFL7 with the interaction of Notch1 and Jagged1 as well as binding of EGFL7 to Notch1 in apposing cells. (**B**) Likewise, HEK293 cell clones permanently expressing each construct were analysed. (**C**) Rat Jagged1-HA and human EGFL7-V5 were co-expressed in HEK293 cells in the presence or absence of the GFP-hN1 E7-12 construct. E7-12 was not able to induce an association between EGFL7 and Jagged1. (**D**) Murine Notch1 was transfected into HEK293 cells that were harvested 24h after transfection and seeded on plastic dishes coated with 5 µg/ml BSA or recombinant Jagged1 in the absence or presence of 1 µg/ml human EGFL7. The next day, cells were lysed and NICD detected using a specific antibody. Densitometry revealed a decrease of Notch1 activation by 76% in the presence of EGFL7. (**E**) TP1-luciferase reporter and β-galactosidase plasmids were expressed in HEK293 cells with or without murine Notch1. After 24h cells were harvested and mixed with HEK293 cells expressing control vector or human EGFL7. The cell mixture was seeded on plastic dishes coated with 5 µg/ml BSA or recombinant Jagged1. Reporter gene activity was reduced by 43% upon co-expression of EGFL7. (**F**) This assay was repeated in the presence of various amounts of human EGFL7. Signalling was reduced in an EGFL7 concentration-dependant manner. At a concentration of 1,000 ng/ml EGFL7 reduced Notch-induced reporter gene activity almost to base line.

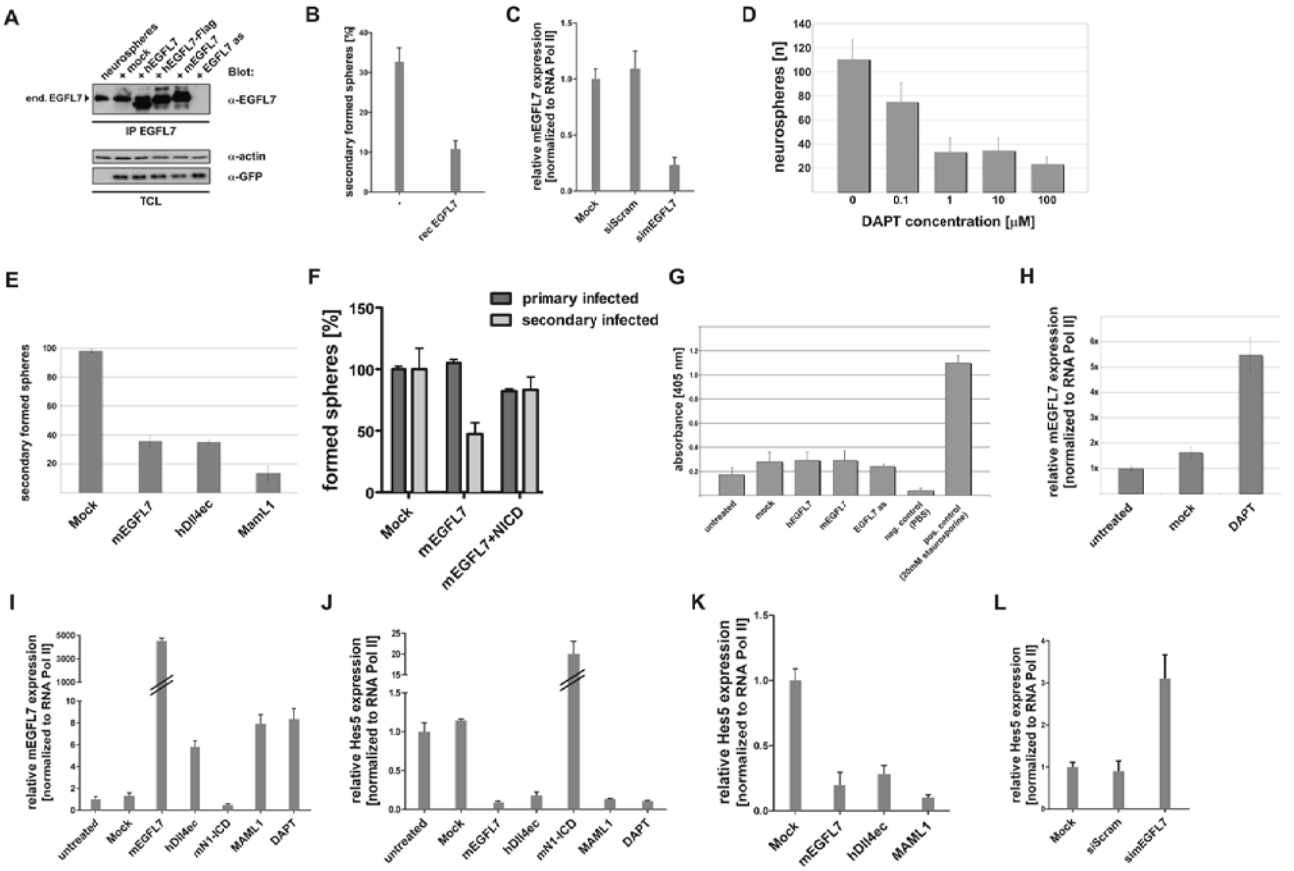

Figure S5 Addendum to EGFL7 affects NSC self-renewal. (**A**) Adenoviruses encoding for human and mouse EGFL7 as well as an EGFL7 antisense structure were created and tested in neurospheres. GFP served as an IRES-driven infection control. The western blot displays infection and expression efficiency of the adenoviral constructs applied to neurospheres. (**B**) Neurospheres were grown at clonal density in 6 well plates and recombinant EGFL7 was applied at a concentration of 1 μg/ml to the medium. NSC self-renewal was reduced by 67%. (**C**) Neurospheres were grown at clonal density in 6 Well plates and transfected with 1 μg siRNA duplexes using LP2000. Efficiency of siRNA targeting scrambled control (siScram) or murine EGFL7 (simEGFL7) was measured by quantitative RT-PCR. (**D**) Treatment of neurospheres with various concentrations of DAPT caused a maximal inhibition of secondary sphere formation at a concentration of 1 μM DAPT (n, number of spheres). Under this condition self-renewal was reduced by 69%. (**E**) Neurospheres were infected by adenovirus with murine EGFL7, the extracellular domain of human Dll4 and a truncated version of MamL1. All three constructs reduced Notch signalling upon infection (Fig. S5K) and reduced the NSC self-renewal capacity to comparable degrees. (**F**) NSC were infected with empty adenovirus (Mock), murine EGFL7 or murine EGFL7 plus the intracellular domain of murine Notch1 (NICD). Co-infection of dominant active Notch1 abolished the EGFL7 effect and completely restored the NSC self-renewal capacity. (**G**) Apoptosis of NSC, as measured by the quantification of the amount of fragmented cytosolic DNA, was not altered upon adenovirus infection. (**H**) Quantitative RT-PCR of murine EGFL7 in neurospheres indicated that mEGFL7 is upregulated upon inhibition of Notch signalling by treatment with 1 μM DAPT as compared to non-treated or mock (DMSO)-treated neurospheres. (**I**) NSC were grown in the presence of Notch-stimulating agents (NICD) or Notch-repressive agents (mEGFL7, hDll4ec, MamL1 or 10 μM DAPT). As measured by quantitative RT-PCR, murine EGFL7 was up-regulated if Notch signalling was low and *vice versa*. (**J**) Notch signalling in NSC was quantified by quantitative RT-PCR of Hes5 under the conditions of (I). (**K**) Neurospheres were infected with murine EGFL7, the extracellular domain of human Dll4 and a truncated version of MamL1. All three constructs reduced Notch signalling. (**L**) The effect of EGFL7 knock-down on Notch signalling after transfection of NSC with 1 μg siRNA targeting scrambled control (siScram) or murine EGFL7 (simEGFL7) was measured by quantitative RT-PCR of the Hes5 target gene.

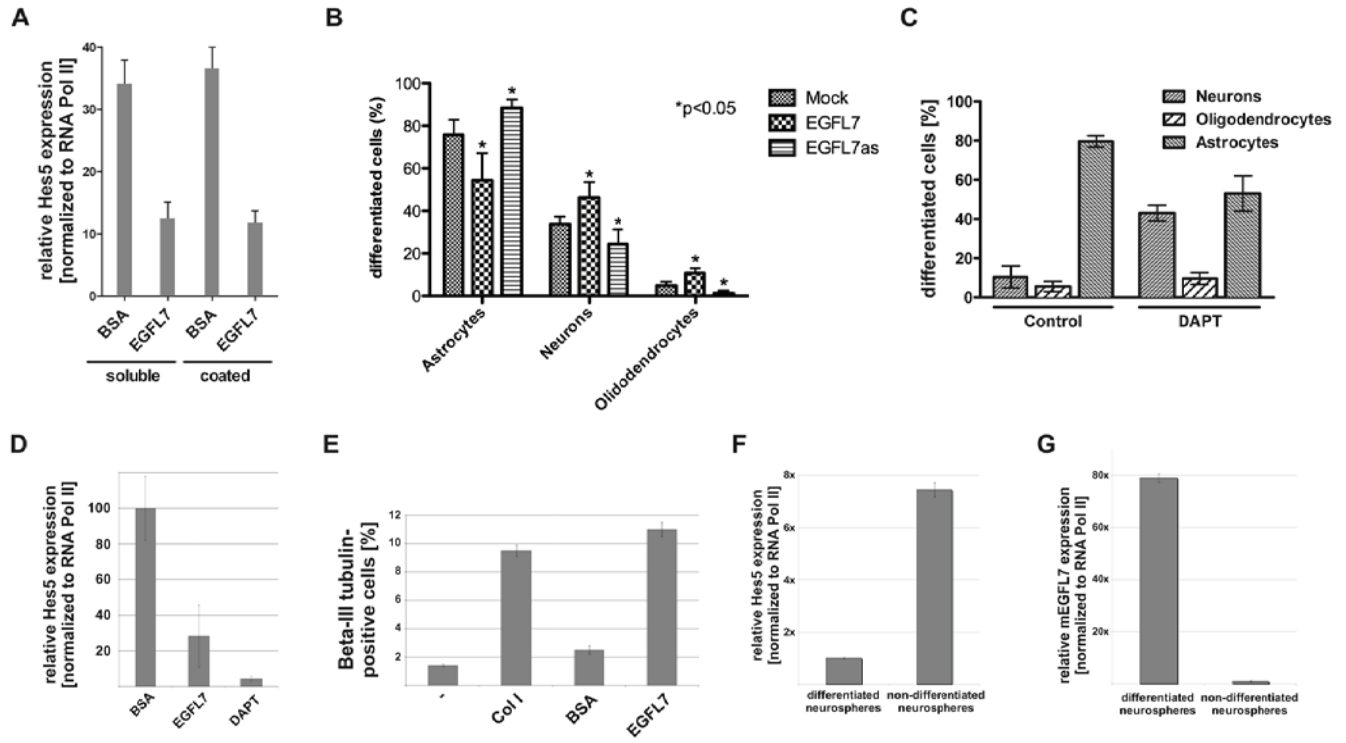

Figure S6 Addendum to EGFL7 affects NSC differentiation. (**A**) Neurospheres were grown in the presence of 1 µg/ml recombinant EGFL7 or BSA or allowed to differentiate on dishes coated with 10 µg/ml rec. EGFL7 or BSA. Subsequently, relative Hes5 expression was determined by quantitative RT-PCR, which was decreased by approximately 60% in both cases. (**B**) 2 day old neurospheres were infected with adenovirus encoding for EGFL7 or an EGFL7 antisense construct. Cells were seeded on coverslips coated with 10 µg/ml poly-l-ornithine and were allowed to differentiate for 12 days. Staining for neurons (Tuj1/NF160), oligodendrocytes (O4) and astrocytes (GFAP) revealed an increase in the amount of neurons and oligodendrocytes formed at the expense of astrocytes in EGFL7-infected cells. The opposite effect was observed upon infection with an EGFL7 antisense construct. (**C**) 2 d old neurospheres were allowed to differentiate for 12 d in the presence of 10 µM DAPT. Staining for neurons, oligodendrocytes and astrocytes revealed an increase in the amount of differentiated neurons and oligodendrocytes in the presence of DAPT as compared to control coverslips coated with 10 µg/ml BSA. (**D**) 2 d old neurospheres were allowed to differentiate for 12 d on 10 µg/ml BSA or EGFL7 or alternatively in the presence of 10 µM DAPT. At the end of this period, *Hes5* transcription was quantified by quantitative RT-PCR and was found significantly reduced in the presence of EGFL7 or DAPT. (**E**) As an alternative differentiation assay, PC12 cells were seeded on dishes coated with 10 µg/ml collagen, BSA or EGFL7. After 24h expression of the neuronal marker beta-III tubulin was quantified by FACS and, as previously described, collagen induced beta-III tubulin expression[1], while BSA had no such effect. Interestingly, EGFL7 induced expression of the neuronal marker, which indicates that EGFL7 drives PC12 differentiation towards a neuronal cell fate. (**F**) Quantitative RT-PCR of the Notch-induced gene product Hes5 in differentiated and non-differentiated neurospheres revealed an 8-fold downregulation of Hes5 upon differentiation of NSC. (**G**) Under the same conditions, EGFL7 was 80-fold upregulated in differentiated neurospheres as measured by quantitative RT-PCR.

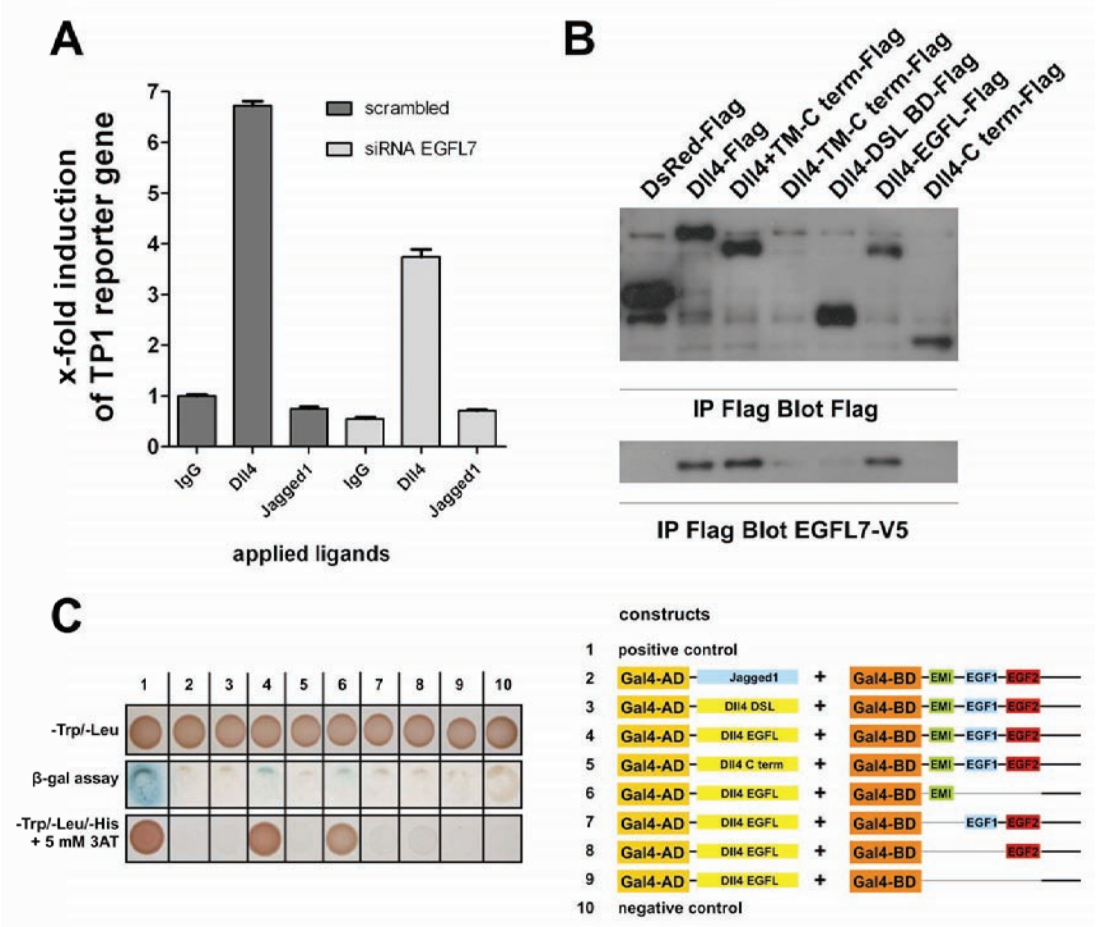

Figure S7 EGFL7 affects Notch signalling in HUVEC. (**A**) Reporter gene assays were performed in freshly prepped HUVEC transfected with TP1-firefly luciferase promoter plasmid and pGL4.70 *Renilla* luciferase as a control. The next day cells were treated with siRNA against EGFL7 or scrambled siRNA and after 24h seeded on IgG-, Dll4- or Jagged1-coated dishes. Subsequently, firefly luciferase activity was measured and normalized to *Renilla* luciferase expression. Dll4 but not Jagged1 induced Notch signalling in HUVEC under these conditions. Knock-down of EGFL7 caused a decrease in Dll4-induced Notch reporter gene activity. (**B**) HEK293 cells were transfected with V5-tagged full-length EGFL7 and various Flag-tagged Dll4 constructs or Flag-DsRed as a negative control. The extracellular region of Dll4, namely the EGF-like domains, associated with EGFL7. (**C**) Yeast two-hybrid assays were performed using various EGFL7 constructs as baits and Jagged1 or various Dll4-constructs as preys. EGFL7 (4) and its isolated EMI domain (6) interacted with the EGF-like domain of Dll4. Jagged1 (2) did not show an interaction with EGFL7.

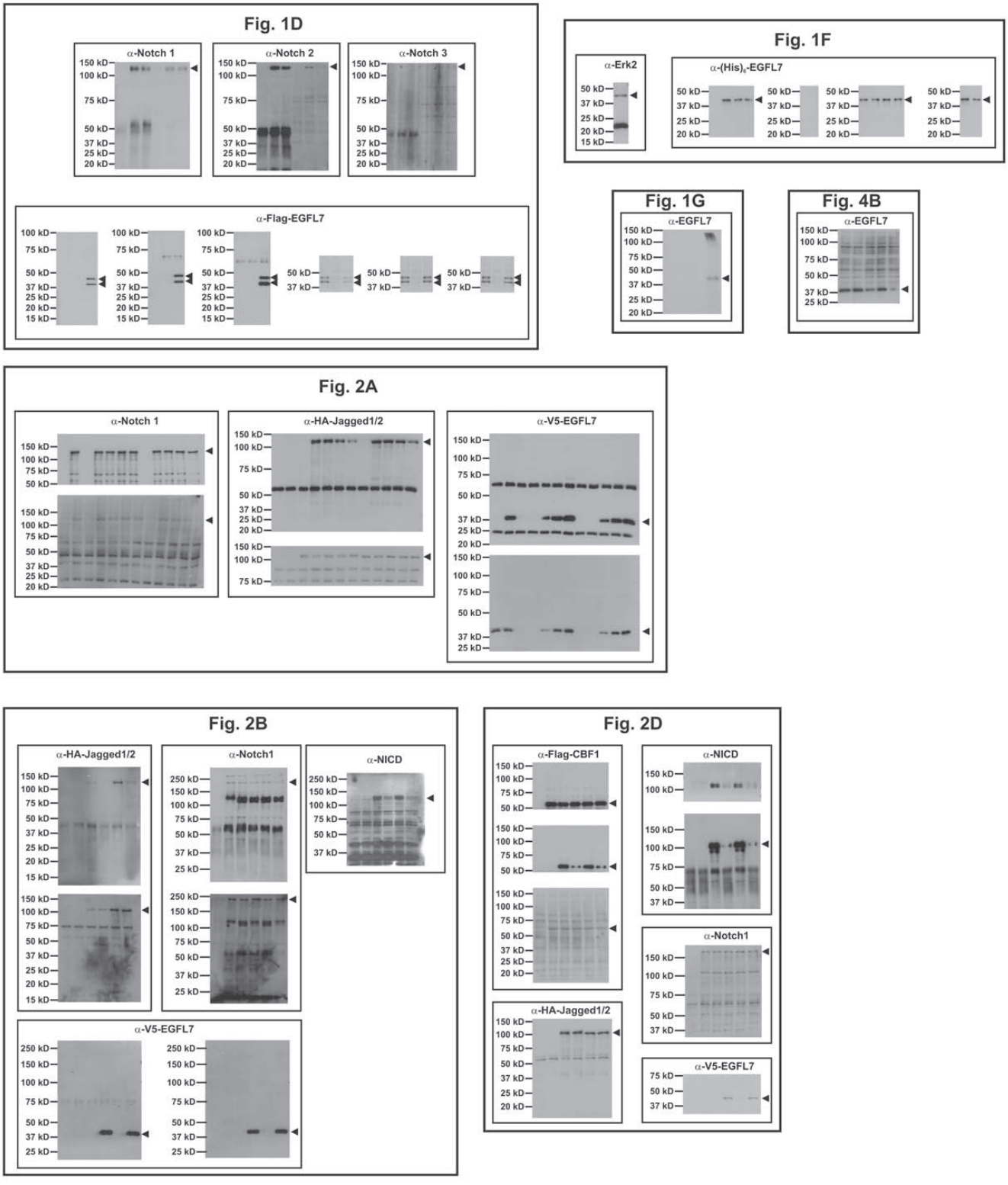

Figure S8 Full scans of key western data shown in Figs. 1D, 1F, 1G, 2A, 2B, 2D, 4D; molecular weight is indicated at the left-hand side; arrows indicate the analyzed protein.

Supplementary methods

Antibodies, constructs, cells and other materials

N-[N-(3,5-difluorophenacetyl)-L-alanyl]-S-phenylglycine t-butyl ester (DAPT) was purchased from Sigma (Deisenhofen, Germany). 3,3´-dithiobis(sulfosuccinimidylpropionate), EZ-Link sulfo-NHS-LC-Biotin as well as streptavidin-conjugated horseradish peroxidase (HRP) coupled to agarose were from Pierce (Rockford, USA). Mouse monoclonal α-HA (F-7), α-actin (C-2) and α-LDLR (C-7), rabbit polyclonal α-EGFL7 (H-90) and (M-135), α-EGFR (1005), α-Erk 2 (C-14), α-Jagged1 (H-66) and (H-114), α-Notch1 (C-20) and (H-131), α-Notch2 (M-20), α-Notch3 (M-134), α-Tie1 (C-18), α-Tie2 (C-20), goat polyclonal α-EGFL7 (R-12) as well as mixes of three siRNA duplexes directed against human (CCA GUC AGA UGU GGA UGA ATT, GAG UGG ACA GUG CAA UGA ATT, GCA AGA AAG ACU CGU GAC UTT) and mouse EGFL7 (CCU UUG UGC AGC GUG UAU ATT, GGG UUG AUG UGC UAG AAC ATT, CAU CCC UAG AUC CCU UGU ATT) were purchased from Santa Cruz Biotechnology (Santa Cruz, USA). Scrambled siRNA controls for human (GAG GAG GGU ACG UUC UAU ATT) and mouse (GAC UUC GUA UAG CCU UAC ATT) EGFL7 siRNAs were purchased from MWG (Munich, Germany). Rabbit polyclonal α-cleaved Notch1 (Val1744) antibody was from Cell Signaling Technology (Boston, USA), mouse monoclonal α-GFP (Living Colours), α-mouse IgG-APC, α-$(His)_6$ and rat monoclonal α-PECAM were from BD (Heidelberg, Germany), mouse monoclonal α-Flag (M2) and α-NF160 were from Sigma (Deisenhofen, Germany), mouse monoclonal α-V5 was from Invitrogen (Karlsruhe, Germany), sheep-α-mouse-HRP from GE Healtcare (Uppsala, Sweden) and mouse monoclonal α-BrdU (Bu20a) was from Dako (Hamburg, Germany). Mouse monoclonal α-GFAP and α-NeuN as well as rabbit polyclonal α-Olig1 were purchased from Millipore (Billerica, USA), mouse monoclonal α-beta-III tubulin was from Promega (Madison, USA), and rabbit polyclonal α-O4 was from Neuromics (Edina, USA).

Recombinant extracellular domains of Jagged1 and Notch1 were from R&D Systems (Minneapolis, USA).

Original cDNAs of human (IRATp970C0316D) and mouse (IRAVp968F1255D) EGFL7 were purchased from imagenes (Berlin, Germany). Full-length and partial sequences were cloned into the bacterial GST vector pDEST15, the mammalian expression vectors pcDNA3.1/nV5-DEST and pDEST40 carrying V5 tags, pDEST47 and pDEST53 carrying GFP tags or pcDNA3.0 N-Flag and pDEST490 carrying Flag tags. For baculoviral expression EGFL7 has been cloned into pAcGP67-B and for adenoviral expression into pDC515. Murine Notch1 and Notch2 as well as human Notch2 were kindly provided by the lab of Anna Bigas. Murine Notch3 was from Urban Lendahl. Human Notch1 and dominant negative MamL1 fragment was provided by Jon Aster, human Notch3 by Anne Joutel, murine Notch4 by Cédric Auffrey and human Notch4 was purchased from RZPD. DSL-BD domains of human Notch receptors were cloned into pDEST53 and N-terminally GFP-tagged. A permanent active form of murine Notch1 ICV wt was provided by Raphael Kopan. HA-tagged rat Jagged1 and 2 were kindly provided by Gerry Weinmaster, while Flag-tagged CBF1 was from Diane Hayward. Human HA-tagged LDLR was from Guojon Bu.

Murine hemangioendothelioma-derived EOMA, human embryonic kidney HEK293, and human lung fibroblast MRC5 cell lines were purchased from ATCC-LGC Promochem (Wesel, Germany). HEK293 cells were transiently transfected using Lipofectamine 2000 reagent (Invitrogen, Karlsruhe, Germany) following the manufacturer's guidelines. These cell lines were cultured under standard conditions (37°C and 5% CO_2) using Dulbecco's modified Eagle's medium (DMEM) supplemented with 10% fetal calf serum (FCS) and antibiotics. PC12 cells were grown in RPMI 1640 supplemented with 10% HS, 5% FCS and antibiotics. Human umbilical vein endothelial cells (HUVEC) were freshly prepared from umbilical cord and human aortic smooth muscle cells (hAoSMC) were purchased from Cambrex (Charles City, USA). Both cell types were cultured in endothelial cell growth medium MV plus

supplements (Promocell, Heidelberg, Germany) under standard conditions. Mouse brain tissues were prepared from six to eight weeks old C57bl6 mice[2].

Mouse brain tissue homogenates

Mouse brain or brain tissues were prepared from six to eight weeks old C57bl6 mice, snap-frozen in liquid nitrogen and grinded with a mortar. Resulting powder was transferred to immunoprecipitation (IP) buffer and homogenized with an UltraTurrax homogenizer for three rounds, 1 min each, on ice. The insoluble fraction was removed by centrifugation at 3,200 x *g* for 5 min at 4°C. The resulting suspension was centrifuged at high speed (16,200 x *g*) five times at 4°C. The cleared supernatants were subjected to immunoprecipitation studies.

Immunohistochemical staining

For immunohistochemical staining of mouse brains, acetone/methanol fixed 10 µm cryosections were blocked with goat serum and stained over night at 4°C with respective primary antibodies. The next day, secondary antibodies (donkey-α-goat-Alexa488, goat-α-mouse-Alexa568, goat-α-rabbit-Alexa568 or goat-α-rabbit-Alexa568, from Dianova, Hamburg, Germany) were applied at room temperature for 1h. In case of double staining, one additional blocking step using non-immune goat serum was added to cover epitopes and avoid species-crosstalk of secondary antibodies. Finally, cell nuclei were stained with TOTO-3 iodide (642/660 from Molecular Probes, Karlsruhe, Germany) for 10 min and analysed by confocal microscopy using a Nikon Eclipse TE2000-E (Nikon, Düsseldorf, Germany).

Interaction of recombinant proteins

Binding of $(His)_6$-tagged recombinant human EGFL7 to recombinant hIgG Fc-tagged rat Notch1 (R&D Systems, Minneapolis) was measured by a modified ELISA. In brief, 96 well plates were coated with 0.4 µg α-hIgG (BD, Heidelberg) per well over night and subsequently

loaded with 1.5 µg recombinant rat Notch1-IgG (R&D Systems, Minneapolis) per well for 1h. Subsequently, increasing amounts of recombinant, purified $(His)_6$-tagged EGFL7 were added. Bound EGFL7 was detected by incubation with 1‰ α-$(His)_6$ primary antibody (BD, Heidelberg, Germany) and 4‰ α-mIgG-HRP (GE Healthcare, Uppsala, Sweden) secondary antibody for 30 min each. 100 µl TMB solution (Pierce, Rockford, USA) was added for quantification and absorbance at 370 nm has been measured using an Infinity plate reader (Tecan, Munich, Germany). Dissociation constants were determined using nonlinear regression in GraphPad Prism software version 5.

Binding of recombinant proteins to the cellular surface

Binding of $(His)_6$-tagged recombinant human EGFL7 and rat Jagged1 (R&D Systems, Minneapolis, USA) to the surface of HEK293 cells expressing Notch1 was shown by FACS analysis using a FACS Canto II instrument (BD, Heidelberg, Germany). In brief, cells were dissociated using accutase, and 3 x 10^5 cells were incubated in binding buffer (PBS plus 2% FCS and 100 µg/ml $CaCl_2$) in a rotating wheel at 4°C. After blocking unspecific binding sites with 10% goat serum for 30 min, cells were incubated with recombinant EGFL7 or Jagged1 for 1 h at 4°C. Cells were incubated with 1‰ α-$(His)_6$ primary and 4‰ α-mIgG-APC secondary antibody (BD, Heidelberg, Germany) for 30 min each. Cells were resuspended in 500 µl binding buffer and analyzed by a FACS Canto II device (BD, Heidelberg, Germany) to determine binding of recombinant EGFL7 or Jagged1 to the cellular surface. For quantitative analysis, the secondary antibody was replaced with a sheep α-mouse IgG-HRP conjugate (GE Healthcare, Uppsala, Sweden) and binding was visualized by addition of 100 µl TMB solution (Pierce, Rockford, USA) and determination of the absorbance at 370 nm in an Infinity plate reader (Tecan, Munich, Germany). Dissociation constants were determined using nonlinear regression in GraphPad Prism software version 5 [3].

Quantitative RT-PCR

RNA from cell lines and neurosphere cultures was prepared using Trizol reagent (Invitrogen, Karlsruhe, Germany) according to the manufactures guidelines. Likewise, RNA from fresh frozen tissue samples was prepared using the RNeasy kit (Qiagen). cDNA was synthesized from 1 µg RNA per sample using the Thermoscript RT-PCR System (Invitrogen, Karlsruhe, Germany). For quantitative real-time PCR the following primers were created: mouse RNA-Polymerase II 5'-CAG ACA GAC AAC AAG AAG AAG A-3' (forward) and 5'-GAC ATA AGA ACC ATC AAA GGA GA-3' (reverse)[4], mouse EGFL7: 5'-CAC CTA CCG AAC CAT CTA CC-3' (forward) and 5'-GGC TTT GTC CCT CCC ATC-3' (reverse), mouse Hes5: 5'-AAG TAC CGT GGC GGT GGA GAT GC-3' (forward) and 5'-CGC TGG AAG TGG TAA AGC AGC TT-3' (reverse)[5]. Real-time PCR was performed using iQ SYBR Green Supermix (Bio-Rad, Munich, Germany) with subsequent detection of the melting curves. Results were normalized to RNA polymerase II expression using the iQ5 Optical System Software (Bio-Rad, Munich, Germany).

Reporter gene assays

Transactivation of Notch-responsive elements was detected as described[6]. In brief, HEK293 cells were seeded in 6 well plates and transfected by Lipofectamine 2000 (Invitrogen, Karlsruhe, Germany) with plasmids indicated plus 200 ng 12x CBF1 TP1-firefly luciferase promoter plasmid pGa981-6 (provided by Ursula Zimber-Strobl and Lothar Strobl)[7] and 50 ng pSV-β-gal encoding for β-galactosidase or pGL4.70 encoding for *Renilla* luciferase as internal transfection controls. Alternatively, 4x CSL-luciferase (provided by Raphael Kopan)[8] or Hes1-luciferase (provided by Alain Israel)[9] reporters have been used. Cells were lysed in SDS-free sample buffer 12h, 24h or 48h after transfection and intracellular luciferase concentration was determined using the chemiluminscent luciferase reporter gene assay (Roche, Mannheim, Germany). Likewise, β-galactosidase activity in each cell extract

was determined using the chemiluminescent β-gal reporter gene assay (Roche, Mannheim, Germany). Alternatively, the "Dual-Luciferase Reporter Assay System" from Promega (Madison, USA) was used. Kits were applied according to the manufacturer's guidelines and samples analyzed in a Victor^3 (Perkin Elmer, Rodgau, Germany) or an Infinity (Tecan, Munich, Germany) microplate reader. Eventually, luciferase concentrations were normalized to β-galactosidase or *Renilla* luciferase units in each sample and blotted as x-fold induction as compared to non-transfected controls.

PC12 differentiation assay

Differentiation of PC12 cells was determined by expression of the neuronal cell marker beta-III tubulin[1]. Quantification was performed by flow cytometry (FACS Canto II, BD, Heidelberg, Germany) as previously described[10]. Differentiation of PC12 cells was induced by seeding cells on dishes coated with 10 µg/ml BSA, collagen or EGFL7 followed by 24h incubation in RPMI medium supplemented with 0.5% HS and 0.25% FCS. Cells were detached with accutase, washed and triturated to a single cell suspension in PBS. Cells were fixed in 2% PFA for 20 min on ice followed by washing and inubation in PBS plus 0.5% saponin for 20 min on ice. Subsequently, cells were incubated over night at 4°C with either primary antibody or IgG control and incubated with Alexa488-α-mouse IgG for 30 min. Cells were washed in PBS plus 0.1% saponin, resuspended in PBS containing 2% FCS and analysed using a FACS Canto II device (BD, Heidelberg, Germany) after determination of >10,000 events and subsequent analysis using FACSDiva 6.0 software.

Supplementary references

1. Ohuchi, T., Maruoka, S., Sakudo, A. & Arai, T. Assay-based quantitative analysis of PC12 cell differentiation. *J Neurosci Methods* **118**, 1-8 (2002).
2. Singec, I.*, et al.* Defining the actual sensitivity and specificity of the neurosphere assay in stem cell biology. *Nat Methods* **3**, 801-806 (2006).
3. Shimizu, K.*, et al.* Mouse jagged1 physically interacts with notch2 and other notch receptors. Assessment by quantitative methods. *J Biol Chem* **274**, 32961-32969 (1999).
4. Radonic, A.*, et al.* Guideline to reference gene selection for quantitative real-time PCR. *Biochem Biophys Res Commun* **313**, 856-862 (2004).
5. Nyfeler, Y.*, et al.* Jagged1 signals in the postnatal subventricular zone are required for neural stem cell self-renewal. *Embo J* **24**, 3504-3515 (2005).
6. Kuroda, K.*, et al.* Regulation of marginal zone B cell development by MINT, a suppressor of Notch/RBP-J signaling pathway. *Immunity* **18**, 301-312 (2003).
7. Sakai, T.*, et al.* Functional replacement of the intracellular region of the Notch1 receptor by Epstein-Barr virus nuclear antigen 2. *J Virol* **72**, 6034-6039 (1998).
8. Saxena, M.T., Schroeter, E.H., Mumm, J.S. & Kopan, R. Murine notch homologs (N1-4) undergo presenilin-dependent proteolysis. *J Biol Chem* **276**, 40268-40273 (2001).
9. Jarriault, S.*, et al.* Signalling downstream of activated mammalian Notch. *Nature* **377**, 355-358 (1995).
10. Sergent-Tanguy, S., Chagneau, C., Neveu, I. & Naveilhan, P. Fluorescent activated cell sorting (FACS): a rapid and reliable method to estimate the number of neurons in a mixed population. *J Neurosci Methods* **129**, 73-79 (2003).

nature cell biology

TGF-β activates Akt kinase through a microRNA-dependent amplifying circuit targeting PTEN

Mitsuo Kato[1,5], Sumanth Putta[1,2], Mei Wang[1], Hang Yuan[1], Linda Lanting[1], Indu Nair[1], Amanda Gunn[2], Yoshimi Nakagawa[4], Hitoshi Shimano[4], Ivan Todorov[1], John J. Rossi[2,3] and Rama Natarajan[1,2,5]

Akt kinase is activated by transforming growth factor-β1 (TGF-β) in diabetic kidneys, and has important roles in fibrosis, hypertrophy and cell survival in glomerular mesangial cells[1–11]. However, the mechanisms of Akt activation by TGF-β are not fully understood. Here we show that TGF-β activates Akt in glomerular mesangial cells by inducing the microRNAs (miRNAs) miR-216a and miR-217, both of which target PTEN (phosphatase and tensin homologue), an inhibitor of Akt activation. These miRNAs are located within the second intron of a non-coding RNA (RP23-298H6.1-001). The *RP23* promoter was activated by TGF-β and miR-192 through E-box-regulated mechanisms, as shown previously[3]. Akt activation by these miRs led to glomerular mesangial cell survival and hypertrophy, which were similar to the effects of activation by TGF-β. These studies reveal a mechanism of Akt activation through PTEN downregulation by two miRs, which are regulated by upstream miR-192 and TGF-β. Due to the diversity of PTEN function[12,13], this miR-amplifying circuit may have key roles, not only in kidney disorders, but also in other diseases.

Diabetic nephropathy is a major complication of diabetes. Its key features include glomerular mesangial expansion, hypertrophy and accumulation of extracellular matrix (ECM) proteins, such as collagen, in the kidney[2,3,7,10,11]. The phosphatidylinositol 3-kinase (PI3K)–Akt pathway is activated in animal models of diabetic nephropathy [4–7], and *Akt1*$^{-/-}$ mice are protected from hyperhexosemia-induced mesangial hypertrophy and ECM accumulation[7]. These results implicate Akt kinase as a key mediator of diabetic nephropathy . Increased expression of TGF-β is observed in renal cells during diabetic nephropathy progression[1–3]. Activation of the PI3K–Akt pathway by TGF-β[4,5,8–10] has been related to increased ECM protein expression[9,10], hypertrophy[5], cell survival and oxidant stress in glomerular mesangial cells[4]. However, the mechanism by which TGF-β activates Akt has not been fully elucidated.

miRNAs are short non-coding RNAs that induce gene silencing, mainly by blocking mRNA translation or promoting mRNA degradation[14,15]. A number of miRNAs are highly expressed in the kidney[16,17]. In TGF-β-treated mouse glomerular mesangial cells (MMCs) and in diabetic mouse glomeruli, miR-192 has been shown to be upregulated and to increase collagen type I α2 chain (Col1a2) expression by downregulating Zeb2 (also known as SIP1 or Zfhx1b), an E-box repressor[3]. Another report showed that miR-377 regulates fibronectin expression in diabetic nephropathy [18]. However, the functional roles and regulation of other renal miRs are unclear. Here we show that in MMCs, miR-216a is upregulated by TGF-β in a dose- and time-dependent manner, similarly to miR-192 (Fig. 1a, b; Supplementary Information, Fig. S1c, k)[3]. *Col1a2* was induced in parallel. miR-216a levels were also increased in renal glomeruli isolated from type 1 (streptozotocin, STZ, -injected) and type 2 (*db/db*) diabetic mice relative to their controls (C57BL/6 and *db/+*, respectively; Fig. 1c).

miR-216a lies in the second intron of a non-coding RNA (RP23-298H6.1-001, RP23) located in the mouse chromosome 11 (miRBase, http://microrna.sanger.ac.uk; Fig. 1d; Supplementary Information, Fig. S2a)[19]. *RP23* levels were also increased by TGF-β in MMCs (Fig. 1a, b; Supplementary Information,Fig. S1b, j). Interestingly, another miRNA, miR-217, was present in the same intron, 6.6 kb downstream of miR-216a (Fig. 1d). Indeed, miR-217 levels were increased in TGF-β-treated MMCs (Fig. 1a, b; Supplementary Information, Fig. S1d, l), and in the glomeruli of diabetic mice (Fig. 1c). Therefore, miR-216a and miR-217 were expressed along with *RP23* and induced by diabetic conditions or TGF-β.

Next, the *RP23* promoter region was examined. We focused on 5'-CAGA-3' repeats (Smad binding elements) and E-boxes (5'-CAXXTG-3'), due to their function in TGF-β response[3,20]. Several 5'-CAGA-3' repeats and E-boxes were found in the *RP23* upstream region, especially from –5 kb to –2 kb (Fig. 1e). Upstream fragments of the *RP23* gene were cloned into a luciferase reporter construct, pGL4–Luc, and transfected into MMCs. The longest construct, RP23–4.8 kb–Luc, had the lowest basal activity, but showed a significant response to TGF-β (Fig. 1f). RP23–3.5 kb–Luc had intermediate basal activity and also responded to TGF-β. The shortest construct, RP23–2.7 kb–Luc, had highest basal activity, but no TGF-β response. The –4.8 to –2.7 kb region

[1]Gonda Diabetes Center, [2]Graduate School of Biological Sciences, [3]Division of Molecular Biology, Beckman Research Institute of the City of Hope, Duarte, CA 91010, USA. [4]Department of Internal Medicine, Metabolism and Endocrinology, Graduate School of Comprehensive Human Sciences, University of Tsukuba, Tsukuba, Ibaraki 305-8575, Japan.
[5]Correspondence should be addressed to R.N. or M.K. (e-mail: rnatarajan@coh.org; mkato@coh.org)

Received 6 January 2009; accepted 20 March 2009; published online 21 June 2009; DOI: 10.1038/ncb1897

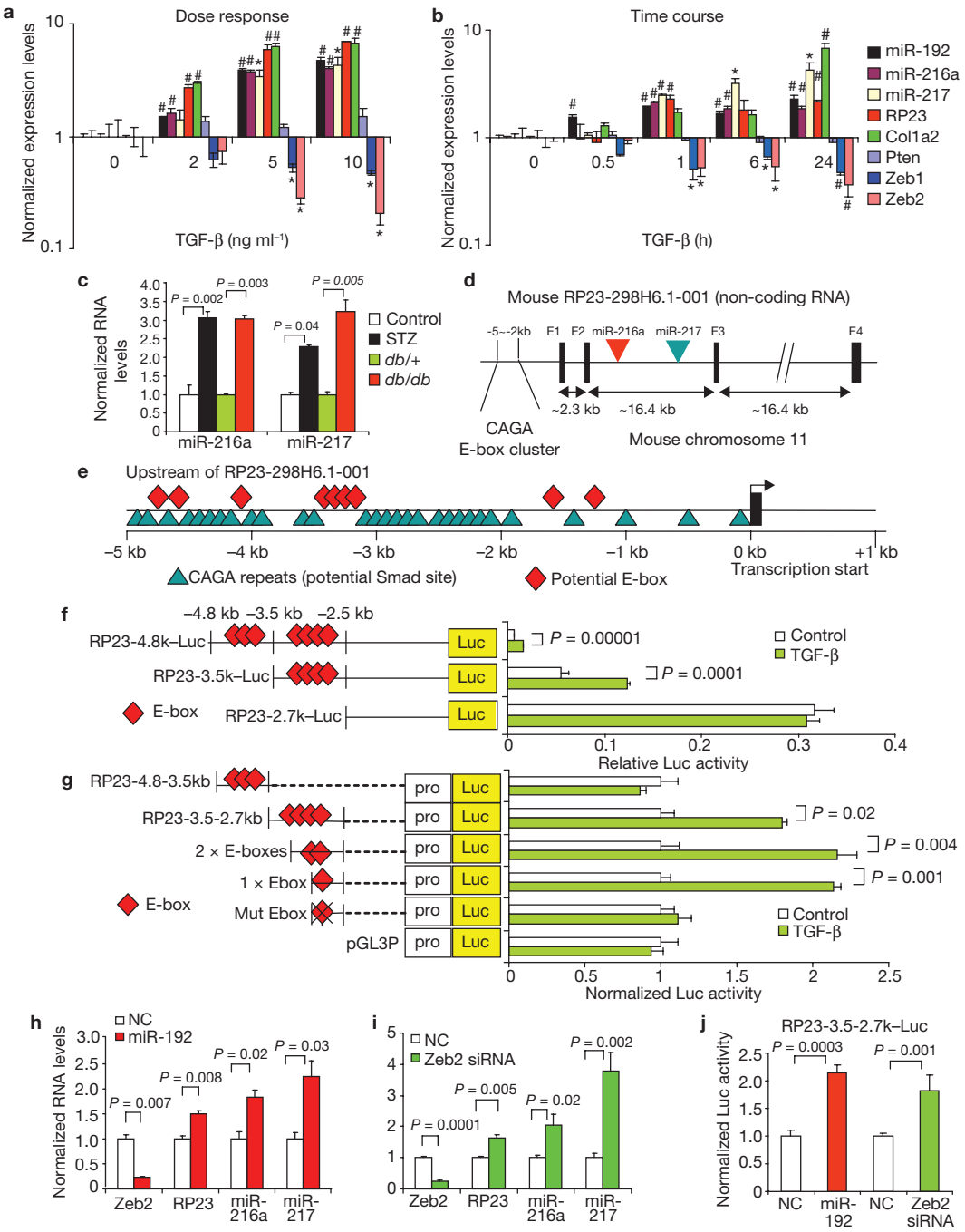

Figure 1 Expression and genomic organization of miR-216a and miR-217. (**a**) Real time (rt) qPCR data showing dose response of TGF-β-treatment (for 24 h) of miRs and related genes in MMCs (*$P < 0.05$, #$P < 0.01$ versus control, $n = 3$). See Supplementary Information, Fig. S1 for details. (**b**) Data from rtqPCR showing a time course of TGF-β effects in MMCs (*$P < 0.05$; #$P < 0.01$, $n = 3$). See Supplementary Information, Fig. S1 for details. (**c**) Data from rtqPCR showing significant increases in miR-216a and miR-217 levels in glomeruli of STZ-injected type 1 and *db/db* type 2 diabetic mice ($n = 4$). (**d**) Schematic representation of mouse non-coding RNA RP23-298H6.1-001 genomic region showing miR-216a and miR-217 locations in the second intron, with upstream 5'-CAGA-3's and E-box clusters. (**e**) Genomic structure of the upstream region of the *RP23* gene. 5'-CAGA-3' repeats (blue triangles) and potential E-boxes (red diamonds) are found in the –2 to –5-kb upstream region. (**f**) Basal activity of *RP23* promoter regions and response to TGF-β. The –4.8-kb and –3.5-kb constructs, but not the –2.7kb construct, responded to TGF-β ($n = 4$). Luc, luciferase (**g**) Response of deletion mutants of the –4.8 to –2.7-kb region to TGF-β, ($n = 4$). The –4.8 to –3.5-kb region includes three E-boxes and ten 5'-CAGA-3' s, whereas the –3.5 to –2.7-kb region has four E-boxes and eight 5'-CAGA-3' s. A significant increase in luciferase activity of the –3.5 to –2.7-kb construct was observed but there was no change in that of the –4.8 to –3.5-kb region ($n = 4$). TGF-β had similar effects in the RP23–3.5–2.7 kb, 2×E-boxes and 1×E-box constructs. One E-box in the most proximal part of –3.5 to –2.7 kb was sufficient for TGF-β response. Mutation of this proximal E-box abrogated the response. (**h**) Data from rtqPCR showing that the miR-192 mimic (10 nM) decreased expression of *Zeb2* and reciprocally increased *RP23*, miR-216a and miR-217 levels ($n = 3$). (**i**) rtqPCRs showing that, similarly to miR-192, ON-TARGETplus SMART pool *Zeb2* siRNA (10 nM) decreased the expression of *Zeb2* but increased *RP23*, miR-216a and miR-217 levels ($n = 3$). (**j**) miR-192 mimic (10 nM) or SMART pool *Zeb2* siRNA (10 nM) increased luciferase activity of RP23–3.5–2.7 kb–Luc ($n = 4$). NC, negative control. Data are mean ± s.e.m.

seemed to have negative elements for basal activity, and positive elements for TGF-β-response. To identify the elements, partial fragments of this region were cloned into pGL3P–Luc. Whereas RP23–3.5–2.7 kb–Luc responded to TGF-β, neither RP23–4.8–3.5 kb–Luc nor pGL3P alone did (Fig. 1g). Deletion of two or three upstream E-boxes from –3.5 to –2.7 kb did not alter TGF-β effects (Fig. 1g). However, mutation of the most proximal E-box completely abrogated the TGF-β response, confirming that E-boxes within –3.5 to –2.7 kb are essential for the TGF-β response in MMCs.

E-boxes are negatively regulated by Zeb1 and Zeb2 (refs 3, 21, 22). miR-192 upregulates *Col1a2* by targeting Zeb2 (ref. 3). In time course experiments, TGF-β induced a significant increase in miR-192 by 30 min, whereas induction of *RP23*, miR-216a and miR-217 required 1 h (Fig. 1b; Supplementary Information, Fig. S1i–l), suggesting that miR-192 may upregulate *RP23*, miR216a and miR-217. *Zeb1* and *Zeb2* were reduced at 1 h (Fig. 1b; Supplementary Information, Fig S1m, n). Transfection of MMCs with a miR-192 mimic or *Zeb2* siRNA (short interfering RNA) significantly decreased *Zeb2* levels and increased the expression of *RP23*, miR-216a and miR-217 (Fig. 1h, i) as well as RP23–3.5–2.7k–Luc activity (Fig. 1j). By inhibiting Zeb2, miR-192 relieves the repression of *RP23* (as well as miR-216a and miR-217) through its upstream E-boxes, similarly to collagen induction by TGF-β[3]. The initial induction of miR-192 by TGF-β may subsequently increase *RP23*, miR-216a and miR-217.

Transcription factor E3 (TFE3) is a positive regulator of E-boxes[20,23]. Ectopic expression of *Tfe3* significantly increased *RP23*–3.5–2.7 kb promoter activity (Supplementary Information, Fig. S2b). Conversely, knockdown of *Tfe3* by shRNAs (short hairpin RNAs)[23] significantly decreased reporter activity (Supplementary Information, Fig. S2c). Chromatin immunoprecipitation (ChIP) assays revealed that Tfe3 occupancy at the RP23–3.5–2.7 kb region was increased by TGF-β, whereas Zeb1 occupancy was decreased (Supplementary Information, Fig. S2d, e). E-box regulators may have key roles in the transcription of *RP23*, miR-216a and miR-217 through TGF-β collaborating with Smads[20] (Supplementary Information, Fig. S2i).

Genomic structures of miR216a and miR-217 are conserved from human to mouse, rat and zebrafish[19,24,25]. As in the mouse genome, in the human genome miR-216a and miR-217 also lie in the second intron of a non-coding RNA (DA732292, DA73) in chromosome 2 and 5'-CAGA-3' and E-box clusters were found in the human *DA73* promoter (–7 kb upstream; Supplementary Information, Fig. S2f). The –7.3 to –6.5 kb upstream region of *DA73* was cloned into pGL3P and transfected into MMCs or human embryonic kidney (HEK-293) cells. The luciferase activity of this construct was significantly enhanced by TGF-β or miR-192 mimics (Supplementary Information, Fig. S2g, h). These results suggest a conserved regulation of miR-216a and miR-217 from mouse to human.

Using miR target predictions (TargetScan, http://www.targetscan.org), we found that PTEN is a potential target of both miR-216a and miR-217 (Fig. 2a). PI3K generates PIP3 (phosphatidylinositol-3, 4, 5-triphosphate) from PIP2 (phosphatidylinositol 4,5-bisphosphate), which then activates Akt[12,13]. PTEN dephosphorylates PIP3 to inhibit Akt activation. PTEN mutations enhance Akt activity in certain cancer cells[12]. Akt activation and decreased Pten are observed in glomerular mesangial cells treated with high glucose or TGF-β[5]. Therefore, PTEN might be a link between TGF-β and Akt activation.

Decreased levels of Pten were confirmed in glomeruli of diabetic *db/db* mice (Fig. 2b–d) and in MMCs treated with TGF-β or high glucose (Fig. 2e). A miR-216a or miR-217 mimic decreased Pten levels in MMCs (to 30~40% of negative control levels; Fig. 2f, g). Simultaneous transfection with these two mimics decreased Pten levels to a greater extent (to ~10% of negative control levels), suggesting an additive effect of these two miRs on Pten downregulation. Despite a significant decrease in Pten protein levels in TGF-β-treated MMCs, no decrease in *Pten* mRNA levels was observed (Fig. 1a, b; Supplementary Information, Fig. S1h, p), suggesting post-transcriptional reduction of Pten by TGF-β in MMCs.

TGF-β activated Akt (Ser 473 phosphorylation) in MMCs (Fig. 2h), consistent with previous reports[4,5]. A parallel increase in Akt activation in MMCs transfected with miR-216a, miR-217 or both (Fig. 2i) further confirmed that miR-216a and miR-217 target Pten in response to TGF-β. A biphasic Akt activation was observed in time course experiments (Supplementary Information, Fig. S3a, c). A rapid response time of 5 min (ref. 4) presumably results from a direct interaction of the TGF-β receptor and PI3K (ref. 8). A second, more robust Akt activation by 6 h to 24 h (Supplementary Information, Fig. S3a, c) occurs through induction of *RP23* (miR-216a and miR-217) and a decrease in Pten (Fig. 2e; Supplementary Information, Fig. S3a, b). Interestingly, a miR-192 mimic decreased Pten levels and promoted Akt activation similarly to miR-216a and miR-217 mimics (Fig. 2i, j), again suggesting that miR-192 functions upstream of miR-216a and miR-217.

To verify whether these miRs target the *Pten* 3'UTR, luciferase reporters containing *Pten* 3'UTR (full-length and shorter form with miR-216a and miR-217 target sites) were constructed. Both miR-216a and miR-217 mimics significantly inhibited *Pten* 3'UTR luciferase activity relative to negative controls, whereas *Pten* 3'UTR containing mutations at miR-216a and/or miR-217 sites lost this response (Fig. 2k; Supplementary Information, Fig. S4a). Similar inhibition was observed with TGF-β treatment, which induced a decrease in luciferase activity; however, miR-216a and miR-217 inhibitors could override this effect (Fig. 2l, m; Supplementary Information, Fig. S4b–g). These results confirm that *Pten* 3'UTR is a target of miR-216a and miR-217.

Transgenic mice with the miR-17–92 cluster had lymphoproliferative diseases due to decreased levels of Pten and Bim, which are targeted by this cluster[26]. They also had enlarged kidney glomeruli, hypercellularity, mesangial expansion and proteinuria (features similar those of diabetic nephropathy). These observations further support the physiological significance of our data that Pten downregulation by miRNAs is an important step in kidney dysfunction.

Next, inhibitors of miR-192, miR-216a and miR-217 were tested to determine the functional relevance of these miRNAs. First, we used MMCs treated with TGF-β, as these cells show features of diabetic nephropathy (Akt activation and ECM accumulation). Inhibitors of miR-216a and miR-217 reversed the effects of TGF-β treatment on Pten and phospho-Akt (P-Akt) levels (Fig. 3a, b), as did the miR-192 inhibitor (Fig. 3c, d). Moreover, a miR-192 inhibitor reversed the effects of TGF-β on RNA expression of miR-192, *RP23*, miR-216a, miR-217, *Zeb2* and *Col1a2* (Fig. 3e), and attenuated TGF-β-induced *RP23* promoter activation (Fig. 3f). Therefore, the miR-192 inhibitor blocked key pathological effects of TGF-β, in MMCs, related to diabetic nephropathy (including Col1a2 and Akt activation).

Next, we examined the *in vivo* consequences of miR-192 inhibition using locked nucleic acid (LNA)-modified oligonucleotides. LNA

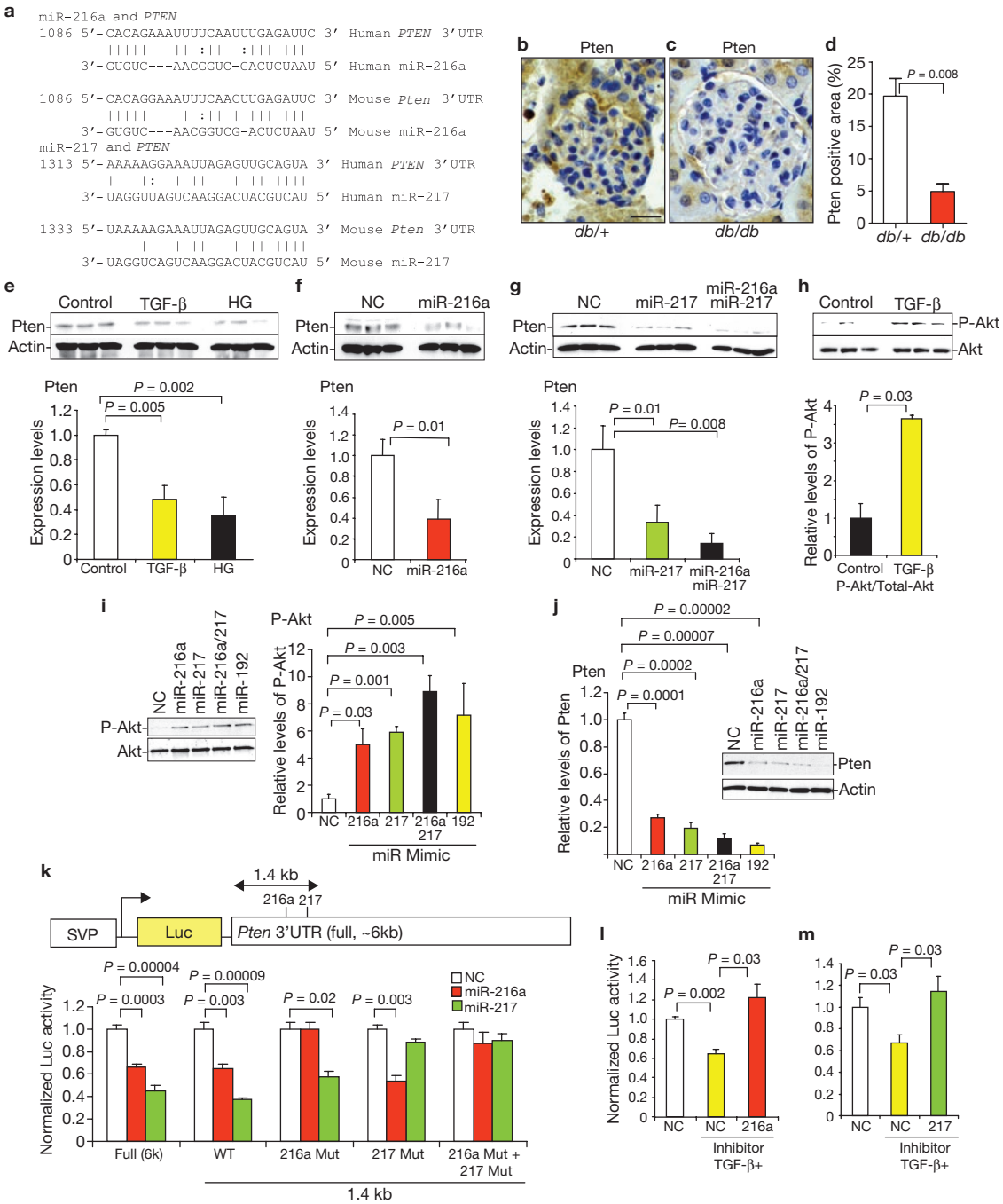

Figure 2 *Pten* is a direct target of miR-216a and miR-217. (**a**) Sequence alignment of human and mouse miR-216a or miR-217 with *Pten* 3′UTR sequences. Seed regions of these miRs are completely complementary to target sites in the *Pten* 3′UTR. Target sequences are highly conserved from human and mouse. Numbers next to the *PTEN* 3′UTR sequence are relative to 3′UTR start sites. (**b**–**d**) Immunostaining of Pten in mouse renal sections. Pten levels in glomeruli from *db/db* diabetic mice (**c**) were significantly lower than in the control *db/+* mice (**b**, **d**; $n = 3$). Scale bar, 20 μm. (**e**-**g**, **j**) Pten protein levels in MMCs treated for 24 h with TGF-β or high glucose (HG; $n = 3$; **e**), for 48 h with an miR-216a mimic (10 nM; $n = 3$; **f**), miR-217 alone or with miR-216a ($n = 3$; **g**), miR-216a, miR-217 or miR-192 mimics ($n = 4$; **j**). (**h**, **i**) Phospho-Akt (p-Akt) levels in MMCs treated for 24 h with TGF-β ($n = 3$; **h**) or for 48 h with miR-216a, miR-217 or miR-192 mimics (10 nM; $n = 4$; **i**). (**k**) Luciferase reporters containing full-length (6 kb) or shorter (1.4 kb) *Pten* 3′UTR, and mutants of miR-216a and miR-217 target sites (SVP, SV40 promoter; Luc, luciferase). miR-216a and miR-217 mimics (10 nM) significantly inhibited *Pten* 3′UTR luciferase (full) activity relative to the negative control (NC). The shorter 1.4-kb construct (WT), which includes the miR-216a and miR-217 target sites, showed similar responses to the full-length construct. The miR-216a site mutant still responded to miR-217 but not to miR-216a, and vice versa. The double mutant did not respond to either of the miRNA mimics ($n = 4$). See also Supplementary Information, Fig. S4a for details of *Pten* 3′UTR constructs. (**l**) Effects of TGF-β and the miR-216a inhibitor on the *Pten* 3′UTR reporters. A plasmid containing luciferase fused to *Pten* 3′UTR (miR-216a target site) was used as a reporter (*Pten* 3′UTR-S). A significant decrease in reporter activity was detected with *Pten* 3′UTR-S by TGF-β ($n = 4$) and this was reversed by the miR-216a inhibitor (10 nM; $n = 4$). (**m**) TGF-β significantly decreased *Pten* 3′UTR-S (miR-217 site) reporter activity ($n = 4$), and this was reversed by the miR-217 inhibitor (5 nM; $n = 4$). See Supplementary Information, Fig. S4. Data are mean ± s.e.m. Full or larger scans of blots in **e**–**j** are shown in Supplementary Information, Fig. S7.

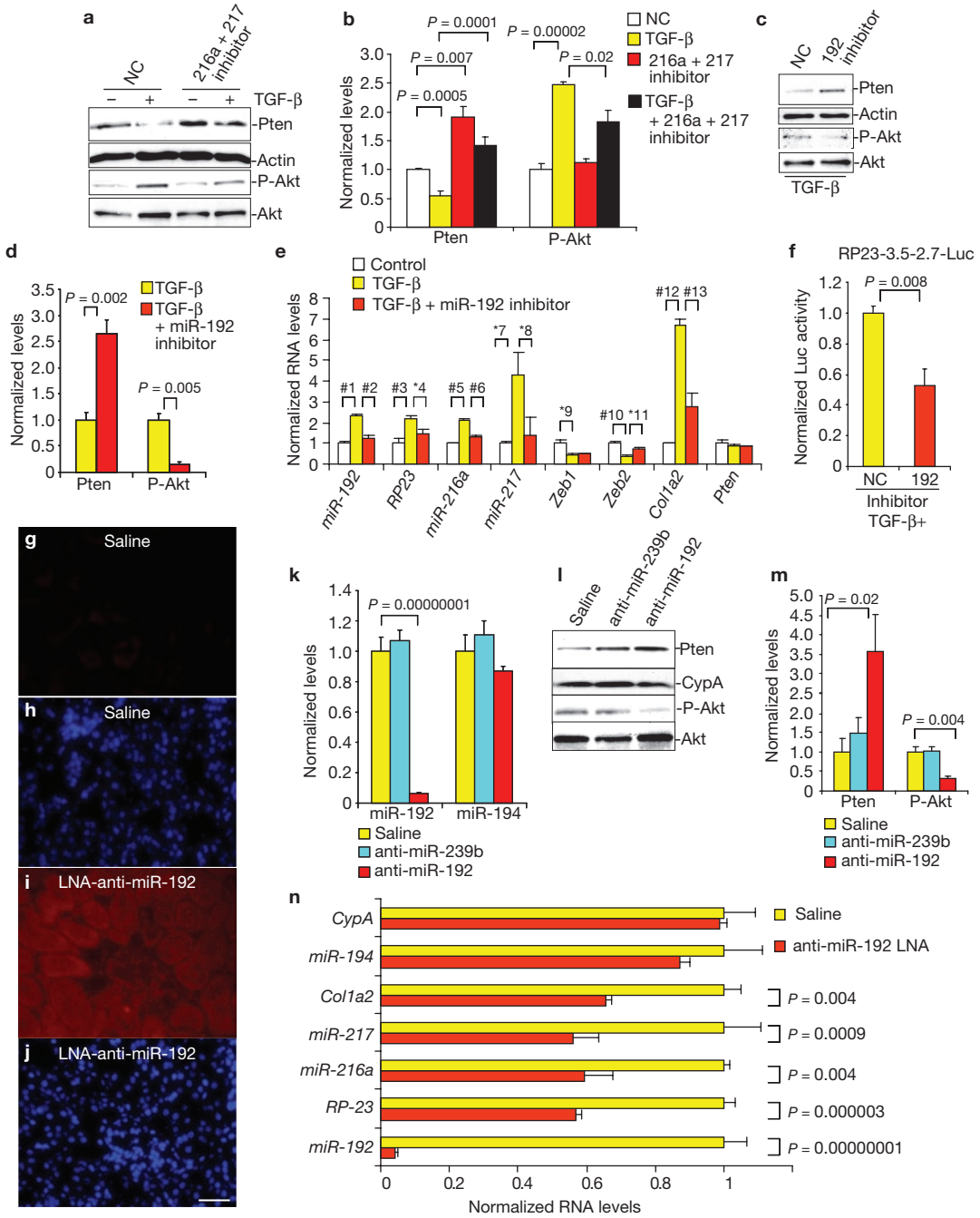

Figure 3 Effects of miRNA inhibitors on downstream signalling *in vitro* and *in vivo*. (**a**, **b**) Effects of miR-216a and miR-217 inhibitors (10 nM) on endogenous Pten and P-Akt levels in MMCs treated with or without TGF-β ($n = 3$). NC, negative control. (**c**, **d**) Effects of miR-192 inhibitor (10 nM) on TGF-β-induced effects on Pten and phospho-Akt (p-Akt) in MMCs. Cells were transfected with inhibitors and then treated with TGF-β, followed by western blotting analysis ($n = 3$). (**e**) Real time (rt) qPCR data showing the effects of a miR-192 inhibitor on endogenous levels of various RNAs in MMCs treated with TGF-β (*$P < 0.05$; #$P < 0.01$, $n = 3$). #1, $P = 0.005$; #2, $P = 0.001$; #3, $P = 0.001$; *4, $P = 0.02$; #5, $P = 0.006$; #6, $P = 0.0007$; *7, $P = 0.02$; *8, $P = 0.02$; *9, $P = 0.04$; #10, $P = 0.01$; *11, $P = 0.02$; #12, $P = 0.002$; #13, $P = 0.003$. (**f**) Effects of miR-192 inhibitor on TGF-β-induced *RP23* promoter (RP23–3.5–2.7 kb–luc) activity in MMCs ($n = 4$). (**g**–**j**) *In vivo* LNA-anti-miR-192 delivery. LNA-anti-miR-192 was subcutaneously injected (2.5 mg kg^{-1}) into normal C57BL/6 mice and renal cortical tissues and collected 6 h later. Representative data is shown of *in situ* hybridization to detect LNA-anti-miR-192 in mouse renal cortical sections 6 h after injections. Very mild fluorescence was detected in the kidney of control vehicle saline-injected mice (saline; **g**). Intense and widespread fluorescence in kidney glomerular and tubular compartments was observed in LNA-anti-miR-192-injected mice (**i**). The kidney cortexes from saline and LNA-anti-miR-192-injected mice were stained with DAPI (**h**, **j**, respectively). Scale bar, 20 μm. (**k**) Data from rtqPCRs of cortical tissues obtained from normal C57BL/6 mice injected subcutaneously with 2.5 mg kg^{-1} LNA-anti-miR-192, LNA-anti-miR-239b (targeting *C. elegans* miR-239b) or saline. A significant decrease in RNA levels of miR-192, but not miR-194, was observed with LNA-anti-miR-192, whereas no change was observed with saline or LNA-anti-miR-239b. (**l**, **m**) A concomitant significant increase in Pten protein levels and decrease in P-Akt levels (P-Akt to total Akt ratios) by LNA-anti-miR-192, but not by LNA-anti-miR-239b, was observed. (**n**) A significant decrease in RNA levels of miR-192, *RP23*, miR-216a, miR-217 and *Col1a2*, but no change in miR-194 or *CypA*, was detected in LNA anti-miR-192-injected mice ($n = 3$). Data are mean ± s.e.m. Full or larger scans of blots in **a**, **c** and **l** are shown in Supplementary Information, Fig. S7.

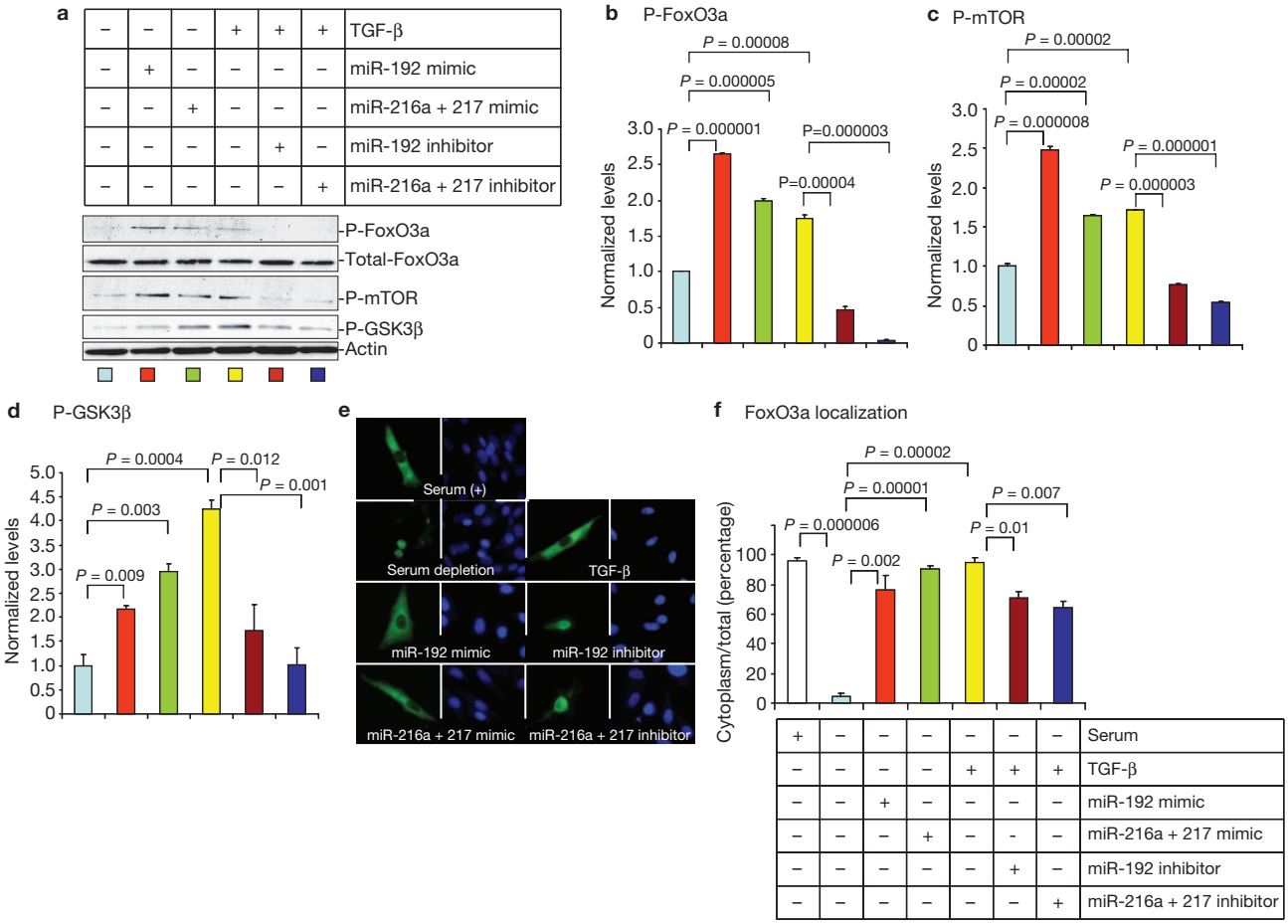

Figure 4 Effects of miR-192 and miR-216a/217 on Akt downstream targets. (**a**) Blots showing that miR-192 and miR-216 + 217 mimics (10 nM) induced phosphorylation of the Akt targets FoxO3a, mTOR and GSK3β similarly to TGF-β. The miRNA inhibitors (10 nM) blocked or attenuated TGF-β effects. Actin and total FoxO3a were used as loading controls. (**b**–**d**) Bar graph quantifications show increased phosphorylation of FoxO3a (P-FoxO3a; **b**), mTOR (P-mTOR; **c**) and GSK3β (P- GSK3β; **d**) in MMC treated with TGF-β, miR-192 and miR-216a + 217 mimics, and attenuation by the miR-192 or miR-216a + 217 inhibitors ($n = 3$). (**e**) Cellular localization of FoxO3a in MMCs. Left panels in each treatment show FoxO3a–GFP cellular localization. Right panels show Hoechst staining (nuclear)[4]. Serum depletion induced nuclear localization of FoxO3a and TGF-β reversed this localization to the cytoplasm. Similarly to TGF-β, miR-192 and miR-216a + 217 mimics induced cytoplasmic translocation of FoxO3a. Conversely, inhibitors of these miRs relocated FoxO3a into the nucleus in TGF-β-treated cells. Scale bar, 20 μm. (**f**) Cells with cytoplasmic or nuclear localization were counted in three fields and the results depicted in the bar graph as the percentage of cells with cytoplasmic fluorescence relative to the total ($n = 3$). FoxO3a was localized in the cytoplasm in 96% of cells under normal culture conditions (Serum +). However, after serum depletion (SD), 96% of cells had nuclear FoxO3a (4% in cytoplasm). FoxO3a translocated back to the cytoplasm after treatment with miR-192 (76%) or miR-216a + 217 (90%) mimic or TGF-β (95%). The miR-192 or miR216a + 217 inhibitor significantly attenuated cytoplasmic FoxO3a to 71% or 64%, respectively, in TGF-β-treated cells. Data are mean ± s.e.m. Full or larger scans of blots in **a** are shown in Supplementary Information, Fig. S7.

anti-miRs are potent miR inhibitors even in primates[27]. Marked accumulation of a subcutaneously injected LNA-modified miR-192 inhibitor (anti-miR-192) was observed in mouse kidneys, relative to injected saline (Fig. 3g–j). LNA-anti-miR-239b targeting *Caenorhabditis elegans* miR-239b (similar sequences are not found in mammalian RNAs) was injected as a negative control. LNA-anti-miR-192, but not LNA-anti-miR-239b, significantly inhibited miR-192 levels in renal cortical tissues (Fig. 3k). The expression of miR-194 was unaffected, indicating the specificity of LNA-anti-miR-192, which also attenuated P-Akt while augmenting Pten levels relative to saline and LNA-anti-miR-239b controls (Fig. 3l, m). Concomitant decreases in *RP23*, miR-216a, miR-217 and *Col1a2* levels (but not miR-194 or cyclophilin A, CypA) were observed (Fig. 3n). These *in vivo* data further support miR-192 as a master regulator of other related miRNAs, and the therapeutic potential of anti-miR-192 for diabetic nephropathy. The possible cell-type differential effects of miRs should however be considered while designing such therapies.

Next, the biological significance and downstream consequences of Akt activation by this miR circuit were evaluated. Phosphorylation of Akt targets, FoxO3a, mTOR and GSK3β, which are associated with cell survival and hypertrophy[4–6,28], was induced by miR-192 and miR-216a + miR-217 mimics as well as TGF-β (Fig. 4a-d). Interestingly, phosphorylation of these proteins by TGF-β was blocked or attenuated by inhibitors of these miRNAs (Fig. 4a–d), suggesting that this miRNA circuit affects key Akt targets. As Akt-induced phosphorylation of FoxO3a transcription factor promotes its nuclear to cytoplasmic translocation and inactivation, we then tested the effects of the miRNAs in MMCs transfected with a vector expressing FoxO3a–GFP[4] (GFP, green fluorescent protein). Serum depletion induced nuclear localization of FoxO3a, whereas TGF-β treatment induced cytoplasmic translocation, presumably due to Akt activation and

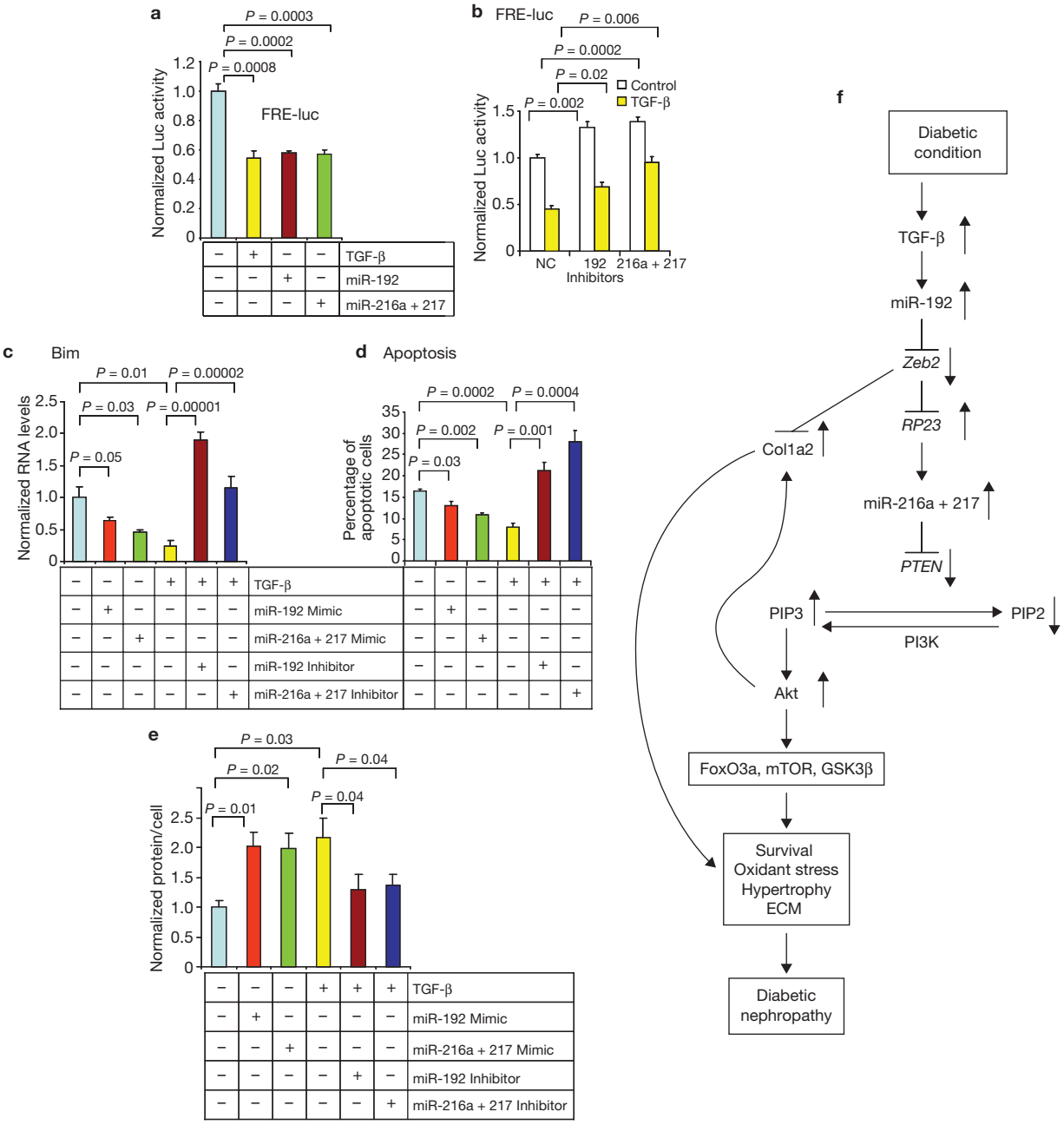

Figure 5 Effects of miR-192 and miR-216a + 217 on FoxO3a activity, MMCs apoptosis and hypertrophy. (**a**) FoxO3a function was monitored by pFRE–Luc. Luciferase activity was decreased by TGF-β. Similarly to TGF-β, miR-192 and miR-216a + 217 mimics (10 nM) decreased reporter activity ($n = 4$). (**b**) Inhibitors (10 nM) of miR-192 and miR-216a + 217 increased the basal activity of pFRE–Luc and also restored the reporter activity inhibited by TGF-β ($n = 4$). (**c**) In serum-depleted cells, *Bim* expression levels (as detected by rtqPCRs) were decreased by miR-192 and miR-216a + 217 mimics as well as TGF-β. Inhibitors of miR-192 and miR-216a + 217 reversed the inhibitory effect of TGF-β on *Bim* expression ($n = 3$). (**d**) TGF-β, as well as miR-192 and miR-216 + 217 mimics, reduced serum depletion-induced apoptosis of MMCs. Inhibitors of miR-192 and miR-216a + 217 reversed the inhibitory effect of TGF-β ($n = 4$). (**e**) Cellular protein levels were calculated as the total amount protein amount / total cell number. Protein levels (hypertrophy) were increased by TGF-β in serum-depleted cells. Mimics of miR-192 and miR-216a + 217 induced hypertrophy to the same extent as TGF-β. Conversely, inhibitors of miR-192 and miR-216a + 217 attenuated TGF-β-induced hypertrophy ($n = 3$). (**f**) Schematic model of miRNA-dependent amplifying mechanisms in the pathogenesis of diabetic nephropathy. TGF-β induced by diabetic conditions upregulates miR-192 which targets *Zeb2*. The ensuing decrease in Zeb2 upregulates the expression of *RP23* which hosts miR-216a and miR-217, both of which target *PTEN*. The decrease in PTEN increases PIP3 and Akt activation, leading to the phosphorylation of Akt target proteins and increased MMC survival, oxidant stress, ECM expression and hypertrophy, all main features of diabetic nephropathy. Data are mean ± s.e.m.

FoxO3a phosphorylation (Fig. 4e), as reported previously[4]. The miR-192 and miR-216a + miR-217 mimics induced a similar cytoplasmic translocation of FoxO3a in serum-depleted MMCs (Fig. 4e). Conversely, inhibitors of these miRNAs induced nuclear localization of FoxO3a in TGF-β-treated MMCs (Fig. 4e). Quantification of the percentage of cells with cytoplasmic FoxO3a (Fig. 4f) confirms that these miRNAs induced significant

nuclear to cytoplasmic translocation of FoxO3a in serum-depleted MMCs, similarly to TGF-β, whereas inhibitors of these miRNAs attenuated TGF-β effects. Therefore, these miRNAs promote FoxO3a phosphorylation and cytoplasmic translocation by inhibiting Pten and activating Akt.

To test whether this miRNA circuit functionally inhibits FoxO3a transcriptional activity, MMCs were transfected with a luciferase reporter containing forkhead-response elements (pFRE–Luc)[4] along with the miRNAs. Both miR-192 and miR-216a + miR-217 inhibited luciferase activity of the reporter, similarly to TGF-β (Fig. 5a). Inhibitors of these miRNAs could override the TGF-β-induced reduction in luciferase activity (Fig. 5b). By downregulating Pten and activating Akt, this miRNA circuit could inhibit FoxO3a function. The expression of the pro-apoptotic gene *Bim*, a FoxO3a target, was inhibited by miR-192 and miR-216a + miR-217 as well as TGF-β, whereas inhibitors of these miRNAs reversed the effects of TGF-β (Fig. 5c). Moreover, miR-192, miR-216a + miR-217 and TGF-β prevented serum-depletion-induced MMC apoptosis, and the TGF-β effect was reversed by miR inhibitors (Fig. 5d). Therefore, similarly to TGF-β, these miRNAs promote MMC survival by downregulating *Bim* through Akt activation (due to Pten reduction) and subsequent FoxO3a phosphorylation. Expression of the antioxidant gene *MnSOD* (manganese superoxide dismutase), another FoxO3a target[4], was also inhibited by TGF-β, miR-192 and miR-216a + miR-217 mimics, whereas miRNA inhibitors restored its expression (Supplementary Information, Fig. S5a), suggesting that this miRNA circuit may also upregulate oxidant stress in MMCs through FoxO3a phosphorylation.

Finally, we evaluated glomerular mesangial cell hypertrophy, a major feature of diabetic nephropathy and a downstream consequence of Akt activation[2,5,6,11,28]. TGF-β significantly increased protein levels (Fig. 5e), confirming that it induces MMC hypertrophy. The miR-192 and miR-216a + miR-217 mimics similarly induced hypertrophy in serum-depleted glomerular mesangial cells, whereas inhibitors of these miRNAs attenuated TGF-β effects (Fig. 5e), suggesting that this miRNA circuit mediates TGF-β-induced MMCs hypertrophy. The Akt downstream proteins mTOR and GSK3β also regulate protein synthesis and hypertrophy[6,28]. Our results from miRNA mimics and inhibitors on mTOR and GSK3β phosphorylation (Fig. 4a–d) further support a role for these miRNAs in TGF-β-induced glomerular mesangial cell hypertrophy. As FoxO3a is implicated in the regulation of autophagy genes[29], these miRNAs might also promote hypertrophy through reducing autophagy.

Notably, cyclin-dependent kinase inhibitor p21-mediated cell-cycle arrest, but not apoptosis, of cancer cells induced by miR-192 through the p53 pathway was reported recently[30], and miR-192 was found to activate the promoter of the anti-apoptotic Survivin gene[31]. Our results show that miR-192 also activates Akt and protects cells from apoptosis (Fig. 5d). Therefore, miR-192 probably induces cell-cycle arrest but not apoptosis. Since p21-mediated cell-cycle arrest is related to glomerular mesangial cell hypertrophy[11], miR-192 might also promote glomerular hypertrophy by activating p21 and p53. Further studies are needed to verify this.

In summary, miR-216a and miR-217 are co-expressed with *RP23* and downregulate the same target (*PTEN*), illustrating an efficient way to control target genes under certain disease states (Supplementary Information, Fig. S6). Co-expression of miR-216a and miR-217 in the pancreas (high in acinar but low in islets)[24,32] and expression of PTEN (high in islets but low in acinar)[33] support such regulation. Our current results also demonstrate a new mechanism for Akt activation by TGF-β through miR-216a and miR-217-mediated PTEN downregulation, controlled by upstream miR-192 (Fig. 5f). Akt activation by this miRNA circuit produced biological effects in MMCs including ECM gene expression, cell survival and hypertrophy, all classic features of diabetic nephropathy . Since the E-box regulators, PTEN and Akt, also have key roles in cancer development and insulin signalling[12,13,23], miR-192, miR-216a and miR-217 may also regulate not only kidney disorders, but also cancer and metabolic diseases. Inhibitors of these miRNAs, their host non-coding RNAs or promoters could therefore serve as new therapeutic modalities for such diseases. □

METHODS

Methods and any associated references are available in the online version of the paper at http://www.nature.com/naturecellbiology/.

Note: Supplementary Information is available on the Nature Cell Biology website.

ACKNOWLEDGEMENTS

This work was supported by grants from the NIH-National Institute of Diabetes and Digestive and Kidney Diseases and the Juvenile Diabetes Research Foundation (to RN). We are grateful to M. C.-T. Hu for a generous gift of plasmids (pFRE–Luc and FoxO3a–GFP), L.Wang and J. Arizala for technical assistance and S. DaCosta for editing the manuscript.

AUTHOR CONTRIBUTIONS

M.K. and R.N. designed research; M.K., S.P., M.W., H.Y., L.L., I.N., A.G., and I.T. performed research; M.K., M.W., Y.N, H.S. and J.J.R. contributed new reagents/analytic tools; M.K., S.P. and I.T. analysed data and M.K. and R.N. wrote the paper.

COMPETING FINANCIAL INTERESTS

The authors declare no competing financial interests.

Published online at http://www.nature.com/naturecellbiology/
Reprints and permissions information is available online at http://npg.nature.com/reprintsandpermissions/.

1. Yamamoto, T., Nakamura, T., Noble, N. A., Ruoslahti, E. & Border, W. A. Expression of transforming growth factor beta is elevated in human and experimental diabetic nephropathy. *Proc. Natl Acad. Sci. USA* **90,** 1814–1818 (1993).
2. Sharma, K. & Ziyadeh, F. N. Hyperglycemia and diabetic kidney disease. The case for transforming growth factor-β as a key mediator. *Diabetes* **44,** 1139–1146 (1995).
3. Kato, M. *et al.* MicroRNA-192 in diabetic kidney glomeruli and its function in TGF-beta-induced collagen expression via inhibition of E-box repressors. *Proc. Natl Acad. Sci. USA* **104,** 3432–3437 (2007).
4. Kato, M. *et al.* Role of the Akt/FoxO3a pathway in TGF-β1-mediated mesangial cell dysfunction: a novel mechanism related to diabetic kidney disease. *J. Am. Soc. Nephrol* **17,** 3325–3335 (2006).
5. Mahimainathan, L., Das, F., Venkatesan, B. & Choudhury, G. G. Mesangial cell hypertrophy by high glucose is mediated by downregulation of the tumor suppressor PTEN. *Diabetes* **55,** 2115–2125 (2006).
6. Nagai, K. *et al.* Gas6 induces Akt/mTOR-mediated mesangial hypertrophy in diabetic nephropathy. *Kidney Int.* **68,** 552–561 (2005).
7. Xin, X., Chen, S., Khan, Z. A. & Chakrabarti, S. Akt activation and augmented fibronectin production in hyperhexosemia. *Am. J. Physiol. Endocrinol. Metab.* **293**, E1036–1044 (2007).
8. Yi, J. Y., Shin, I. & Arteaga, C. L. Type I transforming growth factor β receptor binds to and activates phosphatidylinositol 3-kinase. *J. Biol. Chem.* **280,** 10870–10876 (2005).
9. Runyan, C. E., Schnaper, H. W. & Poncelet, A. C. The phosphatidylinositol 3-kinase/Akt pathway enhances Smad3-stimulated mesangial cell collagen I expression in response to transforming growth factor-β1. *J. Biol. Chem.* **279,** 2632–2639 (2004).
10. Ghosh Choudhury, G. & Abboud, H. E. Tyrosine phosphorylation-dependent PI 3 kinase/Akt signal transduction regulates TGFβ-induced fibronectin expression in mesangial cells. *Cell Signal* **16,** 31–41 (2004).
11. Wolf, G. & Ziyadeh, F. N. Molecular mechanisms of diabetic renal hypertrophy. *Kidney Int.* **56,** 393–405 (1999).
12. Cully, M., You, H., Levine, A. J. & Mak, T. W. Beyond PTEN mutations: the PI3K pathway as an integrator of multiple inputs during tumorigenesis. *Nature Rev. Cancer* **6,** 184–192 (2006).
13. Lazar, D. F. & Saltiel, A. R. Lipid phosphatases as drug discovery targets for type 2 diabetes. *Nature Rev. Drug Discov.* **5,** 333–342 (2006).

14. Stefani, G. & Slack, F. J. Small non-coding RNAs in animal development. *Nature Rev. Mol. Cell Biol.* **9,** 219–230 (2008).
15. Bartel, D. P. MicroRNAs: target recognition and regulatory functions. *Cell* **136,** 215–233 (2009).
16. Sun, Y. *et al.* Development of a micro-array to detect human and mouse microRNAs and characterization of expression in human organs. *Nucleic Acids Res.* **32**, e188 (2004).
17. Tian, Z., Greene, A. S., Pietrusz, J. L., Matus, I. R. & Liang, M. MicroRNA-target pairs in the rat kidney identified by microRNA microarray, proteomic, and bioinformatic analysis. *Genome Res.* **18,** 404–411 (2008).
18. Wang, Q. *et al.* MicroRNA-377 is up-regulated and can lead to increased fibronectin production in diabetic nephropathy. *Faseb J.* **22,** 4126–4135 (2008).
19. Landgraf, P. *et al.* A mammalian microRNA expression atlas based on small RNA library sequencing. *Cell* **129,** 1401–1414 (2007).
20. Hua, X., Liu, X., Ansari, D. O. & Lodish, H. F. Synergistic cooperation of TFE3 and smad proteins in TGF-β-induced transcription of the plasminogen activator inhibitor-1 gene. *Genes Dev.* **12,** 3084–3095 (1998).
21. Sekido, R. *et al.* The delta-crystallin enhancer-binding protein delta EF1 is a repressor of E2-box-mediated gene activation. *Mol. Cell Biol.* **14,** 5692–5700 (1994).
22. Comijn, J. *et al.* The two-handed E box binding zinc finger protein SIP1 downregulates E-cadherin and induces invasion. *Mol. Cell* **7,** 1267–1278 (2001).
23. Nakagawa, Y. *et al.* TFE3 transcriptionally activates hepatic IRS-2, participates in insulin signaling and ameliorates diabetes. *Nature Med.* **12,** 107–113 (2006).
24. Wienholds, E. *et al.* MicroRNA expression in zebrafish embryonic development. *Science* **309,** 310–311 (2005).
25. Lim, L. P., Glasner, M. E., Yekta, S., Burge, C. B. & Bartel, D. P. Vertebrate microRNA genes. *Science* **299,** 1540 (2003).
26. Xiao, C. *et al.* Lymphoproliferative disease and autoimmunity in mice with increased miR-17-92 expression in lymphocytes. *Nature Immunol.* **9,** 405–414 (2008).
27. Elmen, J. *et al.* LNA-mediated microRNA silencing in non-human primates. *Nature* **452,** 896–899 (2008).
28. Glass, D. J. Signalling pathways that mediate skeletal muscle hypertrophy and atrophy. *Nature Cell Biol.* **5,** 87–90 (2003).
29. Salih, D. A. & Brunet, A. FoxO transcription factors in the maintenance of cellular homeostasis during aging. *Curr. Opin. Cell Biol.* **20,** 126–136 (2008).
30. Braun, C. J. *et al.* p53-Responsive MicroRNAs 192 and 215 Are Capable of Inducing *Cell* Cycle Arrest. *Cancer Res.* **68,** 10094–10104 (2008).
31. Gou, D., Zhang, H., Baviskar, P. S. & Liu, L. Primer extension-based method for the generation of a siRNA/miRNA expression vector. *Physiol. Genomics* **31,** 554–562 (2007).
32. Bravo-Egana, V. *et al.* Quantitative differential expression analysis reveals miR-7 as major islet microRNA. *Biochem. Biophys. Res. Commun.* **366,** 922–926 (2008).
33. Perren, A. *et al.* Mutation and expression analyses reveal differential subcellular compartmentalization of PTEN in endocrine pancreatic tumors compared to normal islet cells. *Am. J. Pathol.* **157,** 1097–1103 (2000).

DOI: 10.1038/ncb1897

METHODS

Cell culture. Primary MMCs were isolated and cultured as described previously[3] and used in all experiments. Recombinant human TGF-β1 was from R&D Systems Inc. Cells in 12-well-plates were serum-depleted for 48 h and then treated with TGF-β for the indicated time periods.

Animal studies. All animal studies were approved by Institutional Animal Care and Use Committee. Induction of diabetes with STZ in C57BL/6 mice was carried out as described previously[3]. Mice were used seven weeks after the onset of diabetes. *db/db* mice and genetic control *db/+* mice (ten weeks old) were from Jackson Laboratories. Glomeruli were sieved from mouse renal cortical tissues as described previously[3].

Real time quantitative PCR (rtqPCR). SYBR Green PCR Master Mix and 7300 Realtime PCR System (Applied Biosystems) were used to perform rtqPCR, which was used to detect miRNAs, as reported previously[3]. Sequences of miRNA-specific primers for cDNA synthesis and reverse primers for miR-216a were: 5'-CATGATCAGCTGGGCCAAGACACAGTTGCCAGCTG-3' and 5'-TAATCTCAGCTGGCAA-3'. Primers for miR-217 were: 5'-CATGATCAGCTGGGCCAAGAATCCAGTCAGTT-3' (cDNA synthesis) and 5'-TACTGCATCAGGAACT-3' (reverse primer). Expression levels of miRNA were also confirmed by poly-adenylation of mature miRNA and cDNA synthesis primed by oligo-dT primer tagged with a universal primer sequence (miScript System). cDNA was amplified using miRNA-specific and universal primers. For miR-192, miR-194, miR-216a and miR-217 PCRs, the same reverse primers mentioned above and the primers provided by Qiagen were used as miRNA-specific primers. Either 5S RNA or 18S RNA served as internal control (Ambion). PCR primers for *Col1a2, Zeb1, Zeb2* and *MnSOD* were as described previously[3,4]. Mouse *Pten* PCR primers were from SuperArray Bioscience Corporation. *RP23* PCR primers were: forward (exon 2) 5'- TACTGAACCATCCCCACATCCC -3' and reverse (exon 3) 5'- TGGCCCAGCTGTAGTTCTGTGA -3', reverse (exon 3 and 4 junction) 5'- CTTTCTCCAGCCTCAGAGTG -3' reverse (exon 4) 5'- ATGCAGGCAGTAATCCTTGTG -3'. *Bim* PCR primers were: forward 5'-cCGGAGATACGGATTGCACAGG-3' and reverse 5'-cgcttATACCAGACGGAAGATAAAGcG-3'. CypA primers were: forward 5'-ATGGTCAACCCCACCGTGT-3' and reverse 5'-TTCTTGCTGTCTTTGGAACTTTGTC-3'.

Western blotting analysis. These were performed as described previously[3,4]. Antibodies against PTEN, P-Foxo3a, P-mTOR, P-GSK3β, Cyclophilin A (Cell Signaling) and β-actin (Sigma-Aldrich) were used. All primary antibodies were used at a 1:1000 dilution.

Immunohistochemistry. Immunostaining of renal cortical sections was performed as reported previously[4] using antibodies to PTEN and quantified with Image-Pro Plus 5.1 software (Media Cybernetics, Inc.).

Target prediction and genomic structure of human and mouse miRNAs. We used the online databases miRBase (http://microrna.sanger.ac.uk), TargetScan (http://www.targetscan.org), microRNA.org (http://www.microrna.org/microrna/home.do), NCBI (http://www.ncbi.nlm.nih.gov), Blat (http://genome.ucsc.edu/cgi-bin/hgBlat) and Ensembl (http://www.ensembl.org) for target prediction and analysis of the genomic structure of human and mouse miRNAs.

Cloning of the promoter regions of RP23-298H6.1-001. The promoter regions of *RP23* were cloned by PCR using primers, 5'-AAGGagatctTCACTTCATGAACAAACTGCCTT-3' and 5'-CTTGaagcttCATCACTGGAATGTTATTAAGTCAAG-3' for the proximal –0.5 kb fragment, 5'-CTActcgaGGCTACCCTGCATCCTTTTCTAG-3' and 5'-CTTGaagcttCATCACTGGAATGTTATTAAGTCAAG-3' for the proximal –2.7 kb fragment, 5'-CCAAGCTAGCCAGATCATAATAGTGAGGTTTGG-3' and 5'-CTTGaagcttCATCACTGGAATGTTATTAAGTCAAG-3' for the proximal –3.5 kb fragment, 5'-CCCAGCTAGCCAGATCAAAAGCAGCTTGGG-3' and 5'-CTTGaagcttCATCACTGGAATGTTATTAAGTCAAG-3' for the proximal –4.8 kb fragment, 5'-CCAAGCTAGCCAGATCATAATAGTGAGGTTTGG-3' and 5'-CACTCGAGTCTGATTGGAGTTACCAGTG-3' for the –3.5–2.7 kb fragment, and 5'-CCCAGCTAGCCAGATCAAAAGCAGCTTGGG-3' and 5'-GCACTCGAGTCTGTGTGCAGGCTAAGTGC-3' for the –4.8–3.5 kb fragment. The entire –4.8 k, –3.5 k, –2.7 k and proximal regions were cloned into pGL4. The –3.5 –2.7 kb and –4.8–3.5 kb fragments were cloned into the pGL3-promoter (Promega). Reporter with 2× E-boxes was made by digestion of *Hpa*I site. 1×E-box was generated by PCR using a primer, 5'-TGGGAGATCTTGGCACGTGCCTTCAATCCCA-3' (E-box underlined) and –2.7 k reverse primer, and cloned into the pGL3 promoter. The mutant E-box construct was generated by PCR using primers, 5'-TGGCTAGCGCCTTCAATCCCA-3' (mutant E-box is underlined) and –2.7 k reverse primer, and cloned into the pGL3P.

Plasmids and 3'-UTR reporters. Full-length 3'UTR of mouse *Pten* was amplified using primers, 5'-CATGCTCGAGCTTATCAAGAGGGATAAAATACCATG-3'and 5'-CATGCGGCCGCCACAGGAAGGTATTTCTAGTCTTATG-3'. The PCR fragment was digested with *Xho*I and *Not*I and cloned into psiCheck2 (Promega). The shorter 1.4 kb fragment of *Pten* 3'UTR (which includes the miR-216a and miR-217 sites) was amplified using primers, 5'-CATGCTCGAGCTTATCAAGAGGGATAAAATACCATG-3' and 5'-GTTGCGGCCGCTTTACTGCAACTCTAATTTCTTTTTTAAC-3'. The miR-216a site mutant in the 1.4 kb construct was made by Quick Change site-directed mutagenesis (Stratagene) using primers, 5'- TTCACAGGAAATTTCAACTCCGAATTCAACAGTAA-3' and 5'-TTACTGTTGAATTCGGAGTTGAAATTTCCTGTGAA-3'. Substituted bases are underlined. The miR-217 site mutant was amplified using primers, 5'-CATGCTCGAGCTTATCAAGAGGGATAAAATACCATG-3' and 5'-GTTGCGGCCGCTTGAGATCTACTCTAATTTCTTTTTTAAC-3'. Substituted bases are underlined. Sequences of all the inserts were confirmed by sequence analysis. For *Pten* 3'UTR minimum target site reporters, *Not*I site-tagged potential target sequences in the 3'UTR of mouse *Pten* (for the miR-216a site, sense, 5'-GGCCTTCACAGGAAATTTCAACTTGAGATTC-3'; antisense, 5'-GGCCGAATCTCAAGTTGAAATTTCCTGTGAA-3', for the miR-217 site, sense, 5'-GGCCAAAAGAAATTAGAGTTGCAGTAA-3'; antisense, 5'-ggccTTACTGCAACTCTAATTTCTTTT-3') were cloned into *Not*I site of psiCheck2 (Promega). A plasmid containing a sense *Pten*-3'UTR sequence was used as reporter (psiCheck2mPten-3'UTR-S) and the plasmid containing the 3'UTR sequence in the anti-sense orientation was used as negative control (psiCheck2mPten-3'UTR-AS). The plasmid expressing FoxO3a–GFP and the luciferase reporter plasmid with pFRE–Luc were described previously[4].

Luciferase assays. MMCs were transfected with luciferase reporter plasmids and/or small RNAs using XtremeGENE (Roche) in 24-well-plates and treated with TGF-β as reported previously[3]. After 24 h, luciferase activity was measured as described previously[3]. For miRNA and shRNA experiments, cells were treated for 48 h. Glomerular mesangial cells were also transfected with plasmids and/or small RNAs using Nucleofector (Amaxa Biosystems). Basic Nucleofector Kit for Primary Smooth Muscle Cells (Amaxa) was used. Five programs (A33, D33, P13, P24 and U25) were tested to examine the transfection efficiency of glomerular mesangial cells with pmaxGFP (Amaxa). Program U25 resulted in highest efficiency (~60%) and was used in subsequent experiments (Supplementary Information, Fig. S5b).

miRNA mimics and inhibitor oligonucleotides. miRNA mimics, negative control #1 mimics, miRNA inhibitors, and negative control #1 inhibitors were obtained from Dharmacon. Sequences of mimics and inhibitors are based on Sanger miRBase (http://microrna.sanger.ac.uk). LNA-modified anti-miRNAs were obtained from Exiqon and Integrated DNA Technologies, Inc. LNA–anti-miR-192: 21mer, 5'-gGctGtcAatTcaTagGtcAg-3' (uppercase: LNA; lowercase: DNA, full phosphorothioate) or control LNA-anti-miR-239b; 21mer, 5'-cAgtActTttGtgTagTacAa-3' were subcutaneously injected (2.5 mg kg^{-1}) into normal C57BL/6 mice and renal cortical tissues were harvested 6 h later.

***In situ* hybridization.** To detect LNA-anti-miR-192 accumulation *in vivo, in situ* hybridization was performed as described previously[27]. Briefly, frozen kidney cortex sections from LNA-anti-miR-192-injected and saline control mice ($n = 3$ per group) were fixed in paraformaldehyde (3% for 10 min at room temperature) followed by rinsing in PBS. Slides were pre-hybridized (at 48 °C for 30 min) in hybridization solution (50% formamide, 5× SSC, 500 μg ml^{-1} yeast tRNA and 1×Denhardt's solution), and then hybridized (at 48 °C for 5 min) with a Texas Red-labeled LNA-modified oligonucleotide probe complementary to LNA-anti-miR-192 (21mer, 5'-TexasRed-ctgAccTatGaaTtgAcaGcc-3' (Exiqon) followed by post-hybridization wash (3 × 10 min, 55 °C) in 0.1× SSC. Slides were then stained with DAPI (4,6-diamidino-2-phenylindole), mounted and analysed using a fluorescence microscope.

***Zeb2*-knockdown siRNA.** To knockdown *Zeb2* in MMCs, ON-TARGETplus SMART pool siRNA (Dharmacon) was transfected using Amaxa Nucleofector. Target sequences are 5'-GAGCAGACAGGCUUACUUA-3', 5'-GUAAAUGGCCGAAUGAGAA-3', 5'-GCGACACGGCCAUUAUUUA-3' and 5'-GCAGGUAACCGCAAGUUCA-3'. ON-TARGETplus Non-targeting Pool (Dharmacon) was used as a control.

Cell number and cellular protein levels. To calculate cellular protein content per cell, MMCs were trypsinized and counted using a Coulter Counter with 100-μm aperture (Beckman). Cells were lysed, and the total protein content determined using Bio-Rad Protein Assays (Bio-Rad).

Apoptosis assay. Apoptosis was evaluated with the ApopTag Fluorescein kit from Chemicon/Millipore. Slides were counterstained with DAPI (Sigma), washed and embedded in Vectashield (Vector Labs). Quantitative evaluations were performed with laser scanning cytometry[34]. Briefly, stained slides were scanned through a 40× objective at 0.5-μm steps using iCys laser scanning cytometer (Compucyte) and iCys 3.3.2 software. Nuclei were contoured using the 405-nm laser based on the DAPI fluorescence. TUNEL-positive cells were recorded using the 488-nm laser.

Data Analyses. Results are expressed as mean ± s.e.m. from multiple experiments. Paired Student's t-tests (two-tailed) were used to compare two groups. Statistical significance was detected at the 0.05 level.

34. Omori, K. *et al.* Improvement of human islet cryopreservation by a p38 MAPK inhibitor. *Am. J. Transplant* **7,** 1224–1232 (2007).

nature cell biology

DOI: 10.1038/ncb1897

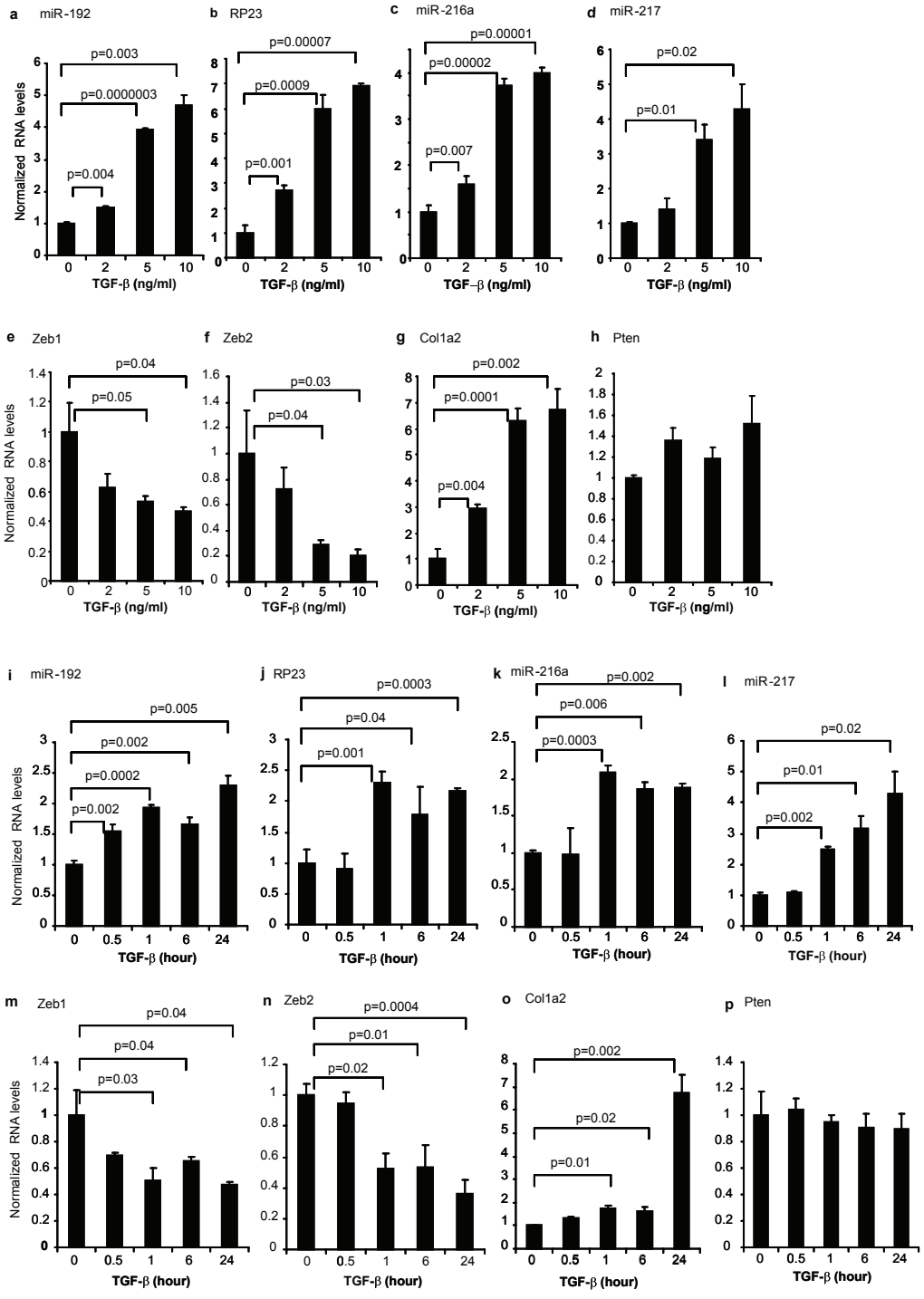

Figure S1 Dose response and time course of the effects of TGF-β on RNA levels of various genes. Dose response. MMC were treated with 0, 2, 5 or 10 ng/ml of TGF-β for 24 hours. Expression levels of miR-192 (**a**), *RP23* (**b**), miR-216a (**c**), miR-217 (**d**), *Zeb1* (**e**), *Zeb2* (**f**), *Col1a2* (**g**) and *Pten* (**h**) were examined by RT-qPCR (mean and s.e.m., n=3). **Time course.** MMC were treated with 10ng/ml TGF-β for 0, 0.5, 1, 6, 24 hours. Expression levels of miR-192 (**i**), *RP23* (**j**), miR-216a (**k**), miR-217 (**l**), *Zeb1* (**m**), *Zeb2* (**n**), *Col1a2* (**o**) and *Pten* (**p**) were examined by RT-qPCR (mean and s.e.m., n=3).

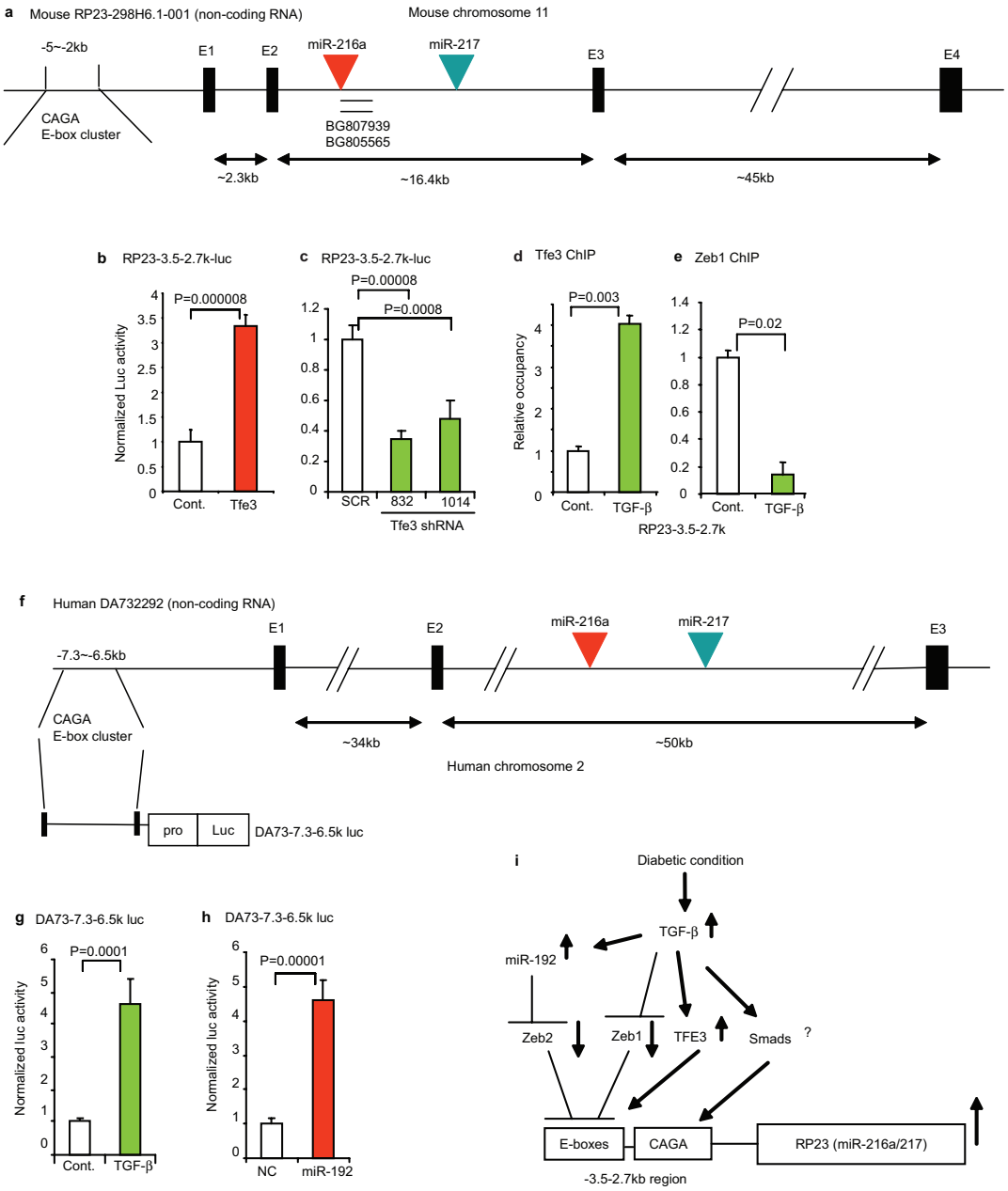

Figure S2 Schematic representations of the genomic structures of mouse (**a**) and human (**f**) non-coding RNAs showing locations of miR-216a and miR-217. **a**, Genomic structures of mouse miR-216a, miR-217 and a non-coding RNA (RP23-298H6.1-001, RP23) located in mouse chromosome 11. Two ESTs (BG807939 and BG805565) were identified just after the miR-216a precursor sequence which could be cropped fragments of the precursor miR-216a RNA. CAGA repeats and potential E-box clusters were found in the -5~-2kb upstream region of mouse *RP23*. **b**, *Tfe3* overexpression in MMC significantly increased promoter-Luc activity of RP23-3.5-2.7k-luc (n=4). *Tfe3* and its shRNA expression vectors were previously described[23]. **c**, Cotransfection with *Tfe3* shRNAs (two constructs targeting different sites, 832 and 1014) significantly decreased RP23-3.5-2.7k-luc activity (n=4). **d**, ChIP analysis showing significant increase in Tfe3 occupancy at the RP23-3.5-2.7k region by 6h of TGF-β treatment (n=3). **e**. ChIP analysis showing decreased occupancy of Zeb1 at RP23-3.5-2.7k region (10% of control) 24 h after TGF-β treatment (n=3). ChIPs were performed with antibodies against Zeb1 (SantaCruz, Santa Cruz, CA), Tfe3 (BD Bioscience, Franklin Lakes, NJ), or IgG (negative control). ChIP-enriched DNA was purified and utilized as template for real time qPCRs using primers, 5'-TGGGAGATCTTGGCACGTGCCTTCAATCCCA-3' (E-box is underlined) and 5'-CACTCGAGTCTGATTGGAGTTACCAGTG-3'. **f**, Genomic structures of human miR-216a, miR-217 and a non-coding RNA (DA732292) on chromosome 2. CAGA repeats and potential E-box clusters are found in the -7.3~-6.5kb upstream region of human DA732292 genes. **g**,**h**, The -7.3-6.5k upstream region of human DA732292 (DA73-7.3-6.5-luc) was amplified using primers, 5'-CTAggtacCAGGTGGGGCAGGGGATTGTAG-3' and 5'-AAGcccgggCAGCTGGCCTACTAATCTACATACCCTT-3' and cloned into pGL3P. This Luc reporter responded significantly to TGF-β in MMC (**g**) and to miR-192 Mimic in human HEK293 cells (**h**) (n=4), similar to mouse *RP23* promoter. Bar graph data expressed as mean and s.e.m. **i**, Schematic model of RP23 promoter regulation. TGF-β increases *RP23* gene (also miR-216a and miR-217) expression by inducing miR-192 that targets and inhibits Zeb2 (E-box repressor), and also by inhibiting Zeb1 (another E-box repressor) (via as yet unknown mechanisms) and upregulating Tfe3 (E-box activator). Therefore, miR-216a and miR-217 may be induced by TGF-β via de-repression at the upstream E-boxes of the host *RP23* gene.

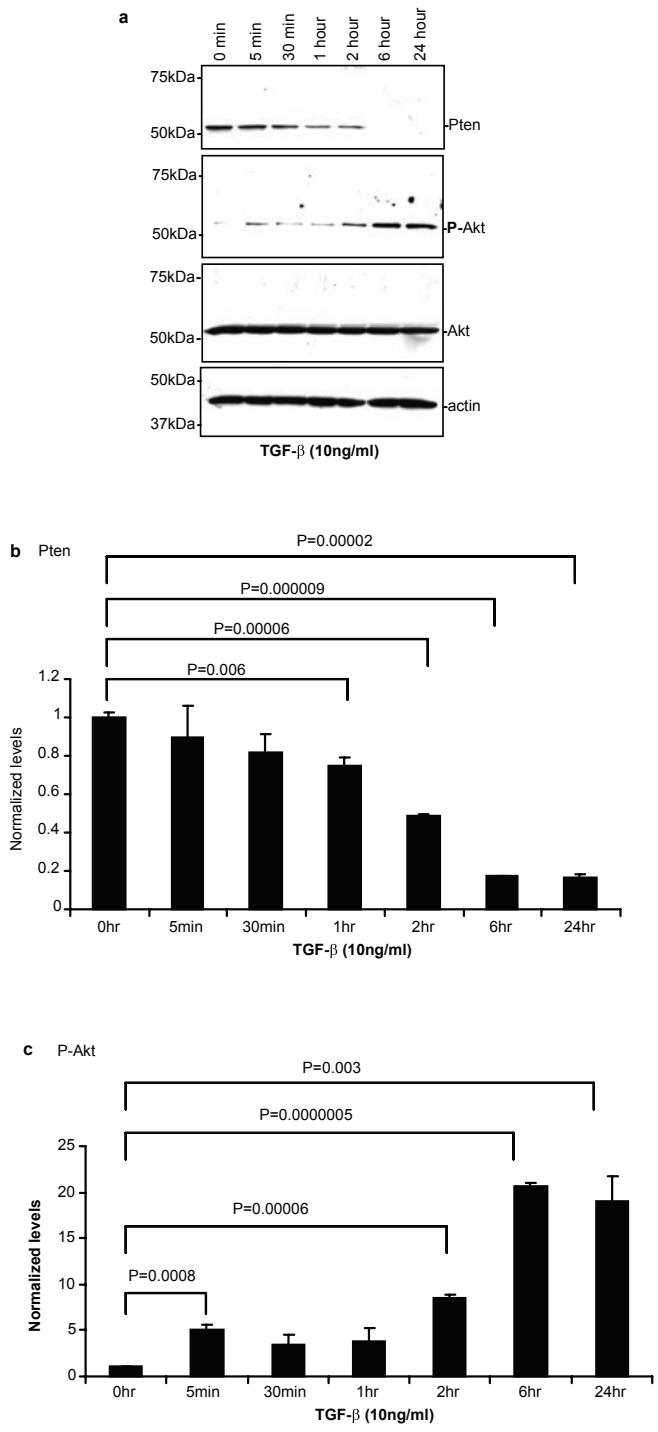

Figure S3 Time course study of Pten and Phospho-Akt in MMC treated with TGF-β. Western Blots showing **a-c**, Time-dependent decrease in Pten levels and parallel increase in P-Akt levels in MMC treated with 10ng/ml of TGF-β for 5 min to 24 hour. β-actin and total Akt levels used as internal controls. Bar graph data expressed as mean and s.e.m. (n=3).

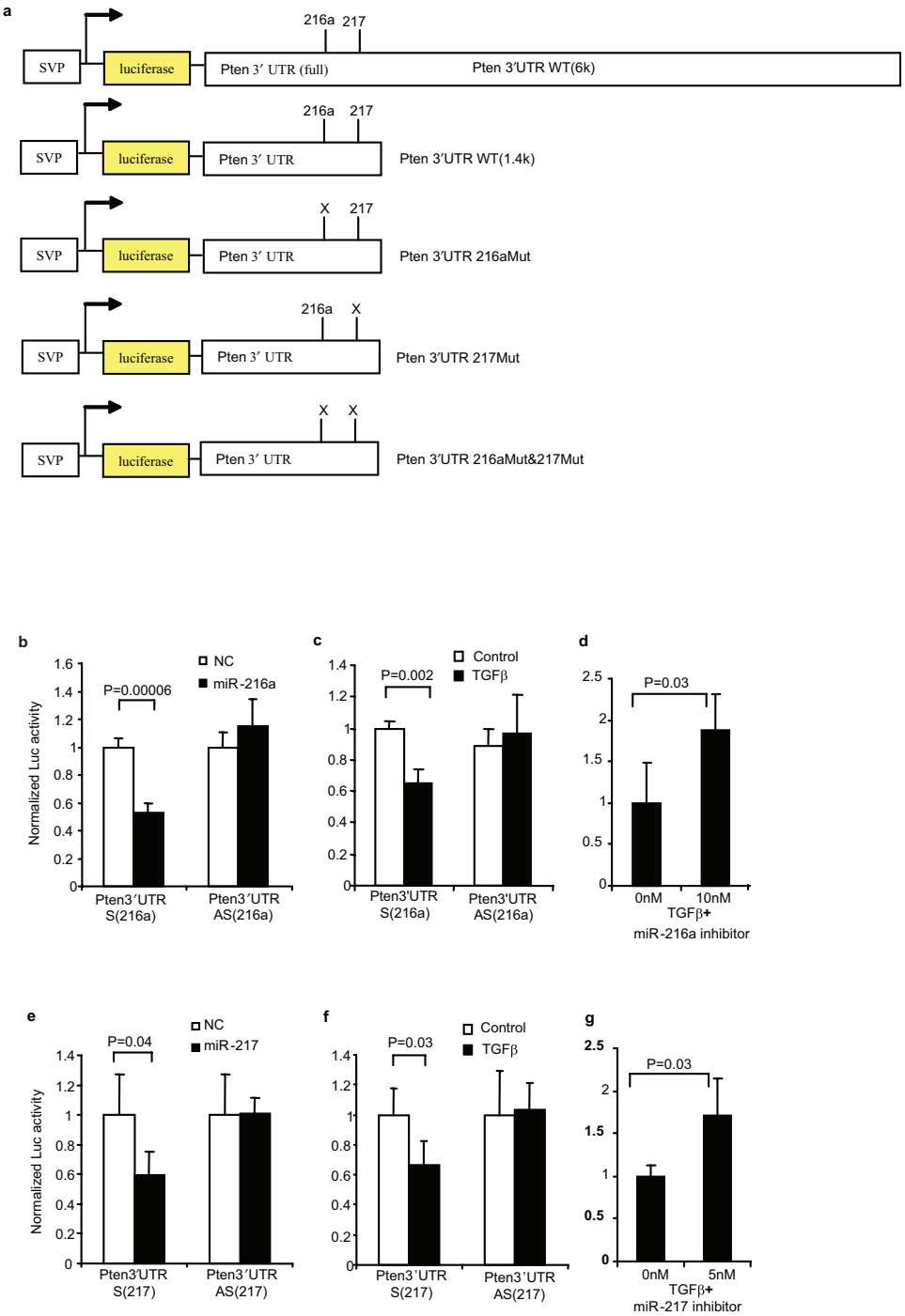

Figure S4 Effects of miR-216a and miR-217 Mimics and TGF-β on the *Pten* 3'UTR reporters. **a**, Pten is a target of miR-216a and miR-217. To verify *Pten* 3'UTR as a direct target of miR-216a, Luc reporters containing full-length (6k) or shorter (1.4 k) *Pten* 3'UTR regions, and mutants of miR-216a and miR-217 potential target sites were constructed. **b**, Plasmid containing luciferase fused to *Pten* 3'UTR (miR-216a minimum target site) was used as reporter (Pten 3'UTR-S). Reporter with antisense (AS) *Pten* 3'UTR (Pten 3'UTR-AS) was used as control. miR-216a Mimic or negative control (NC) was cotransfected with Luc reporters. Significant decrease in Luc activity was observed in *Pten* 3'UTR-S while no significant change was detected with control reporters (n=4). **c**, TGF-β effects on *Pten* 3'UTR reporters. Significant decrease in reporter activity was detected with *Pten* 3'UTR-S, but not with antisense control (n=4). **d**, Effects of miR-216a inhibitor on *Pten* 3'UTR-S. Reporter activity in TGF-β-treated cells was significantly increased by 10 nM miR-216a inhibitor (n=4). **e**, Effects of miR-217 Mimic on the *Pten* 3'UTR (miR-217 minimum target site) reporters. Significant decrease in reporter activity was observed with *Pten* 3'UTR-S by cotransfection of miR-217 Mimic, with no significant change in 3' UTR antisense control (n=4). **f**, TGF-β effects on *Pten* 3'UTR (217 site) reporters. TGF-β significantly decreased *Pten* 3'UTR-S reporter activity, with no change in the antisense reporter (n=4). **g**, Effects of miR-217 inhibitor on *Pten* 3'UTR. Reporter activity in TGF-β-treated cells was significantly increased by 5 nM of miR-217 inhibitor (n=4). Bar graph data expressed as mean and s.e.m.

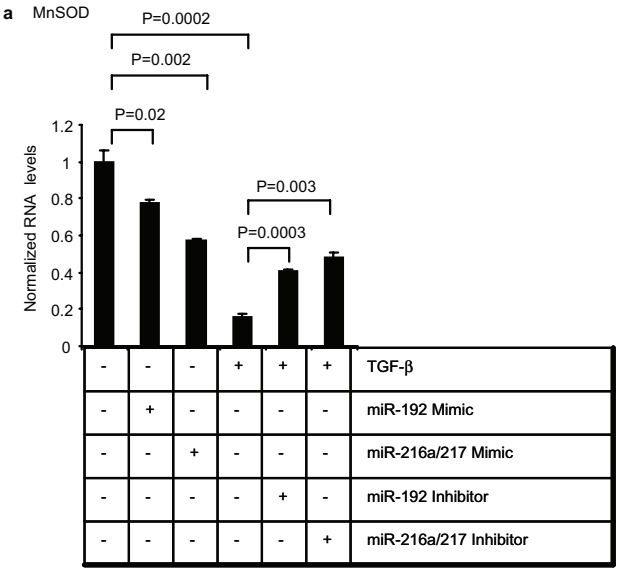

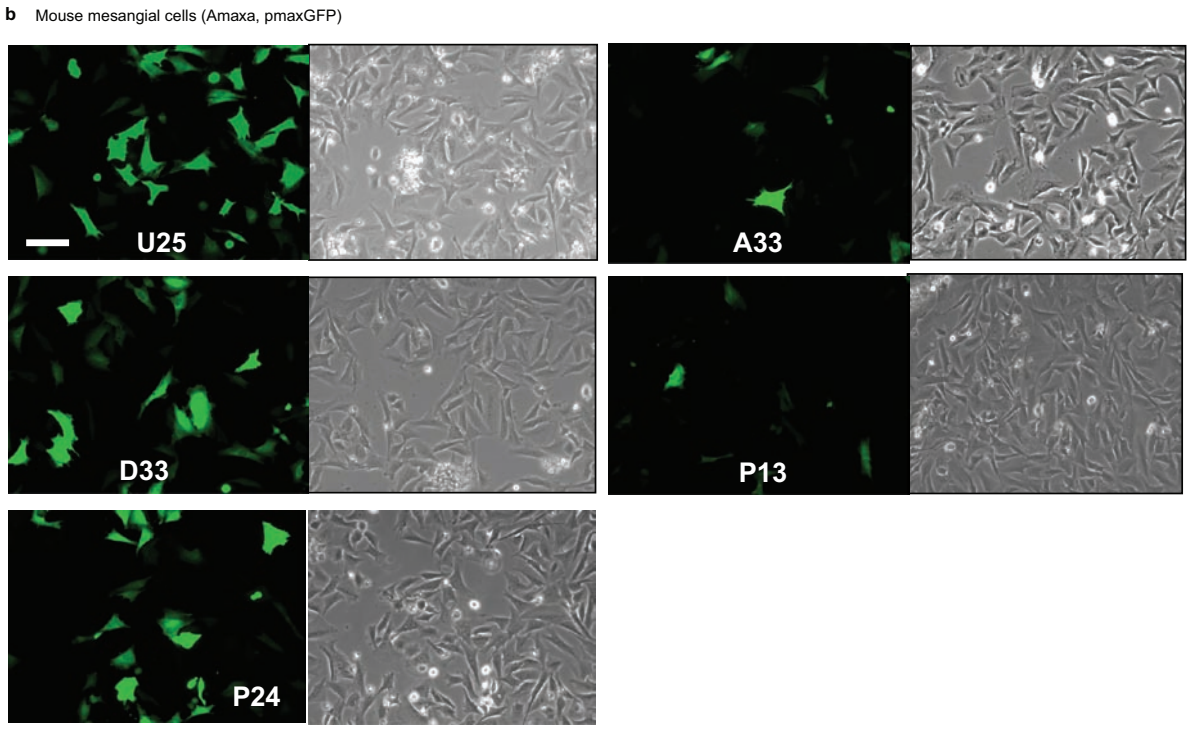

Figure S5 a, Effects of miRs on the expression of *MnSOD* gene, a known target of FoxO3a[4]. RT-qPCR results showing that TGF-β as well as miR-192 and miR-216a/217 mimics significantly reduced *MnSOD* gene expression. Conversely, inhibitors of miR-192 and miR-216a/217 significantly reversed TGF-β-induced decrease in *MnSOD* expression levels. These results suggest that this miR circuit may also lead to increased oxidant stress in response to TGF-β. Bar graph data expressed as mean and s.e.m (n=3). **b**, Efficiency of transfection in MMC. Amaxa Nucelofector was utilized to enhance the transfection efficiency in primary MMC. Basic Nucleofector Kit for Primary Smooth Muscle Cells (Amaxa Inc.) was used. Five programs (A33, D33, P13, P24 and U25) were evaluated to test efficiency of transfecting MMC with pmaxGFP (Amaxa Inc.). Program U25 resulted in the highest transfection efficiency (~60%) and was used in subsequent experiments. Scale bar, 20 μm.

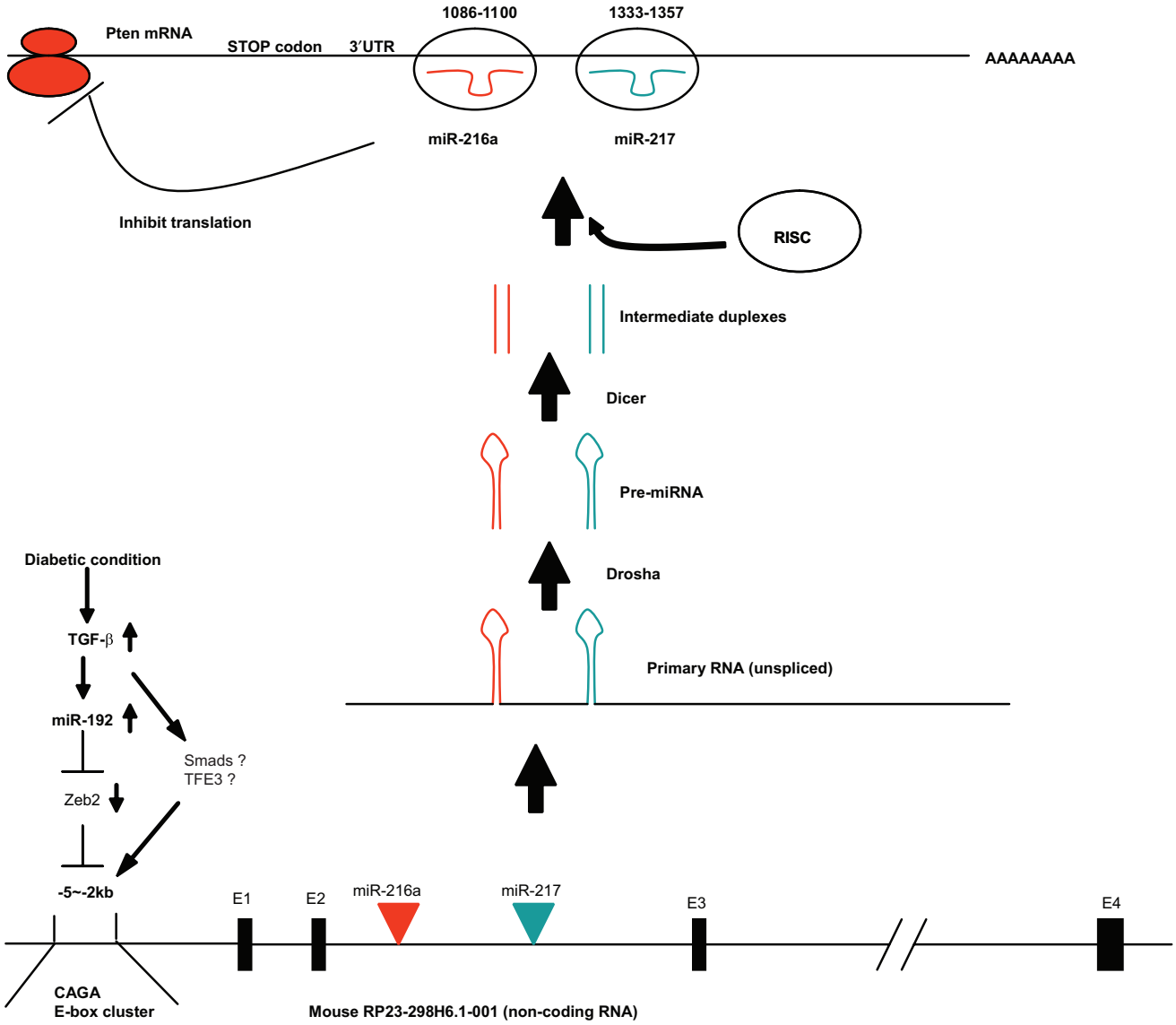

Figure S6 Schematic representation of the downregulation of Pten by TGF-β and diabetic conditions via a non-coding RNA (RP23-298H6.1-001, RP23) along with miR-216a and miR-217. These two miRs are expressed from the same genomic region, the second intron of *RP23*. *RP23* (and miR-216a/217) is regulated by miR-192 via E-boxes present in its promoter region, through similar regulation mechanisms shown for Col1a2 induction by miR-192 via enhancer E-boxes[3]. These E-box regulators might collaborate with Smad proteins activated by TGF-β receptor[20] to increase the *RP23*. Upon TGF-β treatment, miR-216a and miR-217 are upregulated together with their host *RP23*. Mature miRs are recruited into RISC (RNA induced silencing complex) and miR-216a- and miR-217-RISC target 1086-1100 and 1333-1357 regions respectively on the 3'UTR of *Pten* mRNA. This leads to significant decrease in Pten protein levels in MMC treated with TGF-β (Fig. 2e). However, no decrease in mRNA levels of *Pten* was observed (Supplementary Fig. S1h,p). Therefore, Pten protein levels are most likely reduced via translational inhibition by TGF-β and these miRs. This illustrates an efficient manner by which target genes can be controlled in response to TGF-β.

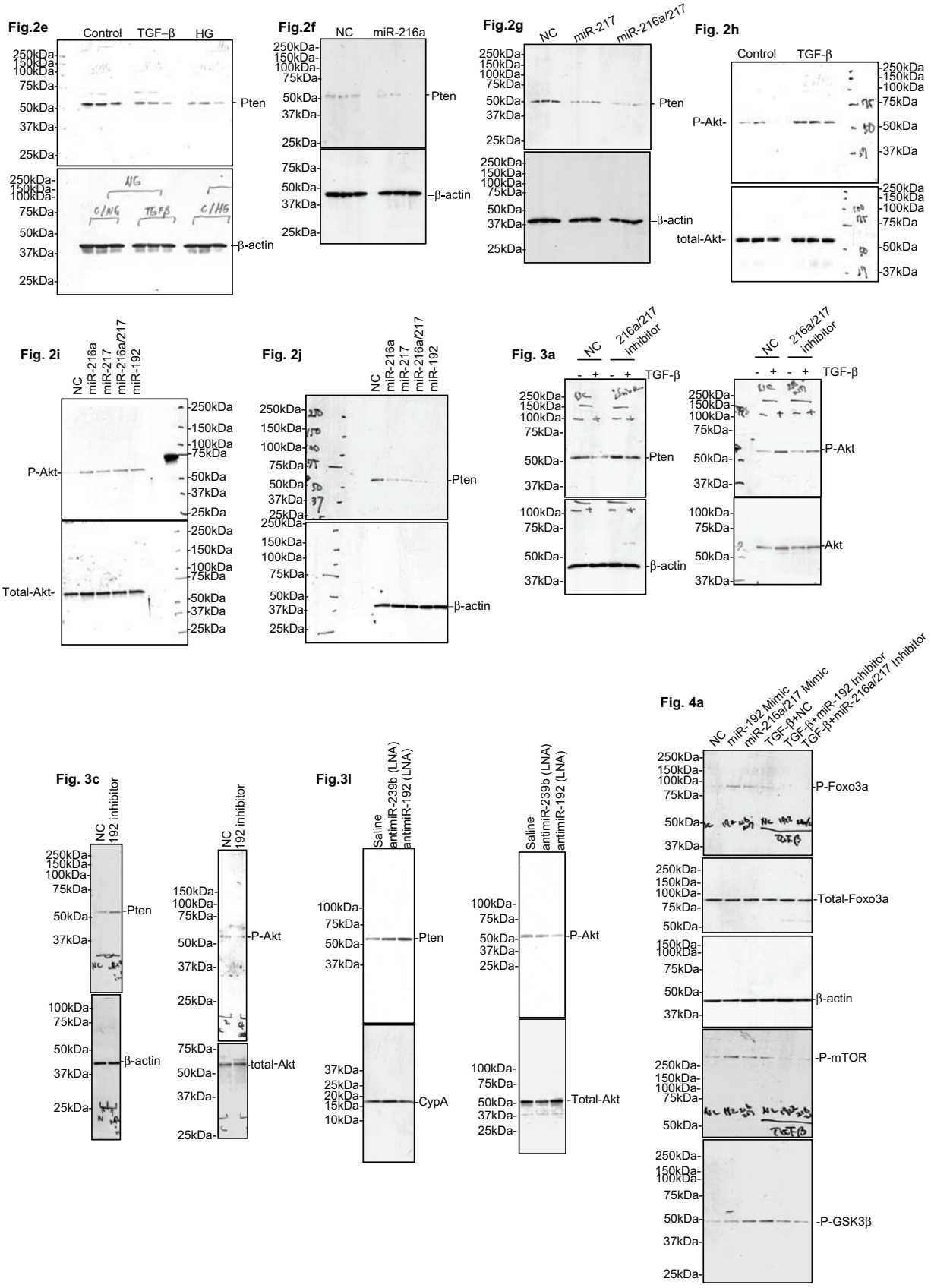

Figure S7 Full-scan or larger scan images for Fig.2e-j, 3a, 3c, 3l and 4a.

nature cell biology

The tyrosine kinase Stitcher activates Grainy head and epidermal wound healing in *Drosophila*

Shenqiu Wang[1], Vasilios Tsarouhas[1], Nikos Xylourgidis[1,2], Nafiseh Sabri[1], Katarína Tiklová[1], Naumi Nautiyal[1], Marco Gallio[1,2] and Christos Samakovlis[1,3]

Epidermal injury initiates a cascade of inflammation, epithelial remodelling and integument repair at wound sites. The regeneration of the extracellular barrier and damaged tissue repair rely on the precise orchestration of epithelial responses triggered by the injury[1,2]. Grainy head (Grh) transcription factors induce gene expression to crosslink the extracellular barrier in wounded flies and mice[3,4]. However, the activation mechanisms and functions of Grh factors in re-epithelialization remain unknown. Here we identify *stitcher* (*stit*), a new Grh target in *Drosophila melanogaster*. *stit* encodes a Ret-family receptor tyrosine kinase required for efficient epidermal wound healing. Live imaging analysis reveals that Stit promotes actin cable assembly during wound re-epithelialization. Stit activation also induces extracellular signal-regulated kinase (ERK) phosphorylation along with the Grh-dependent expression of *stit* and barrier repair genes at the wound sites. The transcriptional stimulation of *stit* on injury triggers a positive feedback loop increasing the magnitude of epithelial responses. Thus, Stit activation upon wounding coordinates cytoskeletal rearrangements and the level of Grh-mediated transcriptional wound responses.

Epidermal cells and their apical extracellular matrix provide a vital shield against physical damage and pathogens. Despite remarkable structural differences between mammalian skin and insect cuticles, Grh emerges as a conserved regulator of epidermal wound healing across phylogeny[1,5,6]. In wounded fly embryos it rapidly activates *Ddc* and *ple* (the genes encoding DOPA decarboxylase and tyrosine hydroxylase, respectively) to facilitate cuticle repair[3]. Similarly, Grhl-3 (mouse Grainy head-like 3) induces transglutaminase-1 expression in neonatal skin wounds to crosslink the stratum corneum. Grhl-3 has also been implicated in epithelial remodelling after wounding[4], but the mechanism by which Grhl-3 controls re-epithelialization is unclear.

We used two conserved Grh-binding elements (Gbes)[7–9] to search the *D. melanogaster* genome for target regions containing clustered binding sites by using the CIS-ANALYST algorithm (see Supplementary Information). We found a cluster of four putative Gbes within the second intron of CG10244 (Fig. 1a). We selected CG10244 for further analysis because it was strongly expressed in all ectodermal tissues, like *grh*, and it encoded an uncharacterized protein with homology to receptor tyrosine kinases (RTKs) (Supplementary Information, Fig. S1a). We renamed CG10244 *stitcher* (*stit*) to reflect its function (see below). *stit* expression initiated at stage 12 in epithelial tissues and was severely decreased in the epidermis of *grh* mutants in comparison with the wild type (Fig. 1b, c). The relative amount of *stit* mRNA in *grh* mutants only reached about 50% of wild-type levels by stage 16 (Supplementary Information, Fig. S1b). Conversely, Grh overexpression in epidermal stripes of *en>grh* embryos activated striped *stit* expression, indicating that Grh controls *stit* during development (Fig. 1d, e). Electrophoretic mobility-shift assays with the Grh DNA-binding region fused to glutathione *S*-transferase revealed direct Grh binding to Gbe3 of *stit* (Supplementary Information, Fig. S1c). To determine whether Grh binding activates *stit* transcription, we first tested the ability of *stit* Gbes to drive epidermal expression of a green fluorescent protein (GFP) reporter[10]. A 5.4-kilobase (kb) DNA fragment (α) encompassing five Gbes directed GFP to the epidermis of transgenic embryos. In *grh* mutants, this expression was severely reduced and limited to only a few cells (Fig. 1f, f′). We split the 5.4-kb DNA segment into a 3.4-kb fragment (β) and a 2-kb fragment (γ) containing the Gbe cluster (Fig. 1a). Both fragments directed epidermal GFP expression in transgenic embryos. However, whereas *stitβ*–GFP expression remained robust in *grh* mutants, *stitγ*–GFP levels were greatly decreased (Fig. 1g–h′). The *stit* regulatory region therefore contains a Grh-dependent enhancer. To test the contribution of Gbes to *stitγ*–GFP expression, we generated *stitδ*–GFP embryos with all four putative Gbes mutated. Epidermal GFP expression was markedly decreased in these embryos in comparison with *stitγ*–GFP (Fig. 1i). Therefore Grh directly activates *stit* during development. Does it also control *stit* expression during wound healing? Aseptic wounding of wild-type embryos induced a rapid accumulation of *stit* transcripts at wound sites (Fig. 1j). We punctured wild-type and *grh* mutants carrying either the *stitα*–GFP or the *stitγ*–GFP reporter.

[1]Department of Developmental Biology, Wenner-Gren Institute, Stockholm University, S-10691 Stockholm, Sweden.
[2]Present addresses: Netherlands Cancer Institute, Department of Tumor Biology, Plesmanlaan 121, 1066 CX Amsterdam, The Netherlands (N.X.); Neurobiology Section, Division of Biological Sciences, University of California, San Diego, 9500 Gilman Drive, La Jolla, California 92093-0649, USA (M.G.).
[3]Correspondence should be addressed to C.S. (e-mail: christos@devbio.su.se)

Received 29 December 2008; accepted 23 March 2009; published online 14 June 2009; DOI:10.1038/ncb1898

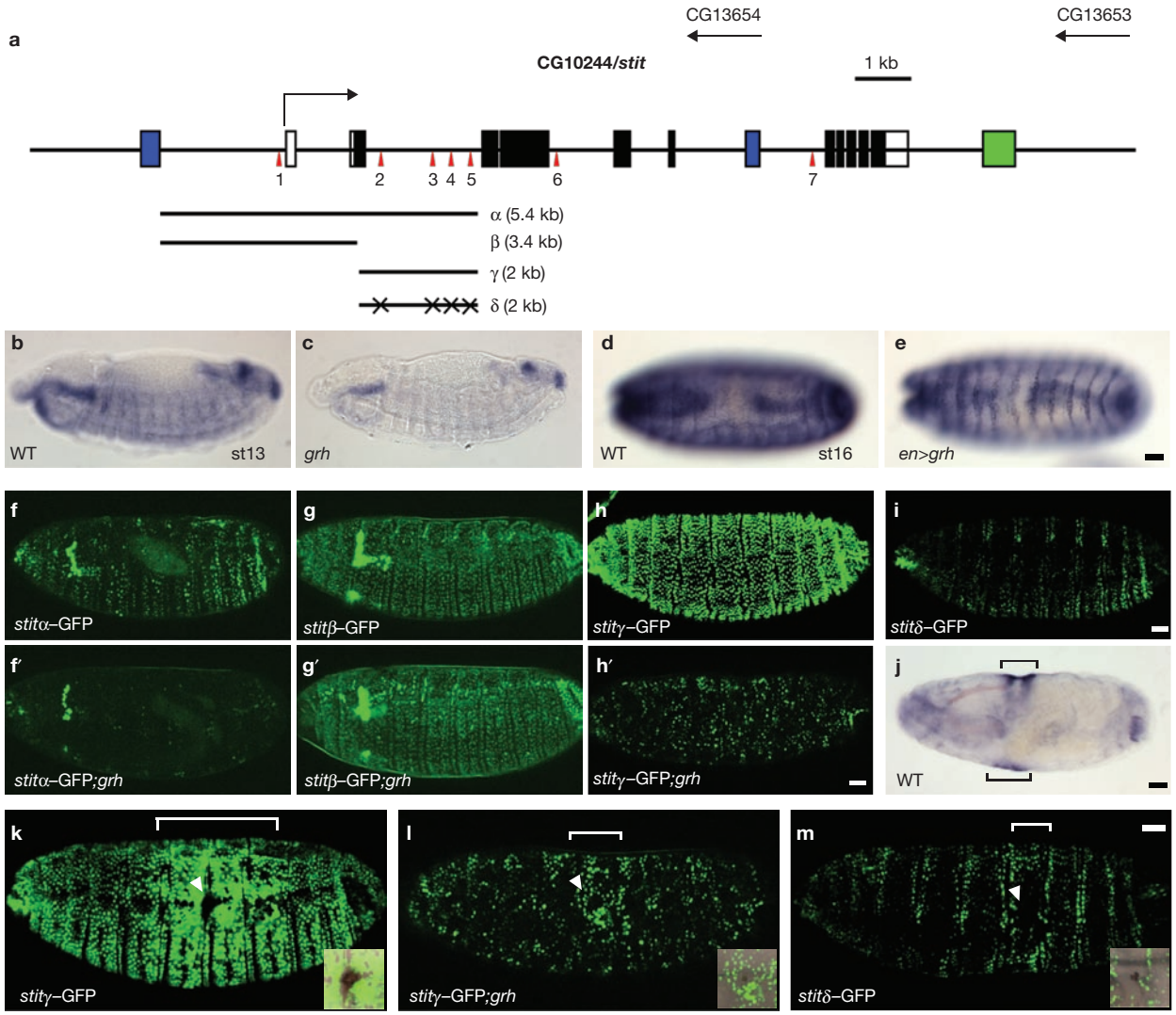

Figure 1 *stit* is a Grh target gene. (**a**) Schematic illustration of the *stit* locus. Blue and green boxes denote predicted exons of the flanking genes CG13654 and CG13653, respectively. *stit* exons are shown in white (non-coding) and black (coding) boxes. Arrows show the direction of transcription. Numbered arrowheads indicate predicted Gbes. The black lines denote the fragments (α, β, γ and δ) contained in *stit*–GFP reporters. Crosses on the *stitδ*–GFP reporter indicate the four mutated Gbes. (**b**–**e**) *In situ* hybridization shows epidermal *stit* expression in wild-type (wt; **b**, **d**), *grh* (**c**) and *en>grh* (**e**) embryos. Epidermal *stit* expression (**b**) is much reduced in *grh* mutants at stage 13 (**c**). Grh overexpression in epidermal stripes activates *stit* expression (**d**, **e**) at stage 16. (**f**–**i**, **k**–**m**) Confocal projections of live embryos expressing *stit–GFP* reporters. (**f**–**h**′) Epidermal *stitα*–GFP and *stityγ*–GFP expression is greatly decreased in *grh* mutants (**f**′, **h**′), whereas *stitβ*–GFP remains unchanged (**g**′). (**i**) Expression of *stitδ*–GFP is very low compared with that of *stityγ*–GFP. (**k**, **l**) Wounding induction of the *stityγ*–GFP reporter is decreased in *grh* mutants (**l**) compared with wild-type embryos (**k**). (**m**) *stitδ*–GFP is barely induced in wounded embryos. Arrowheads indicate wound sites identified by melanization (insets in **k**–**m**). (**j**) *In situ* hybridization shows *stit* mRNA induction around wounds (brackets). Scale bars, 25 μm.

The GFP levels from both reporters were robustly increased around the wounds of wild-type embryos. This induction was severely decreased in *grh* mutants (Fig. 1k, l; Supplementary Information, Fig. S1d). Finally, wild-type embryos carrying the *stitδ*–GFP reporter showed hardly any GFP induction on wounding (Fig. 1m). Grh therefore activates epidermal *stit* expression during development and wound closure.

To elucidate *stit* function, we characterized two null alleles (Supplementary Information, Fig. S2a–c). Homozygous animals for either allele and also the transheterozygotes die at late pupal stages. The lethality of *stit* mutants could be partly rescued by *stit* transgenic expression at low levels in ectodermal tissues by using the *69B*-GAL4 driver (Supplementary Information, Fig. S2d, e). High-level Stit expression caused embryonic lethality. Unlike *grh* mutants[11,12], *stit* embryos showed no developmental defects in ectodermal tissues (Supplementary Information, Fig. S3). Does Stit therefore have a role in wound healing? We punctured wild-type and *stit* embryos and examined survival after 20 h. Most wounded wild-type animals survived, whereas 30% of the mutants succumbed to wounding ($n = 379$; Supplementary Information, Fig. S4a). *stit* therefore facilitates survival on wounding. To address *stit* function in epithelial closure after puncture, we expressed an actin-binding GFP–*moesin* marker (GFP–*moe*) in the epidermis[13,14]. We inflicted 400–800-μm^2 puncture wounds on *69B*>GFP–*moe* and *stit 69B*>GFP–*moe* embryos and imaged them in parallel. Whereas *69B*>GFP–*moe* embryos sealed their wounds within 60 min (62 ± 11 min; $n = 13$), 26% of *stit 69B*>GFP–*moe* embryos failed to close their wounds within 3 h. The remaining mutants took on average 110 min to seal their wounds

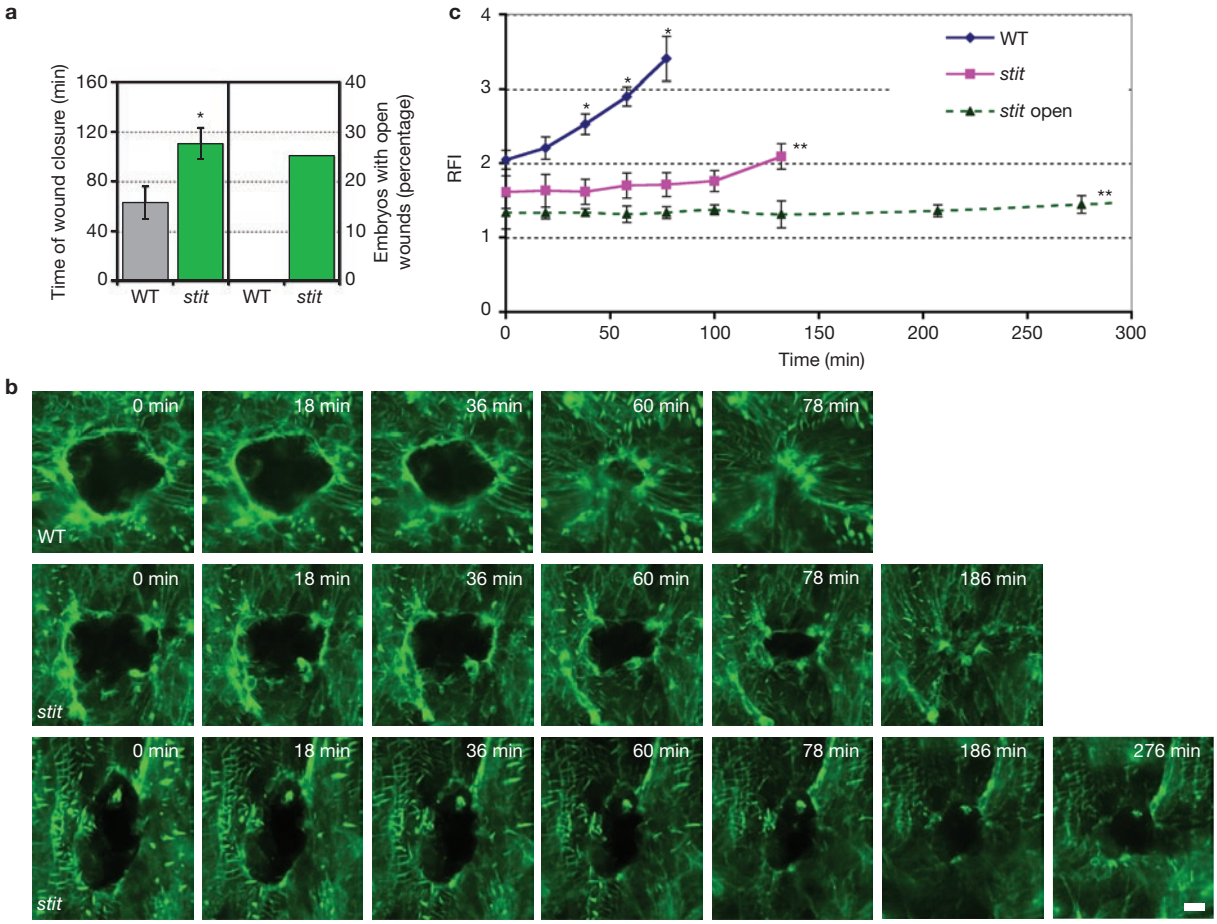

Figure 2 Re-epithelialization defects in *stit* mutants. (**a**) Plot showing delayed re-epithelialization in *stit 69B*>GFP–*moe* (*stit*) mutants compared with *69B*>GFP–*moe* (wt) embryos, which seal wounds within 62 min on average ($n = 13$). In all, 14 of 19 wounded *stit* mutants were significantly delayed (asterisk, $P = 0.0004$), whereas the rest (26%) remained with open wounds for at least 3 h. Data were acquired by wide-field fluorescence microscopy. (**b**) Time-lapse images of wounded *69B*>GFP–*moe* (wt) and *stit 69B*>GFP–*moe* (*stit*) embryos. In the wild type, a cable forms at the wound edge and condenses at closure (top row). Only disconnected patches of GFP–*moe* (middle row) or a very weak cable (bottom row) are found in *stit* wounds. The increased GFP accumulation in the wild-type embryo ($t = 78$ min, wt) is not detected in *stit* mutants. Micrographs are confocal projections and recording times after wounding are indicated. (See also Supplementary Information, Movies S3–S5.) Scale bar, 5 μm. (**c**) Plot of changes in RFI of GFP–*moe* at wound edges for the wild type ($n = 18$, in blue), for *stit* mutants that closed their wounds ($n = 18$, in magenta) and for *stit* mutants with open wounds during the recording period (*stit* open, $n = 9$, in green). RFIs were calculated at defined points of the average wound closure time. Asterisks indicate significant RFI increases compared with the initial time point ($P < 0.01$). Except for the initial time point, RFI levels are significantly lower in *stit* mutants than in the wild type (two asterisks, $P < 0.005$). All data are expressed as means ± s.e.m.

(110 ± 36 min; $n = 19$) (Fig. 2a). To ensure that it was *stit* deficiency that caused the delayed wound closure, we re-expressed Stit in *stit* mutants at low levels by using *69B*-GAL4. Such embryos closed their wounds twice as fast as *stit* mutants treated in parallel (Supplementary Information, Fig. S4b). Thus, Stit is required for rapid re-epithelialization; 25% of the mutants showed at least a threefold delay in epithelial repair, and the other 75% of *stit* mutants required double the time needed for wound closure in wild-type embryos.

To define *stit* function further, we observed changes in cell shape in wounded embryos by confocal microscopy. We used a Neuroglian–GFP (Nrg–GFP) protein-trap marker expressed at endogenous levels in epithelial cell membranes[15]. Wild-type embryos expressing Nrg–GFP repaired their wounds within 73 min (73 ± 9 min; $n = 6$) (Supplementary Information, Fig. S4c, d). Epidermal cells at the margins first extended and then constricted to seal the puncture (Supplementary Information, Fig. S4c and Movie S1). In 27% of the *stit* mutants, margin cells also elongated towards the centre of the wound but failed to close it for at least 5 h (Supplementary Information, Fig. S4c and Movie S2). We did not detect any obvious defects in cell elongation in the remaining mutants, which also showed a delayed wound closure phenotype (118 ± 27min; $n = 11$) in comparison with the wild type (Supplementary Information, Fig. S4d). We also used wide-field epifluorescence microscopy to assess the cell elongation process in living wild-type and *stit* mutant embryos expressing Nrg–GFP. Both wild-type ($n = 12$) and *stit* mutants ($n = 12$) showed characteristic elongated cell shapes during the second half of re-epithelialization. This suggested that Stit functions during the second half of re-epithelialization.

Epidermal healing relies on dynamic filopodia and lamellipodia and on the formation of a continuous actin cable at the wound perimeter[16]. We used confocal microscopy to analyse cytoskeletal dynamics in wounded wild-type and *stit* mutants with the GFP–*moe* marker. We detected no gross defects in the cellular protrusions at wound margins of *stit* mutants

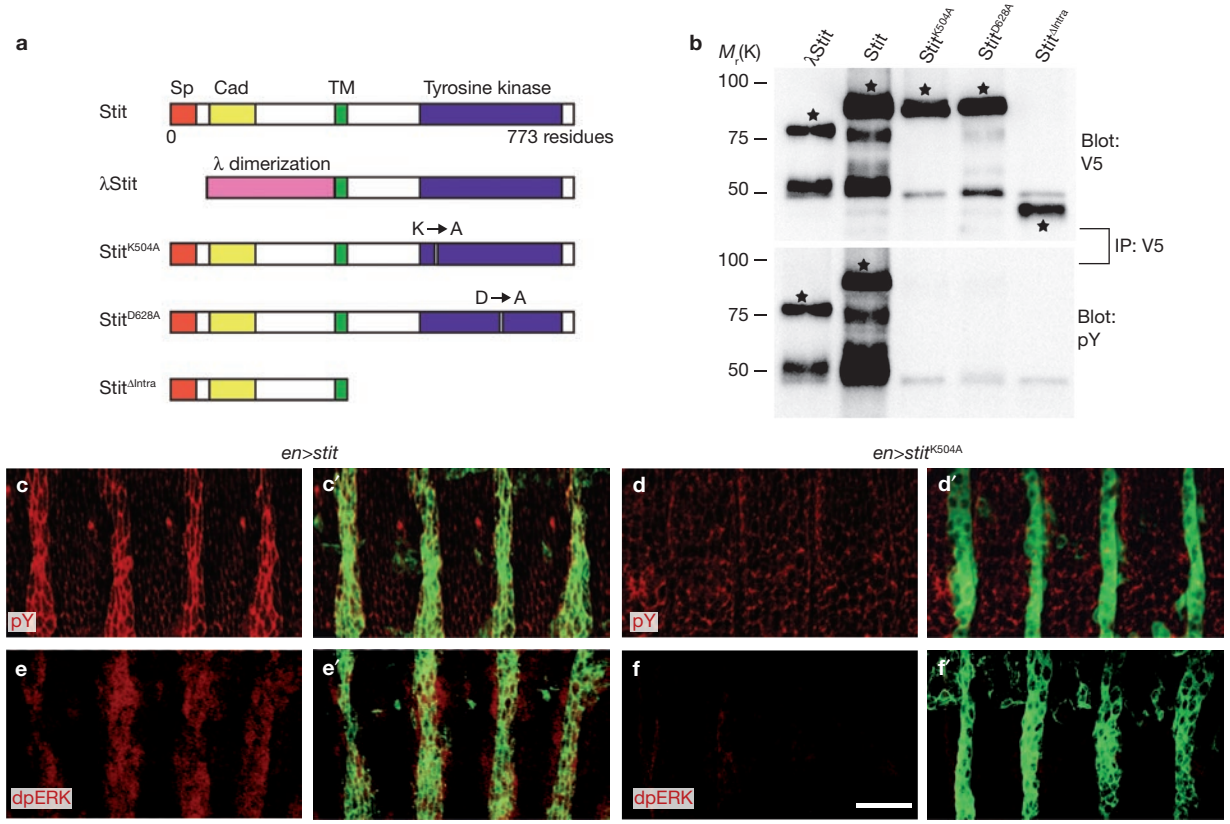

Figure 3 Stit is a tyrosine kinase sufficient for ERK activation *in vivo*. (**a**) Diagram of wild-type and mutated versions of Stit. Sp, signal peptide; Cad, cadherin domain; TM, transmembrane domain. (**b**) Western blots probed with anti-V5 (upper panel) and anti-phosphotyrosine (pY; lower panel) antibodies show immunoprecipitated (IP) wild-type and mutated versions of Stit proteins. Asterisks indicate the bands corresponding to expected molecular masses of the expressed proteins. (**c**–**f**′) Confocal images show ectopic phosphorylation of tyrosine (red; **c**–**d**′) and ERK (red; **e**–**f**′) in *en>stit* embryos (**c**, **c**′, **e**, **e**′) but not in *en>stit*^{K504A} embryos (**d**, **d**′, **f**, **f**′). Expression of Stit and Stit^{K504A} was detected by anti-Stit antiserum (green, **c**′–**f**′). Scale bar, 20 μm.

(Supplementary Information, Fig. S4e, f). Halfway through wound healing, GFP–*moe* revealed a pronounced actin cable around the wound edge of wild-type embryos (Fig. 2b; Supplementary Fig. S4g and Movie S3). In contrast, in *stit* mutants the GFP–*moe* ring was either discontinuous or showed severely reduced intensity (Fig. 2b; Supplementary Fig. S4h and Movies S4 and S5). To quantify cytoskeletelal changes during wound closure, we recorded 18 wild-type and 27 wounded *stit* mutant embryos. We calculated the relative fluorescence intensity (RFI) of GFP–*moe* at the wound edge for each embryo at defined time points of the wound closure period in each phenotypic class. The rate of increase in cytoskeletal RFI during wound closure was much decreased in *stit* mutants in comparison with the wild type. In addition, the RFI at the wounds of *stit* mutants was significantly lower during the second half of the wound healing process than in the wild type (Fig. 2c). Thus, Stit coordinates the formation of the actin cable at the wound perimeter during re-epithelialization.

The predicted Stit protein contains an amino-terminal signal peptide, an extracellular cadherin domain, a transmembrane motif and an intracellular tyrosine kinase domain (Fig. 3a). This domain combination is distinctive for members of the Ret RTK family[17]. RTK activation normally depends on ligand-induced dimerization and the autophosphorylation of tyrosine residues in the intracellular domain[18]. We generated a series of V5-tagged constructs to test whether Stit could function as a RTK in S2 cells. To force ligand-independent dimerization, we replaced the Stit extracellular region by the λ cl repressor dimerization domain (λStit)[19,20]. To eliminate the predicted kinase activity we generated Stit^{K504A}, Stit^{D628A} and Stit$^{\Delta Intra}$ (Fig. 3a). We expressed these constructs and Stit-V5 in S2 cells and analysed tyrosine phosphorylation by immunoprecipitation and western blotting. λStit and overexpressed Stit underwent ligand-independent autophosphorylation, as expected of constitutively active RTKs (Fig. 3b). We did not detect phosphotyrosine on the Stit$^{\Delta Intra}$, Stit^{K504A} and Stit^{D628A} proteins, indicating that Stit itself is a tyrosine kinase. Is the Stit kinase activity needed for Stit function *in vivo*? We compared the ability of a kinase-defective *stit*^{K504A} transgenic construct and a wild-type *stit* transgene to rescue the lethality of *stit* mutants. Only the wild-type construct provided rescuing activity of the lethality phenotype, indicating that the tyrosine kinase activity is required for Stit function (Supplementary Information, Fig. S2d, e).

RTK activation typically leads to phosphorylation of members of the mitogen-activated protein kinase family[21–23]. We used transgenic strains expressing either *en>stit* or the kinase-defective *en>stit*^{K504A} in embryonic epidermis. *en>stit*, but not *en>stit*^{K504A}, produced ectopic phosphorylation of tyrosine and ERK in stripes (Fig. 3c–f′). Thus, Stit can activate ERK, a common RTK effector. To define its endogenous localization, we generated anti-Stit antisera. Double stainings for the membrane markers CAAX–GFP, Crumbs (Crb) and Fasciclin III (FasIII) indicated that Stit was predominantly localized apically in epidermal cells (Fig. 4a–c′). Stit staining was severely decreased in *stit* mutants, indicating the specificity of the antiserum (Fig. 4d, d′). The intensity of Stit staining was markedly increased at the wound edges of wild-type embryos, indicating that Stit levels are elevated at wound sites (Fig. 4e–f′). In summary, Stit is a

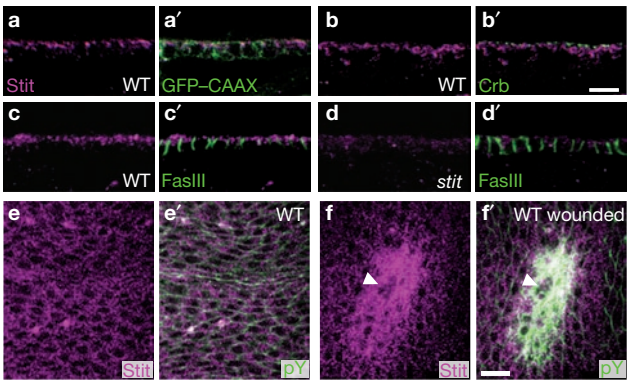

Figure 4 Stit localizes apically in epidermal cells and accumulates at wound sites. (**a**, **a**′) Stit is partly colocalized with the cell membrane marker GFP–CAAX in epidermal cells. GFP–CAAX expression was driven by the epidermal driver *69B*-GAL4. (**b**–**c**′) Stainings show the localization of Stit relative to the apical membrane protein Crb (**b**, **b**′) and the basolateral protein FasIII (**c**, **c**′). Stit is localized predominantly in the apical region of epidermal cells. (**d**, **d**′) Stit staining is severely decreased in *stit* mutants. (**e**–**f**′) Stit is expressed homogeneously in all the epidermal cells (**e**, **e**′) in unwounded wild-type embryos, and accumulates around the wounds after pricking (**f**, **f**′). Anti-phosphotyrosine was used to mark out the wound (white arrowheads). All micrographs are confocal *x*–*y* sections. Scale bars, 5 μm (**a**–**d**′); 10 μm (**e**–**f**′).

wound-responsive, apical membrane tyrosine kinase that can induce ERK activation *in vivo*. ERK activation results in the Grh-dependent induction of *Ddc* and *ple* on wounding[3]. Is Stit also required for ERK activation at wound sites? We pierced wild-type and *stit* mutants and performed double staining for dpERK and FasIII to reveal surrounding epidermal cells. dpERK staining is not detectable in epidermal cells of stage 16 wild-type embryos (Supplementary Information, Fig. S5a–a′′). Wounding induced a robust dpERK signal extending two to three cell diameters around the puncture site of wild-type embryos (Fig. 5a, a′). By contrast, in *stit* mutant embryos, this dpERK signal was weaker and restricted to cells immediately adjacent to the edge (Fig. 5b, b′). Similarly to dpERK, the inducible phosphotyrosine staining was decreased at the wounds of *stit* mutants compared with that in the wild-type (Supplementary Information, Fig. S5b–c′′). Stit is therefore required for the expansion of ERK phosphorylation at wound sites. In wild-type embryos, *Ddc* transcripts readily accumulated in cells located several cell diameters away from the puncture site. This response was limited to far fewer cells in *stit* mutants (Supplementary Information, Fig. S5d–f). We quantified the induction of the *Ddc*–GFP reporter in wild-type and *stit* mutants (Fig. 5c–d′; and Supplementary Information, Fig. S5g). Among *Ddc*–GFP embryos, 85% showed a broad or moderate GFP induction, and only 15% presented a weak signal ($n = 314$). By contrast, 41% of 234 wounded *stit* mutants showed a restricted and weak induction and 59% showed broad or moderate GFP activation. Stit was also required for the extended activation of the *ple*–DsRed wound response reporter (Supplementary Information, Fig. S5h–j). Conversely, *Ddc* mRNA was induced ectopically in *en>stit* embryos but remained unaffected in *en>stit*^{K504A} embryos (Fig. 5e, f). This induction was abolished in *en>stit; grh* mutants (not shown). Collectively, Stit regulates ERK phosphorylation and Grh-dependent activation of cuticle repair genes. The genetic analysis places *stit* both downstream and upstream of *grh*, suggesting a positive feedback loop mechanism in wound repair. Because *stit* mRNA is induced at wound sites, we tested whether the Grh-dependent *stitα*–GFP induction requires endogenous

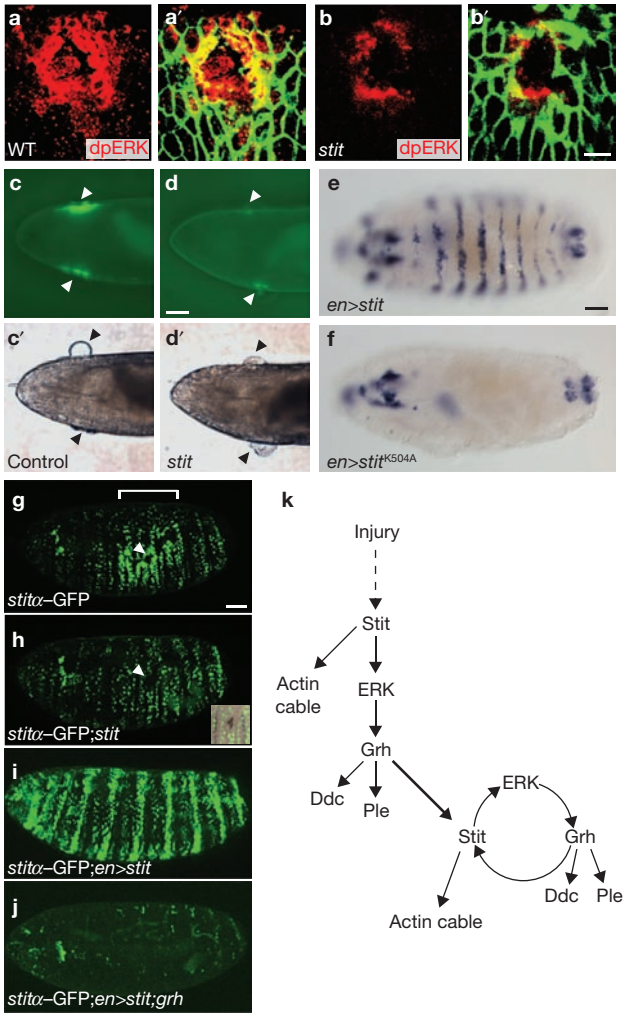

Figure 5 Stit activates the induction of wound reporters dependent on ERK and Grh. (**a**–**b**′) Confocal *x*–*y* projections show robust dpERK staining (red) around wounds in the wild type (**a**). The signal is restricted to fewer cells in *stit* mutants (**b**). Green FasIII staining reveals surrounding cells (**a**′, **b**′). (**c**–**d**′) *Ddc*–GFP wound reporter induction is limited in *stit* mutants in comparison with the control. White arrowheads indicate GFP induction. Puncture sites are identified by lymph leakage (differential interference contrast micrographs in **c**′ and **d**′; black arrowheads). (**e**, **f**) *In situ* hybridization shows striped activation of *Ddc* in *en>stit* embryos (**e**) but not in *en>stit*^{K504A} embryos (**f**). (**g**, **h**) Wounding induction of *stitα*–GFP (**g**) is diminished in *stit* mutants (**h**). Arrowheads indicate the melanized puncture sites (**h**, inset). (**i**, **j**) *en>stit* expression activates *stitα*–GFP in stripes in control embryos (**i**) but not in *grh* embryos (**j**). Panels **g**–**j** are confocal images of live embryos. Scale bars, 5 μm (**a**–**b**′); 25 μm (**c**–**j**). (**k**) Schematic summary of *stit* function in wound closure.

Stit. In contrast with the robust GFP induction in wild-type embryos, *stitα*–GFP expression in wounded *stit* mutants remained unchanged (Fig. 5g, h). Accordingly, *stitα*–GFP was activated in stripes in *en>stit* embryos (Fig. 5i), and this increase was abolished in *en>stit; grh* mutants (Fig. 5j). Thus, Stit function is required for the transcriptional upregulation of *stit* at the wound.

Stit presents the first candidate receptor in *Drosophila* epidermal wound healing. The functional analysis of *stit* proposes a two-tier mechanism in wound healing. Epidermal wounds generate signals[24–27], which presumably activate Stit and other receptors to initiate the expression

of cuticle repair genes and cytoskeletal rearrangements. Stit also further induces its own transcription and a second tier of responses by a Grh-dependent positive feedback loop (Fig. 5k). The proposed amplification mechanism ensures efficient epidermal wound repair and relies on transcriptional regulation without the need for further extracellular stimulation. Several RTKs[2,28–30] have been implicated in mammalian epidermal wound healing, suggesting that similar mechanisms may coordinate and amplify wound responses in insects and vertebrates. □

METHODS

Methods and any associated references are available in the online version of the paper at http://www.nature.com/naturecellbiology/.

Note: Supplementary Information is available on the Nature Cell Biology website.

ACKNOWLEDGEMENTS

We thank W. McGinnis, S. Hayashi, S. Bray, P. Rørth, R. Hodgetts, the Bloomington, the Exelixis–Harvard Stock Centers, Developmental Studies Hybridoma Bank and Drosophila Genomics Resource Center for reagents; H. Jin, J. Hemphälä, M. Björk and I. Granel for technical assistance; and A. Uv, U. Theopold, R. Palmer, K.-A. Senti and colleagues at Wenner-Gren Institute for critical suggestions on the manuscript. Vetenskapsrådet, Cancerfonden and G. Gustafsson Stiftelsen provided financial support.

AUTHOR CONTRIBUTIONS

M.G. and S.W. conducted the bioinformatics analysis. S.W. generated and analysed most strains, helped with live imaging and co-wrote the manuscript. V.T. performed and anlaysed the live imaging and wrote part of the manuscript. N.X. generated and analysed the kinase-dead *stit* strains and performed quantitative polymerase chain reaction and electrophoretic mobility-shift assays. N.S. conducted immunoprecipitation experiments. K.T. performed the electron microscopy analysis. N.N. generated the *stitδ* construct. C.S. designed the project, analysed results and co-wrote the manuscript.

Published online at http://www.nature.com/naturecellbiology.
Reprints and permissions information is available online at http://npg.nature.com/reprintsandpermissions/.

1. Schafer, M. & Werner, S. Transcriptional control of wound repair. *Annu. Rev. Cell Dev. Biol.* **23,** 69–92 (2007).
2. Werner, S. & Grose, R. Regulation of wound healing by growth factors and cytokines. *Physiol. Rev.* **83,** 835–870 (2003).
3. Mace, K. A., Pearson, J. C. & McGinnis, W. An epidermal barrier wound repair pathway in *Drosophila* is mediated by *grainy head*. *Science* **308,** 381–385 (2005).
4. Ting, S. B. *et al.* A homolog of *Drosophila grainy head* is essential for epidermal integrity in mice. *Science* **308,** 411–413 (2005).
5. Harden, N. Cell biology. Of grainy heads and broken skins. *Science* **308,** 364–365 (2005).
6. Stramer, B. & Martin, P. Cell biology: master regulators of sealing and healing. *Curr. Biol.* **15,** R425–R427 (2005).
7. Uv, A. E., Harrison, E. J. & Bray, S. J. Tissue-specific splicing and functions of the *Drosophila* transcription factor Grainyhead. *Mol. Cell. Biol.* **17,** 6727–6735 (1997).
8. Venkatesan, K., McManus, H. R., Mello, C. C., Smith, T. F. & Hansen, U. Functional conservation between members of an ancient duplicated transcription factor family, LSF/Grainyhead. *Nucleic Acids Res.* **31,** 4304–4316 (2003).
9. Narasimha, M., Uv, A., Krejci, A., Brown, N. H. & Bray, S. J. Grainy head promotes expression of septate junction proteins and influences epithelial morphogenesis. *J. Cell Sci.* **121,** 747–752 (2008).
10. Barolo, S., Carver, L. A. & Posakony, J. W. GFP and β-galactosidase transformation vectors for promoter/enhancer analysis in *Drosophila*. *Biotechniques* **29,** 726, 728, 730, 732 (2000).
11. Bray, S. J. & Kafatos, F. C. Developmental function of Elf-1: an essential transcription factor during embryogenesis in *Drosophila*. *Genes Dev.* **5,** 1672–1683 (1991).
12. Hemphala, J., Uv, A., Cantera, R., Bray, S. & Samakovlis, C. Grainy head controls apical membrane growth and tube elongation in response to Branchless/FGF signalling. *Development* **130,** 249–258 (2003).
13. Edwards, K. A., Demsky, M., Montague, R. A., Weymouth, N. & Kiehart, D. P. GFP–moesin illuminates actin cytoskeleton dynamics in living tissue and demonstrates cell shape changes during morphogenesis in *Drosophila*. *Dev. Biol.* **191,** 103–117 (1997).
14. Chihara, T., Kato, K., Taniguchi, M., Ng, J. & Hayashi, S. Rac promotes epithelial cell rearrangement during tracheal tubulogenesis in *Drosophila*. *Development* **130,** 1419–1428 (2003).
15. Morin, X., Daneman, R., Zavortink, M. & Chia, W. A protein trap strategy to detect GFP-tagged proteins expressed from their endogenous loci in *Drosophila*. *Proc. Natl Acad. Sci. USA* **98,** 15050–15055 (2001).
16. Wood, W. *et al.* Wound healing recapitulates morphogenesis in *Drosophila* embryos. *Nature Cell Biol.* **4,** 907–912 (2002).
17. Runeberg-Roos, P. & Saarma, M. Neurotrophic factor receptor RET: structure, cell biology, and inherited diseases. *Ann. Med.* **39,** 572–580 (2007).
18. Fantl, W. J., Johnson, D. E. & Williams, L. T. Signalling by receptor tyrosine kinases. *Annu. Rev. Biochem.* **62,** 453–481 (1993).
19. Lee, T., Hacohen, N., Krasnow, M. & Montell, D. J. Regulated Breathless receptor tyrosine kinase activity required to pattern cell migration and branching in the *Drosophila* tracheal system. *Genes Dev.* **10,** 2912–2921 (1996).
20. Duchek, P., Somogyi, K., Jekely, G., Beccari, S. & Rorth, P. Guidance of cell migration by the *Drosophila* PDGF/VEGF receptor. *Cell* **107,** 17–26 (2001).
21. Brunner, D. *et al.* A gain-of-function mutation in *Drosophila* MAP kinase activates multiple receptor tyrosine kinase signaling pathways. *Cell* **76,** 875–888 (1994).
22. Gabay, L., Seger, R. & Shilo, B. Z. MAP kinase in situ activation atlas during *Drosophila* embryogenesis. *Development* **124,** 3535–3541 (1997).
23. McKay, M. M. & Morrison, D. K. Integrating signals from RTKs to ERK/MAPK. *Oncogene* **26,** 3113–3121 (2007).
24. Martin, P. & Parkhurst, S. M. Parallels between tissue repair and embryo morphogenesis. *Development* **131,** 3021–3034 (2004).
25. Zhao, M. *et al.* Electrical signals control wound healing through phosphatidylinositol-3-OH kinase-γ and PTEN. *Nature* **442,** 457–460 (2006).
26. Jacinto, A., Martinez-Arias, A. & Martin, P. Mechanisms of epithelial fusion and repair. *Nature Cell Biol.* **3,** E117–E123 (2001).
27. Galko, M. J. & Krasnow, M. A. Cellular and genetic analysis of wound healing in *Drosophila* larvae. *PLoS Biol.* **2,** E239 (2004).
28. Wenczak, B. A., Lynch, J. B. & Nanney, L. B. Epidermal growth factor receptor distribution in burn wounds. Implications for growth factor-mediated repair. *J. Clin. Invest.* **90,** 2392–2401 (1992).
29. Chmielowiec, J. *et al.* c-Met is essential for wound healing in the skin. *J. Cell Biol.* **177,** 151–162 (2007).
30. Gurtner, G. C., Werner, S., Barrandon, Y. & Longaker, M. T. Wound repair and regeneration. *Nature* **453,** 314–321 (2008).

DOI: 10.1038/ncb1898

METHODS

Fly genetics and transgenic lines. Crosses were performed at 25 °C on standard medium unless indicated otherwise. The w^{1118} strain was used as wild type. The XP-type P element d07355 is inserted in the first *stit* intron, 1,045 base pairs (bp) upstream of the predicted ATG. Df(3R)Exel9056 carries a 12,191-bp deletion that completely removes the *stit* locus and part of the gene CG13654. Imprecise and precise excisions of the d07355 P element yielded several viable and lethal strains (non-complementing the lethality of Df(3R)Exel9056). One of the lethal strains, excision no. 266, contains a 3,417-bp deletion that removes the *stit* 5′ untranslated region (UTR) and a 136-bp coding sequence. Unrelated lethal mutations in both excision no. 266 and Df(3R)Exel9056 were removed by recombination to w^{1118}. The obtained recombinant Df(3R)Exel9056R#22 strain (*stit* mutants) was used for all wounding experiments. Other mutant alleles used were grh^{B37} and grh^{s2140} (refs 11, 12). *en*-GAL4 was used to drive UAS-grh^{12}, UAS-*stit* and UAS-$stit^{K504A}$ expression in epidermal stripes at 29 °C. The −1.4-kb *Ddc*–GFP and the 3.0-kb *ple*-DsRed wound reporters were used to monitor *Ddc* and *ple* induction on wounding[3]. The GFP trap line P{PTT-GA}Nrg^{G00305} (Nrg–GFP)[15] was used to reveal the epidermal cell shapes. To reveal the actin cytoskeleton, UAS–GFP–*moesin*[14] flies were crossed with the epithelial driver *69B*-GAL4. To rescue the delayed re-epithelialization defect, Stit was re-expressed in the *stit* mutants with *69B*-GAL4 by using a weakly expressed UAS-*stit* line at room temperature (about 22 °C). Appropriate *lacZ* or GFP-marked CyO and TM3 (or TM6) balancers were used to identify homozygous mutant embryos.

stit–GFP reporters were constructed by subcloning the corresponding PCR fragments from genomic DNA of w^{1118} into the pH-Stinger[10]. UAS-*stit* was generated by cloning a RE05926 insertion comprising the 5′ UTR, coding region and 3′ UTR of *stit* into pUAST. UAS-$stit^{K504A}$ was constructed by introducing the K504A mutation (see Supplementary Information) and was cloned into pUAST. Transgenic lines were established by P-element-mediated germline transformation.

Live imaging of wounded embryos. Embryos were collected during early stage 16 (about 14 h after egglaying at 25 °C), and pricked as described previously[16]. Live imaging was performed essentially as described[31]. Individual *Z*-stacks with a step size of 1.5–2.5 μm were taken every 5–6 min over a 2–7-h period. Recording started about 30 min after wounding (sample preparation time). All recorded embryos developed into late stage 17. Time-lapse movies were created from the confocal *Z*-stacks by using NIH ImageJ software from http://rsb.info.nih.gov/ij/index.html.

Aseptic injury assays. Aseptic injury assays were performed as described previously[3], except that embryos were collected for 1 h. Pricked embryos for dpERK and FasIII staining were fixed immediately after wounding. Pricked embryos for phosphotyrosine (pY) and Stit staining were either fixed immediately (shown in Supplementary Information, Fig. S5b–c′′) or incubated in a humid chamber for 1 h before fixation (shown in Fig. 4f, f′). Wounded embryos for RNA *in situ* hybridization were fixed 45 min after wounding. For the induction of *Ddc*–GFP, *ple*–DsRed and *stit*–GFP reporters, pricked embryos carrying the relevant reporter were allowed to develop for 4 h (for *Ddc*–GFP and *ple*–DsRed reporters) or 6 h (for *stit*–GFP reporters) before imaging. For the wound survival assay, pricked embryos were allowed to develop for 20 h before scoring.

Generation of Stit antigens. Stit protein motifs were identified with sequence analysis tools found at http://smart.embl-heidelberg.de/ and http://www.cbs.dtu.dk/services/SignalP/ Stit antisera were generated against a protein corresponding to the amino-acid segment 7–314 of Stit fused to the 6 × His tag of pRSETB. The protein was purified from *Escherichia coli* on Ni^{2+}-nitrilotriacetate resin and injected into guinea-pigs (Eurogentec).

Cell culture, immunoprecipitation and western blotting. λStit was constructed by replacing the extracellular domain of Stit with the λ-repressor dimerization domain that was amplified by PCR from λ-btl^{19}. PCR fragments comprising the full-length *stit*, λ*stit*, $stit^{K504A}$, $stit^{D628A}$ and $stit^{\Delta intra}$ were subcloned in frame with a carboxy-terminal V5 tag into pMT expression vector (Invitrogen) and transfected into *Drosophila* S2 cells using Effectene Kit (Qiagen). At 48 h after transfection, cells were harvested in 10 mM Tris-HCl pH 8, 140 mM NaCl, 1.5 mM $MgCl_2$, 1% Nonidet P40 containing a protease inhibitor cocktail (Roche). Cell lysates were cleared by centrifugation for 10 min at 20,000*g* and supernatants were incubated with anti-V5 antibody for 16 h. Protein A–Sepharose CL-4B (Amersham Bioscience) was added and incubation was continued for 3 h. After several washes in 10 mM Tris-HCl pH 8, 0.1% Nonidet P40, proteins were eluted with 0.5% SDS and analysed by SDS–PAGE and western blotting with anti-V5 (1:5,000 dilution; Invitrogen) and anti-pY (1:500 dilution; Upstate Cell Signaling) antibodies.

To detect Stit protein in embryo extracts, 80 embryos were homogenized in 60 μl of 2 × SDS sample buffer and boiled for 5 min before loading. Extracts equal to about 20 embryos were loaded in each lane and probed with anti-Stit (1:500 dilution) and anti-tubulin (1:1,000 dilution) antibodies.

Immunohistochemistry and TEM. Immunohistochemistry and TEM were performed as described[12]. The following primary antibodies were used: guinea-pig anti-Stit (1:500 dilution), mouse anti-diphosphorylated ERK (dpERK) (1:100 dilution; Sigma), mouse anti-phosphotyrosine (pY) (1:100 dilution, Upstate Cell Signaling), mouse anti-FasIII (1:10 dilution; DSHB), mouse anti-Crb (1:50 dilution; DSHB), rat anti-DE-Cad (1:20 dilution; DSHB), mouse anti-GFP (1:1,000 dilution; Sigma) and rabbit anti-β-gal (1:1,500 dilution; Cappel). Secondary antibodies conjugated to Cy2 or Cy3 (Jackson Immunochemicals) or Alexa Fluor-488 (Molecular Probes) were used at 1:400 dilution.

Semi-quantitative analysis of GFP–*moe* fluorescence intensity. Laser confocal imaging was performed on live wounded embryos for 2–5 h. Wounds were optically sectioned by 10–14 focal planes, which allowed the detection of the entire puncture depth and of the surrounding epithermal tissue. We recorded wound closure of 18 *69B*>GFP–*moe* (wild type) and of 27 *stit 69B*>GFP–*moe* mutant (*stit*) embryos. Wild-type embryos closed their wounds within 77 min on average (77 ± 23 min). Out of 27 mutants, 9 did not close their wounds during the imaging period of 5 h. The rest of them showed a prolonged wound closure period extending to 133 min on average (133 ± 51 min; $P = 0.0093$). We first defined time points at regular intervals of the average wound closure period for each phenotypic class. For wild-type embryos, the time points represent the start, 1/4, 1/2 and 3/4 of the average closure time and the final closure time. For *stit* mutant embryos with delayed wound closure we defined additional time points at 3/4 of their average closure time and at their final closure time. For *stit* mutants that failed to close their wounds during the recording period, we defined additional time points at 3/4 of the average recording time and at the final recording time. Fluorescence intensity was estimated as the projected sum of signals of the *Z*-stack using the NIH ImageJ software. Relative fluorescence intensity (RFI)[32] from projected-stack images was calculated for the defined time points in each embryo by using the ratio $RFI = FI_w/FI_{ep}$, where FI_w represents the average intensity within the area of a ring 1 μm (12 pixels) wide around the wound edge and FI_{ep} represents the average intensity in an equal concentric ring area located at a distance of 8 μm (100 pixels) from the wound border. Mean RFI values were calculated for each defined time point and are plotted in the graph shown in Fig. 2c.

Statistics. Data in the bar graphs are expressed as means ± s.e.m unless indicated. A two-tailed distribution Student's *t*-test was used to estimate statistical significance.

31. Tsarouhas, V. *et al*. Sequential pulses of apical epithelial secretion and endocytosis drive airway maturation in *Drosophila*. *Dev. Cell* **13,** 214–225 (2007).
32. Bement, W. M., Forscher, P. & Mooseker, M. S. A novel cytoskeletal structure involved in purse string wound closure and cell polarity maintenance. *J. Cell Biol.* **121,** 565–578 (1993).

nature cell biology

DOI: 10.1038/ncb1898

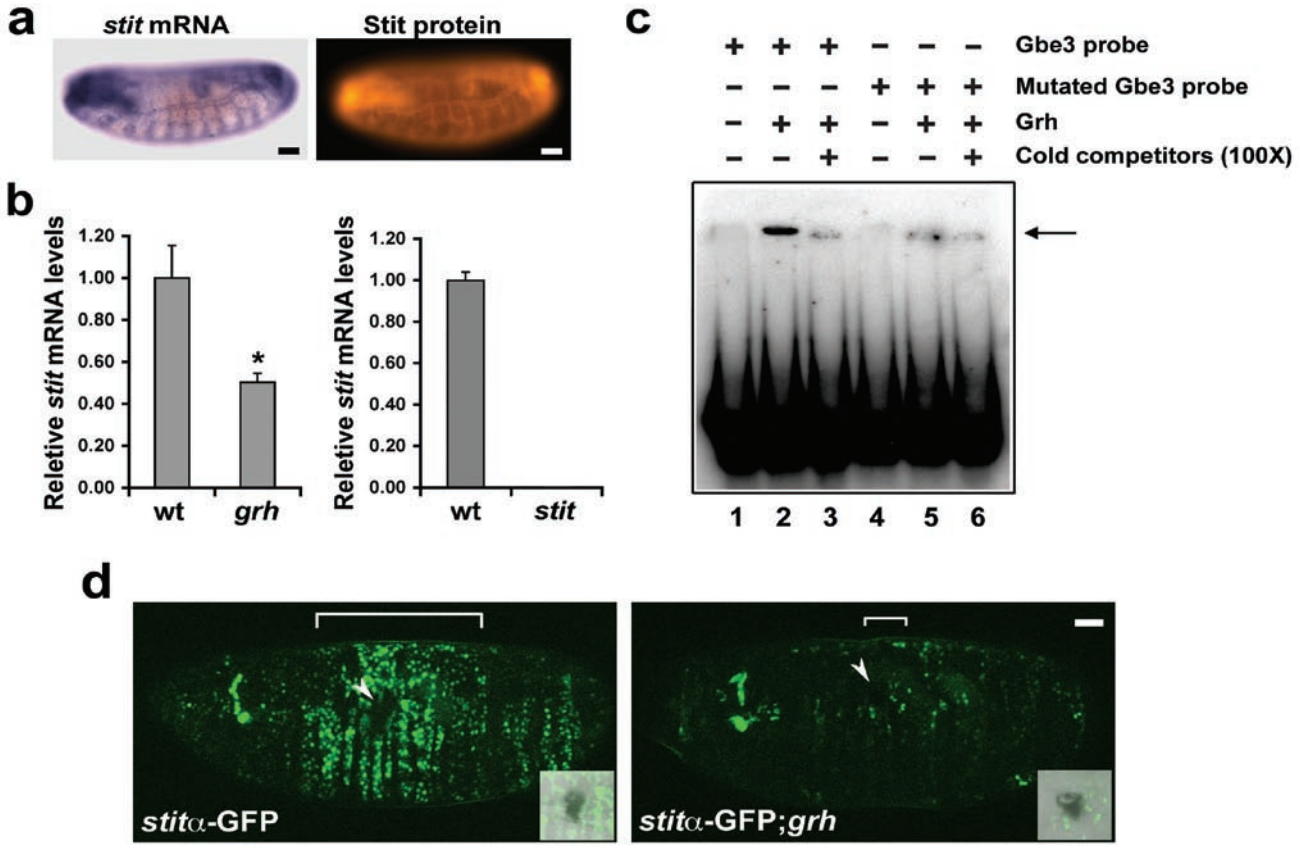

Figure S1 *stit* is a direct target gene of Grh. (**a**) *stit* mRNA and protein were detected in epidermis, foregut and hindgut of wild type embryos. (**b**) Quantitative real-time Reverse-Transcription PCR (q-RT-PCR) showing *stit* mRNA levels in wild type (wt), *grh* and *stit* mutants at late stage 16 (error bars indicate s.d.; * denotes p = 0.00019). (**c**) EMSA shows a complex of Grh and the Gbe3 probe (indicated by arrow). Lanes 1-3: 100-fold excess of the unlabelled Gbe3 probe competes away the signal. Lanes 4-6: A mutated probe does not produce a specific shift.(**d**) Confocal projections of live embryos show that the broad induction of the *stit*α–GFP reporter is decreased in *grh* mutants. Brackets mark the extent of wound-induced GFP signal. Arrowheads indicate wound sites identified by melanization (inserts). Scale bars: 25μm.

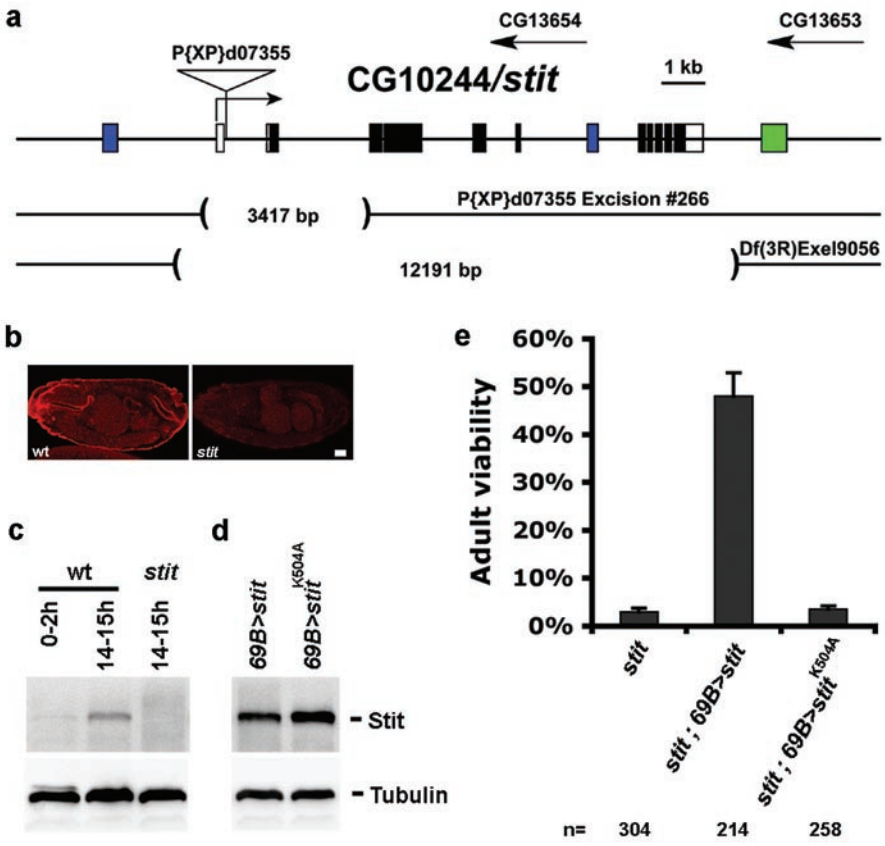

Figure S2 Stit is required for adult viability. (**a**) Schematic presentation of the *stit* locus and the DNA lesions in *stit* mutant strains. Blue and green boxes denote exons of the flanking genes CG13654 and CG13653, respectively. *stit* exons are shown as white (non coding) and black (coding) boxes. Arrows show the transcriptional direction. Position of the transposon insertion P{XP}d07355 is indicated by a white triangle. The *stit*P{XP}d07355 Excision #266 allele contains a 3417bp deletion generated by imprecise excision of the P{XP} element. The Df(3R)Exel9056 with a 12191bp deletion completely removes *stit* and part of the CG13654 gene. (**b**) Immunostaining shows that Stit protein is detected in wild type (wt) but not in *stit* mutant embryos. (**c-d**) Western blot of embryo extracts probed with anti-Stit (upper panel) and anti-Tubulin (lower panel) antibodies. Stit protein is clearly detected in wild type (wt) embryos 14-15 hours after egg laying (AEL). Stit is weakly detected in 0-2 hour wild type embryos. By contrast, Stit protein is not detectable in *stit* mutants at 14-15 hours AEL (**c**). The expression level of the transgenic constructs encoding Stit or the 'kinase dead' version Stit^{K504A} is comparable. *69B*-GAL4 was used to drive the transgenic expression and embryo extracts were prepared from embryos 14-15 hours AEL (**d**). These tested lines were used for the lethality rescue experiment in (**e**). (**e**) Re-expressing Stit but not Stit^{K504} with *69B*-GAL4 in *stit* mutants (*stit*$^{Exel9056R\#22}$ and *stit*$^{d07355Exc\#266}$ transheterozygotes) partially rescue *stit* lethality phenotype. *n* represents the expected number of the viable *stit* homozygous flies according to the cross. Error bars indicate s.d.

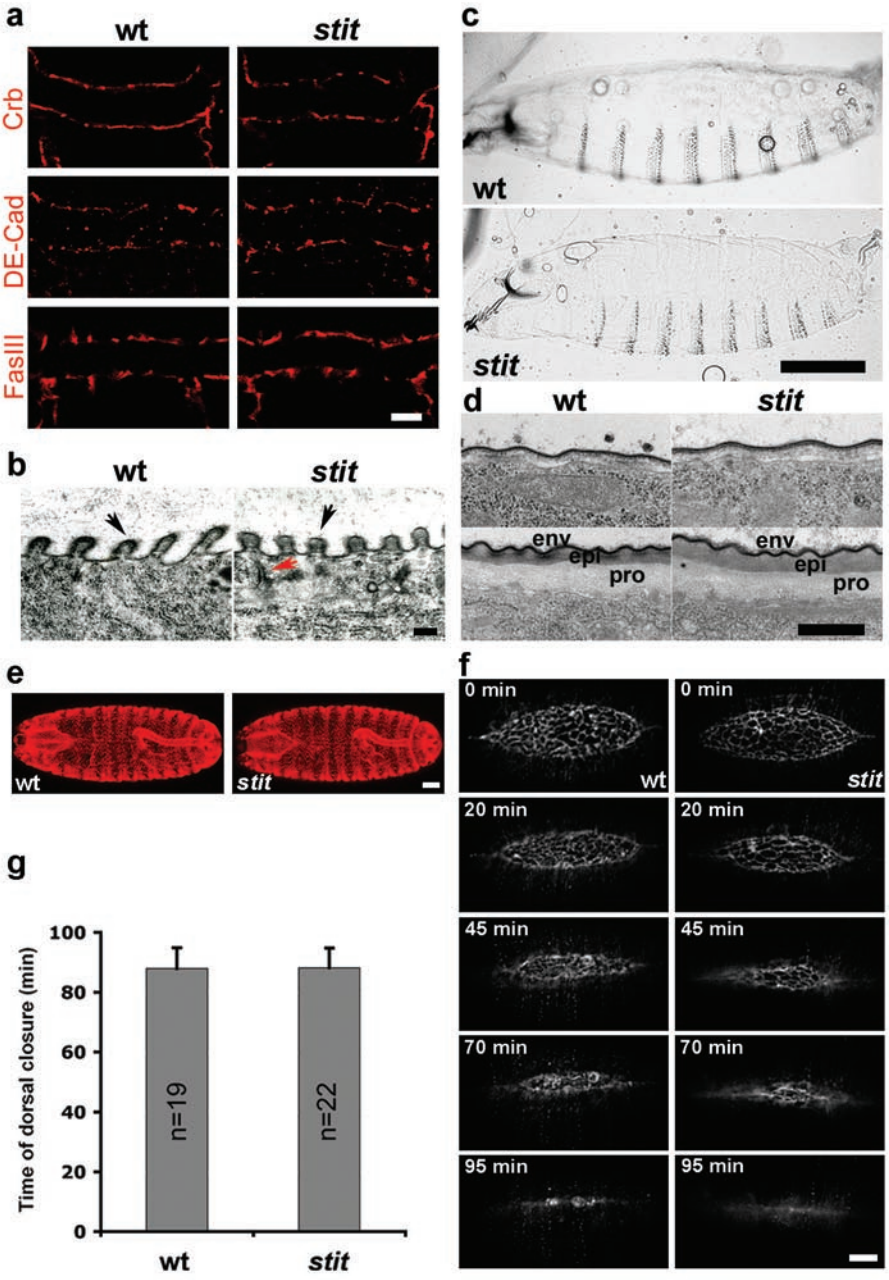

Figure S3 *stit* mutants show no tracheal or epidermal defects. (**a**) Tracheal dorsal trunk confocal x-y sections of wild type (wt) and *stit* mutants stained for Crumbs (Crb), DE-Cadherin (DE-Cad) and Fasciclin III (FasIII). Neither the amount nor localization of the markers is affected in *stit* mutants. (**b**) Transmission electron micrographs of tracheal dorsal trunk cross-sections from late stage 16 wild type (wt) and *stit* mutants. *stit* mutants show normal taenidia (black arrows) and adherens junctions (red arrow). (**c**) Cuticle preparations from wild type (wt) and *stit* mutants. No defect was detected in *stit* mutants. (**d**) Transmission electron micrographs of epidermis in wild type (wt) and *stit* mutant embryos of stage 16 (upper panel) and 17 (lower panel). The epidermal cells and overlying cuticular layers show no defects in *stit* embryos. env, envelope; epi, epicuticle; pro, procuticle. (**e**) Confocal x-y projections of embryos stained with FasIII show no defect in dorsal closure of *stit* mutants. (**f**) Time-lapse images of *69B>GFP-moe* (wt) and *stit 69B>GFP-moe* (*stit*) live embryos show that *stit* mutant embryos complete their dorsal closure at a similar rate compared to wild type. Recording time is indicated. (**g**) Plot showing no significant difference in the dorsal closure time between wt and *stit* mutants. *n* represents the number of animals used for live imaging. Error bars indicate s.d. Scale bars: 5μm (**a**); 100μm (**c**); 0.5μm (**b**) and (**d**);25μm (**e**) and (**f**).

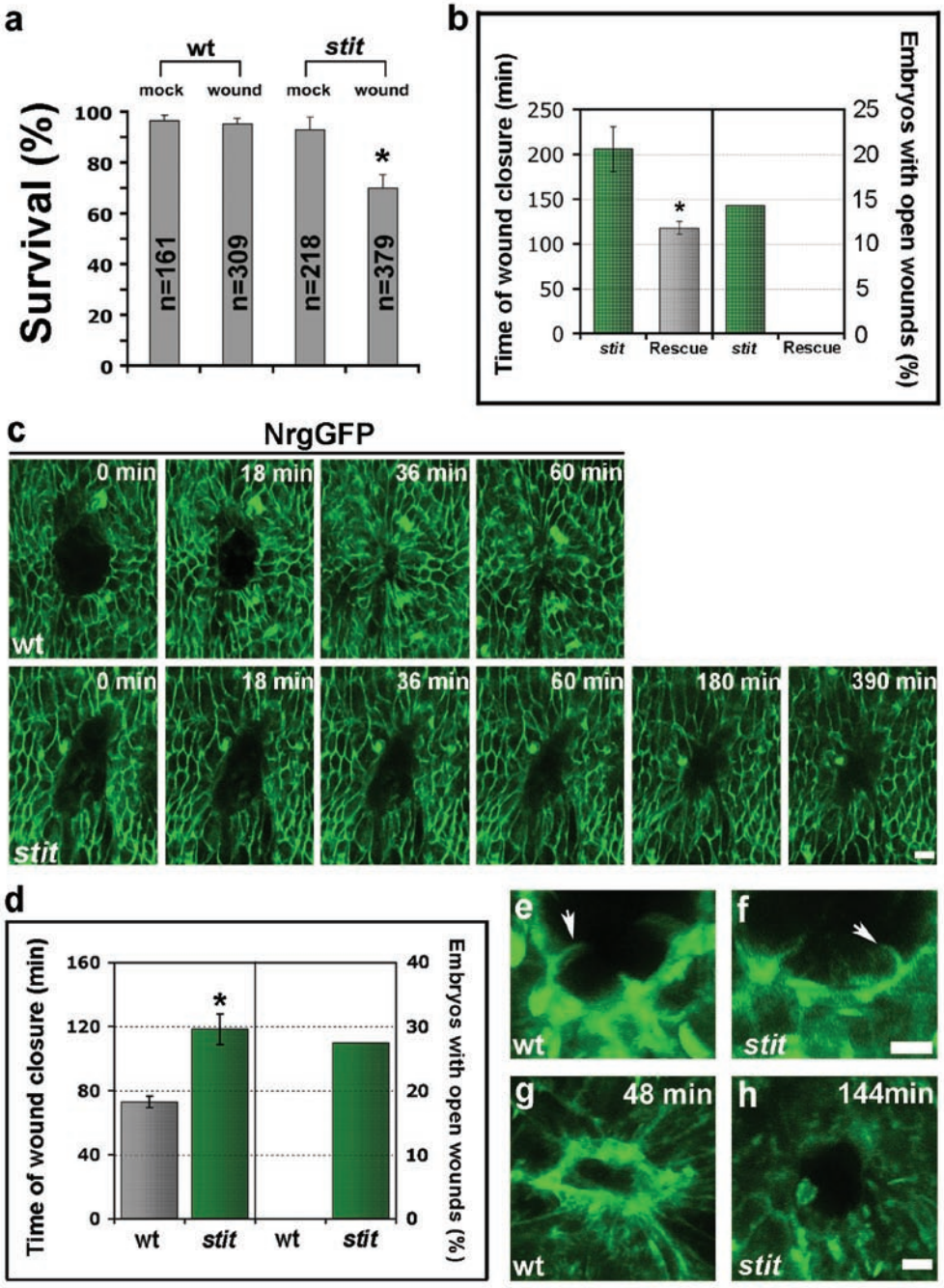

Figure S4 Stit is required for survival after wounding and efficient re-epithelialization. (**a**) Stit is required for survival upon wounding. *n* represents the number of animals used for each indicated treatment (error bars indicate s.d.; * denotes p = 0.0017.). (**b**) Plot showing the rescue of the re-epithelialization phenotype in *stit* mutants by transgenic re-expression of *stit* with the epidermal driver *69B*-GAL4. Rescued embryos closed their wounds twice as fast as *stit* mutants (left graph, * denotes p = 0.0029.). All *stit* mutants (n = 12) carrying the UAS-*stit* transgene under the control of *69B*-GAL4 closed their wounds. 14% of *stit* mutants (n = 14) failed to close their wounds during the 6-hour recording session (right graph). The data derived from movies acquired by wide-field fluorescence microscopy. (**c**) Selected images from time-lapse confocal movies (see also Supplementary Information, Movie S1 and S2) show wound closure in wild type (wt) and *stit* mutant embryos expressing the septate junction marker Nrg-GFP. The recording time after wounding is displayed in minutes (top corner). The wt embryo closed its wound at 60 minutes while the wound in *stit* mutant remained open even after the 390 minutes imaging period. (**d**) Quantifications of the wound closure phenotype in *stit* mutant embryos expressing Nrg-GFP. About 27 % of *stit* embryos failed to close their wounds within the 5-hour recording period. The rest of *stit* mutant embryos required a significant longer wound closure time (118±27min; n= 11; * denotes *p*=0.0008) compared to wild type (73 ±9 min; n= 6). **(e-h)** Stit mutant embryos show numerous filopodial protrusions but a defective actin cable at their wound margins. (**e-f**) Cytoplasmic protrusions (arrows) are detected at wound edges both in *69B*>GFP-*moe* (wt) (**e**) and *stit 69B*>GFP-*moe (stit)* mutant embryos (**f**). No gross defect was found in *stit* mutants. (**g-h**) A pronounced actin cable forms at the wound edges of wt embryos (**g**) half way and towards the end of wound closure. This cable is absent in the *stit* mutant (**h**). All micrographs are confocal x-y projections taken from time-lapse movies. Scale bars: 5μm.

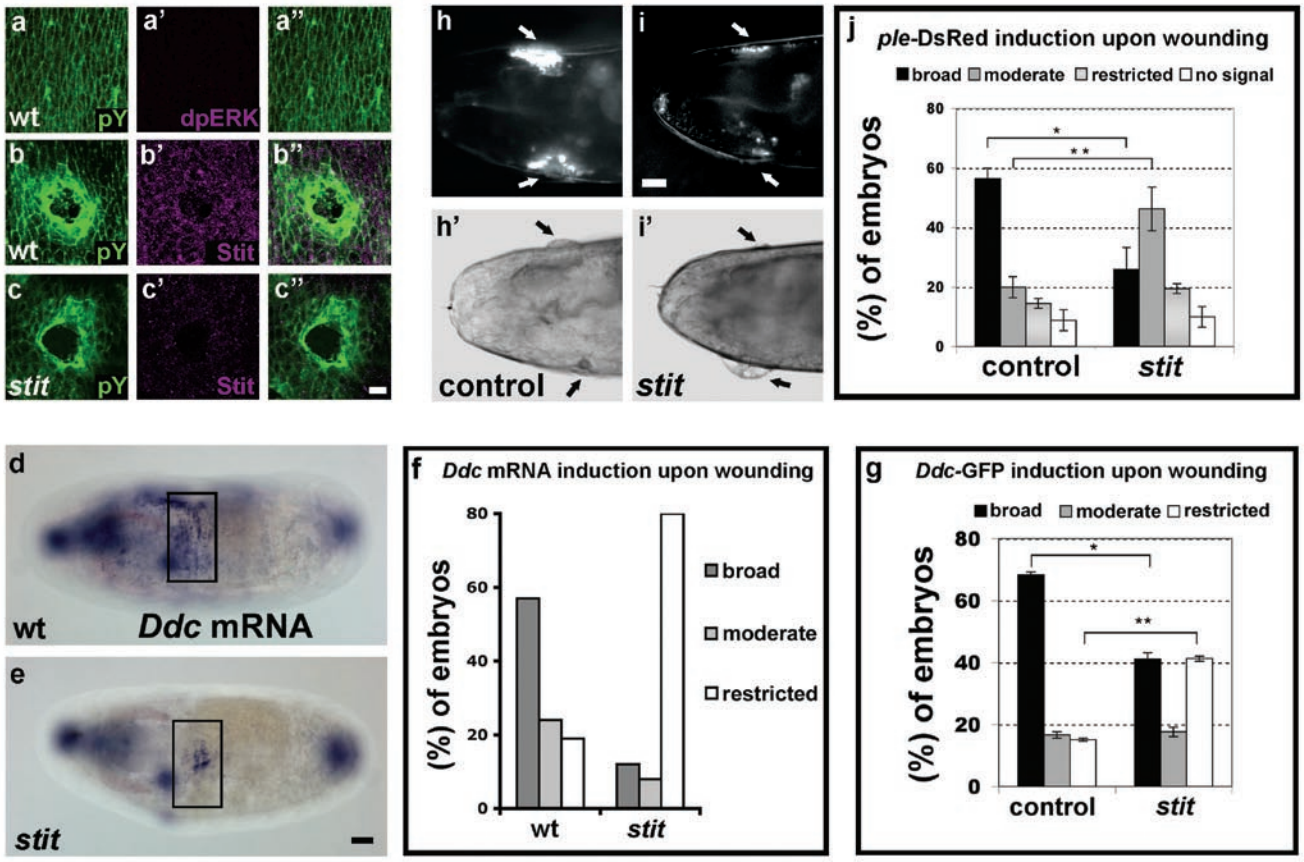

Figure S5 Stit is required for phosphotyrosine accumulation and the efficient activation of cuticle repair genes at wound sites. (**a-a"**) Confocal x-y projections show pY (green) and dpERK staining (magenta) in wild type (wt) untreated embryos at stage 16. pY staining is homogeneous while dpERK signal is not detectable in the epidermal cells. (**b-c"**) Confocal x-y projections show increased pY staining (green) around wounds in wild type (wt). The staining is more restricted in *stit* mutants. Stit staining (magenta) visualized the epithelia cells around wounds in wild type. This staining is absent in *stit* mutants. (**d-e**) *In situ* hybridization shows the induction of *Ddc* mRNA upon wounding in wild type (wt) (**d**) and *stit* mutant (**e**) embryos. Transparent squares indicate the extent of induction of *Ddc* transcripts after wounding. *Ddc* transcripts are detected in much fewer cells around wounds in *stit* mutant embryos than in wt. (**f**) Plot comparing wound-induced *Ddc* transcripts in wt and *stit* mutants. 80% of wounded wt embryos (n = 54) exhibit broad or moderate *Ddc* induction. By contrast, only 20% of *stit* mutants (n = 49) show broad or moderate induction of *Ddc* mRNA. (**g**) Quantification of the *Ddc*-GFP induction in wounded control (*Ddc*-GFP embryos) and *stit* mutant embryos (*Ddc-GFP; stit* embryos) (* indicates p = 0.0076 and ** p = 0.00029; n = 312 for the control and n = 234 for *stit* mutants). (**h-i'**) The induction of *ple*-DsRed wound reporter upon wounding is much restricted in *stit* mutant (*ple*-DsRed; *stit*) compared to control embryos (*ple*-DsRed). Wound induced RFP expression is marked by white arrows (upper panel; fluorescent micrographs). Wound location is identified by the leakage of body fluid (black arrows in the lower panel; DIC micrographs) after puncture. (**j**) Quantification of the *ple*-DsRed induction in wounded control (*ple*-DsRed) and *stit* mutant (*ple*-DsRed*; stit*) embryos (* p = 0.011, ** p = 0.0026. Control embryos, n = 87; *stit* mutant embryos, n = 152). Scale bar: 5µm (**a-c"**); 25µm (**d**), (**e**) and (**h-i'**).

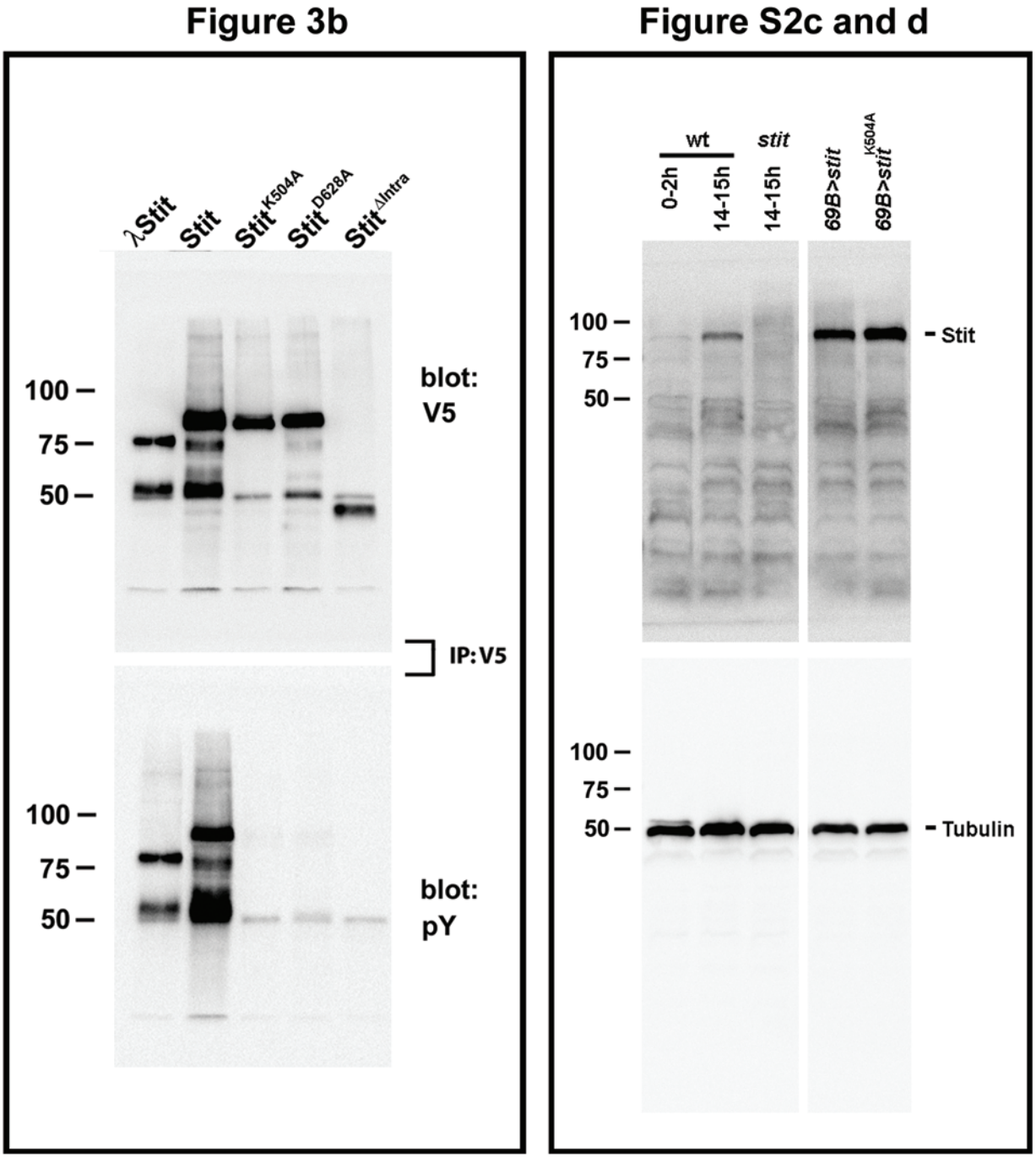

Figure S6 Full scans of cropped western blot panels

Supplementary Movie Legends

Movie S1 Confocal time-lapse movie showing epidermal wound re-epithelialization in a wild type embryo expressing Nrg-GFP. Wound closure takes 60 minutes.

Movie S2 Confocal time-lapse movie showing epidermal wound re-epithelialization in a *stit* embryo expressing Nrg-GFP. Wound closure is not completed even after 390 minutes.

Movie S3 Confocal time-lapse movie showing epidermal wound re-epithelialization of a wild type embryo expressing GFP-*moe* driven by *69B*-GAL4. This embryo seals its wound within 78 minutes.

Movie S4 Confocal time-lapse movie showing epidermal wound re-epithelialization in a *69B*>GFP-*moe*; *stit* embryo. The wound is closed after 186 minutes.

Movie S5 Confocal time-lapse movie showing epidermal wound re-epithelialization in a *69B*>GFP-*moe*; *stit* embryo, which failed to close its wound during the 390 minutes recording period.

Supplementary Methods

Fly stocks. The XP type P element d07355 and Df(3R)Exel9056 are described in [1] and [2], respectively. Transgenic lines were established by P element-mediated germ line transformation according to [3].

Grh binding elements and EMSA. DNA genomic sequences were obtained from http://www.flybase.net. Grh binding elements (Gbes) were predicted using the CIS-ANALYST search tool available at **http://rana.lbl.gov/cis-analyst**[4]. CIS-ANALYST examines sequence windows of defined length (wind_size), selecting only those containing at least a user defined number of binding sites (min_sites). It then collapses all overlapping windows into a single ‘‘cluster”. The parameters used in our search were “wind_size”= 700 base pairs (bp) and “min_sites”= 5. The user-defined motifs were the epidermal specific Gbe be-1 (GAAACCGGTTAT) and the neuron specific Gbe be-2 (TGAACCGGTCCT)[5]. This screen identified 95 Gbe clusters located in either upstream, downstream, or intronic regions of ~100 annotated genes. The p value was 0.0003. One such cluster was located in the second intron of CG10244/*stit*. After confirming that *stit* was indeed a likely Grh target by *in situ* hybridization, and since *stit* is not expressed in neurons, we performed a second search looking for additional epidermal-specific binding sites (be-1) near *stit*, using a window of 10000 bps both upstream and downstream of the coding sequence. The identified Gbes are shown in figure 1a. The p value was also 0.0003. The DNA sequences of identified putative Gbes within the *stit* locus are: Gbe1, GTAAGCGGATAT; Gbe2, ATACCCGGTGTT; Gbe3, TCAACCGGTTAT; Gbe4,

GTCATCGGTTTC; Gbe5, AAAACCGGTACT; Gbe6, ATATGCGGTTAC; Gbe7, GAAATCGGATAG.

EMSA was carried out as described previously, using the bacterial derived GST-Grh fusion protein (g-B/P: aa 603-865)[6]. The following oligonucleotide probes were used (sense strand only given):

Gbe3 probe:

5'-CAAGTGCAAACAACTCAACCGGTTATCACGTCACGTCG-3';

Mutated Gbe3 probe:

5'-CAAGTGCAAACAACTCATACGATCATCACGTCACGTCG-3'

The underlined segment highlights Gbe3 and its mutated version. The Gbe3 probe was selected for EMSA because Gbe3 shows high similarity to the previously identified Grh binding site be-1 (GAAACCGGTTAT)[5].

Site-directed mutagenesis. For site-directed mutagenesis, QuickChange Site-Directed Mutagenesis Kit (Stratagene) was used with the following primers. The mutated bases are shown underlined.

To mutate Gbe2:

Forward: 5'-AGGCGTTTAATGGATTTGGTTTGAACTCTTAATTC-3'

Reverse: 5'-GAATTAAGAGTTCAAACCAAATCCATTAAACGCCT-3'

To mutate Gbe3:

Forward: 5'-GTGCAAACAACTTCCATTTGGATCACGTCACGTC-3'

Reverse: 5'-GACGTGACGTGATCCAAATGGAAGTTGTTTGCAC-3'

To mutate Gbe4:

Forward: 5'-ATCGCTGTGTCGTGCATTTGGTCGACGACCGC-3'

Reverse: 5'-GCGGTCGTCGACCAAATGCACGACACAGCGAT-3'

To mutate Gbe5:

Forward: 5'-CACTTTATAAAACCTTGGCTGTAACATCGGAGAATCTGGC-3'

Reverse: 5'-GCCAGATTCTCCGATGTTACAGCCAAGGTTTTATAAAGTG-3'

To generate a kinase dead mutant Stit (Lys504Ala, $Stit^{K504A}$, this substitution is expected to interfere with ATP binding[7]):

Forward: 5'-GCATTACAACCGTGGCTGTGGCCACGCTCAAGGAAAGTGC-3'

Reverse: 5'-GCACTTTCCTTGAGCGTGGCCACAGCCACGGTTGTAATGC-3'

To generate a kinase dead mutant Stit (Asp628Ala, $Stit^{D628A}$, this substitution was expected to eliminate the kinase activity[8]):

Forward: 5'-CACTTGCAAAGTTGCGGCCTTTGGCTTCGCACGAG-3'

Reverse: 5'-CTCGTGCGAAGCCAAAGGCCGCAACTTTGCAAGTG-3'

Real time quantitative Reverse-Transcription PCR (q-RT-PCR). Total RNA was extracted from 100 embryos using Trizol (Gibco BRL). cDNA was synthesized from total RNA using oligo (dT)20 primers and SuperScript II for the reverse transcriptase reactions (Invitrogene). Real-time PCR was performed using an ABI PRISM 7000 Sequence Detection system (Applied Biosystems) and TaqMan Universal PCR Master Mix (Applied Biosystems). Relative levels and the standard deviation of wild type and mutant samples were calculated from triplicate reactions with at least two different total RNA preparations using the delta-delta Ct method. *RP49* probes were used to normalize

total mRNA levels in each experiment[9]. The Taqman primer/probe sets for *stit* (CG10244) and *Rp49* (CG7939) were the ones recommended by Applied Biosystems.

RNA *in situ* hybridization and cuticle preparations. Digoxigenin-labled RNA probes were transcribed from RE05926 (*stit*) and RE72216 (*Ddc*) and hybridized to embryos according to[10]. Embryos were collected on apple juice agar plates for 4 hours and aged for additional 24 hours. Cuticle preparation was then performed as described in[11].

Analysis of dorsal closure timing. The analysis of dorsal closure timing was performed according to [12].

Aseptic injury assays-supplementary information. To compare the induction of *stit*α-GFP and *stit*γ-GFP upon wounding in wild type, *grh* and *stit* mutant background, 2 independent lines for each reporter were examined. We analyzed GFP expression in: 136 embryos for *stit*α-GFP, in 192 embryos for *stit*α-GFP; *grh* mutants, in 93 embryos for *stit*α-GFP; *stit* mutants, in 247 *stit*γ-GFP embryos and in 202 embryos for *stit*γ-GFP; *grh*. To compare the expression of *stit*γ-GFP to *stit*δ-GFP, we analyzed 4 independent lines of *stit*γ-GFP and 6 independent lines of *stit*δ-GFP. To compare the induction of *stit*γ-GFP and *stit*δ-GFP upon wounding, 2 independent lines for each reporter were used. We analyzed 182 *stit*δ-GFP embryos in this the wounding assay.

References for Supplementary Information

1. Thibault, S. T. et al. A complementary transposon tool kit for Drosophila melanogaster using P and piggyBac. Nat Genet 36, 283-7 (2004).
2. Parks, A. L. et al. Systematic generation of high-resolution deletion coverage of the Drosophila melanogaster genome. Nat Genet 36, 288-92 (2004).
3. Rubin, G. M. & Spradling, A. C. Genetic transformation of Drosophila with transposable element vectors. Science 218, 348-53 (1982).
4. Berman, B. P. et al. Exploiting transcription factor binding site clustering to identify cis-regulatory modules involved in pattern formation in the Drosophila genome. Proc Natl Acad Sci U S A 99, 757-62 (2002).
5. Uv, A. E., Harrison, E. J. & Bray, S. J. Tissue-specific splicing and functions of the Drosophila transcription factor Grainyhead. Mol Cell Biol 17, 6727-35 (1997).
6. Uv, A. E., Thompson, C. R. & Bray, S. J. The Drosophila tissue-specific factor Grainyhead contains novel DNA-binding and dimerization domains which are conserved in the human protein CP2. Mol Cell Biol 14, 4020-31 (1994).
7. Fang, X., Stachowiak, E. K., Dunham-Ems, S. M., Klejbor, I. & Stachowiak, M. K. Control of CREB-binding protein signaling by nuclear fibroblast growth factor receptor-1: a novel mechanism of gene regulation. J Biol Chem 280, 28451-62 (2005).
8. Kornev, A. P., Haste, N. M., Taylor, S. S. & Eyck, L. F. Surface comparison of active and inactive protein kinases identifies a conserved activation mechanism. Proc Natl Acad Sci U S A 103, 17783-8 (2006).
9. Livak, K. J. & Schmittgen, T. D. Analysis of relative gene expression data using real-time quantitative PCR and the 2(-Delta Delta C(T)) Method. Methods 25, 402-8 (2001).
10. Lehmann, R. & Tautz, D. In situ hybridization to RNA. Methods Cell Biol 44, 575-98 (1994).
11. Ostrowski, S., Dierick, H. A. & Bejsovec, A. Genetic control of cuticle formation during embryonic development of Drosophila melanogaster. Genetics 161, 171-82 (2002).
12. Fox, D. T. et al. Rho1 regulates Drosophila adherens junctions independently of p120ctn. Development 132, 4819-31 (2005).

nature cell biology

Centromere assembly requires the direct recognition of CENP-A nucleosomes by CENP-N

Christopher W. Carroll[1], Mariana C.C. Silva[2], Kristina M. Godek[1], Lars E.T. Jansen[2] and Aaron F. Straight[1,3]

Centromeres are specialized chromosomal domains that direct kinetochore assembly during mitosis. CENP-A (centromere protein A), a histone H3-variant present exclusively in centromeric nucleosomes, is thought to function as an epigenetic mark that specifies centromere identity. Here we identify the essential centromere protein CENP-N as the first protein to selectively bind CENP-A nucleosomes but not H3 nucleosomes. CENP-N bound CENP-A nucleosomes in a DNA sequence-independent manner, but did not bind soluble CENP-A–H4 tetramers. Mutations in CENP-N that reduced its affinity for CENP-A nucleosomes caused defects in CENP-N localization and had dominant effects on the recruitment of CENP-H, CENP-I and CENP-K to centromeres. Depletion of CENP-N using siRNA (short interfering RNA) led to similar centromere assembly defects and resulted in reduced assembly of nascent CENP-A into centromeric chromatin. These data suggest that CENP-N interprets the information encoded within CENP-A nucleosomes and recruits other proteins to centromeric chromatin that are required for centromere function and propagation.

Accurate chromosome segregation during mitosis is essential for the maintenance of genome integrity. Eukaryotic cells have evolved complex machinery to ensure the fidelity of chromosome segregation. Each chromosome directs the assembly of a kinetochore that mediates attachment to the mitotic spindle and is required for microtubule-dependent chromosome movement during mitosis. Kinetochores also function as signalling centres for the mitotic checkpoint, which delays the initiation of anaphase in response to improper chromosome attachment to the mitotic spindle (see ref. 1 for review). The centromere is the region of the chromosome on which the kinetochore is assembled. Human centromeric DNA is composed of repetitive α-satellite sequences but centromeres are thought to be epigenetically specified, as centromeric DNA is not well conserved between species and no DNA sequences have been identified that are necessary or sufficient for kinetochore function in vertebrates (see ref. 2 for review). In all eukaryotes, centromeric chromatin contains specialized nucleosomes in which histone H3 is replaced by a histone H3-variant, CENP-A (see ref. 3 for review). This centromere protein is currently the best candidate for the epigenetic mark that specifies centromere identity. It is essential for the centromeric recruitment of most other proteins required for kinetochore function, but the molecular basis for recognition of CENP-A-containing chromatin as the site of kinetochore assembly is poorly understood. Furthermore, the mechanisms that target newly synthesized CENP-A/H4 to established centromeric chromatin to maintain centromere identity have not been determined.

A fundamental limitation in understanding centromere assembly is the lack of well-defined biochemical assays for studying this process. No direct and specific interaction between CENP-A nucleosomes and any of the > 75 proteins that make up a vertebrate mitotic kinetochore has been demonstrated. To identify CENP-A nucleosome-interacting proteins, we developed a simple and rapid binding assay using reconstituted mononucleosomes that contained α-satellite DNA derived from human centromeres and either histone H3 or CENP-A (Fig. 1a). Potential CENP-A nucleosome-interacting proteins were selected for testing in this assay based on the analysis of kinetochore assembly in several organisms. We focused on the constitutive centromere associated network (CCAN) of proteins, which includes the centromere proteins CENP-C, H, I and K–U, because these proteins are localized to centromeres during interphase and are required for the assembly of functional kinetochores in mitosis. Moreover, their localization, observed by immuno-electron microscopy of CENP-C, to the inner kinetochore plate and the recent demonstration that several of these proteins co-purify with CENP-A mononucleosomes suggests that CCAN proteins are likely to be the chromatin proximal elements of kinetochores[4–7]. We also included CENP-B in our analysis because it has been shown previously to bind directly to a conserved 17-nucleotide motif called the CENP-B box, present in α-satellite DNA[8]. We expressed CENP-B, C, H, I, and K–U and labelled them with ^{35}S by coupled *in vitro* transcription and translation (Fig. 1b; Supplementary Information Fig. S1). We then incubated the labelled proteins with or without CENP-A mononucleosomes before resolving the mixtures using native gel electrophoresis. Both CENP-B and CENP-N showed an increased relative migration in the presence of CENP-A nucleosomes assembled with α-satellite DNA, suggesting that CENP-B and CENP-N

[1]Department of Biochemistry, Stanford University School of Medicine, Beckman Center, Room 409, 279 Campus Drive, Palo Alto, CA 94503-5307, USA. [2]Laboratory for Epigenetic Mechanisms, Instituto Gulbenkian de Ciência, Rua da Quinta Grande, 6, 2780-156 Oeiras, Portugal.
[3]Correspondence should be addressed to A.F.S. (e-mail: astraigh@stanford.edu)

Received 5 November 2008; accepted 17 March 2009; published online 21 June 2009; DOI: 10.1038/ncb1899

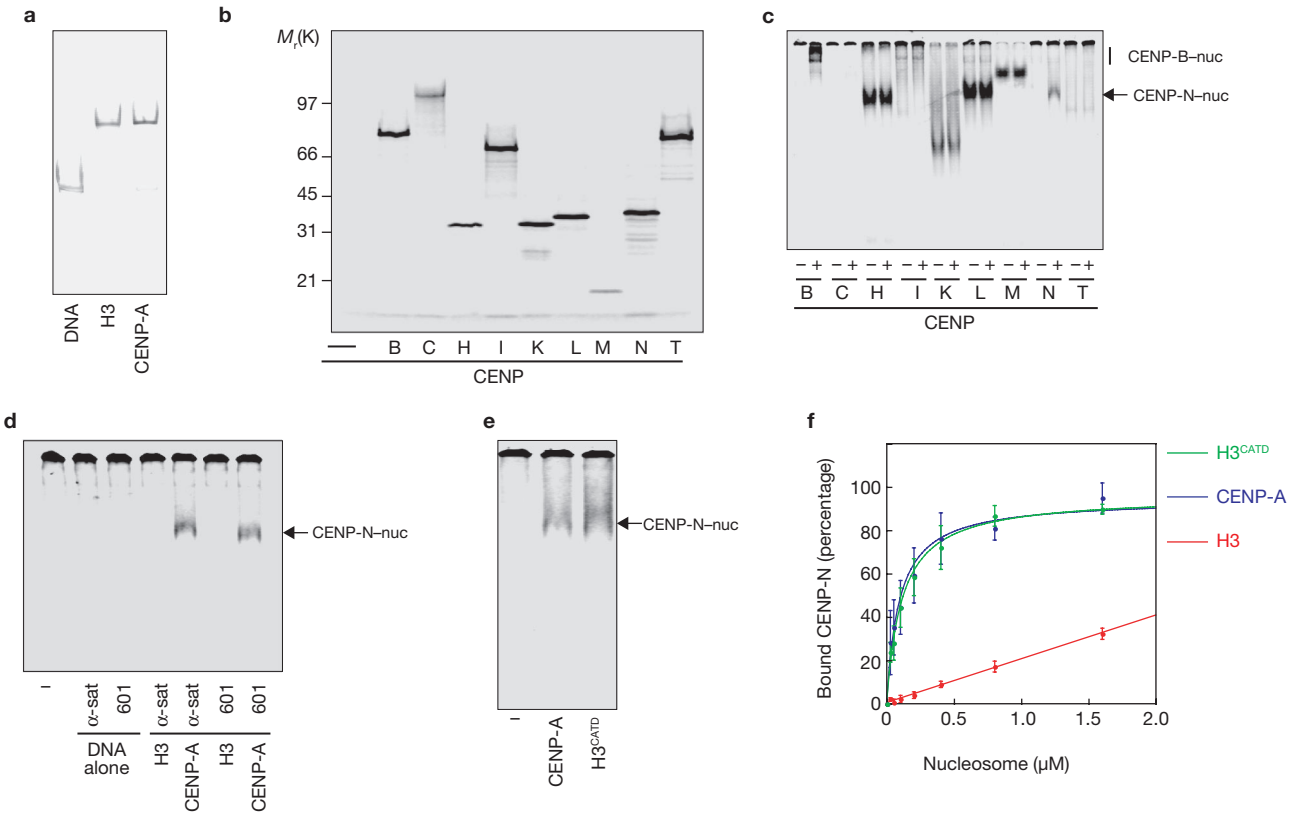

Figure 1 CENP-N binds CENP-A nucleosomes. (**a**) Reconstitution of conventional and centromeric nucleosomes. Free 186 base pair human α-satellite DNA (DNA) or mononucleosomes containing either histone H3 or CENP-A were assembled by salt dialysis and resolved by native gel electrophoresis. (**b**) *In vitro* expression of centromere proteins. Centromere proteins to be used as substrates in nucleosome binding assays were expressed in coupled transcription and translation reactions containing ^{35}S-methionine. (**c**) CENP-A nucleosome binding assay. ^{35}S-labelled centromere proteins (~1 nM) were incubated in the presence (+) or absence (-) of reconstituted CENP-A nucleosomes (50 nM) and separated by native gel electrophoresis. Both CENP-B and CENP-N showed CENP-A-nucleosome dependent changes in migration (CENP-B/N–nuc, nucleosome bound CENP proteins). (**d**) CENP-N binding to nucleosomes depends on CENP-A and not DNA sequence. α-satellite DNA (α-sat) or 601 DNA (601), or H3- or CENP-A-containing nucleosomes reconstituted with α-satellite or 601 DNA were incubated with ^{35}S-labelled CENP-N and resolved by native gel electrophoresis. The faster migrating band (arrow) indicates nucleosome-bound CENP-N (– indicates no nucleosome or DNA, as a control). (**e**) Binding of CENP-N to CENP-A nucleosomes occurs through the CATD region of CENP-A. No nucleosome (–) as a control, CENP-A or H3^{CATD} nucleosomes reconstituted with α-satellite DNA were bound to ^{35}S–CENP-N and assayed as in **c**. (**f**) CENP-N binds with equal affinity to CENP-A and H3^{CATD} nucleosomes. CENP-N binding was assayed as in **c** with increasing nucleosome concentration and was quantified according to the ^{35}S–CENP-N signal in the gel (data are mean ± s.e.m., $n = 3$).

bind directly to CENP-A nucleosomes (Fig. 1c). We did not detect any change in the migration of CENP-C, H, I, K, L, M or O–U (Fig. 1c; Supplementary Information, Fig. S1a). We also tested hMis18α, hMis18β and M18BP1/hKNL-2, which have been implicated in CENP-A assembly, but we did not detect any interaction with CENP-A nucleosomes in this assay (Supplementary Information, Fig. S1b)[9,10].

We determined the contribution of DNA sequence and histone protein composition to CENP-B and CENP-N binding of CENP-A nucleosomes by alternately exchanging the nucleosomal DNA and histones. As expected, CENP-B bound to naked α-satellite DNA as well as both H3 and CENP-A nucleosomes that contained α-satellite DNA (Supplementary Information, Fig. S1c). CENP-B did not bind the synthetically derived 601 nucleosome positioning sequence or nucleosomes that contained the 601 DNA sequence. In contrast, CENP-N bound equally well to CENP-A nucleosomes that contained either the α-satellite DNA or the 601 DNA sequence (Fig. 1d). CENP-N did not bind the α-satellite or 601 DNA fragment or histone H3 nucleosomes assembled on either DNA fragment. CENP-N also bound to CENP-A/H4 tetrasomes reconstituted with α-satellite DNA that lacked histone H2A and H2B, but did not specifically bind to soluble CENP-A/H4 tetramers (Supplementary Information, Fig. S1d–f). Thus, CENP-N binds specifically to CENP-A-associated chromatin.

Domain transfer experiments have previously suggested that a contiguous portion of the loop I and helix II region within the histone fold of CENP-A, called the CENP-A targeting domain (CATD), is sufficient for CENP-A function *in vivo*[11,12]. We tested whether the CATD domain was sufficient for CENP-N binding using reconstituted nucleosomes that contained the histone H3^{CATD} chimaera. CENP-N bound efficiently to H3^{CATD}-containing nucleosomes (Fig. 1e), and dose-response experiments revealed that the affinity of CENP-N for H3^{CATD} nucleosomes was indistinguishable from the affinity of CENP-N for wild-type CENP-A nucleosomes (apparent K_d = 163 nM ± 60 versus 169 nM ± 70, respectively; Fig. 1f; Supplementary Information, Table S1). The CATD domain imparts structural differences to CENP-A nucleosomes, in comparison with H3 nucleosomes, and CENP-A nucleosomes have been suggested to function as an epigenetic mark within chromatin to specify centromere identity[13]. Our data suggest that CENP-N recognizes the unique structural information encoded by the CATD within CENP-A nucleosomes.

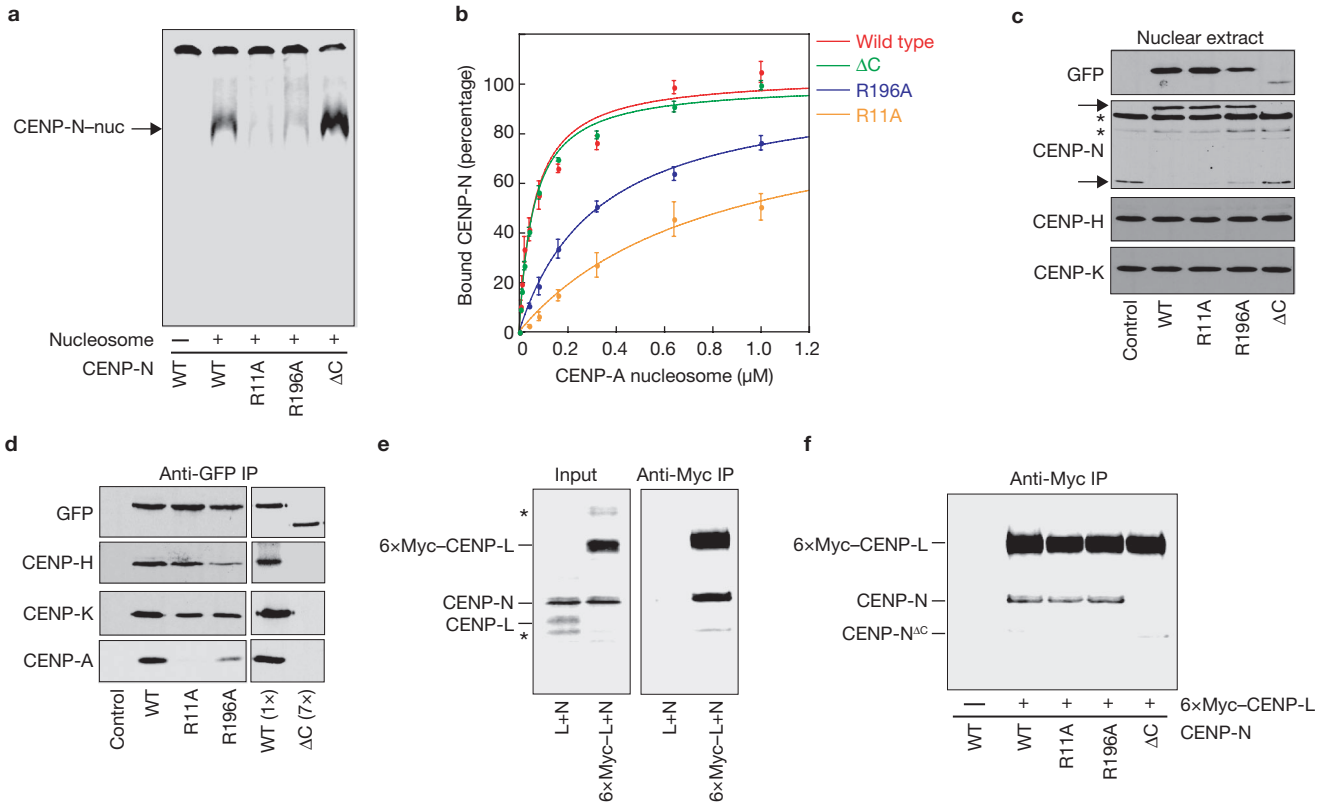

Figure 2 Identification and characterization of CENP-N mutants defective in CENP-A-nucleosome binding. (**a**) CENP-N mutants show a range of affinities for CENP-A nucleosomes. CENP-N wild type (WT) or the indicated CENP-N mutants (R11A, R196A and ΔC) were expressed and an equal concentration (~1 nM) of each was assayed for the ability to bind CENP-A nucleosomes (CENP-N–nuc, bound CENP). The control reaction (–) lacked CENP-A nucleosomes. (**b**) Dose-response experiments for each CENP-N mutant were performed as in **a**, with increasing concentrations of CENP-A nucleosome added to each reaction. Data are mean ± s.e.m., $n = 3$. (**c**) Expression of CENP-N mutants in HEK293 cells. Nuclear extracts from stable HEK293 cell lines expressing GFP–CENP-N (WT) or the indicated GFP–CENP-N mutants were separated by SDS–PAGE and analysed by western blotting using the indicated antibodies. Two nonspecific bands (asterisks) are present in the anti-CENP-N western blot. Upper and lower arrows indicate positions of GFP–CENP-N and endogenous CENP-N, respectively. Quantification of each band is presented in Supplementary Information, Fig. S4a. (**d**) Co-immunoprecipitation of CENP-H, K and A from micrococcal-nuclease solubilized chromatin with CENP-N mutants. Anti-GFP immunoprecipitates (IP) from each cell line were probed with the indicated antibodies. Seven times more nuclear extract from the CENP-N$^{\Delta C}$ cell line than the wild-type cell line was required to achieve equal levels of CENP-N in the immunoprecipitations. Quantification of each band is presented in Supplementary Information, Fig. S4b. (**e**) CENP-N binds to CENP-L. 6×Myc-CENP-L, L and N were expressed and labelled with ^{35}S-methionine and the indicated proteins were mixed at equal stoichiometry. Of each mixture, 20% was resolved as input (left). The remaining 80% was immunoprecipitated with anti-Myc antibodies (right). Two background bands (asterisks) were present in the input reactions. (**f**) CENP-L binding requires the C terminus of CENP-N. Immunoprecipitations were identical to those in **e**, except that equal amounts of wild-type CENP-N or the indicated CENP-N mutant was used in each reaction.

Depletion of CENP-N with siRNA causes defects in kinetochore assembly and chromosome congression during metaphase, and results in the loss of most other CCAN components from the centromere[5,14]. However, the depletion of other CCAN subunits, including CENP-H, I and K, results in mitotic phenotypes similar to those caused by CENP-N depletion[4,5,14,15]. Furthermore, CENP-N co-purifies with CENP-H, I, M, K, L and T, which are all likely to be interdependent for centromere localization, as indicated by pairwise dependency relationships[4,5,14,15]. Accordingly, a specific function for CENP-N in recognizing centromeric chromatin *in vivo* cannot be inferred from siRNA-based studies.

To directly determine the role of CENP-A nucleosome binding by CENP-N in centromere assembly, we generated CENP-N mutants that had specifically reduced CENP-A-nucleosome binding affinity. Conserved charged and polar amino acids within CENP-N were changed to alanine, based on sequence alignments of CENP-N orthologues from several species (Supplementary Information, Fig. S2a). Following an initial characterization of the mutants *in vitro* and *in vivo* (Supplementary Information, Fig. S3 and Table S1), two of the point mutants, CENP-N^{R11A} and CENP-N^{R196A}, were selected for detailed analysis. Both of these mutants showed reduced CENP-A-nucleosome binding when compared with wild-type CENP-N (Fig. 2a). Dose-response experiments indicated that the CENP-N^{R11A} and CENP-N^{R196A} mutants had a 6-fold and a 2-fold reduction in CENP-A-nucleosome binding, respectively (Fig. 2b; Supplementary Information, Table S1), suggesting that both Arg 11 and Arg 196 in CENP-N contribute to the recognition of CENP-A nucleosomes. In addition, the carboxyl terminus of CENP-N (amino-acids 289–339 in human CENP-N) is more highly conserved among vertebrates than the rest of the protein (Fig. S2b). We therefore constructed a truncation mutant of CENP-N, lacking the C terminus (CENP-N$^{\Delta C}$). The CENP-N$^{\Delta C}$ mutant did not affect nucleosome binding when compared with wild-type CENP-N (Fig. 2a, b).

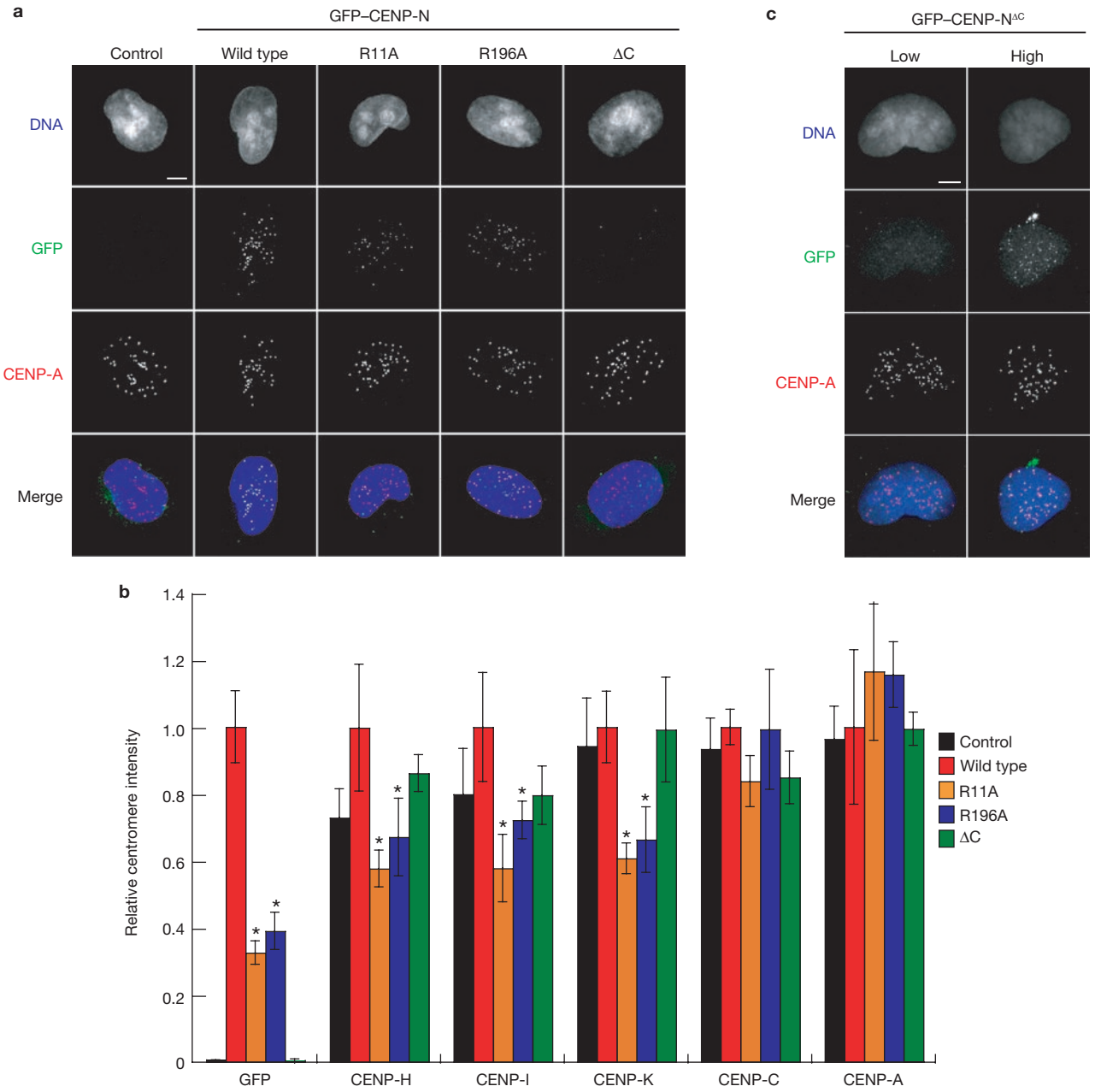

Figure 3 CENP-N mutants show centromere assembly defects. (**a**) Representative images of control HEK293 cells and stable cell lines expressing wild-type or the indicated mutant CENP-N. Scale bar, 5 μm. (**b**) CENP-N mutants cause centromere assembly defects. The fluorescence intensity of the indicated centromere protein at individual centromeres in stable cell lines was measured (see Methods). Data are mean ± s.e.m. from three independent experiments, including > 300 centromeres from > 20 cells for each cell line, $*P < 0.05$ significance compared with wildtype, as determined by Student's *t*-test. (**c**) The C terminus of CENP-N is not required for centromere localization. Representative images from transiently transfected HeLa cells show the localization of GFP–CENP-N$^{\Delta C}$ in low and high expressing cells. Scale bar, 5 μm.

We generated stable HEK293 cell lines that expressed green-fluorescent protein (GFP) fusions to either wild-type CENP-N or the CENP-N mutants to determine how changing the affinity of CENP-N for the CENP-A nucleosome affected CENP-N localization and centromere assembly *in vivo*. Western blotting indicated that each cell line expressed comparable levels of the respective GFP–CENP-N protein, with the exception of the CENP-N$^{\Delta C}$ mutant, which was reduced ~7-fold compared with wild-type GFP–CENP-N (Fig. 2c; Supplementary Information Fig. S4a). HEK293 cell lines express CENP-N from a single genomic locus under the same promoter (see Methods), suggesting that the decreased protein level is a general property of the CENP-N$^{\Delta C}$ mutant. Interestingly, while the levels of CENP-H and CENP-K were not affected in any of the stable cells lines, the expression of wild-type GFP–CENP-N or either of the two GFP–CENP-N point mutants caused a significant reduction in endogenous CENP-N protein (Fig. 2c). Such a reduction has also been described in cells depleted of CENP-H, suggesting that CENP-N is unstable when not associated with other CCAN components[14]. We

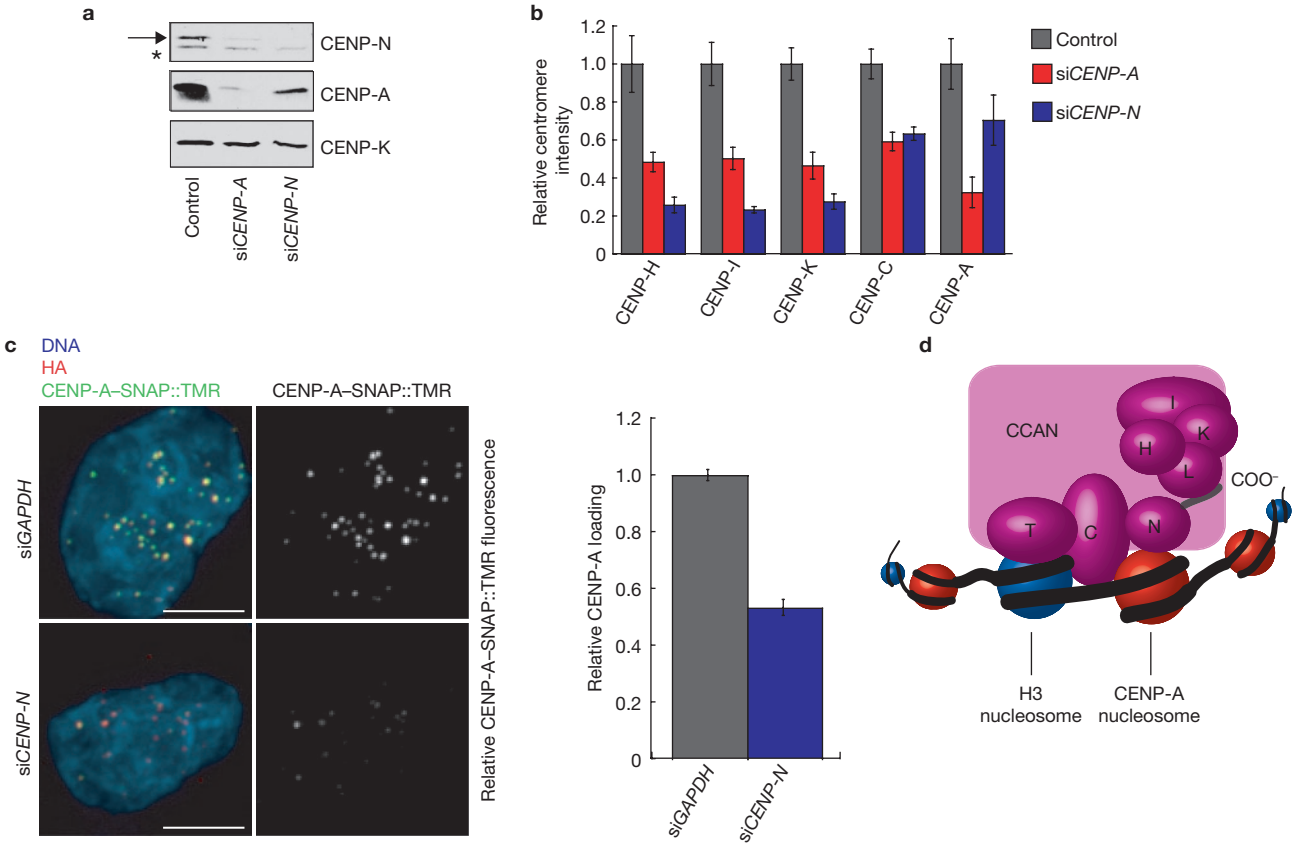

Figure 4 Depletion of CENP-N affects centromere assembly. (**a**) CENP-N depletion leads to a reduction in CENP-A levels. HeLa cells were treated with the indicated siRNAs for 56 h and the abundance of the indicated centromere protein was determined by western blotting. Arrow (top) indicates the position of CENP-N. A background band (asterisk) was present in the anti-CENP-N western blot. CENP-K was included as a loading control. (**b**) CENP-N depletion causes centromere assembly defects. HeLa cells were treated as in **a**, except that the centromere fluorescence intensity of the indicated protein was measured. Data are mean ± s.e.m., from three independent experiments, including > 150 centromeres from > 10 cells for each experiment. (**c**) Reduced CENP-A assembly after *CENP-N* RNAi transfection. CENP-A–SNAP cells were synchronized, transfected with siRNAs against *CENP-N* or *GAPDH* and assayed for CENP-A loading by specifically labelling nascent CENP-A–SNAP using TMR-Star as outlined in Supplementary Information, Fig. S5c. Representative images are shown (left). Haemagglutinin (HA) labels a steady state pool of CENP-A–SNAP and is used as a centromere marker. Scale bar, 5 μm. Data are mean ± s.e.m. from three independent experiments, including the fluorescence intensity of 200 centromeres from 20 cells from each experiment, which was normalized to the *GAPDH* siRNA control. (**d**) A model depicting the multiple roles of CENP-N in CENP-A-nucleosome recognition and centromere assembly, from the recruitment of CCAN proteins to the CENP-N C-terminal region and centromeric chromatin propagation to the CCAN-dependent regulation of CENP-A-nucleosome assembly.

conclude that wild-type GFP–CENP-N and the GFP–CENP-N^{R11A} and GFP–CENP-N^{R196A} mutants effectively replaced endogenous CENP-N in these cell lines.

We directly determined the ability of the CENP-N point mutants to interact with other CCAN proteins and with CENP-A nucleosomes *in vivo*. Immunoprecipitation of wild-type GFP–CENP-N showed that GFP–CENP-N bound to CENP-H, K and A nucleosomes (Fig. 2d; Supplementary Information, Fig. S4b). The GFP–CENP-N^{R11A} and GFP–CENP-N^{R196A} mutants were also associated with CENP-H and CENP-K, although CENP-N^{R196A} bound CENP-H less well than wild-type CENP-N. Importantly, the CENP-N^{R11A} and CENP-N^{R196A} mutants both showed defects in CENP-A-nucleosome binding, the severity of which was consistent with the binding of each mutant to reconstituted CENP-A nucleosomes. Thus, residues Arg 11 and Arg 196 within CENP-N contribute to CENP-A-nucleosome binding *in vitro* and *in vivo*. The comparatively low levels of GFP–CENP-N$^{\Delta C}$ present in stable cells and the inability of this mutant to downregulate endogenous CENP-N protein levels suggests that the GFP–CENP-N$^{\Delta C}$ mutant may not be stably associated with other CCAN proteins. Indeed, GFP–CENP-N$^{\Delta C}$ did not bind to CENP-H, K or A nucleosomes (Fig. 2d).

To understand the mechanism by which the C terminus of CENP-N mediates CENP-N association with CCAN proteins, we expressed epitope-tagged centromere proteins and untagged CENP-N, in reticulocyte extracts, and performed pairwise binding experiments using anti-Myc immunoprecipitation. Myc-tagged CENP-L, but not untagged CENP-L, efficiently co-precipitated with CENP-N, indicating a direct interaction between CENP-N and CENP-L (Fig. 2e). Myc-tagged CENP-L bound the CENP-N^{R11A} and CENP-N^{R196A} mutants as efficiently as it bound wild-type CENP-N (Fig. 2f), consistent with the efficient association of these CENP-N mutants with CENP-H and CENP-K *in vivo*. However, the GFP–CENP-N$^{\Delta C}$ mutant did not bind to CENP-L. These data suggest that CENP-N associates with other CCAN components through a direct interaction with CENP-L that requires the highly conserved C terminus of CENP-N.

We compared the localization of CENP-N^{R11A}, CENP-N^{R196A} and CENP-N$^{\Delta C}$ with wild-type CENP-N. Wild-type GFP–CENP-N localized

exclusively to centromeres as indicated by colocalization with endogenous CENP-A (Fig. 3a). CENP-N^{R11A} and CENP-N^{R196A} also localized to centromeres but did so inefficiently. Quantification showed that the levels of the CENP-N^{R11A} and CENP-N^{R196A} at centromeres was reduced to 32 ± 4% and 39 ± 6%, respectively, from the wild type (Fig. 3b). The difference in localization efficiency between the CENP-N^{R11A} and CENP-N^{R196A} mutants was not as great as would be predicted from their relative CENP-A-nucleosome binding affinities (Fig. 2b, d), suggesting that the other CCAN proteins probably contribute to CENP-N localization efficiency *in vivo*. Nevertheless, these data show that mutations that reduce CENP-A-nucleosome binding by CENP-N result in quantitative defects in the centromere-specific localization of CENP-N.

We did not detect the CENP-N$^{\Delta C}$ mutant at centromeres in our stable cell line, suggesting that association with other CCAN subunits is an important step in the recruitment of CENP-N to centromeres (Fig. 3a, b). However, transiently transfected cells expressing the GFP–CENP-N$^{\Delta C}$ mutant from a strong promoter occasionally contained detectable levels of the mutant protein at centromeres (Fig. 3c). Thus, the C terminus of CENP-N is not absolutely required for CENP-N centromere localization. Instead, our data indicate that association with other CCAN components stabilizes CENP-N and probably increases the efficiency of CENP-N centromere localization.

Mutations in CENP-N that affected CENP-A-nucleosome binding caused dominant defects in centromere assembly in our stable cell lines. Quantification of CENP-H, I and K in cells expressing CENP-N^{R11A} and CENP-N^{R196A} indicated that the levels of each protein at centromeres in interphase cells was significantly reduced when compared with levels in cells expressing wild-type CENP-N (Fig. 3b). Thus, reducing the level of CENP-N at centromeres led to a reduction in the levels of a subset of other CCAN subunits. The defect in CENP-H, I and K localization in the mutant cells was not as severe as that of CENP-N itself, suggesting that a small amount of remaining endogenous CENP-N may also contribute to centromere assembly in these cell lines (Fig. 3b). CENP-N^{R11A} and CENP-N^{R196A} did not alter the levels of CENP-A or CENP-C at centromeres.

Next, we examined the dependence of CENP-H, I and K localization on CENP-N by depleting CENP-N with siRNA in HeLa cells (Fig. 4a; Supplementary Information, Fig. S5a). CENP-N depletion led to a substantial reduction in the levels of CENP-H, I and K at centromeres (Fig. 4b), consistent with previous studies demonstrating CENP-H reduction in cells depleted of CENP-N (ref. 14). The localization defects of CENP-H, I and K in CENP-N-depleted cells were more severe than in cells depleted of CENP-A, indicating that these defects are not an indirect consequence of the reduced CENP-A levels in the CENP-N-depleted cells (Fig. 4b, see below). CENP-C localization to centromeres was also reduced in CENP-N-depleted cells, but not to the same extent as other CCAN proteins (Fig. 4b). Thus, the dependence of CCAN protein localization on CENP-N function was similar between CENP-N-depleted cells and stable cell lines expressing CENP-N mutants with CENP-A-nucleosome binding defects.

Depletion of CENP-N caused a reduction in total levels of CENP-A (Fig. 4a) and CENP-A levels at centromeres (Fig. 4b; Supplementary Information, Fig. S5b). CENP-N is therefore required for the maintenance of centromeric chromatin. Similar defects have been described in *Schizosaccharomyces pombe* cells with mutations in the CENP-N orthologue Mis15, suggesting that CENP-N function is evolutionarily conserved[16]. CENP-H, I and K are required for the deposition of newly synthesized CENP-A at centromeres[4]. We therefore asked whether the reduction in CENP-A levels within centromeric chromatin in CENP-N-depleted cells was due to a failure to load new CENP-A at centromeres. To address this we used the pulse labelling method, based on the SNAP-tag, to determine the fate of newly synthesized protein. Using this strategy, the assembly of nascent CENP-A has been shown previously to be restricted to early G1 phase[17]. The siRNA-mediated reduction of CENP-N levels resulted in a significant reduction in the recruitment of newly synthesized CENP-A–SNAP to centromeres (Fig. 4c; Supplementary Information, Fig. S5c), indicating that the loss of steady-state levels of centromeric CENP-A is caused, at least in part, by a defect in CENP-A assembly.

We have identified CENP-N as the first protein to bind specifically to CENP-A nucleosomes and shown that the direct binding of CENP-A nucleosomes by CENP-N is required for centromere assembly. The DNA sequence-independent binding of CENP-A nucleosomes by CENP-N suggests that CENP-N recognizes the epigenetic mark in chromatin that specifies centromere identity. Importantly, whereas CENP-N targets directly to CENP-A nucleosomes, we found that CENP-N itself is required for recruiting new CENP-A to the centromere, suggesting that CENP-N is part of a feedback loop responsible for propagating centromeric chromatin in dividing cells (Fig. 4d).

CENP-N mutants with a 2-fold or 6-fold reduction in apparent binding affinity for CENP-A nucleosomes, compared with wild-type CENP-N, localized equally efficiently to centromeres *in vivo*, suggesting that CCAN proteins other than CENP-N may also provide direct interactions with chromatin that are important for centromere assembly. The interdependence of several CCAN proteins, including CENP-N and CENP-T, for centromere localization is consistent with this possibility[5]. A complex of CENP-T and CENP-W was recently shown to bind directly to DNA *in vitro* and it associates with histone H3-containing nucleosomes[18]. CENP-N and the CENP-T–W complex are therefore likely to cooperate in providing multiple distinct chromatin contacts that are required for the localization of a subset of other CCAN proteins, including CENP-H, I and K, to centromeres.

CENP-C assembly at centromeres is less sensitive to CENP-N depletion than the other CCAN proteins we examined, consistent with previous results suggesting that CENP-I and CENP-C are independently recruited to centromeric chromatin in human cells[19]. Nevertheless, CENP-A is required for both CENP-N and CENP-C centromere localization, indicating that several centromere localization pathways downstream of CENP-A exist[5,20]. CENP-C has been shown previously to bind directly to DNA *in vitro*, but it is unclear how such an activity could translate into the centromere-specific localization observed for CENP-C *in vivo*[21,22]. Identifying the molecular mechanisms by which CENP-C is recruited to CENP-A chromatin in the absence of CENP-N, and understanding how these distinct centromere-recognition pathways are integrated at the level of chromatin will provide important insights into centromere assembly and structure. □

METHODS

Methods and any associated references are available in the online version of the paper at http://www.nature.com/naturecellbiology/.

Note: Supplementary Information is available on the Nature Cell Biology website.

ACKNOWLEDGEMENTS

The authors would like to thank members of the Straight Lab for helpful comments and support, J. Minshull and DNA2.0 (CA, USA) for gene synthesis, S. H. Hanissian for the CENP-U(50) cDNA, J. Yang, G. Narlikar, M. Resch, K. Luger and J. Hansen for reagents and help with nucleosome reconstitution, S.-T. Liu for the CENP-H and CENP-I antibodies and D. Herschlag for advice. C.W.C. was supported by a postdoctoral fellowship from the Helen Hay Whitney Foundation. K.G. was supported by a predoctoral fellowship from the National Science Foundation and by a NIH grant (T32GM007276). A.F.S. is a Gordon Family Scholar supported by the Damon Runyon Cancer Research Foundation, and this work was supported by a NIH grant (R01GM074728). M.C.C.S. is supported by the Fundação para a Ciência e a Tecnologia (FCT; SFRH/BD33219/2007). LETJ is supported by the FCT, Fundação Calouste Gulbenkian and the EU Seventh Framework Programme.

AUTHOR CONTRIBUTIONS

C.W.C. and A.F.S. designed the experiments and wrote the manuscript; C.W.C. performed all the experiments except those presented in Figure 4c, which were performed by M.C.C.S. and L.E.T.J.; and K.G. purified histones and helped with nucleosome assembly.

COMPETING FINANCIAL INTERESTS

The authors declare no competing financial interests.

Published online at http://www.nature.com/naturecellbiology/.
Reprints and permissions information is available online at http://npg.nature.com/reprintsandpermissions/.

1. Cheeseman, I. M. & Desai, A. Molecular architecture of the kinetochore-microtubule interface. *Nature Rev. Mol. Cell Biol.* **9,** 33–46 (2008).
2. Choo, K. H. Domain Organization at the Centromere and Neocentromere. *Dev. Cell* **1,** 165–177 (2001).
3. Carroll, C. W. & Straight, A. F. Centromere formation: from epigenetics to self-assembly. *Trends Cell Biol.* **16,** 70–78 (2006).
4. Okada, M. *et al.* The CENP-H-I complex is required for the efficient incorporation of newly synthesized CENP-A into centromeres. *Nature Cell Biol.* **8,** 446–457 (2006).
5. Foltz, D. R. *et al.* The human CENP-A centromeric nucleosome-associated complex. *Nature Cell Biol.* **8,** 458–469 (2006).
6. Izuta, H. *et al.* Comprehensive analysis of the ICEN (Interphase Centromere Complex) components enriched in the CENP-A chromatin of human cells. *Genes Cells* **11,** 673–684 (2006).
7. Saitoh, H. *et al.* CENP-C, an autoantigen in scleroderma, is a component of the human inner kinetochore plate. *Cell* **70,** 115–125 (1992).
8. Masumoto, H., Masukata, H., Muro, Y., Nozaki, N. & Okazaki, T. A human centromere antigen (CENP-B) interacts with a short specific sequence in alphoid DNA, a human centromeric satellite. *J. Cell Biol.* **109,** 1963–1973 (1989).
9. Fujita, Y. *et al.* Priming of centromere for CENP-A recruitment by human hMis18α, hMis18β, and M18BP1. *Dev. Cell* **12,** 17–30 (2007).
10. Maddox, P. S., Hyndman, F., Monen, J., Oegema, K. & Desai, A. Functional genomics identifies a Myb domain-containing protein family required for assembly of CENP-A chromatin. *J. Cell Biol.* **176,** 757–763 (2007).
11. Black, B. E. *et al.* Structural determinants for generating centromeric chromatin. *Nature* **430,** 578–582 (2004).
12. Black, B. E. *et al.* Centromere identity maintained by nucleosomes assembled with histone H3 containing the CENP-A targeting domain. *Mol. Cell* **25,** 309–322 (2007).
13. Black, B. E., Brock, M. A., Bedard, S., Woods, V. L. Jr & Cleveland, D. W. An epigenetic mark generated by the incorporation of CENP-A into centromeric nucleosomes. *Proc. Natl Acad. Sci. USA* **104,** 5008–5013 (2007).
14. McClelland, S. E. *et al.* The CENP-A NAC/CAD kinetochore complex controls chromosome congression and spindle bipolarity. *EMBO J.* **26,** 5033–5047 (2007).
15. Cheeseman, I. M., Hori, T., Fukagawa, T. & Desai, A. KNL1 and the CENP-H/I/K complex coordinately direct kinetochore assembly in vertebrates. *Mol. Biol. Cell* (2007).
16. Hayashi, T. *et al.* Mis16 and Mis18 are required for CENP-A loading and histone deacetylation at centromeres. *Cell* **118,** 715–729 (2004).
17. Jansen, L. E., Black, B. E., Foltz, D. R. & Cleveland, D. W. Propagation of centromeric chromatin requires exit from mitosis. *J. Cell Biol.* **176,** 795–805 (2007).
18. Hori, T. *et al.* CCAN Makes Multiple contacts with centromeric *DNA* to provide distinct pathways to the outer kinetochore. *Cell* **135,** 1039–1052 (2008).
19. Liu, S. T., Rattner, J. B., Jablonski, S. A. & Yen, T. J. Mapping the assembly pathways that specify formation of the trilaminar kinetochore plates in human cells. *J. Cell Biol.* **175,** 41–53 (2006).
20. Goshima, G., Kiyomitsu, T., Yoda, K. & Yanagida, M. Human centromere chromatin protein hMis12, essential for equal segregation, is independent of CENP-A loading pathway. *J. Cell Biol.* **160,** 25–39 (2003).
21. Yang, C. H., Tomkiel, J., Saitoh, H., Johnson, D. H. & Earnshaw, W. C. Identification of overlapping *DNA*-binding and centromere-targeting domains in the human kinetochore protein CENP-C. *Mol. Cell Biol.* **16,** 3576–3586 (1996).
22. Trazzi, S. *et al. In vivo* functional dissection of human inner kinetochore protein CENP.-C. *J. Structural Biology* **140,** 39–48 (2002).

METHODS

cDNA isolation and expression. cDNAs encoding CENP-C, N, K, T, and I were amplified from HeLa cell mRNA with gene-specific oligonucleotides using the Super-Script III kit (Invitrogen) and cloned by blunt-end ligation into pCR4 Blunt-TOPO using the Zero-Blunt cloning kit (Invitrogen) according to the manufacturers instructions. cDNAs encoding CENP-B, CENP-H, CENP-L, CENP-M, CENP-O, CENP-P, CENP-Q, CENP-R, CENP-S, Mis18α, Mis18β and Mis18BP1/KNL2 were produced by gene synthesis (DNA 2.0, Palo Alto). All cDNAs were sequenced and subcloned into the AscI and PacI sites of a modified pCS2+-based plasmid for coupled transcription and translation in reticulocyte lysates (Promega). ^{34}S-methionine (Amersham) was added to specifically label each protein. The abundance of the centromere proteins was estimated using western blotting.

Histone expression. Histones H2A, H2B, H3 and H4 were expressed, purified and refolded as described previously[23], except that the soluble H3/H4 tetramer and H2A/H2B dimer, rather than the histone octamer, were assembled and frozen on liquid nitrogen. CENP-A was expressed as a soluble tetramer with histone H4 as described previously[11]. Briefly, BL21 bacterial cells (6 l), transformed with a bi-cistronic vector encoding human CENP-A and *Xenopus laevis* histone H4, were grown to optical density (OD) 600 = 0.2 at 37 °C. The culture was then switched to 23 °C and grown until reaching OD600 = 0.6, at which point IPTG (isopropyl-β-D-thiogalactoside) was added to 0.3 mM for 6 h to induce protein expression. The cells were spun down and frozen directly on liquid nitrogen. Cell pellet was resuspended in 100 ml of lysis buffer (10 mM KPO_4, 0.9 M NaCl and 10 mM β-mercaptoethanol — BME — and 1 mM phenylmethylsulphonyl fluoride — PMSF — at pH 6.8), sonicated and centrifuged at 100,000*g* to clarify the extract. The high-speed supernatant was added to a hydroxyapatite column, which was washed with five column volumes of lysis buffer and eluted with a 0.9 M to 3.5 M NaCl gradient in KPO_4 (10 mM at pH 6.8). Soluble CENP-A/H4 typically elutes in a broad peak between 1.5 and 3.5 M NaCl. Fractions containing CENP-A/H4 tetramers were pooled and dialysed two times against SP-loading buffer (10 mM Tris-HCl, 0.75 M NaCl, 10 mM BME and 0.5 mM EDTA at pH 7.4). The dialysate was loaded onto a 1 ml Hi-Trap SP column (Amershan) and eluted with a 0.75 to 2 M NaCl gradient in Tris-HCl (10 mM) and EDTA (0.5 mM at pH 7.4). Fractions containing CENP-A/H4 were pooled, concentrated and added to a Sephadex 200 gel-filtration column equilibrated with Tris-HCl (10 mM), NaCl (2 M) and EDTA (0.5 mM at pH 7.4). Peak fractions were pooled, concentrated and frozen down for nucleosome reconstitution. Approximately 5 mg of CENP-A/H4 tetramer can be expected from 6 l of cells.

Nucleosome reconstitution. DNA (186-bp) containing the centromere repeat or the 601 nucleosome-positioning sequence was generated by polymerase chain reaction (PCR). CENP-A/H4 tetramer, H2A/H2B dimer and DNA were mixed at a stoichiometry of 1.1:2.2:1 in high-salt buffer (10 mM Tris-HCl, 2 M NaCl and 0.5 mM EDTA at pH 7.4) and the salt concentration was slowly lowered to 2.5 mM NaCl over ~60 h by gradient dialysis. Mononucleosomes were then purified on a 5 ml 5-30% glycerol gradient as described previously[23]. Fractions containing pure mononucleosomes were concentrated and stored at 4 °C.

Gel shift assays. Centromere proteins were run out alone or in the presence of the indicated nucleosome on 5% acrylamide gels in 0.5× TBE for 70 min at 10 mA. Typical binding reactions were carried out for 30 min at room temperature and contained the indicated concentrations of nucleosome and 0.5–1 μl of *in vitro* transcription/translation (ivt) mix in Tris-HCl (10 mM) and glycerol (20%) at pH 7.4. Binding reactions were loaded directly on the gel. After electrophoresis, gels were first stained with ethidium bromide or SYBR-gold (Invitrogen) to visualize and/or quantify the nucleosomes, followed by staining with Coomassie blue to visualize proteins. Gels were then dried and the ^{35}S-methionine-labelled centromere proteins were visualized and quantified with a phosphorimager.

CENP-N mutagenesis and stable cell lines. Point mutants in CENP-N were generated with a site-directed mutagenesis kit (Stratagene) according to the manufacturer's instructions. Stable cell lines were created by co-transfecting HEK293 flp-in target cells (Invitrogen) with pOG44 and a modified version of pcDNA5/FRT engineered to express CENP-N with an N-terminal GFP-tag according to the manufacturer's instructions. For western blotting and co-immunoprecipitation experiments, nuclei were isolated from ~5×10^7 cells and chromatin was solubilized with micrococcal nuclease as described previously[5,8]. After micrococcal nuclease treatment, extracts were centrifuged at 16,000*g* for 10 min in a microfuge and the concentration of each supernatant was determined using Bradford reagent (Biorad). The supernatant (10 μg) was loaded on a 12.5% poly-acylamide gel to determine the levels of the centromere proteins present (Fig. 2c) and the remaining extract (~2 mg) was used in anti-GFP immunoprecipitations. For CENP-A immunofluorescence, cells were fixed with methanol at -20 °C for 2 min without previous extraction and processed using standard techniques. For staining CCAN proteins, HEK293 cells were pre-extracted with 0.1% Triton X-100 in PBS for 1 min and then fixed for 10 min in PBS + 4% formaldehyde and processed using standard techniques. Similar methods were used for staining CCAN proteins in HeLa cells except that cells were pre-extracted for 3 min in 0.3% Triton X-100 before fixation.

siRNA. *CENP-N* (5'-GUAAAUUUCCGACAGAGAAUU-3', 5'-CUACCUACGUGGUGUACUAUU-3', 5'-GAUAUUACCGAAAUGAAGAUU-3', 5'-CCAGAAAGUUUGGGAUGUUUU-3') and *CENP-A* (5'-AACACAGUCGGCGGAGACAAG-3') siRNAs (Dharmacon) were used according to the manufacturer's instructions. Buffer alone or *GAPDH* siRNA was used in control experiments. Cells were processed for immunofluorescence as described above. For western blots, cell extracts were prepared by resuspending cells (20 mM HEPES, 0.5 M NaCl, 1% Triton X-100, 1 mM dithiothreitol, 10 mM EDTA, 10 mM EGTA and 1 mM PMSF), followed by centrifugation for 10 min at 16,000 *g* in a microfuge. Protein concentration in each extract was determined using Bradford reagent (Biorad) and identical amounts of total protein were loaded in each well of the gel.

SNAP pulse labelling. HeLa cells stably expressing near endogenous levels of CENP-A-SNAP-3×HA[17] were treated with thymidine (2 mM) for 17 h to arrest cells in S phase. Following release in deoxycytidine (24 μM) for 3 h, cells were transfected with CENP-N and GAPDH siRNA pools (Dharmacon) according to the manufacturer's instructions. At 9 h after release from thymidine, fresh thymidine was added to synchronize cells at the next G1/S boundary. SNAP-tag was quenched with non-fluorescent BTP (Covalys) after which cells were released into S phase. Newly synthesized CENP-A-SNAP was labelled 7.5 h after release (in G2 phase) with TMR-Star (Covalys), cells were allowed to proceed through the cell cycle for CENP-A assembly and were collected at the next G1/S boundary by the addition of thymidine. Cells were fixed (without pre extraction) and processed for microscopy (see Supplementary Information, Fig. S5c for schematic).

Microscopy. Stacks of fixed cell immunofluorescence images encompassing the entire cell (or cells) were captured at 0.2 μm axial steps using a motorized stage mounted on an Olympus IX70 microsope. Immunofluorescent images were acquired using a ×60 1.4NA PlanApo objective and a CoolSnap-HQ CCD camera (Photometrics) on a DeltaVision Spectris system (Applied Precision). TMR-Star-labelled CENP-A-SNAP images were acquired using a ×100 1.4 NA UPlanSApo objective and a Cascade2 EMCCD camera (Photometrics). Centromere fluorescence intensity in each channel was quantified as described except that intensity measurements were performed on non-deconvolved maximal intensity projections of each *z*-series[24]. The images presented are maximum intensity projections of deconvolved images.

23. Luger, K., Rechsteiner, T. J. & Richmond, T. J. Preparation of nucleosome core particle from recombinant histones. *Methods Enzymol.* **304,** 3–19 (1999).
24. Hoffman, D. B., Pearson, C. G., Yen, T. J., Howell, B. J. & Salmon, E. D. Microtubule-dependent changes in assembly of microtubule motor proteins and mitotic spindle checkpoint proteins at PtK1 kinetochores. *Mol. Biol. Cell* **12,** 1995–2009 (2001).

nature cell biology

DOI: 10.1038/ncb1899

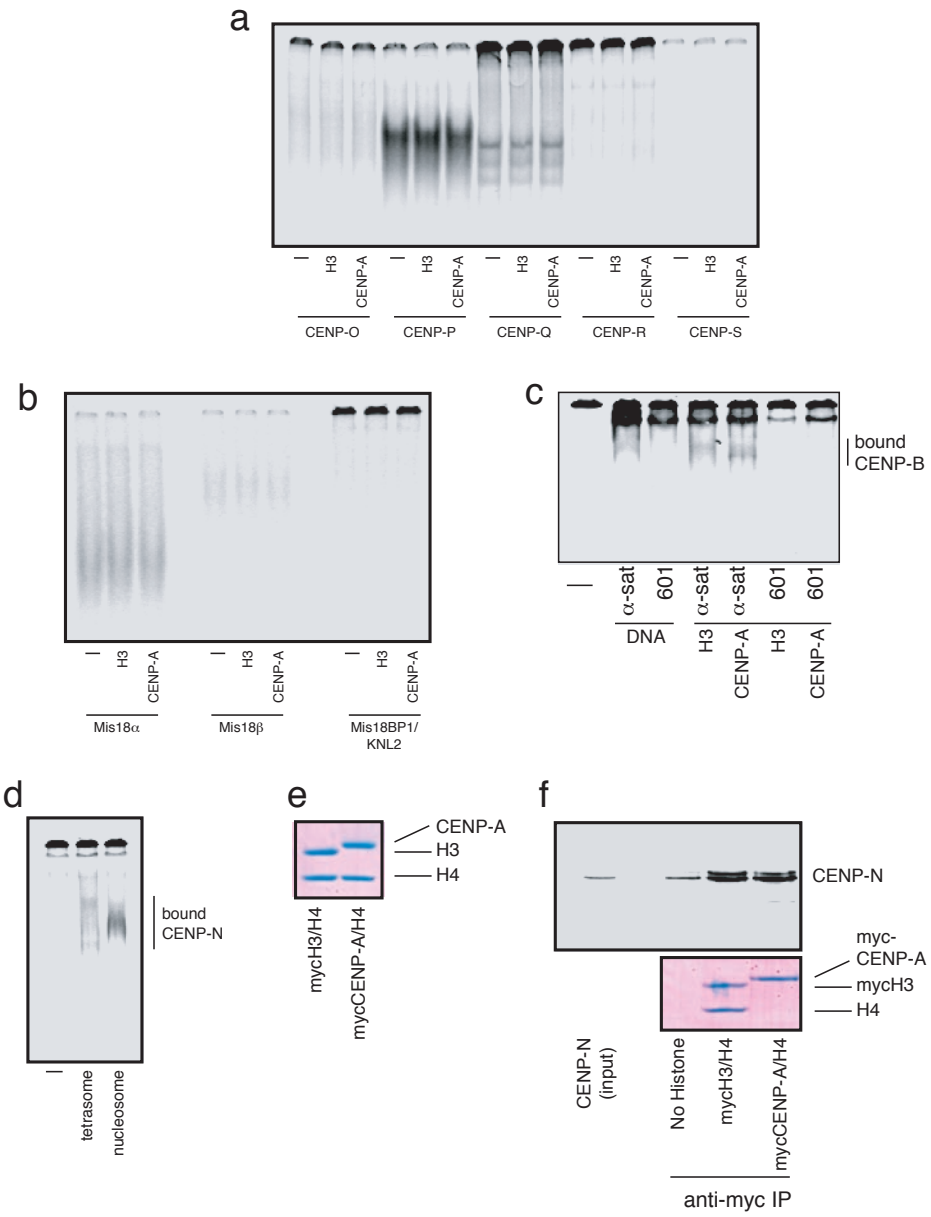

Figure S1 CENP-A nucleosome binding assay. (**a**,**b**) CENP-A or H3 nucleosomes or buffer alone (-) were incubated with the indicated centromere proteins and resolved on native gels as described in Figure 1c and 1d. (**c**) An experiment identical to that presented in Figure 2a was performed except that the nucleosome-binding requirement of CENP-B (1 nM) was determined. (**d**) An experiment identical to that in Figure 1a was performed with ^{35}S-labeled CENP-N (~10 nM) except that 100nM CENP-A/H4 tetrasomes (containing CENP-A/H4 and α-satellite DNA) or 100 nM CENP-A nucleosomes were used. The control reaction (-) contained buffer only. (**e**) Purified myc-CENP-A/H4 and myc-H3/H4 tetramers used in anti-myc immunoprecipitations were resolved on a 17.5% gel and stained with coomassie blue. (**f**) Anti-myc immunoprecipitation of purified myc-CENP-A/H4 and myc-H3/H4 tetramers with ^{35}S-labeled CENP-N. Input represents 10% of total CENP-N in each immunoprecipitation. The myc-CENP-A/H4 tetramer (bottom panel) dissociates at the low salt concentrations used in these experiments.

a

b

	% Identity to HsCENP-N	
	1-289	290-339
BtCENP-N	84	93
MmCENP-N	70	93
GgCENP-N	56	83
XlCENP-N	70	68

Figure S2 Alignment of CENP-N orthologs. (**a**) CENP-N orthologs from several vertebrate species were aligned using Clustal W. Residues identical to those in human CENP-N are shaded in grey. Residues that were mutated to alanine in human CENP-N are indicated (*). The residues deleted in the CENP-NΔC truncation mutant are outlined in blue. (**b**) Comparison of the percent identity between human CENP-N and other vertebrate CENP-N orthologs over amino acids 1-289 or 290-339 of human CENP-N.

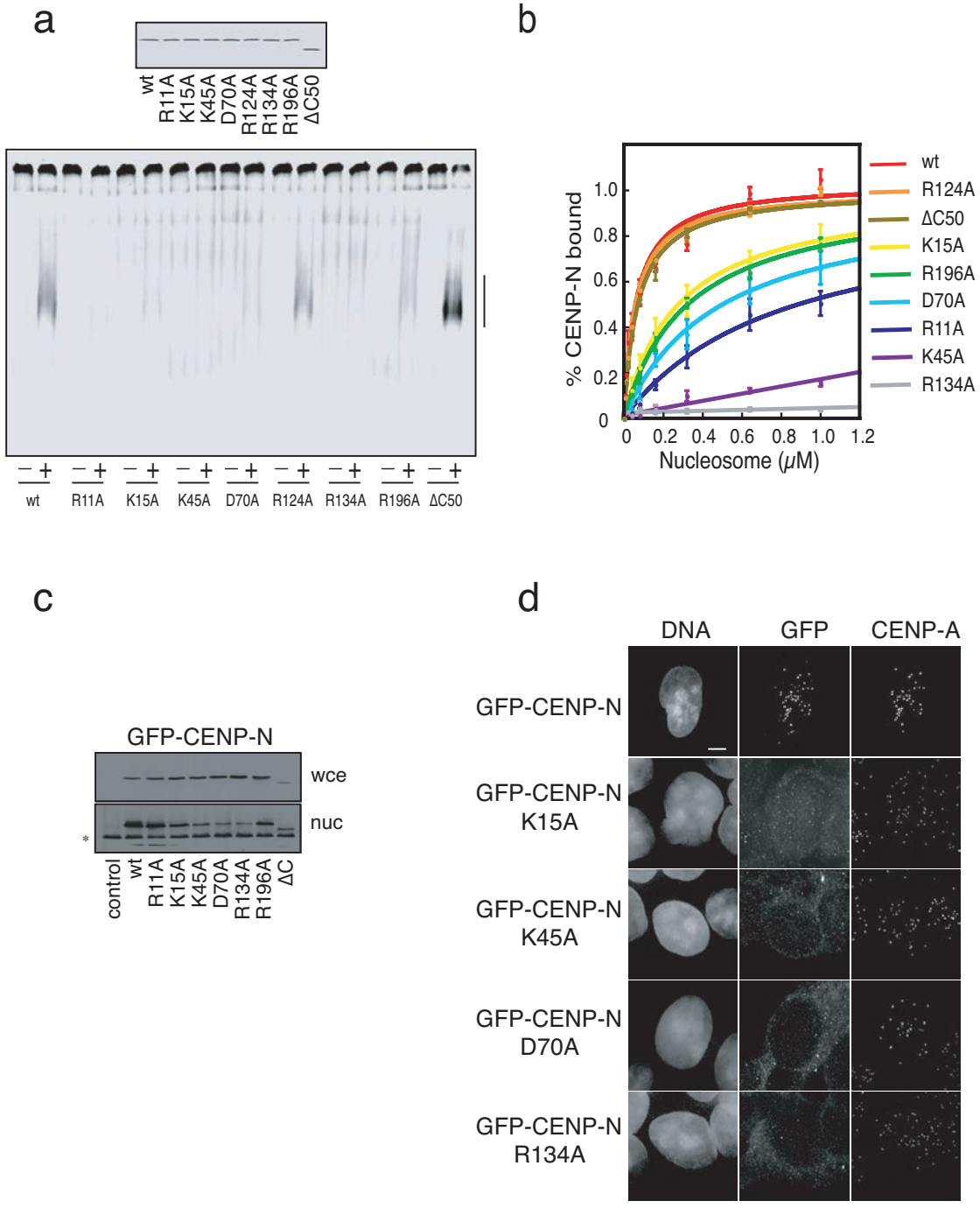

Figure S3 Initial characterization CENP-N point mutants. (**a**) CENP-N mutants exhibit a range of affinities for CENP-A nucleosomes. CENP-N (wt) or individual CENP-N mutants were expressed in reticulocyte extract and resolved by SDS-PAGE (top panel). Each mutant was assayed for its ability to bind CENP-A nucleosomes (bottom panel). Nucleosome gel shift assays included wildtype CENP-N and each CENP-N mutant alone (-) or in the presence of 300 nM CENP-A nucleosome (+). (**b**) Dose-response experiments for each CENP-N mutant were performed as in A (bottom panel) with increasing concentrations of CENP-A nucleosome added to each reaction (N=3, error bars represent SEM). Data for wildtype CENP-N, and the R11A, R196A and ΔC mutants is reproduced from Figure 2b for comparison. (**c**) Expression of CENP-N mutants in HEK293 cells. Whole-cell extracts (wce) or nuclear extracts (nuc) from stable HEK293 cell lines expressing GFP-CENP-N (wt) or the indicated GFP-CENP-N mutant were separated by SDS-PAGE and western blotted with anti-GFP antibodies. A nonspecific band (*) that migrates faster than GFP-CENP-N is present in the nuclear extracts. (**d**) Representative images of HEK293 stable cells expressing GFP-CENP-N or the indicated GFP-CENP-N mutant. The image of cells expressing GFP-CENP-N is reproduced from Figure 3a and is included for reference.

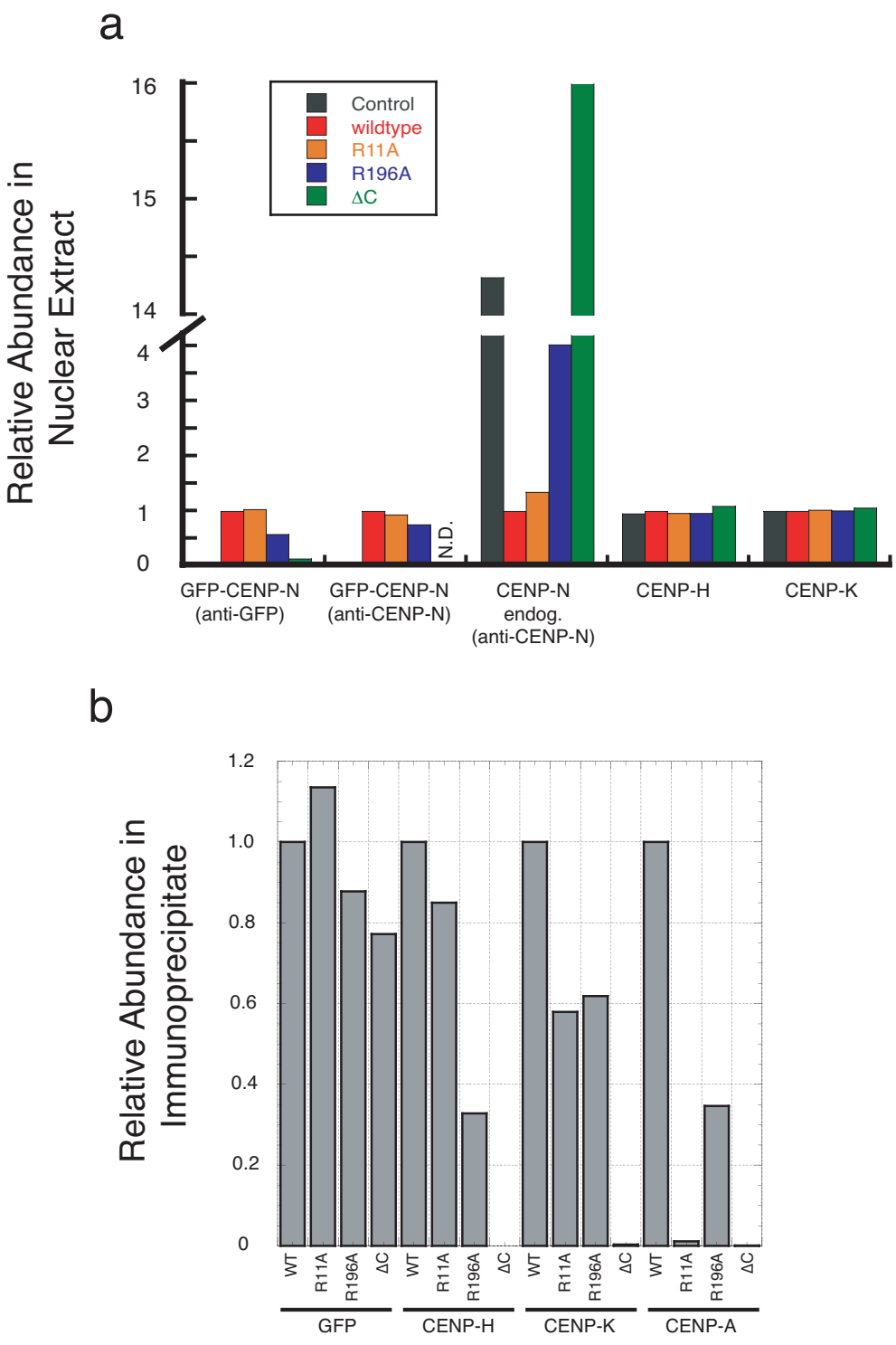

Figure S4 CENP-N mutants show changes in CENP-A nucleosome interaction and CCAN protein association. (**a**) Quantification of the levels GFP-CENP-N, endogenous CENP-N, CENP-H and CENP-K proteins from the western blots shown in Figure 2c. The amount of protein in each case is normalized to the amount of protein presiend in the GFP-CENP-N lane. (**b**) Quantification of GFP-CENP-N wildtype and mutant immunoprecipitations from western blot in Figure 2d. The amount of protein in each case is normalized to the amount present in the GFP-CENP-N wildtype immunoprecipitation.

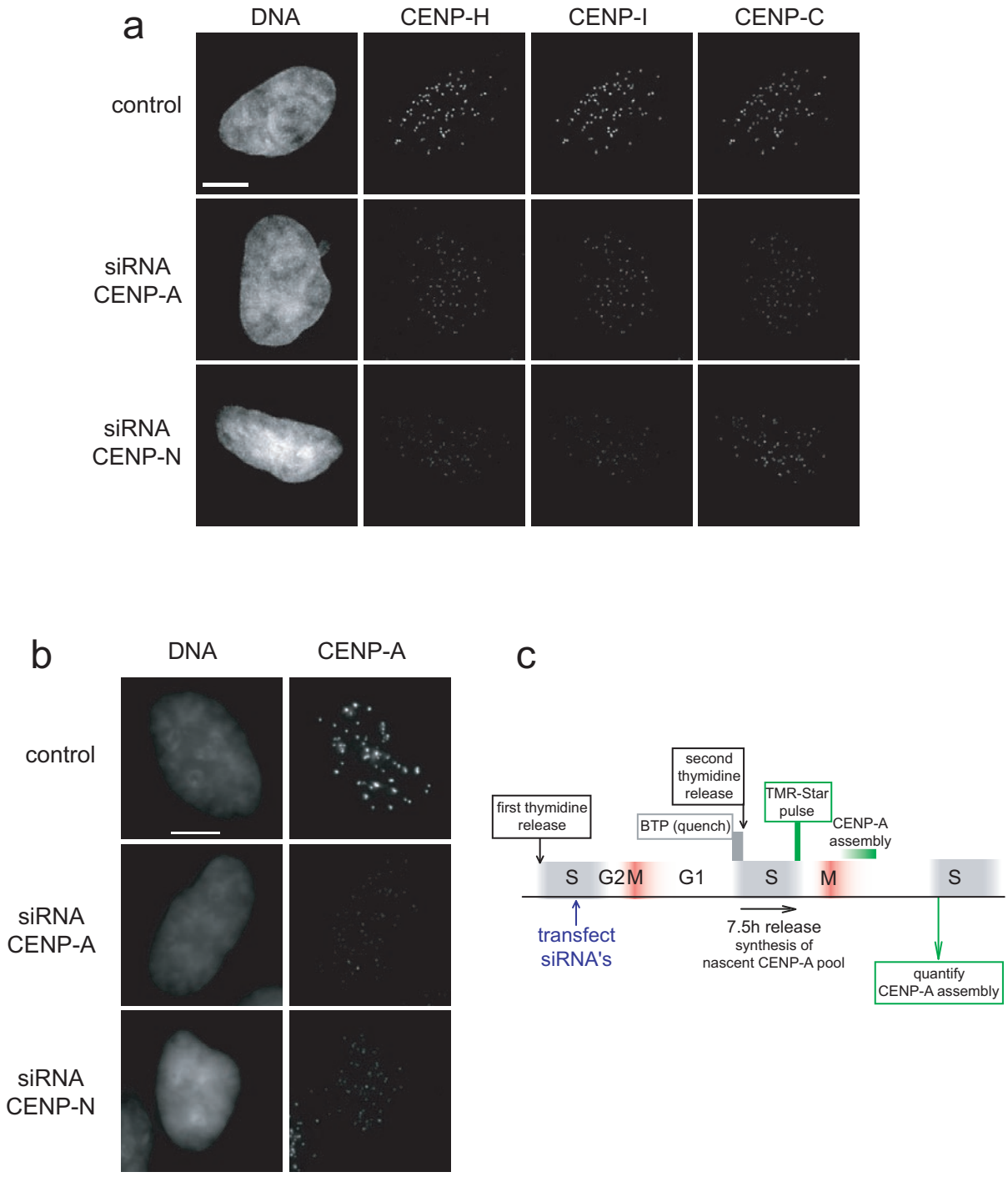

Figure S5 CENP-N is required for centromere assembly. (**a**,**b**) Representative images of control cells or cells depleted of CENP-A or CENP-N with siRNA stained with the indicated antibodies to visualize centromere proteins. Scale bar is 5 μm. (**c**) Experimental scheme for SNAP based CENP-A assembly assay depicting order of synchronization, transfection and SNAP labeling steps described in detail in Material and Methods.

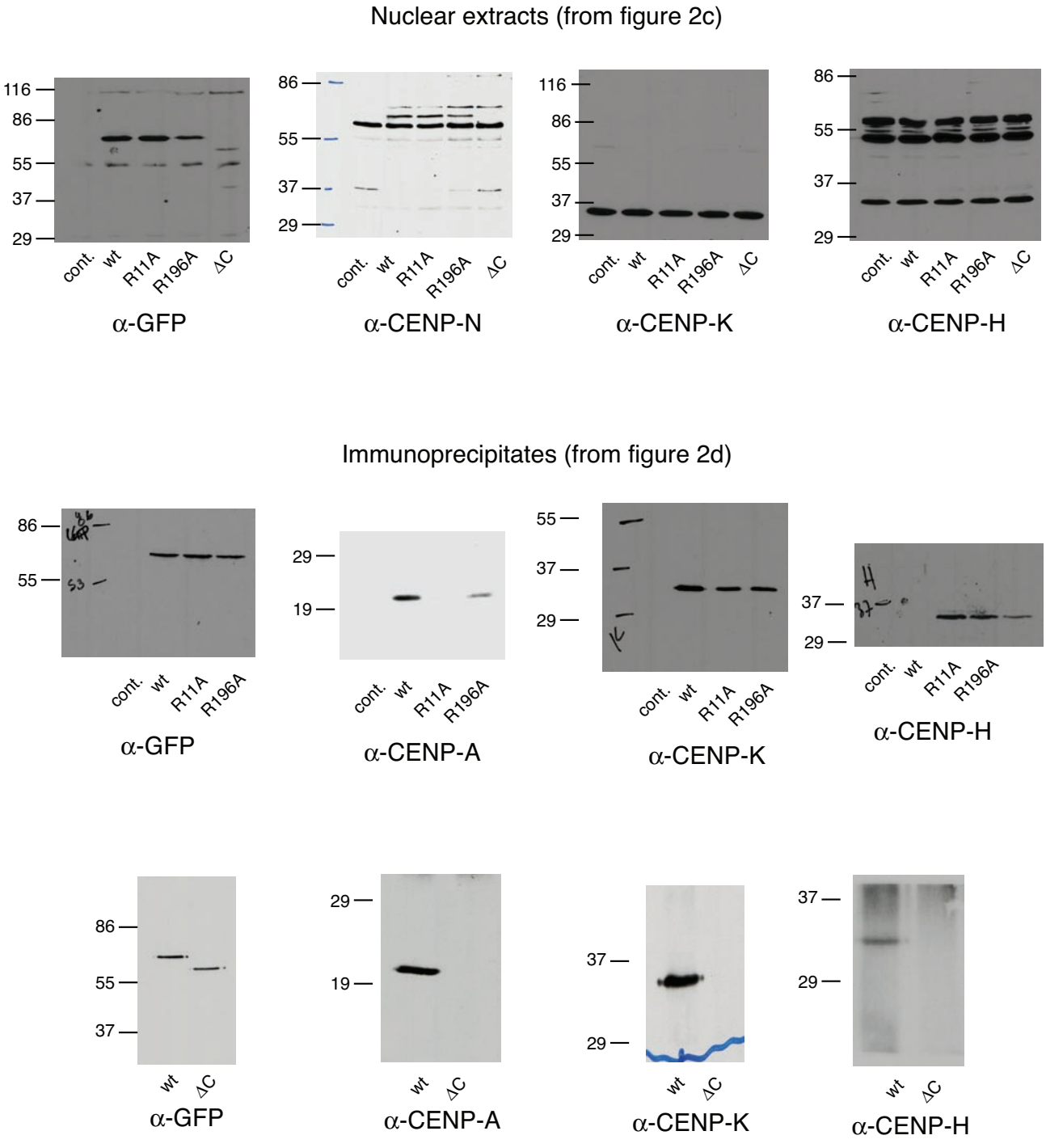

Figure S6 Full scans of western blot images.

CENP-N	K_d apparent (nM)
wt	169±70
R11A	962±259
K15A	297±77
K45A	ND
D70A	546±152
R124A	72±10
R134A	ND
R196A	331±36
ΔC	62±8

Table S1 The apparent dissociation constant of wild-type CENP-N and each CENP-N mutant for reconstituted CENP-A nucleosomes as determined by the dose-response experiments presented in Figure 2b and S5b. Affinites for R134A and K45A were too low to accurately determine a dissociation constant (ND).

nature cell biology

Essential role for eIF4GI overexpression in the pathogenesis of inflammatory breast cancer

Deborah Silvera[1], Rezina Arju[1], Farbod Darvishian[2], Paul H. Levine[3], Ladan Zolfaghari[3], Judith Goldberg[4], Tsivia Hochman[4], Silvia C. Formenti[5,6] and Robert J. Schneider[1,6]

Inflammatory breast cancer (IBC) is the most lethal form of primary breast cancer[1]. IBC lethality derives from generation of tumour emboli, which are non-adherent cell clusters that rapidly spread by a form of continuous invasion known as passive metastasis[2–5]. In most cancers, expression of E-cadherin, an epithelial marker, is indicative of low metastatic potential[6,7]. In IBC, E-cadherin is overexpressed[8] and supports formation of tumour emboli by promoting tumour cell interactions rather than adherence to stroma[2,3,9]. E-cadherin, a surface component of adherens junctions, is anchored by interaction with p120 catenin (p120). We show that the unique pathogenic properties of IBC result in part from overexpression of the translation initiation factor eIF4GI in most IBCs. eIF4GI reprograms the protein synthetic machinery for increased translation of mRNAs with internal ribosome entry sites (IRESs) that promote IBC tumour cell survival and formation of tumour emboli. Overexpression of eIF4GI promotes formation of IBC tumour emboli by enhancing translation of IRES-containing *p120* mRNAs. These findings provide a new understanding of translational control in the development of advanced breast cancer.

Although alterations in translational control have not been studied extensively in human malignancies[10], overexpression of the translation initiation factor eIF4E occurs in some human cancers[11–14]. eIF4E, eIF4A and eIF4GI, form a complex (eIF4F) that recruits ribosomes to the capped end of mRNA to initiate cap-dependent translation[15]. Cap-dependent mRNA translation is regulated by the eIF4E-sequestering protein 4E-BP1, which in turn is controlled by the kinase mTOR[15]. Overexpression of eIF4E preferentially increases translation of mRNAs containing stable 5′ secondary structures[10,16]. A small number of mRNAs continue to be translated during stresses when cap-dependent translation is impaired. These dual function mRNAs contain a cap as well as IRES elements that direct their translation in a cap-independent manner[17,18].

eIF4E, eIF4GI and 4E-BP1 levels were examined in 37 IBC tumour biopsies, 30 stage III (T3, ≥5cm) non-IBC tumours and 10 normal breast epithelium specimens (Fig. 1a; Supplementary Information, Table S1). eIF4GI was markedly overexpressed in nearly 80% of IBC specimens, compared with weak expression in normal breast epithelium ($P < 0.001$). A small number of IBC specimens overexpressed eIF4E, although with no statistical significance (~20%, $P = 0.174$), and even fewer overexpressed 4E-BP1 (~15%, $P = 0.089$), also without statistical significance. Analysis of the two additional eIF4G family members, eIF4GII and DAP5, showed that neither was overexpressed in IBC specimens or normal tissue (Supplementary Information, Table S1). Expression of eIF4GI, eIF4E and 4E-BP1 was different in stage III (T3) invasive ductal carcinomas, which overexpressed eIF4GI and 4E-BP1 in 69% and 87% of tumours, respectively (Supplementary Information, Table S2), as observed previously[17]. Logistic regression analysis demonstrated that of all translation factors examined, eIF4GI overexpression was the only significant predictor of IBC. Moreover, there was no association between eIF4GI overexpression in IBC and levels of eIF4E ($P = 0.30$) or 4E-BP1 ($P = 0.71$). E-cadherin was previously shown to be overexpressed in all of the IBC specimens examined here by more than 2-fold, with a mean of 4-fold, compared with normal breast epithelium[19].

The role of overexpressed eIF4GI in IBC was examined in the SUM149 cell line[20], which is well established as a model for IBC[21]. Compared with normal human mammary epithelial (HME) cells, SUM149 cells overexpressed eIF4GI and E-cadherin, whereas 4E-BP1, eIF4A and eIF4E levels were equivalent (Fig. 1b). In addition, a substantial amount of eIF4GI was free and unbound to eIF4E, because IBC cells have a high proportion of their 4E-BP1 protein in the hypophosphorylated (activated) state and bound to eIF4E, compared with a mammary epithelial cell line (MCF10A) that has similar levels of eIF4GI and total 4E-BP1 (Supplementary Information, Fig. S1). To study the role of high levels of eIF4GI in IBC, we silenced it with short hairpin RNAs (shRNAs) in SUM149 cells. Silencing reduced eIF4GI protein levels by at least 90%, compared with control cells (Fig. 1c), but only slightly decreased overall protein synthesis (15%, Fig. 1d), had no effect on cell viability, and only slightly impaired cell proliferation (data not shown). This is consistent with the previously reported small reduction in protein synthesis on eIF4GI depletion[18].

[1]Department of Microbiology and [2]Department of Pathology, New York University School of Medicine, New York, New York, 10016, USA. [3]George Washington University School of Public Health, Washington, District of Columbia, 20037, USA. [4]Department of Environmental Medicine, Division of Biostatistics, [5]Department of Radiation Oncology and [6]NYU Cancer Institute, New York University School of Medicine, New York, New York, 10016, USA.
Correspondence should be addressed to R.J.S. (e-mail: Robert.schneider@nyumc.org)

Received 5 February 2009; accepted 12 March 2009; published online 14 June 2009; DOI: 10.1038/ncb1900

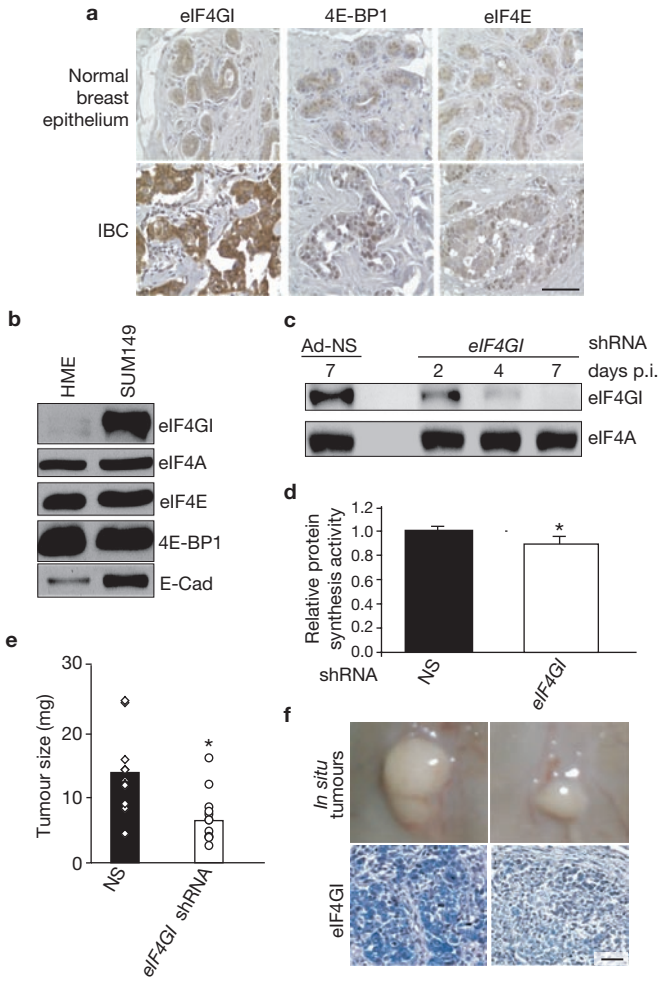

Figure 1 eIF4GI overexpression in IBC drives tumour growth. (**a**) Immunohistochemical staining of representative IBC tumour specimens ($n = 37$) and normal breast epithelium ($n = 10$) for eIF4GI, 4E-BP1 and eIF4E. eIF4GI shown corresponds to +2 intensity in Supplementary Information, Table S1. Scale bar 100 μm. (**b**) Immunoblot analysis of indicated proteins using equal protein amounts from whole-cell extracts of SUM149 (IBC) and normal control human mammary epithelium (HME). A representative blot is shown. (**c**) shRNA silencing of *eIF4GI* in SUM149 cells. SUM149 cells were infected three times over 7 days with non-silencing (NS) or *eIF4GI*-silencing (*eIF4GI*) Adenovirus (Ad) shRNA vectors. Equal amounts of protein lysates from cells 2, 4 and 7 days after final infection were probed with antibodies to eIF4GI and eIF4A (as a loading control). A representative blot of 5 independent experiments is shown. (**d**) Global protein synthesis in *eIF4GI*-silenced cells. SUM149 cells were labelled with ^{35}S-methionine and protein synthesis rates determined. Standard deviation was derived from the mean of four independent experiments. $^*P < 0.001$, paired *t*-test. (**e**) Tumour growth in nude mice is inhibited by *eIF4GI* silencing in SUM149 cells. Mice were injected subcutaneously in both flanks with 3×10^6 NS or *eIF4GI*-silenced cells. After 7 days, tumours were photographed, excised, weighed and fixed. $^*P < 0.001$, paired *t*-test. (**f**) Tumours grown in mice retain reduced levels of eIF4GI protein expression. Tumours excised from nude mice were fixed in formalin and embedded in paraffin before immunostaining. Scale bar, 40 μm.

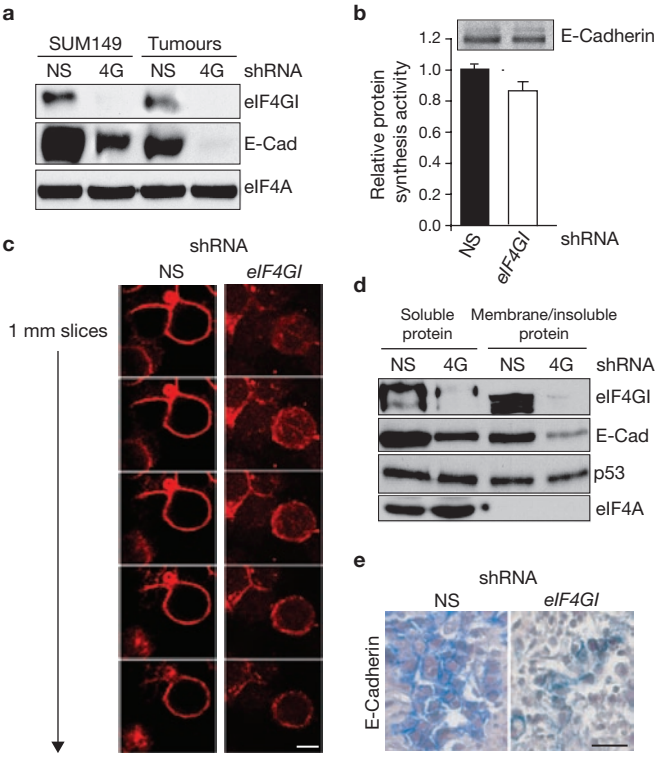

Figure 2 Silencing of *eIF4GI* in SUM149 cells is associated with internalization and destabilization of E-cadherin. (**a**) E-cadherin protein levels are reduced after silencing of *eIF4GI* in both SUM149 cells and tumours. Equal amounts of eIF4GI and NS SUM149 cell tumour and cell protein lysates were resolved by SDS–PAGE and proteins identified by immunoblot analysis with the indicated antibodies. (**b**) *De novo* translation of E-cadherin is not reduced after *eIF4GI* silencing in SUM149 cells. E-cadherin from ^{35}S-methionine metabolically labelled NS and *eIF4GI*-silenced SUM149 cells was immunoprecipitated, resolved by SDS–PAGE followed by autoradiography and quantified by densitometry. Data shown are mean ± s.d. of three independent experiments. (**c**) Internalization of E-cadherin in *eIF4GI*-silenced cells. NS and *eIF4GI*-silenced cells were immunolabeled with antibodies directed against E-cadherin (TRITC-conjugated antibodies, red). Shown are 1-μm *z*-stack slices through the central plane of cells. Scale bar, 10 μm. (**d**) Association of E-cadherin to the membrane fraction is reduced after *eIF4GI* silencing in SUM149 cells. Equal amounts of soluble and insoluble lysates from NS or *eIF4GI*-silenced cells were analysed by SDS–PAGE and immunoblotted with the indicated antibodies. (**e**) Reduction of E-cadherin levels in *eIF4GI*-silenced SUM149 tumours is associated with internalization and loss of the protein. *eIF4GI*-silenced or control tumours grown in mice were immunohistochemically labelled using an antibody against E-cadherin. Scale bar, 20 μm.

Despite the marginal requirement for elevated levels of eIF4GI in overall protein synthesis, eIF4GI might be required for IBC tumour growth. In the nude mouse xenograft model, tumours derived from *eIF4GI*-silenced SUM149 cells were less than half the size of those from control cells (Fig. 1e). TUNEL assay revealed no difference in the viability of tumour cells after *eIF4GI* silencing (data not shown). Silencing of *eIF4GI* was retained by tumours during growth in nude mice (Fig. 1f) without reduction in expression of control eIF4A (data not shown). Similar data were obtained for tumours grown in the chick chorioallantoic membrane (CAM; Supplementary Information, Fig. S2). Thus, silencing of *eIF4GI* impairs IBC tumour growth independently of a significant reduction in overall protein synthesis.

We investigated whether there is a link between the poor growth of *eIF4GI*-silenced IBC tumours and E-cadherin expression. E-cadherin protein levels were modestly reduced in cell lines and strongly reduced in SUM149 tumours with *eIF4GI* silencing (Fig. 2a). There was no corresponding change in *E-cadherin* mRNA levels, but E-cadherin protein was destabilized (Supplementary Information, Fig. S3a, b).

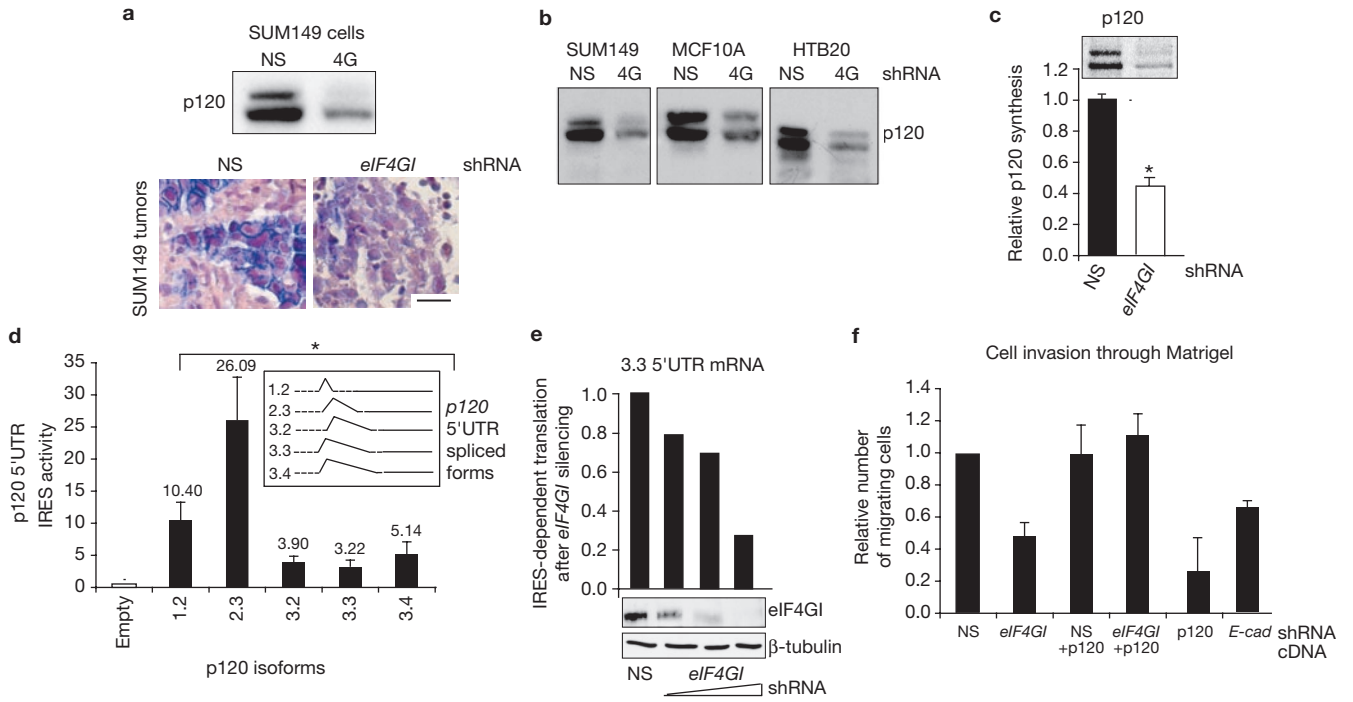

Figure 3 Internalization and destabilization of E-cadherin after *eIF4GI* silencing results from specific reduction in the translation of *p120* mRNA. (**a**) p120 protein levels are reduced after silencing of *eIF4GI* in SUM149 cells and tumours. Equal amounts of eIF4GI and NS whole cell lysates were examined by SDS–PAGE and immunoblotting with the p120 antibody (top panel). Tumours were stained with p120 antibody by immunohistochemistry (bottom panel). Representative fields are shown. Scale bar, 20 μm. (**b**) Levels of p120 protein are reduced in *eIF4GI*-silenced mammary cell lines. Immunoblot analysis of equal amounts of protein from SUM149, MCF10A (immortalized human mammary epithelial cells) and HTB20 (human highly transformed mammary carcinoma) cell lines after *eIF4GI* silencing. (**c**) Translation rates of p120 are reduced after *eIF4GI* silencing in SUM149 cells. Newly synthesized p120 protein was immunoprecipitated from equal amounts of extracts from NS and *eIF4GI*-silenced SUM149 cells metabolically labelled for 2 h with ^{35}S-methionine, resolved by SDS–PAGE and autoradiographed. Levels of newly synthesized p120 protein were quantified by densitometry. Data shown are mean ± s.d of three independent experiments. $*P < 0.01$, paired *t*-test. (**d**) *p120* 5′UTRs (insert) direct internal initiation of translation. SUM149 cells were transfected with bicistronic reporters containing a cap-dependent Renilla luciferase followed by a firefly luciferase driven by the indicated *p120* 5′UTRs[24]. Results are shown as *p120* 5′UTR-dependent firefly translation divided by Renilla translation, normalized to the empty vector, and are the mean ± s.d. of five independent experiments. $*P < 0.05$; paired *t*-test. (**e**) Strong concentration-dependence of eIF4GI for p120 IRES-mediated translation. NS and *eIF4GI*-silenced cells expressing the 3.3 5′UTR *p120* bicistronic mRNA reporter described above. $*P < 0.01$, paired *t*-test. Results are firefly luciferase activity divided by the Renilla luciferase activity normalized to the same values for the NS control. (**f**) Overexpression of eIF4GI promotes IBC cell invasion through increased *p120* mRNA translation. Migration of indicated cells through Matrigel was quantified by counting ten separate fields per filter. Results are normalized to the number of control, non-silenced SUM149 cells and are the mean ± s.d. of three independent experiments.

Furthermore, there was no decrease in *E-cadherin* mRNA translation rates in *eIF4GI*-silenced cells, beyond that of the slight reduction in overall protein synthesis (Fig. 2b). *eIF4GI* silencing caused a marked reduction in E-cadherin associated with the cell surface, accompanied by relocalization of E-cadherin to the cytoplasm, as shown by serial optical sections of control and silenced cells (Fig. 2c). This was confirmed by biochemical fractionation (Fig. 2d), as E-cadherin levels associated with the insoluble protein fraction were sharply reduced. Examination of tumours by immunohistochemistry further confirmed the reduction of E-cadherin protein levels with *eIF4GI* silencing in tumours, where its absence at adherens junctions was apparent (Fig. 2e).

The association of E-cadherin with the cell membrane blocks its degradation, and is mediated by E-cadherin interaction with p120 (refs 22, 23). Levels of p120 protein were significantly reduced in SUM149 cells and tumours after *eIF4GI* silencing, with loss of staining at adherens junctions (Fig. 3a), as well as in other mammary epithelial cell lines (Fig. 3b). *p120* mRNA levels (Supplementary Information, Fig. S3a) and stability of p120 protein were not significantly affected by *eIF4GI* silencing (data not shown). However, translation of the *p120* mRNA in *eIF4GI*-silenced IBC cells was reduced by about 60% (Fig. 3c).

The *p120* gene encodes alternatively spliced mRNAs that generate the four major protein isoforms[24]. These mRNAs contain 5′ untranslated regions (5′UTRs) of varying lengths, from 263 to 590 nucleotides. The major isoforms of *p120* 5′UTRs expressed in SUM149 cells were not altered as a result of *eIF4GI* silencing (Supplementary Information, Fig. S4a). We therefore tested whether the *p120* 5′UTRs contain IRES elements that might require high levels of eIF4GI for efficient translation. The 5′UTRs of the five major forms of *p120* mRNAs in IBC cells were cloned and inserted into bicistronic mRNA expression vectors[17]. All *p120* 5′UTRs enabled translation of the second cistron (Fig. 3d) and maintained full-length intact mRNAs (Supplementary Information, Fig. S4b), indicating IRES activity. The *p120* 5′UTRs showed a remarkably strong concentration-dependence of eIF4GI for translation (Fig. 3e). Thus, the *p120* 5′UTRs contain a strongly active, highly eIF4GI-dependent IRES element that drives efficient *p120* mRNA translation in IBC cells. Other IRES-containing mRNAs, such as pro-angiogenic, survival vascular

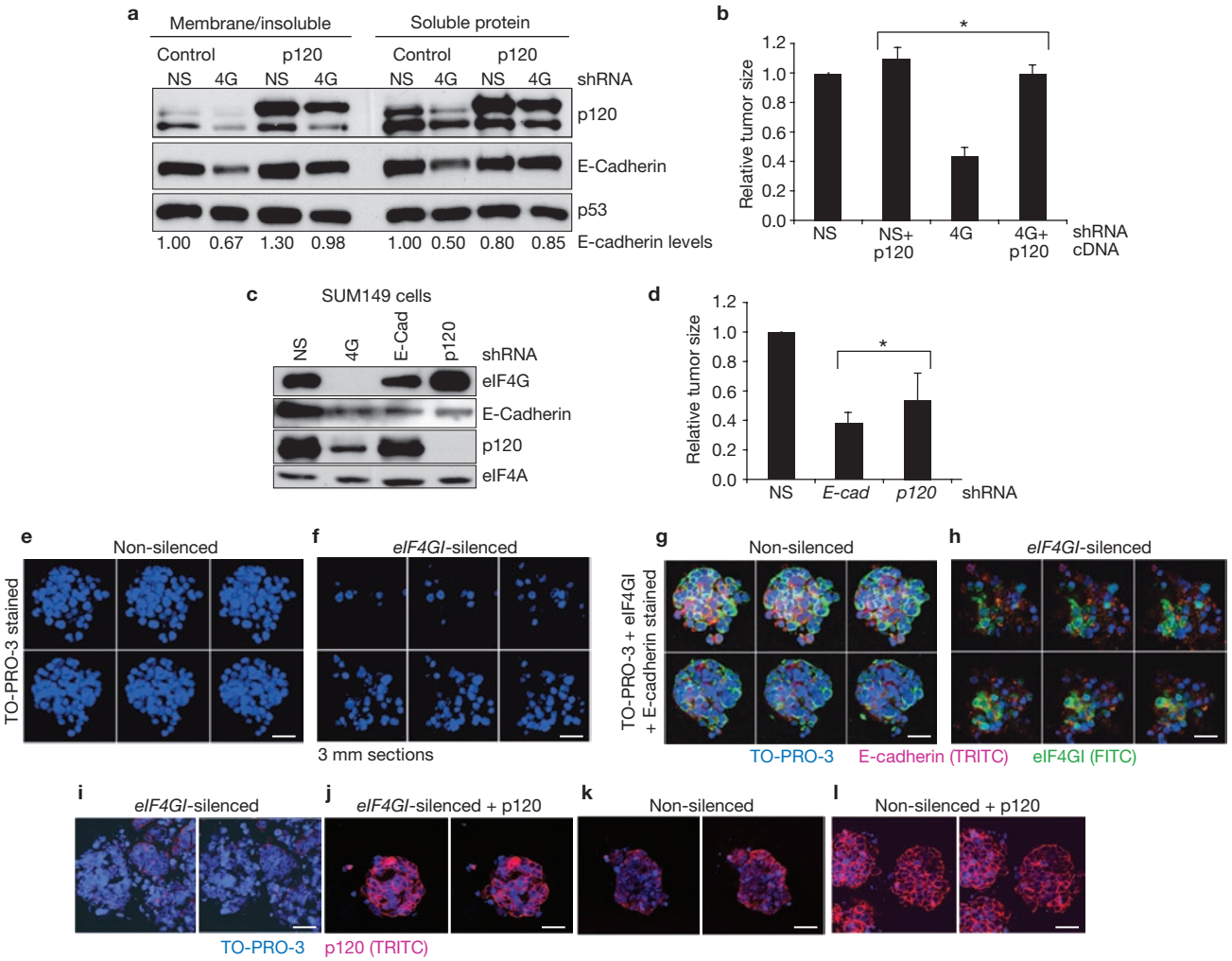

Figure 4 Role of eIF4GI overexpression in tumour growth and tumour cell emboli formation. (**a**) Overexpression of p120 stabilizes E-cadherin expression and localization to the cell surface in *eIF4GI*-silenced cells. NS and eIF4GI cells were co-infected with p120 or GFP adenoviruses, insoluble and soluble fractions were detected with indicated antibodies. E-cadherin levels were quantified by densitometry analysis and normalized to levels of the NS control for each fraction. Numbers indicate the relative levels of E-cadherin in each lane. Typical results of three independent experiments are shown. (**b**) Overexpression of p120 in *eIF4GI*-silenced SUM149 cells increases tumour growth in nude mice. SUM149 cells subjected to NS or *eIF4GI* silencing were co-infected with an adenovirus vector expressing either p120 or GFP, followed by implantation into opposite flanks of nude mice. Tumours were grown for 7 days, excised and weighed. Results are the mean ± s.d. of three independent experiments, normalized to the growth of non-silenced tumours in the absence of p120 overexpression. $*P < 0.01$, paired *t*-test. (**c**) Immunoblot of whole-cell lysates from cells infected with the indicated adenovirus vectors and detected with the indicated antibodies. (**d**) Silencing of *p120* or *E-cadherin* in SUM149 cells decreases tumour growth. SUM149 cells silenced with the indicated shRNAs were implanted into opposite flanks of nude mice. Tumours were excised 7 days after implantation and weighed. Results are the mean ± s.d. of three independent experiments and are normalized to the NS control. (**e**–**l**) Emboli formation requires increased *p120* mRNA translation promoted by eIF4GI overexpression. (**e**–**h**) SUM149 cells silenced with Ad NS or eIF4GI shRNAs were grown on Matrigel, fixed, and immunostained with indicated antibodies (eIF4GI, FITC; E-cadherin, TRITC). Nuclei were stained with TO-PRO-3 (blue). Resulting structures were examined by confocal microscopy. A series of 3-μm *z*-stack images representative of typical results are shown. SUM149 cells expressing NS or *eIF4GI* shRNAs stained with TO-PRO-3 (**e**, **f**), or with TO-PRO-3, eIF4GI (FITC) and E-cadherin (TRITC) (**g**, **h**); for (**i**–**l**), control and *eIF4GI*-silenced cells were infected with a p120 expression adenovirus vector (**i**, **k**) or a vector expressing GFP (**j**, **l**), and stained as indicated. Scale bars, 40 μm.

endothelial growth factor (VEGF-A) also showed eIF4GI dependence for translation in IBC cells without alteration of mRNA levels (Supplementary Information, Fig. S5a, b). Indeed, *eIF4GI* silencing resulted in a 2.5-fold reduction in VEGF-A-mediated neo-vascularization over a period of only three days when tested in the chick CAM assay (Supplementary Information, Fig. S5c).

A hallmark of IBC tumour cells is efficient invasion, which promotes the lymphodermal infiltration of tumour cell emboli. Wild-type IBC SUM149 cells showed strong invasion through a semi-permeable membrane in Matrigel (Fig. 3f). Invasion was diminished 2-fold by *eIF4GI* silencing, 3-fold by *p120* silencing and less so by *E-cadherin* silencing because of an inability to reduce its expression as fully. Overexpression of p120 in wild-type cells had no effect, but in *eIF4GI*-silenced cells invasiveness was fully restored to the levels of control, non-silenced cells (Fig. 3f). Thus, promotion of IRES-dependent *p120* mRNA translation by eIF4GI overexpression promotes IBC cell invasion. To investigate whether reduced IBC tumour growth results in large part from reduced E-cadherin protein levels resulting from the decrease in *p120* mRNA translation in *eIF4GI*-silenced SUM149 cells, we performed a series of overexpression and silencing experiments and assessed their effects on

IBC tumour growth. First, p120 was overexpressed in conjunction with *eIF4GI* silencing. E-cadherin cell surface membrane localization was almost fully restored and its cytoplasmic degradation blocked by p120 overexpression (Fig. 4a). Overexpression of p120 in *eIF4GI*-silenced IBC tumours was sufficient to restore normal tumour growth, but had little effect on the growth of tumours that already overexpress eIF4GI (Fig. 4b). Silencing of *E-cadherin* or *p120* (Fig. 4c) significantly reduced tumour growth in nude mice (Fig. 4d), in a manner similar to that of *eIF4GI* silencing (Figs 1e, 4b). Silencing of *eIF4GI*, *p120* or *E-cadherin* had no effect on SUM149 cell proliferation rates in culture (data not shown). Thus, overexpression of eIF4GI in IBC tumour cells is important for maintaining high levels and cell surface retention of E-cadherin through selective upregulation of p120 IRES-mediated mRNA translation, whereas p120 depletion phenocopies eIF4GI-dependence in IBC tumour growth.

Given the key importance of E-cadherin in the formation of tumour cell emboli, we asked whether silencing of *eIF4GI* impairs emboli formation in an *in vitro* 3-dimensional culture system[25]. Control SUM149 cells gave rise to tightly packed non-adherent spheroid clusters of 50–100 cells that mirrored IBC tumour emboli with tight E-cadherin staining at the adherens junctions (Fig. 4e, g). By contrast, silencing of *eIF4GI* prevented formation of emboli, resulting in diffuse cells with no defined architecture and little evidence for development of adherens junctions (Fig. 4f, h). There was no evidence for decreased cell viability or a significantly decreased proliferation rate of emboli cells after *eIF4GI* silencing (data not shown). Expression of p120 in *eIF4GI*-silenced IBC cells fully restored the ability to generate tumour cell emboli with adherens junctions staining (Fig. 4i–l). These data demonstrate that overexpression of eIF4GI is essential for formation and maintenance of IBC tumour cell emboli by promoting IRES-dependent translation of *p120* mRNA.

Our results provide an important new understanding of the importance of translational control in IBC, the most lethal form of primary breast cancer. We provide a mechanistic understanding for overexpression of eIF4GI in IBC, demonstrating that it promotes IRES and eIF4GI-dependent translation, which is partly responsible for the unusual pathological properties of IBC (overexpression of E-cadherin, strong homotypic IBC cell interaction, formation of tumour emboli and pronounced IBC cell invasion). High levels of eIF4GI and selectively increased mRNA translation therefore drive formation of IBC tumour cell emboli, which promote invasion (passive metastasis). Surprisingly, silencing of eIF4GI only marginally downregulated overall protein synthesis, consistent with previous results[18], but strongly impaired IRES-dependent mRNA translation of p120, thereby blocking formation of tumour cell emboli. It is interesting to note that locally advanced breast cancers (LABC) overexpress eIF4GI and the cap-dependent mRNA translation inhibitor 4E-BP1, comprising a hypoxia-activated translation switch to cap-independent translation, promoting substantial tumour angiogenesis and large tumour size[17]. IBC differs from LABC in that it more strongly overexpresses only eIF4GI in the absence of changes in 4E-BP1 levels.

The *eIF4GI* gene is amplified in 30% of human squamous cell lung carcinomas[26,27]; however, the function of overexpressed eIF4GI in these studies is unknown. Overexpression of eIF4GI in IBC probably acts in concert with several identified genetic alterations to generate the unusual disease phenotype of IBC, particularly overexpression of VEGF-A and the small GTPase RhoC, which increase malignancy and angiogenesis[28,29], and loss of tumour suppressor WISP3[30]. □

METHODS

Methods and any associated references are available in the online version of the paper at http://www.nature.com/naturecellbiology/

Note: Supplementary Information is available on the Nature Cell Biology website.

ACKNOWLEDGMENTS

We thank I. Mohr and members of the Schneider lab for their comments on the manuscript. This study was supported by the US Department of Defence Breast Cancer Center of Excellence Research Program (W81XWH-06-1-0629), the Breast Cancer Research Foundation (15-C6000-33141; R.J.S. and S.C.F.), Shifrin and Myers, the NY State Breast Cancer Research Fund (D.S.) and the Breast Cancer Discovery Fund.

AUTHOR CONTRIBUTIONS

D.S., S.C.F. and R.J.S designed and organized the experiments and wrote the manuscript. D.S. performed most of the studies; R.A. and F.D performed the immunohistochemistry studies; J.G. and T.H. performed the statistical analysis; P.L. and L.Z obtained, verified and prepared the tissue for analysis.

COMPETING INTERESTS

The authors declare that they have no competing financial interest.

Published online at http://www.nature.com/naturecellbiology/
Reprints and permissions information is available online at http://npg.nature.com/reprintsandpermissions/

1. Gong, Y. Pathologic aspects of inflammatory breast cancer: part 2. Biologic insights into its aggressive phenotype. *Semin. Oncol.* **35,** 33–40 (2008).
2. Alpaugh, M. L., Tomlinson, J. S., Kasraeian, S. & Barsky, S. H. Cooperative role of E-cadherin and sialyl-Lewis X/A-deficient MUC1 in the passive dissemination of tumor emboli in inflammatory breast carcinoma. *Oncogene* **21,** 3631–3643 (2002).
3. Colpaert, C. G. *et al.* Inflammatory breast cancer shows angiogenesis with high endothelial proliferation rate and strong E-cadherin expression. *Br. J. Cancer* **88,** 718–725 (2003).
4. Liotta, L. A., Saidel, M. G. & Kleinerman, J. The significance of hematogenous tumor cell clumps in the metastatic process. *Cancer Res.* **36,** 889–894 (1976).
5. Moore, D. H., Rouse, M. B., Massenburg, G. S. & Zeman, E. M. Description of a spheroid model for the study of radiation and chemotherapy effects on hypoxic tumor cell populations. *Gynecol. Oncol.* **47,** 44–47 (1992).
6. Parker, C. *et al.* E-cadherin as a prognostic indicator in primary breast cancer. *Br. J. Cancer* **85,** 1958–1963 (2001).
7. Wheelock, M. J., Soler, A. P. & Knudsen, K. A. Cadherin junctions in mammary tumors. *J. Mammary Gland Biol. Neoplasia* **6,** 275–285 (2001).
8. Kleer, C. G., van Golen, K. L., Braun, T. & Merajver, S. D. Persistent E-cadherin expression in inflammatory breast cancer. *Mod. Pathol.* **14,** 458–464 (2001).
9. Tomlinson, J. S., Alpaugh, M. L. & Barsky, S. H. An intact overexpressed E-cadherin/α, β-catenin axis characterizes the lymphovascular emboli of inflammatory breast carcinoma. *Cancer Res.* **61,** 5231–5241 (2001).
10. Schneider, R. J. & Sonenberg, N. Translational Control in Cancer Development and Progression in *Translational Control in Biology and Medicine*, (eds. Mathews, M. B., Sonenberg, N. & J. W. B. Hershey) 401–432 (Cold Spring Harbor Laboratory Press, Cold Spring Harbor, 2007).
11. Miyagi, Y. *et al.* Elevated levels of eukaryotic translation initiation factor eIF-4E, mRNA in a broad spectrum of transformed cell lines. *Cancer Lett.* **91,** 247–252 (1995).
12. Rosenwald, I. B. *et al.* Upregulation of protein synthesis initiation factor eIF-4E is an early event during colon carcinogenesis. *Oncogene* **18,** 2507–2517 (1999).
13. Rosenwald, I. B., Hutzler, M. J., Wang, S., Savas, L. & Fraire, A. E. Expression of eukaryotic translation initiation factors 4E and 2α is increased frequently in bronchioloalveolar but not in squamous cell carcinomas of the lung. *Cancer* **92,** 2164–2171 (2001).
14. McClusky, D. R. *et al.* A prospective trial on initiation factor 4E (eIF4E) overexpression and cancer recurrence in node-positive breast cancer. *Ann. Surg.* **242,** 584–590 (2005).
15. Gingras, A. C., Raught, B. & Sonenberg, N. mTOR signaling to translation. *Curr. Top. Microbiol. Immunol.* **279,** 169–197 (2004).
16. Gingras, A. C., Raught, B. & Sonenberg, N. Regulation of translation initiation by FRAP/mTOR. *Genes Dev.* **15,** 807–826 (2001).
17. Braunstein, S. *et al.* A hypoxia-controlled cap-dependent to cap-independent translation switch in breast cancer. *Mol. Cell* **28,** 501–512 (2007).
18. Ramírez-Valle, F. *et al.* eIF4GI links nutrient sensing to cell proliferation and inhibition of autophagy by selective mRNA translation. *J. Cell Biol.* **181,** 293–307 (2008).
19. Portera, C. C. *et al.* Evaluation of E-cadherin expression and lymphatic. involvement in inflammatory breast cancer. *Breast Cancer Res. Treatment* **100,** S177 (2006).
20. Ignatoski, K. M., Lapointe, A. J., Radany, E. H. & Ethier, S. P. erbB-2 overexpression in human mammary epithelial cells confers growth factor independence. *Endocrinology* **140,** 3615–3622 (1999).
21. Lerebours, F., Bieche, I. & Lidereau, R. Update on inflammatory breast cancer. *Breast Cancer Res.* **7,** 52–58 (2005).

22. Bryant, D. M. & Stow, J. L. The ins and outs of E-cadherin trafficking. *Trends Cell Biol.* **14,** 427–434 (2004).
23. Xiao, K., Oas, R. G., Chiasson, C. M. & Kowalczyk, A. P. Role of p120-catenin in cadherin trafficking. *Biochim. Biophys. Acta* **1773,** 8–16 (2007).
24. Keirsebilck, A. *et al.* Molecular cloning of the human p120ctn catenin gene (CTNND1): expression of multiple alternatively spliced isoforms. *Genomics* **50,** 129–146 (1998).
25. Lee, G. Y., Kenny, P. A., Lee, E. H. & Bissell, M. J. Three-dimensional culture models of normal and malignant breast epithelial cells. *Nature Methods* **4,** 359–365 (2007).
26. Bauer, C. *et al.* Overexpression of the eukaryotic translation initiation factor 4G (eIF4G-1) in squamous cell lung carcinoma. *Int. J. Cancer* **98,** 181–185 (2002).
27. Comtesse, N. *et al.* Frequent overexpression of the genes FXR1, CLAPM1 and EIF4G located on amplicon 3q26–27 in squamous cell carcinoma of the lung. *Int. J. Cancer* **120,** 2538–2544 (2007).
28. van Golen, K. L., Wu, Z. F., Qiao, X. T., Bao, L. & Merajver, S. D. RhoC GTPase overexpression modulates induction of angiogenic factors in breast cells. *Neoplasia* **2,** 418–425 (2000).
29. van Golen, K. L., Wu, Z. F., Qiao, X. T., Bao, L. W. & Merajver, S. D. RhoC GTPase, a novel transforming oncogene for human mammary epithelial cells that partially recapitulates the inflammatory breast cancer phenotype. *Cancer Res.* **60,** 5832–5838 (2000).
30. van Golen, K. L. *et al.* A novel putative low-affinity insulin-like growth factor-binding protein, LIBC (lost in inflammatory breast cancer), and RhoC GTPase correlate with the inflammatory breast cancer phenotype. *Clin. Cancer Res.* **5,** 2511–2519 (1999).

METHODS

Cells. MCF10A cells were obtained from the American Type Culture Collection and grown in the recommended medium. 293 cells were maintained in DMEM medium supplemented with 10% FBS and 25 μg ml^{-1} gentamicin. SUM149 and HME cell lines were provided by Stephen Ethier (Karmanos Cancer Institute, Wayne State University, MI, USA) and grown in Ham's F12 medium supplemented with 5% FBS, 1 mg ml^{-1} hydrocortisone, 5 μg ml^{-1} gentamycin and 5 μg ml^{-1} insulin. For SUM149 and HME cells, medium also contained 10 μg ml^{-1} EGF and for HME cells only, 100 μg ml^{-1} cholera toxin.

Immunofluorescence studies. Cells grown in multi-well teflon-coated glass slides (Polysciences) were washed twice with PBS, then fixed with 4% paraformaldehyde in PBS. Cells were permeabilized by incubation in 0.25% Triton-X in PBS, blocked in 3% BSA and incubated with the indicated primary antibodies overnight at 4°C, washed 3 times in PBS and incubated for 1 h with FITC or Texas Red-conjugated secondary antibodies (Jackson ImmunoResearch). Cells were mounted using Vectashield mounting medium with DAPI (Vector Laboratories). Image acquisition was performed by confocal microscopy using a Zeiss Axiophot microscope.

Tumour growth in nude mice. For mouse xenograft experiments, 3×10^6 cells were injected subcutaneously into the flanks of female NCR nude mice (Taconic) aged 4–6 weeks. Tumours were allowed to grow for one week before being excised and weighed before either protein extraction by homogenization or fixation overnight in 4% formaldehyde and paraffin embedding.

Immunohistochemistry. All kits and developing substrates were obtained from Vector Laboratories. Paraffin-embedded patient samples were deparaffinized, rehydrated and subjected to antigen retrieval using ARS solution. Sections were incubated in 5% hydrogen peroxide for 30 min before staining using the Universal Vectastain-ABC horseradish peroxidase kit and incubated with the indicated antibodies. Slides were developed with the DAB substrate kit. Sections from mouse tumours were deparaffinized, rehydrated and subjected to antigen retrieval using ARS solution, followed by immunostaining using the Vectastain ABC-AP kit. Stain was developed using the Vector Blue substrate kit. Sections were mounted using VectaMount permanent mounting medium.

Transfections and luciferase assays. Cells were transfected using Lipofectin in combination with PLUS reagent (Invitrogen). For bicistronic constructs, cells were collected two days after transfection and extracted in passive lysis buffer followed by dual luciferase assays (Promega) using a 96-well plate luminometer.

Emboli formation in Matrigel cultures and confocal microscopy analysis. SUM149 cells that had been silenced for the indicated proteins using shRNA adenovirus vectors were overlaid onto 8-well chamber slides coated in 100 μl Matrigel (BD Biosciences), as described previously[25]. Medium containing 4% Matrigel was added to the cells and changed every two days. After 12 days, the resulting emboli were fixed in 2% paraformaldehyde, permeabilized in 0.5% Triton PBS buffer, stained with the indicated primary antibodies and fluorescence-labelled secondary antibodies. Nuclei were stained with TO-PRO-3 (Stratagene). Confocal immunofluorescence microscopy and image acquisition were carried out at room temperature using a Zeiss LSM 510 meta confocal scanning laser microscope. Images were acquired using Lasersharp 2000 software (Carl Zeiss) and converted into TIF files, pseudo-coloured and merged for image processing with Photoshop 7 software.

Cell invasion assays. Invasion assays were performed using the Biocoat Matrigel invasion chambers (BD Biosciences). 1×10^5 SUM149 cells that had been silenced for the indicated proteins using shRNA adenovirus vectors were plated onto each chamber in serum-free growth medium. Chambers were placed in wells containing growth medium with 10% FBS to act as a chemoattractant. After incubation for 24 h, migrating cells were fixed with methanol and stained with crystal violet. Ten fields per chamber were counted using a ×40 objective lens in a light microscope. Results are the mean of three independent experiments.

Statistical analyses. For analysis of experimental data, comparison of categorical data was carried out by Student's *t*-test. Data are presented as the mean ± s.d. All *P*-values are two-sided. A *P*-value <0.05 was considered statistically significant in all experiments. The distributions of eIF4G, 4E-BP1 and eIF4E levels in IBC specimens were compared to control specimens using cross-tabulation methods. Fisher's exact tests (2-sided) were used to assess the differences between and among groups. Logistic regression models were proposed to examine the multivariable nature of the differences between the cases and controls; these models did not converge because of the low variability in biomarker levels in the controls. To address this issue, we developed a regression tree in 'R' using the *rpart* function.

Antibodies. Antibodies to eIF4E, 4E-BP1 and p53 were purchased from Cell Signaling Technologies. E-cadherin and p120 antibodies were obtained from BD Transduction Laboratories. Antibody to eIF4A was provided by William Merrick (Case Western Reserve University, Cleveland, OH). Polyclonal eIF4GI antibodies were generated by immunization of rabbits against the C-terminal portion of eIF4GI, as described previously[31]. Horseradish peroxidase-conjugated donkey anti-rabbit or sheep anti-mouse secondary antibodies were from Amersham. All primary antibodies were used at a 1:1,000 dilution; secondary antibodies were used at a 1:10,000 dilution.

Tumour growth in the chick CAM. To perform the CAM assays, 2.5×10^6 cells were collected by trypsinization and resuspended in 40 μl of RPMI medium before implanting into 10-day old chick embryos. Eggs were incubated in a humidified chamber at 37 °C for 6 days after implantation, collected and photographed before dissection from CAM membranes, weighed and fixed in zinc fixation buffer for 48 h followed by embedding in paraffin.

Branch formation assay. Branch formation assays in the chick CAM were performed as described previously[32]. Briefly, filter discs soaked in 48-h conditioned medium from SUM149 cells that had been silenced for the indicated proteins using shRNA adenovirus vectors were placed on 10-day old chick CAMs. Three days later discs were excised, photographed and new branch formation was quantified by counting ten different fields per disc.

Immunoblot and protein extracts. Cells were washed twice in cold PBS and resuspended in NP-40 lysis buffer (50 mM Hepes, pH 7.0, 150 mM NaCl, 2 mM EDTA, 0.5% NP-40, 25 mM β-glycerophosphate, 2 mM sodium vanadate and complete protease inhibitor cocktail (Roche)), incubated for 10 min on ice and centrifuged. Protein concentrations were determined using the Biorad protein assay. For Triton-soluble and insoluble extract preparation, cells were resuspended in Triton buffer (0.5% Triton X-100, 300 mM sucrose, 10 mM PIPES, pH 6.8, 50 mM NaCl, and 3 mM $MgCl_2$) and incubated for 30 min at 4 °C in a rotator. Soluble and insoluble fractions were separated by centrifugation. Insoluble protein/membrane pellets were resuspended in RIPA buffer (150 mM NaCl, 50 mM Tris-HCl, pH 8.0, 1% NP-40, 0.5% sodium deoxycholate, 0.1% SDS, 1 mM EDTA, 25 mM β-glycerophosphate, 2 mM sodium vanadate and complete protease inhibitor cocktail (Roche)). Protein concentrations were determined by Biorad DC protein assay. Tumours were extracted by homogenization in RIPA buffer using a Tekmar tissumizer and centrifuged at 13,000*g* for 10 min at 4 °C to remove insoluble material. Protein concentration was determined using the Biorad DC protein assay. To determine the total levels of specific proteins, equal amounts of protein from lysates were resolved by sodium dodecyl sulfate–polyacrylamide gel electrophoresis (SDS–PAGE) and analysed by protein immunoblotting with specific antibodies.

Adenovirus vectors. shRNA adenovirus vectors were constructed using the pShuttle-KO vector, generated by ligation of a knockdown cassette from pLKO.1puro[33] into pShuttle using *Xho*I to generate the DNA fragments. Synthetic double-stranded DNA oligonucleotides (IDT DNA) were phosphorylated using T4 PNK kinase and ligated to linearized pShuttle-KO vector digested with *Mlu*I and *Age*I. Positive clones were then recombined with the pAdEasy plasmid and purified according to manufacturer instructions (Stratagene). To generate viruses, 10 μg pAd-KO plasmids were linearized with *Pac*I and transfected into 293 cells. Cells were collected approximately 10 days later (after cytopathic effect was observed). Pellets were sonicated to release virus and used for stock production by re-infection of 293 cells, followed by CsCl gradient purification. Adenoviruses expressing p120 and the control virus were provided by Andrew Kowalczyk[34] (Emory University, Atlanta, GA). For silencing studies, SUM149 cells were infected three times 3 days apart at a multiplicity of infection (MOI) of 100. For combination silencing/overexpression studies, the cells were infected twice with the p120 or E-cadherin viruses (on days 5 and 6) after the initial infection with the Ad-KO viruses. The sequences of cloning and shRNA oligonucleotides are listed in the Supplementary Information.

DOI: 10.1038/ncb1900

PCR and RT–PCR analysis of endogenous and introduced p120 constructs

Primer	Application	Sequence (5′ to 3′)
KO-4GF	Cloning	CGCGTAAAAAGTAGTGTGATGTGTCTGAACTCTCGAGAGTTCAGACACATCACACTAC
KO-4GR	Cloning	CCGGGTAGTGTGATGTGTCTGAACTCTCGAGAGTTCAGACACATCACactacttttta
KO-NSR	Cloning	CGCGTAAAAAAATTCTCCGAACGTGTCACGTCTCGAGACGTGACACGTTCGGAGAATT
KO-ECDF	Cloning	ccggGGAGAGCGGTGGTCAAAGAGCctcgagGCTCTTTGACCACCGCTCTCCttttta
KO-ECDR	Cloning	cgcgtaaaaaGGAGAGCGGTGGTCAAAGAGCctcgagGCTCTTTGACCACCGCTCTCC
KO-p120F	Cloning	ccggGCCAGAGGTGGTTCGGATATActcgagTATATCCGAACCACCTCTGGCttttta
KO-p120R	Cloning	cgcgtaaaaaGCCAGAGGTGGTTCGGATATActcgagTATATCCGAACCACCTCTGGC
p120-5'F	Cloning, RT–PCR	TGAATTACTAGTCTCCAGATCAGTTTGTCACC
p120-iso1R	Cloning	TGAATTGAATTCGAAGGTAAGGGGCGGAGCCGC
p120-iso2R	Cloning	TGAATTGAATTCGAGTGGGTTGGCATCTTGTGG
p120-iso2R	Cloning	TGAATTGAATTCCCTGGGGATGGTGCTATATAG
p120-iso2R	Cloning	TGAATTGAATTCTGTCTTCATAGCTCCTCAAAT
ECDHF4	qRT-PCR	CGACCCAACCCAAGAATCTA
ECDHR4	qRT-PCR	AGGCTGTGCCTTCCTACAGA
p120F	qRT-PCR	TCCAGCAAACGATACAGTGG
p120R	qRT-PCR	GAACCACCTCTGGCTGAAAT
FireflyR	RT-PCR	AGGAACCAGGGCGTATCTCTTCAT
EX1F5	RT-PCR	TGCCCTGCTGGATTTGTCTT
EX5R5	RT-PCR	CGAGTGGTCCCATCATCTG

Protein synthesis analysis. Cells were incubated with 20 μCi of ^{35}S-methionine per ml (Easytag Express protein labelling mix; Dupont/NEN) in methionine-free DMEM for 1 h, washed twice with ice-cold phosphate-buffered saline (PBS) and lysed by incubation in 0.5% NP-40 lysis buffer (0.5% NP-40, 50 mM HEPES, pH 7.0, 250 mM NaCl, 2 mM EDTA, 2 mM sodium orthovanadate, 25 mM glycerophosphate and complete protease inhibitor (Roche)) for 10 min at 4°C. Lysates were clarified by centrifugation at 13,000*g* for 10 min. Specific activity of methionine incorporation was determined by trichloroacetic acid precipitation onto GF/C filters and liquid scintillation counting. All assays were conducted in duplicate and repeated at least three times.

Real-time quantitative RT–PCR analysis of endogenous mRNAs. Total RNA was extracted from cells with Trizol reagent, according to the manufacturer's instructions (Gibco). Equal amounts of total RNA from each sample (25 ng) were then reversed-transcribed and amplified using the SYBR green quantitative RT–PCR kit from Sigma using the indicated oligonucleotides.

^{35}S-methionine incorporation into newly synthesized proteins. Cells were labelled for 2 h with 50 μCi of ^{35}S-methionine per ml (Easytag Express protein labelling mix; Dupont/NEN) in methionine-free DMEM, washed with cold PBS and lysed in RIPA buffer. Immunoprecipitations were carried out by incubation overnight in a rotator at 4 °C with the indicated antibodies in buffer PLB (PBS, 0.1% SDS, 0.1% Triton X-100, 0.05% sodium azide, 1% sodium deoxycholate). Protein A-agarose beads (Santa Cruz Biotechnology) were added and the mixture further incubated for 1 h at 4°C. Beads were washed twice with buffer H-PLB (BDB containing 500 mM NaCl) and three times with PLB, resuspended in SDS–loading buffer and resolved by SDS–PAGE. Gels were fixed in 25% isopropanol/10% acetic acid followed by incubation in amplify reagent (GE Healthcare) and drying under vacuum. Dried gels were exposed to film and bands were quantified by densitometry using the GS800 scanner and software. For determination of E-cadherin half-life after *eIF4GI* silencing, cells were labelled as above but for a 4-h period, washed twice with cold medium, collected at the indicated time-points and immunoprecipitated as described above.

31. Cuesta, R., Laroia, G. & Schneider, R. J. Chaperone hsp27 inhibits translation during heat shock by binding eIF4G and facilitating dissociation of cap-initiation complexes. *Genes Dev.* **14,** 1460–1470 (2000).
32. Brooks, P. C., Montgomery, A. M. & Cheresh, D. A. Use of the 10-day-old chick embryo model for studying angiogenesis. *Methods Mol. Biol.* **129,** 257–269 (1999).
33. Stewart, S. A. *et al.* Lentivirus-delivered stable gene silencing by RNAi in primary cells. *RNA* **9,** 493–501 (2003).
34. Xiao, K. *et al.* p120-Catenin regulates clathrin-dependent endocytosis of VE-cadherin. *Mol. Biol. Cell.* **16,** 5141–5151 (2005).

nature cell biology

DOI: 10.1038/ncb1900

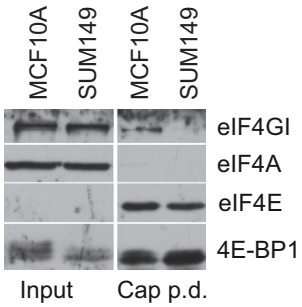

Figure S1 A substantial amount of eIF4GI remains unbound to eIF4E in SUM149 cells. 500 mg of lysates from SUM149 or MCF10A cells were bound to 7-Methyl-G coupled Sepharose beads (cap p.d. panels) and examined by immunoblot analysis with the indicated antibodies. Panels on the right show the initial levels of the indicated proteins in equal amounts of lysates.

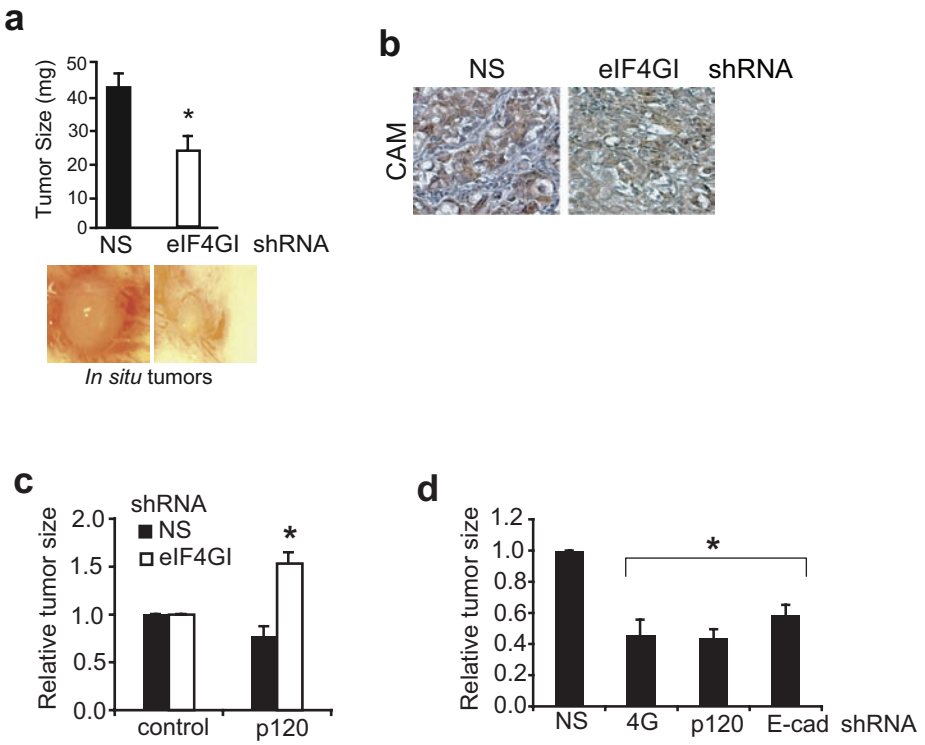

Figure S2 Tumor growth in the chick chorioallantoic membrane (CAM) is reduced by eIF4GI silencing. NS or eIF4GI-silenced SUM149 cells ($2.5x10^6$ cells) were implanted on the CAM of 10 d old chick embryos. Tumors were excised 6 d post-implantation, photographed and weighed. Results are the average of four independent experiments. * $P<0.001$; paired t-test.

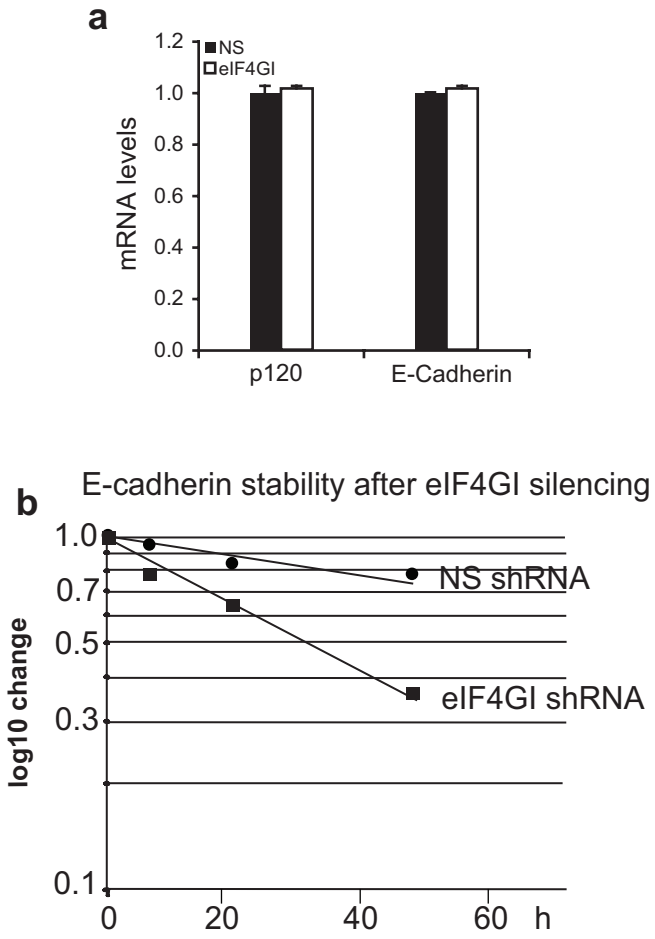

Figure S3 (**a**) Levels of E-cadherin and p120 mRNAs do not change as a result of eIF4GI silencing in SUM149 cells. Trizol extracted total RNA from NS or eIF4GI-silenced SUM149 cells were subjected to real time RT-PCR using oligonucelotides specific to E-cadherin or p120 mRNAs and normalized to eEF2K mRNA levels. (**b**) E-cadherin protein is destabilized as a result of eIF4GI silencing. Cells were metabolically labeled for 4 h with (^{35}S)-methionine and chased with cold medium (time 0). Extracts were immunoprecipitated for E-cadherin at the indicated times and resolved by SDS-PAGE followed by autoradiography and densitometry. Results are normalized to the total E-cadherin protein immunoprecipitated at time 0.

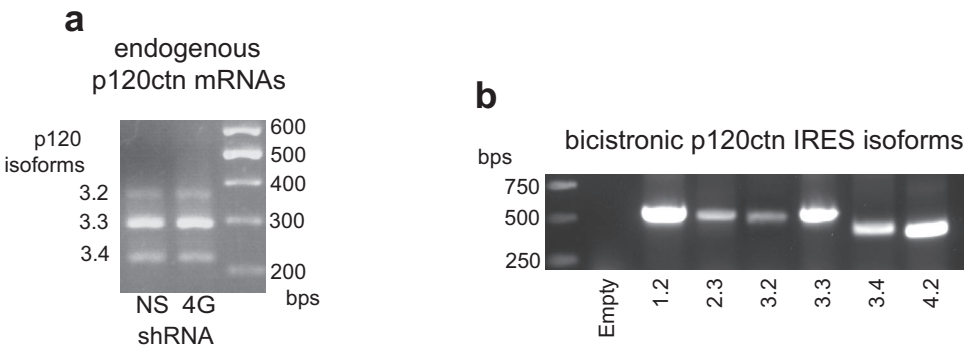

Figure S4 (**a**) Patterns of p120 transcription do no change after eIF4GI silencing in SUM149 cells. Equal amounts of total RNA from NS and eIF4GI-silenced SUM149 cells were subjected to RT-PCR analysis using primers directed to the 5' end of all the p120 isoforms located in exons: mRNA isoforms identified as described [1]. (**b**) Full-length expression of p120 5'UTRs after transfection of bicistronic constructs into SUM149 cells. Bicistronic dual luciferase plasmids containing the indicated p120 5'UTRs in inter-cistronic regions were transfected into SUM149 cells. Total RNA was extracted 48 h later and subjected to RT-PCR analysis using a forward primer at the 5' end of each UTR and a reverse primer that binds inside the firefly luciferase coding region.

1. Keirsebilck, A. *et al.* Molecular cloning of the human p120ctn catenin gene (CTNND1): expression of multiple alternatively spliced isoforms. *Genomics* **50**, 129-146 (1998).

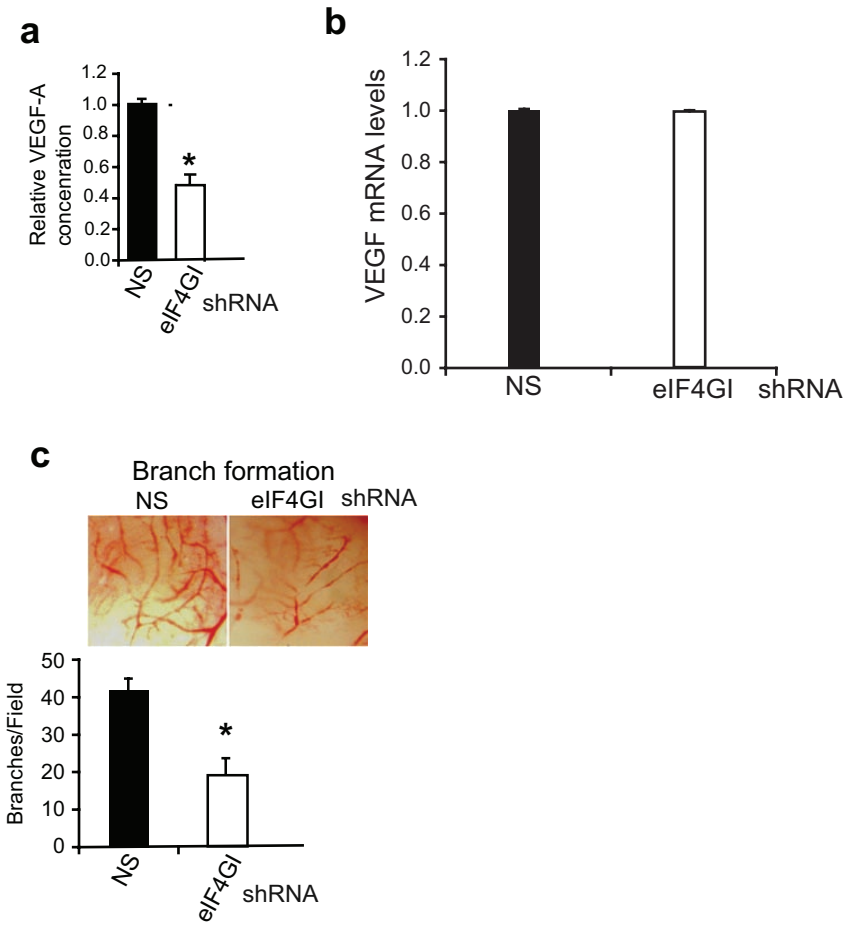

Figure S5 Control of VEGF-A protein synthesis and angiogenesis in SUM149 cells. (**a**) 48 h conditioned media from SUM149 cells with NS (black bar) or eIF4GI silencing (white bar) were analyzed by VEGF ELISA. Results expressed as a ratio of VEGF-A levels from eIF4GI-silenced cells over NS cells, represent an average of three independent experiments. * $P<0.001$; paired t-test. (**b**) Levels of VEGF-A mRNA do not change after eIF4GI silencing in SUM149 cells. Quantitative real time RT-PCR of mRNA from eIF4GI and control silenced SUM149 cells. Cells were silenced for eIF4GI or NS using Ad vectors, then Trizol extracted for total RNA and real time RT-PCR performed using oligonucleotides specific for VEGF-A mRNA, then normalized to eEF2K mRNA levels. (**c**) Angiogenic activity of conditioned media from eIF4GI-silenced SUM149 cells is reduced compared to control media. Filter discs soaked in 48 h conditioned media from eIF4GI-silenced or NS SUM149 cells were placed on 10 d CAMs. Three days post-implantation discs were photographed (right panels) and vascular branch formation quantified (left panel) by counting 10 equally sized fields on each of three discs. * $P<0.001$; paired t-test.

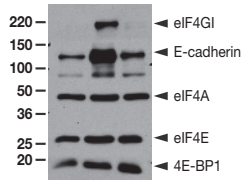

Fig1b

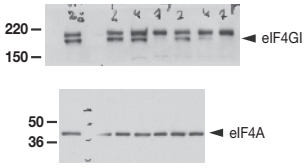

Fig1c

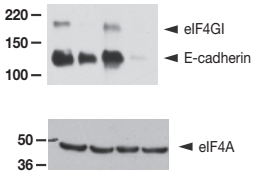

Fig2a

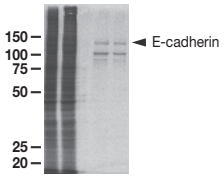

Fig2b

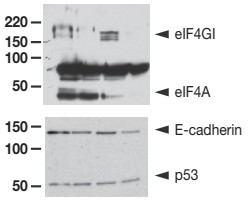

Fig2d

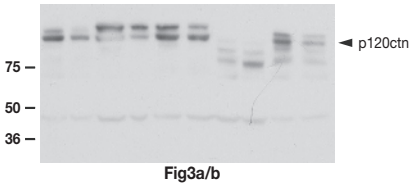

Fig3a/b

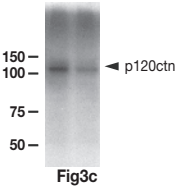

Fig3c

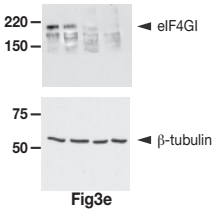

Fig3e

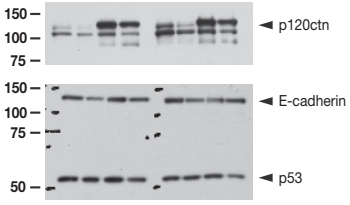

Fig4a

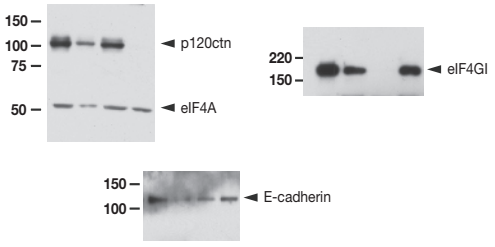

Fig4c

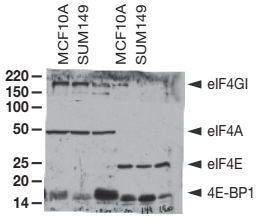

FigS1

Figure S6 Full scans of gels used in all figures.

Supplementary Table S1. Levels of translation factors in IBC, Stage III breast cancers and normal breast epithelium

		IBC		Control		Stage III	
	score	No.	%	No.	%	No.	%
eIF4GI	0	1	2%	0	0%	0	0%
	+1	7	19%	10	100%	9	30%
	+2	21	*57%	0	0%	14	*46%
	+3	8	*22%	0	0%	11	*23%
4E-BP1	0	11	30%	0	0%	0	0%
	+1	13	35%	8	80%	4	13%
	+2	13	35%	2	20%	9	*30%
	+3	0	0%	0	0%	11	*57%
eIF4E	0	8	22%	0	0%		
	+1	17	46%	9	90%		
	+2	11	**30%	1	10%		
	+3	1	2%	0	0%		
eIF4GII	0	7	25%	0	0%		
	+1	8	28%	4	34%		
	+2	10	†36%	7	58%		
	+3	3	†11%	1	8%		
DAP5	0	1	4%	1	8%		
	+1	15	54%	8	67%		
	+2	11	†39%	3	25%		
	+3	1	4%	0	0%		

Fisher's 2-sided Exact test, n=37 IBC specimens, 10 normal breast epithelium; * $P < 0.001$

** No statistically significant increased expression in IBC compared to normal breast epithelium ($P=0.174$)

† Trend toward slightly greater expression in normal breast epithelium compared to IBC that was not statistically significant

nature cell biology

Transmission and spreading of tauopathy in transgenic mouse brain

Florence Clavaguera[1], Tristan Bolmont[2], R. Anthony Crowther[3], Dorothee Abramowski[4], Stephan Frank[1], Alphonse Probst[1], Graham Fraser[3], Anna K. Stalder[5], Martin Beibel[4], Matthias Staufenbiel[4], Mathias Jucker[2], Michel Goedert[3,6,7] and Markus Tolnay[1,6,7]

Hyperphosphorylated tau makes up the filamentous intracellular inclusions of several neurodegenerative diseases, including Alzheimer's disease[1]. In the disease process, neuronal tau inclusions first appear in the transentorhinal cortex from where they seem to spread to the hippocampal formation and neocortex[2]. Cognitive impairment becomes manifest when inclusions reach the hippocampus, with abundant neocortical tau inclusions and extracellular β-amyloid deposits being the defining pathological hallmarks of Alzheimer's disease. An abundance of tau inclusions, in the absence of β-amyloid deposits, defines Pick's disease, progressive supranuclear palsy, corticobasal degeneration and other diseases[1]. *Tau* mutations cause familial forms of frontotemporal dementia, establishing that tau protein dysfunction is sufficient to cause neurodegeneration and dementia[3–5]. Thus, transgenic mice expressing mutant (for example, P301S) human tau in nerve cells show the essential features of tauopathies, including neurodegeneration and abundant filaments made of hyperphosphorylated tau protein[6,8]. By contrast, mouse lines expressing single isoforms of wild-type human tau do not produce tau filaments or show neurodegeneration[7,8]. Here we have used tau-expressing lines to investigate whether experimental tauopathy can be transmitted. We show that injection of brain extract from mutant P301S tau-expressing mice into the brain of transgenic wild-type tau-expressing animals induces assembly of wild-type human tau into filaments and spreading of pathology from the site of injection to neighbouring brain regions.

Transgenic mouse lines ALZ17 and P301S tau were used[6,7]. Mice from line ALZ17, which express the longest human brain tau isoform (441 amino acids) do not have filamentous tau aggregates (Supplementary Information, Fig. S1a). By contrast, mice from line P301S tau, which express the 383 amino acid human tau isoform with the P301S mutation that causes inherited frontotemporal dementia, develop abundant filamentous tau inclusions (Supplementary Information, Fig. S1a). Both the 383 and 441 amino acid tau isoforms contain 4 microtubule-binding repeats, but they differ by the presence of two alternatively spliced amino-terminal inserts of 29 amino acids each[9].

To investigate whether aggregation of tau can be transmitted, we injected diluted extracts of brain homogenates from 6-month-old human P301S tau mice into the hippocampus and the overlying cerebral cortex of 3-month-old ALZ17 mice. Before injection, the homogenates were analysed by immunoblotting and immunoelectron microscopy. Human tau protein bands of 55,000–64,000 (M_r 55–64K) were detected by western blotting (Supplementary Information, Fig. S1b). The slowest migrating tau species were immunoreactive with antibody AT100 (Supplementary Information, Fig. S1b) and other phosphorylation-dependent anti-tau antibodies (data not shown). Immunoelectron microscopy showed that tau filaments were present in the tissue extracts (Supplementary Information, Fig. S1c). Injection of brain extract from human P301S tau mice induced filamentous tau pathology in ALZ17 mice, as indicated by the appearance of Gallyas-Braak silver staining[10,11] (Fig. 1a) and the presence of tau filaments by immunoelectron microscopy (Fig. 1b). Gallyas-Braak staining was present intracellularly 6, 12 and 15 months after injection of brain extract ($n = 5$ per group). In addition to silver-positive nerve cell bodies and processes, injection of brain extract from P301S tau mice resulted in the appearance of immunoreactivity with antibody AT100 (Fig. 1a), which is indicative of tau filaments[6]. By contrast, no silver-positive lesions were observed at corresponding levels of the hippocampus (Supplementary Information, Fig. S2a) of 18-month-old non-injected ALZ17 mice or in ALZ17 mice 15 months after the injection of brain extract from non-transgenic control mice (Fig. 1a). ALZ17 animals injected with P301S extract immunodepleted of tau did not reveal any Gallyas- or AT100-positive structures 6 months after injection (Fig. 1c), demonstrating that the presence of tau in the P301S extract was necessary to induce filamentous tauopathy.

AT8 immunoreactivity (reflecting tau hyperphosphorylation), but not AT100 staining, was present in the hippocampus of 18-month-old

[1]Department of Neuropathology, Institute of Pathology, University of Basel, Basel, Switzerland. [2]Department of Cellular Neurology, Hertie-Institute for Clinical Brain Research, University of Tübingen, Tübingen, Germany. [3]MRC Laboratory of Molecular Biology, Cambridge, UK. [4]Novartis Institutes for Biomedical Research, Basel, Switzerland. [5]Neurology and Neurobiology, University Hospital, Basel, Switzerland.
[6]These authors contributed equally to this work
[7]Correspondence should be addressed to M.T or M.G. (e-mail: mtolnay@uhbs.ch; mg@mrc-lmb.cam.ac.uk)

Received 24 February 2009; accepted 26 March 2009; published online 7 June 2009; DOI: 10.1038/ncb1901

ALZ17 mice, as previously reported[7]. Following the injection of brain extract from human P301S tau mice, AT8 immunoreactivity became more widespread, indicating the promotion of tau hyperphosphorylation (Fig. 1a). Filamentous tau pathology in P301S tau-injected ALZ17 mice was induced in different cell types. Silver-positive structures morphologically indistinguishable from those found in human tauopathies were observed in the brains of injected ALZ17 mice (Supplementary Information, Fig. S2b). They included neurofibrillary tangles (arrows in panels 1 and 2), neuropil threads (arrowheads in panels 1 and 2) and oligodendroglial coiled bodies (arrows in panels 3 and 4). The silver-positive structures were also immunoreactive for phosphorylated tau (Supplementary Information, Fig. S2b panels 2 and 3). Filaments extracted from injected brains were decorated with phosphorylation-dependent anti-tau antibodies and with antibodies specific for tau isoforms with N-terminal inserts (Fig. 1b). It follows that the filaments had formed from the wild-type 441 amino acid human tau isoform expressed in line ALZ17 and were not derived from the injected material. This is also supported by the finding that inclusions in ALZ17 mice injected with P301S brain extract were immunoreactive with antibodies specific for tau with N-terminal inserts (Supplementary Information, Fig. S3). No silver staining was observed in ALZ17 mice 1 day after the injection of P301S tau brain extract (data not shown). No signs of neuronal loss, astrogliosis, inflammation, axonal damage or myelin breakdown were observed in ALZ17 mice 15 months after the injection of P301S tau brain extract when compared with non-injected ALZ17 animals (Supplementary Information, Fig. S4).

Induction of filamentous tau in ALZ17 mice was time- and brain region-dependent. Quantitative assessment in the hippocampus revealed a significant increase in the number of silver-positive lesions between 6, 12 and 15 months after injection (Fig. 2a, c). Neuropil threads were most abundant, followed by coiled bodies and neurofibrillary tangles (Fig. 2b). The same was true for the cerebral cortex, although fewer silver-positive structures developed there over time (Fig. 2a).

Positive silver staining did not remain confined to the injected areas, but spread to neighbouring brain regions, as visualized in three coronal brain sections encompassing the injection sites and the levels 1.7 mm anterior and 1.3 mm posterior to the injection site (Fig. 3; Table 1). At the injection level, abundant silver staining was present in the hippocampus, fimbria, optic tract and thalamus, with fewer abnormal structures in more distant regions, such as medial lemniscus, zona incerta and cerebral peduncle. The hypothalamus was the most distant region where filamentous tau pathology developed (4 mm ventral from the injection sites; an adult mouse brain measures approximately 5.5 mm in height and 13 mm in length). Almost 2 mm anterior to the injection level, filamentous tau pathology was found in the fimbria, thalamus, internal capsule, caudate-putamen, somatosensory cortex, hypothalamus and the amygdala 15 months after the injection of brain extract from human P301S tau mice (Table 1; Supplementary Information, Fig. S5a). More than 1 mm posterior to the injection level, the cerebral peduncle, hippocampus, superior colliculus, substantia nigra, entorhinal cortex, deep mesencephalic nucleus and the pontine nuclei showed filamentous lesions 15 months after injection (Table 1; Supplementary Information, Fig. S5b). Moderate filamentous tau pathology was observed in some brain regions of the contralateral, non-injected hemisphere (Supplementary Information, Fig. S5c).

To determine which kind of tau species was responsible for the induction of aggregated tau in ALZ17 mice, P301S extracts containing either soluble or insoluble tau were injected into ALZ17 mice. Injection of

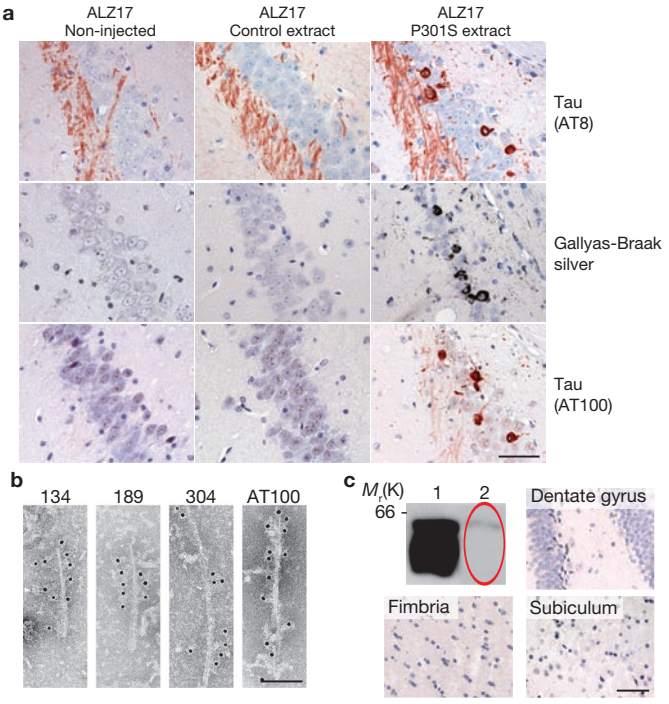

Figure 1 Induction of filamentous tau pathology in ALZ17 mice injected with brain extract from mice transgenic for human P301S tau. (**a**) Staining of the hippocampal CA3 region of 18-month-old ALZ17 mice with anti-tau antibody AT8, Gallyas-Braak silver or anti-tau antibody AT100. Non-injected (left), 15 months after injection with brain extract from non-transgenic control mice (middle) and 15 months after injection with brain extract from 6-month-old mice transgenic for human P301S tau protein (right). The sections were counterstained with haematoxylin. Scale bar, 50 μm (same magnification in all panels). (**b**) Immunoelectron microscopy of filaments extracted from the brain of an ALZ17 mouse 15 months after the injection of brain extract from mice transgenic for human P301S tau. Labelling with anti-tau sera 134, 189 and 304, and antibody AT100. Scale bar, 100 nm. (**c**) No filamentous tau pathology in ALZ17 mice injected with tau-immunodepleted human P301S tau brain extract. Top left panel shows western blot with anti-tau antibody HT7 of P301S brain extract before (lane 1) and after (lane 2) immunodepletion. Top right and lower panels show Gallyas-Braak staining of dentate gyrus, fimbria and subiculum of ALZ17 mice 6 months after injection with tau-immunodepleted P301S brain extract. The sections were counterstained with haematoxylin. Scale bar, 50 μm (same magnification in all panels). The full scan of the western blot data is available in the Supplementary Information, Fig. S7.

insoluble tau induced a large number of Gallyas-Braak-positive structures in ALZ17 animals (Supplementary Information, Fig. S6), similar to that observed after injection of crude P301S extracts. In addition, there was a similar increase and spreading of fibrillar tau pathology over time (data not shown). Injection of soluble tau induced Gallyas-Braak-positive structures to a much lesser extent (<5%), compared with insoluble tau (Supplementary Information, Fig. S6). Thus, it is predominantly the insoluble tau species that induces tau aggregation.

We next injected brain extract from human P301S tau mice into non-transgenic control mice. Interestingly, the wild-type mice showed Gallyas-Braak- and AT100-positive threads and coiled bodies (but no neurofibrillary tangles) 6 months (Fig. 4) and 12 months after injection. They remained confined to the injection site and did not increase in number between 6 and 12 months after injection (data not shown). Gallyas-Braak-positive structures were stained with the anti-murine tau antibody MT1, but not with human-specific tau antibody T14, demonstrating that filamentous tau

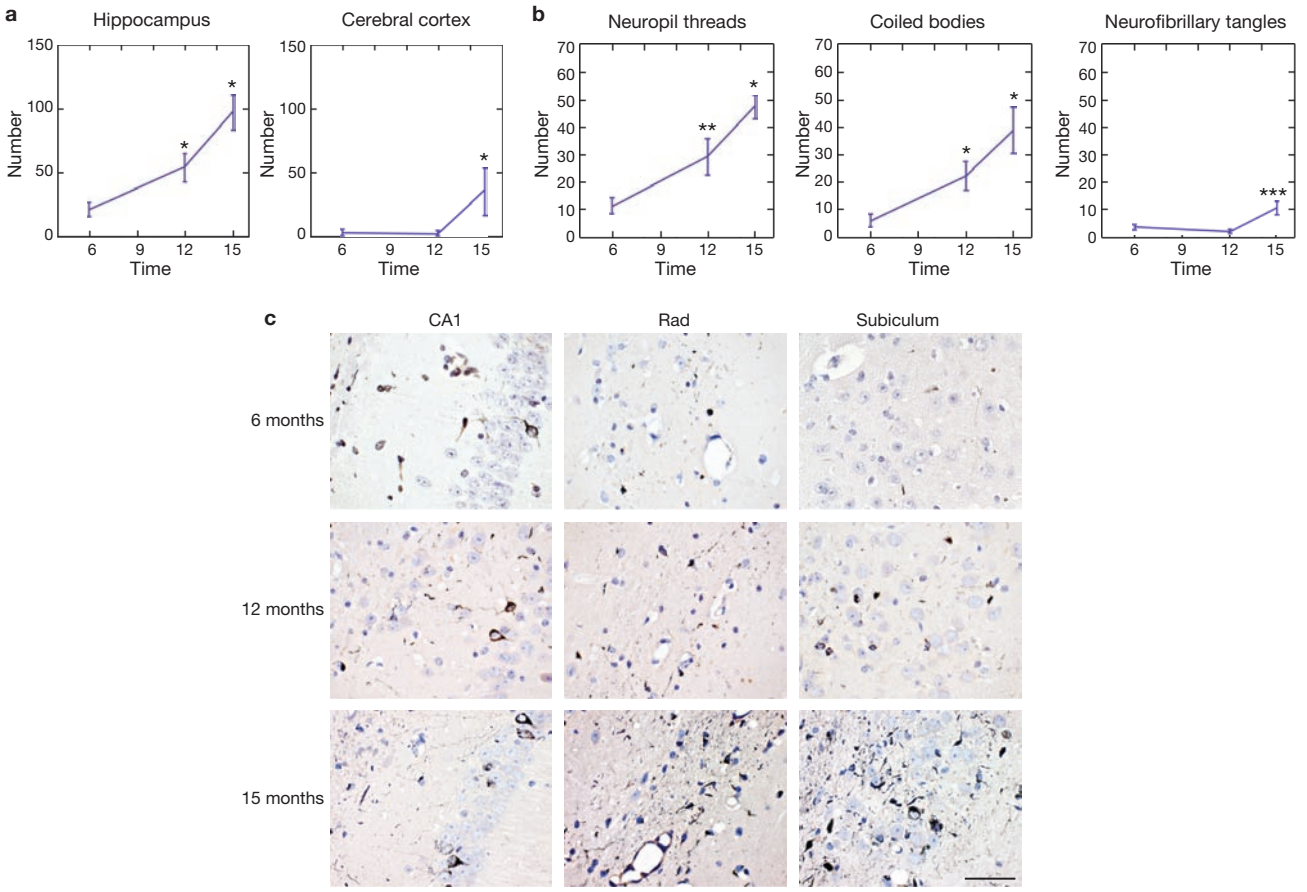

Figure 2 Temporal increase in the number of Gallyas-Braak-positive structures at the injection sites (–2.5 mm from bregma) in ALZ17 mice. (**a**) A statistically significant increase in silver-positive structures was observed in the hippocampus from 6 to 12 months and 12 to 15 months. In the cerebral cortex, a significant increase was observed between 12 and 15 months. The results are expressed as means ± s.e.m. ($n = 5$); $^{*}P < 0.05$. (**b**) In the hippocampus, significant increases in neuropil threads and coiled bodies were observed between 6 and 12 months, and between 12 and 15 months. For neurofibrillary tangles, a significant increase was observed between 12 and 15 months. The results are expressed as means ± s.e.m. ($n = 5$); $^{*}P < 0.05$; $^{**}P < 0.001$; $^{***}P < 0.0001$. (**c**) Gallyas-Braak staining of the hippocampal region (CA1, *stratum radiatum* and subiculum) of ALZ17 mice injected with human P301S tau brain extract 6 (top), 12 (middle) and 15 (bottom) months after injection. The sections were counterstained with haematoxylin. Scale bar, 50 μm (same magnification in all panels).

induced in wild-type mice was made of murine tau (Fig. 4). No tau pathology was observed in sham-lesioned mice (Fig. 4). These results suggest that expression of human tau in ALZ17 mice was essential for the temporal increase and spreading of filamentous tau pathology after injection of human P301S tau brain extract. However, the presence of a small number of mouse tau filaments in the extract could be responsible for the aggregation of murine tau in wild-type animals and explain the modest amount of filamentous tauopathy. The extent to which tau expression levels influence spreading remains to be clarified.

The present findings show that intracerebral injection of brain extract from mice with a filamentous tau pathology induces the formation and spreading of silver-positive aggregates made of hyperphosphorylated tau in mice transgenic for human wild-type tau, demonstrating experimental transmission of tauopathy. During the process leading to Alzheimer's disease, neuronal tau pathology forms in a stereotypical fashion in transentorhinal cortex from where it seems to spread to the hippocampal formation and neocortex[2], consistent with a uniform biological process. We have also shown the appearance over time of silver-positive structures at sites that are at a considerable distance from the injection sites in hippocampus and cerebral cortex. Brain regions that develop pathology are connected anatomically to the injection sites or to each other. This, together with the stereotypical appearance of silver-positive structures in defined brain regions over time in all animals studied (Table 1), is clearly indicative of the active induction and spreading of pathology rather than the passive diffusion of tau aggregates from the injection sites to more distant regions. The lack of obvious signs of neurodegeneration in ALZ17 mice 15 months after injection of brain extract from mice transgenic for human P301S tau contrasts with the nerve cell loss that characterizes the P301S tau mice[6]. This suggests that the molecular tau species responsible for transmission and neurotoxicity are not identical. It remains to be seen whether neurodegenerative changes appear at later time points.

A combination of neuronal and glial tau pathology is the defining feature of a number of human neurodegenerative diseases characterized by the assembly of wild-type four-repeat tau isoforms into filaments. They include progressive supranuclear palsy, corticobasal degeneration and argyrophilic grain disease[12]. By contrast, in Pick's disease, three-repeat tau isoforms are found in the neuronal inclusions; in Alzheimer's disease, both three- and four-repeat tau isoforms make up neurofibrillary tangles[12]. In addition, the morphologies of tau filaments vary widely in different tauopathies[13]. Together with the findings reported here showing

Table1 Semi-quantitative grading of filamentous tau pathology

Anterior (1.7 mm from injection level)			
	Time after injection (months)		
Region	6	12	15
Fimbria	++	+++	+++
Thalamus	+	++	++
Internal capsule	–	+	++
Caudate putamen	–	+	+
Somatosensory cortex	–	+	+
Hypothalamus	–	–	+
Amygdala	–	–	+
Injection level			
	Time after injection (months)		
Region	6	12	15
Hippocampus*,[1]	++	+++	+++
Optic tract	++	++	+++
Fimbria	+	++	+++
Medial lemniscus	+	++	+++
Zona incerta	+	++	+++
Thalamus	+	++	++
Cerebral peduncle	+	++	++
Visual cortex[2]	+	+	++
Hypothalamus	+	+	+
Amygdala	–	+	+
Posterior (1.3 mm from injection level)			
	Time after injection (months)		
Region	6	12	15
Cerebral peduncle	++	+++	+++
Hippocampus*	+	++	+++
Superior colliculus	+	++	++
Substantia nigra	+	+	+
Entorhinal cortex	–	+	++
Deep mesencephalic nucleus	–	+	++
Pontine nuclei	–	–	+

ALZ17 mice were injected with brain extract from mice transgenic for human P301S tau ($n = 5$ for each time point). – No Gallyas-Braak-positive structures; + 1–20; ++ 21–40; +++ >40; *CA1, CA2, CA3, dentate gyrus and subiculum; [1, 2]injection sites

transmission and spreading of filamentous tau pathology, this is reminiscent of mammalian and yeast prions, for which different strains have been described on the basis of the existence of separate conformers of assembled protein[14]. It is tempting to speculate that distinct tau strains may underlie the pathogenesis of different sporadic tauopathies. This hypothesis can now be tested experimentally by injecting ALZ17 mice with brain extracts from patients with sporadic tauopathies.

From the increase in silver-positive structures over time, it seems likely that nerve cell processes and oligodendrocytes are major sites of filament induction. These findings are comparable to previous work using mouse models of prion diseases, β-amyloid deposition and some peripheral amyloidoses[15–22]. However, unlike the extracellular location of filamentous deposits in those other diseases, tau inclusions are intracellular. Mechanisms must therefore exist by which tau aggregates can either gain access to the inside of cells or activate filament-inducing cascades from the outside. Inside cells, tau aggregates could function as seeds for the ordered assembly of transgenic wild-type human tau into silver- and AT100-positive filamentous deposits. Intracellular filamentous tau pathology could also be induced by extracellular tau aggregates. Previous work has indeed shown potentiation of tau pathology by extracellular β-amyloid aggregates in mice transgenic for mutant human tau[18,19]. However, no such effect was observed in mice transgenic for wild-type human tau[23].

It has been suggested that misfolded superoxide dismutase, which causes a subset of familial forms of amyotrophic lateral sclerosis, is secreted from motor neurons[24]. By analogy, spreading of tau pathology may also result from the release of aggregates from affected nerve cells and glial cells. It will be important to investigate whether such mechanisms exist for misfolded tau. The formation of tau aggregates in a single brain cell and their subsequent spreading may therefore be at the origin of sporadic tauopathies. Consequently, the presence of tau aggregates in the extracellular space would be an obligatory step in the events leading to disease. Immunisation strategies may prevent this process[25].

The present findings demonstrate transmission of tauopathy between transgenic mouse lines and describe an experimental system in which to investigate the spreading of pathology and the existence of tau strains. It will be important to identify the molecular tau species capable of inducing transmission, aggregation and spreading. Similar mechanisms may also underlie Parkinson's disease and dementia with Lewy bodies, where α-synuclein pathology seems to spread from brainstem areas to midbrain and neocortex[26]. Furthermore, in Parkinson's disease patients who have undergone transplantation of fetal midbrain neurons, filamentous α-synuclein pathology seems to spread from affected host tissue to the grafted neurons[27]. In contrast to prion diseases[28], human tauopathies are not believed to be infectious. Experimental model systems of the type described here now make it possible to dissect the similarities and differences between tauopathies and prion diseases. □

METHODS

Methods and any associated references are available in the online version of the paper at http://www.nature.com/naturecellbiology/

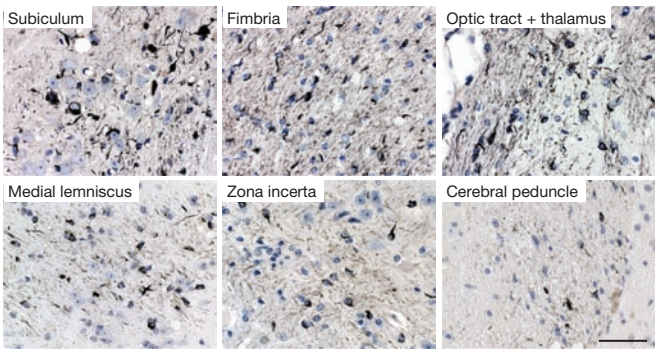

Figure 3 Spreading of filamentous tau pathology in ALZ17 mice injected with brain extract from mice transgenic for human P301S tau. Gallyas-Braak silver staining of brain regions at a distance from the injection sites 15 months post-injection. The sections were counterstained with haematoxylin. Scale bar, 50 μm (same magnification in all panels).

Note: Supplementary Information is available on the Nature Cell Biology website.

ACKNOWLEDGEMENTS

This work was supported by the Swiss National Science Foundation (3100AO-120261) (M.T.), the Alzheimer Association (ZEN-06-27341), the German National Genome Network (NGFN-Plus) and the German Competence Network in Degenerative Dementias (01GI0705) (M.J.), the U.K. Medical Research Council (R.A.C, G.F., M.G.) and the U.K. Alzheimer's Research Trust (M.G.). We thank K.H. Wiederhold (Novartis Institutes for Biomedical Research, Basel) and N. Schaeren-Wiemers (University Hospital Basel) for antibodies and helpful discussions.

AUTHOR CONTRIBUTIONS

F.C., R.A.C., M.G. and M.T. designed the experiments, coordinated the project and wrote the manuscript. M.J. initiated the study. F.C., T.B., R.A.C. D.A., G.F., A.K.S. and M.G. performed the experimental work. A.P. assisted with assessment and interpretation of initiation and neuroanatomical spreading of tau pathology. M.B. performed statistical analyses. M.S., S.F. and M.J. contributed to data and manuscript discussions.

COMPETING INTERESTS

The authors declare that they have no competing financial interest.

Published online at http://www.nature.com/naturecellbiology/
Reprints and permissions information is available online at http://npg.nature.com/reprintsandpermissions/

1. Goedert, M. & Spillantini, M. G. A century of Alzheimer's disease. *Science* **314,** 777–781 (2006).
2. Braak, H. & Braak, E. Neuropathological stageing of Alzheimer-related changes. *Acta Neuropathol.* **82,** 239–259 (1991).
3. Poorkaj, P. *et al.* Tau is a candidate gene for chromosome 17 frontotemporal dementia. *Ann. Neurol.* **43,** 815–825 (1998).
4. Hutton, M. *et al.* Association of missense and 5′-splice-site mutations in *tau* with the inherited dementia FTDP-17. *Nature* **393,** 702–705 (1998).
5. Spillantini, M. G. *et al.* Mutation in the tau gene in familial multiple system tauopathy with presenile dementia. *Proc. Natl Acad. Sci. USA* **95,** 7737–7741 (1998).
6. Allen, B. *et al.* Abundant tau filaments and nonapoptotic neurodegeneration in transgenic mice expressing human P301S tau protein. *J. Neurosci.* **22,** 9340–9351 (2002).
7. Probst, A. *et al.* Axonopathy and amyotrophy in mice transgenic for human four-repeat tau protein. *Acta Neuropathol.* **99,** 469–481 (2000).
8. Frank, S., Clavaguera, F. & Tolnay, M. Tauopathy models and human neuropathology: similarities and differences. *Acta Neuropathol.* **115,** 39–53 (2008).
9. Goedert, M., Spillantini, M. G., Jakes, R., Rutherford, D. & Crowther, R. A. Multiple isoforms of human microtubule-associated protein tau: Sequences and localization in neurofibrillary tangles of Alzheimer's disease. *Neuron* **3,** 519–526 (1989).
10. Gallyas, F. Silver staining of Alzheimer's neurofibrillary changes by means of physical development. *Acta Morphol. Acad. Sci. Hung.* **19,** 1–8 (1971).
11. Braak, H., Braak, E., Ohm, T. & Bohl, J. Silver impregnation of Alzheimer's neurofibrillary changes counterstained for basophilic material and lipofuscin pigment. *Stain Technol.* **63,** 197–200 (1988).
12. Lee, V. M.-Y., Goedert, M. & Trojanowski, J. Q. Neurodegenerative tauopathies. *Annu. Rev. Neurosci.* **24,** 1121–1159 (2001).
13. Crowther, R. A. & Goedert, M. Abnormal tau-containing filaments in neurodegenerative diseases. *J. Struct. Biol.* **130,** 271–279 (2000).
14. Prusiner, S. B. Prions. *Proc. Natl Acad. Sci. USA* **95,** 13363–13383 (1998).
15. Legname, G. *et al.* Synthetic mammalian prions. *Science* **305,** 673–676 (2004).
16. Kane, M. D. *et al.* Evidence for seeding of β-amyloid by intracerebral infusion of Alzheimer brain extracts in β amyloid precursor protein-transgenic mice. *J. Neurosci.* **15,** 3606–3611 (2000).

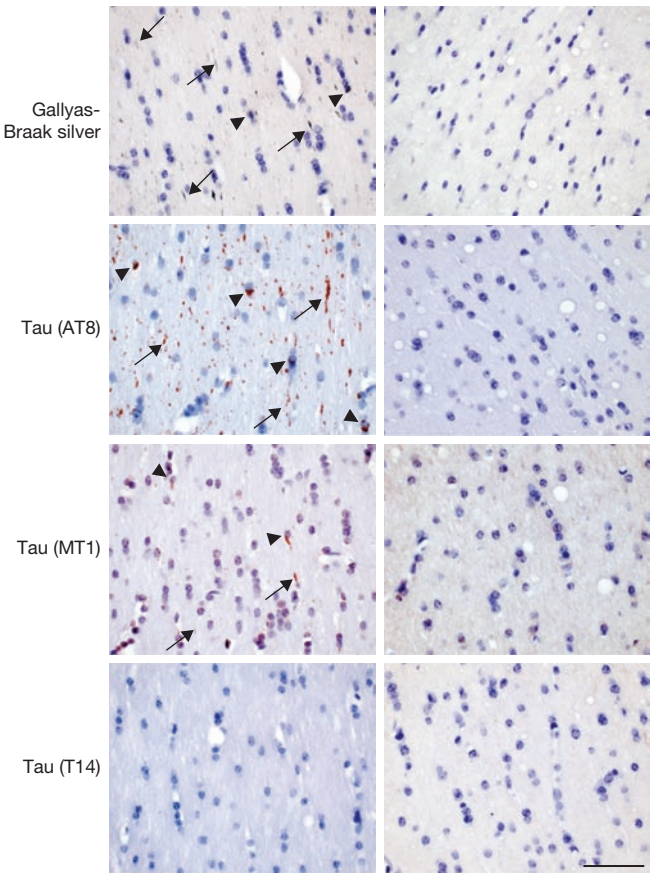

Figure 4 Induction of filamentous tau pathology in non-transgenic C57BL/6 mice injected with brain extract from mice transgenic for human P301S tau. Gallyas-Braak silver staining and immunostaining with the phosphorylation-dependent anti-tau antibody AT8, murine-specific tau antibody MT1 and human-specific tau antibody T14 in the fimbria of a non-transgenic mouse 6 months after the injection with the human P301S tau brain extract (left column). Gallyas-Braak-, AT8- and MT1-positive, T14-negative, tau deposits were observed in neurites (arrows) and in oligodendrocytes (arrowheads). No tau pathology was observed in age-matched sham-lesioned animals (right column). The sections were counterstained with haematoxylin. Scale bar, 50 μm (same magnification in all panels).

17. Meyer-Luehmann, M. *et al.* Exogenous induction of cerebral β-amyloidosis is governed by agent and host. *Science* **313,** 1781–1784 (2006).
18. Götz, J., Chen, F., van Dorpe, J. & Nitsch, R. M. Formation of neurofibrillary tangles in P301L tau transgenic mice induced by Aβ 42 fibrils. *Science* **293,** 1491–1495 (2001).
19. Bolmont, T. *et al.* Induction of tau pathology by intracerebral infusion of amyloid-β-containing brain extract and by amyloid-β deposition in APP X tau transgenic mice. *Am. J. Pathol.* **171,** 2012–2020 (2007).
20. Xing, Y. *et al.* Transmission of mouse senile amyloidosis. *Lab. Invest.* **81,** 493–499 (2001).
21. Lundmark, K. *et al.* Transmissibility of systemic amyloidosis by a prion-like mechanism. *Proc. Natl Acad. Sci. USA* **99,** 6979–6984 (2002).
22. Walker, L. C., LeVine III, H., Mattson, M. P. & Jucker, M. Inducible proteopathies. *Trends Neurosci.* **29,** 438–443 (2006).
23. Boutajangout. *et al.* Characterisation of cytoskeletal abnormalities in mice transgenic for wild-type human tau and familial Alzheimer's disease mutants of APP and presenilin-1. *Neurobiol. Dis.* **15,** 47–60 (2004).
24. Urushitani, M. *et al.* Chromogranin-mediated secretion of mutant superoxide dismutase proteins linked to amyotrophic lateral sclerosis. *Nature Neurosci.* **9,** 108–118 (2006).
25. Asuni, A. A., Boutajangout, A., Quartermain, D. & Sigurdson, E. M. Immunotherapy targeting pathological tau conformers in a tangle mouse model reduces brain pathology with associated functional improvements. *J. Neurosci.* **27,** 9115–9129 (2007).
26. Braak, H. *et al.* Staging of brain pathology related to sporadic Parkinson's disease. *Neurobiol. Aging* **24,** 197–211 (2003).
27. Brundin, P., Li, J.-Y., Holton, J. L., Lindvall, O. & Revesz, T. Research in motion: the enigma of Parkinson's disease pathology spread. *Nature Rev. Neurosci.* **9,** 741–745 (2008).
28. Brown, P. *et al.* Human spongiform encephalopathy: The National Institutes of Health series of 300 cases of experimentally transmitted disease. *Ann. Neurol.* **35,** 513–529 (1994).

METHODS

Mice. Homozygous human wild-type tau ALZ17 transgenic mice[7], homozygous human P301S tau transgenic mice[6] and non-transgenic control mice, all females on a C57BL/6 background, were used. Experiments were performed in compliance with protocols approved by the local Basel Committee for Animal Care and Animal Use.

Preparation of brain extracts. Six-month-old mice transgenic for human P301S tau and age-matched non-transgenic control mice were anaesthetized with sodium pentobarbitone (100 mg kg^{-1}) and killed by decapitation. Brainstems were dissected, snap-frozen in liquid nitrogen and stored at –80 °C. Brainstems from 3 mice were combined and homogenized at 10% (w/v) in sterile phosphate-buffered saline (PBS), briefly sonicated (Branson 450, output 2, 5 × 0.9 s) and centrifuged at 3,000*g* at 4 °C for 5 min. The supernatant was aliquoted, snap-frozen and stored at –80 °C until use.

Separation of soluble and insoluble tau. Brainstem extracts from mice transgenic for human P301S tau were centrifuged at 100,000*g* at 4 °C for 20 min. The supernatants containing soluble tau were aliquoted and stored at –80 °C until use. The pellets containing insoluble tau were resuspended in the original volume of PBS, sonicated (Branson 450, output 1.5, 3 × 0.9 s), aliquoted and stored at –80 °C until use.

Immunodepletion of tau. A mixture of anti-tau antibodies HT7 (Pierce), AT8 (Pierce), and TAU-5 (Biosource) (20 µg of each antibody) was incubated for 2 h with 10 µl of Protein G Sepharose 4 Fast flow (PGS, Pharmacia). Sepharose beads were washed twice with 1 ml PBS and the liquid removed with a glass capillary. P301S brain extract (100 µl, prepared as described above) was added to semi-dry beads and allowed to react overnight at 4 °C on an overhead mixer. The beads were settled by centrifugation (1 min, 200*g*) and 70 µl of the tau-depleted supernatant were removed. Five µl were used for western blot analysis and the remainder stored at –80 °C until use. As a control, P301S extract was treated as above, but in the absence of anti-tau antibodies.

Western blotting. Brain extracts were run on 8% Tris-glycine SDS–PAGE, transferred onto a PVDF membrane (Immobilon P, Millipore) and probed with anti-tau antibodies HT7 (1:1,000), AT8 (1:1,000) and AT100 (1:200, Pierce). HT7 recognizes human tau, but not mouse tau[29], AT8 labels tau phosphorylated at Ser 202 and Thr 205 (ref. 30) and AT100 detects tau phosphorylated at Thr 212, Ser 214 and Thr 217 (ref. 31). The secondary antibody was goat anti-mouse IgG (Chemicon). For signal detection, ECL plus (Amersham) was used in conjunction with Amersham Hyperfilm ECL.

Stereotaxic surgery. Three-month-old ALZ17 mice and non-transgenic C57BL/6 control mice were anaesthetized with a mixture of ketamine (10 mg kg^{-1}) and xylazine (20 mg kg^{-1}). When deeply anaesthetized, the mice were placed on a heating pad to maintain body temperature during surgery. Using a Hamilton syringe, the hippocampus (A/P, –2.5 mm from bregma; L, ±2.0 mm; D/V, –1.8 mm) and the overlying cerebral cortex (A/P, –2.5 mm from bregma; L, ±2.0 mm; D/V, –0.8 mm) each received a unilateral (right hemisphere) stereotaxic injection of 2.5 µl brain extract, at a speed of 1.25 µl min^{-1}. After injection, the needle was kept in place for an additional 3 min before gentle withdrawal. The surgical area was cleaned with sterile saline and the incision sutured. Mice were monitored until recovery from anaesthesia and checked weekly after surgery. For sham-lesioned wild-type mice ($n = 3$), the same procedure was applied without injection of brain extract.

Histology and immunohistochemistry. ALZ17 mice were anaesthetized with sodium pentobarbitone (100 mg kg^{-1}) and killed by transcardial perfusion with 20 ml cold PBS, followed by 20 ml 4% paraformaldehyde in PBS. The brains were dissected and post-fixed overnight. After paraffin embedding, 5-µm coronal sections were prepared. Sections were silver-impregnated using the method of Gallyas-Braak to visualize filamentous tau pathology[10,11]. Haematoxylin and eosin staining (H&E) was performed for morphological analysis. For immunohistochemistry, the following anti-tau antibodies were used: T14 (1:1,000, Zymed), AT8 (1:1,000), AT100 (1:1,000), BR189 (1:500), BR304 (1:500) and MT1 (1:500). T14 is specific for human tau[32]. MT1 was raised against amino acids 114–127 of the longest brain isoform of mouse tau. It is specific for mouse tau and does not recognize human tau[6]. BR189 and BR304 were raised against amino acids 76–87 and 45–73 of tau, respectively (in the numbering of the longest human brain tau isoform). They are specific for tau isoforms with one (BR304) or two (BR304 and BR189) N-terminal inserts[9]. Antibody Olig2 (1:500, Chemicon) was used to stain oligodendrocytes. Antibodies NF200 (1:100, DakoCytomation), Iba1 (1:100, Abcam), GFAP (1:100, Abcam) and MBP (1:500, Abcam) were used to visualize neurofilaments, astrocytes, microglia and myelin basic protein, respectively. Secondary antibodies were from Vector Laboratories (Vectastain ABC kit).

Immunoelectron microscopy. Immunoelectron microscopy of injected P301S brain extract using the anti-tau antibody BR134 was performed as described previously[33]. BR134 was raised against a synthetic peptide corresponding to amino acids 428–441 of tau[9]. In some experiments, sarkosyl-insoluble tau was prepared from injected ALZ17 brains, as described previously[34]. Anti-tau antibodies BR134, BR189, BR304 and AT100 were used to identify tau filaments.

Quantitative analysis of tau pathology. ALZ17 mice injected with P301S brain extract were analysed at 6, 12 and 15 months post-injection (five mice per time point). Gallyas-Braak-stained coronal sections were selected at identical brain coordinates[35] (anterior to the injection level, –0.8 mm from bregma; injection level, – 2.5 mm from bregma; posterior to the injection level, – 3.8 mm from bregma). Silver-positive structures (neurofibrillary tangles, neuropil threads and coiled bodies) were counted at these 3 levels with a ×20 objective (Zeiss). At the injection level (–2.5 mm from bregma), total counts of silver-positive structures were assessed in the hippocampal (CA1, CA2, CA3, dentate gyrus and subiculum) and visual cortex injection sites. In the visual cortex, silver-positive lesions developed just around and at a very short distance from the needle tract. For semi-quantitative assessment, Gallyas-Braak staining was graded as follows: (–), no silver-positive structures; (+), < 20 silver-positive structures; (++), 20–40 silver-positive structures; (+++), > 40 silver-positive structures. For each group there was only slight variation between individual animals.

Statistical analysis. Statistical analysis of quantitative tau pathology data was performed using the Poisson regression algorithm with the help of the SAS 8.02 software. Link function was the logarithm and scale was estimated by deviance (to account for overdispersion). Significance tests for differences between mice at 12 months and at 6 months following brain extract injection, and between mice at 15 months and at 12 months following injection were obtained. No multiplicity correction was applied. The results of the significance tests are reported in Fig. 2a, b as follows: $*P < 0.05$; $**P < 0.001$; $***P < 0.0001$.

29. Mercken, M. *et al.* Affinity purification of human tau proteins and the construction of a sensitive sandwich enzyme-linked immunosorbent assay for human tau detection. *J. Neurochem.* **58,** 548–553 (1992).
30. Goedert, M., Jakes, R. & Vanmechelen, E. Monoclonal antibody AT8 recognises tau protein phosphorylated at both serine 202 and threonine 205. *Neurosci. Lett.* **189,** 167–170 (1995).
31. Yoshida, H. & Goedert, M. Sequential phosphorylation of tau protein by cAMP-dependent protein kinase and SAPK4/p38δ or JNK2 in the presence of heparin generates the AT100 epitope. *J. Neurochem.* **99,** 154–164 (2006).
32. Kosik, K. S. *et al.* Epitopes that span the tau molecule are shared with paired helical filaments. *Neuron* **1,** 817–825 (1988).
33. Crowther, R. A. Straight and paired helical filaments in Alzheimer disease have a common structural unit. *Proc. Natl Acad. Sci. USA* **88,** 2288–2292 (1991).
34. Goedert, M., Spillantini, M. G., Cairns, N. J. & Crowther, R. A. Tau proteins of Alzheimer paired helical filaments: Abnormal phosphorylation of all six brain isoforms. *Neuron* **8,** 159–168 (1992).
35. Franklin, K. B. J. & Paxinos, G. The mouse brain in stereotaxic coordinates. (*Academic Press, New York*, 2001).

nature cell biology

DOI: 10.1038/ncb1901

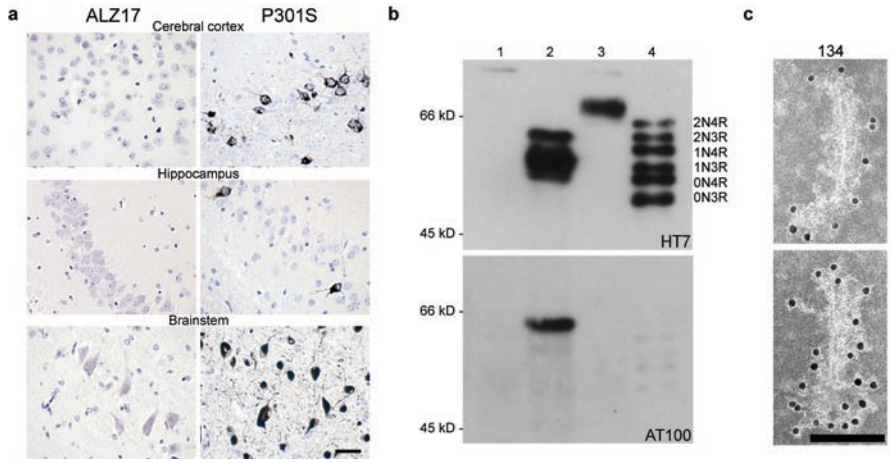

Figure S1 Transgenic mouse lines ALZ17, human P301S tau and characterization of mouse brain extracts. (**a**) Gallyas-Braak staining of cerebral cortex, hippocampus and brainstem of an 18 month-old ALZ17 mouse (left) and a 5 month-old mouse transgenic for human P301S tau (right). Note the absence of silver staining in the ALZ17 mouse and the strong staining in the P301S mouse. The sections were counterstained with haematoxylin. Scale bar, 50 µm (same magnification in all panels). (**b**) Immunoblotting of mouse brain extracts with anti-tau antibodies HT7 (specific for human tau, phosphorylation-independent) and AT100 (phosphorylation-dependent). Lanes: 1, brain extract (125 µg tissue) from non-transgenic control mouse; 2, brain extract used for injection (125 µg tissue) from a 5 month old mouse transgenic for human P301S tau; 3, forebrain extract (125 µg tissue) from 18 month-old ALZ17 mouse; 4, recombinant human tau isoform mixture (10 ng). (**c**) Immunoelectron microscopy using anti-tau serum BR134 to decorate filaments in the brain extract used for injection. Scale bar, 100 nm. The full scan of the Western blot data is available in the Supplementary Information, Fig. S7.

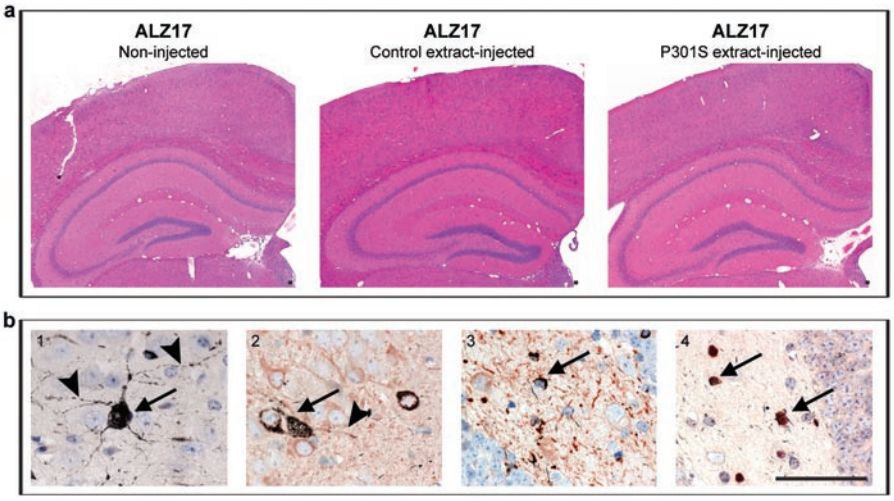

Figure S2 Injection sites and tau pathology. (**a**) H&E staining of corresponding hippocampal levels of non-injected ALZ17 animals (left), ALZ17 mouse injected with control brain extract (middle) and ALZ17 mouse injected with P301S tau brain extract (right). Scale bar, 50 µm (same magnification in all panels). (**b**) Different types of filamentous tau pathology in ALZ17 brains injected with P301S tau brain extract: (1) neurofibrillary tangle (arrow) and neuropil threads (arrowheads) visualized by silver staining; (2,3) double staining with silver and AT8 (red) shows neurofibrillary tangles (2, arrow), neuropil threads (2, arrowhead) and coiled bodies (3, arrow). (4) Double staining of coiled bodies (arrows) with silver and antibody Olig2 (red). The sections were counterstained with haematoxylin. Scale bar, 50 µm (same magnification in all panels).

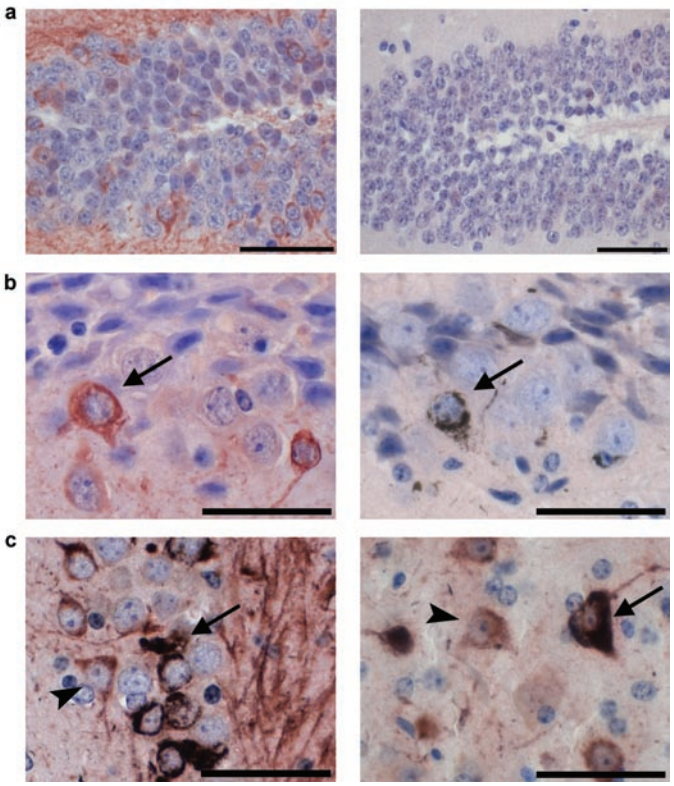

Figure S3 Inclusions in ALZ17 mice injected with P301S brain extract contain tau with N-terminal inserts. (**a**) BR189 staining (specific for tau isoforms with both N-terminal inserts) of the dentate gyrus of an 18-month-old ALZ17 mouse (left) and a 6-month-old homozygous P301S mouse (right). Note the absence of staining in the P301S mouse and the staining of pretangle pathology in the ALZ17 mouse. (**b**) BR304 staining (specific for tau isoforms with the first N-terminal insert; left) and Gallyas-Braak silver staining (right) of the CA3 region of the hippocampus of an ALZ17 mouse 15 months after injection with P301S brain extract. The images are of serial brain sections. The arrows point to a BR304-positive neuron which is also stained by the Gallyas-Braak method. (**c**) Double staining with BR304 and Gallyas-Braak (left) and with BR189 and Gallyas-Braak (right) of the hippocampus of an ALZ17 mouse 15 months after injection with P301S brain extract. Darker neurons (arrows) are double stained for Gallyas-Braak and BR304 (left) or Gallyas-Braak and BR189 (right), indicative of tangles. Single-stained neurons (arrowheads) with BR304 (left) or BR189 (right) represent pretangles. The sections were counterstained with haematoxylin. Scale bars, 50 μm.

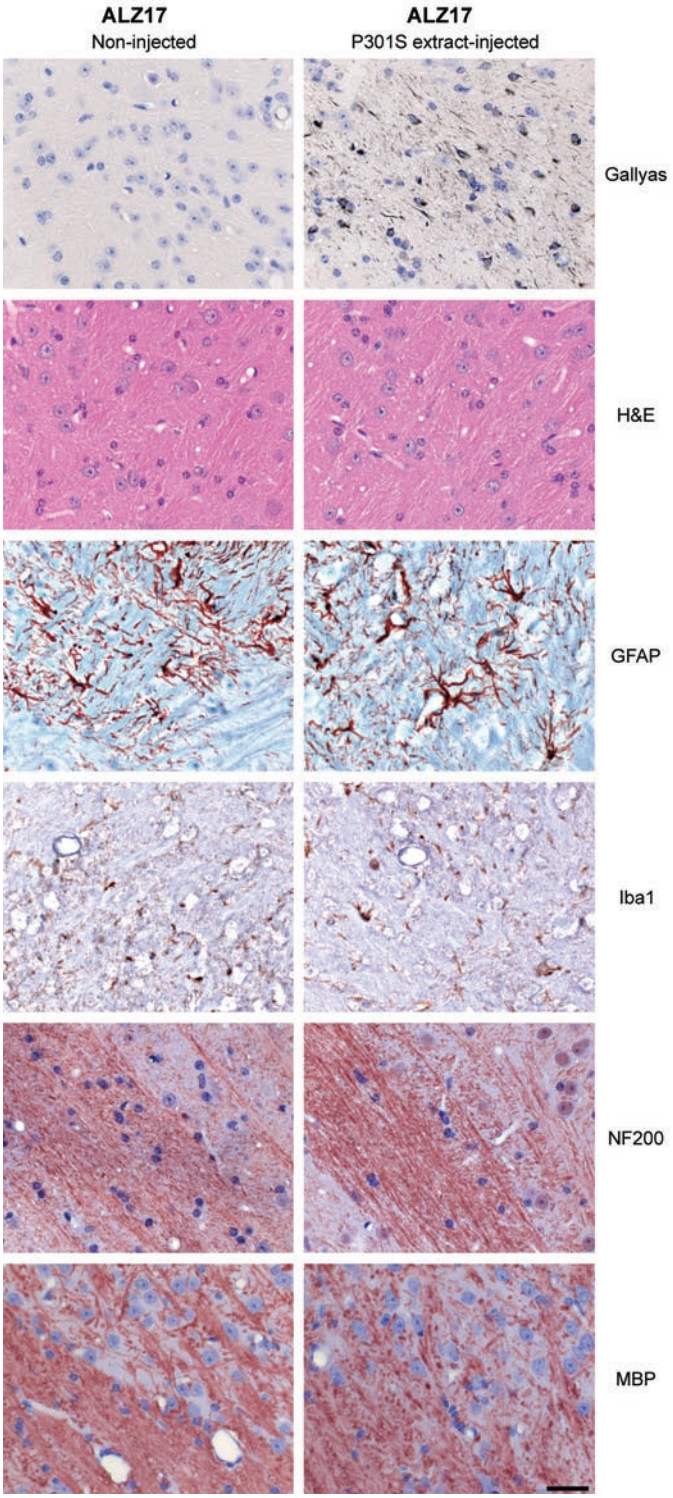

Figure S4 Comparison between non-injected (left) and P301S extract-injected (right) ALZ17 mice (15 months post-injection). High magnification of the thalamic region of ALZ17 animals in which Gallyas-Braak silver staining detects threads and coiled bodies (top). Various stains do not reveal overt neurodegeneration (H&E), astrogliosis (GFAP), microgliosis (Iba1), neurofilament alterations (NF200) or myelin changes (MBP) in ALZ17 mice injected with P301S brain extract. The sections were counterstained with haematoxylin. Scale bar, 50 μm (same magnification in all panels).

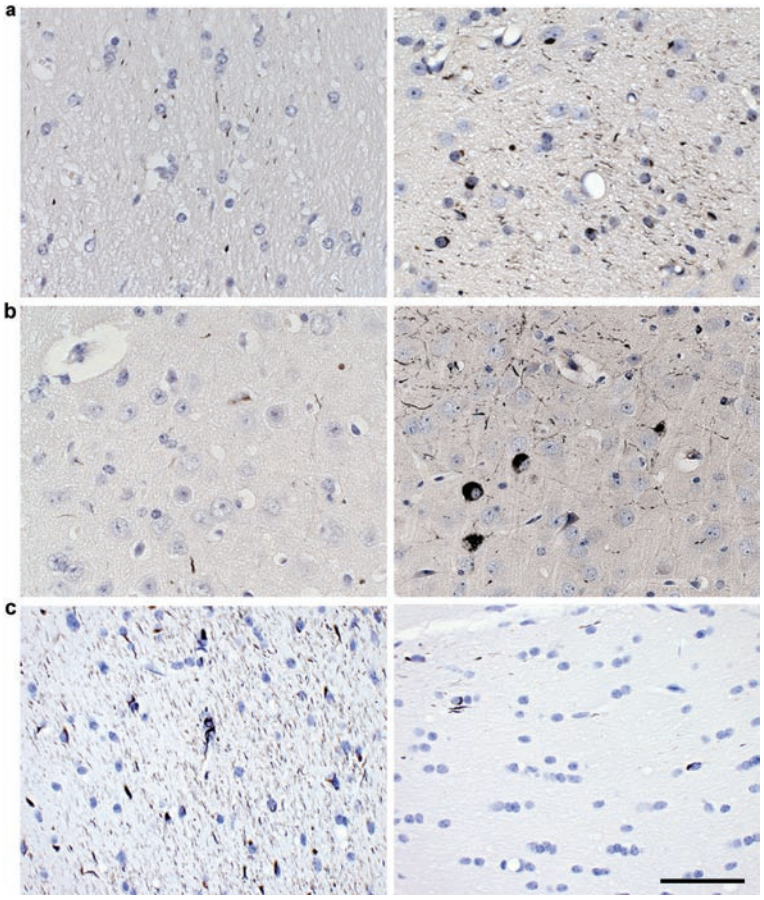

Figure S5 Spreading of filamentous tau pathology. (**a**) Anterior to the injection level (section 1.7 mm from injection level). Gallyas-Braak staining of the fimbria from ALZ17 mice 6 months (left) and 15 months (right) after the injection of brain extract from mice transgenic for human P301S tau. The sections were counterstained with haematoxylin. Scale bar, 50 μm (same magnification in all panels). (**b**) Posterior to the injection level (section 1.3 mm from injection level). Gallyas-Braak staining of the polymorphic layer of the hippocampus from ALZ17 mice 6 months (left) and 15 months (right) after the injection of brain extract from mice transgenic for human P301S tau. The sections were counterstained with haematoxylin. Scale bar, 50 μm (same magnification in all panels). (**c**) Modest contralateral spreading of filamentous tau pathology. Gallyas-Braak staining of the ipsilateral (left) and contralateral (right) fimbria of an ALZ17 mouse 15 months after the unilateral injection of brain extract from mice transgenic for human P301S tau (injection level). Note the few scattered silver-positive lesions on the contralateral side. The sections were counterstained with haematoxylin. Scale bar, 50 μm (same magnification in all panels).

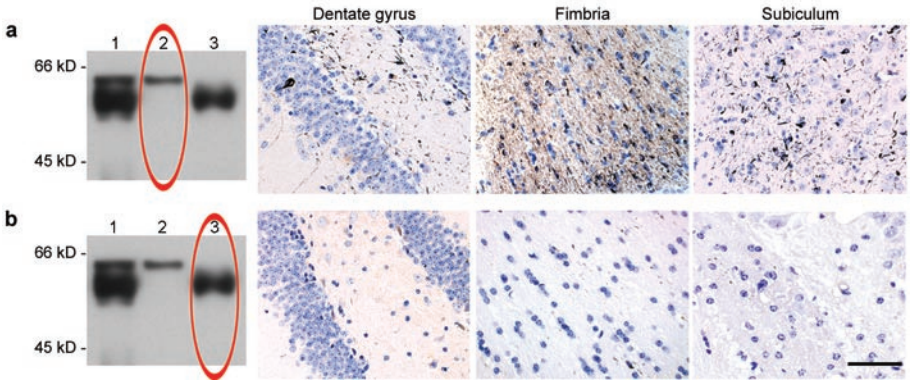

Figure S6 Injection of human P301S tau brain extract containing either insoluble or soluble tau into ALZ17 mice. (**a**) Major induction of filamentous tau pathology after injection of insoluble tau into ALZ17 mice. Left: Western blot using anti-tau antibody HT7 of total human P301S tau brain extract (lane 1), P301S brain extract containing insoluble tau (lane 2) and P301S brain extract containing soluble tau (lane 3). Right: Gallyas-Braak staining of dentate gyrus, fimbria and subiculum of an ALZ17 mouse 12 months after the injection of insoluble tau. (**b**) Minor induction of filamentous tau pathology after injection of soluble tau into ALZ17 mice. Left: Western blot with anti-tau antibody HT7 of total human P301S tau brain extract (lane 1), P301S brain extract containing insoluble tau (lane 2) and P301S brain extract containing soluble tau (lane 3). Right: Gallyas-Braak staining of dentate gyrus, fimbria and subiculum of an ALZ17 mouse 12 months after the injection of soluble tau. The sections were counterstained with haematoxylin. Scale bar, 50 μm (same magnification in all panels). The full scan of the Western blot data is available in the Supplementary Information, Fig. S7.

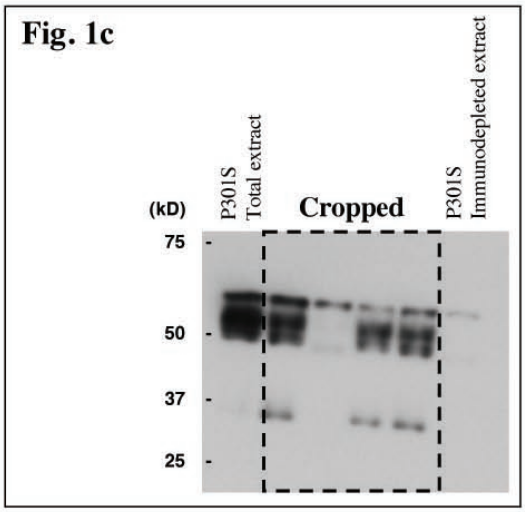

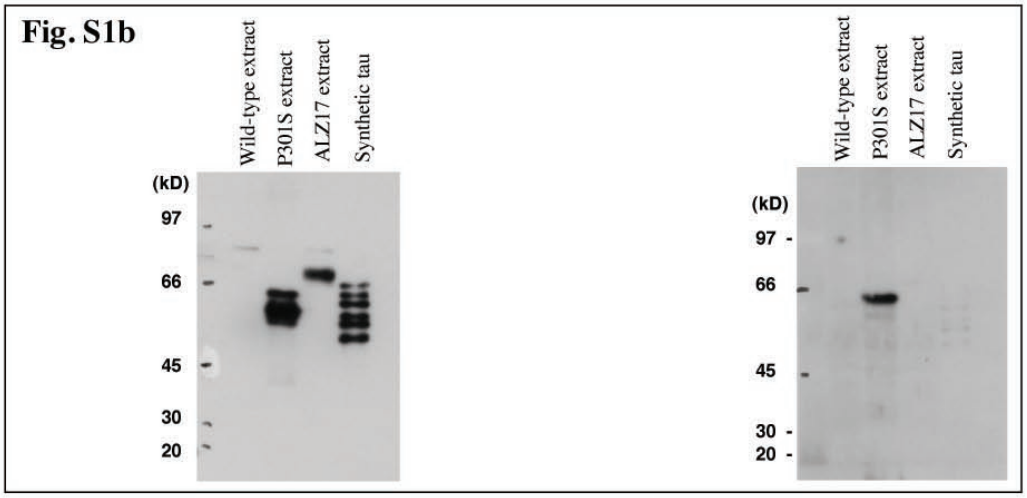

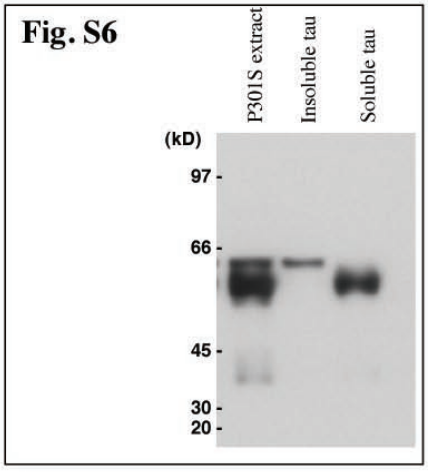

Figure S7 Full scans of the Western blot data shown in Figure 1, Figure S1 and Figure S6.

ERRATUM

p53 controls cancer cell invasion by inducing the MDM2-mediated degradation of Slug

Shu-Ping Wang, Wen-Lung Wang, Yih-Leong Chang, Chen-Tu Wu, Yu-Chih Chao, Shih-Han Kao, Ang Yuan, Chung-Wu Lin, Shuenn-Chen Yang, Wing-Kai Chan, Ker-Chau Li, Tse-Ming Hong and Pan-Chyr Yang

Received 29 October 2008; accepted 19 February 2009; published online 17 May 2009; corrected after print 19 May 2009

In the version of this article initially published, the Myc–Ub label in Figure 3c was incorret. Arrowheads were missing in fig. 5d and 5e. A plus (+) was misplaced from the curve in Fig. 7c. The correct versions of these figures are shown below. These errors have been corrected in the HTML and PDF versions of the article.

Figure 3

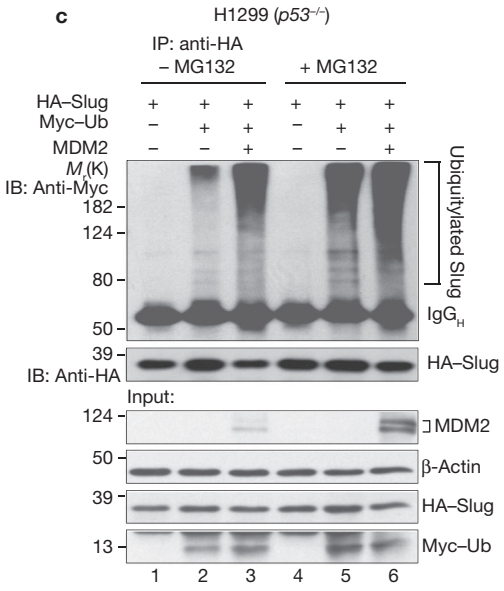

Figure 5

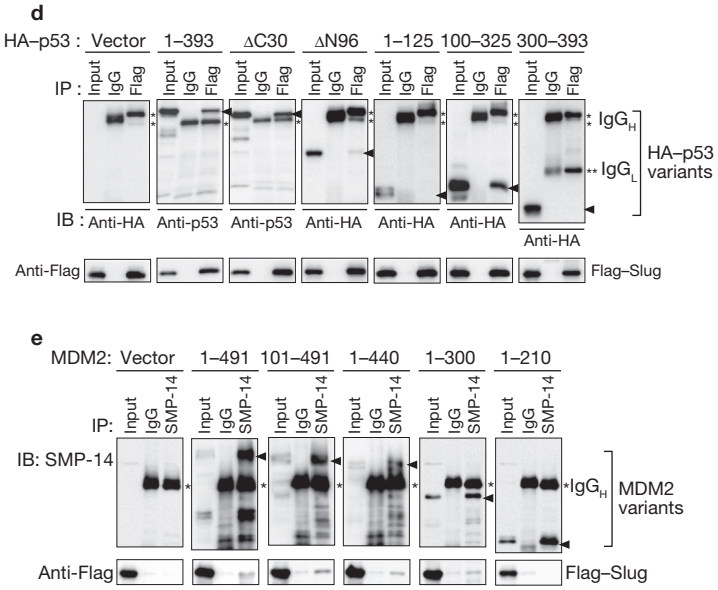

Figure 7